



Proceedings Book

1st Iberian Meeting on Aerosol Science and Technology

RICTA 2013

PROCEEDINGS BOOK



Edited by

Maria João Costa, Ana Maria Silva, Juan Luis Guerrero Rascado,
Sérgio Pereira, Daniele Bortoli and Rui Salgado

1st Iberian Meeting on Aerosol Science and Technology



1st Iberian Meeting on

Aerosol Science and Technology

ISBN: 978-989-20-3962-6

Centro de Geofísica de Évora
Universidade de Évora
Julho 2013

U. Évora 2013

July 1-3, 2013 , Colégio Luís António Verney
Universidade de Évora, Évora, Portugal



1st Iberian Meeting on Aerosol Science and Technology

Évora, Portugal, July 1-3, 2013

PROCEEDINGS BOOK

Edited by

Maria João Costa, Ana Maria Silva, Juan Luis Guerrero Rascado, Sérgio Pereira, Daniele Bortoli and Rui Salgado

Centro de Geofísica de Évora

Universidade de Évora, Évora, Julho 2013



Cover: panel of tiles in room 120, the *Physics Room* at Colégio do Espírito Santo, the main building of the University of Évora (opened in 1553). This panel evokes the celebrated episode of the mirrors of Archimedes, who used the sun rays to set fire to the Roman Armada, which was ready to conquer his city, Syracuse, in Sicily.

In *The Tiles of the University of Évora* by J. F. Mendeiros.

Title: 1st Iberian Meeting on Aerosol Science and Technology - Proceedings Book
Coordinator: Maria João Costa
Editors: Maria João Costa, Ana Maria Silva, Juan Luis Guerrero Rascado, Sérgio Pereira, Daniele Bortoli and Rui Salgado
July 2013
© University of Évora
R. Romão Ramalho, 59
7000-671 Évora
Portugal

<http://www.cge.uevora.pt>
<http://www.uevora.pt>

ISBN: 978-989-20-3962-6

Contents

Editorial Message	7
Committees	9
Acknowledgements	10
Sponsors	11
Communications	13
Noise as an indicator of traffic and ultrafine particles in Huelva city	15
<i>I.M. Brito Cabeza, R. Fernández-Camacho, J.D. de la Rosa</i>	
Carbonaceous aerosols emitted from food cooking	21
<i>C. Alves, M. Duarte, T. Nunes, R. Moreira, S. Rocha</i>	
Total and ultraviolet solar irradiance during a desert dust episode at Cáceres (Spain)	27
<i>M.A. Obregón, A. Serrano, G. Sánchez, M.L. Cancillo</i>	
Suitable altitude for detecting desert aerosol outbreaks in the Iberian Peninsula	33
<i>A. Serrano, M. Á. Obregón, M. L. Cancillo</i>	
Speciation of Metals in Refinery Emissions Particles	39
<i>Y. González-Castanedo, D. A. Sánchez-Rodas, C. Ferrer, J. D. de la Rosa</i>	
Particle Emission from the Aircraft Engine Testing Cycles	43
<i>J.J. Rodríguez-Maroto, V. Archilla, D. Sanz-Rivera, E. Rojas-García, M. Pujadas, J.L. Mosquera, D. Mercader, A. Gonzalez, A. Jimenez, A. Entero, J. Mena, J.M. Fernández-Mainez, J.C. Bezares</i>	
Optical Properties of Saharan Dust Aerosols, Sea Spray and Cloud Droplets from AMISOC-ARN 2012 airborne campaign	49
<i>J. Andrey, A. Quirantes, N. Soane-Vieira, F. J. Olmo, L. Alados-Arboledas, B. de la Morena, M. Gil-Ojeda</i>	
Long-term atmospheric fluxes of radionuclides at a coastal Mediterranean station	55
<i>C. Dueñas, M.C. Fernández, E. Gordo, E. Liger, S. Cañete, M. Pérez</i>	

Behaviour of ⁷Be in air at a sampling point on Southeastern Spain	61
<i>C. Dueñas, M.C. Fernández, E. Gordo, E. Liger, S. Cañete, M. Pérez</i>	
Particulate matter in the indoor and outdoor air of a gymnasium and a fronton	65
<i>C. Alves, A. Calvo, L. Marques, A. Castro, R. Fraile, T. Nunes</i>	
Organic speciation of PM_{2.5} from urban background sites in Oporto and Coimbra	71
<i>C. Alves, T. Nunes, A. Vicente, C. Gonçalves, M. Evtugina, T. Marques, C. Pio</i>	
Effect of gear selection on diesel exhaust particle number and size distributions in steady state	77
<i>A. Domínguez-Sáez, C. Martín, C. C. Barrios</i>	
Comparison between EEPS 3090 and WCPC 3788: differences and similarities in transient and stable measures	83
<i>C. C. Barrios, A. Domínguez-Sáez, C. Martín</i>	
Atmospheric Boundary Layer during AMISOC-ARN: Lidar-derived height as estimated by different methods	89
<i>D. Toledo, C. Córdoba-Jabonero, J.A. Adame, M. Sorribas, D. Grau, J. Andrey, B. de la Morena, M. Gil-Ojeda</i>	
Levels of BTEX in an urban environment: The city of a Coruña	93
<i>G. Blanco-Heras, M.P.Gómez-Carracedo, V. Juncal-Bello, M. Ríos, M. Piñeiro-Iglesias, P. López-Mahía, S. Muniategui, D. Prada</i>	
Measurements of number size distributions of submicron aerosols during summer 2012 at the western part of Spain	97
<i>S. Iglesias-Samitier, V. Juncal-Bello, M. Piñeiro-Iglesias, P. López-Mahía, S. Muniategui, D. Prada</i>	
Impact on air quality operations cleaning and inspection of natural gas pipelines in Central Mexico	101
<i>L.M. Rodriguez, A.M. Sánchez de la Campa, J.D. de la Rosa</i>	
Validation of atmospheric aerosols sampling in equivalent fractions	105
<i>C. M. Oliveira, M. F. Camões, P. Bigus, A. A. Fachado, R. Silva</i>	

AMISOC 2012: Comparison of Aerosol Size Distribution with Airborne and Ground Based Instrumentation	109
<i>N. Seoane-Vieira, J. Andrey, M. Sorribas, A. Corrales-Sierra, R. González-Armengod, M. Gil-Ojeda, B. de la Morena, B. Marqués</i>	
Aerosol optical properties at “El Montsec”, a continental background site in the northeastern Spain	113
<i>Y. Sola, J. Lorente</i>	
The relations between AOD and PM_x from long-term data for north-central Spain	119
<i>Y. S. Bennouna, V. E. Cachorro, M. A. Burgos, C. Toledano, A. Herguedas, J. González Orcajo, A. M. de Frutos</i>	
Spanish activities in the framework of the ChArMEx project since 2009: a summary	125
<i>M. Sicard, J. Pey, J. C. Cerro, D. Lange, S. Caballero, A. Tovar-Sanchez, R. Morales-Baquero, A. Comerón, C. Bujosa, X. Querol, B. Artíñano, L. Alados-Arboledas, S. Basart, A. Alastuey, J. M. Baldasano, F. Rocadenbosch, A. Muñoz, C. Muñoz, D. García-Vízcaíno, A. Rodríguez, J. Bach, X. Bush</i>	
Formaldehyde levels at a common pre-school playroom	131
<i>M. Oliveira, K. Slezakova, C. Delerue-Matos, M.C. Pereira, S. Morais</i>	
Pointing error and field of view of AERONET Cimel-318 Sun photometers	135
<i>B. Torres, C. Toledano, A.J. Berjón, D. Fuertes, V. Molina, R. González, M. Canini, V.E. Cachorro, P. Goloub, T. Podvin, L. Blarel, O. Dubovik, Y. Bennouna, A.M. de Frutos</i>	
A comparison between almucantar and principal plane retrieval products within AERONET network	141
<i>B. Torres, C. Toledano, O. Dubovik, V. Cachorro, A.J. Berjón, T. Lapyonak, P. Goloub</i>	
Study of aerosol hygroscopic growth inside a well-mixed boundary layer by means of multi-wavelength Raman lidar	147
<i>F. Molero, A.J. Fernández, F. J. Gómez-Moreno, E. Alonso, M. Becerril, M. Pujadas, B. Artíñano</i>	
Relation between solar UVB and UV erythemal radiation at the surface	153
<i>V. Salgueiro, M. J. Costa, A. M. Silva, D. Bortoli</i>	

NanoScan SMPS - Key Characteristics of an Innovative, Portable Instrument for Sizing and Counting of Nanoparticles	157
<i>T. Tritscher, S. Elzey, M. Beeston, E. Filimundi, A. F. Zerrath, T. J. Krinke, O. F. Bischof</i>	
Germination Rate of Three Anemophilous Pollen Types After In Vitro Exposure to Gaseous Atmospheric Pollutants	163
<i>L. Duque, H. Ribeiro, C. R. Gomes, J. C. G. Esteves da Silva, I. Abreu</i>	
Long range transport of European fine particulate nitrate in the Central Iberian Peninsula	167
<i>M. A. Revuelta, L. Núñez, F. J. Gómez-Moreno, M. Pujadas, B. Artíñano</i>	
The REDMAAS 2012 SMPS+UFP intercomparison campaign	173
<i>F. J. Gómez-Moreno, E. Alonso, B. Artíñano, V. Juncal Bello, M. Piñeiro Iglesias, P. López Mahía, N. Pérez, J. Pey, A. Alastuey, B. A. de la Morena, M. I. García, S. Rodríguez, M. Sorribas, G. Titos, H. Lyamani, L. Alados-Arboledas</i>	
Inventario del Aerosol Desértico en la Región de Castilla y León (2003 - 2012)	177
<i>V.E. Cachorro, M.A. Burgos, Y. Bennouna, C. Toledano, B. Torres, A. Herguedas, J. González Orcajo, A.M. de Frutos</i>	
Variability of the levels of Particulate Matter in the Madrid Metropolitan Area, during the 1999-2012 period	183
<i>P. Salvador, B. Artíñano, F. Molero, M. Viana, A. Alastuey, X. Querol</i>	
Physical, Chemical and Optical Properties of Aerosol at Ny Ålesund, Svalbard: a Closure Study	189
<i>C. Lanconelli, M. Busetto, M. Mazzola, A. Lupi, S. Becagli, D. Frosini, A. Virkkula, V. Vitale</i>	
Raman lidar observations of Iberian forest fires smoke layers over Portugal	193
<i>S. Pereira, J. Preißler¹, J. L. Guerrero-Rascado, F. Wagner, A. M. Silva</i>	
Influence of atmospheric aerosol characterization on satellite remote sensing of water quality parameters	199
<i>M. Potes, M. J. Costa, R. Salgado</i>	
Sensitivity study of longwave radiative forcing to dust particle properties	205
<i>S. Bertolín, M. Sicard, M. Mallet, P. Dubuisson, A. Comerón</i>	

Editorial Message

This Proceedings Book contains the conference communications (oral and poster) received before the editing deadline and presented at the 1st Iberian Meeting on Aerosol Science and Technology (RICTA 2013), which was held from 1-3 July 2013, in Évora, Portugal.

The event was simultaneously the VI Reunión Española de Ciencia y Tecnología de Aerosoles and the IV Summer School on Aerosol Science and Technology, in 2013 organized and hosted by the Geophysics Centre of the University of Évora (CGE) with the collaboration of the Asociación Española de Ciencia y Tecnología de los Aerosoles (AECTA).

The Meeting, for the first time a Portuguese-Spanish Reunion on Aerosol Science, gathered over 90 participants covering a wide range of aerosol science and technology. As in previous editions of RECTA, the participation of young researchers was especially welcome, with the organization of the 4th Summer School on Aerosol Science and Technology and awards for the best poster and PhD thesis.

The editors would like to express their sincere gratitude to all the participants, in particular, those who contributed to this book by submitting their papers to convey the science discussed at RICTA 2013. Finally, we also thank the referees for their valuable revision of these papers.

Maria João Costa, Ana Maria Silva, Juan Luis Guerrero Rascado, Sérgio Pereira, Daniele Bortoli and Rui Salgado

July 2013



Scientific Committee

Chairs:

José Luis Castillo Gimeno (UNED)
Ana Maria Almeida e Silva (CGE, U.Évora)

Cristina Gutiérrez-Cañas Mateo (U. P.Vasco)
Lucas Alados-Arboledas (CEAMA, U.Gran)
Adolfo Comerón (U. Polit. de Catalunya)
António Heitor Reis (CGE, U. Évora)
António Miguel (CGE, U. Évora)
Antonio Serrano Pérez (U. Extremadura)
Begoña Artíñano (CIEMAT)
Casimiro Pio (CESAM, U. Aveiro)
Filomena Camões (F. Ciências, U. Lisboa)
Francisco J. Olmo Reyes (CEAMA, U. Gra)
Ignacio González Loscertales (U. Málaga)
José A. Martínez Lozano (U. Valencia)
José María Baldasano (BSC-CNS)
Juan Fernández de la Mora (Yale Univ.)
Juan Luis Guerrero Rascado (CEAMA,U.
Granada and CGE, U. Évora)
Maria João Costa (CGE, U. Évora)
Mário Reis (ITN)
Pedro L. García Ybarra (UNED)
Rui Namorado Rosa (CGE, Univ. Évora)
Victoria Cachorro (Univ. Valladolid)
Xavier Querol (IDAEA-CSIC, Barcelona)

Evaluation Comittee - Poster Prize

Francisco Molero (CIEMAT)
Manuel Antón (U. Extremadura)
Maria João Costa (U. Évora)
Rui Brandão (U. Évora)
Rui Salgado (U. Évora)

Organizing Committee

Chair:

Maria João Costa

Co-Chair:

Ana Maria Almeida e Silva

Ana Filipa Domingues
Daniele Bortoli
Dina Santos
Flavio Couto
José Pombinho
Juan Luis Guerrero-Rascado
Marta Melgão
Miguel Potes
Nuno Croino
Rui Salgado
Sérgio Pereira
Vanda Salgueiro

Evaluation Comittee - PhD Prize

José Luis Castillo Gimeno (UNED)
Ana Maria Almeida e Silva (CGE, U.Évora)
Cristina Gutiérrez-Cañas Mateo (U. P. Vasco)
Lucas Alados-Arboledas (CEAMA, U. Grana)
Antonio Serrano Pérez (U. Extremadura)
Filomena Camões (Fac. Ciências, U. Lisboa)
José María Baldasano (BSC-CNS)
Michaël Sicard (U. Polit. de Catalunya)
Victoria Cachorro (U. Valladolid)

Acknowledgements

First of all a special thank you to the Asociación Española de Ciencia y Tecnología de los Aerosoles (AECTA) and in particular to its President, Prof. José L. Castillo Gimeno, who challenged the Évora Geophysics Centre to organize for the first time a joint Portuguese-Spanish Meeting on Aerosol Science.

The organizers want to express their grateful appreciation to all valued participants that attended RICTA 2013, sharing their ideas and expertise. A special thanks also to the Scientific and Evaluation Committees, Lecturers of the Summer School, Invited Speakers and Session Moderators for their effort and contribution to the success of this Meeting.

The Organizing Committee gratefully acknowledges all sponsors and exhibitors for their generous support.

The meeting was also financially supported by Fundação para a Ciência e a Tecnologia (FCT) through FACC program (FCT/6511/12/6/2013/S). In addition, it was financed through FEDER (Programa Operacional Factores de Competitividade - COMPETE) and National funding through FCT in the framework of projects FCOMP-01-0124-FEDER-009303 (PTDC / CTE-ATM / 102142 / 2008), FCOMP-01-0124-FEDER-014024 (PTDC/AAC-CLI/114031/2009) and FCOMP-01-0124-FEDER-029212 (PTDC/GEO-MET/4222/2012).

The organizers also acknowledge the funding provided by the Évora Geophysics Centre, Portugal, under the contract with FCT, PEst-OE/CTE/UI0078/2011.

We are also deeply grateful to the University of Évora for the facilities and support, as well as to a number of people in different services of the University that helped in many ways to make this meeting possible.

Sponsors



Communications

Noise as an indicator of traffic and ultrafine particles in Huelva city

I.M. Brito Cabeza¹, R. Fernández-Camacho¹, J.D. de la Rosa¹

Abstract — Traffic emissions and noise levels are linked to adverse health effects. Vehicle exhaust emissions are the major source of ultrafine particles (UFP) in urban cities. Correlations between ultrafine particles, road traffic emissions and noise levels were studied in an urban city in the Southwest of Spain during winter 2009. The temporal variability of noise was found to be with traffic intensity during every time of the day and with PN1, BC and NO_x concentrations during the rush hours, due to the greater impact of the wind speed on air pollution concentrations at midday.

An estimating of UFP concentrations from noise levels is proposed in the study. The high linearity observed between PN1 and LAeq with the road traffic intensity can be used to estimate the traffic related particle number concentration (PN1) experimentally. Per each 100 vehicles in circulation, 1 dB is increased. It is equivalent to 1500 ultrafine particles per vehicle. This methodology allows low cost sensors to be used as proxy in an urban air quality network for ultrafine particles monitoring. In this way, air quality managers can decrease the ultrafine particles concentrations from vehicles exhaust emissions by limiting the number of vehicles passing a given point. Since studied parameters (UFP and noise) have strong influence on health, this methodology has proved to be of great interest in improving the air quality.

Keywords — noise, ultrafine particles, black carbon, road traffic emissions

1 INTRODUCTION

Road traffic is a dominant source of noise and air pollution in many cities [1], [2]. Several researches have shown associations between exposure to road traffic and adverse health effects. These associations are attributed to traffic-generated air pollution and road noise [3], [4].

Despite the adverse health effects caused by both air pollution and noise sources, a few studies have focused on studying the relationship between the associations of these pollutants. Most of them have investigated the correlation between traffic-related noise and air pollution focusing on gaseous pollutants, PM₁₀ [5], [6], PM_{2.5} and hydrocarbons [2]. Very few studies have evaluated the correlation between noise and ultrafine particles (UFP) [7], [8], [9], [10].

Many researchers express the need to continue measuring both pollutants together, noise and air pollution [2]. The spatio-temporal covariation between particles and noise is believed to be more evident for ultrafine particles (< 100 nm) compared to PM₁₀ or PM_{2.5} [11]. UFP is the metric associated with one of most important epidemiological parameters [12], [13]. Vehicle exhaust emissions are de major source of ultrafine particles in European cities. However, the maintenance of ultrafine particles counters in an air quality network result very expensive [10].

The goal of this work is to obtain a methodology that allows predicting airborne pollutant concentration levels by using noise level meter and avoiding, therefore, expensive measurement methods. The accuracy of these low cost sensors has been tested by recent researches [14]. Specifically, we aimed to: 1) evaluate space-temporal variations among noise, ultrafine particles, black carbon, gaseous pollutants, meteorological parameters and road traffic intensity (number of vehicles per hour); 2) determine the relationship between noise and ultrafine particles; 3) obtain a methodology that allows to determinate the ultrafine particle concentrations according to the road traffic intensity.

2 METHODOLOGY

2.1 Study area

The city of Huelva (Fig. 1A), with around 148.918 inhabitants, is located in SW Spain (Huelva: 37°15'0"N, 6°57'0"W, 54 m.a.s.l.).

The city is surrounded by a ring road that allows road-traffic to connect the city with motorways. The average daily traffic in the two sections of the motorway is between 21000 and 25000 vehicles 24h⁻¹. University Campus monitoring station is situated on the northeast side of the core-center of the city (Fig. 1A). Andalusia and Fuerzas Armadas Avenues are the closest roads, located at 500 m to the north and 1000 m to the south of the measurement site, respectively (Fig. 1B). The weekly mobility in the study area is distributed as following: 44.9% private vehicles, 1.36% public transport and 51.9% pedestrians. Andalusia Avenue (Fig. 1C) has 3-by-3

¹. Associate Unit CSIC-University of Huelva "Atmospheric Pollution", Center for Research in Sustainable Chemistry CIQSO, University of Huelva, 21071, Huelva, Spain.

lane road with central green areas and free time sites and with two additional lanes reserved to car parking. It has a total width around 80 meters.

The second largest Cu-smelter plant in Europe, a fertilizer and phosphoric production plants, and oil refinery and petrochemical plant are located in this industrial city (Fig 1A). The proximity of the industry and the predominance of the sea-land breeze during daylight facilitate the entry of the industrial plumes in the city [15], [16].

Two sources contribute significantly to the particle number PN: road traffic and industrial emissions, accounting for 50% and 44%, respectively [17].



Fig. 1. A) Map of Huelva which details, in addition to the University Campus location, a wind rose for winter 2009 and the two main Industrial Estates: Punta del Sebo and Nuevo Puerto. B) Main roads around University Campus. C) University Campus where monitoring station and sound level meter location are highlighted.

2.2 Experimental data

Road traffic intensity data (number of vehicles per hour) were recorded in the Andalusia Avenue (Fig. 1C). Noise levels were registered in University Campus, at 80 m. to the main road (Fig. 1C). Both, traffic counts and noise levels are managed by the Council of Huelva. Gaseous pollutants (NO_x , O_3 and SO_2), PM_{10} , $\text{PM}_{2.5}$, ultrafine particles and black carbon concentrations were recorded in University Campus, an urban monitoring station belonging to the Air Quality Network of Andalusia Government located at 200 m. from the road approximately. Meteorological parameters (wind speed and wind direction, temperature, relative humidity, precipitation and solar radiation) were recorded in the Huelva North station less than 2 km away managed by The Spanish Meteorological Agency (AEMET). All the measurements were simultaneously performed from January 1st, 2009 to March 31st, 2009 (winter season).

Gaseous pollutants, meteorological parameters and road traffic intensity data had an availability of 100%. Data availability was 70% for particle

number (PN), 75% for noise levels, 94% for black carbon (BC), 94% for PM_{10} and 76% for $\text{PM}_{2.5}$.

PN was monitored using an ultrafine counter particle condensation (UCPC, 3776 model, TSITM). The instrument recorded data at 1-min time resolution and detects particles coarser than 2.5 nanometers (nm) operating in high flow ($1.5 \text{ l} \cdot \text{m}^{-1}$) in order to avoid diffusion losses (see details in [16]). PN is considered representative of ultrafine particle number concentration because of between 80-90% of particles in urban air are $< 100 \text{ nm}$ [18]. BC concentration was monitored by using a ThermoTM Caruso model 5012 Multi-Angle Absorption Photometer (MAAP). BC concentrations were calculated from a mass-specific attenuation cross-section equal to $10.31 \text{ m}^2 \cdot \text{g}^{-1}$ [16]. Both instruments were calibrated for airflow on a weekly basis using a GilibratorTM bubble-flow meter.

Gaseous pollutants concentrations (NO_x , O_3 and SO_2) were monitored with 1-h resolution by using the reference methods of the European air quality directive [19].

Noise levels were measured by the noise level meter IS000814 (SDR 500, EcuDap) placed on a billboard approximately 4 m above ground level (Fig. 1B) [20]. 1-min equivalent continuous sound pressure levels (LA_{eq}) were logged, reported in units of A-weighted decibels dB (A). The noise meter was calibrated monthly without presenting deviations that may indicate errors. This noise meter belongs to UrbaNoise Red.

Hourly levels of PM_{10} and $\text{PM}_{2.5}$ were monitored using a beta attenuation monitor and a GRIMMTM 1107 optical particle counter, respectively. Their concentrations were converted to the gravimetric equivalent by comparing with the EU (gravimetric) reference method following the EU standardized procedure [21].

2.3 Components of ultrafine particles

In order to distinguish the road traffic and industrial emissions sources in the study area, particle number concentration was split into two components following the methodology of [22]:

$$\begin{aligned} \text{PN1} &= \text{S1} \cdot \text{BC} & (1) \\ \text{PN2} &= \text{PN} - \text{PN1} & (2) \end{aligned}$$

$\text{S1} = 6.0 \cdot 10^6 \text{ particles} \cdot \text{ng}^{-1} \text{ BC}$, being the minimum slope observed in the PN vs BC plot in our measurement site. It represents the minimum number of particles formed/emitted per nanogram of BC emitted by vehicle exhausts (see details in [16], [23]). PN1 is representative of the components directly emitted in particle phase (light-absorbing elemental carbon, carbonaceous material, trace metals, etc) and components nucleating immediately after the vehicle exhaust emission (eg. sulphates, condensed hydrocarbons and unburned oil). PN2 accounts for the particles formed from enhancement

in new particle formation processes during the dilution and cooling of vehicle exhaust emissions or in ambient due to photochemistry processes and/or in gas-to-particle conversion processes in precursor plumes.

3 RESULTS AND DISCUSSION

3.1 Noise levels, traffic and ambient air quality parameters

Table 1 shows the mean, maximum and minimum and standard deviation hourly levels for each measured variable during the sampling period. The ambient temperature averaged 12 °C, with a maximum during the daylight of 27°C and a minimum temperature at night of -2°C. The predominant wind direction was from 1st and 4th quadrant, principally (Fig. 1A). The mean value for relative humidity was around 79%. Accumulated precipitation of 123 mm · h⁻¹ was recorded in the study. Wind speeds were also low, with a mean value of 0.3 m · s⁻¹. The mean PM₁₀ concentration was 33 µg · m⁻³, with a maximum and minimum value of 179 and 20 µg · m⁻³, respectively. 16 µg · m⁻³ of PM_{2.5} was observed.

The road traffic intensity showed an average of 754 vehicles per hour, reaching a maximum value of 3772 vehicles / hour. Particle number concentrations were on average 29000 cm⁻³, while noise levels reached a mean value of 57 db.

Table 1. Mean, maximum and minimum and standard deviation of hourly levels for particle number (PN), BC, gaseous pollutants (O₃, NO_x and SO₂), meteorological parameters (wind speed and wind direction, temperature, relative humidity and precipitation), PM₁₀ concentrations, road traffic intensity and noise levels during winter 2009 in Huelva city

	Winter 2009			
	Mean	SD	Max.	Min.
PN (cm ⁻³)	28979	37711	612600	925
BC (ng · m ⁻³)	1041	1011	8390	47
NO _x (µg · m ⁻³)	33	30	292	5
O ₃ (µg · m ⁻³)	56	24	125	7
SO ₂ (µg · m ⁻³)	14	8	136	4
WS (m · s ⁻¹)	0.3	0.2	1.5	0
T (°C)	12	5	27	-2
RH (%)	79	20	100	25
Precipitation (mm · h ⁻¹)	123*			
PM ₁₀ (µg · m ⁻³)	33	20	179	1
PM _{2.5} (µg · m ⁻³)	16	8	93	5
Vehicles · h ⁻¹	754	536	3772	7
LAeq (dB)	57	6	88	41

*Accumulated precipitation

3.2 Temporal patterns of noise levels, traffic and air pollution parameters

Fig. 2 shows the hourly average values for particle number PN, PN1, PN2 and black carbon BC

concentrations, gaseous pollutants (NO_x and SO₂), the road traffic intensity, wind speed and noise levels for each day of the week. The sharp increase in BC and NO_x concentrations during the morning and evening rush hours on working days pointed to the relation of these pollutants with the vehicle exhaust emissions. PN shows a high correlation with these parameters explaining its common origin (Fig 2A). During the morning rush hours, PN reached an average concentration of 38700 cm⁻³, accounting PN1 for 34% of PN. This characteristic peak during the morning rush hours has been reported from a number of streets canyon and kerbside [7]. However, at midday, a high peak of PN is recorded. When PN is segregated in PN1 and PN2 following the methodology of [21], PN1 is related with primary particles due to vehicle exhaust emissions, and therefore with BC and NO_x (Fig 2B) and new particles formation by nucleation processes not related with vehicle exhaust emissions is included in PN2. The high correlation between PN2, reaching an average concentration of 40600 cm⁻³ and accounting for 78% of PN, SO₂, solar radiation and wind speed after the morning rush hours (Fig 2D) is due to the new particle formation in the SO₂ industrial plumes that reach the monitoring site when the sea breeze is blowing inland [16].

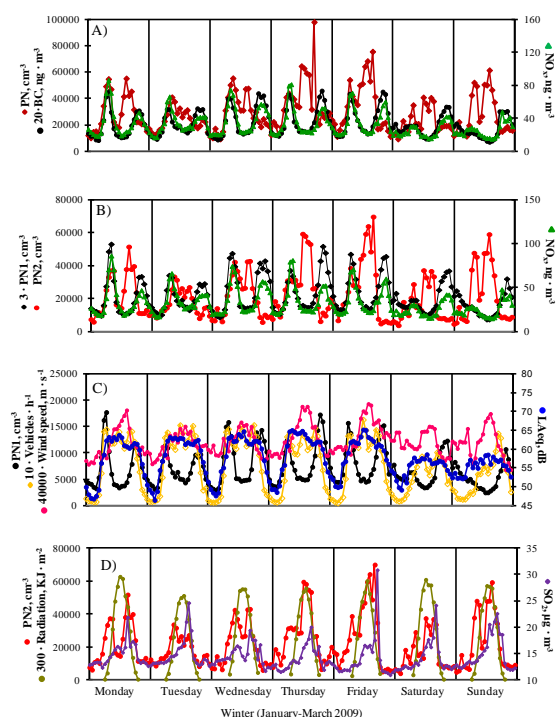


Fig. 2. Hourly average values of particles (PN, PN1, PN2 and BC) and NO_x gas pollutant, and road-traffic intensity (number of vehicles per hour), wind speed and noise levels (LAeq), and radiation and SO₂ gas pollutant, for every day of the week.

The high correlation between noise levels LAeq with road traffic intensity and PN1 during rush hours suggests the noise is linked to vehicle exhausts

emissions as main source of pollution in urban areas [10]. Noise levels increase in the morning strongly at around 8:00 h GMT and decrease precipitously after 20:00 h GMT (Fig. 2C), ranged between 58 and 61 dB. The significantly coupled in the spatial distribution between noise levels and road traffic intensity is due to the little influence of meteorological conditions on these pollutants [8], [10], [11]. However, wind speed has a significant impact on ultrafine particles (Fig.2.C) [24]. Note that during the colder months, the daily PN1 and BC concentrations are strongly influenced by diurnal sea breeze undergoing a decrease after the morning rush hours (Fig.2B) [16].

The decrease from working days to weekdays of traffic related pollutants (including noise) is evident in Fig. 2A, 2B, 2C.

3.3 Correlation between noise and ultrafine particles

Few works have studied the correlation between noise levels and ultrafine particles in urban air due to vehicle exhaust emissions [7], [10]. We have analyzed the relationship between noise levels and ultrafine particles related to vehicle exhaust emissions (PN1) by simple correlation analysis during the winter 2009. Fig. 3 shows PN1 versus LAeq scatter plot for every hour of the day. It can be observed the high linearity between both parameters.

$$y = 720.32x - 31367 \quad (3)$$

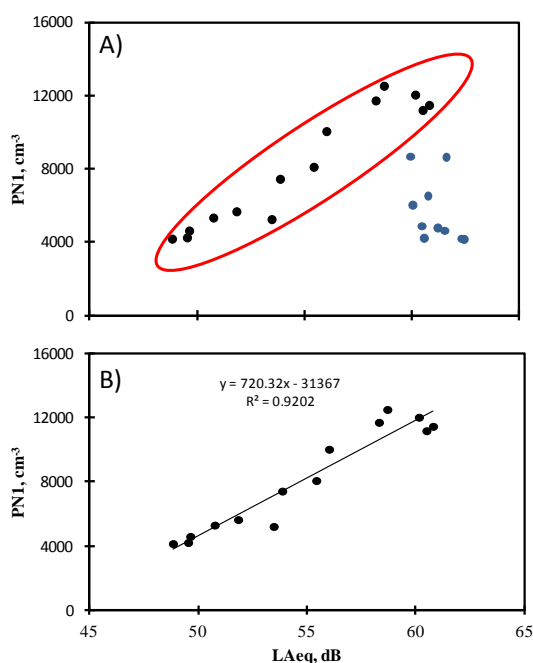


Fig. 3. A) Hourly average concentrations of PN1 particles versus noise levels LAeq for every hour of the day during the winter of 2009. Points off the slope are in blue colour. B) PN1/LAeq slope without blue dots.

The PN1/LAeq slope (Fig. 3B) showed a value of 720 particles / dB with a R^2 correlation coefficient of 0.92. This value confirms the role of the traffic noise as the main noise source on the variation of PN1 in the study area.

Points observed out the slope (Fig. 3A) are attributed to the local road traffic intensity during the central hours of the day. At this time, while meteorological conditions have only a very small influence on noise levels, particle number concentrations are strongly modulated by the enhancement in the dilution conditions and air mass renewal by breeze regime (Fig. 2C).

3.4 Noise as traffic indicator

In order to quantify the relationship between PN1 concentrations and LAeq noise levels with the road traffic intensity, PN1 and LAeq levels were averaged in ranges of 100 vehicles during the winter season. For the analysis, the data corresponding to sunshine hours (between 9:00 h and 18:00 h GMT) have been removed. The data were grouping between 19:00 and 8:00 h GMT period time in order to decrease the strongly impact of wind speed on PN1 concentrations at midday and give more importance to noise levels correlated to vehicles exhaust emissions.

From noise data and according to equation 3 (PN1 vs LAeq in winter season), PN1 concentrations can be determined experimentally. The overall correlations between estimated and measured PN1 concentrations are shown in Fig. 4. Increases in noise levels by 1 dB per 100 vehicles are estimated, which is equivalent to 1500 particles per vehicle.

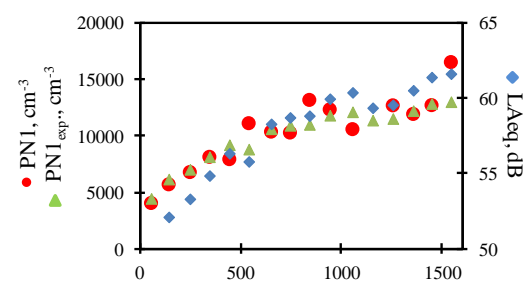


Fig. 4. Particle number concentrations PN1, PN1 exp. and LAeq versus vehicles / hour ratio during the winter season. Traffic intensity data are average in 100 vehicles ranges.

This interesting result points to low-cost noise sensors may be used to predict the ultrafine particles concentrations [14].

3 CONCLUSIONS

Correlations between ultrafine particles, road traffic emissions and noise levels were studied in an urban

city in the Southwest of Spain during winter 2009, where a motorway with a traffic intensity of about 23000 vehicles per day was located. The temporal variability of noise was found to be with traffic intensity during every time of the day and with PN1, BC and NO_x concentrations during the rush hours, due to the greater impact of the wind speed on air pollution concentrations at midday.

In this work, an estimating of UFP concentrations from noise levels is proposed. The high linearity observed between PN1 and LAeq with the road traffic intensity can be used to estimate the traffic related particle number concentration (PN1) experimentally. Per each 100 vehicles in circulation, 1 dB is increased. It is equivalent to 1500 ultrafine particles per vehicle. Estimated ultrafine particles concentrations were improved by grouping data with no sea breeze conditions. The obtained methodology allows low cost sensors to be used as proxy in an urban air quality network for ultrafine particles monitoring.

This methodology can be taking into account for air quality management in order to predict the impact of the pollutant on air quality and provide data for implementation of traffic control plans in the large cities and for future UFP regulations.

ACKNOWLEDGMENT

This work was supported by the P11-RNM-7800 research project, Department of Environmental, Rural and Marine of the Andalusian Autonomous Government, the Eygema Company and the Council of Huelva.

REFERENCES

- [1] Foraster, M., Deltell, A., Basagaña, X., Medina-Ramón, M., Aguilera, I., Bouso, L., Grau, M., Phuleria, H.C., Rivera, M., Slama, R., Sunyer, J., Targa, J., Künzli, N., "Local determinants of road traffic noise levels versus determinants of air pollution levels in a Mediterranean city", *Environmental Research* 111, 177–183, 2011.
- [2] Ross, Z., Kheirbek, I., Clougherty, J.E., Kazuhiko, I., Matte, T., Markowitz, S., Eisl, H., "Noise, air pollutants and traffic: Continuous measurement and correlation at a high-traffic location in New York City", *Environmental Research* 111, 1054-1063, 2011.
- [3] Beelen, R., Hoek, G., Houthuijs, D., van den Brandt, P.A., Goldbohm, R.A., Fischer, P., et al., "The joint association of air pollution and noise from road traffic with cardiovascular mortality in a cohort study", *Occupational and Environmental Medicine* 66 (4), 243–250, 2009.
- [4] Van Kempen, E., Fischer, P., Janssen, N., Houthuijs, D., van Kamp, I., Stansfeld, S., Cassee, F., "Neurobehavioural effects of exposure to traffic-related air pollution and transportation noise in primary school children", *Environmental Research* 115, 18–25, 2012.
- [5] Linares, C., Díaz, J., Tobías, A., De Miguel, J.M., Otero, A., "Impact of urban air pollutants and noise levels over daily hospital admissions in children in Madrid: a time series analysis", *Int Arch Occup Environ Health* 79, 143–152, 2006.
- [6] Kim, K-H., Duy Xuan Ho, Brown, R.J.C., Oh, J.M., Park C.G., In Cheol Ryu., "Some insights into the relationship between urban air pollution and noise levels", *Science of the Total Environment* 424, 271-279, 2012.
- [7] Weber, S., "Spatio-temporal covariation of urban particle number concentration and ambient noise", *Atmospheric Environment* 43, 5518–25, 2009.
- [8] Allen, R.W., Davies, H., Cohen, M.A., Mallach, G., Kaufman, J.D., Adar, S.D., "The spatial relationship between traffic-generated air pollution and noise in 2 US cities", *Environmental Research* 109 (3), 334–342, 2009.
- [9] Boogaard, H., Borgman, F., Kamming, J., Hoek, G., "Exposure to ultrafine and fine particles and noise during cycling and driving in 11 Dutch cities", *Atmospheric Environment* 43, 4234–42, 2009.
- [10] Can, A., Rademaker, M., Van Renterghem, T., Mishra, V., Van Poppel, M., Touhafi, A., Theunis, J., De Baets, B., Botteldooren, D., "Correlation analysis of noise and ultrafine particle counts in a street canyon", *Science of the Total Environment* 409, 564–572, 2011.
- [11] Weber, S., Litschke, T., "Variation of particle concentrations and environmental noise on the urban neighbourhood scale", *Atmospheric Environment* 42, 7179–83, 2008.
- [12] Oberdörster, G., Sharp, Z., Atudorei, V., Elder, A., Gelein, R., Kreyling, W., Cox, C., "Translocation of Inhaled Ultrafine Particles to the Brain", *Inhalation Toxicology* 16, 1-9, 2004.
- [13] Araujo, J.A., Barajas, B., Kleinman, M., Wang, X., Bennett, B.J., Gong, K.W., Navab, M., Harkema, J., Sioutas, C., Lusis, A.J., Nel, A.E., "Ambient particulate pollutants in the ultrafine range promote early atherosclerosis and systemic oxidative stress", *Circulation Research* 102(5), 589-596, 2008.
- [14] Van Renterghem T, Thomas P, Botteldooren D, Dominguez F, Touhafi A, Dauwe S., "The use of cheap microphones in extensive outdoor noise monitoring networks", *Proceedings of the Joint Institute of Acoustics (IOA) and Belgium Acoustical Society (ABAV) Congress*; April 2010.
- [15] Fernández-Camacho, R., De la Rosa, J., Sánchez de la Campa, A.M., González-Castanedo, Y., Alastuey, A., Querol, X., Rodríguez, S., "Geochemical characterization of Cu-smelter emission plumes with impact in an urban area of SW Spain", *Atmospheric Research* 96, 590-601, 2010a.
- [16] Fernández-Camacho, R., Rodríguez, S., De la Rosa, J., Sánchez de la Campa, A.M., Viana, M., Alastuey, A., and Querol, X., "Ultrafine particle formation in the inland sea breeze airflow in Southwest Europe", *Atmospheric Chemistry and Physics*, 10, 9615-9630, 2010b.
- [17] Fernández-Camacho, R., Rodríguez, S., De la Rosa, J., Sánchez de la Campa, A.M., Alastuey, A., Querol, X., González-Castanedo, Y., García-Orellana, I., Nava, S., "Ultrafine particle and fine trace metal (As, Cd, Cu, Pb and Zn) pollution episodes induced by industrial emissions in Huelva, SW Spain", *Atmospheric Environment* 61, 507-517, 2012.
- [18] Putaud, J.-P., Van Dingenen, R., Alastuey, A., Bauer, H., Birmili, W., Cyrys, J., Flentje, H., Fuzzi, S., Gehrig, R., Hansson, H.C., Harrison, R.M., Herrmann, H., Hittenberger, R., Hüglin, C., Jones, A.M., Kasper-Giebl, A., Kiss, G., Kousa, A., Kuhlbusch, T.A.J., Loschau, G., Maenhaut, W., Molnar, A., Moreno, T., Pekkanen, J., Perrino, C., Pitz, M., Puxbaum, H., Querol, X., Rodríguez, S., Salma, I., Schwarz, J., Smolik, J., Schneider, J., Spindler, G., Ten Brink, H., Tursic, J., Viana, M., Wiedensohler, A., Raes, F., "A European aerosol phenomenology-3: Physical and chemical characteristics of particulate matter from 60 rural, urban and kerbside sites across Europe", *Atmospheric Environment* 44, 1308-1320, 2010.
- [19] EU, 2008b. 2008/107/EC. Council Directive on ambient air quality and cleaner air for Europe. *Official Journal* L 152, 0001-0044.
- [20] EU, 2002. 2002/49/EC. Council Directive relating to the assessment and management of environmental noise. *Official Journal* L 189, 0012-0025.
- [21] EC Working group on particulate matter: REPORT-Guidance to Member States on PM10 Monitoring and Intercomparisons with the Reference Method, January 2002.

- [22] Rodríguez, S., Cuevas, E., “The contributions of ‘minimum primary emissions’ and ‘new particle formation enhancements’ to the particle number concentration in urban air”, *Journal of Aerosol Science* 38, 1207-1219, 2007.
- [23] Reche C, Querol X, Alastuey, A., Viana, M., Pey, J., Moreno, T., Rodríguez, S., González, Y., Fernández-Camacho, R., Sánchez de la Campa, A.M., de la Rosa, J., Dall’Osto, M., Prévôt, A.S.H., Hueglin, C., Harrison, R.M., Quincey, P., “New considerations for PM, Black Carbon and particle number concentration for air quality monitoring across different European cities. *Atmospheric Chemistry Physics* 11, 6207-6227, 2011.
- [24] Kumar, P., Fennel, P., Langley, D., Britter, R., “Pseudo-simultaneous measurements for the vertical variation of coarse, fine and ultrafine particles in an urban street canyon”, *Atmospheric Environment* 42, 4304–19, 2008b.

Carbonaceous aerosols emitted from food cooking

Célia Alves, Márcio Duarte, Teresa Nunes, Rita Moreira, Sónia Rocha

Abstract — PM_{2.5} samples were collected from the exhaust stacks on the roofs of an university canteen, a charcoal-grilled chicken restaurant and a wood-oven roasted piglet restaurant. The use of thick exhaust hood filters and of gas and electricity as energy sources for cooking in the kitchen of the university canteen contributed to the emission of much lower PM_{2.5} levels (24-127 µg/m³) compared to the restaurants. The charcoal-grilled chicken restaurant emitted particles at concentrations from 26 to 127 mg/m³. In the exhaust of the wood-oven roasted piglet restaurant, PM_{2.5} ranged from 192 mg/m³, when vine cuttings were used to fire up the ovens, to 203 µg/m³, at the final stage of roasting. Organic carbon (OC) represented, on average, 49% of the PM_{2.5} mass in samples from the canteen, while elemental carbon (EC) accounted for 1-6%. The OC and EC contents in aerosols from the charcoal-grilled chicken restaurant ranged from 73 to almost 95% and from 0.4 to 1%, respectively. Very high organic contents in the smoke exhausted from the piglet restaurant were also determined. However, the EC mass percentages in PM_{2.5} from this restaurant are higher than those found in samples from the other establishments.

Keywords — EC, OC, PM_{2.5}, cooking emissions

1 INTRODUCTION

Atmospheric particles are of major scientific interest due to their demonstrated role in climate change and their effect on human health [1]. Current European Directive on Air Quality 2008/50/CE targets the mass concentration of airborne particulate matter under 2.5 µm (PM_{2.5}). The threshold values are frequently exceeded in many urban areas. Source apportionment studies performed worldwide indicated that, along with vehicle and biomass burning emissions, cooking activities may represent an important source of PM_{2.5}, until now neglected [2-5]. In addition, it has long been known that cooking can create high concentrations of aerosol indoors [6]. It has been demonstrated recently that the health effects of cooking emissions are relevant to people across the globe [7]. Some emission profiles have been obtained for American [2, 8, 9] and Chinese [10-14] cooking styles. However, emissions depend strongly on the cooking method and food ingredients, and nothing is known about particle emissions from the Mediterranean cuisine.

The main goal of this study consisted in obtaining particle concentrations and the respective carbonaceous content in the exhaust fumes from representative restaurants serving traditional Portuguese meals. Quantitative knowledge of individual source emissions to the atmosphere is crucial to devise cost-effective abatement strategies.

2 METHODOLOGIES

2.1 Sampling

In 2012, low-volume PM_{2.5} samples were collected from the exhaust stacks on the roofs of an university canteen, a charcoal-grilled chicken restaurant and a wood-oven roasted piglet restaurant, during the preparation of lunches and/or dinners. The University of Aveiro owns 4 canteens where 5000-6000 meals are daily prepared. The selected canteen serves about half of the total meals. Throughout Portugal there are numerous restaurants located in towns, cities, and also by roadside on national highways offering the typical fare of barbecued chicken. The selected restaurant provides table service and takeaway. Despite being made across the country, the Bairrada region, in central Portugal, is specialised in serving up spit-roasted, crispy skinned and pepper-spiced piglets to thousands of visitors. In this region, around 15 tons of sucking pigs are eaten a day.

The PM_{2.5} samples were collected onto pre-baked (6 h at 500°C) 47 mm diameter quartz filters at a flow of 2.3 m³/h using Echo TCR Tecora samplers, following the EN 14907 norm. Two pairs of parallel samples were collected directly from the exit of exhausts during variable periods, depending on the smoke loads. In the case of the university canteen, the sampling campaign lasted for several weeks and collection times ranged from about 2 to 12 hours. The longest periods are associated with sampling of fumes from the preparation of boiled dishes, for which it was necessary to accumulate the emissions of two or three lunches and/or dinners onto the same filters. Because of the very dense

Authors are with the Centre of Environmental and Marine Studies, Department of Environment, University of Aveiro, 3810-193 Aveiro, Portugal.

E-mails in successive order: celia.alves@ua.pt; marcioduarte@ua.pt; tnunes@ua.pt; rita.moreira@ua.pt; rocha.sonia@ua.pt

smoke emitted through the stacks, sampling times for the other two establishments ranged from 5 to 75 minutes.

2.2 Analytical techniques

Before weighing, the filters were conditioned in a desiccator at least for 24 h in a temperature- and humidity-controlled room. Previous to and after sampling, gravimetric determination was performed with a microbalance Mettler Toledo AG245 (readability 0.1 mg/0.01 mg). Filter weights were obtained from the average of several measurements, with weight variations less than 5%.

After gravimetric determination of the $PM_{2.5}$ mass, filter punches were analysed by a thermo-optical transmission system in order to obtain the carbonaceous content (OC and EC). Controlled heating in anoxic and oxic conditions was performed to separate, respectively, OC into two fractions of increasing volatility and EC, which were measured in the form of CO_2 by an infrared non-dispersive analyser. The first fraction corresponds to the volatilisation at $T < 200^\circ C$ of lower molecular weight organics (OC1). The second fraction is related to the decomposition and oxidation of higher molecular weight species at temperatures ranging from 200 to $600^\circ C$ (OC2). However, pyrolysed organic carbon (PC), formed during the previous heating steps, is only released in oxic conditions, when the sample is heated up to $850^\circ C$, evolving simultaneously with EC. The interference between PC and EC can be controlled by continuous evaluation of the blackening of the filter using a laser beam and a photodetector that measures the light transmittance. The split between the PC and EC is assigned when the initial (baseline) value of the filter transmittance is reached. All carbon removed before the split is considered organic, and that removed after the split is considered elemental.

3 RESULTS AND DISCUSSION

The use of thick exhaust hood filters, which were changed at the beginning of the first day of sampling, and gas and electricity as energy sources for cooking in the kitchen of the university canteen contributed to the emission of much lower $PM_{2.5}$ levels compared to the restaurants (Table 1). The $PM_{2.5}$ samples from the canteen exhausts presented concentrations between 24 and $127 \mu g/m^3$. The highest concentrations were obtained in samples from the fry and stew stations, while the lowest corresponded to the boiled food station. The charcoal-grilled chicken restaurant emitted particles at concentrations from 26 to $127 mg/m^3$, averaging $71 mg/m^3$. In the exhaust of wood-oven roasted piglet restaurant, $PM_{2.5}$ ranged from $52-78 mg/m^3$, when vine cuttings and pine slats were used to fire up the brick ovens in which piglets were roasted, to

$203 \mu g/m^3$, at the final stage of roasting. This confirms the results reported in a recent review paper in which it was demonstrated that the elevated concentrations derive largely from the combustion of the fuel used for cooking rather than from the cooking itself [6]. In accordance with other works [15], in the present study it was also observed that, in general, foods containing a higher percentage of fat generate higher emission rates than those with less fat percentage. See and Balasubramanian [16] analysed various cooking methods (steaming, boiling, stir-frying, pan-frying and deep-frying). The authors observed that the highest concentration of $PM_{2.5}$ measured at 20 cm from the cooker was produced during deep frying ($190 mg/m^3$) and the lowest level was registered during steaming ($72 \mu g/m^3$). It has been also demonstrated that cooking with oil contributes to the generation of more particles than cooking with water [15-17]. In a comparison of emissions from Chinese, Indian and Malay food stalls it was reported that the highest mass concentrations of $PM_{2.5}$ were measured in the Malay stall ($245 \mu g/m^3$), while the lowest were observed in the Indian stall ($187 \mu g/m^3$) [18]. It should be noted, however, that these studies were carried out in the kitchens of residential houses or in domestic kitchens set-up inside a laboratory, and do not refer to stack emissions.

Table 1. Concentrations of particles, organic carbon and elemental carbon in the stack exhausts from cooking operations.

Description	$PM_{2.5}$	OC	EC
UNIVERSITY CANTEEN ($n = 20$; units: $\mu g/m^3$)			
Boiled chicken with vegetables	41±11	14±0.33	1.8±0.27
Fried fish, seafood rice	97±23	39±2.5	1.4±0.32
Veal stroganoff stew	63±2.3	30±0.79	1.5±0.34
Boiled pork meat with vegetables	27±1.5	8.5±0.57	1.0±0.19
Roasted ribs	127±2.0	33±0.58	6.0±0.01
Alentejo pork meat with clams; stewed pork chops with sausages	45±8.1	27±0.28	1.8±0.43
Grilled pork	107±3.1	69±1.8	1.2±0.58
Beef with rice, pork with boiled potatoes	29±6.7	10.4±1.3	1.7±0.66
Grilled and boiled fish	44±11	34±1.1	1.3±0.02
Chicken stew, turkey stew with rice	55±4.0	39±1.2	2.1±0.01
CHARCOAL-GRILLED CHICKEN RESTAURANT ($n = 7$; units: mg/m^3)			
Smoke-roasted chicken	71±39	62±37	0.37±0.12
WOOD-OVEN ROASTED PIGLET RESTAURANT ($n = 11$)			
Over preheating with remains of pruning vines and pine slats	70 mg/m^3	52 mg/m^3	7.5 mg/m^3
Burning of pruning vines and pine slats (flaming)	31 mg/m^3	28 mg/m^3	1.24 mg/m^3
Pine slats burning like in a fireplace (door open) after refueling; flaming phase and beginning of smouldering phase	192 mg/m^3	178 mg/m^3	9.24 mg/m^3
Smouldering and glowing embers	16.0±2.58 mg/m^3	8.13±3.07 mg/m^3	5.02±0.739 mg/m^3
Tray with rice soaked in chicken's blood, glowing embers at the bottom; door open occasionally to spread ashes on the glowing embers	31.4±2.24 mg/m^3	10.3±2.29 mg/m^3	5.02±0.739 mg/m^3
3 piglets in the oven; glowing embers at the bottom; door open	1393±142 $\mu g/m^3$	809±106 $\mu g/m^3$	107±21 $\mu g/m^3$
Final phase of roasting; oven door closed	207±6.1 $\mu g/m^3$	158±29 $\mu g/m^3$.5 $\mu g/m^3$

OC represented, on average, 49% of the PM_{2.5} mass in samples from the canteen, whilst EC accounted for 1-6%. The OC and EC particle mass fractions from the charcoal-grilled chicken restaurant ranged from 73 to around 100% and from 0.4 to 1%, respectively. Very high organic contents in the smoke exhausted from the piglet restaurant were also determined. However, the EC mass percentages in PM_{2.5} from the latter place are higher than those found in samples from the other eateries.

Previous studies have also indicated that OC carbon is the major constituent found in cooking fumes [16, 19-22]. Comparison of different culinary methods showed that those using oil release higher concentrations of EC and OC than those using boiling (i.e. boiling and steaming) [6].

In a recent study in a rural area in the Indo-Gangetic-Plains [23], it was observed that black carbon (BC) levels, both indoors and outdoors, have anomalously large twice-daily peak concentrations reaching 60 µg/m³ for indoor and 30 µg/m³ for outdoor, during the early morning, 05:00-08:00, and early evening, 17:00-19:00, coinciding with the morning and evening cooking hours. The peak indoor BC concentrations reached as high as 1000 µg/m³. The large diurnal peaks, due to cooking activities, seen in this research lead to the conclusion that satellite based aerosol studies that rely on once-daily daytime measurements may severely underestimate the BC loading of the atmosphere. The concentration of OC was a factor of 5 larger than BC and furthermore optical data show that absorbing brown carbon was a major component of the OC. It should be stressed that the term EC or BC is defined operationally in the literature and refers to the same absorbing component (i.e. dark-coloured “soot”) in carbonaceous aerosols. Destructive analytical techniques (such as thermal-optical method) that use the thermal resistance, oxidative resistant and chemical inert nature of highly polymerised graphitic-like fraction of soot termed it as EC. Non-destructive analytical techniques (such as optical methods) that use the light absorbing characteristic of soot termed it as BC. The definition of BC includes EC as well as all components in the soot that absorb light such as some OC fractions (known as brown carbon) that show strong absorption in near-UV region of solar spectrum [24].

The OC/EC ratio can be helpful in differentiating between aerosol sources [25]. Typically mean OC/EC ratios for fossil fuel dominated aerosol in urban cities (range from about 1 to 3), while in regions impacted by biomass burning emissions these ratios are substantially higher [25]. OC and EC measurements performed in a busy roadway tunnel in central Lisbon showed an OC/EC ratio in the range of 0.3-0.4, which reflected the composition of fresh vehicular exhaust emissions [26]. Schauer et al. [27] reported OC/EC values in the range 16.8-40.0 for wood combustion. Schmidl et al. [28] found

OC/EC ratios between 2.7-3.3 for hard- and 2.6-5.7 for softwood during the combustion of mid-European Alpine species in a domestic tiled stove. Values ranging from 3.99 to 52.6 were obtained by Gonçalves et al. [2011] in PM_{2.5} emissions from fireplace and woodstove combustion of typical Portuguese wood species. Roden et al. [30, 31] reported OC/EC ratios between 0.5 and 13 (mean value of 2.3) during field measurements from a traditional Honduran wood-fired cookstove. The authors argued that the large amount of EC emitted during cook stove combustion may not be able to distinguish between fossil and biofuel combustion aerosols when cooking with biofuel is dominant.

Relatively low OC/EC ratios (3.34±1.63) were obtained in our study for the cooking emissions of the university canteen. Much higher ratios, between 76.9 and 247 (average = 155), were found in the very greasy fumes of the charcoal-grilled chicken restaurant. Since chicken skin is very high in fat, cooking it on an underfired charbroiler yields high amounts of OC, which superimpose the EC emitted from the combustion of charcoal. OC/EC values in the range 2.5-10.5 have been reported for residential coal burning [32]. Emissions from the piglet restaurant produced an average OC/EC of 21.1 once the thin vine twigs were lit, and small pieces of pine wood were added, achieving a very intense flaming phase. The ratio decreased to values of 1-2 after heating the oven up to high temperatures and glowing coals covered the bottom. The highest average value (35.5) was achieved during the roasting process. A large fork is used to place the pig's carcass in the oven, while hot water is applied to it to cause the skin to tighten. The piglet is roasted at high temperature until meat is tender and skin is crispy. Ratios from 32.9 to 81.6, i.e. between those of the piglet and chicken restaurants, have been described in the literature for kitchen emissions [17].

4 CONCLUSIONS

Commercial cooking is a surprisingly large source of particle emissions that could pose risks to human health and the environment. While that mouth-watering smell may whet our appetite, emissions likely involving hazardous pollutants in the smoke from the cooking processes are ejected into the air that we breathe. Mechanical and environmental engineering solutions aiming at mitigating emissions recommend the combined application of air pollution control equipments (e.g. grease filter, electrostatic precipitator, hydrovent, etc.) together with a suitably located exhaust outlet. The outlets should be located at a place where ventilation is good and sufficient separation distance from the neighbourhood is maintained. The emission from the exhaust system should be adequately dispersed and

should not be restricted or deflected by any plates, caps or other obstacles.

The emissions of cooking aerosol are highly diverse, depending upon factors such as the raw-food composition, cooking temperature, cooking style and energy sources. Although it is possible to clearly distinguish the OC/EC ratios of vehicle exhausts from those of cooking emissions, the separation between the latter and biomass burning is tricky, because overlapping of values may occur.

While further knowledge the chemical composition of cooking emissions would be beneficial, quantitative source apportionment will remain imprecise and potentially inaccurate in situations with mixed cooking source types contributing to atmospheric concentrations. This provides a considerable challenge to receptor models, such as Chemical Mass Balance (CMB), where it is necessary to input a source profile.

ACKNOWLEDGMENT

This work was funded by the Portuguese Science Foundation (FCT) through the project "Source apportionment of URban Emissions of primary particulate matter", PTDC/AAC-AMB/117956/2010 (URBE). We would also like to acknowledge the restaurant owners and staff for their cooperation.

REFERENCES

- [1] A.I. Calvo, C. Alves, A. Castro, V. Pont, A.M. Vicente, R. Fraile, "Research on aerosol sources and chemical composition: past, current and emerging issues," *Atmos. Res.*, vol. 120-121, pp. 1-28, 2013.
- [2] J. McDonald, B. Zielinska, E.M. Fujita, J.C. Sagebiel, J.C. Chow, J.G. Watson, "Emissions from charbroiling and grilling of chicken and beef," *J. Air Waste Manage. Assoc.*, vol. 53, pp. 185-194, 2003.
- [3] C. Alves, A. Vicente, C. Pio, G. Kiss, A. Hoffer, S. Decesari, A.S.H. Prevot, M.C. Minguillón, X. Querol, R. Hillamo, G. Spindler, E. Swietlicki, "Organic compounds in aerosols from selected European sites - biogenic versus anthropogenic sources," *Atmos. Environ.*, vol. 59, pp. 243-255, 2012.
- [4] C. Mohr, P.F. DeCarlo, M.F. Heringa, R. Chirico, J.G. Slowik, R. Richter, C. Reche, A. Alastuey, X. Querol, R. Seco, J. Peñuelas, J.L. Jiménez, M. Crippa, R. Zimmermann, U. Baltensperger, A.S.L. Prévôt, "Identification and quantification of organic aerosol from cooking and other sources in Barcelona using mass spectrometer data," *Atmos. Chem. Phys.*, vol. 12, pp. 1649-1665, 2012.
- [5] A.L. Robinson, R. Subramanian, N.M. Donahue, A. Bernardo-Bricker, W.F. Rogge, "Source apportionment of molecular markers and organic aerosol. 3. Food cooking emissions," *Environ. Sci. Technol.*, vol. 40, pp. 7820-7827, 2006.
- [6] K.L. Abdullahi, J.M. Delgado-Saborit, R.M. Harrison, "Emissions and indoor concentrations of particulate matter and its specific chemical components from cooking: A review," *Atmos. Environ.*, vol. 71, pp. 260-294, 2013.
- [7] K.H. Kim, S.K. Pandey, E. Kabir, J. Susaya, R.J.C. Brown, "The modern paradox of unregulated cooking activities and indoor air quality," *J. Haz. Mat.*, vol. 195, pp. 1-10, 2011.
- [8] J.J. Schauer, M.J. Kleeman, G.R. Cass, B.R.T. Simoneit, "Measurement of emissions from air pollution sources. 4. C₁-C₂₇ organic compounds from cooking with seed oils," *Environ. Sci. Technol.*, vol. 36, pp. 567-575, 1999.
- [9] C. Mohr, J.A. Huffman, M.J. Cubison, A.C. Aiken, K.S. Docherty, J.R. Kimmel, I.M. Ulbrich, M. Hannigan, J.L. Jimenez, "Characterization of primary organic aerosol emissions from meat cooking, trash burning, and motor vehicles with high-resolution aerosol mass spectrometry and comparison with ambient and chamber observations," *Environ. Sci. Technol.*, vol. 43, pp. 2443-2449, 2009.
- [10] L.Y. He, M. Hu, X.F. Huang, B.D. Yu, Y.H. Zhang, D.Q. Liu, "Measurement of emissions of fine particulate organic matter from Chinese cooking," *Atmos. Environ.*, vol. 38, pp. 6557-6564, 2004.
- [11] L.Y. He, Y. Lin, X.F. Huang, S. Guo, L. Xue, Q. Su, M. Hu, S.J. Luan, Y.H. Zhang, "Characterization of high-resolution aerosol mass spectra of primary organic aerosol emissions from Chinese cooking and biomass burning," *Atmos. Chem. Phys.*, vol. 10, pp. 11535-11543, 2010.
- [12] Y. Zhao, M. Hu, S. Slanina, Y. Zhang, "Chemical compositions of fine particulate organic matter emitted from Chinese cooking," *Environ. Sci. Technol.*, vol. 41, pp. 99-105, 2007.
- [13] Y. Chen, K.F. Ho, S.S.H. Ho, W.K. Ho, S.C. Lee, J.Z. Yu, E.H.L. Sit, "Gaseous and particulate polycyclic aromatic hydrocarbons (PAHs) emissions from commercial restaurants in Hong Kong," *J. Environ. Monit.*, vol. 9, pp. 1402-1409, 2007.
- [14] C.T. Li, Y.C. Lin, W.J. Lee, P.J. Tsai, "Emission of polycyclic aromatic hydrocarbons and their carcinogenic potencies from cooking sources to the urban atmosphere," *Environ. Health Persp.*, vol. 111, pp. 483-487, 2003.
- [15] G. Buonanno, L. Morawska, L. Stabile, "Particle emission factors during cooking activities," *Atmos. Environ.*, vol. 43, pp. 3235-3242, 2009.
- [16] S.W. See, R. Balasubramanian, "Chemical characteristics of fine particles emitted from different gas cooking methods," *Atmos. Environ.*, vol. 42, pp. 8852-8862, 2008.
- [17] C. He, L. Morawska, J. Hitchins, D. Gilbert, "Contribution from indoor sources to particle number and mass concentrations in residential houses," *Atmos. Environ.*, vol. 38, pp. 3405-3415, 2004.
- [18] S.W. See, S. Karthikeyana, R. Balasubramanian, "Health risk assessment of occupational exposure to particulate-phase polycyclic aromatic hydrocarbons associated with Chinese, Malay and Indian cooking," *J. Environ. Monit.*, vol. 8, pp. 369-376, 2006.
- [19] M.J. Kleeman, J.J. Schauer, G.R. Cass, "Size and composition distribution of fine particulate matter emitted from wood burning, meat charbroiling, and cigarettes," *Environ. Sci. Technol.*, vol. 33, pp. 3516-3523, 1999.
- [20] M.J. Kleeman, M.A. Robert, S.G. Riddle, P.M. Fine, M.D. Hays, J.J. Schauer, M.P. Hannigan, M.P., "Size distribution of trace organic species emitted from biomass combustion and meat charbroiling," *Atmos. Environ.*, vol. 42, pp. 3059-3075, 2008.
- [21] J.J. Schauer, M.J. Kleeman, G.R. Cass, B.R.T. Simoneit, "Measurement of emissions from air pollution sources. 1. C₁ through C₂₉ organic compounds from meat charbroiling," *Environ. Sci. Technol.*, vol. 33, pp. 1566-1577, 1999.
- [22] J.C. Chow, J.G. Watson, H. Kuhns, V. Etyemezian, D.H. Lowenthal, D. Crow, S.D. Kohl, J.P. Engelbrecht, M.C. Green, "Source profiles for industrial, mobile, and area sources in the Big Bend Regional Aerosol Visibility and Observational study," *Chemosphere*, vol. 54, pp. 185-208, 2004.
- [23] H. Rehman, T. Ahmed, P. S. Praveen, A. Kar, V. Ramanathan, "Black carbon emissions from biomass and fossil fuels in rural India," *Atmos. Chem. Phys.*, vol. 11, pp. 7289-7299, 2011.
- [24] M. O. Andreae, A. Gelencser, "Black carbon or brown carbon? The nature of light-absorbing carbonaceous aerosols," *Atmos. Chem. Phys.*, vol. 6, pp. 3131-3148, 2006.

- [25] T. Novakov, M.O. Andreae, R. Gabriel, T.W. Kirchstetter, O.L. Mayol-Bracero, V. Ramanathan, "Origin of carbonaceous aerosols over the tropical Indian Ocean: Biomass burning or fossil fuels?," *Geophys. Res. Lett.*, vol. 27, pp. 4061-4064, 2000.
- [26] C. Pio, M. Cerqueira, R.M. Harrison, T. Nunes, F. Mirante, C. Alves, C. Oliveira, A. Sanchez de la Campa, B. Artñano, M. Matos, "OC/EC ratio observations in Europe: re-thinking the approach for apportionment between primary and secondary organic carbon," *Atmos. Environ.*, vol. 45, pp. 6121-6132.
- [27] J.J. Schauer, M.J. Kleeman, G.R. Cass, B.R.T. Simoneit, "Measurement of emissions from air pollution sources. 3. C₁-C₂₉ organic compounds from fireplace combustion of wood," *Environ. Sci. Technol.*, vol. 35, pp. 1716-1728, 2001.
- [28] C. Schmidl, I.L. Marr, A. Caseiro, P. Kotianova, A. Berner, H. Bauer, A. Kasper-Giebl., H. Puxbaum, "Chemical characterization of fine particles emissions from wood stove combustion of common woods growing in mid-European Alpine regions," *Atmos. Environ.*, vol. 42, pp. 126-141, 2008.
- [29] C. Gonçalves, C. Alves, A.P. Fernandes, C. Monteiro, L. Tarelho, M. Evtugina, C. Pio, "Organic compounds in PM_{2.5} emitted from fireplace and woodstove combustion of typical Portuguese wood species," *Atmos. Environ.*, vol. 45, pp. 4533-4545, 2011.
- [30] C.A. Roden, T.C. Bond, S. Conway, A.B.O. Pinel, "Emission factors and real-time optical properties of particles emitted from traditional wood burning cook stoves," *Environ. Sci. Technol.*, vol. 40, pp. 6750-6757, 2006.
- [31] C.A. Roden, T.C. Bond, S. Conway, A.B.O. Pinel, N. MacCarty, D. Still, "Laboratory and field investigation of particulate and carbon monoxide emissions from traditional and improved cookstoves," *Atmos. Environ.*, vol. 43, pp. 1170-1181, 2009.
- [32] Y. Chen, G. Zhi, Y. Feng, J. Fu, J. Feng, G. Sheng, B.R.T. Simoneit, "Measurements of emission factors for primary carbonaceous particles from residential raw-coal combustion in China," *Geophys. Res. Lett.*, vol. 33, doi:10.1029/2006GL026966, 2006.

Total and ultraviolet solar irradiance during a desert dust episode at Cáceres (Spain)

M.A. Obregón¹, A. Serrano², G. Sánchez³, M.L. Cancillo⁴

Abstract —This work focuses on the study of the influence of a particular Saharan desert dust episode on total and ultraviolet (UV) solar irradiance as recorded at Cáceres station (Spain) from 5 to 7 August 2005. The transport of dust from the Sahara region towards the Iberian Peninsula is a frequent phenomenon that notably influences the radiation balance as well as the atmospheric visibility at those sites influenced by these aerosols.

This Saharan dust event has been detected to significantly affect the values of several aerosol in-column radiometric properties, such as aerosol optical depth, Ångström exponent α , single scattering albedo and aerosol volume size distributions, as recorded by a CIMEL Sun photometer located at Cáceres (Spain), which participates in the NASA AERONET (Aerosol Robotic NETwork) network. This Saharan event is characterized by a strong intensity, (aerosol optical depth greater than 0.5) and coarse particles (Ångström exponent α lower than 1).

The total and ultraviolet erythemal solar irradiances were measured with Kipp&Zonen broadband instruments installed at the Cáceres radiometric station. During this episode the total solar irradiance decreased, on average, between 10 and 16%. For the UV erythemal irradiance the attenuation shows high variability ranging from 15 to 33%. These strong effects emphasize the important role of aerosols in the radiation balance of the Earth-atmosphere system.

Keywords —AERONET, desert dust, Earth's radiation balance

1 INTRODUCTION

Solar radiation is the main source of energy for the Earth-atmosphere system. It is well known that any change in the atmospheric composition would significantly affect the radiative budget and, as a result, the global temperature of the Earth. One of these components is the atmospheric aerosol, with natural and anthropogenic origins.

It is known that atmospheric aerosols, in general, modify the energy balance of the Earth-atmosphere system, but there is still a large source of uncertainty concerning their climate effects. They directly interact with solar and terrestrial radiation through scattering, and absorption as well as through emission processes. They also indirectly affect the radiation balance by influencing the cloud formation and modification. According to the Intergovernmental Panel on Climate Change 2007, the global average aerosol direct radiative forcing is estimated to be about -0.5 [-0.9 to -0.1] W/m² and the global indirect forcing about -0.7 [-1.8 to -0.3] W/m², therefore contributing to the cooling of the

planet. However there are still many uncertainties and accurate and reliable measurements and analyses are demanded to reduce those uncertainties.

An important source of mineral aerosol in the Iberian Peninsula and in the Northern Hemisphere [1] is the Saharan Desert, playing an important role in the radiation balance of the Climate System [2]. Moreover, due to the proximity of the Saharan Desert to the Iberian Peninsula and the annual latitudinal displacement of the general atmospheric circulation, desert dust events in the Iberian Peninsula show a typical seasonal pattern [3], [4] associated to certain synoptic situations [5], [6], [7]. These intrusions have been widely studied by means of active and passive remote sensing techniques at different stations in the Iberian Peninsula by different authors [8], [9], [10], [11], [12], [13], [14], [15], [16]. However, few studies analyze the effects of desert dust aerosols on surface radiation, both total and ultraviolet (UV), over this region [17], [18], [19], [20], [21].

Therefore, the aim of this work is to monitor an intense Saharan dust event in the atmospheric column over Cáceres station, Spain, and analyze the influence of this event on total and UV irradiance recorded at Cáceres. This work is organized as follows: a brief description of the study region and instrumentation is presented in Section 2; data set and methodology are provided in section 3; results are discussed in section 4. Finally, conclusions are given in section 5.

1. M.A. Obregón is with the Department of Physics, University of Extremadura. Avda. De Elvas, s/n, 06006 Badajoz. Spain. E-mail: nines@unex.es
2. A.Serrano is with the Department of Physics, University of Extremadura. Avda. De Elvas, s/n, 06006 Badajoz. Spain. E-mail: asp@unex.es
3. G. Sánchez is with the Department of Physics, University of Extremadura. Avda. De Elvas, s/n, 06006 Badajoz. Spain. E-mail: guadalupesh@unex.es
4. M.L. Cancillo is with the Department of Physics, University of Extremadura. Avda. De Elvas, s/n, 06006 Badajoz. Spain. E-mail: mcf@unex.es

2 STUDY REGION AND INSTRUMENTATION

The location of Cáceres radiometric station is shown in Figure 1. It is installed at the Campus of the University of Extremadura, on the roof of the Polytechnic School building, guaranteeing a free horizon (39.47°N, 6.34°W, 397 m a.s.l.).

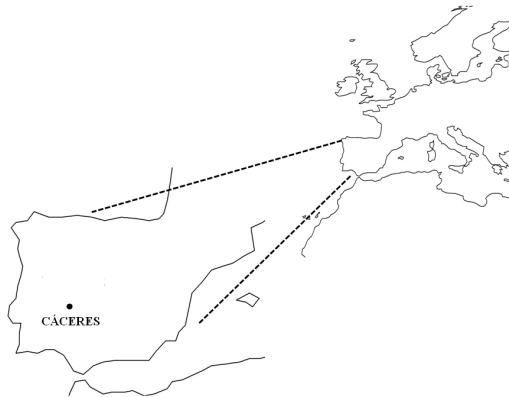


Figure 1. Iberian Peninsula showing the location of Cáceres station.

Cáceres station is managed by the AIRE (Atmósfera, clima y Radiación en Extremadura) research group of the Physics Department, at the University of Extremadura (Spain). This station is equipped with a CIMEL CE-318 sunphotometer, which is integrated in the NASA AERONET (Aerosol Robotic NETWORK) network. This instrument makes direct sun measurements with a 1.2° full field of view at 340, 380, 440, 500, 675, 870, 940 and 1020 nm. In addition, the CIMEL measures sky radiances, both in almucantar and principal plane, at 440, 675, 870 and 1020 nm. Calibration of this instrument was performed by AERONET-RIMA network. More details about this instrument are given by Holben et al. [22]. All radiance measurements are processed by AERONET protocol as described by Holben et al. [22], obtaining aerosol parameters at different quality levels (1.0, 1.5 and 2.0).

Radiation data set consists of one-minute simultaneous measurements of total (285-2800nm) and UV erythemat (280-400nm) irradiance. The total solar irradiance was measured using a Kipp & Zonen CM6B pyranometer which is classified as a “first class” instrument by the WMO. Diurnal signals were corrected for night offsets estimated as the averaged value recorded at solar zenith angle higher than 100°. UV erythemat irradiance was measured using a Kipp & Zonen UVS-E-T broadband radiometer. This instrument has been calibrated biannually at the Atmospheric Sounding Station of the National Institute for Aerospace

Technology (ESAt/INTA) located at “El Arenosillo”, Huelva, Spain. UV data used in this paper were obtained by applying the coefficients obtained in the calibration campaign carried out in September 2003.

Data sets of both instruments have been submitted to a quality control to detect and remove possible erroneous data. Additionally, only cloud-free measurements corresponding to solar zenith angle lower than 80° have been considered in this study. The cloud presence was detected analyzing the short-term fluctuations in the total solar irradiance.

3 DATASET AND METHODOLOGY

In this study, a desert dust episode over Cáceres station, from 5 to 7 August 2005, has been identified. For this purpose, we have analyzed 4 aerosol properties: aerosol optical depth (τ), Ångström α exponent (440-870) (α), single scattering albedo (ω) and aerosol volume size distributions (VSD). During this episode, level 2.0 data [22] are available, and have been used. However, since the conditions to reach level 2.0 are particularly restrictive for ω , there are very few values of this parameter and, therefore, level 1.5 was preferred.

The back trajectories of air masses arriving at Cáceres during this event have also been analyzed. For this, 120-hour back trajectories ending at Cáceres were calculated using the HYSPLIT (Hybrid Single-Particle Lagrangian Integrated Trajectory) version 4 [23], [24]. All trajectories have been calculated at 12:00 UTC, at 3000 m a.s.l. (corresponding to approximately 700 hPa). This height has been chosen because of being representative of the free troposphere, where there are hardly any aerosols except desert dust, which are produced by movements at high altitudes above the boundary layer. The back-trajectories were used to identify this episode, paying special attention to its origin over North Africa.

To calculate the effect of desert dust episode on total and UV irradiance, the values for each day have been compared with the values of the days before the episode.

4 RESULTS

a) Identification of Saharan dust episode

In this section, τ , α , ω , VSD and air mass back trajectories, during the period 4 – 7 August, have been analyzed in order to verify that this is a desert dust episode. Figure 2 shows the time evolution of τ_{500} and α during the Saharan dust episode occurred between 5 and 7 August 2005. On 5 August there is an increase of τ from about 0.1 to

0.6 and a simultaneous significant decrease of α from about 1.2 to 0.5.

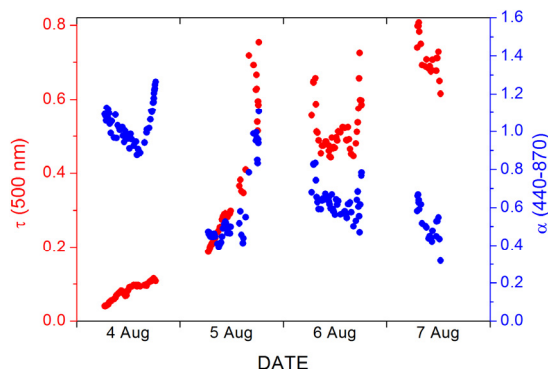


Figure 2. Evolution of $\tau_{500 \text{ nm}}$ and α during the time period 4-07/08/2005 which includes the desert dust event (5-7/08).

Daily average values, computed using all available data for each day, of aerosol optical depth τ at 500, Ångström exponent α and single scattering albedo ω at 675 nm, during the days of dust influence, have been calculated (Table 1).

Table 1. Daily average values of aerosol optical depth at 500, Ångström α exponent (440-870) and single scattering albedo ω at 675 nm during the time period 4-7/08/2005 at Cáceres. For day 7th August, values correspond to hours between 8 and 10 am because they are the only data available.

Day	τ_{500}	α	ω_{675}
04-08-2005	0.079	1.042	0.817
05-08-2005	0.345	0.572	0.925
06-08-2005	0.517	0.631	0.916
07-08-2005	0.718	0.520	0.963

On 4 August τ is very low, significantly increasing on 5 August as α decrease. As shown in Table 1, on 5, 6 and 7 August, the highest daily average values of τ (0.345, 0.517 and 0.718) and the lowest daily average values of α (0.572, 0.631 and 0.520) were detected in Cáceres. The data presented in Figure 2 and Table 1 agrees with the back trajectories at 3000m a.s.l shown in Figure 3. On 4 August (Figure 3a) the trajectory illustrates an atmospheric circulation from the North Atlantic area. On 5, 6 and 7 August (Figure 3b, 3c and 3d), all trajectories overpass North Africa transporting desert aerosol. On 8 and 9 August (Figure 3e, 3f) the back trajectories arrive again from the Atlantic area, as in the days before of the dust event.

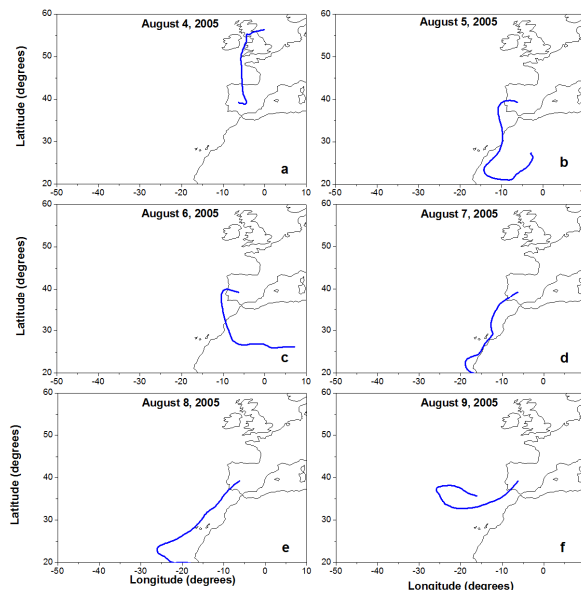


Figure 3. 120 h back trajectories at 3000 m a.s.l. arriving at Cáceres station from 4 to 9 August 2005.

Concerning ω (Table 1 and Figure 4), its values are greater during desert dust episode, increasing with the wavelength as is expected for desert dust aerosols [25].

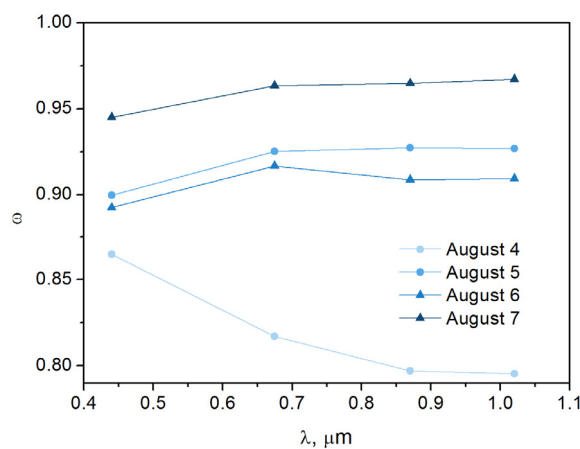


Figure 4. Relation between the average single scattering albedo values and the wavelengths during the time period 04-07/08/2005.

The behaviour of α during the desert dust episode is consistent with the measured aerosol volume size distributions (VSD) (Figure 5). On 5, 6 and 7 August, the proportion of coarse aerosols is clearly higher than before the beginning of the episode (4 August).

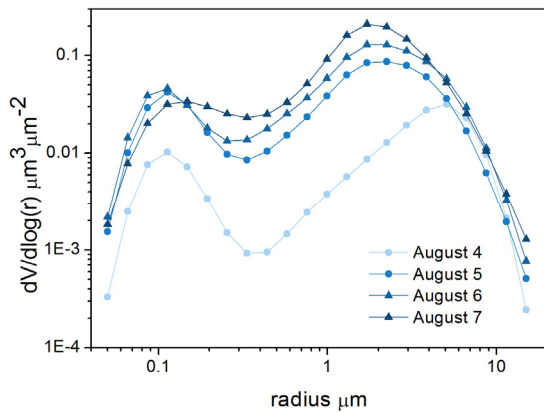


Figure 5. Daily average values of aerosol volume size distribution during the time period 04-07/08/2005.

a) Effect of the dust episode on total and UV solar irradiance

In this section, the effect of desert aerosol on the irradiance measured at Cáceres station has been analyzed. For this analysis, irradiance measured during the event (days 5, 6 and 7 August) has been divided by the irradiance measured at the same hour on 4 August, when dust aerosol event had not begun yet. This normalization is widely used to show relative changes whilst [26]. Figures 6 and 7 show the evolution of these ratios for total and UV irradiance, respectively, together with the τ evolution for each day of the desert dust episode. The analysis of total irradiance has been developed using aerosol optical depth at 500 nm while aerosol optical depth at 380 nm has been used for UV irradiance.

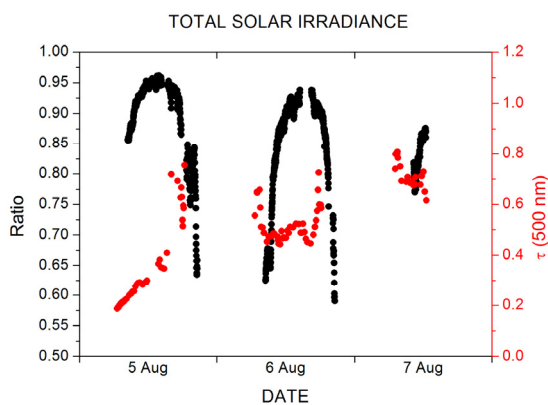


Figure 6. Evolution of τ and the irradiance ratio between total irradiance during the event (5, 6 and 7 August) and reference values (4 August).

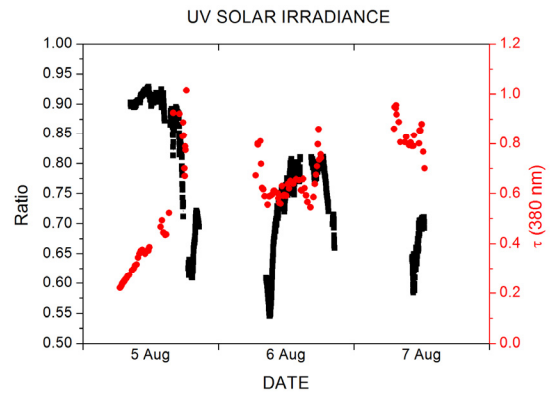


Figure 7. Evolution of τ and the irradiance ratio between UV irradiance during the desert dust event (5, 6 and 7 August) and reference values (4 August).

Figure 6 shows that on 5 August, τ increases continuously along the day while the desert aerosol mass arrives over Cáceres. High values of τ at later hours cause a notable decrease of the irradiance ratio. On 6 August, τ remains approximately constant except for sunrise and sunset where high values are reached producing a remarkable decrease of the irradiance ratio. On August 7 τ shows the highest values though unfortunately no cloud-free data are available after 10 AM.

The general behavior of the irradiance ratios is similar for total and UV wavelengths although the latter shows higher attenuation, mainly on 6 and 7 August (Figure 7). Another characteristic of this desert aerosol intrusion is the continuous decrease in the daily maximum irradiance. For our location the lower solar zenith angle is reached around 12:30 UTC. At this time total irradiance for days 4, 5 and 6 is 957, 908 and 899 W/m², respectively, and UV irradiance is 0.23, 0.20 and 0.19W/m².

Additionally, the attenuation of total and UV solar irradiance by desert aerosol has been quantified with its relative difference with respect to the irradiance measured on 4 August before the intrusion. Table 2 shows the daily average relative difference obtained for total and UV irradiance for each day of the episode. As can be observed, total irradiance decreased, on average, between 10 and 16%. For the UV irradiance the attenuation shows high variability ranging from 15 to 33%.

Table 2. Daily average relative difference for total and UV irradiance with respect to day 4 August.

	Total irradiance (%)	UV irradiance (%)
5 August	9.8	15
6 August	14.9	26.1
7 August	16.5	33.3

5 CONCLUSIONS

This study contributes to the identification of a Saharan dust event from 5 to 7 August 2005 over Cáceres station (Spain). This event has been detected by the analysis of different aerosol in-column radiometric properties, and the back-trajectories of the air masses carrying the aerosols. Monitoring total and UV solar irradiance measured at Cáceres station during this episode indicated a substantial decrease. The analysis of relative difference of irradiance with respect to values measured the 4 August (before the intrusion) shows a 10 to 16% decreasing, on average, in the total irradiance measured during this episode. The UV irradiance shows even higher attenuation with a notable variability ranging from 15 to 33%. This high attenuation emphasizes the important role of aerosols in the radiation balance of the Earth-atmosphere system.

ACKNOWLEDGMENT

This work was partially supported by the research project CGL2011-29921-C02-01/CLI granted by the “Ministerio de Economía y Competitividad” of Spain, Ayuda a Grupos GR10131 granted by Gobierno de Extremadura and Fondo Social Europeo. Thanks are due to AERONET/PHOTONS and RIMA networks for the scientific and technical support. CIMEL calibration was performed at the AERONET-EUROPE GOA calibration center, supported by ACTRIS under agreement no. 262254 granted by European Union FP7/2007-2013. The provision of the HYSPLIT model is due to the NOAA Air Resources Laboratory (ARL).

REFERENCES

- [1] J. M. Prospero, P. Ginoux, O. Torres, S. E. Nicholson, and T. E. Gill, “Environmental characterization of global sources of atmospheric soil dust identified with the NIMBUS 7 Total Ozone Mapping Spectrometer (TOMS) absorbing aerosol products”, *Rev. Geophys.*, vol. 40, no. 1, 1002, doi:10.1029/2000RG000095, 2001.
- [2] R. Arimoto, “Eolian dust and climate: relationship to sources, tropospheric chemistry, transport and deposition”, *Earth Sci. Rev.*, vol.54, pp.29-42, 2001.
- [3] V.E. Cachorro, C. Toledano, A.M. de Frutos, M. Sorribas, J.M. Vilaplana, and B. de la Morena, “Aerosol characterization at El Arenosillo (Huelva, Spain) with an AERONET/PHOTONS CIMEL sunphotometer”, *Geophys. Res. Abstract*, vol.7(08559), 2005.
- [4] C. Toledano, “Climatología de los aerosoles mediante la caracterización de propiedades ópticas y masas de aire en la estación El Arenosillo de la red AERONET”. PhD thesis, Universidad de Valladolid, Spain, 2005.
- [5] S. Rodríguez, X. Querol, A. Alastuey, G. Kallos, and O. Kakaliagou, “Saharan dust contributions to PM10 and TSP levels in Southern and Eastern Spain”, *Atmos. Environ.*, vol.35, pp.2433–2447, 2001.
- [6] X. Querol, S. Rodríguez, E. Cuevas, M.M. Viana, and A. Alastuey, “Intrusiones de masas de aire africano sobre la Península Ibérica y Canarias: mecanismos de transporte y variación estacional”, 3rd Asamblea Hispano portuguesa de Geodesia y Geofísica, Inst. Nac. de Meteorol. Esp., Valencia, 2002.
- [7] M. Escudero, S. Castillo, X. Querol, A. Avila, M. Alarcón, M.M. Viana, A. Alastuey, E. Cuevas, and S. Rodríguez, “Wet and dry African dust episodes over eastern Spain”, *J. Geophys. Res.*, vol.110, D18S08, doi:10.29/2004JD004731, 2005.
- [8] L. Alados-Arboledas, H. Lyamani, and F.J. Olmo, “Aerosol size properties at Armilla, Granada (Spain)”, *Q. J. R. Meteorol. Soc.*, vol.129, pp.1395-1413, 2003.
- [9] H. Lyamani, F.J. Olmo, and L. Alados-Arboledas, “Saharan dust outbreak over southeastern Spain as detected by Sun photometer”, *Atmos. Environ.*, vol.39, pp.7276-7284, 2005.
- [10] Elias, T., A.M. Silva, N. Belo, S. Pereira, P. Formenti, G. Helas, and F. Wagner, “Aerosol extinction in a remote continental region of the Iberian Peninsula during summer”, *J. Geophys. Res.* 111(D14204), 1–20, 2006.
- [11] V.E. Cachorro, R. Vergaz, A.M. de Frutos, J.M. Vilaplana, D. Henriques, N. Laulainen, and C. Toledano, “Study of desert dust events over the southwestern Iberian Peninsula in year 2000: two cases studies”, *Ann., Geophys.*, vol.24, pp.1-18, 2006.
- [12] Toledano, C., V.E.Cachorro, A.M. de Frutos, M. Sorribas, N. Prats, and B. de la Morena, “Inventory of African desert dust events over the southwestern Iberian Peninsula in 2000-2005 with an AERONET CIMEL Sun photometer”, *J. Geophys. Res.* 112 (D21201), 1–14, 2007.
- [13] Cachorro, V.E., Toledano, C., Prats, N., Sorribas, M., Mogo, S., Berjón, A., Torres, B., Rodrigo, R., de la Rosa, J., De Frutos, A.M.” The strongest desert dust intrusion mixed with smoke over the Iberian Peninsula registered with Sun photometry”. *J. Geophys. Res.* 113, D14S04, 2008, <http://dx.doi.org/10.1029/2007JD009582>.
- [14] Guerrero-Rascado, J.L., Ruiz, B., Alados-Arboledas, L. “Multispectral lidar characterization of the vertical structure of Saharan dust aerosol over southern Spain”. *Atmos. Environ.* 42, 2668–2681, 2008.
- [15] Wagner, F., Bortoli, D., Pereira, S., Costa, M.J., Silva, A.M., Weinzierl, B., Esselborn, M., Petzold, A., Rasp, K., Heinol, B., Tegen, I. “Properties of dust aerosol particles transported to Portugal from the Sahara desert”. *Tellus B* 61, 297–306, 2009.
- [16] Valenzuela, A., Olmo, F.J., Lyamani, H., Antón, M., Quirantes, A., Alados-Arboledas, L., “Analysis of the desert dust radiative properties over Granada using principal plane sky radiances and spheroids retrieval procedure”. *Atmos. Res.* 104–105, 292–301, 2012a, <http://dx.doi.org/10.1016/j.atmosres.2011.11.005>.
- [17] Díaz, J.P., Expósito, F.J., Torres, C.J., Herrera, F., Prospero, J.M., Romero, M.C., “Radiative properties of aerosols in Saharan dust outbreaks using ground-based and satellite data: applications to radiative forcing”. *J. Geophys. Res.* 106, 18403-18416, 2001.
- [18] Santos, D., Costa, M.J., Silva, A.M., “Direct SW aerosol radiative forcing over Portugal”. *Atmos. Chem. Phys.* 8, 5771–5786, 2008.

Obregón et al: TOTAL AND ULTRAVIOLET IRRADIANCE DURING A DESERT DUST EPISODE AT CÁCERES (SPAIN)

- [19] Antón, M., Sorribas, M., Bennouna, Y., Vilaplana, J.M., Cachorro, V.E., Gröbner, J., Alados-Arboledas, L., “Effects of an extreme desert dust event on the spectral ultraviolet irradiance at El Arenosillo (Spain)”, *J. Geophys. Res.*, 117, D03205, 2012a, doi:10.1029/2011JD016645.
- [20] Antón, M., Valenzuela, A., Cazorla, A., Gil, J.E., Fernández-Gálvez, J., Lyamani, H., Foyo-Moreno, I., Olmo, F.J., Alados-Arboledas, L., “Global and diffuse shortwave irradiance during a strong desert dust episode at Granada (Spain)”. *Atmospheric Research*, 118, 232-239, 2012b, doi: 10.1016/j.atmosres.2012.07.007
- [21] Valenzuela, A., Olmo, F.J., Lyamani, H., Antón, M., Quirantes, A., Alados-Arboledas, L., “Aerosol radiative forcing during African desert dust events (2005–2010) over Southeastern Spain”. *Atmos. Chem. Phys.*, 12, 10331–10351, 2012b. doi:10.5194/acp-12-10331-2012.
- [22] B. Holben, T.F. Eck, I. Slutsker, D. Tanre, J. Buis, K. Setzer, E. Vermote, J. Reagan, Y. Kaufman, T. Nakajima, F. Lavenu, I. Jankowiak, and A. Smirnov, “AERONET-A Federated Instrument Network and Data Archive for Aerosol Characterization”. *Remote Sens. Environ.*, vol. 66, pp.1–16, 1998.
- [23] R. Draxler, and G.D. Hess, “An overview of the HYSPLIT 4 modelling system for trajectories, dispersion and deposition”, *Aust. Met. Mag.*, vol.47, pp.295–308, 1998.
- [24] R. Draxler, and G. Rolph, “HYSPLIT (HYbrid Single-Particle Lagrangian Integrated Trajectory) Model access via NOAA ARL READY Website”, (<http://www.arl.noaa.gov/ready/hysplit4.html>), NOAA Air Resources Laboratory Silver Spring, MD, 2003.
- [25] O. Dubovik, B. Holben, T. Eck, A. Smirnov, Y. Kaufman, M. King, D. Tanré, and I. Slutsker, “Variability of absorption and optical properties of key aerosol types observed in worldwide locations. *J. Atmos. Sci.*, vol.59, pp.590–608, 2002.
- [26] Badarinath, K. V. S., Kharol, S. K., Kaskaoutis, D. G. and Kambezidis, H. D. "Case study of a dust storm over Hyderabad area, India: its impact on solar radiation using satellite data and ground measurements". *Sci. Total Environ.* **384**(1–3), 316–332, 2007.

Suitable altitude for detecting desert aerosol outbreaks in the Iberian Peninsula

Antonio Serrano¹, María Ángeles Obregón², and María Luisa Cancillo³

Abstract — This work focuses on the selection of the best altitude for detecting desert dust aerosols coming from Sahara and arriving at Cáceres station (Spain). Aerosols of this kind are particularly usual in the Iberian Peninsula due to the proximity of the Saharan Desert. These episodes last between one and three days and are characterized by a high number of coarse particles traveling mainly at high altitude. Since desert dust aerosols travel at high levels, 3000 m is generally selected as suitable arrival altitude for their detection by means of the analysis of back-trajectories. In the present study the suitability of 3000 m for identifying Saharan desert aerosols is analyzed in comparison with the performance obtained for other altitudes. For this aim, aerosol measurements obtained from the AERONET station at Cáceres and back-trajectories calculated by means of the HYSPLIT model are used. Main results indicate that altitudes between 2000 and 3700 m perform better than lower ones, with no specific value significantly better than other. Percentages of success achieved for altitude higher than 2000 m range between 56% and 70% of total cases.

Keywords — AERONET, aerosols, back-trajectory, desert dust, typical altitude

1 INTRODUCTION

One of the most interesting type of aerosol affecting Southern Europe and particularly the Iberian Peninsula is the desert dust aerosol coming from the Saharan Desert. This area in Northern Africa is an important source of aerosols for the whole Mediterranean region. Thus, events of dust desert aerosols irrupting into the Iberian Peninsula occur quite frequently driven by propitious synoptic conditions [1], [2], [3]. In principle, these episodes are most frequent during summertime [4], [5], when air masses from Northern Africa are favored to reach higher latitudes. These episodes last between one and three days. They are characterized by a high number of coarse particles traveling mainly at high altitude.

From the point of view of the ground-based remote sensing of aerosols, these episodes present concurrent high values of aerosol optical depth and low values of Ångström α coefficient (big size particles). In order to investigate the possible Saharan origin of such aerosols, a back-trajectory analysis is usually performed, inspecting those areas overpassed by the air mass at different altitudes. Since desert dust aerosols usually travel at high levels, the back-trajectory corresponding to arrival altitude of 3000 m is generally selected as suitable for their detection in the Iberian Peninsula [6], [7],

[8], [9]. Other studies focusing on Eastern Mediterranean region prefer the altitude of 4000 m for being more representative for this area [10], [11].

In the present study the suitability of the altitude of 3000 m for identifying Saharan desert aerosols outbreaks in the Iberian Peninsula by means of back-trajectory analyses is discussed in comparison with the performance obtained for other altitudes.

2 METHODS

For this aim, aerosol measurements achieved at the AERONET station at Cáceres (Spain), and air mass back-trajectories calculated by means of the HYSPLIT model are used.

The aerosol measurements correspond to radiometric variables as measured by sun-photometers CIMEL CE-318 installed at the station of Cáceres (Spain), with geographical coordinates 39°28'44" N, 06°20'34" W, and 397 m a.s.l. This station belongs to AERONET (Aerosol Robotic NETwork) and RIMA (Red Ibérica de Medida fotométrica de Aerosoles) networks since July 2005, and it is operated by the AIRE (Atmósfera, cIIma y Radiación en Extremadura) research group of the Physics Department of the University of Extremadura.

Radiometric measurements at 340, 380, 440, 500, 675, 870, 940 and 1020 nm wavelengths are routinely processed according to AERONET protocols [12], obtaining aerosol parameters at different quality levels (1.0, 1.5 and 2.0). The high-quality level 2.0 data are used in this study. The period of study spans from 2005 July to 2012 June. The long time series, encompassing almost seven years, ensures that a great variety of atmospheric conditions are sampled.

-
1. A. Serrano is with the Department of Physics, University of Extremadura, 06006 Badajoz, Spain. E-mail: asp@unex.es
 2. M. A. Obregón is with the Department of Physics, University of Extremadura, 06006 Badajoz, Spain. E-mail: nines@unex.es
 3. M. L. Cancillo is with the Department of Physics, University of Extremadura, 06006 Badajoz, Spain. E-mail: mcf@unex.es

Along this long period different sun-photometers have been operating at the station of Cáceres, with the following serial numbers: #341, #353, #243, #422, #411, and #382. They all have been periodically calibrated by AERONET/PHOTONS and its federated network RIMA according to their standard protocols.

Among all atmospheric conditions, 50 days were identified as corresponding to desert dust events and selected for the study. These cases were classified in aerosol types by means of the joint analysis of the magnitude and evolution of the aerosol optical depth (τ) and the Ångström α parameter. To be consistent with the back-trajectories, which are computed for 12:00 UTC, the classification was performed looking at the aerosol measurements nearest to 12:00 UTC. Since the study focuses on the typical traveling altitude of desert aerosols, the 50 selected days correspond to cases clearly identified as desert dust type and no doubtful cases were considered.

Subsequently, five-day (120 hours) back-trajectories were calculated for the selected days by means of the HYSPLIT4 model. The Hybrid Single Particle Lagrangian Integrated Trajectory Model (HYSPLIT) allows for computing air parcel trajectories, among other applications [13], [14], [15]. The most recent version 4 of the HYSPLIT model was used in this study. Meteorological data correspond to GDAS (Global Data Assimilation System) global reanalysis provided by NCEP (National Center for Environmental Prediction). The three-dimensional model option was used to calculate the vertical motion, as recommended by Martin et al. [16], Draxler [17] and Stohl [18].



Fig. 1. North Africa region source of desert dust aerosols.

Since the aim of this study is to analyze the suitable altitude for detecting desert aerosols, back-trajectories starting at 12:00 UTC for different arrival altitudes from 100 to 4000 m by steps of 100 m were computed. The back-trajectories for each arrival altitude were analyzed and cases were

identified as desert if, for the considered altitude, the air mass overpasses Northern Africa (Fig. 1) at any time within the last five days.

3 RESULTS

The analysis of the selected cases shows a notable variability in the altitudes where aerosols travel.

Fig. 2 shows the profiles for two example cases when the aerosols traveling altitudes significantly differ. These profiles have been built from the back-trajectories calculated for the 40 different altitudes. It must be noted that the altitude represents the arrival altitude of the air mass and not the actual

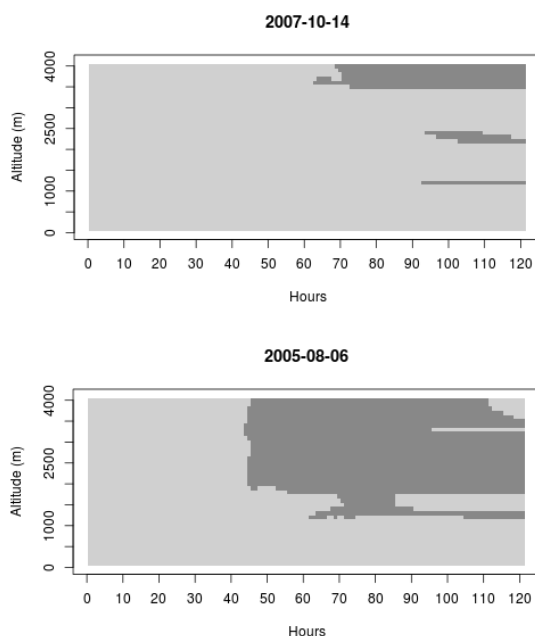


Fig. 2. Two cases of study corresponding to aerosol intrusions at very different arrival altitudes.

altitude of the air mass. The color indicates whether the air mass have overpassed the North Africa region (dark gray color) or not (light gray color).

Thus, the desert event detected at Cáceres station on 2005 August 6 corresponds to desert aerosols arriving at a wide range of altitudes above 1800 m, meanwhile on 2007 October 14 the desert aerosols arrived mainly at altitudes higher than 3500.

In this section, τ and α during these days have been analyzed in order to verify that they are desert dust episodes. Fig. 3 shows the time evolution of the aerosol optical depth at 500 nm and α Angström parameter during these two Saharan dust episodes occurring on 2005 August 6 and 2007 October 14. The aerosol parameters as measured by the Cáceres CIMEL during these dates and two days before and after have been represented. As can be seen, on 6

August there is an increase of τ from about 0.1 to 0.5 and a simultaneous significant decrease of α from about 1.2 to 0.5, with respect to the previous days. On 14 October τ increases from 0.1 to 0.3 and α decreases from 1.7 to 0.5.

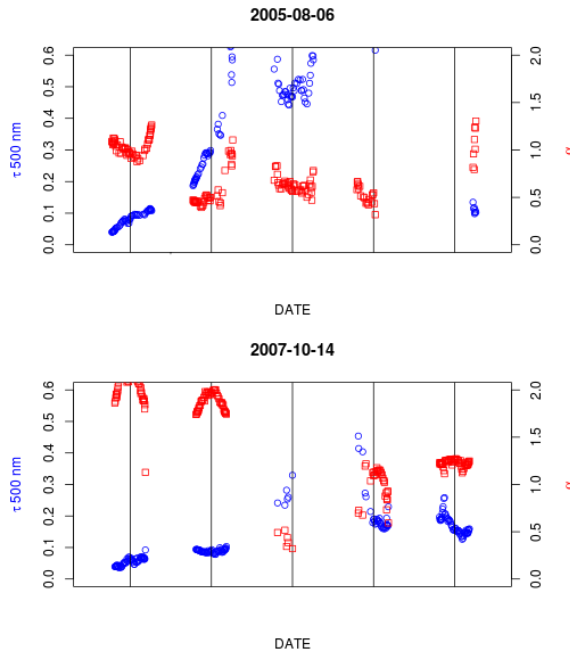


Fig. 3. Evolution of τ (at 500 nm) and α during two Saharan dust episodes.

Since desert dust aerosols travel at high levels, the altitude of 3000 m is generally selected as suitable for their detection by means of the analysis of their back-trajectory. The back-trajectories that finally arrive at 3000 m over the station during these two desert dust episodes are showed in Fig. 4.

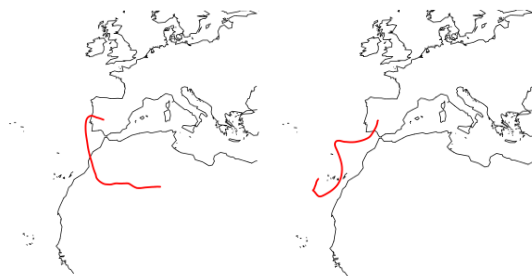


Fig. 4. Back-trajectories arriving at Cáceres station at 3000 m a.s.l. on 2005 August 6 and 2007 October 14, respectively.

As can be seen, the back-trajectory arriving at Cáceres on 2005 August 6 spent many hours over North Africa while the corresponding to 2007 October 14 does not overpass North Africa. These examples indicate the variety of aerosol traveling altitudes and suggest the study of the altitudes which best represent the travel of aerosols to Cáceres.

Fig. 5 presents the relative frequency (%) of the successful identification of desert cases based on each altitude.

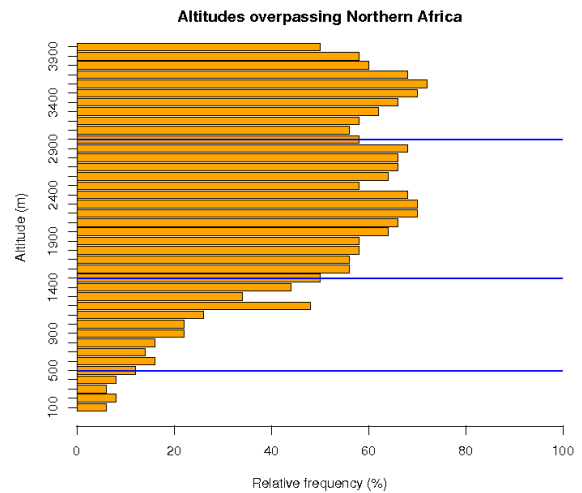


Fig. 5. Successful identification (%) of desert cases for each altitude and period threshold.

It must be noted that maximum values are lower than 72%. As it was expected, this success score is very low (less than 50%) for altitudes lower than 1500 m. For higher altitudes the success ranges from 56% to a maximum value of 72% obtained at 3600 m. Values higher than 70% are found for 2200, 2300, 3500 and 3600 m. The levels 500, 1500 and 3000 m (corresponding to 950, 850 and 700 hPa approximately) usually selected for aerosol classification are plotted with blue lines, showing success score of 12%, 50% and 58%, respectively.

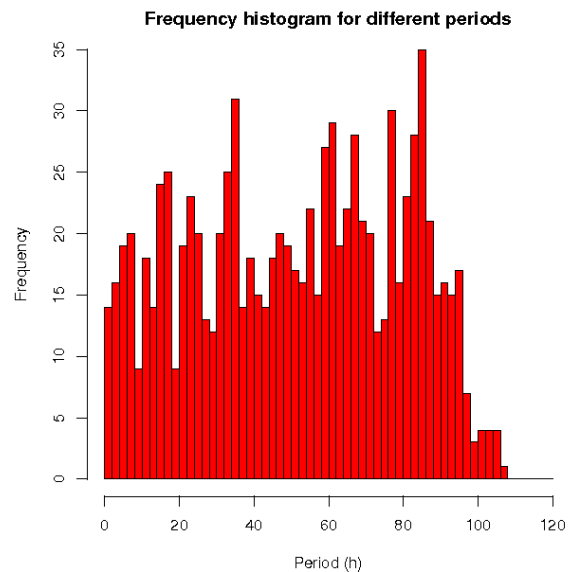


Fig. 6. Histogram of period spent over North Africa

region regardless the altitude considered.

The number of cases in regard to the time spent over North Africa region regardless of the altitude considered is shown in Fig. 6. It can be observed that the frequency rapidly decreases for periods longer than 95 hours. For lower periods the histogram shows a high variability with no preferred duration.

4 DISCUSSION AND CONCLUSIONS

The study conducted here provides interesting information about the attempt to identify desert aerosols events by means of the analysis of the back-trajectories of the air mass that arrives at a radiometric station at a certain altitude. The suitability of this approach and the selection of a proper altitude is analyzed. The need for this kind of study is stressed by several results, particularly by the two example cases presented in Fig. 2 and the low maximum success score (lower than 72%) shown by Fig. 5, showing the limits of this widely used approach.

Main results indicate that altitudes between 2000 and 3700 m perform better than lower ones, with no specific value remarkably better than other (Fig. 5).

The widely used altitude of 3000 m performs better (58%) than 1500 m (50%) and 500 m (12%) but not as well as it could be expected. In addition it performs a bit worse than other altitudes within the range 2000 – 3700 m. This fact should not be considered highly significant since there is a high variability in the performance score and the somewhat better values obtained by altitudes around 2200 and 3600 m could likely be due to the limited size of the sample of cases.

In general it can be said that no single altitude allows to successfully identify the desert aerosol events considered in this study. Even the best performance altitudes fail to identify nearly 30% of cases. This fact questions the suitability of the 3000 m unique altitude and suggest the proposal of other methodologies which consider not just one but a range of altitudes.

Regarding the time spent over the North Africa region a high variability is found (Fig. 6), with cases ranging from 1 to 95 hours over the area of interest. This result confirms that an efficient incorporation of desert aerosols into the air mass can happen in a short time.

The present results have implications for the methodologies used to identify the desert aerosols events based on the air mass trajectories. Thus, it has offered some evidences on the unsuitability of considering single altitudes for desert aerosols events detection and it has suggested directions for future research regarding the development of methodologies based the consideration of the complete profile.

ACKNOWLEDGMENT

This work was partially supported by the research project CGL2011-29921-C02-01/CLI granted by the “Ministerio de Economía y Competitividad” of Spain, Ayuda a Grupos GR10131 granted by Gobierno de Extremadura and Fondo Social Europeo. Thanks are due to AERONET/PHOTONS and RIMA networks for the scientific and technical support. CIMEL calibration was performed at the AERONET-EUROPE GOA calibration center, supported by ACTRIS under agreement no. 262254 granted by European Union FP7/2007-2013. The provision of the HYSPLIT model is due to the NOAA Air Resources Laboratory (ARL). J.A. García is acknowledged for his programming assistance.

REFERENCES

- [1] S. Rodriguez, X. Querol, A. Alastuey, G. Kallos, and O. Kakaliagou, “Saharan dust contributions to PM10 and TSP levels in Southern and Eastern Spain”, *Atmos. Environ.*, vol.35, pp.2433–2447, 2001.
- [2] X. Querol, S. Rodriguez, E. Cuevas, M.M. Viana, and A. Alastuey, “Intrusiones de masas de aire africano sobre la Península Ibérica y Canarias: mecanismos de transporte y variación estacional”, 3rd Asamblea Hispano portuguesa de Geodesia y Geofísica, Inst. Nac. de Meteorol. Esp., Valencia, 2002.
- [3] M. Escudero, S. Castillo, X. Querol, A. Avila, M. Alarcón, M.M. Viana, A. Alastuey, E. Cuevas, and S. Rodríguez, “Wet and dry African dust episodes over eastern Spain”, *J. Geophys. Res.*, vol.110, D18S08, doi:1029/2004JD004731, 2005.
- [4] V.E. Cachorro, C. Toledano, A.M. de Frutos, M. Sorribas, J.M. Vilaplana, and B. de la Morena, “Aerosol characterization at El Arenosillo (Huelva, Spain) with an AERONET/PHOTONS CIMEL sunphotometer”, *Geophys. Res. Abstract*, vol.7(08559), 2005.
- [5] C. Toledano, “Climatología de los aerosoles mediante la caracterización de propiedades ópticas y masas de aire en la estación El Arenosillo de la red AERONET”. PhD thesis, Universidad de Valladolid, Spain, 2005.
- [6] V. Estellés, J.A. Martínez-Lozano and M.P. Utrillas, “Influence of air mass history on the columnar aerosol properties at Valencia, Spain”, *Journal of Geophysical Research - Atmospheres*, vol. 112, D15, doi:10.1029/2007JD008593, 2007.
- [7] F.J. Olmo, A. Quirantes, V. Lara, H. Lyamani and L. Alados-Arboledas, L. “Aerosol optical properties assessed by an inversion method using the solar principal plane for non-spherical particles”, *Journal of Quantitative Spectroscopy and Radiative Transfer*, vol. 109, 8, pp. 1504–1516, 2008.
- [8] C. Toledano, V.E. Cachorro, A.M. de Frutos, B. Torres, A. Berjón, M. Sorribas and R.S. Stone, “Airmass classification and analysis of aerosol types at El Arenosillo (Spain)”, *Journal of Applied Meteorology and Climatology*, vol. 48, 5, pp. 962-981, 2009.

- [9] H. Lyamani, F.J. Olmo and L. Alados-Arboledas, L., “Physical and optical properties of aerosols over an urban location in Spain: seasonal and diurnal variability”, *Atmos. Chem. Phys.*, vol. 10, pp. 239–254, doi:10.5194/acp-10-239-2010, 2010.
- [10] G. Pace, A. di Sarra, D. Meloni, S. Piacentino and P. Chamard, “Aerosol optical properties at Lampedusa (Central Mediterranean). 1. Influence of transport and identification of different aerosol types”, *Atmospheric Chemistry and Physics*, vol. 6, pp. 697–713, 2006.
- [11] D.G. Kaskaoutis, P.G. Kosmopoulos, H.D. Kambezidis and P.T. Nastos, “Identification of the aerosol types over Athens, Greece: the influence of air-mass transport”, *Advances in Meteorology*, 15 pp., doi:10.1155/2010/168346, 2010.
- [12] B. Holben, T.F. Eck, I. Slutsker, D. Tanre, J. Buis, K. Setzer, E. Vermote, J. Reagan, Y. Kaufman, T. Nakajima, F. Lavenu, I. Jankowiak, and A. Smirnov, “AERONET-A Federated Instrument Network and Data Archive for Aerosol Characterization”. *Remote Sens. Environ.*, vol. 66, pp.1–16,1998.
- [13] R.R. Draxler and G.D. Hess, “Description of the HYSPLIT_4 modeling system”, NOAA Tech. Memo. ERL ARL-224, NOAA Air Resources Laboratory, Silver Spring, MD, 24 pp., 1997.
- [14] R.R. Draxler and G.D. Hess, “An overview of the HYSPLIT_4 modeling system of trajectories, dispersion, and deposition”, *Aust. Meteor. Mag.*, vol. 47, pp. 295-308, 1998.
- [15] R.R. Draxler, *HYSPLIT4 user's guide*, NOAA Tech. Memo. ERL ARL-230, NOAA Air Resources Laboratory, Silver Spring, MD, 1999.
- [16] D. Martin, G. Bergametti and B. Strauss, “On the use of the synoptic vertical velocity in trajectory model: Validation by geo-chemical tracers”, *Atmos. Environ.*, vol. 24, pp. 2059-2069, 1990.
- [17] R.R. Draxler, “Boundary layer isentropic and kinematic trajectories during the August 1993 North Atlantic Regional Experiment Intensive”, *J. Geophys. Res.*, vol. 101, pp. 29255-29268, 1996.
- [18] A. Stohl, “Computation, accuracy and applications of trajectories: A review and bibliography”, *Atmos. Environ.*, vol. 32, pp. 947-966, 1998.

Speciation of Metals in Refinery Emissions Particles

González-Castanedo Y.¹, Sánchez-Rodas D.A.¹, Ferrer C.¹, de la Rosa J.D.¹

Abstract —The total metal concentration in particulate matter has been widely used as a criterion to assess the possible effects on human health in industrial areas. However, this paper deals with speciation of particulate matter since all forms of a given metal emitted by an industry has not an equal impact on the environment. A sequential extraction procedure was applied to airborne emissions samples in order to evaluate the potentially most bio-available specie of the main metals (V, Cr, Co, Mo, La, Ce and Pb) emitted by the San Roque refinery complex (Spain). There is a great variation in the bioavailability of metalliferous particulate matter which depends on the size particle range and the industrial process considered. The results show that the refinery is a potent source of bioavailable Cr, V, La and Ce in fine and very fine particles which are deeply inhalable by the human body through the respiratory tract.

Keywords — metal bioavailability, particulate emissions, refinery

1 INTRODUCTION

The Bay of Algeciras (Spain), is a well documented industrial pollution hot spot, with relatively high concentrations of metals such as Ni, V, Cr and La in PM10 and PM2.5, being attributed to both industry [1] and shipping emissions [2].

These metals were identified in the cocktail of pollutants emanating from different emissions stacks from San Roque refinery complex located in the Bay of Algeciras by [3]. These metal release inevitably impact on the local ecosystem and surroundings populations. San Roque refinery complex lies in a densely populated area that includes two major towns, Algeciras (120,000 inhabitants) and La Linea (65,000 inhabitants), which lie 9 km apart and diametrically opposite each other on the SW and NE sides of the bay. The refinery has a capacity of 240,000 b/d (annual distillation of 12×10^6 tonnes of oil), making it the largest in Spain.

V and Ni are related to the refining of crude oil and processing of its downstream products in the petrochemical complex, while La is specifically used in the form of La-concentrates in fluid catalytic cracking unit (FCC) where cracking heavier crude oil distillation fractions into lighter compounds takes place [4].

The total metal concentration has been widely used as a criterion to assess the possible effects on human health. However, all form of a given metal has not an equal impact. The goal of this work is to evaluate the potentially most bio-available specie of the main metals emitted by the refinery (including V, Cr, Co,

Mo, La, Ce and Pb) located in the Bay of Algeciras. A chemical speciation scheme was applied to four different size particles emissions samples, from coarse ($>17 \mu\text{m}$) to very fine ($<0.33 \mu\text{m}$), in order to determine the chemical form available to the human body through the respiratory tract.

2 METHODOLOGY

Four steps Tessier sequential extraction procedure modified by [5] was applied to airborne emissions samples collected from the most polluting chimney stack emissions in the refinery complex: Sulpholane plant (106 m) where aromatic hydrocarbons are extracted from hydrocarbon mixtures, HDS unit (60 m), where catalytic removal of S from naphtha is carried out, and Fluid Catalytic Cracking (FCC) unit, where heavy fuels are cracked into lighter compounds and processed to form gasoline.

This speciation scheme determines the chemical form in which the metals are present: 1st step: soluble and exchangeable metals, 2nd step: carbonates, oxides and reducible metals, 3rd step: bound to organic matter, oxidizable and sulphidic metals and 4th step: residual metals. This paper show the first metallic fraction results so the dissolved metals in the first matrix (H_2O Milli-Q) are the most potentially toxic for the human health. The chemical speciation scheme was applied to four cut off stage diameter emissions samples (very coarse $>17 \mu\text{m}$, coarse 5-14 μm , fine 0.67-1.3 μm , very fine $< 0.33 \mu\text{m}$) from each stack in order to find a possible relation between size particle and bioavailability.

A portion of each filter was extracted with 15 ml H_2O Milli-Q (pH=7.4) using a shaker during 3 hours at room temperature. The final solutions obtained of

1. Unit CSIC-University of Huelva "Atmospheric Pollution", Center for Research in Sustainable Chemistry (CIQSO), Campus El Carmen s/n, University of Huelva, 21071, Spain

each extraction step, were analyzed by Inductively Coupled Plasma- Mass Spectrometry (ICP-MS). The analytical error was controlled and estimated by repeated analysis of NBS-1633a (fly ash) certified reference material. The error range for most elements was 5-10%. An unexposed filter and a reagent blank were analysed using the same procedure.

3 RESULTS AND DISCUSSION

The PM chimney stacks samples selected from the San Roque refinery are rich in metalliferous fly ash particles. Sulpholane stack emissions are characterized by high V, Cr content in particles with diameter $<0.33\mu\text{m}$. HDS unit emit high V concentration in particles with diameter $<14\mu\text{m}$ and Cr in particles with diameter $<0.33\mu\text{m}$. The FCC stack emissions are specially characterized by Cr in particles with diameter $<0.33\mu\text{m}$ and La in particles with diameters between 0.67 and $14\mu\text{m}$ (Table 1).

Table 1. Concentration ($\mu\text{g m}^{-3}$) and particle size (μm) distribution from Sulpholane, HDS and FCC particulate stack emissions. D_p : particle diameter (adapted from [3])

	D_p	V	Cr	Co	Mo	La	Ce	Pb
Sulpholane	>17	2.11	1.68	0.11	1.15	0.40	0.07	0.33
	5-14	15.0	42.0	1.44	5.17	1.66	0.80	0.34
	0.67-1.3	27.7	18.6	1.61	1.72	1.86	$<LD$	0.18
	<0.33	85.4	240	8.44	14.6	0.77	0.31	3.36
HDS	>17	9.02	0.45	0.58	$<LD$	3.10	0.31	0.07
	5-14	61.6	1.21	2.25	0.06	12.0	0.40	0.37
	0.67-1.3	85.2	1.38	4.38	0.38	1.54	0.11	1.14
	<0.33	106	211	7.15	19.2	0.57	0.07	1.49
FCC	>17	2.74	3.59	0.37	0.97	64.5	5.77	0.29
	5-14	9.68	21.8	2.04	1.72	175	15.8	0.67
	0.67-1.3	43.1	336	7.38	26.6	215	18.9	1.59
	<0.33	11.9	74.8	1.90	12.1	14.8	1.53	0.53

3.1 Metal bioavailability in Sulpholane stack emission samples

Co is the most bioavailable element emitted by this stack. The extraction rates were above 50% in all size fractions. Cr extraction rate was around 50% in coarse and fine fractions. Elements such as V, La, Ce (40%) and Mo and Pb (20%) were less bioavailable regardless of size fraction.

Fig. 1 shows the metal extraction obtained in H_2O Milli-Q matrix from Sulpholane stack emissions samples. The highest bioavailable concentration were Cr ($65.5\mu\text{g m}^{-3}$), V ($21.5\mu\text{g m}^{-3}$), Co ($9.17\mu\text{g m}^{-3}$) and Mo ($1.57\mu\text{g m}^{-3}$) in the very fine size fraction ($<0.33\mu\text{m}$). The concentration of the rest of the elements (La, Ce and Pb) was below $1\mu\text{g m}^{-3}$ in all size particles samples (Fig. 1).

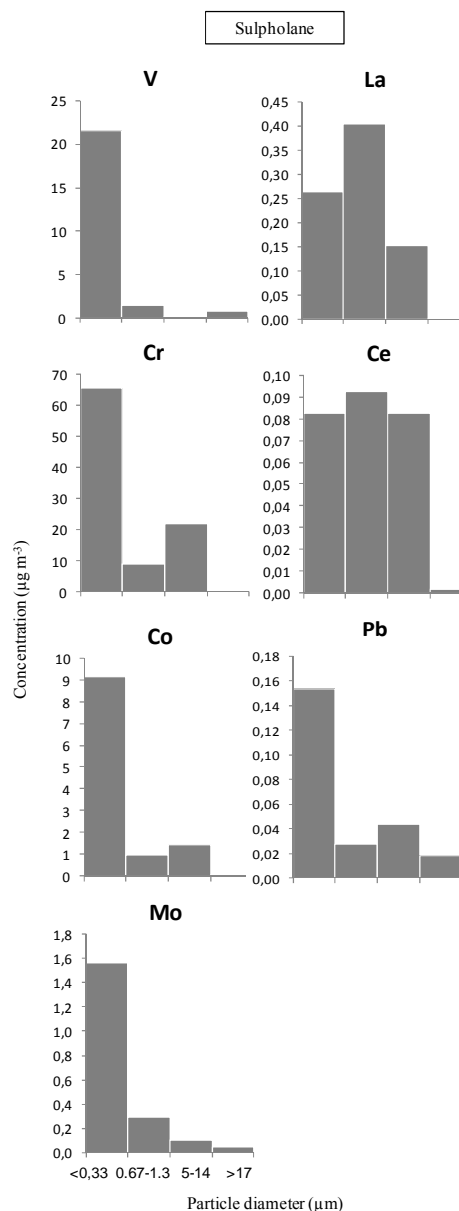


Fig. 1. Concentration ($\mu\text{g m}^{-3}$) and particle size distribution (μm) from Sulpholane stack emissions.

3.2 Metal bioavailability in HDS stack emission samples

The elements most bioavailable emitted during the HDS process are Co, Ce and V. Extraction percentages are greater than 50% in all size fractions except for Co and Ce in the coarse fraction and V in the finest size mode. Fig. 2 shows the metal concentration obtained in H_2O Milli-Q matrix from HDS stack emissions samples.

The highest bioavailable metal concentration in the HDS stack emissions were reached by Cr ($205\mu\text{g m}^{-3}$) in the very fine fraction and V in the fine size mode ($86.6\mu\text{g m}^{-3}$), coarse ($34.1\mu\text{g m}^{-3}$) and very coarse ($8.38\mu\text{g m}^{-3}$),

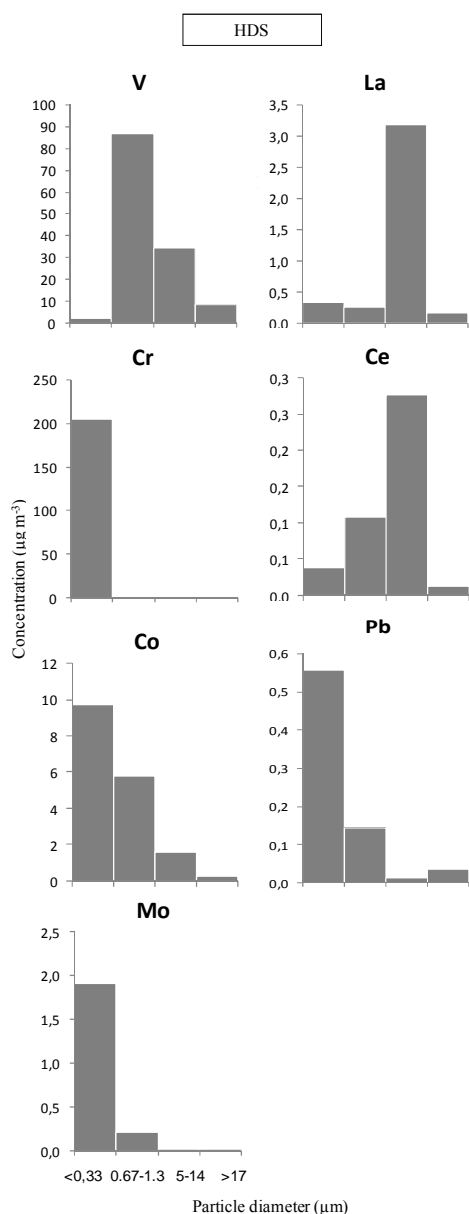


Fig. 2. Concentration ($\mu\text{g m}^{-3}$) and particle size distribution (μm) from HDS stack emissions.

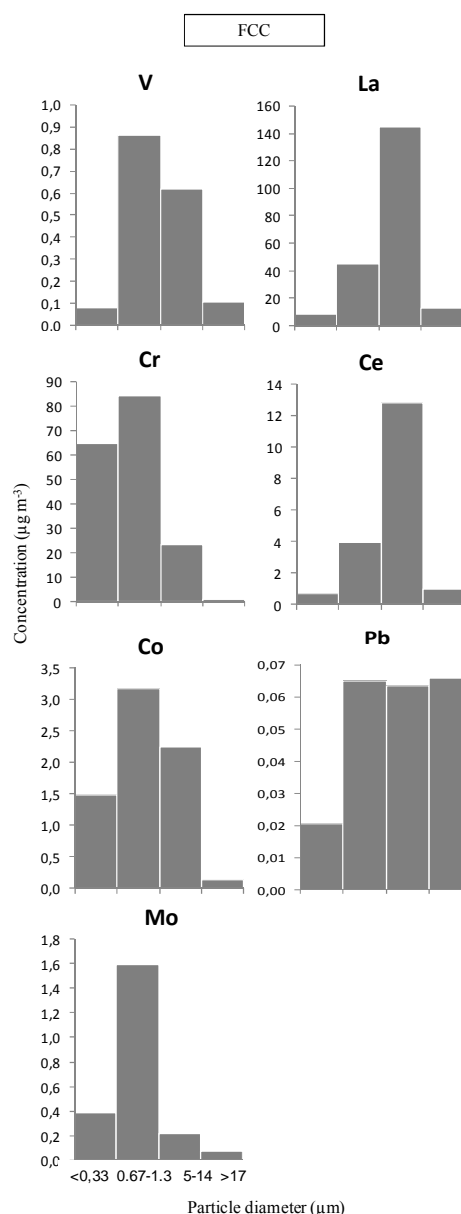


Fig. 3. Concentration ($\mu\text{g m}^{-3}$) and particle size distribution (μm) from FCC stack emissions.

3.3 Metal bioavailability in FCC stack emission samples

The higher extraction percentages were obtained in the coarse and very fine sized particles, for Cr, Co, La and Ce. The rest of the elements (V, Mo and Pb) were less bioavailable with extraction percentage lower than 20%, regardless of the particle size.

Fig. 3 shows the metal extraction obtained in H₂O Milli-Q matrix from FCC stack emissions samples.

Among the elements emitted by FCC stack, Cr, La and Ce are the most potentially bioavailable. The mean Cr concentration is high in the fine ($84.4 \mu\text{g m}^{-3}$), coarse ($23.3 \mu\text{g m}^{-3}$) and very fine ($64.5 \mu\text{g m}^{-3}$) size mode.

The highest bioavailable La concentration was obtained in the coarse ($144 \mu\text{g m}^{-3}$) and fine fraction ($44.8 \mu\text{g m}^{-3}$). The concentration in the rest of the size particles is lower ($8.78 \mu\text{g m}^{-3}$ in the fine fraction and $12.3 \mu\text{g m}^{-3}$ in the coarse fraction, Fig.3).

4 CONCLUSIONS

The bioavailability of the concentration of V, Cr, Co, Mo, La and Ce emitted during production processes called Sulpholane, HDS and FCC has been studied in the San Roque refinery. The study includes four sizes of particles, including very fine particles (< 0.33 μ m), emitted by three chimney stacks in order to assess their potential impact on human health.

All elements are more or less bioavailable since all of them are present in the first matrix of the sequential extraction procedure which corresponds to soluble and exchangeable metals. The extraction percentage obtained for each metal depends on the industrial process and size fraction considered.

The most bioavailable elements are Cr, V, La and Ce. The bioavailable Cr content is mainly emitted by FCC and HDS chimney stacks. The highest concentrations of bioavailable La and Ce are emitted during the FCC process. The highest concentration of V into exchangeable fraction is mainly emitted by the HDS focus and to a lesser extent the Sulpholane source. The elements Co, Mo and Pb are poorly bioavailable. Considering the size distribution of the particles emitted, it is noteworthy to highlight:

-The high concentration of bioavailable Cr obtained in fine and very fine particles emitted by HDS and FCC process.

- The high concentration of V emitted by the Sulpholane chimney stack in very fine particles and by the HDS focus in coarse and fine size particles.

- The high concentration of La obtained in the emission samples from the FCC process in coarse and fine size particles.

The metal release, Cr, V, La and Ce specially, in fine and very fine particles during the refinery process studied are a risk due to its toxic potential effect to human health and its high capacity to be inhaled and absorbed by the body.

ACKNOWLEDGMENT

This work was funded by the Projects 2007-RNM027329 and 2011-RNM7800: Department of Innovation Science and Enterprise, Andalusian Autonomous Government and the Project CGL2011-28025: Spanish Ministry of Science and Innovation (MINECO).

REFERENCES

- [1] de la Rosa J.D., Sánchez de la Campa A.M., Alastuey A., Querol X., González-Castanedo Y., Fernández-Camacho R., Stein A.F., 2010. Using PM10 geochemical maps for defining the origin of atmospheric pollution in Andalusia (Southern Spain). *Atmospheric Environment*, 44, 4595-4605.
- [2] Pandolfi M., Gonzalez-Catanedo Y., Alastuey A., de la Rosa J.D., Mantilla E., Querol X., Pey J., Amato F., Moreno T. Source apportionment of PM10 and PM2.5 at multiple sites in the Strait of Gibraltar by PMF: impact of shipping emissions. *Environmental Science Pollution Research*, 18, 260-269.
- [3] Sánchez de la Campa A.M., Moreno T., de la Rosa J.D., Alastuey A., Querol X., 2011. Size distribution and chemical composition of metalliferous stack emissions in the San Roque petroleum refinery complex, southern Spain. *Journal of Hazardous Materials*, 190, 713-722.
- [4] Moreno T., Querol X., Alastuey A., de la Rosa J., Sánchez de la Campa A.M., Minguillón M., Pandolfi M., González-Castanedo Y., Monfort E., Gibbons W., 2010. Variations in vanadium, nickel and lanthanoid element concentrations in urban air. *Science of the Total Environment*, 408, 4569-4579.
- [5] Fernández Espinosa A.J., Ternero M., Fernández F., Gutiérrez A., Trigo D., 2006. Chemical speciation of trace metals in fine airborne particles: advances in operational performance of a new sequential extraction scheme. *Inter. J. Environ. Anal. Chem.* 86, 641-651.

Particle Emission from the Aircraft Engine Testing Cycles

J.J. Rodríguez-Maroto¹, V. Archilla², D. Sanz-Rivera¹, E. Rojas-García¹, M. Pujadas¹,
J.L. Mosquera¹, D. Mercader², A. Gonzalez² (ISDEFE), A. Jimenez², A. Entero² (ISDEFE),
J. Mena², J.M. Fernández-Mainez¹ and J.C. Bezares¹

Abstract — Present work shows the results of a study on emission of particulate matter (PM) during a series of tests carried out in the Turbojet Engine Test Centre of INTA. Engines are subjected to different operation cycles in which the power delivered by the engine is varied. The measurements were performed in the facility stack. The hot gas from the engine goes through an exit conduct where the emissions (gas and particles) are mixed with ambient air sucked from the test cell by exhaust gas flow, resulting in its dilution and cooling. These phenomena are able to alter the original emission, given its high sensitivity, to change physical-chemical properties, bringing them closer to the ones that will produce the real environmental impact at local level. Given the geometric complexity of the exit conduct and stack, numerical flow simulations were performed before choosing the sampling point. There, an aerosol sample was extracted and both particle concentration and size distribution were simultaneously measured and continuously recorded. The temporal evolution of the concentration and distribution of particle sizes reflect the evolution of the power delivered by the engine. Some statistical parameters of particle size distribution vary in the same way as the applied power. Submicron particles size distribution is bimodal, with two modes found in 25 nm and 50 nm. Depending on the power applied to the engine, both of them are present or one of them prevails, becoming a monomodal size distribution. INTA may be converted into a useful Platform to enabling assessment of the environmental impact from aircraft engine at local and regional levels

Keywords — aircraft, engines, turbofan, emission, particles, PM, turbojet testbed, combustion

1 INTRODUCTION

The global effects of aircraft particulate matter emissions (PM) are a key concern from the point of view of human health and climate change. The most significant effect of these types of emissions is at ground level where they have an important influence on air quality in areas close to airports, but there are also potentially high altitude effects that are a focus of scientific research. Although a significant effort is being made to identify, quantify, simulate and predict these effects, at present, no appropriated method exists for its objective evaluation yet. At the moment, it seems reasonable that some fundamental parameters for characterization of PM (such as mass and number size distribution and concentration) will be useful in the standardized test under engine certification conditions.

The Aircraft Engine Test Facilities allow the assessment of some of the environment impacts from aircraft engine at local and regional levels. During the tests, engines are subjected to different operation cycles in which the power delivered by the engine is varied. The engines certification protocol proposed by the International Civil Aviation Organization (ICAO) considers the following power

points named takeoff (100%), climb-out (85%), approach (30%), and idle (7%). All the pollutants emitted (gases and particles) can be known close to the point where they are generated, which is of great interest for engine manufacturers. Moreover, they can be also assessed after dilution in air, which is very interesting from the environmental point of view.

This paper details the emission measurements from the Turbojet Engine Test Centre, (CET) located in INTA (National Institute for Aerospace Technology) during a campaign on a large turbofan aircraft engine. For these measurements, a first prototype of particle sampling and measurement system was used, which is located in the exhaust stack of the facility, where emissions are already diluted. Although the results reflect the evolution of the concentration and size distribution of particles emitted during the test cycles of the aircraft engine, numerous gaps exist about of its behavior with the variations in test and sampling conditions.

2 MATERIALS AND METHODS

2.1 INTA/Turbojet engine Test Centre (CET)

Before being put into service, an aviation engine is subjected to an exhaustive testing process that guarantees its perfect operation. INTA has one of the most advanced installations in the world for testing aircraft engines, whilst also cooperating with

1. Environment Department, CIEMAT, Ave. Complutense 40, Madrid, Spain, jesus.maroto@ciemat.es

2. Turbojet Test Centre (CET), INTA, Ctra. Torrejón-Ajalvir, Km. 4, Torrejón de Ardoz, Spain, archillapv@inta.es

companies for developing commercial engines, and participating in the R&D Frame-work programme of the European Union for studying and developing new generation engines (higher power/efficiency ratios, and less contamination including acoustic contamination). The INTA test cell is an indoor jet engine test stand, with a 14.5 meters cross-section test chamber and being 114 meters in length, Figure 1.

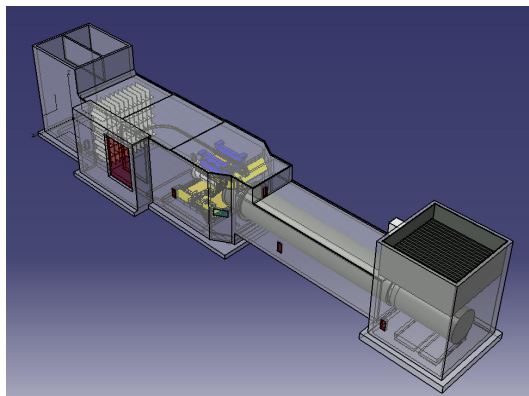


Fig. 1. INTA/Turbojet engine Test Centre.

Key features of the facility include; acoustically treated air intake and exhaust stack (22 meters height), 60 meters length test cell (14.5 meters cross-section), exhaust collector (“detuner”, 48 meters length) and exhaust diffuser (basket).

When the engine is on test, the turbofan engine has a large fan at the front, which sucks in air required for the combustion process from the intake chimney. Most of the air flows around the outside of the engine, making it quieter and giving more thrust at low speeds. Most of today's airliners are powered by turbofans. In a turbojet all the air entering the intake passes through the gas generator, which is composed of the compressor, combustion chamber, and turbine. In a turbofan engine only a portion of the incoming air goes into the combustion chamber. The remainder passes through a fan, or low pressure compressor, and is ejected directly as a "cold" jet or mixed with the gas-generator exhaust to produce a "hot" jet. The objective of this sort of bypass system is to increase thrust without increasing fuel consumption. It achieves this by increasing the total air mass flow and reducing the velocity within the same total energy supply. Then, the emission gases, which comes from the “hot” jet (primary flow), are mixed with the “cold” jet (secondary flow) and the facility flow and expelled into environment through the “detuner” which ends in the basket and the stack (14.5 x 14.5 meters section).

2.2 Sampling Point

Emissions, after crossing "detuner", go through a perforated cylinder ("basket") before leaving by the stack. This “basket” contributes to addressing the

flow of emission.

Additionally, a series of soundproofing panels exist in the stack exists at a height of about 16 m. The sampling point was selected to that height, where it is supposed there is more possibility that the flow is more developed. In this section the sampling point was fixed from a simulation using ANSYS 12.1 version program, and a machine Blade Work-station with 24 GB of RAM. For calculations, it was considered a generic engine (a large turbofan), to which is applied a maximum power of 95%, and assuming an ideal incompressible gas.

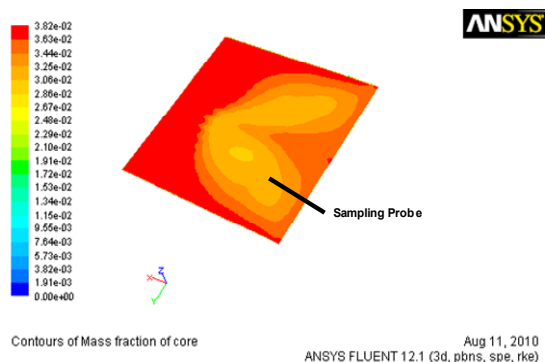


Fig. 2. Mass fraction distribution in a section of stack

Calculations show that the flow distribution is neither homogeneous nor symmetrical in the section. Therefore, for choosing the coordinates of the sampling point, structural and logistic dispositions in the installation were considered. Moreover, the localization was selected where the calculated local particle mass fraction was as close as possible to the mean value in the stack cross section (Figure 2).

2.3 Sampling and Measurement Station

The sampling station is located at 16 m above the ground level, over a structure of 5 m high on the “detuner” and right beside the stack. The structure is fixed through appropriate anchors and anti-vibration systems.

The sampling system basically consists of a seamless stainless steel probe (3.5 m long) with a probe inlet, pointed to the flow, which consist of a conical calibrated orifice of 0.635mm in diameter, where the flow around the inlet is unrestricted without any obstructions affecting the air flow in the vicinity of the probe. A control unit for automatic sampling, a system of aerosol sample dilution with two ejector type diluters (VKL 10E, PALAS), two particle measuring devices: condensation particle counter, (3022CPC, TSI) and a measure system by electrical mobility, (3934SMPS, TSI) to determine the particle size distribution and other additional devices for control and data acquisition (Figure 3).

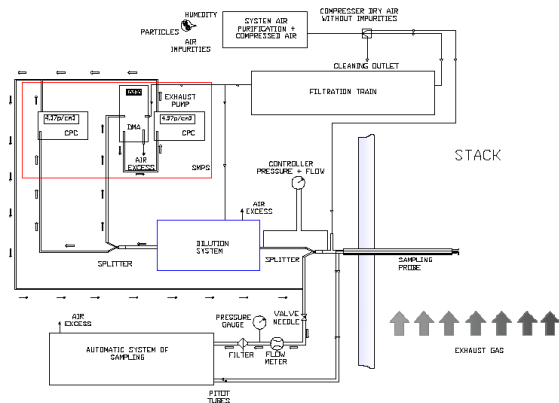


Fig. 3. Particle sampling and measurement system

Aerosol sample is extracted from the stack and a part of the same is diluted up to 100 times, being the rest of sample collected on filters or substrates for later physical-chemical analysis. The diluted sample is divided through splitter into two samples to simultaneously determine the concentration of particles and size distribution. The response of the CPC is fast enough to measure the concentration during the transient test cycles. However, the response time of SMPS (longer than 1 min.) requires measurements to be performed only during long enough stationary periods of the cycle.

2.4 Procedure

Environmental emission measurements in the stack of INTA/Turbojet engine Test Centre were performed, while a large Rolls-Royce turbofan engine was being tested. All tests used a fuel type JET A-1. "Standards" values for this fuel are:

Table1. Main characteristics of the Fuel

JET A-1	
Kinematic viscosity at 20°C	1.563-1.639 mm ² /s
Density at 15 °C	0.7962-0.7965 kg/L
Smoke Point	25.0-26.0 mm
Naphthalene Content	0.40-0.42 % v/v
Sulphur	11-39 mg/kg
Hydrogen Content	13.8 % m/m
Aromatics	17.8-19.6% v/v
Heat of Combustion	43.189-43.233 MJ/kg
Distillation	
Flash Point	153.8-154.3 °C
10% recovered	165.1-166.3 °C
20% recovered	170.2-172.0 °C
50% recovered	188.9-191.3 °C
90% recovered	229.6-231.2 °C
Final Point	250.7-251.7 °C
Residue	1.2-1.3 % v/v
Loss	0.5-0.6 % v/v

3 RESULTS AND DISCUSSION

3.1 Particle number concentration

It is current belief that volatile particles do not exist at "hot" engine exit, and the PM generated by aircraft are composed of non-volatile particles (soot), but owing to the sampling point is located at some distance from the engine exit, the measurement system is measuring non-volatile particles that exist at engine exit conditions and volatile particles that form downstream from the condensable gases because of the fact that the "hot" engine exit mixes and cools when diluted by the engine bypass and entrained air around the engine.

Although the sampling point is located in the stack at some distance from the source of emission, and there is also a dilution and cooling of exhaust gases, changes in the power applied to engine are detected from PM measures carried out. The evolution of engine test cycles is reflected through the measurement of the particle emission concentrations.

The emission factor (index) has been regarded as amount of particles by fuel consumption. The emission index expressed as particles by kg of fuel is a parameter used by engine manufacturers and it can facilitate the comparison among different engines, fuels, test cycles and test facilities (Figure4).

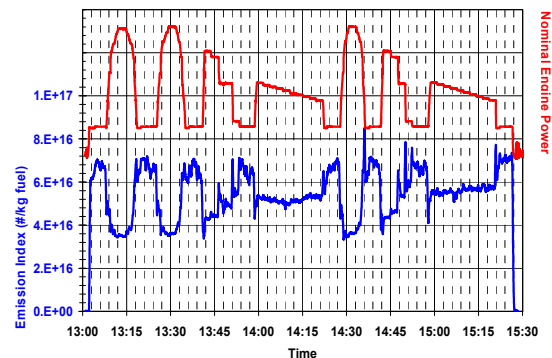


Fig. 4. Evolution of particle emission index during a test

The emission index varied during the test from 4×10^{16} (particles/kg of fuel) at high power up to 8×10^{16} (particles/kg of fuel) at low power. The emission index evolves in a manner contrary to as the power of the engine, i.e. an increase in power represents a decrease of the emission index, in accordance to the result of Kinsey et al, [1] The best efficiency of the combustion in the highest regimes would justify the least amount of particles despite a greater fuel consumption.

When the parameter used to characterize the emission is the concentration of particles expressed as mass/volume, two different behaviours are observed. The evolution is sometimes parallel to that of the cycle of power (figure 5) and other times contrary. Usually, the smoke number increases with

higher engine power output [2], the same as the particle mass [3], [4]. However, the contrary effect has been found when measured away from engine exit [5]. Some studies have reported a decrease in particle concentration with increasing engine power beyond the stage point of the engine [6].

The maximum concentration of particles during test operation engine was of approx. 3×10^7 (particles/cm³), about four orders of magnitude higher than the air particle concentration.

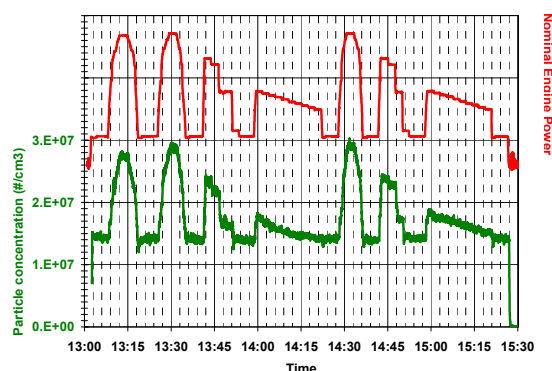


Fig. 5. Evolution of particle concentration during a test, (corresponding to the same test as Figure4)

The exhaust gas flows directly from the combustion chamber from the engine and represents the emission primary flow. This flow joins with a secondary flow constituted by air from the turbo fan; both having their origin in the engine. But at the INTA / Turbojet engine Test Centre, we have to consider a third flow due to the configuration of the test cell, made up of drag air when the engine is running. The secondary and the third flows constitute an air dilution of the emission from the engine.

As a consequence, it is considered that the concentration measured corresponds to an emission diluted, with a factor of dilution which varies along the test cycle because it is engine power dependent, and is different for each engine. Since the sample point is installed in the stack of the facility, some additional emissions need to be taken into account. In normal engine operation, the engine vent and drain system collects and discharges drain fluids, or air, overboard Breather air, containing oil mist, is discharged at high velocity from a nacelle of a gas turbine engine through an exhaust port (breather outlet / drain mast) at the surface of the nacelle. These flows will condense on particulate matter at the stack and its contribution would be added in the readings. Future tests will be focussed on the characterization of lubrication oils emitted from the breather outlet in the exhaust.

As mentioned previously, discrepancies in the results obtained in terms of the evolution of the concentration have been observed. Sometimes the trend of the results coincides with the power rate and sometimes it does not. Some explaining hypotheses

have been identified. First, the flow velocity "profile" in the corresponding sampling stack's cross section may vary depending on engine power (i.e. flow rate). In our case this problem is exacerbated by the non-symmetrical and two-dimensional nature of the flow. Also, the dilution that occurs by the drag of the engine into the stack may affect the results. Or, finally, the process of measurement itself may be affected by the change in pressure at the point of sampling caused by variation of engine power, which can breakdown sample flow rate. All these effects will require a further investigation.

3.2 Particle size distribution

A size distribution skewed with a long tail to bigger sizes has been observed. The biggest particles have a size lower than 600 nm considering electric mobility diameter. Size distributions generally have two modes which coincide with typical nucleation and accumulation modes, in 20-30 and 40-50 nm, predominating one or the other depending on the power applied to engine. Increasing power of engine makes the smaller size mode decrease and larger size mode increase and vice versa. In such a way that at high or low applied engine power the size distribution become a monomodal distribution (Figure 6).

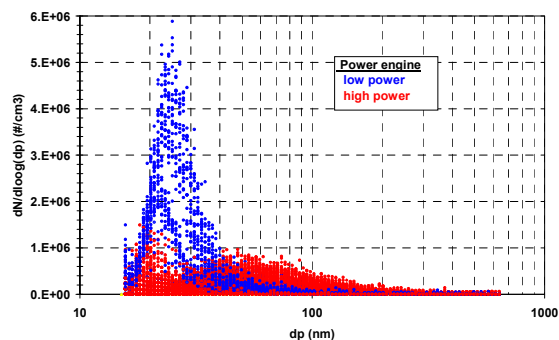


Fig. 6. Particle Size Distribution

When the engine power was increased, the accumulation mode was found to be dominant and nuclei was not significant, while if it was decreased then the main mode was the nuclei one, in accordance with other studies, [6], [7], [8] and [9] in which smaller particles are found at lower engine power output, all of them measured in test beds and next to airport courses.

Results show that the changes in engine power produced variation in the size of the particles. A likeness in the evolutions of the different statistical parameters has been observed typical of the size distribution: mode, median, mean, geometric mean against the power curve of the test cycle. Mode (most frequent diameter) presented values in operation cycles from 20 nm to minimum power to 70 nm at maximum power. Median (diameter for which half total number of particles are larger and

half smaller) varied between 20 nm (low power) and 80 nm (high power) in all tests. Mean or arithmetic average diameter changed since 25 to 90 nm and finally the geometric mean was 25–70 nm. (Figure7).

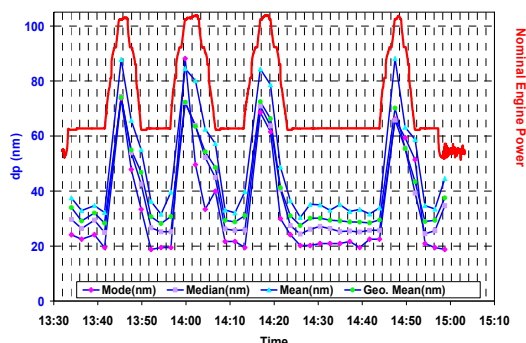


Fig.7. Evolution of statistics parameters and the engine power applied

At present, after the preliminary chemical analysis by SEM/EDX of the particles collected, the presence of some chemical elements has been confirmed. These include C, K, Cl, O, Na, Si, S, K, Fe, etc. Also the PAHs (polycyclic aromatic hydrocarbons), has been analysed by liquid chromatography. The most significant PAHs were naphthalene amount of 20 ppm and phenanthrene approx, 5 ppm, benz(a)pyrene about 3 ppm and the rest (acenaphthene, fluorene, anthracene, fluoranthene, pyrene, benz(a)anthracene, chrysene, benz(b)fluoranthene, benz(k)fluoranthene, dibenz(a)anthracene, benz(ghi)perylene, indeno [1,2,3-cd]pyrene) were present in a concentration of less than 2ppm.

4 CONCLUSIONS

A series of measurements of particulate emissions from turbojet engine testing cycles were made at the INTA facility and from results obtained it is showed that:

-Despite the distance from the exhaust to the sampling point the testing cycles of power applied to the engine are faithfully reflected for the evolution of particulate emissions.

-The measurement system seems appropriate to characterize emissions of particles in this facility and will be subject of future developments, to carry out a global characterization.

-Due to the non-volatile and volatile nature of the particles measured by the probe, the measures made in the output stack of the facility assume a valuation closer to the current environmental impact. These measures could be comparable to that make in the same engine exhaust, allowing additional studies in the emissions, in the evolution of the volatile particles and in the new particle formation and growth.

-The environmental and human health issues associated with submicron particulate matter emissions require more detailed measurement of the mass, size and quantity of these particle emissions. INTA/Turbojet engine test Centre is modern facility which seeks effective systems to measure and characterize pollutant emissions in the most relevant measurement plane closest to the environment.

-Endurance testing allows measurements in the different phases on current airport activities (approach, taxi, take off and climb-out). CET could be a strategy platform to enable assessment of the environmental impact from aircraft engines at local and regional levels in order to encourage better decision-making.

ACKNOWLEDGMENT

This work was supported by INTA and CIEMAT into Framework Agreement for collaboration, to make CET/INTA a Strategic Platform to allow assessment of the environmental impact.

REFERENCES

- [1] J. S. Kinsey, Y. Dong, D. C. Williams and R. Logan. "Physical Characterization of the Fine Particle Emissions from Commercial Aircraft Engines during the Aircraft Particle Emissions Experiment (APEX) 1-3". Atmospheric Environment 44, 2010, pp2147-2156.
- [2] EPA. "Air Pollutant Emission Factors for Military and Civil Aircraft". 1978, EPA-450/3-78-117.
- [3] D.E. Hagen, P. Lobo, P.D. Whitefield. "Physical Characterization of PM Emissions from In-Service Commercial Gas Turbine Engines—Projects APEX and JETS APEX2". Proceedings of the TAC-Conference, June 26 to 29, 2006, Oxford, UK, pp 247-251.
- [4] S.C. Herndon, T.B. Onasch, J.T. Jayne, E.C. Wood, P.E. Yelvington, J. Wormhoudt, M.J. Northway, P. Mortimer, D.R. Worsnop, M.S. Zahniser, D.D. Nelson, J.H. Shorter, J.B. McManus, R.C. Miake-Lye, L.C. Marr, B.E. Anderson, C.L. Wey and P.D. Whitefield. "Aircraft Emissions Characterization". Proceedings of the TAC-Conference, June 26 to 29, 2006, Oxford, UK, pp 252-255.
- [5] R.C. Miake-Lye, E.C. Wood, M.T. Timko, Z. Yu, S.C. Herndon, B. Lee, G. Santoni and W.B. Knighton. "Effects of Alternative Fuels on Hydrocarbon and Particle Emissions from Aircraft Engines". TAC-2 Proceedings, June 22nd to 25th, 2009, Aachen and Maastricht, pp26-32.
- [6] A Crayford & M Johnson. "SAMPLE III. Contribution to aircraft engine PM certification requirement and standard. First Specific Contract-Final Report". EASA. 2010/FC10 SC01. 2011, pp163.
- [7] P. Lobo, D.E. Hagen, and Ph.D. Whitefield. "Comparison of PM Emissions from a Commercial Jet Engine Burning Conventional, Biomass, and Fischer Tropsch Fuels". Environ. Sci. Technol. 2011, 45, pp10744–10749.
- [8] R. Marsh, A. Crayford, A. Petzold, M. Johnson, P. Williams, A. Ibrahim, P. Kay, S. Morris, D. Delhay, D. Lottin, X. Vancassel, D. Raper, S. Christie, M. Bennett, M. Miller, Y. Sevenco, C. Rojo, H. Coe, P. Bowen. "Studying, sampling and measurement of aircraft particulate emissions II .SAMPLE II. Final report." EASA. 2009/4. 2011, pp153.
- [9] P.D. Whitefield, P. Lobo, D.E. Hagen. "PM Emissions from Advected Aircraft Plumes at the Oakland International Airport". Proceedings of the TAC-Conference, June 26 to 29, 2006, Oxford, UK, pp95-100.

Optical Properties of Saharan Dust Aerosols, Sea Spray and Cloud Droplets from AMISOC-ARN 2012 airborne campaign

Javier Andrey¹, Arturo Quirantes², Neves Soane-Vieira³, Francisco José Olmo⁴,
Lucas Alados-Arboledas⁵, Benito de la Morena⁶, Manuel Gil-Ojeda⁷

Abstract – In the frame of AMISOC-ARN project an airborne campaign was held at "El Arenosillo" sounding station in the south-west of the Iberian Peninsula. Three vertical profiles were developed by the INTA C212 atmospheric research aircraft characterizing aerosol size distribution and scattering properties among other parameters. Scattering cross sections measured by a CAS-DPOL optical particle counter have been used as input data for a new refractive index retrieval algorithm. Preliminary results from this algorithm show a good agreement with the different kind of aerosols sampled during the campaign. The uncertainties of the algorithm are lower for particles above 5-8 μm , finding its maximum magnitude for particles in the range from 1 to 3 μm .

Keywords – Airborne measurements, Refractive index, Size distribution, Tropospheric aerosols

1 INTRODUCTION

The largest uncertainty in estimating the Earth radiative balance is caused by aerosols [1]. Aerosols affect the solar radiation by scattering and absorption processes. The impact of each aerosol type on radiation depends in factors such as refractive index or particle shape.

In-situ characterizations of tropospheric aerosols provide valuable information about the state of these particles in the free troposphere. These characterizations require the use of airborne instrumentation on-board balloons or airplanes. The Spanish National Aerospace Technique Institute (INTA) owns an atmospheric research aircraft instrumented with different optical particle counters (OPC) devoted to the measurement of cloud and aerosol size distribution (SD). This kind of instruments is based on analyzing the scattered radiation at given directions and sizing the particles by using Mie theory.

In order to get the correct aerosol size with an OPC, a value for the particle refractive index must be assumed to carry out the corresponding Mie computations. The detection of the light scattered by one particle at different directions simultaneously allows to retrieve the aerosol refractive index of this particle. This procedure prevents making assumptions about this index, in order to get the correct size of the aerosol.

During late May and June of 2012, INTA carried out an airborne campaign in the frame of AMISOC (Atmospheric Minor Species relevant to the Ozone Chemistry at both sides of the subtropical jet) at "El arenosillo" sounding station (ARN) in the south of the Iberian Peninsula (IP). Several measurements of different gases and aerosols were carried out both on-board INTA aircraft and ground level, being this work focused in the CAS-DPOL (Cloud Aerosol Spectrometer with Depolarization Option) instrument, mounted on the aircraft. The latter provides measurements of scattered radiation in forward and backward directions for single particles. This combination of measurements allows to retrieve the real part of aerosol refractive index. Particle asphericity can also be derived by using an empirical approach based on three signals registered by the probe: forward, backward and polarized backward.

In this work, measurements from AMISOC-ARN campaign measurements are shown. These data are used to validate an algorithm devoted to retrieve the refractive index of aerosol particles sampled CAS-DPOL instrument.

¹J. Andrey is with the Spanish National Aerospace Technique Institute (INTA), email: javier.andrey@gmail.com

²A. Quirantes is with the Andalusian Center for Environmental Research (CEAMA) and the Department of Applied Physics of Granada University (UGR), email: aquiran@ugr.es

³N. Soane-Vieira is with the Spanish National Aerospace Technique Institute (INTA), email: nevessoane@gmail.com

⁴F.J. Olmo is with the Andalusian Center for Environmental Research (CEAMA) and the Department of Applied Physics of Granada University (UGR), email: fjolmo@ugr.es

⁵L. Alados-Arboledas is with the Andalusian Center for Environmental Research (CEAMA) and the Department of Applied Physics of Granada University (UGR), email: alados@ugr.es

⁶B. de la Morena is with the Spanish National Aerospace Technique Institute (INTA), email: morenab@inta.es

⁷M. Gil-Ojeda is with the Spanish National Aerospace Technique Institute (INTA), email: gilm@inta.es

2 AMISOC-ARN 2012 CAMPAIGN

AMISOC is a research project funded by the Spanish R&D program devoted to improve the knowledge of minor constituents playing a role in ozone chemistry [2]. AMISOC-ARN campaign was conceived as a multi-instrumented campaign in order to study the behavior of minor trace gases under heavy aerosol loading. This situation is frequent in spring- and summertime when Saharan dust intrusions arrive to the SW-IP [3, 4].

ARN is a multi-instrumented platform for studying several topics on atmospheric sciences located in the coast of Huelva (N37.1 W6.7) near the Doñana national park. The main aerosol types at this sampling site are coastal marine, continental and desert dust. The main atmospheric circulations are the regional (sea-land breeze phenomenon) and synoptic-scale patterns. This observatory is equipped with different instrumentation for monitoring different parameters, such as aerosol (by in-situ and remote sensing techniques), gaseous pollutant concentration (O_3 , NO_2 and NO_x) and meteorological parameters.

2.1 Instrumentation

INTA C212-200 Aircraft is twin turboprop-powered medium transport designed and built by EADS-CASA as civil and military transport. This aircraft has a maximum payload of 2.800 kg. The ceiling service is 26.000 ft / 7.925 m. The cabin is not pressurized so oxygen is required when 10.000 ft / 3.000 m.a.s.l. of altitude is exceeded. It has been instrumented to carry out atmospheric studies keeping instrumentation both inside and outside the cabin. Two hard points are located under each wing to hold sondes from Droplet Measurements Technologies (DMT). Inlets for cabin instruments are located in the emergency trap aircraft behind the cockpit.

The CAS-DPOL instrument is part of the DMT multi-instrument *Cloud, Aerosol and Precipitation Sonde* (CAPS) which is compound by five instruments in total registering aerosol/cloud SD, liquid water content, cloud droplet 2D images, GPS position, pressure, temperature and relative humidity (RH). The CAS-DPOL installed on-board the C212 characterizes the aerosol SD through 30 channels in the range 0.5 to 50 μm [5]. The forward detector collects the light scattered by the particles in the range of angle between 4° to 12° (fig. 1). This information is used by the probe to size the particles. Two additional detectors collect scattered light in backward direction (168° to 176°), being a linear polarizer in front of the second backward detector. Acquisition time and records from this three detectors are registered in a 'Particle By Particle' (PBP) file.

Temperature and relative humidity measurements from the CAPS instrument have been also used.

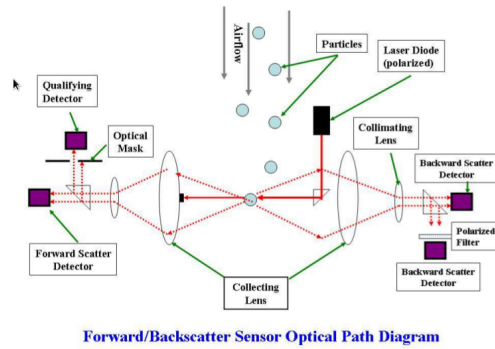


Figure 1: CAS-DPOL scheme taken from the instrument manual [5]

2.2 Flight Descriptions

AMISOC-ARN campaign took place from 21 May to 13 June being developed three flights in this period. The first and second flights took place on 31 May and 1 June, when a Saharan Air Layer (SAL) arrived to ARN. The third flight of the campaign was performed on 13 June, under no-SAL conditions, the last campaign available date.

The flight tracks described by the aircraft consisted in an ascent over ARN following spirals and a descent in steps to improve the quality of certain measurements at previously determined altitudes. The ceiling of the SAL flights was above 22.000 ft for the SAL flights, and 13.000 ft was the ceiling reached in the no-SAL flight.

3 METHODOLOGY

The refractive index algorithm has been run over the PBP files from the campaign taking around one hour and a half to analyze the approximated four millions particles registered. Ten different possible real components of the refractive index have been considered in this analysis.

3.1 Analysis of Acquired Vertical Profiles

Temperature, RH and CAS-DPOL aerosol SD measurements collected by the CAPS instruments over ARN have been averaged within 100 m layers. Temperature and RH profiles have been used to determine the boundary layer (BL) and detect the presence of cloud droplets. SD vertical profiles has also been plotted with the same purposes.

3.2 Calibration Curves from CAS-DPOL Detectors

The algorithms used to retrieve refractive indexes in an experiment require the knowledge of a-priori calibration curves. When a particle reaches the laser

beam of the probe it is illuminated scattering radiation, and the particle cross section (XS) is converted into an electrical signal expressed in terms of counts by each probe photo-detectors. The calibration curves of CAS-DPOL instrument relate the XS with the counts registered in the PBP file. The following steps are followed to determine them in the laboratory:

1. Particles of known size and refractive index are sampled by the instrument (Polystyrene Latex Spheres, PSL, and Glass Beads, GB).
2. The XS of these particles are determined by calculating the phase function of the particle, and integrating it in the angle range for each detector (4° - 12° for forward detector, XS_{fwd} , and 168° - 176° for backward detector, XS_{bck} and XS_{dpol}). [6] codes have been used for this purpose.
3. Particle count data stored in the PBP file are plotted using histograms for each detector. Three histograms from the PBP file are obtained.
4. The histogram class with maximum concentration is associated to the theoretically calculated XS.

3.3 Refractive Index Algorithm

The refractive index is derived using a look-up table that has the theoretical values for the forward and backward scattering cross sections as a function of refractive index. Fig. 2 shows various pairs of XS_{fwd} and XS_{bck} for three different refractive index. For large enough particles, the relationship of forward to backward XS remains fairly constant.

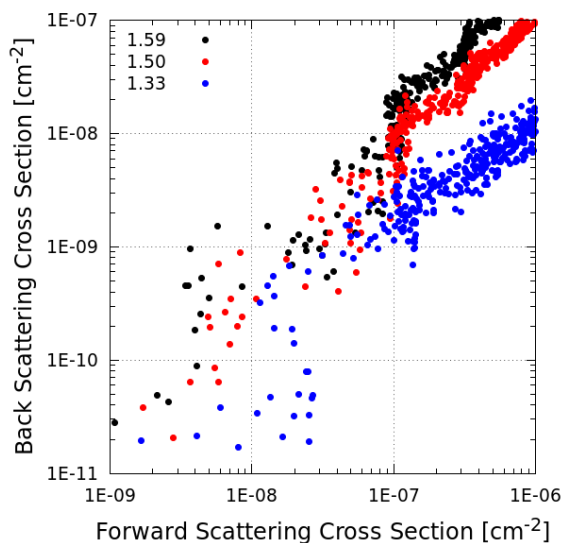


Figure 2: Forward and Backward scattering cross sections as a function of three different refractive indexes

The first step to derive the refractive index is to convert the counts information included in the PBP file into the corresponding XS_{fwd} and XS_{bck} through the calibration curves. After obtaining the particle XS a threshold around them is set up as an exact match will not be necessarily found when searching for occurrences in the lookup table. When a pair of forward and backward scattering cross sections is found that match those measured within the specified error for acceptance, this will indicate the refractive index for that particle.

In some cases, there may not be an unique answer, i.e., according to fig. 2 there are overlapping regions in the plot where particle with different refractive indexes correspond to similar pairs of XS. If the particle population is assumed to be composed of approximately the same composition, then for an ensemble of particles of many sizes, those sizes that have a unique forward to backward relationship will help decide the correct refractive index for those particles whose size is associated with more than one forward to backward scattering pair [5].

Note that in this work particles are assumed to be spherical as [6] does not consider aspherical particles. A posterior revision of the lookup table used in this work will include the code from [7] considering a 50% mix of oblate and prolate spheroids. In addition, the lookup tables used in this do not take into account any light absorption by the particles, i.e. the complex refractive indexes only include the real component. Tables can also be calculated to include imaginary components but this increases the complexity of the analysis as well as the resulting uncertainty.

4 RESULTS

A low pressure system located in the Sahara projected Saharan dust aerosols to the Atlantic being transported towards the IP. On the contrary to other SAL airborne campaigns developed by INTA [8, 9], a presence of clouds in the upper levels of the Saharan dust intrusion was observed (fig. 3).

As well as the previous flights, a depression system was located over the Sahara dessert, but the high pressure system located over the Azores archipelago prevent Saharan dust particles from the IP (fig. 4).

4.1 Vertical Profiles of Aerosols and Clouds in AMISOC-ARN Campaign

Vertical profiles of Temperature, RH and SD taken during the first flight are shown in fig. 5. The mixed Saharan dust-cloud layers observed by the crew during the SAL flights was located between 4 and 7 km above sea level (asl), where the RH increases up to 80%. The increase in larges particles concentration, above $5-8 \mu\text{m}$, is precisely associated to the RH incre-

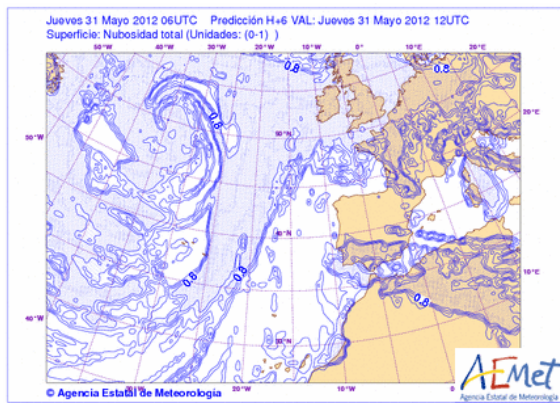


Figure 3: Cloudiness map from May 31, 2012. Data from the Spanish Meteorological Agency (AEMET)

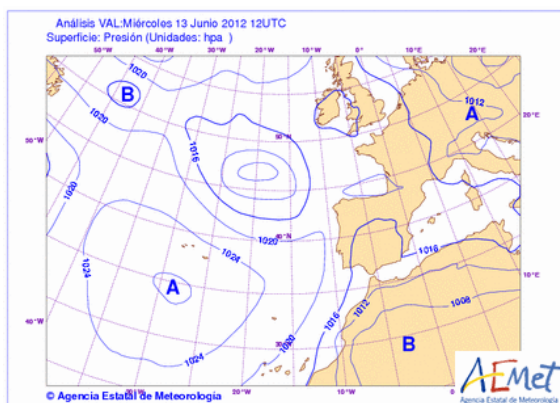


Figure 4: Pressure map from 13 June 2012. Data from the Spanish Meteorological Agency (AEMET)

ment, being these particles cloud droplets. No clear BL is observed both at RH or temperature profiles. The structure of vertical profiles taken during the first and second campaign flights are similar (fig. not shown). Two different groups of particles have been considered for the refractive index analysis: wet layer, between 4 and 7 km asl, and dry layer, from near sea surface up to 4 km asl considered as a pure Saharan dust aerosols layer.

A well-defined BL is observed around 2.1 km asl in the profile taken on June 13 (fig. 6). The particle concentrations observed in the SD profile are reduced precisely above this height. As the vertical profile was carried out over the sea with non-SAL conditions it has been assumed that aerosol particles observed are sea spray aerosols. BL and free troposphere (FT) layers have been configured to carry out the refractive index analysis.

4.2 Refractive Index Analysis

Particles belonging to each of the four layers detailed in the previous section have been used as input data for the refractive index retrieval algorithm. This re-

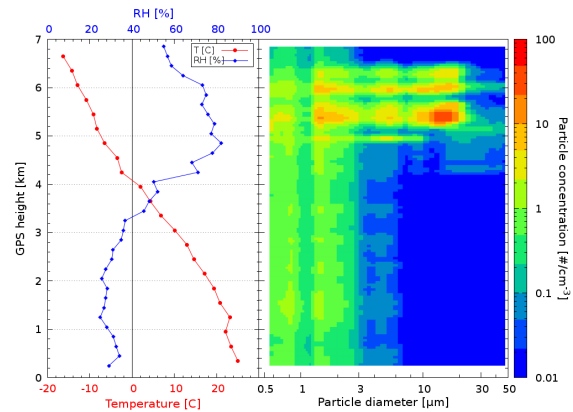


Figure 5: Vertical profiles of Temperature, RH and SD from the first AMISOC-ARN flight (31-May-2012).

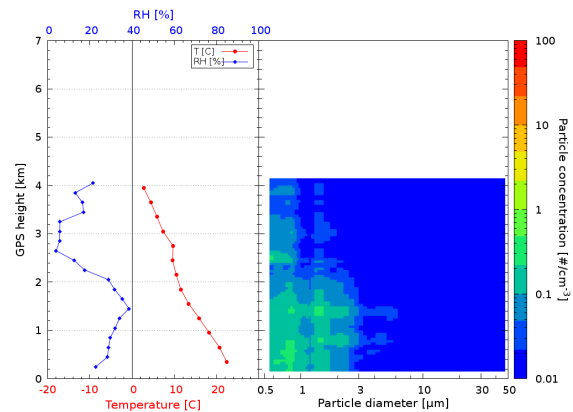


Figure 6: Vertical profiles of Temperature, RH and SD from the third AMISOC-ARN flight (13-June-2013).

sults have been classified into 10 classes according to ten possible real refractive indexes: 1.30, 1.33, 1.36, 1.39, 1.42, 1.46, 1.50, 1.53, 1.56 and 1.59. The frequency obtained for each class has been divided by the corresponding total number of particles analyzed in each layer with the aim to compare the results easily.

Fig. 7 shows the results obtained for the first campaign flight. The frequency of cloud droplets having a refractive index of 1.33 is higher in the wet layer than in the dry one as it was expected according to the RH profiles shown in fig. 5. A well formed peak is also found for particles with a refractive index value of 1.53. These particles correspond with Saharan dust aerosols which refractive index values reported by previous works is in the range from 1.53 to 1.56 [10, 11, 12].

Fig. 8 presents the results of the algorithm applied to the third flight data. The histogram corresponding to the BL shows two peaks, centered on the 1.33, and 1.53 classes. The first class should correspond with water droplets lifted from the sea, whereas the 1.53 class is associated with sea spray aerosols, which have a real refractive index of 1.50.

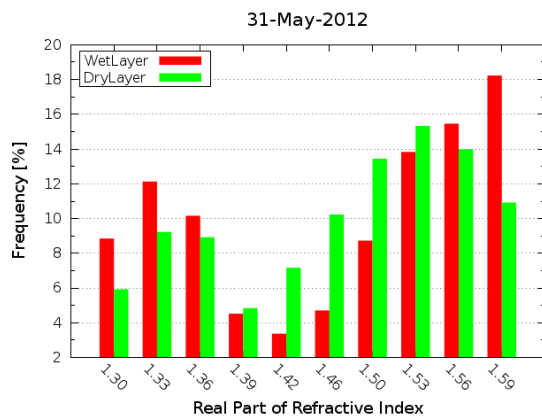


Figure 7: Refractive index algorithm results from the first flight on May 31. Frequencies are expressed in percent values.

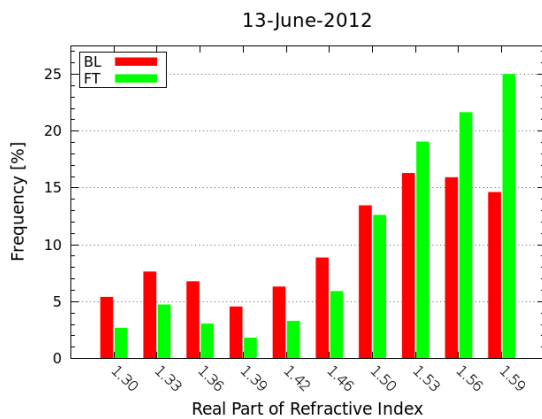


Figure 8: Refractive index algorithm results from the third campaign flight on June 13. Frequencies are expressed in percent values.

The high concentration of particles with a refractive index of 1.59 observed in the first flight wet layer and third flight FT layer apparently seems to be an artifact of the algorithm, as it tend to assign to sampled particles the same refractive index value than the one of the particles used during the calibration.

Although preliminary results show a good agreement with the expected results during AMISOC-ARN campaign, an error analysis must be performed. According to the lookup tables, the retrieval error for large particle (above 5-8 μm) is lower than for medium size particles (around 2.3 μm). A deeper analysis of retrieved refractive index values as a function of particle size is required to asses the algorithm uncertainties. This study is planned to be done before RICTA (*Reunión Ibérica de Ciencia y Tecnología de Aerosoles*) meeting on July 2013.

5 CONCLUSIONS

Data from AMISOC-ARN campaign were used to obtain preliminary results of a refractive index retrieval algorithm. This algorithm is based in the measurements of the CAS-DPOL OPC mounted on-board the INTA C212 atmospheric research aircraft. Three different kind of aerosols were sampled during AMISOC-ARN campaign.

Preliminary results show a good agreement with previously reported refractive indexes of Saharan Dust, sea spray and cloud droplets. Algorithm uncertainties will be presented in the RICTA 2013 meeting, at Evora on July 2013.

ACKNOWLEDGEMENTS

The authors are grateful to INTA Aerial Platforms, belonging to the Spanish ICTS program, and the Spanish Air Force for their efforts maintaining and operating the aircraft. This work was supported by the Spanish Ministry for Economy and Competitiveness (MINECO) under grant CGL2011-24891 (AMISOC project). The Spanish Meteorological Agency (AEMET) is also thanked for their support during the airborne campaign. This work was supported by the Andalusia Regional Government through projects P08-RNM-3568 and P10-RNM-6299, by the Spanish Ministry of Science and Technology through projects CGL2010-18782, CSD2007-00067 and CGL2011-13580-E/CLI; and by EU through ACTRIS project (EU INFRA-2010-1.1.16-262254). The authors thankfully acknowledge the computer resources, technical expertise and assistance provided by the Barcelona Supercomputing Center. ALFA database computation was partly supported by RES (Spanish Supercomputation Network) computing resources (projects AECT-2009-1-0012, AECT-2011-3-0016).

REFERENCES

- [1] IPCC, *Climate Change 2007: The Physical Science Basis. Contribution of Working Group I to the Fourth Assessment Report of the Intergovernmental Panel on Climate Change*. Cambridge University Press, Cambridge, United Kingdom and New York, NY, USA, 2007.
- [2] O. Puentedura, M. Gil, J. Adame, J. Andrey, C. Córdoba-Jabonero, L. Gómez, T. Hay, M. Navarro, C. Prados-Román, A. Saiz-López, M. Sorribas, D. Toledo, and B. de la Morena, "AMISOC 2012: Multi-instrumented campaign for gases-aerosols interaction assessment," in *European Aerosol Conference*, 2012.
- [3] C. Toledano, V. Cachorro, A. Berjon, A. De Frutos, M. Sorribas, B. De la Morena, and P. Goloub, "Aerosol optical depth and ångström exponent climatology at el arenosillo aeronet site (huelva, spain)," *Quarterly Journal of the Royal Meteorological Society*, vol. 133, no. 624, pp. 795–807, 2007.

- [4] C. Córdoba-Jabonero, M. Sorribas, J. Guerrero-Rascado, J. Adame, Y. Hernández, H. Lyamani, V. Cachorro, M. Gil, L. Alados-Arboledas, E. Cuevas, *et al.*, “Synergetic monitoring of saharan dust plumes and potential impact on surface: a case study of dust transport from canary islands to iberian peninsula,” *Atmospheric Chemistry and Physics Discussions*, vol. 10, pp. C11227–30, 2010.
- [5] Droplet Measurement Techniques (DMT), *The Cloud Aerosol Spectrometer – Depolarization Option (CAS-DPOL)*.
- [6] W. J. Wiscombe, “Improved mie scattering algorithms,” *Applied optics*, vol. 19, no. 9, pp. 1505–1509, 1980.
- [7] M. I. Mischenko, L. D. Travis, and A. A. Lacis, *Scattering, absorption, and emission of light by small particles*. Cambridge university press, 2002.
- [8] J. Andrey, M. Gil, and O. Serrano, “Size distribution vertical profiles of saharan dust over the eastern atlantic during the 2005-2006 summer outbreaks,” in *European Aerosol Conference*, (Salzburg, Austria), September 9-14 2007.
- [9] J. Andrey, M. Sorribas, J. Adame, M. Navarro-Comas, M. Gil, and B. de la Morena, “Vertical and ground base aerosols and gases characterization at ‘El Arenosillo’ station during July 2009,” in *VI Reunión Española de Ciencia y Tecnología de Aerosoles (RECTA 2011)*, 2011.
- [10] O. Dubovik, A. Smirnov, B. Holben, M. King, Y. Kaufman, T. Eck, and I. Slutsker, “Accuracy assessments of aerosol optical properties retrieved from Aerosol Robotic Network (AERONET) Sun and sky radiance measurements,” *JOURNAL OF GEOPHYSICAL RESEARCH-ATMOSPHERES*, vol. 105, pp. 9791–9806, APR 27 2000.
- [11] J. Haywood, P. Francis, S. Osborne, M. Glew, N. Loeb, E. Highwood, D. Tanré, G. Myhre, P. Formenti, and E. Hirst, “Radiative properties and direct radiative effect of saharan dust measured by the c-130 aircraft during shade: 1. solar spectrum,” *Journal of Geophysical Research: Atmospheres (1984–2012)*, vol. 108, no. D18, 2003.
- [12] A. Petzold, K. Rasp, B. Weinzierl, M. Esselborn, T. Hamburger, A. Dörnbrack, K. Kandler, L. Schütz, P. Knippertz, M. Fiebig, *et al.*, “Saharan dust absorption and refractive index from aircraft-based observations during samum 2006,” *Tellus B*, vol. 61, no. 1, pp. 118–130, 2009.
- [13] A. Quirantes, F. J. Olmo, H. Lyamani, and A. Valenzuela, “Investigation of fine and coarse aerosol contributions to the total aerosol light scattering: Shape effects and concentration profiling by raman lidar measurements,” *Journal of Quantitative Spectroscopy and Radiative Transfer*, 2012.

Long-term atmospheric fluxes of radionuclides at a coastal Mediterranean station

C. Dueñas¹, M.C. Fernández¹, E. Gordo¹, E. Liger², S. Cañete¹ and M. Pérez³

Abstract — Radioactive composition of bulk deposition sample, which were collected monthly over a 8 year period (January 2005-December 2012) at a site located 30 m.a.l. in Málaga (4 °28' 8" W; 36° 43'40"N) have been analysed. Samples were collected monthly in an area of 1 m² using a collector that is a slightly tilted stainless steel tray and filling 25 or 50 L polyethylene vessels with bulk deposition. The radionuclides present in all samples are ⁷Be, ²¹⁰Pb and ⁴⁰K appears approximately in 50% of the samples. The specific activities of ⁷Be, ²¹⁰Pb and ⁴⁰K varied from 0,6 to 8,3 Bq L⁻¹ (mean = 2,6 Bq L⁻¹), 0,05 to 1,3 Bq L⁻¹ (mean = 0,41 Bq L⁻¹) and 0,02 to 0,84 Bq L⁻¹ (mean= 0,23 Bq L⁻¹) respectively. The temporal variations of radionuclides exhibit similar seasonal behaviour with low values in winter-autumn months and maximum values in spring-summer months. The time variations of the different radionuclides concentrations have been discussed in relation to various meteorological factors and the mean values have been compared to those published in recent literature for other sites located at different latitudes. Bulk depositional fluxes of ⁷Be, ²¹⁰Pb and ⁴⁰K varied between 0,18 and 1779 Bq m⁻² month⁻¹ (annual mean = 1300 Bq m⁻² year⁻¹), and 0,035 to 81 Bq m⁻² year⁻¹ (annual mean = 140 Bq m⁻² year⁻¹ and 0,53 to 81 Bq m⁻² year⁻¹ (annual mean = 70 Bq m⁻² year⁻¹) respectively. Data on the atmospheric depositions of radionuclides in Málaga show that the seasonal variation is not uniform from year to year and the amount of rainfall controls the depositional fluxes. There is a statistically relationship between ⁷Be and ²¹⁰Pb fluxes indicating that removal behaviour from the atmosphere is relatively similar.

Keywords — depositional flux, gamma radionuclides, rainwater, Mediterranean region

1 INTRODUCTION

The deposition of radionuclides on the ground represents an important factor in environmental radioactivity monitoring and an important input parameter in radioecological models. To predict the long-term radiological consequences of an accidental deposition of the radionuclides to the ground, it is a prerequisite to know the environmental long-term behaviour of these radionuclides and a relatively large number of values are required for statistically meaningful conclusions. It is well known that the main part of radioactivity deposition of natural as well as artificial radionuclides from the global nuclear weapons fallout takes place through wet precipitation and dry depositions: [1], [2], [3], [4], [5]. Precipitation scavenging is the removal of particulate matter and gases from the atmosphere through various types of precipitation. The process involves the incorporation of radioactivity into the rain water and the subsequent deposition of the material onto the

surface of the Earth. The deposition rates which determine the residence time of the material in the atmosphere can affect the downwind surface and airborne concentration patterns

The removal of radioactive particles and gases from the atmosphere by precipitation scavenging depends on complicated microphysical and micro chemical processes which are conditional functions both within and outside the natural cloud-bearing layers.

Nuclides of the natural decay chains, especially for ²³⁸U decay chain, are widely applied into atmospheric research, oceanography and marine geology. In marine aquatic environment, budget studies in trace element and in sediment are correspondence to constant supply of ²¹⁰Pb to the sea [6]. ⁷Be is an another nuclide as tracer and chronometers in aquatic and atmospheric systems [7]. Different from ²¹⁰Pb that is original from ground, ⁷Be is product of the spallation of oxygen and nitrogen nucleus with energetic cosmic rays. ⁷Be and ²¹⁰Pb are highly active particles and are easily scavenged by aerosols. Both have been used as aerosol tracers in studying the vertical transport and residence time of aerosols in the troposphere based on modified versions of the general circulation model. [8], [4]. Numerous applications in studies of transport processes have been found in atmospheric and aquatic systems [7]. ⁷Be is removed from the atmosphere by radioactive decay (half-life 53.2 days) and by wet and dry depositions. Most of the ²¹⁰Pb in the atmosphere is formed as a decay product of ²²²Rn emanating from soil. Little attention is paid

1. :Department of Applied Physics, University of Málaga Campus of Teatinos s/n, 29017 Málaga. E-mail: mcduenas@uma.es.

2. Department of Applied Physics II, Faculty of Computer Engineering, S. A University of Málaga. E-mail: eliger@uma.es.

3. Department of Radiology and Health Physics, Ophthalmology and OTL, Faculty of Medicine. University of Málaga 29071 Málaga (SPAIN) E-mail: mperez@uma.es.

to ^{40}K in airborne materials. Its origin is lithogenic and is mainly originated from the suspension of soil. ^{40}K is found in most types of soil and can easily be transported by re-suspended material. This nuclide has been previously associated with the arrival of coarse re-suspended material (PM10, particulate matter with a diameter below 10 μm) from the African continent [9].

2 MATERIAL AND METHODS

2.1 Area of study

The sampling site is one of the environmental radioactivity monitoring network stations operated by the Spanish Nuclear Security Council (CSN), under cooperative agreement with the University of Málaga through the Environmental Radioactivity Research Group. The site where the measurements were carried out is in the North-West of the city ($4^{\circ} 28' 8'' \text{ W}$; $36^{\circ} 43' 40'' \text{ N}$), 5 km away from the coastline. The sampling point was located 14 m above the ground, on the flat roof of the SCAI building, University of Málaga. Málaga is the major coastal city of Andalusia region, south Spain. This Spanish city on the Mediterranean is distinguished by its mild, temperate and warm climate with low rainfall (550 mm yr^{-1}) and around 320 days of sun a year. The coast is backed by a series of mountains that have to be crossed to reach the inland valleys. As Málaga is located on the coast, its ambient air is influenced by both continental and maritime air masses. Due to the influence of the local orography, SE and NW winds prevail and these winds can be observed in the sea-land and land-sea breezes, respectively.

2.2 Sampling and radionuclide measurements.

Samples of bulk deposition were collected on a monthly basis in an area of 1 m^2 using a collector that is a slightly tilted stainless steel tray and filling 25 or 50 l polyethylene vessels for bulk samples reservoirs. Monthly precipitation and dry fallout samples were routinely collected from January 2005 to December 2012. At the end of each month, if there was no rain, the sampler was cleaned with acidified distilled until a sample volume of at least 6.8 l was achieved. Even if there was rain during the last 2-3 days in the collection period, the surface was also cleaned with small amount of acidified distilled water to remove adsorbed radionuclides from the surface. The collector was also cleaned with distilled water to avoid contamination between each collection period. Then the liquid samples were acidified with hydrochloric acid to a pH lower than 1 to minimize sorption of radionuclides on the container wall. Since the rain collector was exposed to the atmosphere continuously, the sum of the wet and dry fallout (bulk deposition) was collected.

Measurements by γ spectrometry were performed to determine the ^7Be and ^{210}Pb activity of the aerosols and bulk deposition samples. Details of the low-background gamma-ray detection system used and the calibration of the resulting samples for gamma spectrometry have been previously described [10]. The weekly filter samples were bulked to form a sample for the ^7Be and ^{210}Pb monthly determination. To determine the monthly depositional flux a volume of 6 l was evaporated at 80°C down to approximately 1 l and transferred to a Marinelli geometry container. This large sample size was required because of the low activity of the samples. The Marinelli and filter samples were counted using an intrinsic germanium coaxial detector, ReGe-type made by CANBERRA. The counting time was in the order of 90000-172000 s. The concentrations were corrected for decay to the mid-collection period using a 53 day half-life and 477.6 keV gamma-ray of ^7Be and 22.3 yr half-life and 46.5 keV line of ^{210}Pb . The errors reported are propagated errors arising from the one sigma counting uncertainty due to detector calibration and background correction.

The standard meteorological data: rainfall, duration of rainfall, number of dry days and number of wet days were obtained from the Spanish National Institute of Meteorology, AEMET, located 500 m away from the sampling site. Data for the number of days with high probability of episodes of Saharan intrusions that may affect levels of particulate matter collected on the surface air have been obtained from the CALIMA project.

3. RESULTS AND DISCUSSION

3.1 Variations in the specific activities of gamma radionuclides in bulk deposition.

Table 1 summarises the main statistical variables calculated for the measured gamma radionuclides (^7Be , ^{210}Pb and ^{40}K) over the whole sampling period. All activities are given in Bq l^{-1} .

Table 1. Statistical summary of the specific activities of gamma radionuclides.

	^7Be (Bq l^{-1})	^{210}Pb (Bq l^{-1})	^{40}K (Bq l^{-1})
N of cases	96	96	37
Average	2.6	0.41	0.21
Geo. mean	2.2	0.34	0.17
Maximum	8.3	1.32	0.84
Minimum	0.6	0.05	0.02
Std. deviation	1.7	0.24	0.16
Std. error	0.17	0.02	0.026
Variation coef.	64%	58%	75%
Skewness(GI)	4.7	5.5	5.6

The measurements were performed once the short-lived radon daughter had decayed. The radionuclides present in all samples are ^7Be and ^{210}Pb . The specific activities of ^7Be , ^{210}Pb and ^{40}K varied from 0,6 to 8,3 Bq l⁻¹ (mean = 2,6 Bq l⁻¹), 0,05 to 1,3 Bq l⁻¹ (mean = 0,41 Bq l⁻¹) and 0,02 to 0,84 Bq l⁻¹ (mean = 0,21 Bq l⁻¹), respectively. Due to value of skewness (GI), the specific activities of ^7Be , ^{210}Pb and ^{40}K in rainwater should fit approximately to log normal distribution. The geometric mean was used in further analysis and comparisons as the main characterization factor of specific activities of ^7Be , ^{210}Pb and ^{40}K . The highest concentration was of 8.3 Bq l⁻¹ obtained for ^7Be while the lowest measured concentration was in the order of 20 mBq l⁻¹ obtained for ^{40}K . Fig. 1 displays seasonal specific activities of ^7Be , ^{210}Pb and ^{40}K during the measurement period. The specific activities of ^7Be exhibit their maximum values in the spring.

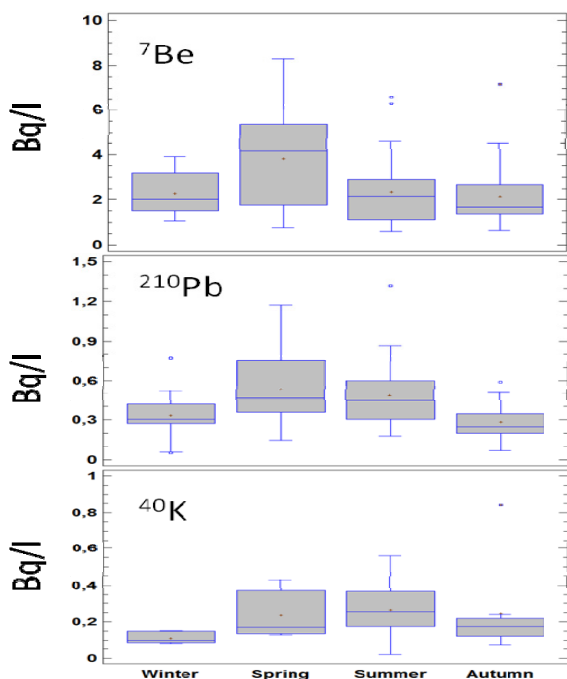


Fig. 1. Seasonal variation of ^7Be , ^{210}Pb and ^{40}K in rainfall

The higher values of ^7Be may be due and the rapid exchange of aerosols between stratosphere and troposphere by contraction of tropopause in the spring season. The highest value of specific activity of ^7Be occurs in May(2009) and the lowest occurs in December (2009).The specific activity of ^{210}Pb and ^{40}K show minimum values in winter and autumn and maximum values in summer and spring. The highest value of specific activity of ^{210}Pb occurs in July (2006) and the lowest occurs in December (2005). The highest specific activity of ^{40}K occurs in October 2008 and the lowest occurs September (2010).

Table 2 displays the annual minimum and maximum values of rainfall, the annual minimum and maximum values of rainfall duration, the sum of monthly amounts of rainfall and the annual number of wet days for the measurement period. The minimum annual rainfall was 239.6 mm (2005) and the maximum value was 903mm (2010). The total amount of rainfall during from 2005 to 2012 was 3658 mm corresponding to a number of 498 wet days.

Table 2. Annual minimum, maximum and sum values for monthly amounts of rainfall, maximum and minimum values for rainfall duration and the sum of annual number of wet days (n_w)

Year	Rainfall Amount (mm)			Rainfall Duration (min)		Number of wet days
	Max.	Min.	Sum	Max.	Min.	n_w
2005	84	0.8	239.6	3363	110	54
2006	160.3	0.5	476.1	2300	20	58
2007	126.7	0.1	351	1670	10	66
2008	96.5	3.4	313.6	1270	310	70
2009	188.5	0.1	435.2	3680	10	59
2010	243.6	0.2	903	4420	20	78
2011	125.2	0.4	401.6	2880	10	55
2012	232.5	12.3	537.9	4160	290	58

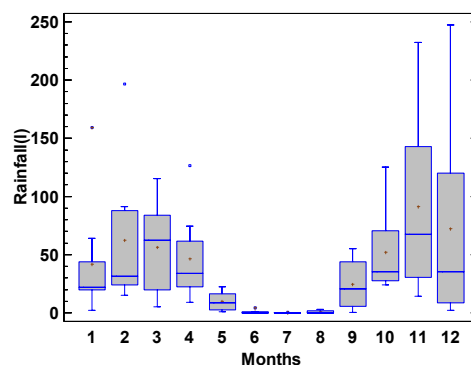


Fig.2 .Monthly precipitation data observed in Málaga during 2005-2009.

In Fig.2 the box and whisker diagrams of the amount of rainfall through eight years are represented. There are various outliers in January, February and April.

The variations in the specific activities of ^7Be , ^{210}Pb and ^{40}K in the bulk deposition samples may be due to several factors such as cloud height, the amount and duration rainfall, the time elapsed between successive rain events and the vertical mixing of air masses at the sampling site.

Taking into account the local features of precipitation in Málaga, with heavy rain events followed by long dry period, five different

parameters have been considered: rainfall amount, rainfall duration, number of dry days, number of wet days and the number of Saharan intrusions due to position of Málaga .

Table 3. Linear correlation studies between the specific activities of studied radionuclides with some parameters

	⁷ Be	²¹⁰ Pb	⁴⁰ K
The amount of rainfall(mm)	-0.10	-0.30	-0.10
Rainfall duration (min)	-0.04	-0.29	-0.18
Number of dry days	0.03	0.40	0.18
Number of wet days	-0.01	-0.38	-0.11
Number of intrusions	0.27	0.48	0.47

A positive correlation has been found with the number of day days and the number of Saharian intrusions. The coefficients range between 0.03 and 0.48 indicating relatively weak relationship between the variables. The weak relationship in this study suggests that radionuclide activities at our site might be controlled by the interactions of complex processes, such as source and scavenging intensity. The highest correlation coefficients have been found between ²¹⁰Pb and ⁴⁰K with the number of Saharian intrusions and number of dry days. Based on the available data and the low dependencies found between the different variables, no predictive model could be built.

The linear correlation between specific activity of ⁷Be and rainfall is very poor (r = -0.10). However, other investigators reported significant correlations between specific activity of ⁷Be and the amount of precipitation [11], [12], [13] suggested that the specific activity of ⁷Be in rainfall may be higher during the drier months and periods characterized by short-duration precipitation events. A poor correlation has also reported by [2], [14] who suggested that the dilution is not the only process that controls the ⁷Be specific activity in rainwater.

2.2 Activity deposition of ⁷Be, ²¹⁰Pb and ⁴⁰K

Table 4 summarises the main statistical variables calculated for ⁷Be, ²¹⁰Pb and ⁴⁰K atmospheric deposition fluxes over the whole sampling period: 1 January 2005 until 31 December 2012

Table 4.- Statistical summary of the fluxes of gamma radionuclides

	⁷ Be Flux (Bq m ⁻² month ⁻¹)	²¹⁰ Pb Flux (Bq m ⁻² month ⁻¹)	⁴⁰ K Flux (Bq m ⁻² month ⁻¹)
N of cases	96	96	43
Arit. Mean	109	12	7
Geo. Mean	48	7.7	3.0
Maximum	1779	102	81
Minimum	4.02	1.17	0.53
Std. deviation	223	17	14
Std. error	23	1.8	2.4
Variation coef.	189	146	210
Skewness(GI)	20	10	12

Due to value of the skewness (GI) the deposition fluxes of ⁷Be, ²¹⁰Pb and ⁴⁰K should fit approximately to log normal distributions. The monthly fluxes varied widely for ⁷Be varied 4.02-1779 Bq m⁻² month⁻¹ and the average annual deposition is approximately 1300 Bq m⁻² year⁻¹. The monthly fluxes varied also widely for ²¹⁰Pb (1,17 - 102 Bq m⁻² month⁻¹) and the average annual deposition is 140 Bq m⁻² year⁻¹. The monthly fluxes varied widely for ⁴⁰K (0.53 - 81 Bq m⁻² month⁻¹) and the average annual is approximately 80 Bq m⁻² year⁻¹. The highest fluxes of ⁷Be and ²¹⁰Pb was found during December 2010 and November 2012 when the monthly rainfall have been 247,4 and 232,5 mm respectively. The highest flux of ⁴⁰K occurred in October 2008 when a grand Saharian intrusion penetrate in Malaga and the specific activity of ⁴⁰K in rainfall has been 81Bq l⁻¹ [15]. The minimum fluxes of ⁷Be, ²¹⁰Pb and ⁴⁰K occurred in June 2005, August 2008 and September 2010 respectively.

The fluxes of ⁷Be, ²¹⁰Pb and ⁴⁰K within a sampling period were shown in Fig. 4.

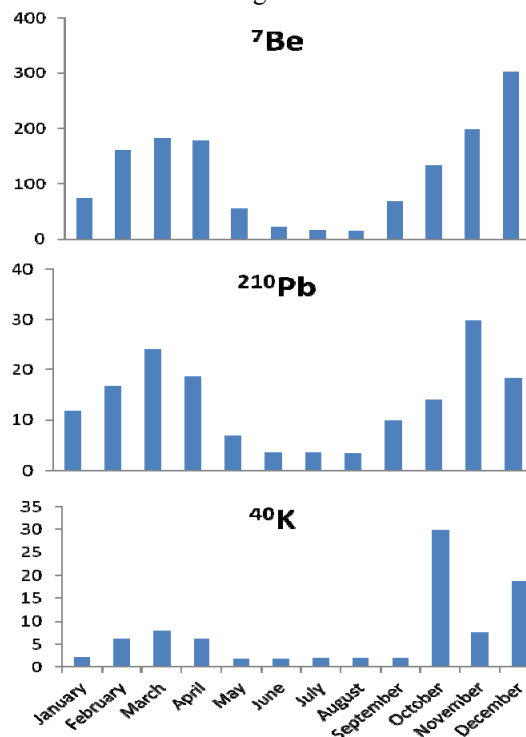


Fig. 3. Monthly variation of fluxes of ^7Be , ^{210}Pb and ^{40}K .

The activity fluxes of ^7Be , ^{210}Pb and ^{40}K are changed in the same tendency of various months. These results suggest seasonal character of deposition flux. The fluxes show a marked seasonal variation with higher values in autumn and winter months and lower values in spring and summer. The sampling area has hot and dry summers due to its Mediterranean characteristics. The fluxes of ^7Be and ^{210}Pb are correlated ($r = 0.74$) suggesting that their removal behaviour from the atmosphere are relatively similar. It further indicates that these nuclides cannot be used as independent air mass tracers at least for the areas similar to Málaga.

We have performed a correlation study to identify parameters associated with fluctuations of deposition to ground. The four parameters have been considered: rainfall amount, rainfall duration, number of dry days and number of wet days. Table 4 shows the correlation coefficients between monthly deposition fluxes and those parameters. There is a statistically significant relationship at 95% of confidence level between depositions of ^7Be , ^{210}Pb and ^{40}K with all parameters, since of p-value is less than 0.05. The correlation coefficients indicate a relatively weak relationship between the variables with the exception for the depositional fluxes of ^7Be and ^{210}Pb with rainfall.

Table 5. Linear correlation studies between deposition fluxes and some parameters.

	^7Be	^{210}Pb	^{40}K
The amount of rainfall(mm)	0.84	0.90	0.66
Rainfall duration (min)	0.32	0.85	0.59
Number of dry days	-0.51	-0.69	-0.55
Number of wet days	0.53	0.72	0.61

In the majority of studies, a moderate correlation between the deposition fluxes of radionuclides and rainfall is observed. Such relationships have been commonly observed and explained by the fact the rainfall constitutes the mayor depositional pathway of the radionuclides [14], [16], [5], [17].

As previously observed, correlation of rainfall with ^{210}Pb seems better than with ^7Be due to a relatively greater contribution of ^{210}Pb from dry deposition

4 CONCLUSIONS

We have evaluate a time series of specific activities of gamma radionuclides in rainwater and atmospheric deposition fluxes for ^7Be , ^{210}Pb and ^{40}K obtained for eight years (2005-2012). Seasonal variations have been observed. The minima specific activities of radionuclides are registered in winter

months while the maximum ones fundamentally in spring-summer months.

Specific activity data sets for the radionuclides show negative correlations with the number of wet days, the rainfall duration and the amount of rainfall. A positive correlation has been found with the number of dry days. The correlation coefficient ranges between 0.32 and 0.90 and indicating a relatively weak relationship between the variables.

Mean values of annual deposition fluxes of ^7Be , ^{210}Pb and ^{40}K are : 1300, 140 and 70 Bq $\text{m}^{-2}\text{y}^{-1}$ respectively. The depositional fluxes of ^7Be and ^{210}Pb are correlated indicating that removal behaviour from the atmosphere is relatively similar. This study suggests that continuous monitoring of radioelement fluxes is necessary to examine both episodic and long-term changes in annual and seasonal fluxes atmospheric fluxes.

REFERENCES

- [1] J.E. Dibb, "Atmospheric deposition of berillium 7 in the Chesapeake Bay region Dibb", *J. Geophys. Res.* vol.94, pp. 2261-2265, 1989.
- [2] J. F. Todd, G.T.F. Wong, C.R. Olsen and I.I. Larsen, "Atmospheric deposition characteristics of Berillyum 7 and lead 210 along the southeastern Virginia coast", *J. Geophys. Res.* vol.94, pp.106-11, 116, 1989.
- [3] M. Baskaran, "A search for the seasonal variability on the depositional fluxes of ^7Be and ^{210}Pb ", *J. Geophys. Res.*, vol. 199, pp. 2833-2840, 1995.
- [4] M. Baskaran, C.H. Coleman and P.H. Santschi, "Atmospheric depositional fluxes of ^7Be and ^{210}Pb at Galveston and College Station Texas", *J. Geophys. Res.*, vol.98, pp.20,555-20,571, 1993;
- [5] J. Du, J. Zhang, J. Zhang and Y. Wu, "Deposition patterns of atmospheric ^7Be and ^{210}Pb in coast of Esat China sea, Sanghai, China", *Atmos. Environ.* vol.42, pp.101-5109, 2008.
- [6] J.P. Beks, D.J. Eisma, J.U. Van der Plicht, "A record of Atmospheric ^{210}Pb deposition in The Netherlands", *Science of the Total Environment* vol 222, pp. 35-44, 1998.
- [7] S. Rehfeld and M. Heimann, "Three dimensional atmospheric trasport simulation of radioactive tracers ^{210}Pb , ^7Be , ^{10}Be and ^{90}Sr ", *J. Geophys. Res.*, 100(D12), vol. ,pp. 26,141-26,161, 1995.
- [8] R.A. Brost, T. Feichter, and M. Heima, "Three dimensional simulation of Be-7 in a global climate model", *J. Geophys. Res.*, vol. 96, pp.22,423- 22445, 1991.
- [9] F. Hernández, J. Hernández-Armas, A. Catalán, J.C. Fernández-Aldecoa and

- L.Karlson,"Gross alpha, gross beta activities and gamma emitting radionuclides composition of airborne particulate samples in an oceanic island",*Atmos. Environ.*,vol 39,pp. 4057-4066, 2005b.
- [10] C.Dueñas, M.C Fernández, E. Liger,and J. Carretero," Gross alpha, goss beta activities and ⁷Be concentrations in surface air:analysis of their variation and prediction model".*Atmos. Environ.*, vol. 33,pp.3705-3715 , 1999.
- [11] C.R. Olsen,I.L. Larsen, P.D. Lowry,N.H. Cutshall, J.F. Todd, G.T.F. Wong and W.H. Casey,"Atmospheric fluxes and marsh-soil inventories of ⁷Be and ²¹⁰Pb", *J. Geophys. Res.*, vol.90,pp. 10,487-10,495,1985.
- [12] E. A. Canuel,C.S. Martens, and L.K. Benninger," Seasonal variations of ⁷Be activity in the sediments of Cape Lookout Bight, North Carolina", *Geochim. Cosmochim. Acta*, vol.54,pp.237-245, 1990.
- [13] A.A. Renfo, J. K. Cochran and B.A. Colle, "Atmospheric fluxes of ⁷Be and ²¹⁰Pb on monthly time scales and during rainfall events at Stony Brook, New York(USA)",*J. Environ. Radio.*,vol. 116, pp. 114-123, 2013.
- [14] C.R. Benítez-Nelson,K.O. Buesseler, Phosphorous-32,Phosphorous-37,Beryllium-7 and Lead-210:atmospheric fluxes and utility in tracing stratosphere/trophosphere exchange,*J. Geophys. Res.*,vol. 104,pp.11745-11754, 1999.
- [15] M. Cabello, J.A.G. Orza, M.A. Barrero, E. Gordo, A. Berasaluce, L. Cantón, C. Dueñas M.C. Fernández y M. Pérez, Spatial and temporal variation of the impact of an extreme Saharan dust even. *J. Geophys. Res.*, vol. 117, D11204, doi: 1029/2012JD017513, 2012.
- [16] S. Caillet,P. Arpagaus,F. Monna and J. Dominik,"Factors controlling ⁷Be and ²¹⁰Pb atmospheric deposition as revealed by sampling individual rain events in the region of Geneve,Switzerland",*J. Environ. Radioact.* Vol. 2,pp.241-246, 2001.
- [17] A. Ugur,B. Özden,I. Filizok "Determination of ²¹⁰Po and ²¹⁰Pb concentrtrions in atmospheric deposition in Izmir(Aegean Sea-Turkey), *Atmos. Environ.*, doi:10.1016 ,2010.

Behaviour of ^7Be in air at a sampling point on Southeastern Spain

C. Dueñas¹, M.C. Fernández^{*1}, E. Gordo¹, E. Liger², S. Cañete¹ and M. Pérez³

Abstract — ^7Be is a natural radionuclide tracer of aerosols originated over a range of high altitudes in the atmosphere. ^7Be concentrations in air were continuously monitored with a high-volume air sampler between 2009 and 2011 in Málaga (Spain). Time series analysis techniques have been applied to study the ^7Be activity concentration in air and the seasonal data have been correlated with solar radiation, concentrations of particulate matter fraction PM10, Total Suspended Matter (TSP), rainfall and sunspot number. The results of the Principal Component Analysis yielded two components, which accounted for 58,4% and 24,5% of the total variance. The results of our study reveal that aerosol behaviour is represented by two principal components which explain 82.9% of total variance. The first component is related to production of ^7Be , while the second one explains the cyclical and seasonal pattern of ^7Be

Keywords — Atmospheric aerosols, ^7Be , PM10, sunspot number.

1 INTRODUCTION

Long-term measurements of cosmogenic radionuclides such as ^7Be ($T_{1/2} = 53\text{d}$) provide important data in studying global atmospheric processes and comparing environmental impact of radioactivity from man-made sources to natural ones. ^7Be is a natural radionuclide originating over a range of high altitudes in the atmosphere and it is produced in the stratosphere and upper troposphere by the spallation of oxygen and nitrogen nuclides and is subsequently absorbed onto aerosols. This radionuclide has become recognized as a potentially powerful tool when studying environmental processes such as precipitation, wash-out (precipitation scavenging), atmospheric particle deposition and deposition patterns of airborne contaminants. Therefore ^7Be has been frequently used as a tracer of stratospheric intrusions of gases and aerosols into the troposphere. However, there are few available studies on the impact of the suspension and transport of continental aerosols on the concentration of this radiotracer in the troposphere. In this work is important not only to know ^7Be activity concentration in air but also his temporal evolution and behaviour, which could depend both on dry and wet deposition and seasonal variations. Additionally, it is well known that the galactic cosmic-ray intensity at the earth's orbit is inversely related to solar activity. So, a decrease in the galactic cosmic-ray intensity has accompanied

the recent increase in the solar activity, which will be followed by a decrease in the production rate of cosmic-ray products, such as Beryllium-7 that is therefore expected in a global scale. The solar activity in that case is described by the sunspots number. In the 11-year solar cycle, the highest ^7Be activity concentration, the lowest solar activity and vice versa occurred [1]. That means, in the minimum solar activity, the sunspots number is very low, and then, the ^7Be activity concentration in the atmosphere becomes very high. In order to investigate the behaviour of the cosmogenic nuclide ^7Be concentrations in surface air at Málaga (Southeastern Spain), aerosols samples have been continuously recording. The monthly average data set includes observations from 2009 to 2011, during which period the solar activity was on its minimum at the beginning of the 24th cycle in 2008.

2 MATERIAL AND METHODS

2.1 Sampling site and collection of samples

Beryllium-7 in air was continuously monitored with a high-volume air sampler (ASS-500C). The sampling station was located on the roof (12 m above the ground) of the SCAI building, University of Málaga (36° 43' 40" N; 4° 28' 8" W) in the north-west part of the city of Málaga. The sampling point was located approximately 5 km from the coastline, near the airport and surrounded by roads with traffic exhaust (Figure 1). Málaga is the major coastal city of the Andalusia region, south Spain, with a population of 570000 inhabitants.

Airborne dust samples were weekly collected and the sampler uses polypropylene square filters (44x44 cm²) with collection efficiency 93-99%, at a flow rate of 90,000 l min⁻¹. Gamma spectrometric analyses of samples were performed to determine

1. C. Dueñas. Department of Applied Physics I, Faculty of Science, University of Málaga. E-mail: mcduenas@uma.es
2. M.C. Fernández. Department of Applied Physics I, Faculty of Science, University of Málaga. E-mail: mafeji@uma.es
3. E. Gordo. Department of Applied Physics I, Faculty of Science, University of Málaga. E-mail: elisagp@uma.es
4. E. Liger. Department of Applied Physics II, Faculty of Computer Engineering, University of Málaga. E-mail: eliger@uma.es
5. S. Cañete. Department of Applied Physics I, Faculty of Science, University of Málaga. E-mail: scanete@uma.es
6. M. Pérez. 3Department of Radiology and Health Physics, Ophthalmology and OTL, Faculty of Medicine, University of Málaga. E-mail: mperez@uma.es

the ⁷Be activities using an intrinsic REGe detector. Dust content on the filters was determined by weighting the filters before and after exposure under the same conditions of temperature and humidity (Metler AJ100 analytical balance). The difference between the two weights gives the aerosol mass concentration in µg m⁻³ (TSP).

The sunspot number as an index of solar activity has been registered by the Solar Influences Data Analysis Center (SIDC), in Brussels, Belgium, (<http://www.swpc.noaa.gov/>). The meteorological parameters studied in the present work included the amount of precipitation. Meteorological data the sampling site was not available, however, for each sampling period, the data were supplied by the Spanish Meteorological Agency (AEMET) located 500 m away from the sampling point.

PM10 concentrations were measured every ten minutes by beta attenuation method at Carranque station (CS) (36° 40' 29" N; 4° 26' 3" W) in Málaga city. This sampling station is part of the Atmospheric Pollution Monitoring network managed by the Environmental Health Service of the Andalusian Government.



Fig. 1. Map of Spain showing the location of the sampling point near the city of Málaga, on the Mediterranean coast.

3 RESULTS AND DISCUSSION

Atmospheric processes and meteorological parameters might contribute to the variations of ⁷Be activity concentrations in surface air. The effects of sunspot number, amount of precipitation, concentrations of PM10, TSP on ⁷Be activity in the aerosol samples are examined and discussed below.

3.1 Temporal variations

The periodic pattern of mean monthly ⁷Be activity concentrations in surface air during the three years under study are shown in Figure 2. The measured concentrations for ⁷Be are comparable with those found at other locations and the periodic

peaks of ⁷Be concentrations in aerosols observed are in agreement with the findings of other authors.

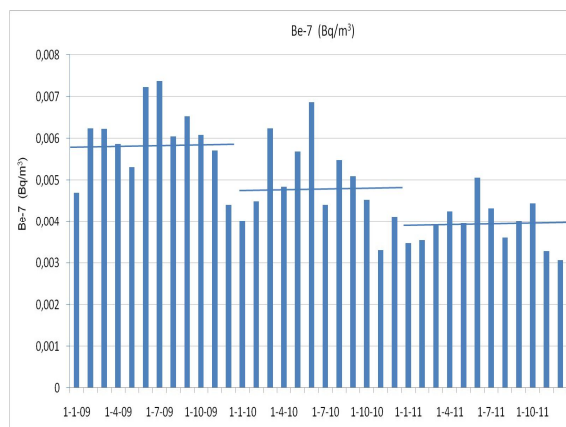


Fig. 2. Temporal variations of ⁷Be concentrations from January 2009 to December 2011 in Málaga.

Fluctuations of atmospheric ⁷Be are commonly ascribed to oscillations of meteorological parameters and depend mainly of the air temperature and the amount precipitation. The highest concentrations of ⁷Be were found during late spring-summer. An increase of ⁷Be concentrations occurs during summer months, when there is very little amount of precipitation and the rising of air temperature produces vertical air mixing with consequent transport of cosmogenic radionuclides to ground level. In this process, importance assumes the intrusion of stratospheric air into troposphere as a consequence of the upward movement of tropopause level in the warm months and owing on the higher frequency of tropopause folding events occurred during the spring period [2].

In order to study the effect of solar activity on the measurements conducted in this work, the correlation between the monthly average activity of ⁷Be concentration and the monthly number of sun spots (as an index of solar activity) is examined in Figure 3.

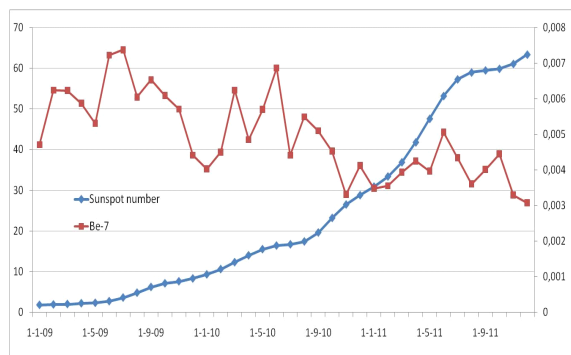


Fig. 3. Temporal variations of the sunspot number and concentrations of ⁷Be (Bq m⁻³) from January 2009 to December 2011.

The inverse relationship between the ⁷Be concentration in air and the sunspot number is

clearly evident. This effect can be interpreted as follows: The solar wind is consistent with the relative low-energy particles eliminated by the passage of the galactic cosmic radiation through the solar system to the earth and therefore it influences by reducing the production rate of cosmogenic origin radionuclides [3].

Monthly values of PM10 are recorded at the time of collection of atmospheric aerosols samples and are plotted in Figure 4. On examining this figure it can be said that the higher values of PM10 are those recorded on July, August and September. These months are the most favourable ones for the intrusions of African air masses that may occur throughout the year [4]. These masses contribute with high dust levels in suspension which overlapped with the local anthropogenic contamination and conditions of atmospheric stability. The lower values of PM10 concentrations were registered in February, March, April and May. The data of our sampling site show a seasonal variation in concentration that increase from June to January. This behaviour is similar to the evolution of the radioactive aerosols in this Mediterranean city [4].

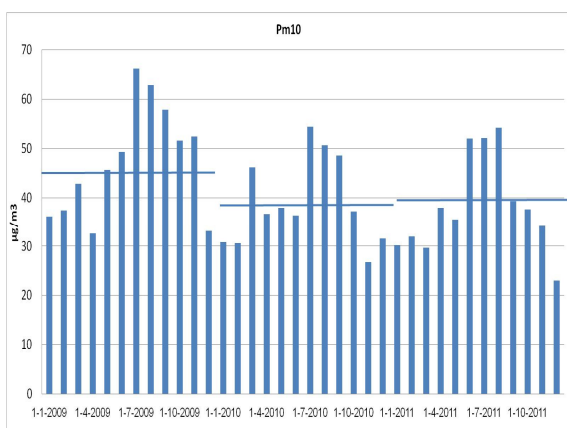


Fig. 4. Temporal variations of PM10 concentrations during the studied period at CS sampling point in Málaga city.

3.2 Statistical Analysis and Data Treatment

The concentrations of ^7Be in weekly samples collected and analyzed during this study are reported monthly. Table 1 provides statistical information of the different variables, such as maximum (MAX) and minimum (MIN) values, mean values and standard deviation (SD). The correlation between the ^7Be concentrations and PM10, TSP, precipitation and number of sunspot was obtained in the form of Pearson correlation coefficients from the raw data. Principal Component Analysis (PCA) was used to reduce large number of variables to representative factors called Principal Components (PC).

Table 1. Statistical summary of the data collected from January 2009 till December 2011.

	Max	Min	Mean	SD
^7Be (mBq m ⁻³)	7.38	3.07	4.94	1.18
PM10 (µg m ⁻³)	66	23	41	11
TSP (µg m ⁻³)	112	27	59	19
Rainfall(mm)	244	0	48	65
Sunspot (n)	63	2	24	21

The Pearson's correlation matrix for ^7Be and the different variables has been studied. Strong and positive correlations was observed between ^7Be concentration and TSP and PM10 and negative correlations with sunspot and precipitation.

Table 2. The Pearson's correlation matrix for ^7Be and the different variables.

	^7Be			
	TSP	PM10	Sunspot	Rainfall
p-value	0.8	0.002	0	0.01
r	0.75	0.60	-0.69	-0.31

In an attempt to find and identify the principal components explaining the matrix of samples and the variables studied, a varimax rotation has been applied to study the data sets (Table 3). The results of our study reveal that aerosol behaviour is represented by two principal components which explain 82.9% of total variance. The first component had positive loading for all parameters, except for the sunspot number. The second component had a positive loading for all parameters, except for precipitation. PC1 is related to production of ^7Be , while PC2 explains the cyclical and seasonal pattern of the ^7Be .

Table 3. Principal Component Analysis.

	Component	
	PC1	PC2
Rainfall	0.034	-0.913
Sunspot	-0.922	0.162
^7Be	0.856	0.358
PM10	0.424	0.769
TSP	0.790	0.423
Variance	58.4%	24.5%

4 CONCLUSIONS

The continuous monitoring conducted over a three-year period allow for the determination of mean monthly concentrations of ^7Be . The monthly activity for ^7Be shows a fluctuation which has

oscillatory characteristics with enhanced activity in spring-summer months during each year. The ground level concentration of ^7Be is influenced by a few atmospheric processes, such as wet (via precipitation) and the change in the atmospheric production rate due to solar activity, strong stratospheric-tropospheric exchange

Inverse correlation have been observed between mean annual ^7Be concentration and sunspot number and was quantified by the computed value of the correlation coefficient r .

The results of the Principal Component Analysis yielded two components which explain 82.9% of total variance

5 ACKNOWLEDGMENT

The authors wish to thank to Spanish Nuclear Safety Council (CSN) for financial support. The authors gratefully acknowledge to Spanish Meteorological Agency (AEMET), Solar Influences Data Analysis Center (SIDC) and Environmental Health Service of the Andalusian Government for the provision of data used in this study.

REFERENCES

- [1] Larsen RJ. "Global decrease of Beryllium-7 in surface air". *Journal of Environmental Radioactivity*, 18, 1993. Pages 85–87.
- [2] F Cannizzaro, G Greco, M Raneli, M.C Spitale, E Tomarchio. "Concentration measurements of ^7Be at ground level air at Palermo, Italy—comparison with solar activity over a period of 21 years". *Journal of Environmental Radioactivity*. Volume 72, Issue 3, 2004, Pages 259–271.
- [3] S. Rodríguez, X. Querol, A. Alastuey, G. Kallos O. Kakaliagou. "Saharan dust contributions to PM10 and TSP levels in Southern and Eastern Spain". *Atmospheric Environment*. Volume 35, Issue 14, May 2001, Pages 2433–2447.
- [4] C. Dueñas, M.C. Fernández, E. Liger, J. Carretero. "Gross alpha, gross beta activities and ^7Be concentrations in surface air: analysis of their variations and prediction model". *Atmospheric Environment*. Volume 33, Issue 22, September 1999, Pages 3705–3715
- [5] C. Papastefanou, A. Ioannidou. "Beryllium-7 and solar activity". *Applied Radiation and Isotopes*. Volume 61, Issue 6, December 2004, Pages 1493–1495

Particulate matter in the indoor and outdoor air of a gymnasium and a fronton

Célia Alves¹, Ana Calvo², Liliana Marques³, Amaya Castro⁴, Roberto Fraile⁵, Teresa Nunes⁶

Abstract — An indoor/outdoor monitoring programme of PM₁₀ was carried out in two sports venues (a fronton and a gymnasium) belonging to the University of León. Levels always below 50 µg m⁻³ were obtained in the fronton and outdoor air. Due to the climbing chalk and the constant process of resuspension, concentrations above 150 µg m⁻³ were registered in the gymnasium. The chalk dust contributed to CO₃²⁻ concentrations of 32±9.4 µg m⁻³ in this sports facility, which represented, on average, 18% of the PM₁₀ mass. Here, the carbonate levels were 128 times higher than those registered outdoors. Much lower concentrations, around 1 µg m⁻³, were measured in the fronton. The chalk dust is also responsible for the high Mg²⁺ concentrations in the gym (4.7±0.89 µg m⁻³), unfolding a PM₁₀ mass fraction of 2.7%. The secondary ions NO₃⁻ and SO₄²⁻ made up, respectively, 1-5% and 6-7% of the outdoor particle mass concentrations. The other ions represented minor mass fractions, either in the two sports facilities or outdoors. Total carbon (organic and elemental carbon) accounted for almost 30% of PM₁₀ in both indoor spaces. The indoor carbonaceous content decreases during weekend, approaching the outdoor levels. Concentration and size distributions revealed a clear dependence on physical activities and attendance to sports facilities.

Keywords — EC, OC, PM₁₀, size distribution, water soluble ions

1 INTRODUCTION

People in modern societies spend about 90% of their time indoors. Hence, indoor air quality (IAQ) has a significant impact on public health. Several IAQ monitoring programmes have been carried out in schools [e.g. 1-4], homes [5-9] and offices [10-12]. Comparatively, almost nothing is known about IAQ in recreation facilities [13-16]. Particulate matter is one of the most important pollutants in indoor air. Athletes and other sports practitioners can be at risk when they are training or exercising because the amounts of pollutants drawn into the lungs increase proportionally with increasing ventilation rates and the air is inhaled through the mouth, bypassing the normal nasal mechanisms for filtration of particles [17]. Particle size determines its deposition site and fraction in human lungs and its potential translocation to other target organs [18, 19]. Organic

and metal constituents have been identified as capable of inducing pro-inflammatory effects in the lung due to their ability to produce oxidative stress [20]. Particle size distribution is also one of the key characteristics related to formation and post-formation processes [21].

In this study, an indoor/outdoor monitoring programme of particulate matter levels and the associated chemical composition was carried out in two sports venues with distinct characteristics. The particle size distributions were also obtained. Knowledge and understanding of the presence and location of modes in particle distributions is of utmost importance not only for evaluating sources and understanding the mechanisms of atmospheric processes, but also for exposure and risk assessment, principally for setting standards and guidelines for air quality.

2 METHODOLOGIES

2.1 Description of sports facilities

Two sports facilities belonging to the University of León, Spain, were chosen to carry out the monitoring programme: a fronton and a gymnasium. A fronton is a court used as playing area for a variant of paddleball. It is made up of a rectangular floor and three vertical walls, named *frontis*; the front wall is the main one, where the hits are directed according to the rules. The University of León fronton building is a closed court. Part of the fourth wall (the one that is not part of the court) is windowed and has a 4 tiered wooden bench seating. The global dimensions of the building are 36 m length × 20 m width × 27 m height. A total of 16

1. Célia Alves is with the Centre for Environment and Marine Studies, Department of Environment, University of Aveiro, 3810-193 Aveiro, Portugal. E-mail: celia.alves@ua.pt
2. Ana Calvo is with the Centre for Environment and Marine Studies, Department of Environment, University of Aveiro, 3810-193 Aveiro, Portugal. E-mail: anacalvo@ua.pt
3. Liliana Marques is with the Centre for Environment and Marine Studies, Department of Environment, University of Aveiro, 3810-193 Aveiro, Portugal. E-mail: lrmarques@ua.pt
4. Amaya Castro is with Department of Physics (IMARENAB), University of León, León 24071, Spain. E-mail: amaya.castro@unileon.es
5. Roberto Fraile is with Department of Physics (IMARENAB), University of León, León 24071, Spain. E-mail: roberto.fraile@unileon.es
6. Teresa Nunes is with the Centre for Environment and Marine Studies, Department of Environment, University of Aveiro, 3810-193 Aveiro, Portugal. E-mail: tnunes@ua.pt

vents are evenly distributed at the top of the front and opposite walls to provide permanent natural air exchange. During the sampling campaign, 2-h long matches were organised, between 10:00 and 14:00 and between 16:00 and 20:00, involving 4 players. The games took place without or with only few spectators (up to 6).

The gymnasium is 15 m wide, 27 m long and has a height of 10.6 m. It has no windows and a half-cylinder skylight (5 m diameter and 20.3 m length) centred on the roof. The vinyl flooring is practically coated with gym mats and safety mattresses. The sports equipments included asymmetric bars/high bar, rings, parallel bars, beams, pommel horse, tumble track, trampolines, wall bars, and dug pit with foam cubes. Due to the high temperatures reached after the late morning hours, a side gate was frequently open when the gymnasium was busy. The gym does not have any mechanical ventilation system. During the sampling campaign, it was occupied by college athletes between 9:00 and 14:00 and between 17:00 and 19:00. A much higher attendance was observed until mid-morning, because sports activities were included in the summer academy for kids sponsored by the university.

2.2 Sampling and measurement equipments

The monitoring campaign was carried out between 8 and 22 July, 2012. During the first week, measurements took place in the fronton. In the second week, samplers were deployed in the gymnasium. On working days, during the occupancy periods, simultaneous indoor and outdoor sampling of particulate matter with equivalent aerodynamic diameter less than 10 μm (PM_{10}) was performed. At weekends, a 48-h sampling schedule was adopted. The PM_{10} samples were collected onto pre-baked (6 h at 500 °C) 47 mm diameter quartz filters using Echo TCR Tecora samplers, following the EN 12341 norm. In addition, the 0.1-10 μm latex particle size spectra were measured in 31 discrete channels (size ranges) using a laser spectrometer probe (Passive Cavity Aerosol Spectrometer Probe, PMS Model PCASP-X).

2.3 Analytical techniques

Following the gravimetric determination of the PM_{10} mass under controlled temperature and relative humidity conditions, samples were analysed by a home-made thermo-optical transmission system in order to obtain the carbonaceous content. After exposure of filter punches to HCl vapours to remove carbonate carbon, controlled heating in anoxic and oxic conditions was performed to separate, respectively, OC into two fractions of increasing volatility and EC, which were then measured in the form of CO_2 by an infrared non-dispersive analyser. The first fraction corresponds to the volatilisation at

$T < 200^\circ\text{C}$ of lower molecular weight organics (OC1). The second fraction is related to the decomposition and oxidation of higher molecular weight species at temperatures ranging from 200 to 600°C (OC2). However, pyrolysed organic carbon (PC), formed during the previous heating steps, is only released in oxic conditions, when the sample is heated up to 850 °C, evolving simultaneously with EC. The interference between PC and EC can be controlled by continuous evaluation of the blackening of the filter using a laser beam and a photodetector that measures the light transmittance. The split between the PC and EC is assigned when the initial (baseline) value of the filter transmittance is reached. All carbon removed before the split is considered organic, and that removed after the split is considered elemental. Carbonates present in PM_{10} samples were analysed through the release of CO_2 , and measurement by the same non-dispersive infrared analyser coupled to the thermo-optical system, when a punch of each filter was acidified with orthophosphoric acid (20%) in a free CO_2 gas stream.

For the determination of water soluble inorganic ions, small punches of the filters were extracted with ultra pure Milli-Q water. Dionex AS14 and CS12 chromatographic columns with Dionex AG14 and CG12 guard columns coupled to II Dionex CMMS III suppressors, respectively for anions and cations, have been used. For the final results, blank values were taken into account.

3 RESULTS AND DISCUSSION

3.1 Particle levels and carbonaceous content

High PM_{10} concentrations, between 154 and 198 $\mu\text{g m}^{-3}$, were obtained during the occupancy periods in the gymnasium. On the weekend, indoor PM_{10} decreased to 17 $\mu\text{g m}^{-3}$, which is comparable to the levels measured outdoors throughout the week. Lower indoor levels, ranging from 38 to 43 $\mu\text{g m}^{-3}$, were measured in the fronton. The weekend level in this sports venue was 13 $\mu\text{g m}^{-3}$ (Table 1). On working days, I/O ratios close to 2 and from 7 to 57 were, respectively, determined for the fronton and the gymnasium. There is no common threshold limit for PM_{10} in indoor spaces. Depending on organisations or IAQ class, the guideline values can range from 20 to 180 $\mu\text{g m}^{-3}$. Regardless of the standards considered, it can be seen that sports practitioners are exposed to potentially harmful concentrations of PM_{10} in the gym. The use of climbing chalk as drying agent for hands and the constant process of resuspension of sedimented material due to physical activities represent the main causes for the high particle levels in this venue.

Total carbon ($\text{TC}=\text{OC}+\text{EC}$) accounted for almost 30% of PM_{10} in both indoor spaces. In the fronton, the carbonaceous content decreased during the

weekend, approaching the outdoor levels ($TC/PM_{10}=18-20\%$). An I/O ratio around 1.4 during the occupancy periods suggests the presence of indoor sources of carbonaceous material. In the gymnasium, the particle mass fractions represented by TC remained relatively constant throughout the whole week. However, the TC absolute concentrations dropped from an average value of $27 \mu\text{g m}^{-3}$ during gymnastics activities to $20 \mu\text{g m}^{-3}$ over the weekend.

Table 1. PM_{10} ($\mu\text{g m}^{-3}$) measured during weekdays (WD) and weekends (WE) and indoor-to-outdoor ratios (I/O).

	Fronton	
	WD	WE
Indoor	40.0 ± 3.54	13.3
Outdoor	22.7 ± 1.77	12.6
I/O	1.77 ± 0.02	1.01
	Gymnasium	
	WD	WE
Indoor	177 ± 17.4	16.8
Outdoor	27.3 ± 22.0	17.5
I/O	11.3 ± 7.84	0.96

OC represented an overwhelming mass fraction of TC. Independently of the day of the week, OC/EC ratios around 6 were observed in the fronton, whereas an average ratio of 72 was determined for the occupancy periods in the gymnasium. OC/EC ratios in the 4-10 range were found for outdoor particles. During occupancy periods in the fronton, OC accounted for 23.4% of PM_{10} , whilst mass percentages around 15-17% were obtained for the vacant period (weekend), as well for outdoors (Fig. 1).

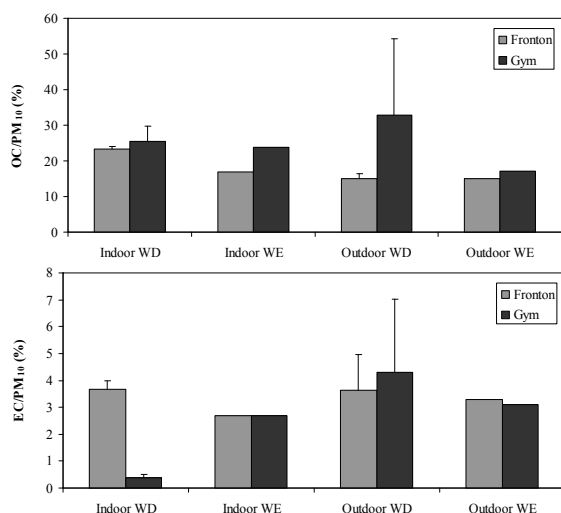


Fig. 1. Organic and elemental carbon PM_{10} mass fractions.

An average OC mass percentage close to that of the fronton was determined for the gymnasium on weekdays. A higher percentage (33%) was obtained for the corresponding period in the outdoor environment. The increase in the PM_{10} mass fraction of OC during the second week of the monitoring

programme is likely associated with enhanced secondary organic aerosol formation due to rising temperatures and, consequently, intensified photochemical activity. In fact, the mean temperature values increased from $18 \text{ }^\circ\text{C}$ (1st week) to $23 \text{ }^\circ\text{C}$ (2nd week), reaching several daily maxima around $37 \text{ }^\circ\text{C}$.

For the whole monitoring programme in the fronton, the EC particle mass fractions were relatively constant (3-4%), both indoors and outdoors. Nevertheless, indoor EC concentrations around $1.5 \mu\text{g m}^{-3}$ during the occupancy periods concurrently with outdoor levels in the range $0.65-0.98 \mu\text{g m}^{-3}$ ($I/O = 1.5-2.3$) indicate the presence of indoor sources. The detection of higher EC levels indoors than outdoors may be related to the fact that a corner of the fronton was used as parking spot of a lawn tractor mower. Several entrances and exits of this vehicle during the monitoring programme and the associated fossil fuel emissions may have contributed to this curious result. In the gymnasium, excepting for the occupancy periods, the EC mass fractions measured, both indoors and outdoors, were 3-4% of the PM_{10} mass concentrations. Due to the very high inorganic content in indoor particles, EC represented a very low mass fraction ($EC/PM_{10} < 0.4\%$) in this facility when physical activities were taking place.

2.4 Water insoluble inorganic ions

The use of climbing chalk (magnesia alba) in the gymnasium contributed to carbonate (CO_3^{2-}) concentrations of $32 \pm 9.4 \mu\text{g m}^{-3}$, which represented, on average, 18% of the PM_{10} mass (Fig. 2). The carbonate levels in this sports venue were 128 times higher than those registered outdoors. Much lower concentrations, around $2.6 \mu\text{g m}^{-3}$, were measured in the fronton. It is possible that the strong alkaline nature of the climbing chalk could contribute to the absorption of CO_2 from air to form more carbonate. The chalk dust is also responsible for the high Mg^{2+} concentrations in the gym ($4.7 \pm 0.89 \mu\text{g m}^{-3}$), unfolding a PM_{10} mass fraction of 2.7%. The excess of carbonate in relation to magnesium indicates that CO_3^{2-} is present in other forms (e.g. CaCO_3 and Na_2CO_3), besides magnesia alba (hydrated magnesium carbonate hydroxide). In addition to a crustal origin of particles entrained from outdoors, CaCO_3 may also be associated with construction materials (concrete, sandstone or cinder-concrete blocks). Besides an origin in crustal materials, Na_2CO_3 may be formed in the atmosphere by reaction between the precursor ions. The good correlations found between CO_3^{2-} and Mg^{2+} ($r^2=0.99$), Na^+ ($r^2=0.82$) and Ca^{2+} ($r^2=0.78$) corroborates the existence of various carbonate salts in particles from the gym. It should be noted, yet, that the presence of different carbonate salts as impurities in magnesia alba cannot be disregarded.

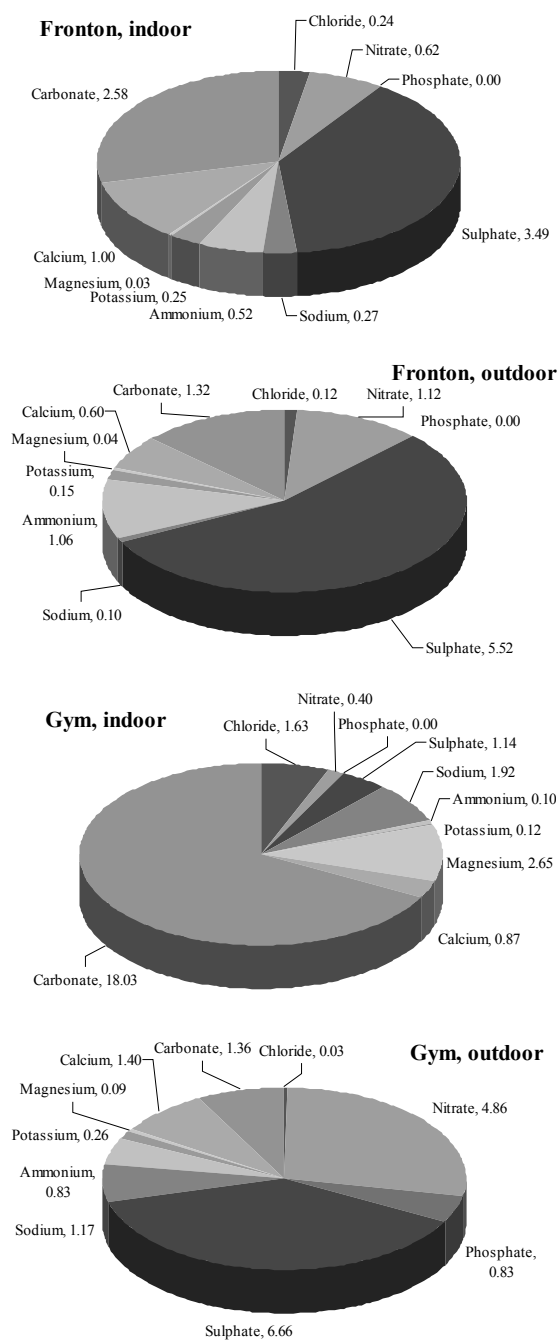


Fig. 2. Mass percentages of water soluble ions in PM₁₀.

As far as we know, the toxicological properties of climbing chalk have not been studied so far. Magnesium carbonate is the material with the closest chemical composition for which health hazards have been evaluated [22]. Although MgCO₃ is not a carcinogen, it can cause coughing and wheezing, as well as some tightness in the chest. Chronic exposure for a number of years can trigger or exacerbate respiratory problems [23]. The use of liquid chalk instead of the common magnesia alba, has been recently proven to be an effective and inexpensive measure to reduce particle levels in gymnasiums [24].

Sodium and chloride made up, respectively, 1.9

and 1.6% of the PM₁₀ mass in the gymnasium. These two species are the predominant minerals in sweat. High occupancy rates, intense physical activities and temperatures sometimes reaching 37 °C may help explain the detection at appreciable amounts of bioeffluent components in indoor aerosols. Secondary water soluble ions (SO₄²⁻ and NO₃⁻) dominated the outdoor PM₁₀. The other ions represent minor mass fractions, either in the two sports facilities or outdoors.

3.4 Size distributions

During the periods of sports activities, the number of particles ranged between 200 and 600 particles cm⁻³ for the fronton and between 250 and 750 particles cm⁻³ for the gymnasium. A decrease in the number of particles was observed during vacant periods. However, during nocturnal periods, the number of particles increased significantly, reaching values as high as 1200 particles cm⁻³. This increase is mainly experienced in the fine mode. Formation of new aerosol particles by nucleation and growth has been recently observed at night by Ortega et al., [25] in chamber experiments. The nocturnal events have been explained by the oxidation of volatile organic compounds (VOCs). Thus, VOCs emitted during the cleaning activities in the late afternoon may have contributed to nocturnal nucleation events. Molinié et al. [26] observed astonishing concentrations during the night in an office with no active indoor sources. The authors explained this result with the penetration of outdoor particles, which presented night-time enhanced concentrations due to stagnant conditions that prevented mixing. Fig 3 shows an example of the evolution of the number of particles throughout a day in both sports venues.

A significant increase in the coarse fraction was observed in the gymnasium when magnesia alba was being used (Fig. 3b). In the fronton, a noteworthy increase in the number of particles, either in the fine or the coarse modes, was registered during cleaning activities, reaching values up to 2400 particles cm⁻³ (Fig. 4).

During the weekend, the number of particles was significantly higher in the gymnasium, with a mean value of 410±140 particles cm⁻³. In the fronton, a mean concentration of 300±100 particles cm⁻³ was observed. In both sports venues, the highest number concentrations were reached at night-time.

A limited number of measurements were performed outdoors. The availability of only a single aerosol spectrometer, associated with its high sensitivity, has restricted the number of displacements of this unit to the outside. The outdoor number of particles varied from day to day, registering higher values during the first week. A mean value of 351±154 particles cm⁻³ with a peak concentration of 725 particles cm⁻³ was observed.

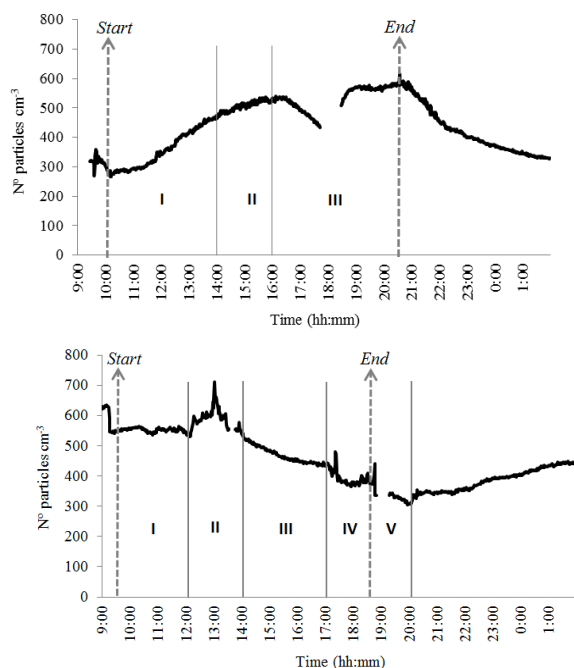


Fig. 3 Evolution of the number of particles. Upper panel - in the fronton: I and III: sports activities, II: vacant period; Lower panel - in the gymnasium: I and IV: sports activities without using magnesia alba; II: sport activities using magnesia alba; III: vacant period; V: cleaning activities.

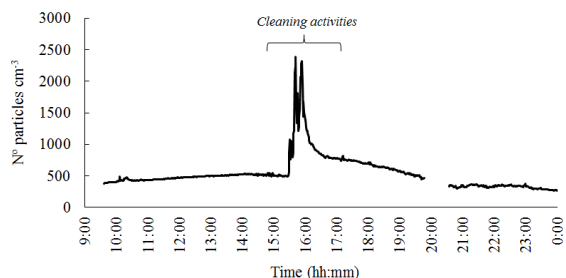


Fig. 4. Total N° particles cm^{-3} registered during cleaning activities in the fronton.

CONCLUSIONS

PM_{10} concentrations in the indoor environment of sports venues are highly variable due to various influencing factors: source types, building characteristics, the activities of practitioners, occupancy rates, etc. Some activities, such as gymnastics lead to a constant resuspension process of particles from the surfaces. Furthermore, the use of magnesia alba as drying agent for hands contributes to very high loads of particulate material, which is very rich in carbonate and magnesium. Taking into account that the health effects of these particles are not well established, the precautionary

principle should be applied. Prevention and remediation actions should be envisaged to reduce the indoor levels.

Additional investigations are needed to characterise the composition of indoor particles and their toxicological properties compared to particles from outdoor origin.

ACKNOWLEDGMENTS

This study was partially funded by the Centre of Environmental and Marine Studies (CESAM) of the University of Aveiro and by the Spanish Ministry of Science and Innovation (Grant TEC2010-19241-C02-01). Ana Calvo acknowledges the postdoctoral grant SFRH/BPD/64810/2009 from the Portuguese Science Foundation (FCT).

REFERENCES

- [1] C. Alves, T. Nunes, J. Silva, M. Duarte, "Comfort parameters and particulate matter (PM_{10} and $PM_{2.5}$) in school classrooms and outdoor air," *Aerosol Air Qual. Res.*, in press.
- [2] P.N. Pegas, T. Nunes, C.A. Alves, J.R. Silva, S.L.A. Vieira, A. Caseiro, C. Pio, "Indoor and outdoor characterisation of organic and inorganic compounds in city centre and suburban elementary schools of Aveiro, Portugal," *Atmos. Environ.*, vol. 55, pp. 80-89, 2012.
- [3] S.M. Almeida, N. Canha, A. Silva, M.C. Freitas, P. Pegas, C. Alves, M. Evtugina, C. Pio, "Children exposure to air particulate matter in indoor of Lisbon primary schools," *Atmos. Environ.*, vol. 45, pp. 7594-7599, 2011.
- [4] M. Stranger, S.S. Potgieter-Vermaakand, R. Van Grieken, "Characterization of indoor air quality in primary schools in Antwerp, Belgium," *Indoor Air*, vol. 18, pp. 454-463, 2008.
- [5] H. Guo, N.H. Kwok, H.R. Cheng, S.C. Lee, W.T. Hung, Y.S. Li, "Formaldehyde and volatile organic compounds in Hong Kong homes: concentrations and impact factors," *Indoor Air*, vol. 19, pp. 206-217, 2009.
- [6] S. Semple, C. Garden, M. Coggins, K.S. Galea, P. Whelan, H. Cowie, A. Sánchez-Jiménez, P.S. Thorne, J.F. Hurley, J.G. Ayres, "Contribution of solid fuel, gas combustion, or tobacco smoke to indoor air pollutant concentrations in Irish and Scottish homes," *Indoor Air*, vol. 22, pp. 212-223, 2012.
- [7] S. Batterman, L. Du, G. Mentz, B. Mukherjee, E. Parker, C. Godwin, J.-Y. Chin, A. O'Toole, T. Robins, Z. Rowe, T. Lewis, "Particulate matter concentrations in residences: an intervention study evaluating stand-alone filters and air conditioners," *Indoor Air*, vol. 22, pp. 235-252, 2012.
- [8] M.C. McCormack, P.N. Breyse, N.N. Hansel, E.C. Matsui, E.S. Tonorezos, J. Curtin-Brosnan, D.L. Williams, T.J. Buckley, P.A. Eggleston, G.B. Diette, "Common household activities are associated with elevated particulate matter concentrations in bedrooms of inner-city Baltimore preschool children," *Environ. Res.*, vol. 106, pp. 148-155, 2008.
- [9] H. Huang, J.J. Cao, S.C. Lee, C.W. Zou, X.G. Chen, S.J. Fan, "Spatial variation and relationship of indoor/outdoor $PM_{2.5}$ at residential homes in Guangzhou city, China," *Aerosol Air Qual. Res.*, vol. 7, pp. 518-530, 2007.
- [10] G. Sangiorgi, L. Ferrero, B.S. Ferrini, C. Lo Porto, M.G. Perrone, R. Zangrando, A. Gambaro, Z. Lazzati, E. Bolzacchini, "Indoor airborne particle sources and semi-volatile partitioning effect of outdoor fine PM in offices," *Atmos. Environ.*, vol. 65, pp. 205-214, 2013.
- [11] H.J. Salonen, A.L. Pasanen, S.K. Lappalainen, H.M. Riuttala, T.M. Tuomi, P.O. Pasanen, B.C. Bäck, K.E.

- Reijula, "Airborne concentrations of volatile organic compounds, formaldehyde and ammonia in Finnish office buildings with suspected indoor air problems," *J. Occup. Environ. Hyg.*, vol. 6, pp. 200-209, 2009.
- [12] C. Jia, S. Batterman, C. Godwin, S. Charles, J.Y. Chin, "Sources and migration of volatile organic compounds in mixed-use buildings," *Indoor Air*, vol. 20, pp. 357-369, 2010.
- [13] R.O. Salonen, A.S. Pennanen, M. Vahteristo, P. Korkeila, S. Alm, J.T. Randell, "Health risk assessment of indoor air pollution in Finnish ice arenas," *Environ. Int.*, Vol. 34, pp. 51-57, 2008.
- [14] G. Buonanno, F.C. Fuoco, S. Marini, L. Stabile, "Particle resuspension in school gyms during physical activities," *Aerosol Air Qual. Res.*, vol. 12, pp. 803-813, 2012.
- [15] H. Guo, S.C. Lee, L.Y. Chan, "Indoor air quality in ice skating rinks in Hong Kong," *Environ. Res.*, vol. 94, pp. 327-335, 2004.
- [16] K.W. Rundell, "High levels of airborne ultrafine and fine particulate matter in indoor ice arenas," *Inhal. Toxicol.*, vol. 15, pp. 237-250, 2003.
- [17] A. Carlisle, N. Sharp "Exercise and outdoor ambient air pollution," *Br. J. Sports Med.*, vol. 35, pp. 214-222, 2001.
- [18] K. Donaldson, V. Stone, P.S. Gilmour, D.M. Brown, W. MacNee, "Ultrafine particles: Mechanisms of lung injury," *Philos. Trans. R. Soc. London, Ser. A.*, vol. 358, pp. 2741-2748, 2000.
- [19] W.G. Kreyling, M. Semmler-Behnke, W. Moller, "Ultrafine particle-lung interactions: Does size matter?," *J. Aerosol Med.*, vol. 19, pp. 74-83, 2006.
- [20] P.H.N. Saldiva, R.W. Clarke, B.A. Coull, R.C. Stearns, J. Lawrence, G.G.K. Murthy, E. Diaz, P. Koutrakis, H. Suh, A. Tsuda, J.J. Godleski, "Lung inflammation induced by concentrated ambient air particles is related to particle composition," *Am. J. Respir. Crit. Care Med.*, vol. 165, pp. 1610-1617, 2002.
- [21] L. Morawska, D. U. Keogh, S.B. Thomas, K.L. Mengersen, "Modality in ambient particle size distributions and its potential as a basis for developing air quality regulation," *Atmos. Environ.*, vol. 42, pp. 1617-1628, 2008.
- [22] S. Weinbruch, T. Dirsch, M. Ebert, H. Hofmann, K. Kandler, "Dust exposure in indoor climbing halls," *J. Environ. Monit.*, vol. 10, pp. 648-654, 2008.
- [23] D. Majumdar, S.P.M. William, "Chalk dustfall during classroom teaching: particle size distribution and morphological characteristics," *Environ. Monit. Assess.*, vol. 148, pp. 343-335.
- [24] S. Weinbruch, T. Dirsch, K. Kandler, M. Ebert, G. Heimbürger, F. Hohenwarter, "Reducing dust exposure in indoor climbing gyms," *J. Environ. Monit.*, vol. 14, pp. 2114-2120, 2012.
- [25] J. Molinié, V. Clotaire, T. Plocoste, R.H. Petit, « Night outdoor air as a major source of indoor air particle concentrations in an office," Proceedings of the 91st American Meteorological Society, Washington, USA.
- [26] I.K. Ortega, T. Suni, M. Boy, T. Grönholm, H.E. Manninen, T. Nieminen, M. Ehn, H. Junninen, H. Hakola, H. Hellén, T. Valmari, H. Arvela, S. Zegelin, D. Hughes, M. Kitchen, H. Cleugh, D.R. Worsnop, M. Kulmala, V.-M. Kerminen, "New insights into nocturnal nucleation", *Atmos. Chem. Phys.*, vol. 12, pp. 4297-4312, 2012.

Organic speciation of PM_{2.5} from urban background sites in Oporto and Coimbra

Célia Alves, Teresa Nunes*, Ana Vicente, Cátia Gonçalves, Margarita Evtuygina, Telma Marques, Casimiro Pio

Abstract — Winter aerosol samples were daily collected during one-month long campaign in Oporto and Coimbra. The high-volume PM_{2.5} samples were solvent extracted and their organic content separated into several functional groups, which were then analysed by gas chromatography - mass spectrometry. The organic compounds identified and quantified revealed some differences between samples from Oporto and Coimbra. In general, the levels of total hydrocarbons in the urban background station of Oporto were higher than those of Coimbra. Concentration ratios between specific compounds and the presence of molecular markers derived from petroleum, such as hopanes, pristane and phytane, point out vehicles as the main source of pollutants. The contribution of biogenic compounds, mainly hydrocarbons associated with the waxy cuticle of vegetation, is also observable in both cities. The benzo[a]pyrene equivalent daily values were frequently higher than 1 ng m⁻³ in Oporto suggesting an additional cancer risk for the population. The PM_{2.5} mass attributable to vehicle emissions is higher in the background atmosphere of Oporto than in Coimbra. Biomass burning markers were detected at higher concentrations in Coimbra.

Keywords — GC-MS, organic speciation, PM_{2.5}, source apportionment

1 INTRODUCTION

It has long been recognised that atmospheric aerosols interact both directly and indirectly with the Earth's radiation budget and climate [1] and may have detrimental effects on human health, such as impairment of pulmonary function [2, 3]. The organic content of aerosols accounts for a substantial fraction of the global aerosol burden [4].

More than half of the world's population live in towns and cities. Thus, most of the aerosol characterisation and risk assessment studies have been carried out in urban areas [e.g. 5-9]. Among the target organic compounds, great efforts have been made to speciate, quantify, and understand the sources and reactivity of polycyclic aromatic compounds (PAHs), particularly due to their carcinogenic potential [10-16].

In Portugal, only a few reports have dealt with the organic composition of aerosols in urban environments [17, 18]. Comprehensive information on the chemical composition of atmospheric aerosols is useful to improve climate models, to propose emission abatement strategies and to estimate public health impacts. Aiming at better understanding the organic composition and sources of urban aerosols, a monitoring campaign was carried out in two cities: Oporto and Coimbra.

2 METHODOLOGY

2.1 Sampling

Fine (PM_{2.5}) and coarse (PM_{2.5-10}) aerosol samples were daily collected during one-month long campaign, simultaneously in Oporto and Coimbra, between January 27 and February 27, 2007. Urban background sites of the air quality network were, respectively, selected: Ermesinde (41°12.40'N; 8°33.17'W) and Geophysical Institute (10°13.33'N; 8°24.65'W). Samples were collected onto pre-fired quartz fibre filters with high volume samplers operating at 1.13 m³ min⁻¹.

2.2 Analytical Determinations

After gravimetric determination of particle concentration, small punches of the filters were analysed by a thermal-optical transmission technique to obtain the organic carbon (OC) content [19]. The PM_{2.5} samples were extracted for 24-h by refluxing dichloromethane and the nitrogen-dried extract was separated into 5 different organic fractions by flash chromatography with silica gel and various eluents of increasing polarity. The detailed description of the methodology for the extraction of organic compounds could be found in [20] and [17]. The fractionated extracts were analysed by gas chromatography-mass spectrometry (GC-MS). Before injection, the compounds with hydroxylic and carboxylic groups were converted into the corresponding TMS ether or TMS ester derivatives, respectively, by addition of a mixture of N,O-

*Authors are with the Centre for Environmental and Marine Studies, Department of Environment, University of Aveiro, 3810-193 Aveiro, Portugal. *E-mail: tnunes@ua.pt*

bis(trimethylsilyl)trifluoroacetamide and trimethylchlorosilane (BSTFA/TMCS; 99:1), followed by 3 h in an oven at 70°C. Extracts were injected within 24 h after the derivatisation procedure. Two quadrupole GC-MS were used, a HP 6890 MSD 5973 and a GC Trace Ultra, DSQ II from Thermo Scientific. Both instruments were operated with TRB-5MS 60 m × 0.25 mm × 0.25 μm columns. Helium was used as carrier gas at a constant flow of 1 mL min⁻¹. The heating programme was as follows: 60°C (1 min); 60-150°C (10°C min⁻¹); 150-290°C (5°C min⁻¹); 290°C (27 min). The acquisition mode was electronic impact at 70 eV and the scanned masses ranged from 50 to 850 m/z. Calibration for GC-MS analysis was based on a total of more than 200 standards in five different concentration levels with relative response factors determined individually for the majority of compounds. For those compounds with no authentic standards available, relative response factors were obtained as an average from the overall homologous series or from compounds of similar chemical structure and retention time. Standards and samples were both co-injected with two internal standards: tetracosane-D50, 1-chlorohexadecane or 1-chlorododecane. In the case of PAHs, an internal standard mix was used: 1,4-dichlorobenzene-D4, naphthalene-D8, acenaphthene-D10, phenanthrene-D10, chrysene-D12 and perylene-D12. Compound identification was based on comparison of resulting spectra with mass spectra libraries (Wiley and Nist), co-injection with authentic standards and analysis of fragmentation patterns. Quantification was performed by single ion monitoring and total ion chromatogram analysis.

3 RESULTS AND DISCUSSION

The daily mean PM_{2.5} concentrations during the sampling campaign were 29.9±25.0 and 19.3±13.3 μg m⁻³, in Oporto and Coimbra, respectively. PM_{2.5} represented 66.7±17.8 of the PM₁₀ mass in the northern city, whilst the percentage was 70.6±16.1% in Coimbra. On some days, in Oporto, the daily mean PM₁₀ concentrations exceeded the limit value of 50 μg m⁻³ set by the Air Quality Directive 2008/50/CE. Organic carbon accounted for 32.5±14.6% and 33.9±18.5% of the PM_{2.5} concentrations measured in Oporto and Coimbra, respectively. In general, the lowest concentrations of both PM_{2.5} and OC were associated with air masses from the Atlantic, while stagnant conditions, regional atmospheric circulation and/or continental air masses coincided with the most polluted days. The chromatographically resolved organic compounds encompassed aliphatic and aromatic hydrocarbons, carbonyls, methyl esters of carboxylic acids, alcohols, anhydrosugars and several types of acids. Anhydrosugars and acids will not be discussed in this manuscript.

3.1 Aliphatic Compounds

The aliphatic fraction of particulate matter comprised *n*-alkanes (Fig. 1), *n*-alkenes, hopanes, the unresolved complex mixture (UCM) of cyclic branched and unsaturated hydrocarbons and acyclic isoprenoids (pristane and phytane). Levels of total *n*-alkanes in the urban background station of Oporto (34.0±31.1 ng m⁻³) were higher than those of Coimbra (16.5±14.4 ng m⁻³). The contribution of biogenic hydrocarbons associated with the waxy cuticle of vegetation was observable in both cities. The wax *n*-alkanes represented, on average, 19 and 25% of the total concentrations in Oporto and Coimbra, respectively. Wax percentages from 14 to 25 have been described as typical for urban areas [11].

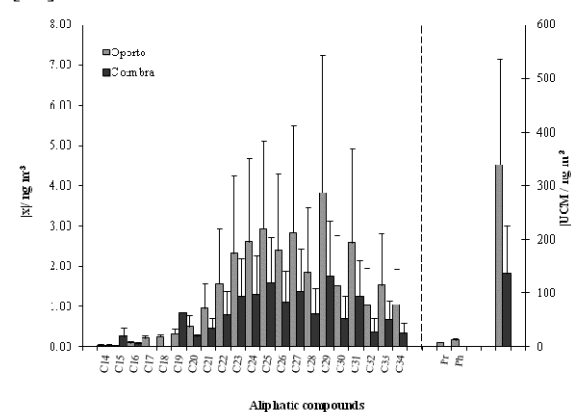


Fig. 1. Concentrations of *n*-alkanes, acyclic isoprenoid hydrocarbons and unresolved complex mixture in PM_{2.5} from Oporto and Coimbra.

The highest *n*-alkane concentrations were observed for the homologues C₂₅, C₂₇, C₂₉ and C₃₁. While the C₂₅ homologue has been associated with fossil fuel emissions, lubricating oils and unburnt heating oil, the other carbon numbers derive from epicuticular waxes from higher plants waxes [21]. The carbon preference index (CPI) is a diagnostic tool that identifies contributions arising from biogenic and anthropogenic inputs [22, 24]. The *n*-alkane CPI values obtained for both cities are indicative of a petrogenic signature (Table 1). Much higher CPI values are generally obtained in rural and forest environments [18, 21, 22]. The petrogenic input is confirmed by the high proportion between the chromatographically unresolved and resolved compounds (UCM/R). Pure hydrocarbon mixtures from plant waxes have UCM/R < 0.1, i.e. they have no UCM [24].

The hopanoid hydrocarbon series found in aerosols (Fig. 2) is derived from precursors in the cell membranes of prokaryotes (bacterial source) and cyanobacteria (blue-green algae source) in sedimentary organic matter over geological time [12]. C₃₀ hopanoids are also known to be present in certain higher plants (e.g. fern and moss). Accompanying the geological evolution, plant

remains undergo physical, chemical and biochemical transformations yielding a series of coals of increasing rank of maturity [25]. In this study, the total hopane concentrations in PM_{2.5} from Oporto and Coimbra were 6.17±3.35 and 2.61±1.73 ng m⁻³, respectively. These concentrations are of the same order as those determined in PM₁ aerosols in urban areas of the Czech Republic [12]. Concentrations 10 times higher (65±24 ng m⁻³) have been reported for wintertime samples collected in the urban atmosphere of Baoji, inland China [14]. Depending on the site, Herlekar et al. [8] obtained hopane concentrations from 7.81±2.00 to 94.1±28.7 ng m⁻³ in Mumbai, India.

Table 1. Diagnostic parameters applied to concentrations of organic compounds

Diagnostic parameters	Oporto	Coimbra
CPI <i>n</i> -alkanes	1.57±0.44	1.37±0.12
UCM/R	1.62±0.48	1.34±0.09
Wax <i>n</i> -alkanes (%)	25.4±8.08	19.1±4.02
Homohopane index	0.56±0.03	0.54±0.05
Bishomohopane index	0.59±0.01	0.59±0.05
C ₂₉ αβ/C ₃₀ αβ	1.16±0.04	1.11±0.07
Ts/Tm	0.89±0.10	0.88±0.09
CPAHs/TPAHs	0.90±0.03	0.88±0.04
IcdP/(IcdP+BghiP)	0.59±0.09	0.58±0.03
Flu/(Flu+Pyr)	0.52±0.04	0.52±0.12
BaA/(BaA+Chry)	0.63±0.15	0.52±0.11
Pyr/BaP	1.04±0.43	0.99±0.47
BghiP/BaP	0.89±0.43	0.74±0.36
BFs/BghiP	2.15±0.58	2.92±0.63
BaPE	0.93±0.86	0.29±0.25
CPI <i>n</i> -alkanols	4.82±3.92	6.27±5.90
Wax <i>n</i> -alkanols (%)	73.9±19.4	67.8±20.6

CPI_{alkanes} = Σ(C₁₃-C₃₅)/Σ(C₁₂-C₃₄); CPI_{alkanols} = Σ(C₁₂-C₃₄)/Σ(C₁₃-C₃₅); Wax C_n = [(C_n)-((C_{n+1}+C_{n-1})/2)]; Homohopane index = C₃₁αβ[S/(S+R)]; Bishomohopane index = C₃₂αβ[S/(S+R)]; CPAHs/TPAHs = concentrations of nine major nonalkylated compounds to the total concentration of PAHs; BFs = sum of concentrations of benzo[fluoranthenes]; BaPE = BaA × 0.06 + BFs × 0.07 + BaP + DBahA × 0.6 + IcdP × 0.08. See Figures 2 and 3 for other acronyms.

The homohopane and bishomohopane indexes obtained in both Portuguese cities are in the ranges described for vehicular emissions, whilst the C₂₉αβ/C₃₀αβ is within the values suggested for coal combustion. Rogge et al. [26] obtained indexes from 0.5 to 0.6 for gasoline and diesel emissions. Oros and Simoneit [27] reported C₂₉αβ/C₃₀αβ, C₃₁αβ[S/(S+R)] and C₃₂αβ[S/(S+R)] ratios, respectively, in the ranges 0.6-2.0, 0.1-0.4 and 0.2-0.4 for coal combustion. The Ts/Tm ratio is an additional indicator for the type of hopane emission sources, because during catagenesis 18α(H)-22,29,30-trisnorhopane (Ts) is more stable than 17α(H)-22,29,30-trisnorhopane (Tm) [9]. The ratio decreases when the impact of less mature fossil fuel (e.g. coal) increases or when instantaneous thermal maturation of biogenic hopanoids by biomass burning occurs. Ts/Tm values from 0.3 to 0.7 have

been found in aerosols impacted by biomass burning [28]. Song et al. [29] obtained Ts/Tm ratios of 1.33 and 1.09 for the particulate matter accumulated on the ceiling surfaces of vehicular tunnels in Hong Kong and Guangzhou, respectively. An average ratio of 1.07 has been reported for PM_{2.5} samples collected in a roadway tunnel in Marseille, France [30]. Thus, the Ts/Tm ratios around 0.9 obtained in the Portuguese cities indicate a mixed imprint of emissions from the combustion of both fossil and less thermally mature fuels.

Pristane (2,6,10,14-tetramethylpentadecane) and phytane (2,6,10,14-tetramethylhexadecane) were only detected in some samples from Oporto at an average Pr/Ph ratio of 0.69. Since it is highly infrequent to find phytane in biological materials (excepting some bacteria), most biogenic samples present Pr/Ph much higher than 1 [24]. Low ratios are indicative of a petrogenic hydrocarbon signature.

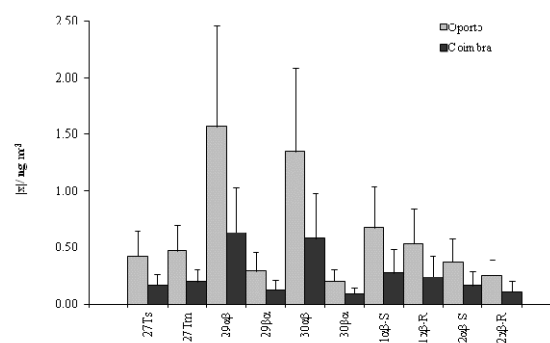


Fig. 2. Concentrations of hopanes in Oporto and Coimbra. 18α(H)-22,29,30-Trisnorhopane (Ts); 17α(H)-22,29,30-Trisnorhopane (Tm); 17α(H),21β(H)-30-Norhopane (29αβ); 17β(H),21α(H)-30-Norhopane (29βα); 17α(H),21β(H)-Hopane (30αβ); 17β(H),21α(H)-Hopane(30βα); 17α(H),21β(H)-22S or R-Homohopane (31αβ-S/R); 17α(H),21β(H)-22S or R-Bishomohopane (32αβ-S/R).

3.2 Polyaromatic Hydrocarbons

Polycyclic aromatic hydrocarbons were found at concentrations of 17.7±17.6 ng m⁻³ in the northern city, while lower levels of 7.3±7.4 ng m⁻³ were obtained in Coimbra (Fig. 3). In contrast with other PAH species, retene, a trace of wood combustion [31], was found at similar concentrations in both cities. The benzo[a]pyrene equivalent concentration (BaPE) has been introduced instead of the sole benzo[a]pyrene, a classical carcinogen and one of the most powerful mutagens, since the later is easily decomposed in reactive air. It tries to parameterise the health risk for humans related to ambient PAH exposure and is calculated by adding weighted concentrations of each carcinogenic congener [21]. Among the PAHs measured, the mass percentage of carcinogenic species was 63-64% in both cities. However, the average values of BaPE indicate a higher cancer risk in Oporto than in Coimbra. In the northern city, on most days, the BaPE daily values

exceeded the maximum permissible risk level of 1 ng m⁻³ set by the World Health Organisation. The BaPE concentrations obtained in Oporto and Coimbra are within the values reported for Barcelona and Zurich [21] and much lower than those obtained for Chinese cities [10, 15, 16].

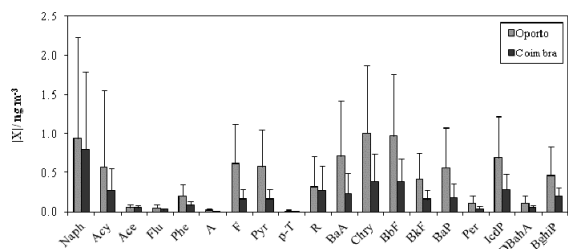


Fig. 3. Concentrations of major PAHs: naphthalene (Naph), acenaphthylene (Acy), acenaphthene (Ace), fluorene (F), phenanthrene (Phe), anthracene (A), fluoranthene (F), pyrene (Pyr), retene (R), benzo[a]anthracene (BaA), chrysene (Chry), benzo[b]fluoranthene (BbF), benzo[k]fluoranthene (BkF), benzo[a]pyrene (BaP), perylene (Per), indeno[1,2,3-cd]pyrene (IcdP), dibenzo[a,h]anthracene (DBahA), benzo[ghi]perylene (BghiP)

Various diagnostic concentration ratios of PAHs have been used to differentiate between petrogenic and pyrogenic sources (Table 1). The CPAHs/TPAHs, Pyr/BaP and BghiP/BaP ratios are consistent with the ranges of PAH emitted by vehicles, especially diesel-powered, whilst BFs/BghiP is closer to the values reported for wood burning [7, 21, 24]. A Fl/(Fl+Py) ratio around 0.51 is used as a tracer of domestic heating gas oil [32]. The IcdP/(IcdP+BghiP) and BaA/(BaA+Chry) ratios reveal mixed influences of wood burning and vehicle emissions [24].

3.3 Carbonyl Compounds

In both cities, *n*-alkanones from C₁₃ to C₃₁, with mixed origins, were present in the aerosol samples at similar concentrations (~ 0.5 ng m⁻³). Discontinuous series of *n*-alkanals, encompassing some of the homologues in the range C₁₀-C₂₉, were also observed. An even carbon number predominance for the homologues > C₂₀ was generally registered in Oporto. The homologue with highest mean concentrations was tetradecanal (1.1 ng m⁻³). The higher molecular weight homologues were not detected in most samples of Coimbra. The major carbonyl compound present in all aerosol samples was 6,10,14-trimethylpentadecanone-2-one, an oxidation product of farnesol and phytol in chlorophyll, also known as phytone [33]. It was found at average concentrations of 3.4 and 4.1 ng m⁻³ in Oporto and Coimbra, respectively. In PM_{2.5} samples from Augsburg, Germany, Schnelle-Kreis et al. [9] detected maximum levels (101 ng m⁻³) in July, while a 10-fold decrease was observed in wintertime. Thus, phytone was classified as a good marker for secondary biogenic aerosol. However,

Alves et al. [21] have detected this carbonyl compound at appreciable amounts in the winter aerosol from Zurich, pointing out biomass burning as another plausible source. The pyrogenic origin is corroborated by the detection of the isoprenoid ketone (225-2176 ng m⁻³) in the smoke plumes of prescribed fires [34].

A multifunctional carbonyl present in some samples, at concentrations up to 200 pg m⁻³, was 3,5-di-*tert*-butyl-4-hydroxybenzaldehyde (BHT-aldehyde). It has been previously detected in hourly in situ measurements made at Chebogue Point, Nova Scotia [35] and in PM_{2.5} samples collected in Birmingham, UK [36]. Alam et al. [36] have pointed out an origin in emissions from food industries where this chemical is used as food additive. However, an origin in emissions from motor vehicles is also plausible since many multifunctional carbonyls have been identified in PM_{2.5} collected in a highway tunnel [37].

Polycyclic aromatic ketones and aldehydes, such as 7H-benzo[c]fluoren-7-one, benzo[a]anthracene-7,12-dione, 9H-fluoren-9-one, hydroxy-9H-fluoren-9-one, 9,10-anthraquinone, phenanthrene-carboxaldehyde, 9-anthracenecarboxaldehyde and pyrenecarboxaldehyde, constituted oxy-PAHs present in almost all samples at individual levels in the order of tens or hundreds of pg m⁻³.

α-Hexylcinnamaldehyde was found in many samples (from undetectable to 400 pg m⁻³). It is a fragrance used in various consumer products and occurs naturally in the bark of some species [38]. It has also been detected in particle emissions from fireplace combustion of different wood species [39].

Nopinone and pinonaldehyde are secondary carbonyl aerosol products, formed from the ozonolysis of pinenes [40]. These pinenic products were present in PM_{2.5} at concentrations up to 0.35 and 9.2 ng m⁻³, respectively. In spite of their high vapour pressures, these constituents may partition into organic layers condensed onto pre-existing particles. Moreover, acid-catalysed polymerisation reactions can produce secondary organic aerosol (SOA) products that condense onto particles even though vapour pressure of the original compound is itself too high for partitioning [41].

3.4 Hydroxyl Compounds

The homologous series of *n*-alkanols (C₁₀-C₃₂) accounted for concentrations in the ranges 3-736 ng m⁻³ in Oporto and 21-630 ng m⁻³ in Coimbra. Around 70% of the levels of the higher molecular weight *n*-alkanols derived from vegetation waxes, while the lower homologues originated mainly from anthropogenic sources [21]. The *n*-alkanol levels followed the same temporal patterns as those observed for PM_{2.5}. Good (*r* = 0.92) or reasonable (*r* = 0.65) correlations were observed between both variables in Oporto and Coimbra, respectively. In general, the CPI values decreased with increasing

PM_{2.5} levels. This suggests that PM_{2.5} spikes were associated with anthropogenic pollution sources.

Some sterol compounds were present in the PM_{2.5} samples. Among them, phytosterols, such as sitosterol and stigmasterol, are plant-derived compounds, which are introduced into smoke by volatilisation during burning [31]. Sitosterol was detected at concentrations ranging from undetectable levels to 29.8 and 63.5 ng m⁻³ in Oporto and Coimbra, respectively. Stigmasterol was only found in aerosols from Coimbra, never exceeding 13.0 ng m⁻³. Lupeol, a tracer of angiosperm smoke, was also identified in both cities (Oporto: 0.112-10.3 ng m⁻³; Coimbra: undetectable-18.6 ng m⁻³).

3.5 Other Compounds

Methyl esters of *n*-alkanoic acids represent other subgroup of compounds present in atmospheric aerosols from the Portuguese cities. The homologous series ranged from methyl tetradecanoate to methyl hexacosanoate. Maximum total concentrations of 11.3 and 156 ng m⁻⁵ and mean values of 15.3 and 3.5 ng m⁻³ were registered in Oporto and Coimbra, respectively. Methyl alkanates have been previously detected in fine particles from distinct European regions and have been apportioned to biomass burning [9, 21]. The detection of methyl alkanates in PM_{2.5} emissions from residential wood combustion [42], wildfires [19] and prescribed fires [34], and their absence from vehicular emissions [26], support this assignment.

Tracers for the burning of plastics [43] have been detected at trace levels in the PM_{2.5} samples of both cities: Irganox 1076 and Irgafos 168. Their presence, although sporadic, is more visible in Coimbra. Some phthalates were also detected in the aerosol samples (1-100 ng m⁻³). Terephthalates were the most representative species. Phthalates have been classified as toxic, carcinogenic and/or endocrine disruptors [44, 45].

4 CONCLUSIONS

Some differences between Oporto and Coimbra were observed. The urban background atmosphere of Oporto showed the highest levels of PM_{2.5}, OC and hydrocarbon compounds. Molecular ratios and the presence of petroleum markers point out vehicle exhausts, especially from diesel powered engines, as the major pollutant source. Biomass burning also represents a significant emission source of organic compounds in both cities. Taking into account the rising prices of fossil fuels and electricity, it is expected that a growing band of residents who want cheaper and locally-available fuels will be increasingly looking at wood fuel boilers and stoves instead of those traditional forms of energy. This will certainly change the atmospheric pollution

patterns. To devise cost-effective mitigation measures, monitoring programmes, carried out in a regular basis, are recommended. This is even more important because, in this study, PM_{2.5} and the carcinogenic content exceeded the recommended levels on several days. Thus, it is imperative to control regional combustion sources to reduce the health risks associated with air pollution.

ACKNOWLEDGMENTS

The sampling campaign were performed within the project POCI/AMB/60267/2004 funded by the Portuguese Science Foundation (FCT). The analytical work was also funded by the FCT through the project "Source apportionment of URBan Emissions of primary particulate matter", PTDC/AAC-AMB/117956/2010 (URBE).

REFERENCES

- [1] K.S. Carslaw, O. Boucher, D.V. Spracklen, G.W. Mann, J. G.L. Rae, S. Woodward, M. Kulmala, "A review of natural aerosol interactions and feedbacks within the Earth system," *Atmos. Chem. Phys.*, vol. 10, pp. 1701-1737, 2010.
- [2] T. Islam, W.J. Gauderman, K. Berhane, R. McConnell, E. Avol, J.M. Peters, F.D. Gilliland, "Relationship between air pollution, lung function and asthma in adolescents," *Thorax*, vol. 62, pp. 957-963, 2007.
- [3] D.R. Riva, C.B. Magalhães, A.A. Lopes, T. Lanças, T. Mauad, O. Malm, S.S. Valença, P.H. Saldiva, D.S. Faffe, W.A. Zin, "Low dose of fine particulate matter (PM_{2.5}) can induce acute oxidative stress, inflammation and pulmonary impairment in healthy mice," *Inhal Toxicol.*, vol. 23, pp. 257-267, 2011.
- [4] Q. Zhang, J.L. Jimenez, M.R. Canagaratna, I.M. Ulbrich, N.L. Ng, D.R. Worsnop, Y. Sun, "Understanding atmospheric organic aerosols via factor analysis of aerosol mass spectrometry: a review," *Anal Bioanal Chem.*, vol. 401, pp. 3045-3067, 2011.
- [5] G. Wang, K. Kawamura, T. Watanabe, S. Lee, K. Ho, J. Cao, "High loadings and source strengths of organic aerosols in China," *Geophys. Res. Lett.*, vol. 33, L22801, doi:10.1029/2006GL027624, 2006.
- [6] X. Bi, B.R.T. Simoneit, G. Sheng, S. Ma, J. Fu., "Composition and major sources of organic compounds in urban aerosols," *Atmos. Res.*, vol. 88, pp. 256-265, 2008.
- [7] M. Tsapakis, E. Lagoudaki, E.G. Stephanou, I.G. Kavouras, P. Koutrakis, P. Oyola, D. von Baer, "The composition and sources of PM_{2.5} organic aerosol in two urban areas of Chile," *Atmos. Environ.*, vol. 36, pp. 3851-3863, 2002.
- [8] M. Herlekar, A.E. Joseph, R. Kumar, I. Gupta, "Chemical speciation and source assignment of particulate matter (PM₁₀) phase molecular markers in Mumbai," *Aerosol Air Qual. Res.*, vol. 12, pp. 1247-1260, 2012.
- [9] J. Schnelle-Kreis., M. Sklorz, A. Peters, J. Cyrys, R. Zimmermann, "Analysis of particle-associated semi-volatile aromatic and aliphatic hydrocarbons in urban particulate matter on a daily basis," *Atmos. Environ.*, vol. 39, pp. 7702-7714, 2005.
- [10] M. Xie, G. Wang, S. Hu, Q. Han, Y. Xu, Z. Gao, "Aliphatic alkanes and polycyclic aromatic hydrocarbons in atmospheric PM₁₀ aerosols from Baoji, China: Implications for coal burning," *Atmos. Res.*, vol. 93, pp. 840-848.
- [11] M.A.B. Mazquiarán, L.C.O. Pinedo, "Organic composition of atmospheric urban aerosol: Variations and sources of aliphatic and polycyclic aromatic hydrocarbons," *Atmos. Res.*, vol. 85, pp. 288-299, 2007.

- [12] K. Krupal, P. Mikuska, Z. Vecera, "Polycyclic aromatic hydrocarbons and hopanes in PM₁ aerosols in urban areas," *Atmos. Environ.*, vol. 67, pp. 27-37, 2013.
- [13] S. Wei, B. Huang, M. Liu, X. Bi, Z. R., G. Sheng, J. Fu, "Characterization of PM_{2.5}-bound nitrated and oxygenated PAHs in two industrial sites of South China," *Atmos. Res.*, vol. 109-110, pp. 76-83, 2012.
- [14] G. Wang, K. Kawamura, M. Xie, S. Hu, S. Gao, Z. An, Z. Wang, "Size- distributions of *n*-alkanes, PAHs and hopanes and their sources in the urban, mountain and marine atmospheres over East Asia," *Atmos. Chem. Phys.*, vol. 9, pp. 8869-8882, 2009.
- [15] W. Wang, S. Tao, W. Wang, G. Shen, J. Zhao, K.C. Lam, "Airborne particulates and polycyclic aromatic hydrocarbons (PAHs) in ambient air in Donghe, Northern China," *J. Environ. Sci. Health A*, vol. 44, pp. 854-860, 2009.
- [16] Y. Chen, Y. Feng, S. Xiong, D. Liu, G. Wang, G. Sheng, J. Fu, "Polycyclic aromatic hydrocarbons in the atmosphere of Shanghai," *Environ. Monit. Assess.*, vol. 172, pp. 235-247, 2011.
- [17] C. Alves, C.A. Pio A. Duarte, "Composition of extractable organic matter of air particles from rural and urban Portuguese areas," *Atmos. Environ.*, vol. 35, pp. 5485-5496, 2001.
- [18] C. Oliveira, C. Pio, C. Alves, M. Evtuygina, P. Santos, V. Gonçalves, T. Nunes, A. Silvestre, F. Palmgren, P. Wahlin, S. Harrad, "Seasonal distribution of polar organic compounds in the urban atmosphere of two large cities from the North and South of Europe," *Atmos. Environ.*, vol. 41, pp. 5555-5570, 2007.
- [19] C.A. Alves, A. Vicente, C. Monteiro, C. Gonçalves, M. Evtuygina, C. Pio, "Emission of trace gases and organic components in smoke particles from a wildfire in a mixed-evergreen forest in Portugal," *Sci. Total Environ.*, vol. 409, pp. 1466-1475, 2011.
- [20] A. Gogou, M. Apostolaki, E. Stephanou, "Determination of organic markers in marine aerosols and sediments-one-step flash chromatography compound class fractionation and capillary gas chromatographic analysis," *J. Chromatogr. A*, vol. 799, pp. 215-231, 1998.
- [21] C. Alves, A. Vicente, C. Pio, G. Kiss, A. Hoffer, S. Decesari, A.S.H. Prevot M.C. Minguillón, X. Querol, R. Hillamo, G. Spindler, E. Swietlicki, "Organic compounds in aerosols from selected European sites - biogenic versus anthropogenic sources," *Atmos. Environ.*, vol. 59, pp. 243-255, 2012.
- [22] S. Yadav, A. Tandon, A.K. Attri, "Monthly and seasonal variations in aerosol associated *n*-alkane profiles in relation to meteorological parameters in New Delhi, India," *Aerosol Air Qual. Res.*, vol. 13, pp. 287-300, 2013.
- [23] R.M. Harrison, J. Yin, "Chemical speciation of PM_{2.5} at urban background and rural sites in the UK atmosphere," *J. Environ. Monit.*, vol. 12, 1404-1414, 2010.
- [24] C. Alves, "Characterisation of solvent extractable organic constituents in atmospheric particulate matter: an overview," *An. Acad. Bras. Ciênc.*, vol. 80, pp. 21-82, 2008.
- [25] B.R.T. Simoneit, X. Bi, D.R. Oros, P.M. Medeiros, G. Sheng, J. Fu, "Phenols and hydroxyl-PAHs (arylphenols) as tracers for coal smoke particulate matter: source test and ambient aerosol assessments," *Environ. Sci. Technol.*, vol. 41, pp. 7294-7302, 2007.
- [26] W.F. Rooge, L.M. Hildemann, M. Mazurek, G.R. Cass, "Sources of fine organic aerosol: 2. Noncatalyst and catalyst-equipped automobiles and heavy-duty diesel trucks," *Environ. Sci. Technol.*, vol. 27, pp. 636-651, 1993.
- [27] D.R. Oros, B.R.T. Simoneit, "Identification and emissions ratios of molecular tracers in coal smoke particulate matter," *Fuel*, vol. 79, pp. 515-536, 2000.
- [28] M. Fang, M. Zheng, F. Wang, K.L. To, A.B. Jaafar, S.L. Tong, "The solvent-extractable organic compounds in the Indonesia biomass burning aerosols - characterization studies," *Atmos. Environ.*, vol. 33, pp. 783-795, 1999.
- [29] Z. Song, M. You, N.S. Duzgoren-Aydin, "Characterization of particulate organics accumulated on the ceiling of vehicular tunnels in Hong Kong and Guangzhou, China," *Atmos. Environ.*, vol. 39, pp. 6398-6408, 2005.
- [30] I.E. Haddad, N. Marchand, J. Dron, B. Temine-Roussel, E. Quivet, H. Wortham, J.L. Jaffrezou, C. Baduel, D. Voisin, J.L. Besombes, G. Gille, "Comprehensive primary particulate organic characterization of vehicular exhaust emissions in France," *Atmos. Environ.* 43, 6190-6198.
- [31] C. Gonçalves, C. Alves, A.P. Fernandes, C. Monteiro, L. Tarelho L., M. Evtuygina, C. Pio, "Organic compounds in PM_{2.5} emitted from fireplace and woodstove combustion of typical Portuguese wood species," *Atmos. Environ.*, vol. 45, pp. 4533-4545, 2011.
- [32] M.B. Yunker, R.W. Macdonald, R. Vingarzan, R.H. Mitchell, D. Goyette, S. Sylvestre, "PAHs in the Fraser River basin: a critical appraisal of PAH ratios as indicators of PAH sources and composition," *Org. Geochem.*, vol. 33, pp. 489-515, 2002.
- [33] J.F. Rontani, P. Cuny, V. Grossi, "Photodegradation of chlorophyll phytyl chain in senescent leaves of higher plants," *Phytochem.*, vol. 42, pp. 347-351, 1996.
- [34] C.A. Alves, C. Gonçalves, M. Evtuygina, C.A. Pio, F. Mirante, H. Puxbaum, "Particulate organic compounds emitted from experimental wildland fires in a Mediterranean ecosystem," *Atmos. Environ.*, vol. 44, pp. 2750-2759, 2010.
- [35] B.J. Williams, A.H. Goldstein, D.B. Millet, R. Holzinger, N.M. Kreisberg, S.V. Hering, A.B. White, D.R. Worsnop, J.D. Allan, J.L. Jimenez, "Chemical speciation of organic aerosol during the International Consortium for Atmospheric Research on Transport and Transformation 2004: Results from in situ measurements," *J. Geophys. Res.*, vol. 112, D10S26, doi:10.1029/2006JD007601.
- [36] M.S. Alam, C.E. West, A.G. Scarlett, S.J. Rowland, R.M. Harrison, "Application of 2D-GCMS reveals many industrial chemicals in airborne particulate matter," *Atmos. Environ.*, vol. 65, pp. 101-111, 2013.
- [37] X. Rao, R. Kobayashi, R. White-Morris, R. Spaulding, P. Frazier, J.M. Charles, "GC/ITMS measurement of carbonyls and multifunctional carbonyls in PM_{2.5} particles emitted from motor vehicles," *J. AOAC Int.*, vol. 84, pp. 699-705, 2001.
- [38] A. Gursale, V. Dighe, G. Parekl, "Simultaneous quantitative determination of cinnamaldehyde and methyl eugenol from stem bark of *Cinnamomum zeylanicum* Blume using RP-HPLC," *J. Chromatogr. Sci.*, vol. 48, pp. 59-62, 2010.
- [39] P.M. Fine, G.R. Cass, B.R.T. Simoneit, "Chemical characterization of fine particle emissions from fireplace combustion of woods grown in the northeastern United States," *Environ. Sci. Technol.*, vol. 35, pp. 2665- 2675, 2001.
- [40] M. Jaoui, R.M. Kamens, "Gaseous and particulate oxidation products analysis of a mixture of α -pinene + β -pinene/O₃/air in the absence of light and α -pinene + β -pinene/NOx/air in the presence of natural sunlight," *J. Atmos. Chem.*, vol. 44, pp. 259-297, 2003.
- [41] M. Kallio, M. Jussila, T. Rissanen, P. Antilla, K. Hartonen, A. Reissell, R. Vreuls, M. Adachhour, T. Hyötyläinen, "Comprehensive two-dimensional gas chromatography coupled to time-of-flight mass spectrometry in the identification of organic compounds in atmospheric aerosols from coniferous forest," *J. Chromatogr. A*, vol. 1125, pp. 234-243, 2006.
- [42] P.M. Fine, G.R. Cass, B.R.T. Simoneit, "Chemical characterization of fine particle emissions from the fireplace combustion of wood types grown in the midwestern and western United States," *Environ. Eng. Sci.*, vol. 21, pp. 387-409, 2004.
- [43] B.R.T. Simoneit, P.M. Medeiros, B.M. Didyk, "Combustion products of plastics as indicators for refuse burning in the atmosphere," *Environ. Sci. Technol.*, vol. 39, pp. 6961-6970, 2005.
- [44] W.M. Kluwe, "Carcinogenic potential of phthalic acid esters and related compounds: structure-activity relationships," *Environ. Health Perspect.*, vol. 65, pp. 271-278, 1986
- [45] L. Sax, "Polyethylene terephthalate may yield endocrine disruptors," *Environ. Health Perspect.*, vol. 118, pp. 445-448, 2010.

Effect of gear selection on diesel exhaust particle number and size distributions in steady state

Aida Domínguez-Sáez¹, Carlos Martín², Carmen C. Barrios³

Abstract — This study investigates the influence of gear selection on pollutant emissions (CO₂, NO_x), focusing especially on the emission of particle number and size distribution. The study was conducted on a diesel engine 2.0 TDI 140 hp EURO 4. One basis of the eco-driving claims that selecting the highest gear as early as possible to avoid high engine speeds leads to a reduction of emissions and fuel consumption savings. The results show that this is true for the CO₂ and NO_x emissions, but the total number of fine and ultrafine particles in the range 5.6-560 nm presents some exceptions (with n<1500 rpm, the total particle number increases). The lower gears at high speeds (over 70 km/h) can cause a high emission of smaller particles (dp < 50 nm) that are most harmful to health.

Keywords — Diesel Engine, Eco-driving, Particle Number Concentration and Particle Size Distributions

1 INTRODUCTION

Population living in urban areas is exposed to high levels of pollutants. Fine and ultrafine particles from diesel vehicles are one of the most alarming pollutants. Diesel exhaust particulate matter enhances allergic response, facilitates the development of new allergy to aeroallergens [1] and airway inflammation [2]. Ultrafine particles (UPFs) from vehicle emission have the potential to damage pulmonary cell [3] among many other adverse health effects. Due to these negative effects, the air quality regulations are becoming more demanding and compelling need to reduce pollutant concentration levels in urban areas. Conventionally, measures to reduce the concentration of pollutants are focused mainly in two ways. The first focuses on reducing traffic congestion, change the typology of vehicles on the city and all measures that can be taken by the competent public authorities. The second type of measures is focused on reducing consumption and emissions of each vehicle individually (aftertreatment technology, driving style,...). It is demonstrated [4], [5] that an effective way to reduce emissions and fuel consumption is to promote the use of environmentally friendly driving style. One characteristic of the so-called eco-driving is to avoid high engine speeds making selective use of the gearshift.

Other authors have studied emissions depending

on the gear and/or type of driving [6]. In [7] was determined by emission models (VETESS tool software) that levels of CO₂, NO_x and HC (measured in g/km) were reduced and CO increased while driving a normal driver compared to an aggressive driver. However, one the results of the same study was that the PM (mass) showed too much randomness and can not identify any relationship between particle emissions and the type of driving. In [8] emissions were modelled depending on the speed (km/h) and gear, concluding that the results for CO₂, CO and HC confirm the hypothesis and show that can save fuel and decrease vehicle exhaust emissions by changing up gear. The results for NO_x and PM, on the other hand, differ slightly.

The main aim of this study is to quantify the emission of particles in number and size distribution depending on different gear selection at a same speed and relate it to the basis of the so-called eco-driving techniques (driving to minimize fuel consumption and the emission of carbon dioxide). A study that relates the selected gear number with the emission of particle number and size distribution are presented for the first time to the best of the authors' knowledge.

2 MATERIAL AND METHODS

2.1 Instrumentation

The test bench used consisted of a diesel engine and a dynamometer (SCHENK W150) controlled by a HORIBA's SPARC system. The diesel engine tested is a 2.0 TDI 140 hp EURO 4 Volkswagen Group (Fig. 1), with turbocharging and direct injection. The exhaust gases are catalyzed by an oxidation catalyst.

The measurement system used during the experiments is a system developed by the authors [9] whose validity and reliability has been established in

1. Aida Domínguez-Sáez is with the Pollutant Emissions Unit, Environmental Department, CIEMAT Avda. Complutense, 40 28040, Madrid, Spain. E-mail: aida.dominguez@ciemat.es

2. Carlos Martín is with the Department of Mechanical Engineering, Polytechnic University of Madrid, C. José Guterrez Abascal, 2, 28006, Madrid, Spain. E-mail: carlos.martin.jimenez@alumnos.upm.es

3. Carmen C. Barrios is with the Pollutant Emissions Unit, Environmental Department, CIEMAT Avda. Complutense, 40 28040, Madrid, Spain. E-mail: carmen.barrios@ciemat.es

many experimental trials dynamometer, closed trials and real urban traffic. The particle measurement was carried out using an EEPS 3090 (TSI Inc.) which has a total of 32 channels between 5.6 and 560 nanometres and a rotating disc diluter MD 19-2E (Eng Matter) which was chosen because of the high dilutions that it allows. The concentration of pollutants in exhaust gases (CO, CO₂, NO_x and THC) were measured using OBS 2200 (HORIBA Inc.). The system is fully described in [9].



Fig. 1. Diesel engine 2.0 TDI 140 hp EURO 4 Volkswagen Group

2.2 Experiments

To determine the influence of gear at a steady state on the ultrafine particle emission, each experimental condition were maintained enough time to stabilize the emission (from one minute to four minutes). From the test bench we can control engine torque (Nm) and the engine speed (rpm). Knowing all the characteristics (diameter wheel drive ...) of a vehicle with a 2.0 TDI engine, it's possible to assign a value of engine speed and torque to reproduce a specific gear in a constant speed. For 50 km/h were reproduced the conditions of engine speed and torque required for the gears II, III, IV and V, for 70 km/h were reproduced gears III, IV, V and VI, finally, for 90 and 120 km/h were reproduced gears IV, V and VI. The values of engine speed and torque for each experimental condition are shown in Table 1 and Fig. 5.

Table 1- Engine speed and torque for the Diesel engine 2.0 TDI 140 hp EURO 4 in each condition of vehicle speed and gear selection

Speed (km/h)	Gear	Engine speed (rpm)	Torque (Nm)
50	II	3323	15.3
50	III	2108	24.1
50	IV	1556	32.7
50	V	1282	39.6
70	III	2952	30.6
70	IV	2178	41.5
70	V	1795	50.3
70	VI	1499	60.3
90	IV	2800	53.3
90	V	2308	64.6
90	VI	1927	77.4
120	IV	3734	76.5
120	V	3078	92.8
120	VI	2570	111.1

One of the bases of eco-driving is to change to a higher gear as soon as possible avoiding high engine speeds. For most internal-combustion engines the peak of efficiency (the greatest amount of power with the lowest possible fuel consumption) is reached around 1800-2500 rpm for petrol engines cars or 1500-2000 rpm for diesels. The experimental conditions in steady state that correspond to ecological driving are underlined in blue in Table 1.

3 RESULTS

3.1 Pollutant emissions

Fig. 2, Fig. 3 and Fig. 4 present the pollutant emission as a function of vehicle speed and gear selection for the EURO 4 diesel engine. Fig 2. shows the high influence of gear selection in CO₂ emission and, therefore, on fuel consumption. The CO₂ emission fulfils one of the basic techniques of eco-driving, meaning that the emission of CO₂ can be reduced changing up gear as soon as possible. The NO_x emission shows the same trend (Fig. 3), becoming more significant at 120 km/h. The high value of the emission of nitrogen oxides at 120 km/h -IV gear is due to two phenomena: a) the fuel injected is very high b) The engine speed is 3734 rpm, in this condition it is not activated the exhaust gas recirculation valve (EGR=0%), thereby increasing the temperature and NO_x.

Fig. 4 shows that the principles of the eco-

driving is fulfilled for 50, 90 and 120 km/h, observing a reduction in the emission of fine particle and UFP per km (5.6-560 nm size range) when the gear shifts up. However, at 70 km/h the lowest particle concentration emission is observed for gear IV. At 90 km/h, from the point of view of particle emissions, the optimal gears are V and VI. At 120 km/h the optimal is VI as shown in table 2.

3.2 Particle size distributions

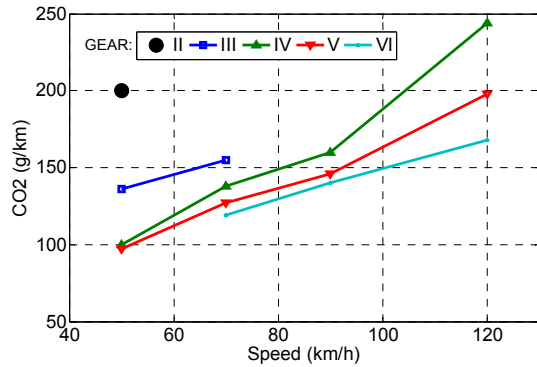


Fig.2. Carbon dioxide emissions in function of the vehicle speed and gear selection.

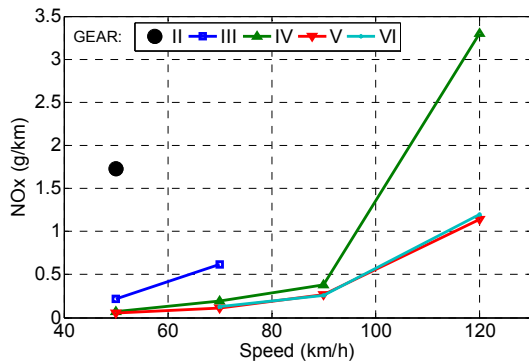


Fig. 3. Nitrogen oxides emissions in function of the vehicle speed and gear selection.

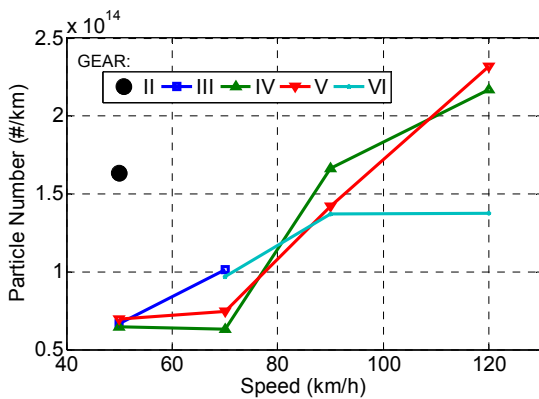


Fig. 4. Particle number emissions (per kilometer) in function of the vehicle speed and gear selection.

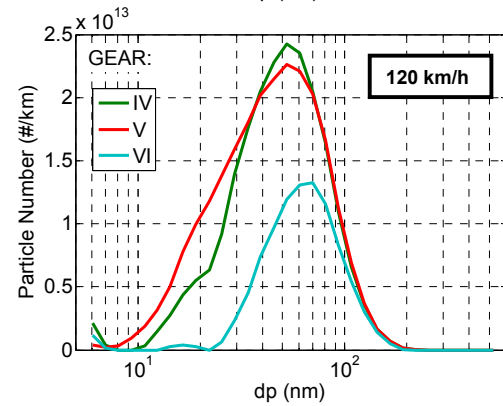
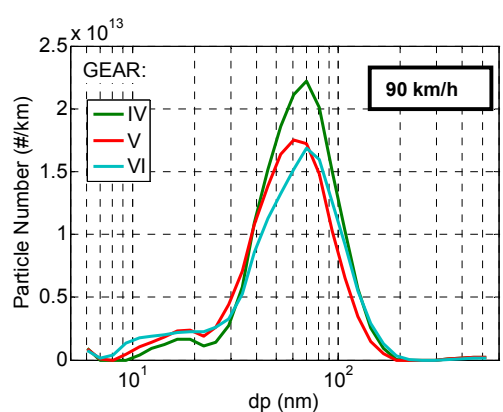
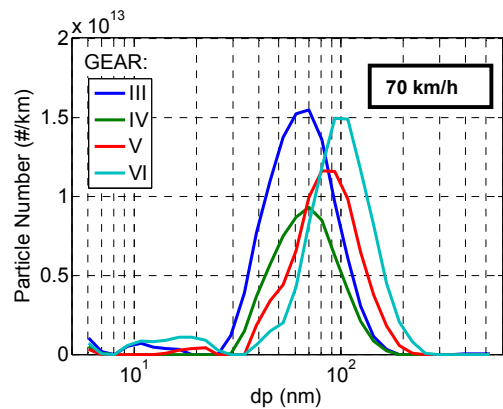
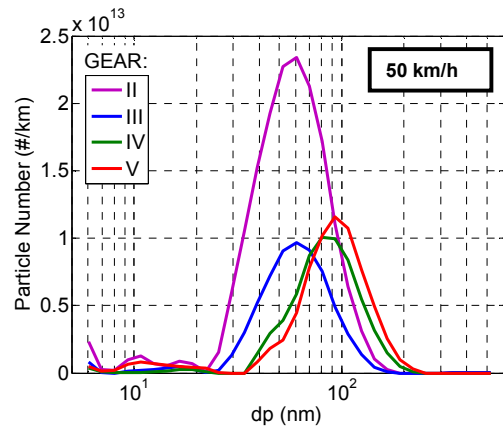


Fig. 5. Particle size distribution as a function of the vehicle speed and gear selection.

Table 2- Air fuel ratio (A/F), exhaust flow (Q), total particle number per cubic centimeter (PN cc), total particle number per kilometer (PN km) and geometric mean diameter (GMD) depending on vehicle speed and gear selection.

Speed-Gear	A/F	Q (m ³ /min)	PN cc	PN km	GMD (nm)
50-II	64.1	3.2	4.5E+07	1.6E+14	57.7
50-III	37.2	1.13	5.2E+07	6.6E+13	60.7
50_IV	27.9	0.6	9.5E+07	6.5E+13	83.5
50_V	22.3	0.5	1.2E+08	7.0E+13	92.0
70_III	42.8	2.03	6.2E+07	1.0E+14	63.7
70_IV	27.1	1.19	6.6E+07	6.3E+13	84.84
70_V	22.5	0.91	1.0E+08	7.5E+13	84.8
70_VI	22.4	0.82	1.5E+08	9.7E+13	99.4
90_IV	29.6	1.93	1.4E+08	1.7E+14	65.2
90_V	25.9	1.59	1.4E+08	1.4E+14	60.4
90_VI	22.9	1.31	1.7E+08	1.4E+14	65.6
120_IV	33.9	4.49	1.0E+08	2.2E+14	52.8
120_V	26.1	2.88	1.7E+08	2.3E+14	51.7
120_VI	23.8	2.7	1.1E+08	1.4E+14	62.6

Fig. 5 shows the particle distributions for all experimental conditions. The fine and ultrafine particle number and size distribution curves used were obtained from the median curve of each experimental speed-gear condition. Table 2 presents a summary of the characteristics of particle emissions and fuel air ratio and exhaust gas flow. These two last parameters can be of great interest to understand and evaluate the particle emissions.

At 50 km/h and gear II, the particle number emission per kilometer is significantly higher than for III, IV and V gears (no significant differences observed between these three gears). In addition, at 50 km/h and gear II, the GMD is low (57.7 nm), these particles being the most harmful to health. 50-II represents an operating condition of the high engine speed (3323 rpm) and low torque (15.3 Nm), consequently the A/F ratio is very low and the exhaust gas flow is very high. Under these conditions the volume concentration of the number of particles is very low and the concentration of particles per kilometer is very high due to the high exhaust flow rate. The high engine speed causes a decrease in the residence time in the combustion chamber, reducing accumulation phenomenon and therefore decreasing the GMD.

At 70 km/h in III, IV and V gears, the behaviour for the number size distribution is similar to that presented for 50 km/h. The main difference at 70 km/h gear happens in VI gear, where one would expect a low particle emission per kilometer and the

actual emission is similar to the emission in III gear. At 70-VI the low engine speed causes a decrease in the combustion temperature, this being more incomplete. The GMD is 99.4 nm, the highest of the experimental conditions tested, this is due to low engine speed and the emergence of the accumulation phenomenon.

At 90 and 120 km/h highlights the high emission of UFPs and nanoparticles under 50 nm. This is due to the low A/F ratio (i.e., highly enriched mixture) which increases the total number concentration of particles (#/cm³) and the high engine speed that reduces the size of them.

This study was conducted with an engine without DPF (Diesel Particle Filter), but the results obtained for particles with diameter less than 50 nm can be extrapolated to vehicles with DPF. Volatile and semi-volatile fraction - nucleation mode (NM) and particles with mean diameter < 50 nm are not retained with current particle filters [10].

4 CONCLUSIONS

This work has brought a deeper knowledge of pollutant emissions of a diesel vehicle depending on gear selection, and, therefore, the type of driving. The novelty of our approach lies in the inclusion of the particle number and size distribution. From the point of view of CO₂ (or fuel consumption) the results show that the basis of eco-driving are satisfied. NOx emissions are also improved with ecological driving but the results show that the same amount of NOx is emitted in the V and VI gear. The particle number concentration (#/cm³) depends on the A/F ratio. The particle number emission per kilometer depends on A/F ratio and on the exhaust flow, in general, the best compromise to reduce the emission of particles coincides with the basics of eco-driving (except high gear with n <= 1500 rpm). The size depends especially on engine speed. Engine speeds higher than 3000 rpm increase the particles with dp < 50 nm. The low gears involve the emission of particles more harmful to health.

Therefore, an aspect than needs to be studied more in detail is the impact of gear selection on fine, ultrafine and nanoparticle emission. This study demonstrates that how a selective use of gears can contribute to a more environmentally friendly driving behaviour from the point of view of particle number and not only fuel consumption. To complete the knowledge of particle emission and its relationship to ecological driving is necessary to extend the study to other types of engines, focusing on modern cars with gear shift indicator.

ACKNOWLEDGMENT

The authors wish to thank Jose Alberto Martín, Lab Specialist of the Pollutant Emissions Unit, for their

assistance during the experimentation. This work was supported in part by Ministerio de Economía y Competitividad, Gobierno de España under contract grant IPT-310000-2010-031.

REFERENCES

- [1] California Environmental Protection Agency Office of Environmental Health Hazard Assessment, Prioritization of Toxic Air Contaminants Under the Children's Protection Act, http://www.oehha.org/air/toxic_contaminants/SB25finalreport.html, 2001
- [2] A.J. Ghio, C.B. Smith and M.C. Madden, "Diesel Exhaust Particles and Airway Inflammation" *Curr. Opin. Pulm. Med.* 18:144–150, 2012.
- [3] R.J. Delfino, C. Sioutas and S. Malik, "Potential Role of Ultra-fine Particles in Associations between Airborne Particle Mass and Cardiovascular Health" *Environ. Health Perspect.* 113:934–946, 2005.
- [4] H. Johansson, P. Gustafsson, M. Henke and M. Rosengren, "Impact of EcoDriving on Emissions". *International Scientific Symposium on Transport and Air Pollution*, Avignon, France, 2003.
- [5] J.N. Barkenbus, "Eco-driving: an Overlooked Climate Change Initiative". *Energy Policy*, 38 762–769, 2010.
- [6] E. Ericsson, "Variability in Urban Driving Pattern", *Transp. Res.* 5D:337, 2000.
- [7] C. Beckx, L. Int Panis, I. De Vlieger and G. Wets, "Influence of Gear Changing Behaviour on Fuel-use and Vehicular Exhaust Emissions", *Highway and Urban Environment*, G.M. Morrison, S. Rauch, eds., Springer, The Netherlands, pp 45-51, 2007.
- [8] C. Beckx, L. Int Panis, D. Janssens, I. De Vlieger and G. Wets, "The Influence of Gear Change on Vehicle Exhaust Emissions. Calculations with the Vetess Emission Tool", *International Conference on Urban Air Quality*, Limassol, Cyprus, 2007.
- [9] C. C. Barrios, A. Domínguez-Sáez, J. R. Rubio and M. Pujadas, "Development and Evaluation of On-Board Measurement System for Nanoparticle Emissions from Diesel Engine", *Aerosol Sci. Technol.* 45:5, 570-580, 2011.
- [10] E. Vouitis, L. Nitzachrios and Z. Samaras, "Theoretical Investigation of the Nucleation Mode Formation Downstream of Diesel after-Treatment Devices", *Aerosol Air Qual. Res.*, 8:1, 37-53, 2008.

Comparison between EEPS 3090 and WCPC 3788: differences and similarities in transient and stable measures

Carmen C. Barrios¹, Aida Domínguez-Sáez², Carlos Martín³

Abstract — This study compares two particle measurement devices of the same manufacturer (TSI Inc.) that use two different technologies. The Engine Exhaust Particle Sizer (EEPS) is based on electrical mobility of the charged particles and the Nano Water-based Condensation Particle Counter (WCPC) is based on optical detection. The comparison was made with both devices measuring in parallel the particle concentration from two engines (diesel and petrol, Euro 4) under different operating conditions (steady-state condition and transient condition in driving cycles). A great influence of particle size distribution in the correlation between devices is observed. The WCPC shows greater measurement stability under all conditions than EEPS, but EEPS is able to measure particle size distribution.

Keywords — EEPS, WCPC, Diesel Engine, Petrol Engine and Particle Number Concentration

1 INTRODUCTION

Nowadays, the particles from internal combustion engines are of most interest to the scientific community [1], because of its impact on community health, particularly nanoparticles that can reach the deeper lung sections [2]. In recent years there has been considerable interest in obtaining the concentration of particles emitted during transient engine operation, where the total number of particles can change dramatically and also environmental impact. Two of the most modern commercial devices for measuring the particle concentration are the Engine Exhaust Particle Sizer 3090 (EEPS 3090, TSI) and the Nano Water-based Condensation Particle Counter 3788 (WCPC 3788, TSI).

Other authors have studied diesel engine particle emissions with several devices. Ayala [3] concludes that relative CPC particle count is reasonable at all concentrations, multi-channel instruments (EEPS) generally agree well with CPC's during transient cycles, but not during cruise and idle, and are noisy at low concentrations (<10.000 #/cc).

The objective of this study is to determine the advantages and disadvantages of the WCPC 3788 and the EEPS 3090 during their application in car engines. The comparison was made with both devices measuring in parallel, the particle concentration from different engines (diesel and petrol, Euro 4) under different operating conditions (steady-state condition and transient condition in driving cycles).

2 MATERIAL AND METHODS

2.1 Instrumentation

The diesel engines tested were a 2.0 TDI 140 hp EURO 4 Volkswagen Group (with turbocharging and direct injection system) and a 2.0 FSI 150 hp EURO 4 Volkswagen Group (direct injection) and two dynamometers same brand SCHENK (W150), controlled by a HORIBA's SPARC system (Fig. 1). The particle measurement was carried out using the EEPS 3090 (TSI Inc.), which has a total of 32 channels between 5.6 and 560 nanometres, the WCPC 3788, whose measurement range is between 2.5 and 3000 nm and a rotating disc diluter MD 19-2E (Eng Matter), the system is fully described in [4]. The concentration of pollutants in exhaust gases (CO, CO₂, NO_x and THC) were measured using OBS 2200 (HORIBA Inc.).

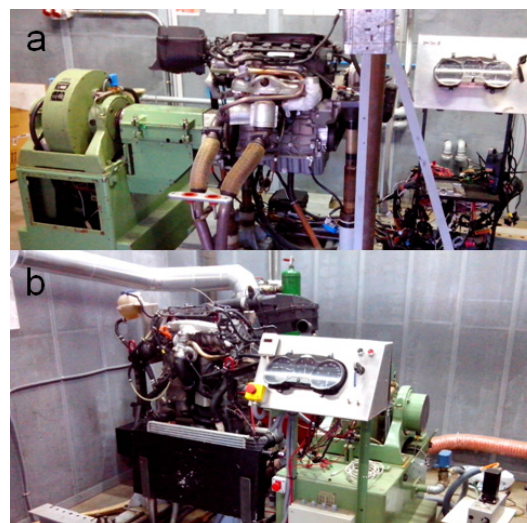


Fig. 1. Petrol engine 2.0 FSI 150 hp VW Euro 4 (a) and Diesel engine 2.0 TDI 140 hp VW Euro 4 (b)

1. Carmen C. Barrios is with the Pollutant Emissions Unit, Environmental Department, CIEMAT Avda. Complutense, 40 28040, Madrid, Spain. E-mail: carmen.barrios@ciemat.es
2. Aida Domínguez-Sáez is with the Pollutant Emissions Unit, Environmental Department, CIEMAT Avda. Complutense, 40 28040, Madrid, Spain. E-mail: aida.dominguez@ciemat.es
3. Carlos Martín is with the Department of Mechanical Engineering, Polytechnic University of Madrid, C. José Gutiérrez Abascal, 2, 28006, Madrid, Spain. E-mail: carlos.martin.jimenez@alumnos.upm.es

2.2 Experiments

To compare both particle measurement devices, WCPC and EEPS, engine bench tests were carried out simulating normal operating conditions of a vehicle operation, with the main aim to cover a wide range of engine operation. The objective of the study is to compare the measuring equipment, not to compare particle emission of both engines, therefore, we consider that is experimental condition can be different in each engine. For both engines (diesel and petrol) steady state conditions (speed and torque) were reproduced in engine bench as shown in Fig. 2 and Fig. 3. The steady state conditions simulate engine operating conditions in a hypothetical vehicle being driven at constant speeds between 15 km/h and 120 km/h. Also, for diesel engine, 8 repetitions of the European Urban Driving Cycle (UDC) were reproduced.

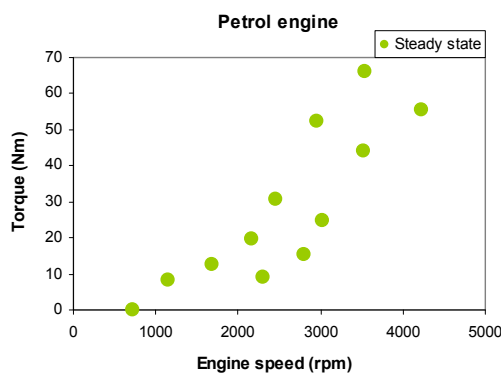


Fig. 2. Petrol engine 2.0 FSI 150 hp VW operating conditions

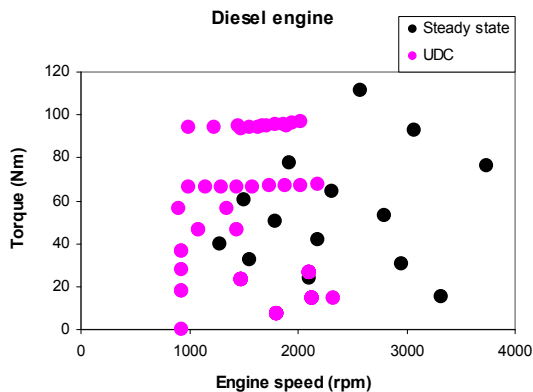


Fig. 3. Diesel engine 2.0 TDI 140 hp VW operating conditions

All experiments were performed in a continuously data recording at intervals of 1 s, taken from the same sample. A total of 9845 valid data were recorded, which 1926 (1061 in steady state and 865 in transient state) correspond to the petrol engine and 7919 (5299 in steady state and 2620 in transient state) to the diesel engine.

3 RESULTS

To analyze the difference between both devices is not necessary to correct data with the dilution factor. The dilution factor used in the experiments was 3400. All figures in the paper show diluted sample concentration (i.e. not corrected with the dilution factor). Fig. 4 shows the global correlation between measures EEPS and WCPC, using as input the 9845 data. Mean particle concentration measured with EEPS is 28% higher than WCPC measurement, with $R^2 = 0.945$. Analyzing the points recorded with the engine running at steady state compared to those recorded in transient state (Fig. 5), no significant differences are observed, which agrees with the expected because the sampling frequency is 10 Hz.

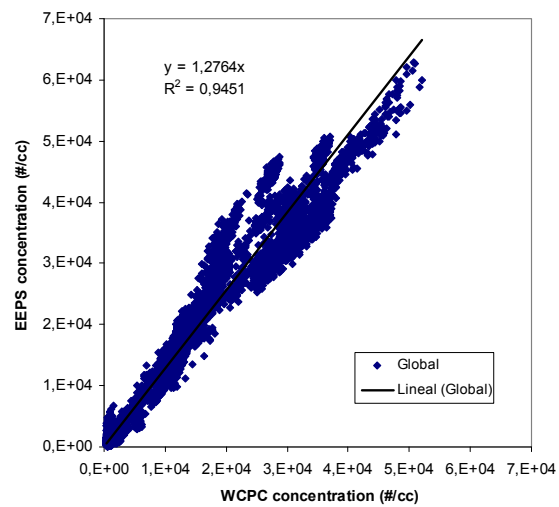


Fig. 4. Global correlation EEPS vs WCPC

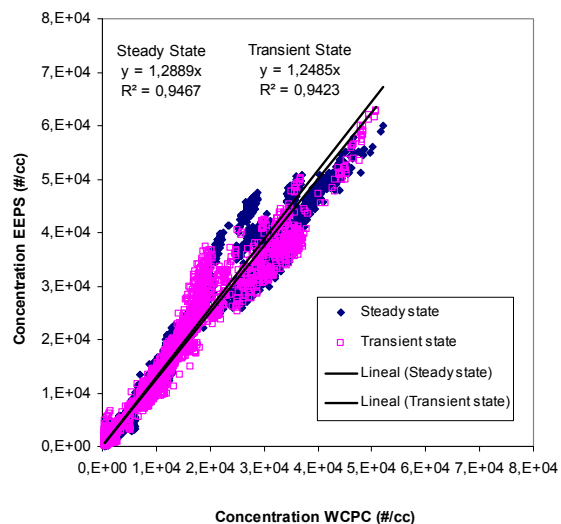


Fig. 5. Correlation EEPS vs WCPC in stable and transient measures

The analysis of the temporal evolution of the concentration of both devices (Fig. 6a, Fig. 7, Fig. 8a and Fig. 9a) shows that the EEPS signal is noisy, especially at low concentrations. In Fig. 6a, the

temporal evolution of the petrol engine measurements is represented, in which the total concentration is always less than $7E+03$ #/cc and EEPS signal has a high noise. To quantify it, the variance is calculated in relation to the moving average of 5 data (5 s), subsequently only the values corresponding to steady states have been selected and finally the standard deviation has been calculated (Table 1). For low concentrations recorded in the experiments with the petrol engine, standard deviation of EEPS is 542, which is higher than standard deviation data recorded under stable conditions with WCPC (SD=32). In the case of the experiments made with diesel engine, the EEPS standard deviation is 507 and the WCPC standard deviation is 250. The optical technology of WCPC improves the signal and noise ratios in comparison with EEPS technology, that is based on electrical mobility of the charged particles.

Table 1- Concentration standard deviation in steady state conditions

Standard Deviation	EEPS	WCPC
Global	513	229
Petrol engine	542	32
Diesel engine	507	250

In steady state experiments with smooth transitions between steady state conditions (Fig. 7) the difference between measurements of the devices remains approximately linear in relation to concentration (the EEPS concentration is 29% higher than the concentration measured with the WCPC), but in the Urban Driving Cycle (UDC), concentration peaks are observed in accelerations (Fig 8a). These concentration peaks are more pronounced in EEPS than WCPC. In the correlation of the UDC data (Fig. 8b) this effect is evident. For WCPC concentrations higher than $2E+04$ #/cc corresponding to accelerations, the concentrations recorded by EEPS are more than 42% higher than the concentrations recorded by WCPC. In this type of acceleration the Fuel/Air ratio increases due to the low speed and high load of the engine, so that the particle geometric mean diameter (GMD) increases [5], [6] and the difference between both devices increases.

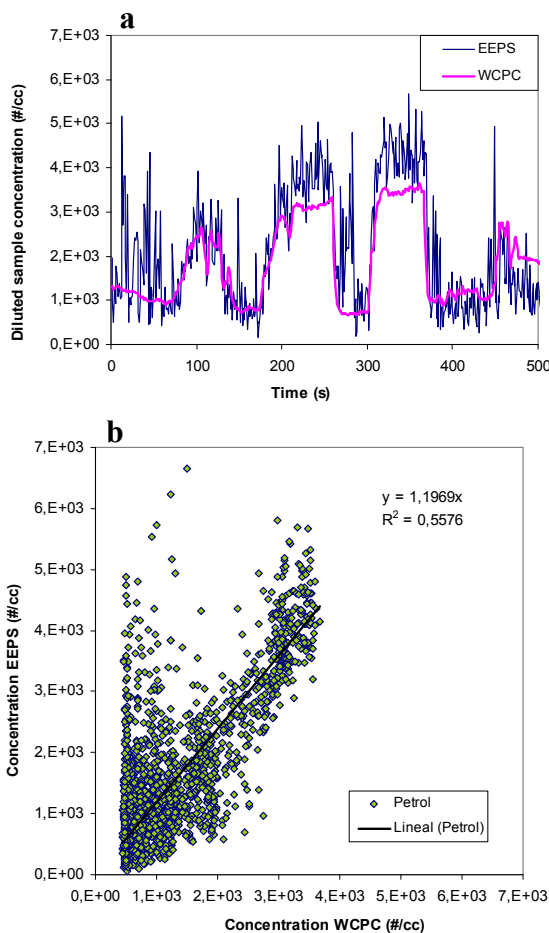


Fig. 6. Temporal evolution of the concentration (a) and correlation EEPS vs WCPC (b) for petrol engine

Fig. 6b shows the correlation between WCPC and EEPS for the petrol engine. The high noise present in low EEPS concentrations deteriorate the correlation of the total data, although measurements of the devices get closer and the EEPS measurement is 20% higher than the WCPC measurement.

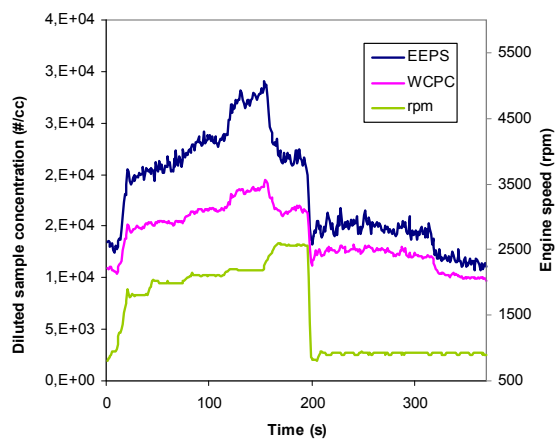


Fig. 7. Temporal evolution of the concentration in steady state experiments with smooth transitions

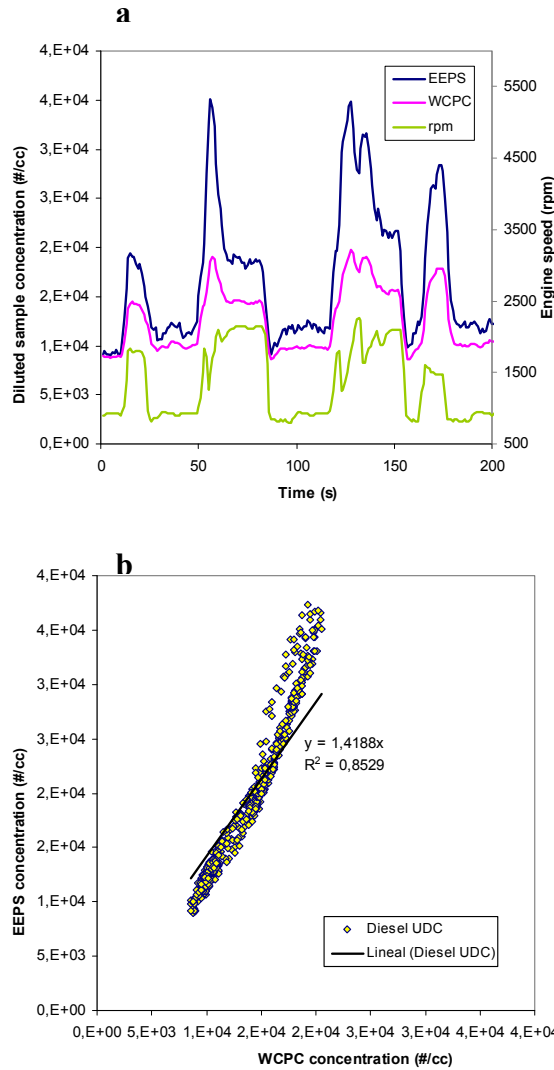


Fig. 8. Temporal evolution of the concentration (a) and correlation EEPS vs WCPC (b) for diesel engine in UDC

Finally, for the diesel engine condition at 3800 rpm (Fig. 9), both concentrations get closer significantly, becoming EEPS measurement only 4% higher than the WCPC. In this operating condition, the high engine speed decreases the residence time of the particles in the combustion chamber, which reduces the accumulation of the particles and favors the occurrence of a larger number of nucleation mode particles (<30 nm). Considering the measurement ranges of the devices, a minimum of 5.6 nm (EEPS) versus 2.5 nm (WCPC) means that there are nucleation mode particles that are measured with WCPC device but are not measured with EEPS device. This decreases the EEPS measurement and both concentration measurements approach. This result is consistent with the petrol engine tests, in which a greater presence of nucleation mode particles, compared to diesel engine tests, encourages EEPS overestimation decrease.

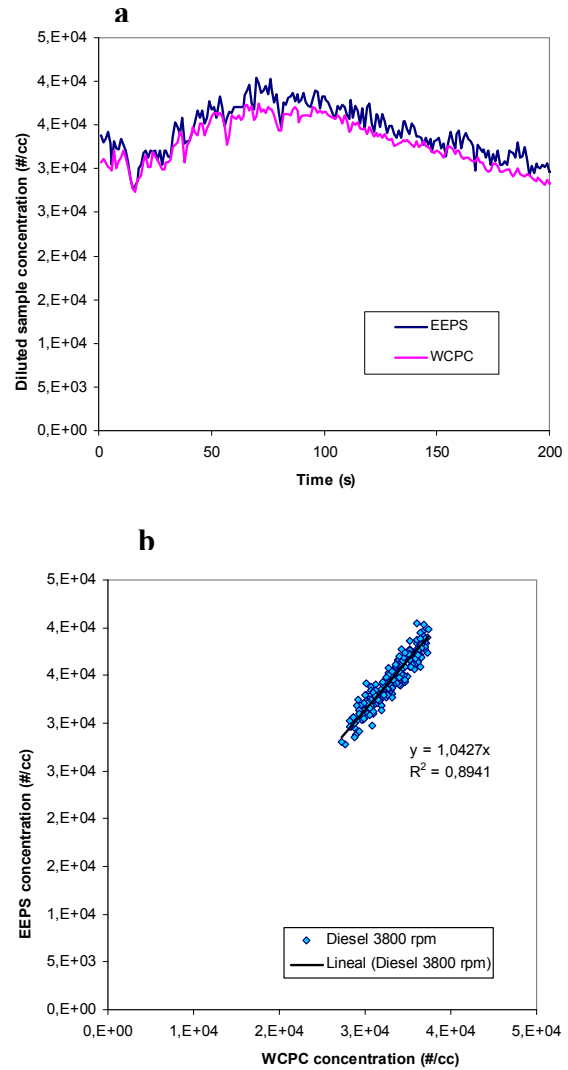


Fig. 9. Temporal evolution of the concentration (a) and correlation EEPS vs WCPC (b) for diesel engine at steady state 3800 rpm and 70 Nm

4 CONCLUSIONS

Several important conclusions were seen from this comparative study of particle measurement devices:

- Generally the EEPS shows a higher particle concentration for any condition in comparison with CPC. EEPS overestimates the total particle concentration proportionally, although the size distribution of the sample modifies this ratio.
- Increasing the geometric mean diameter (GMD) of the particle sample increases the overestimation of EEPS concentration measurement. On the other hand, increasing the nucleation mode particles reduces the overestimation even at high concentrations.
- For particle concentrations below 1E+04 #/cc, the EEPS shows a high level of noise. To

measure the particle size distribution of a petrol engine with EEPS, will be necessary to adjust the dilution ratio for increasing the total concentration of the sample into the proper range.

- Both devices are suitable for measuring steady and transient conditions. The WCPC shows greater measurement stability under all conditions than EEPS, which makes it more desirable when necessary to know only the total concentration. Conversely, if in the study the size distribution is required, it is necessary to take into account the observations about the EEPS presented in this study.

ACKNOWLEDGMENT

The authors wish to thank Jose Alberto Martín, Lab Specialist of the Pollutant Emissions Unit, for their assistance during the experimentation. This work was supported in part by Ministerio de Economía y Competitividad, Gobierno de España under contract grant IPT-310000-2010-031.

REFERENCES

- [1] S. Vedal, "Ambient particles and health: lines that divide", *J. Air Waste Manage. Assoc.*, 47, 551-581, 1997
- [2] D. Schwela, "Air Pollution and Health in Urban Areas", *Rev. Environ. Health*, 15:13-42, 2011
- [3] A. Ayala, J. D. Herner, T. Huai, "California's Efforts for Advancing Ultrafine Particle Number Measurements for Clean Diesel Exhaust", *Diesel Engine-Efficiency and Emissions Reduction Research Conference Detroit, Michigan*, 2006
- [4] C. C. Barrios, A. Domínguez-Sáez, J. R. Rubio, M. Pujadas, "Development and Evaluation of On-Board Measurement System for Nanoparticle Emissions from Diesel Engine", *Aerosol Sci. Technol.* 45:5, 570-580, 2011.
- [5] X. Li, Z. Huang, J. Wang, W. Zhang, "Particle size distribution from a GTL engine", *Sci. Total Environ.*, 382(2-3):295-303, 2007
- [6] C. C. Barrios, A. Domínguez-Sáez, C. Martín, "Evolution of the Particle Size and Number Concentration from Diesel Engine from Idle to High Load", *19th International Transport and Air Pollution Conference*, Thessaloniki, Greece, 2012

Atmospheric Boundary Layer during AMISOC-ARN: Lidar-derived height as estimated by different methods

D. Toledo^{1,*}, C. Córdoba-Jabonero¹, J.A. Adame¹, M. Sorribas², D. Grau¹, J. Andrey¹,
B. de la Morena¹ and M. Gil-Ojeda¹

Abstract — The Atmospheric Boundary Layer (ABL) height is calculated from lidar data by using different methods. These methods represent different mathematical approaches with particular application to lidar measurements. Among them, there are: the Gradient (1-D and 2-D) and Logarithm (log-D) Derivative methods, the Centroid/Variance (VAR) and the Wavelet Covariance Transform (WCT), in addition to the Cluster Analysis (CA), which is applied to lidar measurements as a novel method for ABL height estimation. The Spanish Institute for Aerospace Technology (INTA) deployed a Micro Pulse Lidar (MPL) system at the Atmospheric Sounding Station “El Arenosillo” (ARN), Huelva (Spain), for aerosol vertical measurements in the AMISOC-ARN campaign performed during May-June 2012 within the framework of the AMISOC (Atmospheric Minor Species relevant to the Ozone Chemistry at both sides of the jet) project. The goal of this work is an assessment of the results obtained on ABL top height estimation from the application of each one of those methods to lidar measurements in comparison with radiosounding data. Differences with respect to daily radiosoundings as a reference are analyzed in order to establish the most reliable methods for ABL determination. In particular, the best agreement is found when using 1-D, 2-D, WCT and CA.

Keywords — Atmospheric Boundary Layer (ABL), LIDAR, mathematical methods, radiosoundings.

1 INTRODUCTION

The Atmospheric Boundary Layer (ABL) is the lowest part of the troposphere which is directly influenced by the Earth surface with a timescale of one hour or less [1]. Factors like the season, the orography, the time of the day and the weather act over the ABL. The determination of the ABL height is decisive for pollution dynamics studies and weather forecasting modeling. Once pollutants are emitted into the ABL, they are dispersed by turbulent movements and mixed with air masses located in upper layers. Radiosoundings, typically used for this purpose, are launched in 1-2/day basis, at best. Then they cannot provide a suitable evolution of the ABL along the day.

The fact that higher aerosol concentrations are usually present in the ABL respect to those in the Free Troposphere (FT) allows the ABL height estimation by means of lidar measurements [i.e., 2]. Indeed, a sharp difference in lidar backscattered signal is found by “crossing” from ABL to FT altitudes. In addition, since lidar systems can be in full-time operation with a vertical resolution of a

few meters and an integration time of seconds to minutes, they are a good solution for a continuous ABL top monitoring.

2 METHODOLOGY

2.1 Lidar system and data acquisition

The Spanish Institute for Aerospace Technology (INTA) deployed a Micro Pulse Lidar (MPL) system at the Atmospheric Sounding Station “El Arenosillo” (ARN, 37.1°N 6.7°W, 40 m a.s.l.), Huelva (Spain), for aerosol vertical measurements in the AMISOC-ARN campaign performed from 20 May to 15 June 2012 in the framework of the AMISOC (Atmospheric Minor Species relevant to the Ozone Chemistry at both sides of the jet) project.

The MPL system used in this study is a single-wavelength (523 nm), high-repetition (2500 Hz), low-power (~ 7 μJ), eye-safe commercially available backscatter lidar, capable of determining the range of aerosols and clouds in full-time unattended operation mode. MPL is in routine operation within MPLNET (Micro Pulse Lidar NETWORK, mplnet.gsfc.nasa.gov) at the subtropical station of AEMET/Sta. Cruz de Tenerife Observatory (SCO, 28°N 16°W, 52 m a.s.l.). More instrumental details are found in [3].

MPL measurements were performed on a daily basis, and raw signal profiles were acquired with 1-min integrating time and a vertical resolution of 15 m. Then, these 1-min profiles were averaged over 30

1. Instituto Nacional de Técnica Aeroespacial (INTA), Atmospheric Research and Instrumentation Branch, Torrejón de Ardoz, Madrid, Spain

2. Andalusian Center for Environmental Research (CEAMA), Group of Atmospheric Physics, Universidad de Granada-Junta de Andalucía, Granada, Spain

* Now at: GSMA, Université de Reims Champagne Ardenne, Reims, France

minutes, obtaining thus 2 profiles per hour (48 profiles per day).

2.2 Description of the methods

Different methods are used to calculate the ABL height from lidar measurements. They are based on two approaches: 1) the vertical distribution of the aerosol concentration, as by the Gradient Derivative Methods, i.e. the first (1-D) [4, 5], second (2-D) [6] and Logarithm (log-D) [7] derivative methods, and the Wavelet Covariance Transform (WCT) [8, 9]; and 2) the statistical analysis as by the Centroid/Variance Method (VAR) [10]. A new procedure combining both these approaches is also used in this work: the Cluster Analysis (CA), which is applied to lidar measurements as a novel method for ABL height estimation [11].

2.2.1 Derivative methods (DM)

There are three different ways to analyze the derivative of the lidar signal respect to height: the first derivative (1-D), the second derivative (2-D), and the derivative of the logarithm of the signal (log-D). These methods assume that the concentration of aerosols is higher in the ABL than in the FT, and therefore the height position corresponding to the absolute minimum of the first or second derivatives of the lidar signal is identified as the top height of the ABL.

2.2.2 Wavelet covariance transform (WCT)

The wavelet covariance method (WCT) analyzes the aerosol signature of the lidar profile, being less affected by the signal noise than others methods. WCT is defined as:

$$W_f(a,b) = \frac{1}{a} \int_{z_b}^{z_t} f(z) h\left(\frac{z-b}{a}\right) dz \quad (1)$$

where $f(z)$ is the lidar range-corrected signal (RCS), z is the height, and z_b and z_t are the bottom and top height limits of the signal profile, respectively. The parameters a and b represent the extend and the location of the Haar function, defined as:

$$h\left(\frac{z-b}{a}\right) = \begin{cases} +1 & b - \frac{a}{2} \leq z \leq b \\ -1 & b \leq z \leq b + \frac{a}{2} \\ 0 & \text{elsewhere} \end{cases} \quad (2)$$

where $W_f(a, b)$ is a measurements of the similarity of the lidar signal and the Haar function.

Lidar signals are higher in the ABL than the FT, since the aerosol concentration is higher in the ABL. Due to this fact, WCT takes a clear local maximum at a given height for an appropriate value of a . This height is indeed the ABL top value found. This method is described in more detail in [9].

2.2.3 Centroid/Variance method (VAR)

The entrainment zone (EZ) is an interfacial layer between the ABL and the FT, where clear air masses from the FT are mixed with those more turbid

coming from the ABL. Thus, the variability of the aerosol concentration in that EZ is very high. Based on this fact, the averaged ABL ‘centroid’ (VM) height is identified as the lowest height position of a local maximum in the variance profile function, defined as:

$$VAR(Z) = \frac{1}{(N-1)} \sum_{i=1}^N [S(Z, t_i) - \bar{S}(Z)]^2 \quad (3)$$

where $S(Z, t)$ is the lidar range-corrected signal (RCS) at time t and height Z , and the upper bar means the averaged profile from N signal profiles. The height position corresponding to the absolute maximum of the $VAR(Z)$ function establishes the ABL top height.

2.2.4 Cluster analysis (CA)

Cluster analysis (CA) is the task of assigning a set of objects into groups (clusters), where the objects in the same cluster are similar. In particular, the distance between objects is the similarity used to form the clusters. These distances (similarities) can be based on a single dimension or multiple dimensions, where each dimension represents a rule or condition in order to group the objects. In this study, Euclidean distances in 3 dimensions are used. In our case, each dimension represents the height, the lidar signal and the variance of the signal. This distance $dis(x, y)$ between two given signal points is defined as:

$$dis(x, y) = \left\{ \begin{aligned} &(\text{height}(x) - \text{height}(y))^2 + \\ &(\text{variance}(x) - \text{variance}(y))^2 + \\ &(\text{RCS}(x) - \text{RCS}(y))^2 \end{aligned} \right\}^{\frac{1}{2}} \quad (4)$$

Different clusters can be formed by using these distances. Therefore the distribution of the aerosols in the atmosphere and variations of their concentration can be studied by this method. A complete description of the method can be found in [11].

2.3 Meteorological soundings

A total of 26 daily radiosoundings were launched at around noon during the AMISOC-ARN campaign, but only 24 radiosoundings were available for simultaneous comparison with lidar measurements. ABL heights were calculated from radiosounding data using potential temperature and mixing ratio profiles [1, 12].

ABL height values between 1265 ± 290 m and 1508 ± 374 m were found by using radiosounding data, in average, under different breeze conditions for the overall campaign.

3 RESULTS AND DISCUSSION

Lidar-derived ABL heights calculated by the 1-D, 2-

D, log-D, VAR, WCT and CA methods are compared to that obtained from daily radiosoundings (launched at noon, approximately) as a reference in order to determinate the degree of agreement as well as the robustness of each method on ABL height monitoring under different conditions present during the AMISOC-ARN campaign.

Figure 1 shows the absolute differences $|\Delta|$ (in %) found between the lidar-derived ABL height by each 1-D, 2-D, log-D, VAR, WCT and CA methods and that reported from the corresponding radiosounding profile along the overall campaign.

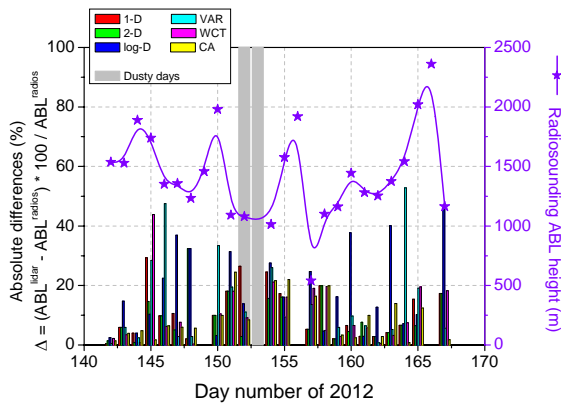


Fig. 1. Lidar-derived ABL height absolute differences (in %) respect to radiosounding data depending on the method applied: 1-D, 2-D, log-D, VAR, WCT and CA, along the overall AMISOC-ARN campaign.

The lowest value of those differences is found for WCT (0.3%), whereas the highest difference is obtained for VAR, with a value 52.8% (see Fig. 1). However, the smallest maximum of the absolute value of the differences is given for 2-D and WCT with values of 4.7% and 4.9%. This fact is very important for studying the stability of each method since this smallest maximum gives an estimation of the difference between the method and the ABL height obtained by the reference radiosounding.

Mean values of these differences ($\langle |\Delta| \rangle$, in %) for all the days together to their one-standard-deviation (1σ) is shown in Fig. 2 in order to examine the robustness of different methods.

CA presents the lowest values of both $\langle |\Delta| \rangle$ and 1σ , being below 10%, whereas log-D and VAR methods retrieve the highest mean differences. 1-D, 2-D, WCT and CA methods can determinate the ABL height with mean differences respect to those calculated by the radiosoundings below 12%. Among them, the best results are obtained by CA with $\langle |\Delta| \rangle$ and 1σ values of 9.1% and 7.5%, respectively. Limitations are found for log-D and VAR since these methods present outliers under different conditions, increasing their mean differences (and 1σ). Therefore, the signal averaging period used for calculating the variance is too short in some cases for a suitable ABL top height

estimation by using VM. In the basis of robustness of the different methods, 1-D, 2-D, WCT and CA appear as the most adequate methods for an automated ABL top monitoring. As a result log-D and VAR are prone to have outliers.

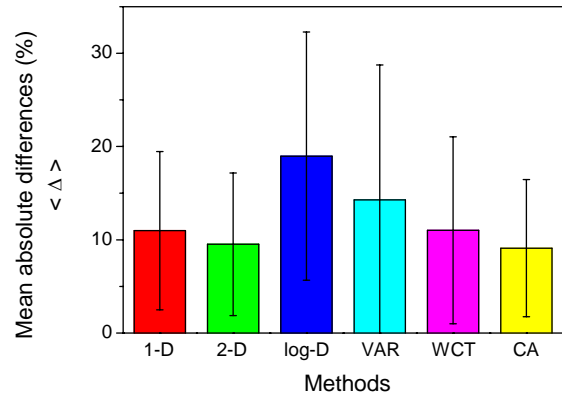


Fig. 2. Mean values of the absolute differences (%) for each method together to their 1σ values (error bars).

4 CONCLUSIONS

This work shows a preliminary analysis of the lidar/radiosoundings comparison for ABL height estimation during the AMISOC-ARN campaign, as a first step to extend our understanding about the evolution of the ABL under different aerosol scenarios: dusty and non-dusty cases, and/or particular atmospheric conditions: pure and non-pure breeze regimes.

In the basis of robustness of different methods, 1-D, 2-D, WCT and CA, appear as the most adequate for an automated ABL top monitoring along the day. Application of these methods to lidar measurements is an useful tool for ABL top height estimation. Results show lidar systems are a reliable instrumentation for a continuous and precise ABL evolution assessment.

ACKNOWLEDGMENT

This work has been supported by the Spanish Ministerio de Economía y Competitividad (MINECO) under grant CGL2011-24891 (AMISOC project). Authors specially thank the INTA/Atmospheric Sounding Station 'El Arenosillo' (ESAt) staff for their valuable assistance and support in the lidar system maintenance and radiosoundings launchings.

REFERENCES

- [1] Stull, R. B., *An introduction to boundary layer Meteorology*. Kluwer Academic Publishers, Dordrecht, Netherlands, 666 pp, 1988.

Toledo et al: Atmospheric Boundary Layer during AMISOC-ARN: Lidar-derived height as estimated by different methods

- [2] Russell, P. B., E. E. Uthe, F. L. Ludwig, and N. A. Shaw, A comparison of atmospheric structure as observed with monostatic acoustic sounder and lidar techniques. *J. Geophys. Res.*, **79**, 5555-5566, 1974.
- [3] Campbell, J. R., D. L. Hlavka, E. J. Welton, C. J. Flynn, D. D. Turner, J. D. Spinhirne, V. S. Scott III, and I. H. Hwang, Full-time, eye-safe cloud and aerosol lidar observation at Atmospheric Radiation Measurement program sites: Instruments and data processing. *J. Atmos. Oceanic Technol.*, **19**, 431-442, 2002.
- [4] Hayden, K. L., K. G. Anlauf, R. M. Hoff, J. W. Strapp, J. W. Bottenheim, H. A. Wiebe, F. A. Froude, J. B. Martin, D. G. Steyn, and I. G. McKendry, The Vertical Chemical and Meteorological Structure of the Boundary Layer in the Lower Fraser Valley during Pacific '93'. *J. Atmos. Environ.*, **31**, 2089-2105, 1997.
- [5] Flamant, C., J. Pelon, P. H. Flamant, and P. Durand, Lidar determination of the entrainment zone thickness at the top of the unstable marine atmospheric boundary layer. *Bound.-Lay. Meteorol.*, **83**, 247-284, 1997.
- [6] Senff, C., J. Bösenberg, G. Peters, and T. Schaberl, Remote Sensing of Turbulence Ozone Fluxes and the Ozone Budget in the Convective Boundary Layer with DIAL and Radar-RASS: A Case Study. *Contrib. Atmos. Phys.*, **69**, 161-176, 1996.
- [7] Menuet, L., C. Flamant, J. Pelon, and P. H. Flamant, Urban boundary-layer height determination from lidar measurements over the Paris area. *Appl. Opt.*, **38**, 945-954, 1999.
- [8] Davis, K. J., N. Gamage, C. R. Hagelberg, C. Kiemle, D. H. Lenschow, and P. P. Sullivan, An objective method for deriving atmospheric structure from airborne lidar observations. *J. Atmos. Oceanic Technol.*, **17**, 1455-1468, 2000.
- [9] Brooks, I., Finding Boundary Layer Top: Application of a wavelet covariance transform to lidar backscatter profiles. *J. Atmos. Ocean. Tech.*, **20**, 1092-1105, 2003.
- [10] Hooper, W. P., and E. W. Eloranta, Lidar measurements of wind in the planetary boundary layer: The method, accuracy and results from joint measurements from radiosonde and kyttoon. *J. Climate Appl. Meteor.*, **25**, 990-1001, 1986.
- [11] Toledo, D., C. Córdoba-Jabonero and M. Gil-Ojeda, Cluster Analysis: A new approach applied to Lidar measurements for Atmospheric Boundary Layer height estimation. *J. Atmospheric and Oceanic Technology*, submitted for publication, 2013.
- [12] Heffter, J. L., *Air Resource Laboratories atmospheric transport and dispersion model*. NOAA Tech. Memo. ERL ARL-81, 24 pp, 1980.

Levels of BTEX in an urban environment: The city of a Coruña

G. Blanco-Heras¹, M.P.Gómez-Carracedo¹, V. Juncal-Bello¹, M. Ríos³, M. Piñeiro-Iglesias²,
P. López-Mahía^{1,2}, S. Muniategui¹, D. Prada^{1,2}

Abstract — Road traffic is the main source of volatile organic compounds in urban areas, particularly of benzene and alkylbenzenes. Some are considered carcinogenic and therefore it is necessary to evaluate them, along with other contaminants in urban air. An assessment of BTEX concentrations in 25 points of the city of A Coruña was performed. Two campaigns were conducted during 2011. Selected points were representative of the different areas of the city (entering and wide avenues surrounding the town, narrow streets with tall buildings, parks and squares, ...). Passive sampling was employed to collect volatile organic compounds (VOCs) by adsorbent tubes (Radiello®), followed by thermal desorption and analysis by gas chromatography coupled with mass spectrometry (TD-GC-MS). Meteorological and other pollutant data provided by different monitoring stations in the city have been used also in this study.

Keywords — BTEX, passive diffusion, Radiello, urban environment

1 INTRODUCTION

VOCs are present in the atmosphere as a result of anthropogenic activities, mainly related to incomplete combustion processes of carbon-containing fuels (gasoline, diesel, wood, coal, natural gas), fuel storage and distribution, use of paints and solvents, various industrial processes such as production, refining and distribution of petroleum and massive natural gas, refined oil, timber industry, etc.[1-2]. The sources of VOCs in urban areas tend to be dominated by emissions from vehicles and the use of solvents and paints. The fraction associated to aromatic hydrocarbons corresponds to typical road traffic: benzene, toluene, ethylbenzene and xylenes (BTEX) [3-4].

Besides its role in the tropospheric chemistry BTEX compounds represent a health risk [5]. Their effects can vary greatly depending on the nature of each compound and the degree and length of exposure. They range from no adverse effects to a high degree of toxicity (carcinogenic or mutagenic actions), with intermediate effects such as odor nuisances, skin irritations, heart problems, and digestive and respiratory issues.

The International Agency for Research on Cancer (IARC) classified benzene and 1,3-butadiene in group 1 (carcinogenic to humans) and ethylbenzene and isoprene in group 2B (possible carcinogenic to humans) [6]. WHO established air quality guideline

values for benzene, toluene and ozone (WHO, 2005) [7] and the Environmental Protection Agency of the United States (U.S. EPA) classified hexane, toluene and xylenes as potentially toxic pollutants (besides benzene, ethylbenzene and 1,3-butadiene)[8].

In general, the low VOCs concentrations in ambient air require sampling techniques selective preconcentration of the analytes prior to their analysis to achieve acceptable detection limits. An example is the capture of the pollutants by adsorption on a solid adsorbent [9]. Sampling may be active or passive, the latter is also called diffusion technique and was used in this study. There are different types of passive samplers for the determination of VOCs. The most used one is Radiello® (350 ± filler Carbograph 10mg 4TM 35-50 mesh size), which has been used in numerous studies, and also here [10].

In Directive 2008/50/EC and in Spanish Legislation a limit value (VL) for the annual average benzene in ambient air of 5 µg/m³ (include upper and lower thresholds of evaluation: UES (3.5 µg/m³) and UEI (2 µg/m³) was established. Also recommendations for measuring VOCs ozone precursors were given and these include monitoring BTEX compounds.

2 METHODOLOGY

2.1 Sampling points

The different sampling points in which BTEX levels were measured are indicated in Fig. 1. These sites represent different areas of traffic density (main roads and around the town, wide streets, narrow streets with tall buildings in their environment, parks, plazas, areas at different heights above the sea level, etc.).

1. Department of Analytical Chemistry, University of A Coruña (UDC), Campus A Zapateira, 15071 A Coruña, Spain. E-mail: purmahia@udc.es

2. Institute of Environmental Sciences, University of A Coruña, Pazo de Lóngora, 15179, Oleiros, A Coruña, Spain. E-mail: purmahia@udc.es

3. Sección de Medio Ambiente, Ayuntamiento de A Coruña, Spain.

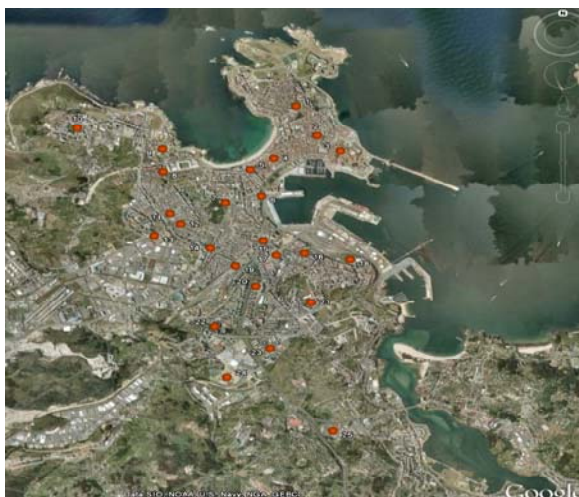


Fig. 1. Map of "google earth" with the locations of the sampling points.

2.2 Sampling

Two sampling campaigns were made in 2011, the first (Campaign 1) from June 29 to July 6, coincided with a warm period without rain, whereas the second (Campaign 2) was from 21 to 31 October with cold weather and heavy rains.

In some sampling points two passive sensors (Fig. 2) were put to check for precision, which yielded satisfactory coefficients of variation less than 5%. Furthermore, field blanks considering tubes identical to those used for sampling. The field blank values obtained were less than 4% of the value obtained for the samples.



Fig. 2. Sampling assembly.

2.3 Method of analysis

Thermal desorption and gas chromatography with mass spectrometry detection (TD-GC-MS) was employed. Electron ionization and ion trap detection with the following conditions:

- Column: SGE BPX-VOL 30 m x 0.25 mm x 1.4 mm
- Thermal Desorption: $T_{\text{tube}}=370^{\circ}\text{C}$; $t=8$ min; $T_{\text{cold tramp } 1}=-30^{\circ}\text{C}$; $T_{\text{cold tramp } 2}=350^{\circ}\text{C}$; desorb flow tube= 60 mL/min and desorb flow tramp= 3 mL/min.
- Chromatographic elution: 35°C (2 min) \rightarrow 119°C , $5^{\circ}\text{C}/\text{min}$ \rightarrow 119°C , (2 min) \rightarrow 150°C , $2.4^{\circ}\text{C}/\text{min}$ \rightarrow 150°C (5 min). Constant flow: 1 mL/min. Transfer line at 260°C .
- Full-scan detection mode.

Calibration and quantitation: Given the difficulty of calibration with liquids on Radiello® tubes, we chose to use Carbograph™ tubes (200 mg). There, BTEX standard solutions in methanol of concentrations between 1 and 2000 ng were injected. **Instrumental quantification limits:** were 0.19 ng for benzene, 0.30 ng for toluene, 0.24 ng for ethylbenzene, 0.47 ng for m + p-xylene and 0.25 ng for o-xylene.

We have also made laboratory blanks, being below 0.1% of the value found in the samples.

Validation: To calculate the analytical recovery five tubes were spiked with different concentrations of the analytes of interest between 1 and 4000 ng. The assay was done in triplicate and results are shown in Table 1.

Table 1. Study of analytical recovery (B=benzene, T=toluene, EB=ethylbenzene, m+p-o-X= m+p-o-xylenes).

	B	T	EB	m+p-X	o-X
%R	98,7	93,0	92,4	95,1	91,4
Cv%	6,6	5,7	5,9	4,9	7,1

3 RESULTS AND DISCUSSION

3.1 Weather conditions

For this study included variables such as temperature, solar radiation, precipitation, relative humidity and wind direction and wind intensity. We used data provided by the meteorological monitoring stations in the city [13-14], as well as those provided by the Department of Environmental affairs of the City of A Coruña (Fig.3). The average temperature during campaign 1 was $18.0 \pm 0.5^{\circ}\text{C}$ while in season 2 it dropped to $13.4 \pm 0.6^{\circ}\text{C}$. The temperature is directly related to the concentration of these compounds in air, mainly those from emissions of fuels, solvents, varnishes and paints due to evaporation processes and / or volatilization. Relative humidity values averaged $74.6 \pm 5.5\%$ and $80.0 \pm 4.3\%$ for the first and second campaigns respectively. During campaign 1 with warm and sunny weather, the average was $280.4 \pm 5.7 \text{ W}\cdot\text{m}^{-2}$, which decreased significantly in campaign 2 to $93.5 \pm 9.0 \text{ W}\cdot\text{m}^{-2}$ due the cold weather and rain. During the study rainfall occurred during campaign 2, with an average accumulated precipitation of $6.4 \pm 1.9 \text{ L}\cdot\text{m}^{-2}$, being practically null in campaign 1, with $0.10 \pm 0.05 \text{ L}\cdot\text{m}^{-2}$. Overall, in the study area the predominant wind circulation is N-NE during spring and summer (warm season) while in autumn and winter (cold season) the predominant direction is S - SE.

3.2 Levels of BTEX

BTEX concentrations were similar to those obtained in other urban areas: ΣBTEX of $17.2 \mu\text{g}\cdot\text{m}^{-3}$ and

8.40 $\mu\text{g}\cdot\text{m}^{-3}$ for the first and second season, respectively (Fig. 3).

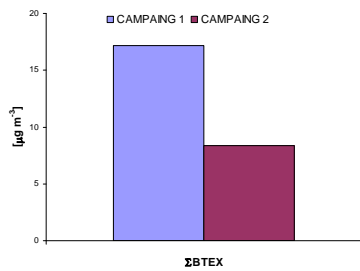


Fig. 3. Variation of ΣBTEX in the two campaigns.

There was a sufficient number of samples to compare the obtained concentrations of benzene with legal value (minimum coverage time will be about 14% with a random measurement per week and / or 8 weeks evenly distributed throughout the year), none of the sampling points (and therefore the average value of benzene in the city) exceeded the annual average limit of 5 $\mu\text{g}\cdot\text{m}^{-3}$ (Fig. 4).

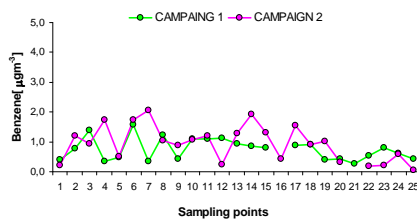


Fig. 4. Levels of benzene.

3.3 Compositional profiles

Differences between the two campaigns were clearly observed: in the first, toluene contributed 69.3%, followed by m+p-xylenes with 11%, benzene and ethylbenzene with 7.2%, each; and finally o-xylene with 5.3%. In the second season, both toluene and m+p-xylenes contributed similarly to total BTEX, and very different from the first campaign, with 37% and 30.1%, respectively. Benzene remained essentially at similar levels in both campaigns and xylenes increased their concentrations in the second (Fig. 5). The ratios of BTEX with other pollutants and/or wetaher parameters showed that traffic was the main source of emission of these compounds in both campaigns in the city of A Coruña. It is also noted that in the first campaign, with highest temperatures, there was a significant contribution of emissions from evaporation and/or volatilization processes from fuels, paints and solvents, together with the fact that photochemical processes were favored. Furthermore, in both campaigns the relative relationships between BTEX suggested a contribution from other emission sources. These may be certain activities that took place in the city (harbour, industrial area, etc.).

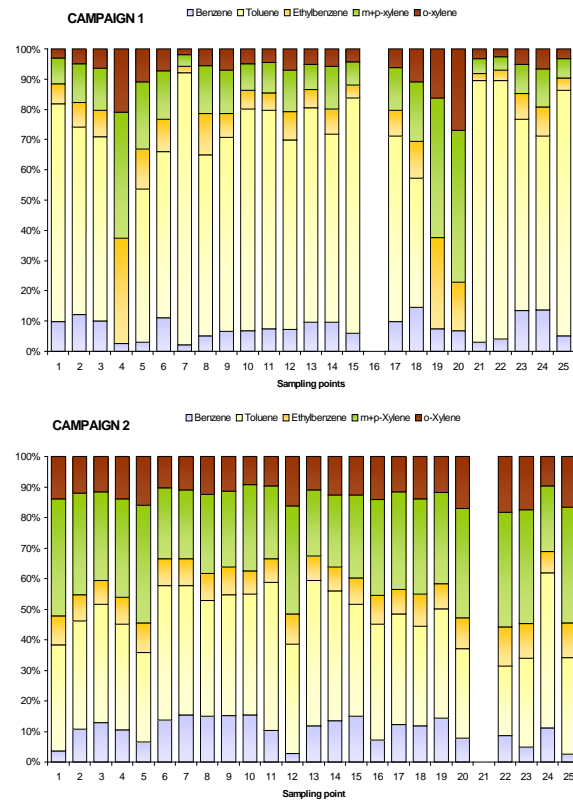


Fig. 5. Compositional profiles of BTEX in the two campaigns.

3.4 Contour plots

To visualize the BTEX levels in the city during the two sampling campaigns the contour plots for benzene and toluene will be displayed as a matter of example. The estimate of the points was made using the kriging method, representing only the area bounded by the sampling points. These representations allow a simplified vision of the concentration levels of the BTEX in different parts of the city, according to a color scale (Fig. 6,7).

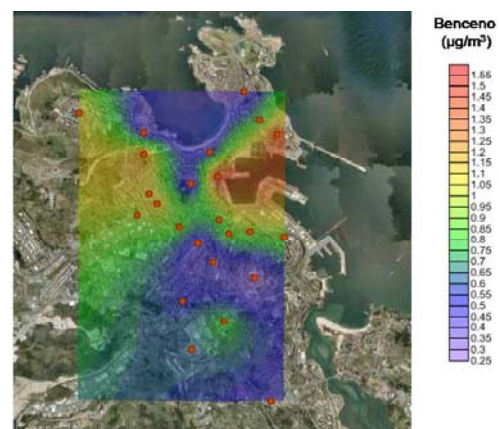


Fig. 6(a). Contour plot of benzene in the campaign 1.

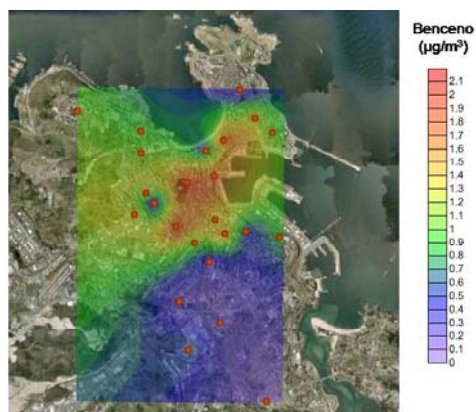


Fig. 6(b). Contour plot of benzene in the campaign 2.

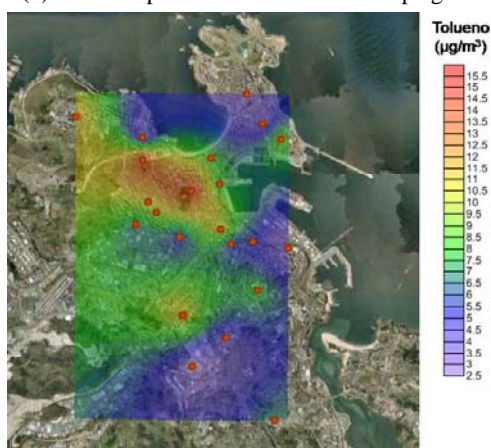


Fig. 7(a). Contour plot of toluene in the campaign 1.

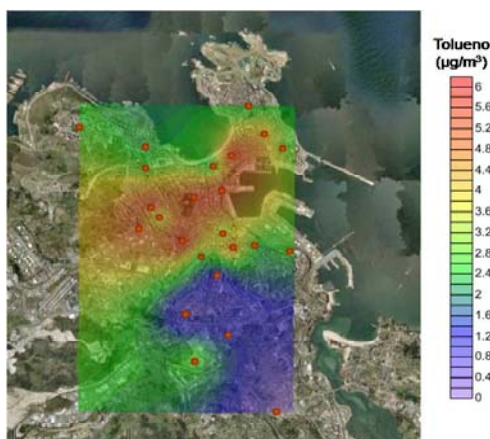


Fig. 7(b). Contour plot of toluene in the campaign 2.

4 CONCLUSIONS

The study presented here must be as a preliminary assessment of the levels of BTEX in the city of A Coruña. There were evaluated at two different periods: from June to July (warm and dry) and October (cold and rainy). The average of Σ BTEX values were of $17.2 \mu\text{g}\cdot\text{m}^{-3}$ and $8.40 \mu\text{g}\cdot\text{m}^{-3}$ for the first and second season, respectively. During the first campaign the major compounds were toluene and ethylbenzene at all points. Benzene remained essentially constant in both campaigns and xylenes increased their concentrations in the second period.

The average values obtained for benzene were $0.76 \mu\text{g}\cdot\text{m}^{-3}$ and $0.94 \mu\text{g}\cdot\text{m}^{-3}$, for the first and second season, respectively.

ACKNOWLEDGMENTS

This work has been supported by the Council of the city of A Coruña. Guillermo Leira is greatly recognized for his technical support, as well as the Research Support Services (SAI) of the University of A Coruña. The authors express also their gratitude to P. Esperon for her valuable help.

REFERENCES

- [1] Vanesa Juncal Bello. Tesis de Licenciatura: "Método semiautomático para la medida de precursores de ozono". Universidad de A Coruña. Marzo de 2006.
- [2] Débora Pérez Rial. Tesis Doctoral: "Monitorización compuestos orgánicos volátiles antropogénicos y biogénicos en aire ambiente y agua de mar. Universidad de A Coruña. Abril de 2011.
- [3] Buczynska A. J., Krata A., Stranger M., Godoi A. Flavia L., Kontozova-Deutsch V., Bencs L., Naveau I., Roekens Edwardand G. R. Van. Atmospheric BTEX-concentrations in an area with intensive street traffic. *Atmospheric Environment*, 43 (2009) 311-318.
- [4] D. Pérez-Rial, P. López Mahía, S. Muniategui Lorenzo, D. Prada Rodríguez. Temporal distribution, behaviour and reactivities of BTEX compounds in a suburban Atlantic area during a year. *J. of Environmental Monitoring* 11 (2009) 1216-1225.
- [5] Pilidis Georgios A., Karakitsios Spyros P., Kassomenos Pavlos A., Kazos Elias A. and Stalikas Constantine D. Measurements of benzene and formaldehyde in a medium sized urban environment. Indoor/outdoor health risk implications on special population groups. *Environment Monitoring Assessment*, 150 (2009) 285-294
- [6] IARC. International Agency for Research on Cancer. <http://monographs.iarc.fr/>. (2011).
- [7] WHO. Guías de calidad del aire de la OMS. WHO air quality guidelines global update 2005. World Health Organization. <http://www.euro.who.int/Document/E87950.pdf>, (2005). EPA. Environmental Protection Agency. <http://www.epa.gov/ttn/uatw/188polls.txt>. (1999).
- [8] Ras M.R., M. R. Borull Francesc. Characterization of ozone precursor volatile organic compounds in urban atmospheres and around the petrochemical industry in the Tarragon region. *Science of the Total Environment*, 407 (2009) 4312-4319.
- [9] Bomboí, M.T.; Pérez A.; Rodríguez B., Galán, D; Díaz A., Fernández R. Spatial and temporal distribution of volatile organic compounds in the area of Madrid (Spain) during a year. *Fresenius Environmental Bulletin* 65 (2005), 1233-1240.
- [10] Pennequin-Cardinal A., Plaisance H., Locoge N., Ramalho O., Kirchner S., Galloo J.C. Dependence on sampling rates of Radiello diffusion sampler for BTEX measurements with the concentration level and exposure time. *Talanta* 11(8) (2002), 437-440.
- [11] Directiva 2008/50/CE del Parlamento Europeo y del Consejo de 21 de mayo de 2008 relativa a la calidad del aire ambiente y a una atmósfera más limpia en Europa (DO L152 de 11.6.2008).
- [12] Real Decreto 102/2011, de 28 de enero, relativo a la mejora de la calidad del aire.
- [13] <http://aire.medioambiente.xunta.es/>
- [14] <http://www2.meteogalicia.es/galego/observacion/estacions/estacions.asp>

Measurements of number size distributions of submicron aerosols during summer 2012 at the western part of Spain

S. Iglesias-Samitier^{1,2}, V. Juncal-Bello², M. Piñeiro-Iglesias², P. López-Mahía¹,
S. Muniategui^{1,2}, D. Prada^{1,2}

Abstract — The ambient nanoparticles number concentration and size distribution have been measured at Institute of Environment (University of A Coruña) during summer period, June-July 2012. This sampling point is located in a suburban area in the outskirts of the city of A Coruña, influenced by traffic and characterized by an Atlantic climate. Measurements of number size distributions were carried out by a Scanning Mobility Particle Sizer (SMPS) consisted of TSI 3080 Electrostatic Classifier with TSI 3081 long-DMA and TSI 3785 Water Condensation Particle Counter, to measure particles between 7,64 and 289 nm. During this period a large number of nucleation events have been identified, specially in June. This process coincided with sea breeze, high solar radiation and temperature. A “clean” atmosphere favour the particle formation process. Other events have been observed: particle growth, evaporation and combustion processes.

Keywords— Atmospheric nanoparticles, nucleation event, Scanning Mobility Particle Sizer, sea breeze, size distribution.

1 INTRODUCTION

The study of atmospheric nanoparticles has been great interest in recent years due to their potential adverse health effects, this fraction has a major contribution to the total particle number concentration [1], but less in the particle volume or mass. The evolution of atmospheric aerosols in the urban environment is affected by processes such as dilution, coagulation, condensation or deposition, which modify the number and/or the size distribution, and are influenced by meteorological parameters such as temperature, relative humidity, wind speed, or amount of solar radiation [2].

2 METHODOLOGY

2.1 Site of study

The measures of size distribution of atmospheric nanoparticles have been carried out at the Institute of Environment (University of A Coruña), in the province of A Coruña (43°19'N, 8°24'W, 115 m.a.s.l.) during summer 2012. The site of study is a suburban area and it is located in a residential zone with low industrial influence (Figure 1). The nearest populations are Santa Cristina and Santa Cruz de Oleiros from 1,6 and 1,5 km, respectively. The city of A Coruña is the biggest population more coming

of the Institute from 5,5 km and with 246.000 habitants approximately. At the proximities of the site of study it can be located a group of industries that can affect the air quality, which are of energy sector, production and transformation of metals, chemical industry, waste management and wastewater, paper manufacturing and processing, food and beverage industry, as well as ports and airports, hospitals, funeral homes, printers, laundries, and other diverse activities. However the main source of particulate matter is the road traffic around the proximities of the Institute.



Fig. 1. Location of the Institute of Environment, sampling point.

1. Department of Analytical Chemistry, University of A Coruña, Campus da Zapateira, 15071, A Coruña-Spain, purmahia@udc.es

2. Institute of Environment, University of A Coruña, Pazo de Lóngora, 15179, Oleiros-A Coruña-Spain

This suburban area is characterized by present an Atlantic climate, with an average temperature during 2012 of 13°C and 17°C during the cold and hot periods, respectively. The local winds, like sea breeze, are the more important circulation during summer, to the point of masking the winds associated to the general atmospheric circulation. The winds were most common from N-NW, wind direction around 300°, indicating that air came from sea.

2.2 Instrumentation

Measurements of number size distributions of submicron aerosols were carried out by a Scanning Mobility Particle Sizer (SMPS) during summer 2012. SMPS consisted of TSI 3080 Electrostatic Classifier with TSI 3081 long-DMA and TSI 3785 Water Condensation Particle Counter. The SMPS was set to the sheath and polydisperse aerosol flow rates of 10.0 and 1 l/min, respectively, to scan the size range 7,64–289 nm. A pre-impactor with nozzle 0,0514 cm was used. The SMPS sampled periodically every 5 minutes with two scans per sample and 120 seconds scan up. The distributions were corrected for multiple charging and diffusion.

On the other hand, several meteorological parameters were measured at the site of study by the meteorological station (Model 03002, R.M. Young Company, Michigan, EEUU): wind direction and velocity, solar radiation, temperature, pressure, relative humidity and precipitation. In addition, PM₁₀, PM_{2.5} and PM₁ concentrations were measured by the GRIMM 1107 Particle Monitor.

3 RESULTS AND DISCUSSION

The average total concentration of particle between 7,64–289 nm was higher during June–July 2012 period (3978 cm⁻³) than during the same period in 2011 (2854 cm⁻³). Figure 2 shows the particle size distributions during the measurement period. June showed a bimodal distribution with two maximum (10,9–14,6 nm and 55,2–71 nm). The first maximum is due to the large number of nucleation events in this month. On the other hand, July showed one maximum around 49,6 nm.

The particle number concentrations have been integrated from the number size distributions for different intervals: the nucleation mode (D_p < 30 nm), the Aitken mode (within 20 and 100 nm) and the accumulation mode (D_p > 90 nm), where D_p is the particle diameter [3]. The daily evolution of these modes was similar for both months, they presented high concentrations during firsts and late hours of the day because traffic. The sampling point is influenced by traffic during summer because the beach is near, and the affluence of visitants is high, thus, accumulation mode presented high concentrations (Figure 3 shows the results of July).

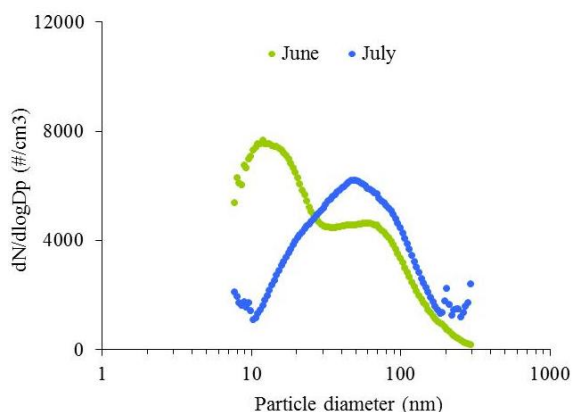


Fig. 2. Particle number concentration during June and July 2012.

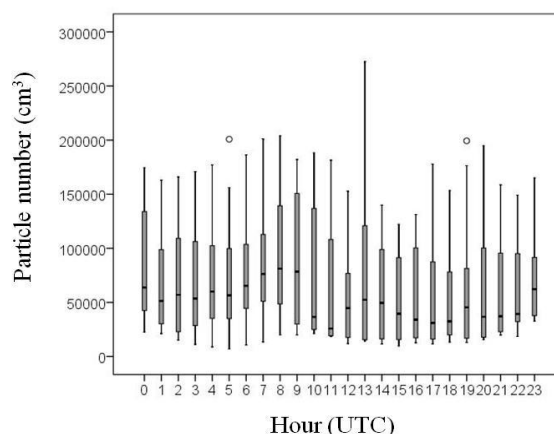


Fig. 3. Daily evolution of the accumulation mode in July.

On the other hand, a large number of nucleation events have been identified during June, this processes were observed during central daily hours when temperature and solar radiation was maximum (Figure 4).

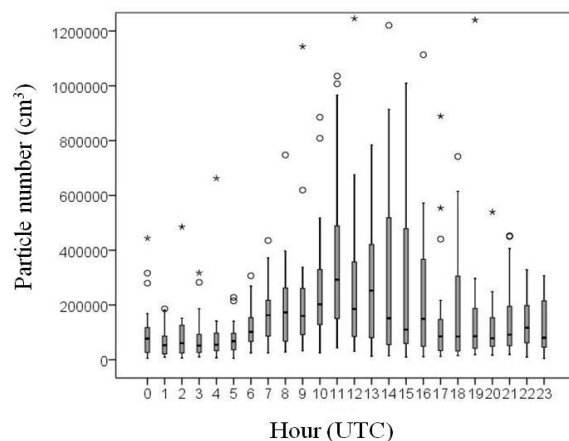


Fig. 4. Daily evolution of the nucleation mode during June.

In addition, the nucleation events identified during sampling period coincided with the sea breeze, as show in Figure 5. In July the number of nucleation events was smaller, but the difference was that the particle matter concentration of PM₁₀,

PM_{2,5} and PM₁ were 29, 25, and 21 µg/m³ respectively, unlike with June that this concentrations were 26, 23, 18 µg/m³, respectively too. This suggested that a “clean” atmosphere can favour the nucleation process.

Moreover, during sample period different process have been identified, like particle growth and evaporation of volatile compounds over particle surface. Figure 6 shows the growth of Aitken mode particles to sizes of accumulation mode and Figure 7 shows an evaporation process. The evaporation process occurred during the hours of maximum solar radiation, which favoured the evaporation of volatile

compounds over particle surface and thus the particles reduced to smaller sizes.

Finally, a combustion process has been identified. During the night of 24th June in A Coruña is celebrated the “San Juan Festivity”, this is a traditional party where thousands of bonfires are burnt in the city and their surroundings. The start of the fire occur around 20 h (UTC) of 23th and they still burn until the early hours of 24th of June. The consequence of this celebration is the emission of particles with diameters within Aitken and accumulation modes (Figure 8).

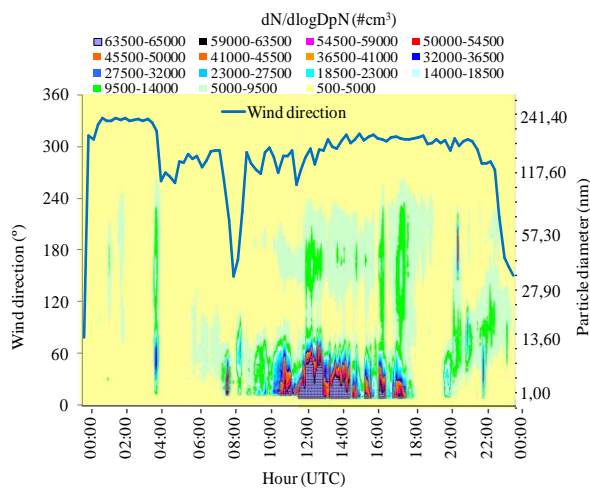


Fig. 5. Nucleation event during 21st June.

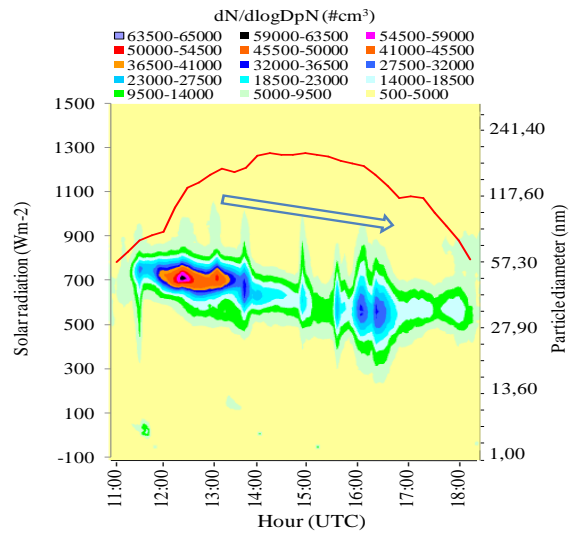


Fig. 7. Evaporation process during 21st July.

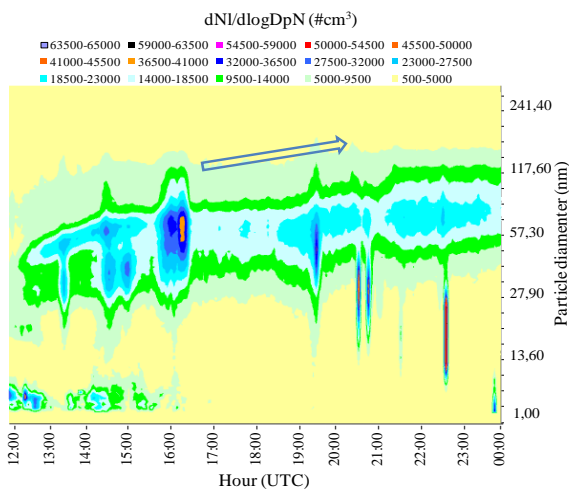


Fig. 6. Growth of particles during 31st May.

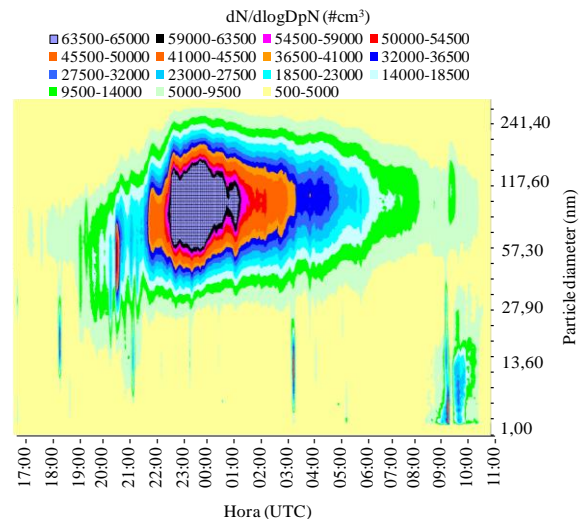


Fig. 8. Combustion process during “San Juan Night 2012”.

4 CONCLUSIONS

The average total concentration of particle between 7,64-289 nm was higher during June-July 2012 period (3978 cm^{-3}) than during the same period in 2011 (2854 cm^{-3}). Also, a large number of nucleation events have been identified at the Institute of Environment (University of A Coruña), especially in June. The atmospheric conditions were sea breeze and high solar radiation and temperature when the new particles formation occurred. A “clean” atmosphere favoured the process of new particle formation too. In addition, other events were observed: growth particles, evaporation process and combustion event during “San Juan Festivity”.

ACKNOWLEDGMENT

The authors acknowledge the financial assistance of Ministerio de Ciencia e Innovación (Plan Nacional de I+D+I 2008-2011) (Ref. CGL2010-18145), Xunta de Galicia (Programa de Consolidación y Estructuración de Unidades de Investigación Competitivas 2010-2012, 2010/52) and FEDER (UNLC00-23-003). The authors also express thanks to P. Esperon for her valuable help.

REFERENCES

- [1] Dall'Osto, M., Beddows, D.C.S., Pey, J., Rodriguez, S., Alastuey, A., Harrison, R.M. and Querol, X. “Urban aerosol size distributions over the Mediterranean city of Barcelona, NE Spain”, *Atmospheric Chemistry and Physics* 12 (2012) 10693.
- [2] Pey, J., Rodríguez, S., Querol, X., Alastuey, A., Moreno, T., Putaud, J.P. and Van Dingenen, R. “Variations of urban aerosols in the western Mediterranean”, *Atmospheric Environment* 42 (2008) 9052-9062.
- [3] Gómez Moreno F. J., Pujadas M., Plaza J., Rodríguez-Maroto J. J., Martínez-Lozano P. and Artífano B. “Influence of seasonal factors on the atmospheric particle number concentration and size distribution in Madrid”, *Atmospheric Environment* 45 (2011) 3169-3180.

Impact on air quality operations cleaning and inspection of natural gas pipelines in Central Mexico

L.M. Rodriguez^{1,2}, A.M. Sánchez de la Campa¹, J.D. de la Rosa¹

Abstract — Methane anthropogenic emissions are generated by the production of oil and natural gas leaks. The main processes impacting on the atmosphere are transport and storage of natural gas, including fugitive emissions in pipeline derived from the maintenance activities. The Cleaning/ Inspection Process of Oil Pipelines (PLITTH), is a preventative maintenance procedure used to monitor the mechanical integrity of the pipelines, which requires natural gas emission to the atmosphere. Hybrid Single Particle Lagrangian Integrated Trajectory (HYSPLIT) model has been used to predict transport and dispersion of PLITTH emissions. The results showed that Air Quality of Metropolitan Area of Mexico (ZMVM) can be modify in least 12 of the analyzed events in 2011. The impact of PLITTH contaminant in ZMVM is identified using PM₁₀. One of the main important episodes of impact occur on 11th January 2011, in which the Metropolitan Environmental Commission (CAM) of the ZMVM, activated the Atmospheric Environmental Contingency Program on 11th - 12th January by high PM₁₀ values recorded at station XALOSTOC (XAL) to Northwest of the ZMVM. The high levels obtained were favored by a high pressure system coupled to the emissions for the PLITTH, and dominant local wind of W, NW and SW.

Keywords — Emissions, HYSPLIT, PLITTH, natural gas

1 INTRODUCTION

It is increasingly common to use natural gas around the world, among other reasons for its environmental advantages compared to other energy sources such as oil and coal. Specialists in this field argue that in 2030, natural gas will displace coal, driven by its increasing use in emergent countries like China and India. It is necessary to consider that the main constituent of natural gas is the methane [1], a greenhouse gas, to which are attributed to global changes on mean temperature and to which recently it is considered an increase in the warming atmospheric.

In Mexico, the main sources of methane emissions are relief (intentionally opening release valve to atmosphere to eliminate / reduce line pressure) and combustion in high and pit-type burners [2]. The latter is mainly in the fields of oil and gas producers. In 1984, relief gas and combustion of natural gas was 5.7% of commercial production, which is close to 98.92 billion cubic meters [3]. The absence of direct measurements of this fraction, its contribution to atmospheric overall impact is unclear, although it was assumed that 20% of the natural gas delivered by the relief pipe escapes directly into the atmosphere [4].

The Cleaning/ Inspection Process of Oil Pipelines (CIPOP), is a preventative maintenance procedure

used to monitor the mechanical integrity of the pipelines, which requires natural gas emission to the atmosphere. In 2011, 69 CIPOP were performed in central Mexico. The CIPOP is an established maintenance process, which has supported the mechanical integrity of the pipeline and to consider alternatives such as gas reinjection relieved to the atmosphere, the gas available elsewhere in the supply chain, electricity cogeneration. These options allow the CIPOP continue as one of the most widely used practices in the oil industry nationally and globally.

In this work, we evaluate the impact of CIPOP in the air quality of several cities of Central and Western Mexico, including the megacity of Mexico DF. We use the levels of contaminant gases and atmospheric particulate matter obtained in the Air Quality Network of the region.

2 METHODOLOGY

2.1 Air Quality

In 2012, the Central and Western Mexico Government management 35 automated sampling stations, through which monitor carbon monoxide (CO), nitrogen dioxide (NO₂), ozone (O₃), sulfur dioxide (SO₂), respirable suspended particles (PM₁₀), and in some cases (PM_{2.5}). 27 monitoring stations are located in the Central (Mexico DF) and 8 in the West (Guadalajara). The information is analyzed in accordance with the methodology called Air Quality Index (AQI) as the basis for calculating the Index Metropolitan Air Quality (IMECA). The environmental standard for the Federal District

1. Author is with Associate Unit CSIC-UHU "Atmospheric Pollution". Center for Research in Sustainable Chemistry (CIQSO), University of Huelva, Campus El Carmen E21071 Huelva, Spain.

2. PEMEX, address Cerro Azul No. 115 Colonia PEMEX Salamanca E36730 Guanajuato, Mexico

NADP-009-AIR-2006, establishes the requirements to design and calculate the IMECA, also used by other entities that perform the measurement and assessment of air quality in Mexico.

The sampling for every compound was performed hourly from January 1st to December 31st 2011 and the data were stored in the monitoring systems of Central and Western Mexico. Information Atmospheric Monitoring System Mexico City (SIMAT) and Atmospheric Monitoring System of Jalisco (SIGA) was exported to Excel® for statistical management, and average hourly information, air station, conversion parameters, processing graphs and trends by pollutant. Data monitoring systems are reported in ppm or ppb, so conversions are performed g/m^3 , based on local conditions of pressure (1013.25 hPa Hg) and temperature (20° C).

2.2 CIPOP 2011 Program

CIPOP Program 2011 considers 69 events for the Southern and Central Mexico. Of these events, 44 were conducted in the Southeast and 25 in Central Mexico. 98% of the generated CIPOP in Southeast impacts on population are not considered in the evaluation of the air quality.

The CIPOP involves two main aspects: a) sending or launching, and b) receiving mechanical or electronic device. The relief and de-pressing out of the "bucket" eliminate any risk of overpressure that might exist when inserting the device. In this part of the process, the first emission to the atmosphere of methane is performed, which depends on the pressure, cell volume, product rate and the pipe diameter (60 to 120 cm), estimating 0.7 to 4.8 m^3 per event [6]. Once the device is inserted, it is drained from the "bucket", which implies a second step of minor concentration of methane to the atmosphere. The inspection process is preferably performed after a cleaning process in order to optimize the quality and reliability of data obtained by the electronic device. The cleaning process is carried out independently. The cleaning and inspection of pipelines is performed without stopping the transport process, so are critical relief activities, de-pressing out and drain pipe.

The 69 CIPOP conducted in 2011, reported volumes of more than 24,000 Tn of solid and 6,000 liter of liquid waste.

2.3 HYSPLIT

Emissions of methane gas, generated by the selected events for the year 2011, are the point source of atmospheric emissions. The process will be analyzed by using the trajectory and HYSPLIT dispersion modelling [7].

Emission trajectories have been calculated for five days. Starting heights was 50 m and source emission duration of 5 hrs, with simulation time of

48 hours. The trajectories have been described in terms of the origin of the prevailing winds in each region and dates emissions. We have selected two domains of calculation: Central (Lat 19° N 99° W) and West (Lat 20° N 103° W).

2.4 Chemical Analysis

Trace elements analyses of the solid residual of CIPOP were conducted by inductively coupled plasma mass spectrometry (ICP-MS) on a HP-7700 instrument of University of Huelva with detection limits close to $0.01 \mu\text{g L}^{-1}$ for all the determinations. Doubly charged and oxide interferences were lesser than 1.5% and 0.5% respectively, and minimized during the tuning operation of the instrument. The average precision and accuracy fall in the range of 5–10% relative standard deviation (RSD), and they were controlled by repeated analyses of NIST 1663b international standard.

3 RESULTS

3.1 Air Quality

For the assessment of air quality we considered the information obtained from their respective databases of the atmospheric monitoring systems and the application of the established methodology for calculating the IMECA. During year 2011, 9 days were classified as regular for ozone in Central Mexico, while in the West were recorded 32 days. For PM_{10} the results were up to 111 regular days, 6 bad and 1 very bad in Central Mexico and of 119 to 5 bad regular in the West. However, the highest values of $\text{PM}_{2.5}$ were recorded in the central region corresponding to 96 regular days, 28 bad and one very bad. For the West region are: 152 regular days, 92 bad, 23 very bad and 3 extremely bad. Recall that for the case of air pollution, particulate matter and Ozone, are contaminants which will have high important in climate change scenario. Ozone shows association with cardiovascular mortality in warm season. The direct relationship between increases in air pollutants and hospital admissions for cardiovascular diseases associated to the effect of carbon monoxide and ozone is because the lungs represent the entry on the air pollutants in the blood. The effect is greater for heart disease than for other circulatory diseases [5].

3.2 Trajectory of Air Mass by HYSPLIT

One of the main important episodes of impact occur on 11th January 2011, in which the Metropolitan Environmental Commission (CAM) of the ZMVM, activated the Atmospheric Environmental Contingency Program on 11th - 12th January by high PM_{10} values recorded at station XALOSTOC (XAL) to Northwest of the ZMVM (Fig 1).

In the hours before of the intrusion of methane, the air quality was classified as fair and during the hours of the intrusion evolved to extremely bad and bad. During the first period of intrusion (18 hrs), there is a general increase in the values of the seasons TLA (Tlalnepantla), XAL (Xalostoc), MER (Merced), CES (Centro Sur), TLI (Tultitlan), where air quality changes from good to bad. The station XAL has extremely bad values at 6 and 8 pm the same day 11 (329 and 405 $\mu\text{g}/\text{m}^3$) but the values are increasing to 618 and 418 $\mu\text{g}/\text{m}^3$ at 17 and 18 hrs, respectively, at times which present natural gas intrusion - methane. They also have extremely bad values in TAH (Tláhuac) and SAG (San Agustín) stations, at 17 and 18 hrs (546 and 337 $\mu\text{g}/\text{m}^3$). The maximum values recorded on the previous day at these stations were 114 $\mu\text{g}/\text{m}^3$ for 21 hrs at the station TAH, and 162 $\mu\text{g}/\text{m}^3$ for 18 hrs at the SAG station.

The second period of intrusion, which originated in 13th January, does not record significant changes in the values recorded by pollutants in the air quality monitoring stations.

The values of the pollutants on 11th January exceed permissible exposure limits outlined by the World Health Organization (WHO) and Official Standard (NOM). The high levels obtained were favored by a high pressure system coupled to the emissions for the CIPOP, and dominant local wind of W, NW and SW.

According to the annual report of air quality of Mexico City, in 2011, were 5 activations Environmental Contingency Program, once caused by PM_{10} and O_3 four occasions, on 26 March, 12 May, 16 June and November 13th.

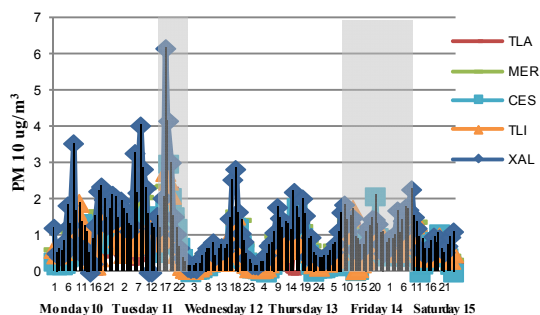


Fig.1. Impact of the emission (the emission period in gray) 11 and 13 January, 2011 in the Center area, showing the variations in the measurement of pollutants PM_{10} ($\mu\text{g}/\text{m}^3$) for the period from 10 to 15 January.

3.3 Trace Elements Analysis of Solid Residual

A solid residual of CIPOP was analyzed using Inductively Coupled Plasma (ICP-MS). 48 toxic potentially elements, among which Pb (1040 ppm), Zn (571 ppm), Sr (343 ppm), Cr (312 ppm), Ba (188 ppm), V (23.9 ppm), Zr (12.5 ppm), and Rb (7.94

ppm), and less proportion of Mo, Cu, Sn, Nb were characterize.

CIPOP is common in the production of solid / liquid to a greater or lesser volume depending on the frequency of cleaning and the distance covered by the cleaning device. In the sample of the waste collected on 4th July, 2012, in the pipeline diameter of 24 inches (60.96 centimeters), called Valtierrilla-Lazaro Cardenas-Nueva Italia Zirahuen stretch, and analyzed by chemical analysis yields the presence 48 trace elements. To compare the results CIPOP chemical residue in the present study, we consider the estimates of trace elements in the composition of the upper continental crust [8].

4 CONCLUSIONS

The main conclusions can be summarized in the following points:

1. – High concentration of toxic potentially elements such as Pb, Zn, Sr, Cr, Ba, V, Zr and Rb, and less proportion of Mo, Cu, Sn, Nb were characterized in solid residual of CIPOP.
2. - During CIPOP, several of toxic elements can be incorporated into the atmosphere as particulate matter with methane and its derivatives, and can impact negatively on air quality of megacities.
3. - Some of the atmospheric monitoring stations in the Central and Western Mexico, have limited monitoring capacity (CO , NO_2 , SO_2 , O_3 and PM_{10}). This fact difficults the identification of the impact of oil and other pollutants such as, Pb, Cr, V. This justifies the fact that the values of CIPOP emissions are reflected in PM_{10} or $\text{PM}_{2.5}$, although it could also be reflected in the Ozone, since methane is a precursor of the latter.

As final conclusion, approximately 82% of CIPOP impacts were developed at cities or states, most of which have not air quality networks, making difficult to assess the impact on the population and the environment.

ACKNOWLEDGMENTS

The researchers from the University of Huelva that facilitated appropriate technology for residual analysis CIPOP.

Petróleos Mexicanos PEMEX for providing the information necessary for the development of this research.

REFERENCES

- [1] Finlayson-Pitts Barbara J., Pitts Jr James N., *Chemistry of the Upper and Lower Atmosphere*, Academic Press, USA, Page 777, 2000.
- [2] United States Environmental Protection Agency, *Methane Emissions from the Natural Gas Industry*, Volume 6: Vented and Combustion Source Summary, Chicago, USA, Page 2, 7, 9, 15 and 25, 1996.
- [3] Fung I, *Three-Dimensional Model Synthesis of the Global Methane Cycle*, Journal of Geophysical Research, Vol. 96, No. D7, Pages 13,033-13,065, July 20, 1991.
- [4] Darmstadter J, *Impacts of world development on selected characteristics of the atmosphere: An integrative approach*, Rep. ORNL/Sub/86-22033, Oak Ridge Nat'l Lab. Oak Ridge Tennessee, 1987.
- [5] Ballester Ferrán, Díaz Julio, Moreno José Manuel, *Cambio climático y salud pública: escenarios después de la entrada en vigor del Protocolo de Kioto*, Gaceta Sanitaria, España, 163, 164-167, 2006.
- [6] United States Environmental Protection Agency, *Reducción de las emisiones de metano Durante el mantenimiento y reparación de ductos*, Taller de Transferencia de Tecnología, Argentina, 2008.
- [7] Draxler, R.R., *Hybrid single-particle Lagrangian integrated trajectories (HY-SPLIT): Version 4.0 -- User's guide and model description*. NOAA Tech. Memo. ERL ARL-224, 27 pp. and Appendices, 1997.
- [8] Rudnick, R. L and Gao S., *Composition of the Continental Crust*, Treatise on Geochemistry, Volume 3, page 1-64.

Validation of atmospheric aerosols sampling in equivalent fractions

C. M. Oliveira¹, M. F. Camões¹, P. Bigus², A. A. Fachado¹, R. Silva¹

Abstract — Physical properties and chemical composition of atmospheric aerosols are of extreme importance, in many fields of interest, namely the Environment even with legal implications. Atmospheric sampling poses inherent problems with consequent demands on sampling optimisation, with sampling strategies requiring validation. In this work a study was conducted aiming at validating the collection of atmospheric aerosols in equivalent fractions. Aerosols were actively collected using a sampling system consisting of a PM₁₀ ($\leq 10 \mu\text{m}$) inlet coupled to a manifold with six channels of filter holders. The set up was mounted on the roof of building C8 of FCUL, in Lisbon. Samples were treated and analysed by Ion Chromatography (IC) for chloride, nitrate and sulphate anions, in the aerosol water-soluble fraction. The evaluation of the compatibility of measurement results was used to validate sampling and analytical procedures. The results obtained for the measurements in the six filter holder positions are, in general, compatible and the positions can be considered metrologically equivalent.

Keywords — atmospheric aerosols, equivalent sampling, ion-chromatography, validation.

1 INTRODUCTION

Atmospheric aerosols consist of relatively stable suspensions of solid or liquid particles in air that may be either directly emitted (primary) into the atmosphere or formed there (secondary) by chemical reactions [1: 100]. The importance of particulate matter (PM) in terms of atmospheric pollution is a matter of great concern, especially because of its health effects in the populations which led the European and American legislations to impose limits on their emissions “[2],[3: 298-299]”. In order to take decisions about air quality control measures in urban areas it is very important to know the mass and chemical composition of particulate matter in air. Atmospheric aerosol sampling is a key issue, since the particles to be sampled and studied have a great variability of sizes and chemical properties. This diversity often imposes the use of different types of filters, conveniently selected according to the respective target measurand, the analytical methodology that will be used and the flow rate used for active sampling [3: 9-12]. Ion chromatography (IC) is considered one of the most powerful analytical tools available for analysing ions in the water soluble aerosols fraction “[4],[5]”. In an attempt to attain a flexible sampling programme and multiple results with low uncertainty, a multichannel sampling system has been developed and was used. It consists of a manifold made out of two main stainless steel tubes, connected by six channels with filter holders, adapted to the common PM₁₀

($\leq 10 \mu\text{m}$) inlet, and to a vacuum pump for active sampling, figures 1 and 2. A series of sets of combinations of channels and filters allowed the evaluation of the compatibility of measurement results leading to validation of this sampling procedure. The ions chosen as indicators for quantitative assessment are chloride, Cl⁻, nitrate, NO₃⁻ and sulphate, SO₄²⁻.

2 EXPERIMENTAL PROCEDURE

2.1 Sampling set up

The sampling system was placed on a roof terrace of building C8 of the FCUL, in Lisbon. The aerosol samples were collected using a sampling system (Fig.1), equipped with a PM₁₀ inlet, connected by a stainless steel tube to a manifold of six channels, each coupled to a filter holder (Fig.2). The system was connected to a vacuum pump operating 24 h, at a flow rate of 12 L min⁻¹, controlled by a flow meter. Aerosols were collected, onto Whatman® 41 filters of 47 mm in diameter, between April and May 2012. Filters were manually replaced daily.

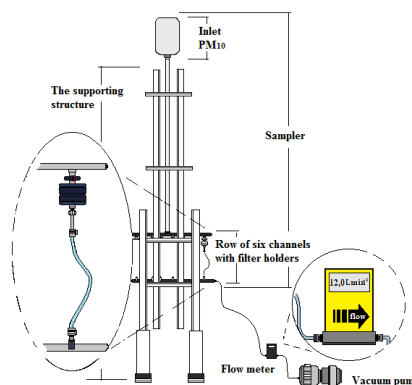


Fig. 1. Schematic representation of sampling system.

1. C. M. Oliveira, M. F. Camões, A. A. Fachado and R. Silva are with CCMM - Department of Chemistry and Biochemistry, Faculty of Sciences of the University of Lisbon, Edifício C8, Campo Grande, 1749-016 Lisbon, Portugal. E-mail: cmoliveira@fc.ul.pt
2. P Bigus is with the Department of Analytical Chemistry, Chemical Faculty, Gdańsk University of Technology, ul. Narutowicza 11/12, 80-233 Gdańsk, Poland E-mail: bigus.paulina@gmail.com

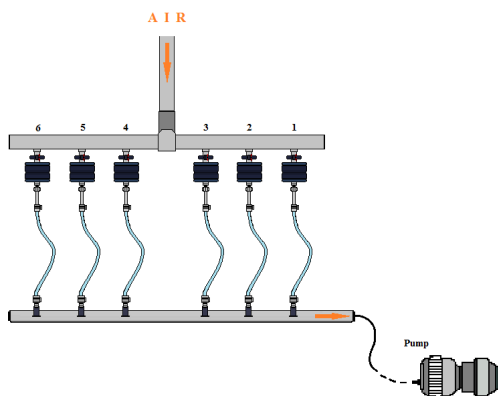


Fig. 2. Schematic representation of the manifold of six channels with filter holders.

Three sets of samples, each set on a different day, were collected with filter holders in different positions (Set A - 1, 2, 3, 4, 5, 6; Set B - 4, 5, 6 and Set C - 4, 5), aiming at comparison of results within each set.

2.2 Analytical assay

The standard calibration solutions and the eluent were prepared with compounds of analytical reagent grade and the water used in all steps was ultra-pure deionised water (18.2 MΩ cm). In order to avoid sample contamination filters were handled with plastic gloves and tweezers, in a clean air bench. Mixed (Cl^- , NO_3^- , SO_4^{2-}) calibration standards were prepared from each anion stock standard solution according to the procedure shown in fig. 3.

Fig. 3. Schematic representation of the dilution procedure of the stock solutions for the preparation of the calibration standards [6]. γ is the mass concentration of the considered ion in the solution.

Each filter with collected aerosol was inserted in a PTFE bottle to which 10 mL, V_1 , of water was added. The capped bottles were sonicated in an ultrasonic bath at $(45 \pm 1)^\circ\text{C}$ for (45 ± 2) min after which the extracted solutions were filtered through a pre-washed Whatman 41[®] filter. If needed, a portion V_2 of the sample extract was diluted with a water volume V_3 [dilution factor, $F_{\text{dil}} = (V_2 + V_3)/V_2$], before being analyzed by ion chromatography (IC). The IC measurements were performed in an ion chromatograph Dionex[®] DX500 system with conductivity detection (CD20). The eluent was a 3.5 mmol dm⁻³ Na₂CO₃ + 1 mmol dm⁻³ NaHCO₃ buffer solution. Daily calibration with four equidistant

mass concentration calibration standards (Fig.3) fit for the application of the linear unweighted regression model [7] was performed using duplicate measurements.

3 EVALUATION OF THE MEASUREMENT UNCERTAINTY

The evaluation of the measurement uncertainty involves different steps, namely: definition of the measurand, identification of the sources of uncertainty, quantification of the uncertainty components, combination of the uncertainty components and expansion of the combined standard uncertainty “[8],[6]”. In this study, the measurand was the mass of a specific anion (chloride, nitrate or sulphate) in the aerosol water soluble fraction collected in a specific filter. The mass, m , of an ion was estimated from eq. (1):

$$m = \gamma \cdot V_1 \cdot \frac{(V_2 + V_3)}{V_2} = \gamma \cdot V_1 \cdot F_{\text{dil}}$$

where γ is the mass concentration of the ion in the diluted sample extract, V_1 is the volume of aerosol extract and F_{dil} the dilution factor. The identified sources of uncertainty to be considered are schematically represented by the cause and effect diagram of Fig. 4 “[6],[7]”.

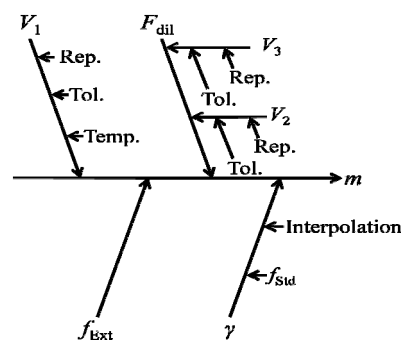


Fig.4. Cause and effect diagram representing the identified sources of uncertainty; Rep., repeatability; Tol., tolerance calibration components; Temp., temperature effect [6].

All volumetric operations are affected by the repeatability of the volumetric material manipulation (Rep.) and by its tolerance nominal value (Tol.). The volumetric measurement V_1 , is also affected by the temperature effect (Temp.). The estimated concentration of the diluted extract (γ) is affected by the statistical interpolation of the sample signal in the calibration curve (Interpolation) and by the uncertainty associated with the concentration of calibration standards (f_{Std}).

The quantification of the sources of uncertainty [9] requires considering several components, namely:

- The uncertainty associated with the dilution factor F_{dil} , $u(F_{\text{dil}})$.
- The relative standard uncertainty of dilution factor $u^r(F_{\text{dil}})$.
- The statistical interpolation uncertainty u_{Int}

- The relative standard uncertainty of stock mother solution $u'_{\text{stock solution}}$.
- The relative combined standard uncertainty, u'_c .
- The expanded uncertainty, U_c .

All these components were estimated according to the procedure described in Silva et al., 2012.

According to VIM [10] the compatibility of measurement results is “the property of a set of measurement results for a specified measurand, such that the absolute value of the difference of any pair of measured quantity values from two different measurement results is smaller than some chosen multiple of the standard measurement uncertainty of that difference”. In order to carry out the test of compatibility of measurement results from different positions of filter holders in the chosen sets, eq. (2) was used:

$$|x_i - x_j| \leq 2 (u_i^2 + u_j^2) \quad (2)$$

where $|x_i - x_j|$ is the difference of mass ion in filters i and j and u_i and u_j are the standard uncertainties of x_i and x_j values. If this condition is true, results are compatible and positions are equivalent (Eq.). Otherwise the positions are different (Dif.). The evaluation of the compatibility of measurement results from filters in different positions at the row of six channels was used to validate the sampling equipment and procedure.

4 RESULTS

The results presented in Table 1 represent the mass values, m , with their corresponding expanded uncertainty values, U , for chloride, nitrate and sulphate ions, in the aerosols water soluble extract, obtained from the respective concentrations values assessed by ion chromatography according to the procedure described previously, in section 2.

Table 1. Results of mass of chloride, Cl^- , nitrate, NO_3^- and sulphate, SO_4^{2-} , ions and the corresponding expanded uncertainty values for filters placed in the various selected filter holder positions. Results of the equivalent positions (Eq. or Dif.) for Set A: 1-6, Set B: 4-6 and Set C: 4-5.

	$m\text{Cl}^- \pm U$	$m\text{NO}_3^- \pm U$	$m\text{SO}_4^{2-} \pm U$	
Set A	1	0.017 ± 0.0046	0.0044 ± 0.0024	0.0024 ± 0.0012
	2	0.016 ± 0.0041	0.0042 ± 0.0019	0.0020 ± 0.00093
	3	0.019 ± 0.0049	0.0060 ± 0.0026	0.0036 ± 0.0013
	4	0.018 ± 0.0048	0.0051 ± 0.0025	0.0029 ± 0.0012
	5	0.018 ± 0.0044	0.0050 ± 0.0020	0.0031 ± 0.00098
	6	0.019 ± 0.0048	0.0058 ± 0.0021	0.0033 ± 0.0010
Set B	4	0.017 ± 0.0061	0.0049 ± 0.0025	0.0060 ± 0.0015
	5	0.018 ± 0.0062	0.0034 ± 0.0023	0.0058 ± 0.0015
Set C	4	0.019 ± 0.0051	0.0073 ± 0.0033	0.015 ± 0.0029
	5	0.019 ± 0.0052	0.0094 ± 0.0036	0.015 ± 0.0029

The observation of the condition stated in eq.2 determines the equivalence of the sampling positions hence the compatibility of measurement results. Table 2 shows the outcome of the results of the comparison of the different positions of the filter holders in the tested manifold.

Table 2. Results of the equivalent positions (Eq. or Dif.) for Set A: 1-6, Set B: 4-6 and Set C: 4-5.

Samplers	Equivalence of positions					
	1	2	3	4	5	6
1						
2	Eq.					
3	Eq.	Dif				
4	Eq.	Eq.	Eq.			
5	Eq.	Eq.	Eq.	Eq.		
6	Eq.	Eq.	Eq.	Eq.	Eq.	

4						
5				Eq.		
6				Eq.	Eq.	

4						
5				Eq.		

Results show systematic compatibility. One single exception, for sulphate, in positions 2 and 3 of Set A, due to non-investigated reasons, was considered of negligible significance.

5 CONCLUSIONS

Comparison and validation of aerosol sampling in equivalent portions was performed in different days with filter holders in different positions of a six channels manifold. Results do not show evidence of significant difference introduced by eventual variation of the hydrodynamic conditions present in the differently positioned channels. The systematic compatibility observed for the mass results of the analysed specific anions led to conclude on the equivalence of fractions for the different filters holders positions. This validates the possibility of using the presented multichannel sampling system for multiple parallel sampling with uncertainty of acceptable magnitude, therefore enabling increased sampling efficiency, without loss of quality. With this system simultaneous sampling can be done in order to carry out replicate analysis of single events as well as multi-parameter studies.

ACKNOWLEDGMENT

The authors thank Fundação para a Ciência e Tecnologia for financial support. A. A. Fachado thanks University of A Coruña for his Erasmus Praticas grant and P. Bigus thanks Gdansk University of Technology for her Erasmus grant.

REFERENCES

- [1] Seinfeld, J. H., Pandis, N. Spyros. "Atmospheric Chemistry and Physics From Air pollution to climate Change". Wiley-Interscience Publication, USA, pp. 100,1998.
- [2] Directive 2008/50/EC on ambient air quality and cleaner air for Europe.
- [3] Vincent J. H. (). Aerosol Sampling. Science, Standards, Instrumentation and Applications. John Wiley & Sons, USA, pp.298-299 and 9-12, 2007.
- [4] Lopez-Ruiz B. "Advances in the determination of inorganic anions by ion chromatography" *Journal of Chromatography A*, 881, 607-627, 2000.
- [5] Mouli P. Ch., S. V. Mohan and S. J. Reddy, "The study on major inorganic ion composition of atmospheric aerosols at Tirupati", *Journal of Hazardous Materials B*, 96, 217-228, 2003.
- [6] Silva R. J. N., A. Arias, C. M. R. R. Oliveira, M. F. G. F. C. Camões, "Assessment of the determination of water-soluble ionic composition of atmospheric aerosols from the analysis of crossed halves of filters", *Accred Qual Assur*, 17, 147-157, 2012.
- [7] Silva R. J. N., M. F. Camões, "The Quality of Standards in Least Squares Calibrations", *Analytical Letters*, 43, 1257-1266, 2010.
- [8] Eurachem, CITAC, "Quantifying uncertainty in analytical measurement", 3rd ed., Eurachem. <http://www.eurachem.org>, 2012.
- [9] JCGM, "Evaluation of measurement data—guide to the expression of uncertainty in measurement (GUM)", JCGM 100, BIPM. /www.bipm.org, 2008.
- [10] JCGM, "International vocabulary of metrology—basic and general concepts and associated terms (VIM)". JCGM 200, Joint Committee for Guides in Metrology, BIPM, 2012. http://www.bipm.org/utis/common/documents/jcgm/JCGM_200_2012.pdf

AMISOC 2012: Comparison of Aerosol Size Distribution with Airborne and Ground Based Instrumentation

N. Seoane-Vieira¹, J. Andrey², M. Sorribas³, A. Corrales-Sierra⁴, R. González-Armengod¹, M. Gil-Ojeda², B. de la Morena⁵, B. Marqués⁴

Abstract — During May and June 2012 AMISOC campaign was carried out. Ground based and onboard instruments were used for the study and characterization of the atmosphere particle size distribution under conditions of Saharan dust intrusion in the south of the Iberian Peninsula. This work shows the comparison of size distribution measurements with two different instruments (CAPS probe on-board INTA C212 aircraft and ground based APS from “El Arenosillo” Atmospheric Sounding Station ARN) at low altitude. The results show a good agreement between both instruments for particle size distribution between 0.8 and 10 μm .

Keywords — Aerosols, Airborne measurements, Optical Particle Counter. Saharan dust

1 INTRODUCTION

The Saharan dust intrusion over the Iberian Peninsula as primary source of atmospheric aerosols is well known, but there is not much information on the vertical profiles of the particle size distribution by airborne instrumentation. This work aims to contribute to the improvement of its knowledge, as well as to compare surface and airborne measurements. The representativeness of surface measurements will be also analyzed.

This work describes the aerosol size distribution of the atmosphere during the AMISOC (Atmospheric Minor Species relevant to the Ozone Chemistry at both sides of the jet) campaign [1], which was carried out in May and June 2012. AMISOC is a R&D project supported by “Plan Español de I+D+I” (Spanish R&D programme of the Ministry for Research and Innovation - MINECO) devoted to the research of the minor atmospheric components that play a role on the atmospheric chemistry. These components are studied under aerosol intrusions in different places (Huelva and Canary Islands).

This campaign combined remote sensing, ground based, and airborne instrumentation to measure aerosols in the presence and absence of Saharan dust

outbreaks.

Measurements were made in the South-West of Spain at “El Arenosillo” Atmospheric Sounding Station (ARN) (37.1N, 6.7W in Huelva). Selected dates for the campaign were chosen by using an atmospheric dust alert system based on different dust forecast models (DREAM, NAAPS, and SKIRON). 31 May and 1 June 2012 were representative of Saharan dust intrusion while 13 June 2012 was representative of non-dusty conditions.

2 METHODS

The characterization of the vertical profiles at “El Arenosillo” Atmospheric Sounding Station (ARN) (37.1N, 6.7W in Huelva) of several atmospheric parameters was done by using a CAPS (Cloud, Aerosol and Precipitation Spectrometer) atmospheric probe (Droplet Measurements Technology (DMT), Boulder, CO).

Additionally, dry ambient sub-micron size distribution within (0.542-10) μm size ranges was monitored by an Aerodynamic Particle Sizer (APS) (TSI Mod. 3321) at surface level.

2.1 CAPS Probe (CAS)

The three DMT instruments included in the CAPS are: the Cloud Imaging Probe (CIP), the Cloud and Aerosol Spectrometer (CAS) and the Hotwire Liquid Water Content Sensor (Hotwire LWC).

The CAPS probe measures temperature, pressure, relative humidity, liquid water content, aircraft velocity and altitude, aerosol particle and cloud hydrometeor size distributions and other miscellaneous data (see Table 1). The CAPS is an acknowledged instrument for cloud and aerosol study [2, 3].

1. Laboratorio de Teledividida e Instrumentación, Área de Ensayos en Vuelo y Armamento (AEVA), Instituto Nacional de Técnica Aeroespacial (INTA), 28850 Torrejón de Ardoz, Madrid, Spain nevesseoane@gmail.com

2. Área de Investigación e Instrumentación Atmosférica (AIIA), INTA, 28850 Torrejón de Ardoz, Madrid, Spain

3. Andalusian Center for Environmental Research, University of Granada, 18006 Granada, Spain

4. Plataformas Aéreas de Investigación (PAI), Subdirección General de Experimentación y Certificación, INTA, 28850 Torrejón de Ardoz, Madrid, Spain

5. Estación de Sondeos Atmosféricos El Arenosillo, INTA 21130 Mazagón - Moguer, Huelva, Spain

Table 1. Specifications CAS probe [4].

Specifications	CAS
Technique:	Forward and Back Scatter Light Sensors, dual back measurement with S and P polarization of the scattered light.
Measured particle Size Range:	0.51 μm to 50 μm
Sample Area	1.1 mm x 120 μm
Upper Concentration Range:	Greater than particles/cm ³ after corrections for coincidence that are about 25% at 800 and 30% at 1,000 particles/cm ³
Air Speed Range:	10-200 m/sec
Number of Size Bins:	30
Laser:	658 nm, ~50 mW
Calibration Verification:	Precision glass beads and latex spheres for sub-micron range
Non-absorbing Refractive Index:	1.3 – 1.7
Light Collection Angles:	4° - 12°, 168°-176°
Auxiliary Parameters:	Ambient Temperature, Relative Humidity, Static Pressure, Dynamic Pressure (CIP)
Data System Interface and Software	System data: RS-232 or RS-422, 56.6 kb/sec Baud Rate. PADS software
Weight:	45 lbs./20.4 kg
Power Requirements	28 VDC: 10A for probe system, and 45A for anti-ice heaters.
Environmental Operating Conditions	Temperature: -40°C to +40°C, RH: 0-100%, Altitude: 0-50,000 ft

In this work the measurements of the CAS probe (Cloud and Aerosol Spectrometer) were used an Optical particle Counter (OPC) ranging particles from 0.5-50 μm (Specifications in Table 1). The CAS, which measures smaller particles, relies on light-scattering rather than on imaging techniques. Particles scatter light from a laser, and collecting optics guide the light scattered from 4° to 12° into a forward-sizing photodetector. This light is measured and used to infer particle size.

Backscatter optics also measure light in the 168° to 176° range, which allows determination of the real component of a particle refractive index for

spherical particles (Table 1). This probe was installed on the Spanish National Aerospace Technique Institute (INTA) CASA C-212 atmospheric research aircraft. The sample collection was made during the ascendant profiles of the C-212 aircraft.

2.2 CASA C212 SN 301 Aircraft

INTA acquired this aircraft to operate its own infrastructure for aerial research in 1994. This aircraft was manufactured and modified for its adaptation as Aerial Platform for Research by EADS-CASA. It is an instrumented aircraft for environmental research, equipped with a FTI installation, pods under the wings for probe installation (Droplet Measurement technologies probes) and a modification in the fuselage for synthetic aperture radar. Is a turboprop-powered STOL medium transport aircraft; designed and built in Spain for civil and military use. It is a non-pressurized aircraft (oxygen is required when 4000 m (13000 ft) of altitude is exceeded). Its reliable, robust and simple design makes these platforms one of the most suitable as a scientific aircraft for research.

Table 2. Specifications C212 NS 301 aircraft.

Specifications	C212 NS 301
MTOW:	7700 kg
MPL:	2800 kg
Range:	Max. Payload: 408 km Max. Fuel: 1760 km
Endurance:	Max. Payload: 1h Max. Fuel: 4h 10'
Speed:	Maximum operation speed: 370 Km/h (200 KIAS) Stall speed: 158 Km/h (85 KCAS)
Take off and landing distances:	Take off: 630 m Landing: 505 m
Service ceiling:	7620 m (25000 ft)
Length:	15.20 m
Tail height:	6.30 m
Wingspan:	19.00 m
Main cabin height:	1.80 m
Main cabin length:	6.50 m
Scientific cabin	Multiple emergency exits, 400 A generators, Rails for racks and instrumentation installation, Battery starting (access to remote areas), rear ramp door.

2.3 APS

The ‘El Arenosillo’ Atmospheric Sounding Station (37°N 6.7W) (INTA), is a multi-instrumented site station for the study of the atmosphere. It is located in the coast of Huelva (near to the Doñana National Park). In this sampling site marine, continental and desert atmospheric aerosols are often detected.

Aerodynamic Particle Sizer (APS) (TSI Mod. 3321) is an instrument capable of measuring dry ambient sub-micron size distribution within (0.542-1) μm and super-micron size distribution within (1-10) μm . It is a time-of-flight spectrometer measuring the particle velocity in an accelerating air flow through a nozzle and using the relation between the particle velocity and the aerodynamic diameter (D_a) to evaluate the particle size distribution. Dataset was corrected for Stokes correction and for losses caused by the sampling system.

2.4 Aircraft Measurements

Atmospheric profiles, with and without Saharan dust, were characterized by their particle number concentrations.

Data were collected with the ground and the on-board instrumentation at the same time.

The profile measurements were done during ascending and descending spirals (but our results are based on the ascending data because the descending data were influenced by operative aircraft issues).

The spirals were carried out from an altitude of 300 to 6500 (1000 – 21300 ft).

Out of this spirals data from a single altitude 1200 m were chosen for the comparison. This altitude gave stable measurements and is fairly low to allow the comparison with the ground measurements.

3 RESULTS AND DISCUSSION

In the work presented here, the focus was set on the comparison of measurements made on May 31 2012, which is a clear example of Saharan dust intrusion as seen below.

The synoptic situation on 31 May was governed by the existence of the Azores anticyclone (in this case is centered in the North of Iberian Peninsula over the Atlantic Ocean), which induces dry, sunny and hot weather in the Iberian Peninsula and its influence arrives to the North of Morocco. This situation favors the flow of air masses from the Sahara desert into the Peninsula with the typical pattern of atmospheric Saharan dust intrusion. At ground level there was no evidence of Saharan dust, with a low-pressure system centered in the west of the UK. This situation promotes cloud at medium and high altitudes, as seen on AEMET’s map of this location (ESAT, Huelva, Spain) (Fig. 1).

The air-mass backward-trajectories from the HYSPLIT model indicated the entry of Saharan dust

at 1500 and 3000 m asl, promoted by the high-pressure system at these heights over the North of Morocco (Fig. 2).

Although vertical profiles have been taken up to an altitude of 21,500 ft with the CAPS probe, values are represented only at surface level since the ground instrumentation, in this case the APS.

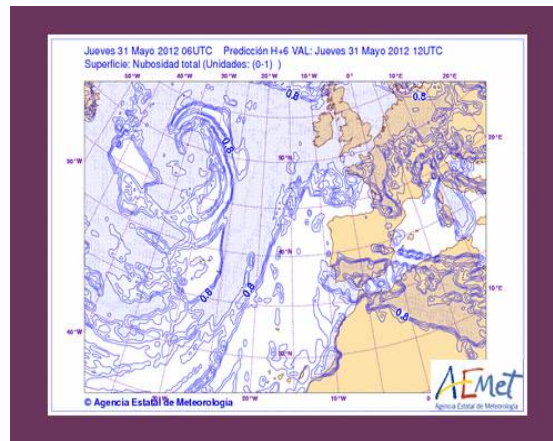


Fig. 1. AEMET’s cloud forecast for 31 May 2012 (www.aemet.es).

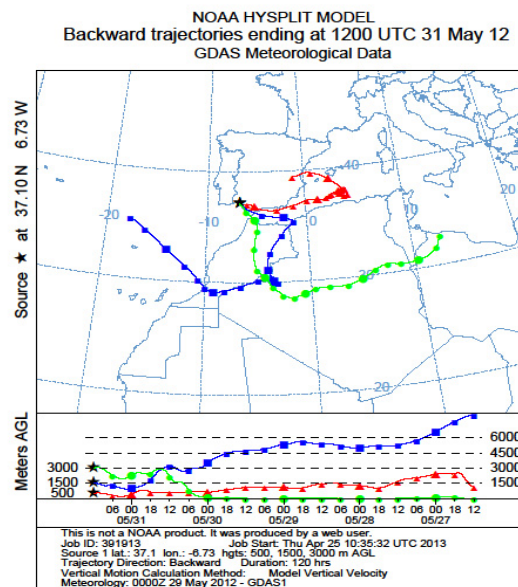


Fig. 2. Air mass backward trajectories for 31 May 2012 from the HYSPLIT model (generated by NOAA Air Resources Laboratory <http://ready.arl.noaa.gov/>).

Fig. 3 shows the comparison of simultaneous ground and airborne based measurements (taken at lower height levels), showing a good agreement for a particle size between 0.8 and 10 μm , on the dust intrusion days. It is noteworthy to see (on Fig.3) that for particle size between 0.5 and 0.7 μm the results cease to agree. It can be due to a decrease of the counting efficiency for APS within this size range or because the CAPS probe being very close to its size detection limit (were noise is more important) or due to differences on the particle size distributions with

height for this very low size particle aerosol (the airborne measurements were made at 1200 m asl).

The agreement between instruments was not so good on the no-intrusion days (figure not shown) because the standard deviation of the data was greater (noisy measurements due to the low number of particles present)

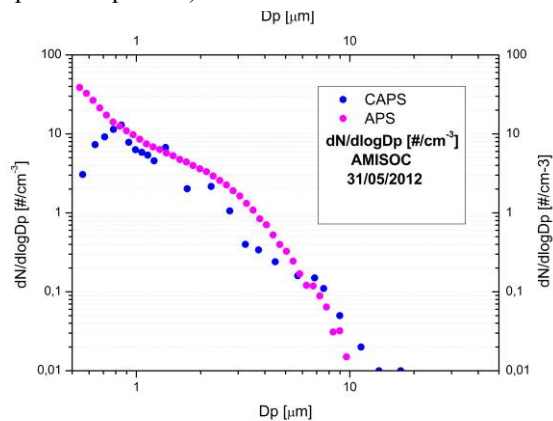


Fig. 3. Particle number size distribution during the AMISOC campaign (dust conditions). This graph shows measurements of CAPS probe and APS

Fig. 3 also shows that the measurements made with the CAPS probe are noisier showing evidence of the difficulties of airborne measurements.

The Saharan dust intrusion analyzed in this work took place in the presence of clouds. This cloud condition allows the investigation of the interactions between cloud droplets and Saharan dust aerosol that will be the topic of a future work.

4 CONCLUSIONS

The AMISOC campaign studies the minor atmospheric components under the presence of Saharan dust intrusions. On this work we compared aerosol particle size distributions between two instruments. One ground based (APS) and another on-board INTA's C212 aircraft (CAPS-CAS probe). This comparison shows a good agreement for particles between 0.8 and 10 μm . A slight disagreement is also seen for particles between 0.5 and 0.7 μm probably due to a decrease of the counting efficiency for APS within this size range or because it is close to the CAPS resolution limit (0.5 μm). Future works will focus on the study of the interactions between cloud droplets and Saharan dust aerosols.

ACKNOWLEDGMENT

This work is supported by the Spanish Ministry for Research and Innovation (MINECO) under grant CGL2011-24891 (project AMISOC) and the Andalusian Regional Government through TASTESOS project (P10-RNM-6299). The authors

of this study are grateful to the CLAEX unit of the Spanish Air Force for operating the C-212. The work of Luis Otero (C212's security and logistics from PAI) is gratefully acknowledged. Jafar Tabrizi and Fernando Lahoz and the rest of the staff of the Laboratorio de Telemetría e Instrumentación (AEVA) are also acknowledged for their technical and personal support.

REFERENCES

- [1] Puentedura, O et al., 2012. "AMISOC 2012: Multi-instrument campaign for assessment of trace gas-aerosol interaction," European Aerosol Conference, Granada, Spain.
- [2] Baumgardner, D., H. Jonsson, W. Dawson, D. O'Connor and R. Newton. "The cloud, aerosol and precipitation spectrometer (CAPS): A new instrument for cloud investigations," *Atmos. Res.* 2001: 59-60, 251-264
- [3] Padmakumari B, Maheskumar RS, Morwal SB, Harikishan G. Konwar M, Kulkarni JR, Goswami BN. 2012. "Aircraft observations of elevated pollution layers near the foothills of the Himalayas during CAIPEEX-2009." *Q. J. R. Meteorol. Soc.* DOI:10.1002/qj.1989
- [4] Droplet Measurements Technologies, Inc. "Cloud Aerosol and Precipitation Spectrometer (CAPS) Operator Manual (DOC-0066 Revision F)," Boulder (CO) 2011.

Aerosol optical properties at “El Montsec”, a continental background site in the northeastern Spain

Yolanda Sola¹, Jerónimo Lorente²

Abstract — Ground-based measurements of aerosol properties play an important role in the validation of satellite retrievals. During the last years the networks of photometers have grown in number and locations. Additionally, background remote stations are useful to study aerosol mechanism formation. This work is focused on the analysis of aerosol optical properties, such as the aerosol optical depth (AOD) and the Ångström exponent, at El Montsec, a background continental site located in the northwestern of the Mediterranean Basin at 1574 m a.s.l. Measurements were performed during one year with an AERONET photometer. The AOD at 440 nm shows a seasonal pattern with lower values in winter than in summer months, thus the mean annual average is 0.09 (typical of background stations). The Ångström exponent is also characterized as background continental sites (1.21) although the frequency distribution has a bimodal pattern with a principal peak at 1.5, mixture of aerosols, and a second one at 0.3, related to African air masses. According to the frequency distribution, 30% of the cases are below 1.0 and an appreciable 10% below 0.4. Cases greater than 1.2 represent 60% of the total.

Keywords — aerosol optical depth; Ångström exponent; remote background station; AERONET Cimel

1 INTRODUCTION

The aerosol radiative forcing is one of the main uncertainties in the climate change assessments [1]. Just as it is quite well known the impact of greenhouse gases on global warming, the role of atmospheric aerosols is still under research. The future predictions of the climate response to aerosol forcing are mainly based on models that nowadays are subject to large uncertainties in some topics, needing more realistic interpretations of the aerosol effects on climate [2]. One of the main uncertainties is the aerosol distribution, both spatially and temporally, and sources such as dust, biomass burning, and sea salts. For this reason, during the last decades the number of measurement has increased including both satellite and ground-based instruments. Each technique results in different complementary approaches of the aerosol characterization, so the satellite-based retrievals give great spatial coverage although limited by the horizontal and temporal resolution and ground-based measurements complement with larger temporal resolution but less global representation.

The aerosol optical and physical properties can be monitored with different in-situ instruments, although in the last years international networks of photometers have developed and extended

worldwide, such as AERONET [3] and SKYNET [4]. These networks keep a series of standards and calibrations protocols to ensure the quality of the measurements.

Remote background stations are located far away from urban and industrial areas, sources of anthropogenic aerosols. These stations are important to study aerosol mechanism formation and to validate aerosol properties and air quality monitoring from satellite measurements [5],[6].

The objective of this work is the characterization of aerosol optical depth (AOD) and Ångström exponent at “El Montsec”, a background remote station in the northeastern of Spain. The results are focused on the first one year of continuous measurements in the station where chemical and granulometric aerosols retrievals are also performed from 2009 [7].

2 DATA

The station of El Montsec is located in the pre-Pyrenees Mountains (42° 3' 5.10" N, 0° 43' 46.88" E) at 1574 m a.s.l. The distance from urban areas and the low influence from anthropogenic emissions define the station as a continental background site. Moreover, its altitude with lower surrounding mountains and free-horizon is an advantage for remote-sensing instruments.

The station of El Montsec is a complete station with optical and granulometric measurements. In November 2009, the Institute of Environmental Assessment and Water Research (IDAEA-CSIC) set up different monitoring instruments (particle counter, absorption photometer, high-volume sampler) and started

1. Yolanda Sola is with the Department of Astronomy and Meteorology, University of Barcelona. Martí i Franquès 1, E-08028 Barcelona, Spain. E-mail: ysola@am.ub.es

2. Jerónimo Lorente is with the Department of Astronomy and Meteorology, University of Barcelona. Martí i Franquès 1, E-08028 Barcelona, Spain. E-mail: jeroni@am.ub.es

measuring real time concentrations of PM₁₀, PM_{2.5}, PM₁, Black Carbon (BC) and particle number (N). The PM₁₀ samples are also used to derive complete chemical characterization. The instruments for granulometric retrievals are described by [7], [8].

In 2011 the station was complemented with a sun photometer Cimel CE-318, the standard instrument of AERONET network and property of the University of Barcelona. Since the first installation, two instruments have been operating, Cimel #416 to 8 March 2012 and then it was replaced by Cimel #411. The instrument #416 has seven channels for aerosol measurements at 340, 380, 440, 500, 675, 870 and 1020 nm and another additional at 935 nm for water vapor retrievals. The instrument #411 has an additional filter at 1640 nm. Both belong to the Red Ibérica de Medida de Aerosoles (RIMA), federated with AERONET and were calibrated by the Atmospheric Optics Group of the University of Valladolid (GOA-UVA).

All the instruments are located on the roof of a measurement unit of the network for monitoring and forecast pollution of Catalonia that is equipped with different gas analyzers (SO₂, NO_x and O₃). Additionally, at the same place the Meteorological Service of Catalonia has an automatic meteorological station with real-time measurements of temperature, humidity, and solar radiation and wind components.

According to previous studies [8], the most frequent air masses are from Atlantic advection (65% of occurrence) that it is also the dominant air mass in the Iberian Peninsula [9] [10]. That class is followed by air masses from North Africa, Europe and regional conditions influenced by Mediterranean area. European air masses are more frequent in winter and, on the other hand, African episodes are more common in summer months when higher PM levels are usually also measured because the station is inside the atmospheric mixing layer.

The aerosol optical properties used in this work are based on AERONET level 1.5 AOD data, that are automatically cloud cleared but without a final calibration. The period spans from March 2012 to April 2013 when the Cimel #411 has been routinely operative. Level 2.0 AOD data is still unavailable for this period in the AERONET database because the post field calibration has not been performed to the instrument yet. The AERONET cloud screening is described in [11].

The AERONET algorithm to retrieve the AOD is based on the Beer-Bouguer law and uses the cloud-screened direct sun measurements. It requires a good quality calibration to derive the AOD. The absolute error for AOD retrieval with the sun photometer is 0.01-0.02 [3]. From the spectral AOD, the Ångström exponent is also derived. There are different possibilities of spectral ranges used to determine the exponent but in this work we use the interval 440-870 nm, including four wavelengths. Its value is used to characterize the aerosol size, the lower the value the larger the particles. According to Toledano et al. [12],

incorrect AOD determination introduces large errors in the exponent and it is strongly dependent on the absolute value of the AOD, the lower the AOD the greater the error in the Ångström exponent.

3 RESULTS

The analysis of the temporal evolution of AOD (see Fig. 1 for channel 440 nm) shows a clear seasonal cycle with lower values in winter and larger ones in summer months. Moreover, AOD has more variability than in winter when the mean values are around 0.1; on the other hand, high turbidity events with values ranging from 0.3 to 0.5 are more frequent in summer. There are a few number of episodes with AOD larger than 0.6 and in this case, the most extreme concentrations are detected in late winter and early spring.

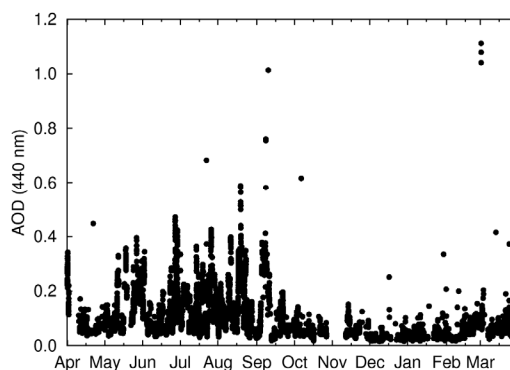


Fig. 1. Time variation of AOD (440 nm) at El Montsec over a year (from April to March)

The low AOD values are characteristic of continental background areas since they are not affected significantly by local anthropogenic pollution [13]. Similar AOD values have been detected in other stations [14],[15],[16]. The granulometric analysis at the station is in agreement with these results, showing an increase of the PM concentration during summer due to recirculation processes and mountain breezes that cause the accumulation of regional particles [8].

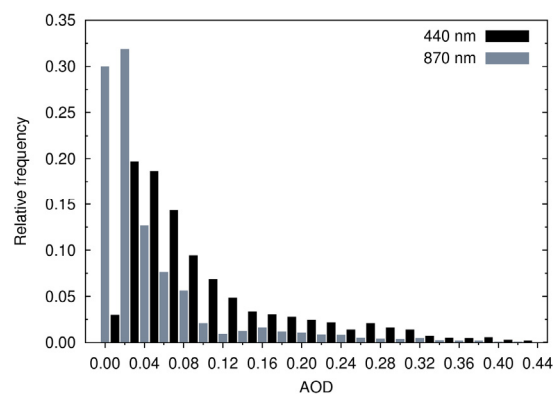


Fig. 2. Relative frequency distribution of AOD at 440 nm and 870 nm during one year

Fig. 2 shows the distribution of relative frequencies of the AOD for two wavelengths (440 and 870 nm). The distribution at 870 nm is narrower and peaks at lower AOD than the distribution at 440 nm. Moreover, 88% of the values are below 0.1 at 870 nm and 65% at 440 nm. The tail of the distribution spans up to 0.44 for channel 440 nm, with 9% of the values larger than 0.25. On the other hand, at 870 nm only the 3% of the measurements are above 0.25.

Table 1. Monthly mean averages of AOD at 870 and 440 nm and Ångström exponent (α). Last row shows the annual averages. Minimum and maximum values are in brackets

	AOD (870 nm)	AOD (440 nm)	α (440–870)
Jan	0.02 (0.005-0.36)	0.03 (0.02-0.33)	1.21 (0.001-2.2)
Feb	0.03 (0.004-1.77)	0.06 (0.02-1.50)	1.40 (0.01-2.5)
Mar	0.06 (0.02-1.27)	0.08 (0.02-1.20)	0.77 (0.03-1.7)
Apr	0.04 (0.01-0.44)	0.11 (0.04-0.45)	1.34 (0.03-2.1)
May	0.06 (0.01-0.27)	0.14 (0.04-0.40)	1.32 (0.3-1.8)
Jun	0.08 (0.009-0.43)	0.13 (0.03-0.47)	1.18 (0.1-2.1)
Jul	0.06 (0.01-0.70)	0.14 (0.03-0.68)	1.44 (0.08-2.1)
Aug	0.10 (0.009-0.44)	0.15 (0.03-0.59)	0.93 (0.2-1.8)
Sep	0.05 (0.005-0.90)	0.12 (0.02-1.01)	1.43 (0.1-2.0)
Oct	0.03 (0.006-0.67)	0.06 (0.02-0.62)	1.13 (0.1-1.9)
Nov	0.03 (0.008-0.11)	0.06 (0.02-0.15)	0.84 (0.05-1.7)
Dec	0.01 (0.003-0.28)	0.03 (0.02-0.25)	1.58 (0.05-2.4)
Annual	0.05	0.09	1.21

Table 1 summarizes the annual variation of the monthly means for AOD and Ångström exponent. The AOD at 440 nm shows its lowest values in

winter and the largest ones in summer with a maximum in August (0.15). In winter, AOD remains below 0.06 (0.03 at 870 nm). The location of the site above the boundary layer [8] and a major number of rain episodes during winter are the responsible of these detected low values. On the other hand, high turbidity episodes in summer are related to drier days and more Saharan dust events.

The most pristine days has background values as low as 0.02 and are detected throughout the year. At 870 nm, values are even smaller, up to 0.004 in February, although in spring the differences with AOD at 440 nm are smaller.

Table 1 also shows the high variability at each month. It is especially interesting the maximum values detected in winter month when the background AOD is low. For example, in February the AOD ranges from 0.02 to 1.50. Although the African dust events are more common in summer, some authors have reported its importance in February and March [12].

The Ångström exponent has a strong variability with values up to 2.5 in some cases (Fig. 3). In a very few cases, negative values are detected but they are related with cloud contamination [12]. The highest variability is detected in winter months when the largest Ångström exponents, consequently small particles, were detected. This fact coincides with low AOD period. During summer the most frequent value is around 1.5 due to mixed aerosols when the station is inside the mixed boundary layer.

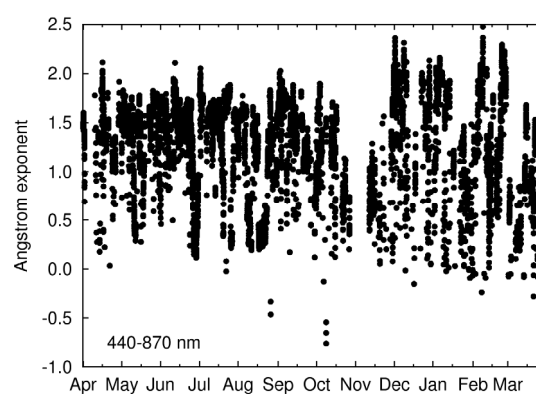


Fig. 3. Temporal evolution of the Ångström exponent during one year of cloud-screened measurements at El Montsec station

The relative frequency (Fig. 4) shows a bimodal distribution with a principal peak around 1.5 and a second one at 0.3. The annual mean average of 1.21 (Table 1) is typical of background continental sites and it has been also reported by other authors [16], nevertheless it masks the two frequency modes detected analyzing individual observations. The second mode of 0.3 is, on the other hand, related to Saharan dust events that are characterized by high AOD and low Ångström exponent. According to the frequency distribution, 30% of the cases are below 1.0

and an appreciable 10% below 0.4. Cases greater than 1.2 are 60% of the total.

According to Ripoll et al. [8], 12% of the days are dominated by North African air masses with high levels of big size particles with high proportion of mineral matter and sulphate. On the contrary, 65% of the days have Atlantic influence.

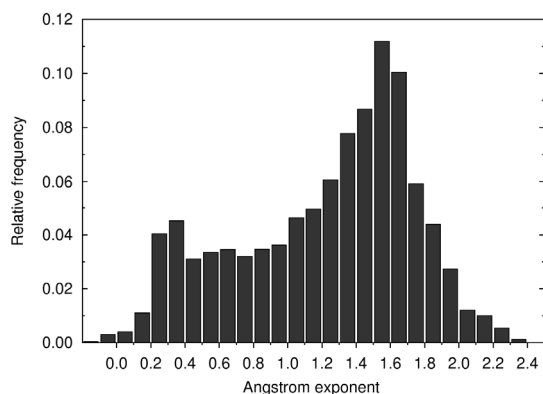


Fig. 4. Relative frequency of Ångstrom exponent during one year of cloud-screened measurements at “El Montsec” station

4 CONCLUSIONS

In this work we have presented preliminary results in the characterization of the aerosol optical properties at “El Montsec” station, located at 1540 m a.s.l. in the northeastern Spain. A first year of measurements with an AERONET photometer from April 2012 to March 2013 shows an AOD at 440 nm of 0.09 and an Ångstrom exponent of 1.21, both typical of background continental sites, as it was reported in other places by other authors [14],[16]. Both variables have high seasonal variability. The lowest AOD values are detected in winter months when the site is commonly above the boundary layer; on the other hand, larger values derived in summer are related to intrusion of air masses from North Africa, regional air masses and the site inside the mixed layer. A deep insight in the relative frequency of the Ångstrom exponents shows a bimodal distribution with principal mode at 1.5, related to mixed small aerosols, and a second peak at 0.3 describing big size aerosols from Saharan air masses.

The wide variety of measurements at “El Montsec” station, from granulometric and chemical to optical and physical data, opens new possibilities of analyses. These preliminary results show the general characteristics of optical properties but it is necessary a deeper analysis of the values related to each air mass, as well as the absorption/scattering properties of the aerosols.

ACKNOWLEDGMENT

This work was funded by the Spanish Ministry of Economy and Competitiveness under the project CGL2012-38945.

The authors thank the Group of Atmospheric Optics, Valladolid University, for the provision of the CÆLIS tool (www.caelis.uva.es) used in this publication. We thank the AERONET, PHOTONS and RIMA staff for their support. The research leading to these results has received funding from the European Union Seventh Framework Programme (FP7/2007-2013) under grant agreement Nr. 262254 [ACTRIS].

REFERENCES

- [1] IPCC, “Climate change 2007: The physical science basis”. Contribution of Working Group, S. Solomon, D. Qin, M. Manning, Z. Chen, M. Marquis, K.B. Averyt, M. Tignor, and H.L. Miller (eds.), Cambridge University Press, Cambridge, UK and New York, USA, 996 pp., 2007.
- [2] S. Menon, “Current uncertainties in assessing aerosol effects on climate,” *Rev. Environ. Res.*, vol. 29, pp. 1-30, doi:10.1146/annurev.energy.29.063003.132549, 2004.
- [3] B.N. Holben, T.F. Eck, I. Slutsker, D. Tanré, J.P. Buis, A. Setzer, E.F. Vermote, J.A. Reagan, Y.J. Kaufman, T. Nakajima, F. Lavenue, I. Jankowiak, and A. Smirnov, “AERONET – A federated instrument network and data archive for aerosol characterization,” *Remote Sensing Environ.*, vol. 66, pp. 1-16, 1998.
- [4] T. Takamura, and T. Nakajima, and SKYNET community group, “Overview of SKYNET and its activities,” *Optica Pura y Aplicada*, vol. 37, pp. 3303-3303, 2004.
- [5] W. Di Nicolantonio, A. Cacciari, and C. Tomasi, “Particulate matter at surface: Northern Italy monitoring based on satellite remote sensing, meteorological fields, and in-situ samplings,” *IEEE J. Sel. Top. Appl. Earth Obs. Rem. Sens.*, vol. 2, pp. 284-292, 2009.
- [6] W. Di Nicolantonio, A. Cacciari, A. Petritoli, C. Carnevale, E. Pisoni, M.L. Volta, P. Stocchi, G. Curci, E. Bolzacchini, L. Ferrero, C. Ananasso, and C. Tomasi, “MODIS and OMI satellite observations supporting air quality monitoring,” *Radiat. Prot. Dosimetry*, vol. 137, pp. 280-287, doi:10.1093/rpd/ncp231, 2000.
- [7] A. Ripoll, J. Pey, A. Alastuey, M. Pandolfi, N. Pérez, M. Cusack, and X. Querol, “Atmospheric PM episodes affecting a continental background site in the Western Mediterranean Basin,” *Proc. RECTA-2010*
- [8] A. Ripoll, J. Pey, A. Alastuey, M. Pandolfi, N. Pérez, and X. Querol, “Atmospheric PM episodes affecting a remote site (Montsec) in the Western Mediterranean Basin,” *Proc. RECTA 2011*
- [9] J.J. Capel Molina, “El clima de la Península Ibérica,” *Ariel Geografía*, Barcelona, Spain, 2000.
- [10] R. Vergaz, V.E. Cachorro, A.M. de Frutos, J.M. Vilaplana, B.A. de la Morena, “Columnar characteristics of aerosols by spectroradiometer measurements in the maritime area of Cadiz Gulf (Spain),” *Int. J. Climatol.*, vol. 25, pp. 1781-1804, 2005.
- [11] A. Smirnov, B.N. Holben, T.F. Eck, O. Dubovik, and I. Slutsker, “Cloud screening and quality control algorithms for the AERONET database,” *Remote Sensing Environ.*, vol. 73, pp. 337-349, 2000.
- [12] C. Toledano, V.E. Cachorro, A. Berjon, A.M. de Frutos, M. Sorbías, B.A. de la Morena, and P. Goloub, “Aerosol optical depth and Ångstrom exponent climatology at El Arenosillo AERONET site (Huelva, Spain),” *Q.J.R. Meteorol. Soc.*, vol. 133, pp. 795-807, doi:10.1002/qj.54, 2007.
- [13] B.N. Holben, D. Tanré, A. Smirnov, T.F. Eck, I. Slutsker, N. Abuhassan, W.W. Newcomb, J. Schafer, B. Chatenet, F. Lavenue, Y.J. Kaufman, J. Vande Castle, A. Setzer, B.

- Markham, D. Clark, R. Frouin, R. Halthore, A. Karnieli, N.T. O'Neill, C. Pietras, R.T. Pinker, K. Voss, and G. Zibordi, "An emerging ground-based aerosol climatology: Aerosol optical depth from AERONET," *J. Geophys. Res.*, vol. 106, pp. 12067-12097, 2001.
- [14] O.E. García, J.P. Díaz, F.J. Expósito, A.M. Díaz, O. Dubovik, Y. Derimian, P. Dubuisson, and J.-C. Roger, "Shortwave radiative forcing and efficiency of key aerosol types using AERONET data," *Atmos. Chem. Phys.*, vol. 12, pp. 5129-5145, doi:10.5194/acp-12-5129-2012, 2012.
- [15] S.K. Satheesh, K. Krishna Moorthy, S. Suresh Babu, and J. Srinivasan, "Unusual aerosol characteristics at Challakere in Karnataka," *Current Sci.*, vol. 104, pp. 615-621, 2013.
- [16] Y.S. Bennouna, V.E. Cachorro, B. Torres, C. Toledano, A. Berjón, A.M. de Frutos, I. Alonso Fernández Copel, "Atmospheric turbidity determined by the annual cycle of the aerosol optical depth over north-center Spain from ground (AERONET) and satellite (MODIS)," *Atmos. Env.*, vol. 67, pp. 352-364, doi:10.1016/j.atmosenv.2012.10.065, 2012.

The relations between AOD and PM_x from long-term data for north-central Spain

Yasmine S. Bennouna¹, Victoria E. Cachorro¹, M. Angeles Burgos¹, Carlos Toledano¹, Andrés Herguedas², Jaime González Orcajo² and Angel M. de Frutos¹

Abstract — This work examines the relations between columnar and surface aerosol loadings based on long records of Aerosol Optical Depth (AOD) and Particulate Matter (PM_x) parameters. The region of interest here is the north-central area of Spain, where AERONET and EMEP networks have nearby sites, Palencia and Peñausende (Zamora) respectively. The measurements of the two sites overlap for a period spanning from 2003 to 2011, presenting 1698 days of coinciding data. Based on this 10 year period, the annual cycle and interannual variability of PM₁₀ - PM_{2.5} are analysed together with those of the AOD at 440 nm. The correlation results between these parameters are also presented both for daily data and monthly averages. The annual cycle of PM_x shows a clear bimodality related to the frequency of desert dust intrusions, which does not appear in that of the AOD. However year to year variations shows that most peaks of PM_x coincide with those of the AOD, and are very variable from one year to the other. Daily data are found to be moderately correlated with a correlation coefficient of 0.56. The correlation is improved when considering the monthly means rising up to 0.70.

Keywords — Aerosol, AOD, Particulate Matter, EMEP, AERONET

1 INTRODUCTION

In the last decade, it has become clear that particulate pollution represents a serious global problem adversely affecting human health.

A common reference indicator for air quality is the concentration of particulate matter (PM) at ground level which is given in units of mass per unit volume of air. Since the toxicity of air pollution particles appears to relate most consistently with aerodynamic diameters, PM is classified according to size fraction noted PM_x. PM₁₀ refer to the mass fraction of particles with an aerodynamic diameter equal to or less than 10 µm, chosen to represent those particles that most likely reach the lower region of the respiratory tract. In the same way, PM_{2.5} is defined as particulate mass less than 2.5 µm in aerodynamic diameter.

To protect public health and environment, various national and international institutions have set limits and guide values for the concentration of various PM size fractions. In consequence, a significant effort has been dedicated to the implementation of operational and continuous monitoring networks to measure pollution associated to this type of particles. Nowadays, many European cities provide detailed air quality information on a regular basis. Some networks such as the European Monitoring and Evaluation Programme (EMEP) network have been established with the objective to study Long-Distance Atmospheric Pollution, thus providing governments with quantitative information on the transport of air pollutants across national boundaries

and resulting deposition and concentration levels. Despite all these efforts, PM observations are too scarce to resolve the large spatial and temporal variation of aerosol fields, and therefore limit the potential of environmental and health assessment for regulating impacts.

Observations of atmospheric aerosol can also be provided by remote sensing techniques, and in particular satellite imagery, which is the only tool capable to achieve full spatial coverage. Despite the fact that satellite measurements are not as accurate as in-situ ones, they represent a cost-effective method to improve the insight in PM spatial distribution and transport patterns, especially in a context of increasing availability of satellite observations. A primary parameter provided by remote sensing observations is the Aerosol Optical Depth (AOD), describing the extinction of the electromagnetic radiation in an atmospheric column attributed to aerosols at a given wavelength. Therefore, in recent years several authors have investigated the relationships between the AOD and PM_x. Some of these studies use ground-based AOD measurements, such as those of the AERONET (Aerosol Robotic Network) operational network known to provide well calibrated data often used for the validation of satellite inversion algorithms [1].

A characteristic source of aerosols from natural origin affecting Southern Europe is the dust transported from the Sahara and Sahel deserts. In particular, because of its proximity to the African continent and favourable atmospheric circulation, the area of the Iberian Peninsula is frequently affected by strong episodes of desert dust. Airmasses are advected from the Saharan desert to the Iberian Peninsula under specific synoptic conditions described in [2]. These dust outbreaks have an

1. Atmospheric Optics Group (GOA), University of Valladolid, 47014 Valladolid. Spain. Corresponding author E-mail: yasmine@goa.uva.es
2. Departamento de Control de Calidad y Cambio Climático, Consejería de Fomento y Medio Ambiente de la Junta de Castilla y León, Valladolid. Spain.

important impact on air quality, and some studies have highlighted that most PM₁₀ exceedance observed at regional background stations are associated to those events [3]. Moreover, owing to the dry climate and scarcity of precipitations, the particles accumulate in the atmosphere as removal mechanisms such as rainout or growth to even larger particles is very slow. Two different types of episode associated with mineral dust can be linked to the increase of PM concentration levels in the central area of the Iberian Peninsula: regional recirculation during summer months, and long-range transport processes spring to autumn time.

The objective of this work is to investigate in detail the relations between PM_X and AOD data at different temporal scales in the northern central region of Spain. This is done using two nearby rural regional background sites from the EMEP and AERONET networks, Peñausende and Palencia respectively. Based on a period of nearly 10 years, the annual cycle and interannual variability of PM₁₀/PM_{2.5} are examined in relation to those of the AOD at 440 nm. The correlation results between these parameters are also presented both for daily data and monthly averages.

Table 1. Yearly statistics of EMEP and AERONET data counts for the period 2003-2011 based on daily values.

Year	Ndays (PM ₁₀)	Ndays (PM _{2.5})	Ndays (AOD 440 nm)
2003	321 (88 %)	321 (88 %)	163 (45 %)
2004	334 (91 %)	334 (91 %)	271 (74 %)
2005	336 (92 %)	336 (92 %)	295 (81 %)
2006	326 (89 %)	326 (89 %)	173 (47 %)
2007	330 (90 %)	330 (90 %)	271 (74 %)
2008	315 (86 %)	315 (86 %)	266 (73 %)
2009	327 (90 %)	327 (90 %)	109 (30 %)
2010	347 (95 %)	335 (92 %)	68 (19 %)
2011	333 (91 %)	333 (91 %)	226 (62 %)
Average	329.9 (90 %)	328.6(90 %)	204.7 (56.0 %)
Total	2969 (90 %)	2957 (90 %)	1842 (56.0 %)

2 SITE AND DATA DESCRIPTION

Both cities of Peñausende (41.24N 5.90W, 985 m asl) and Palencia (41.989N, 4.516W, 750 m asl) belongs to the autonomous community of "Castilla y León" (CyL), lying on the northern plateau of Spain (Castilian Plateau). These two sites separated by about 200 km are relatively well isolated from big urban and industrial centers, Valladolid being the closest of relevant size, and can therefore be classified as rural regional background sites.

At Peñausende, PM_X measurements were performed by gravimetric methods using high volume samplers, following the standard procedures described in the

European Air Quality Directives. PM₁₀ and PM_{2.5} sampling is carried out on a daily basis (one PM₁₀ and one PM_{2.5}, 24 h sample/day). Table 1 summarizes the number of PM_X measurements available for each year back to 2003. On average for a year, data are provided about 90% of the time. It can be seen that PM_{2.5} was also continuously measured with PM₁₀, except for the year 2010, for which 12 days are missing. This leads to totals of 2969 and 2957 days for PM₁₀ and PM_{2.5} datasets respectively.

A CIMEL sunphotometer located in the town of Palencia and operating in the frame of AERONET [1], has been providing continuous aerosol measurements from 2003 to 2011 with the exception of 15 months between 2009 and 2010. The direct sun measurements of this sunphotometer were used to derive the AOD at several wavelengths. In this study the AOD at 440 nm was used. The AERONET dataset is "cloud screened" and "quality assured" (Level 2), except for a period between May 2007 and April 2007 for which Level 1.5 data are used. In addition, the latter were post-corrected for calibration errors as explained in [4], and the dataset is identical to that used in this other study [4]. It must also be recalled that in this dataset, all days presenting less than 3 available measurements had been filtered out from the time series. The corresponding AERONET data counts on a daily basis are also included in Table 1 with those of PM_X.

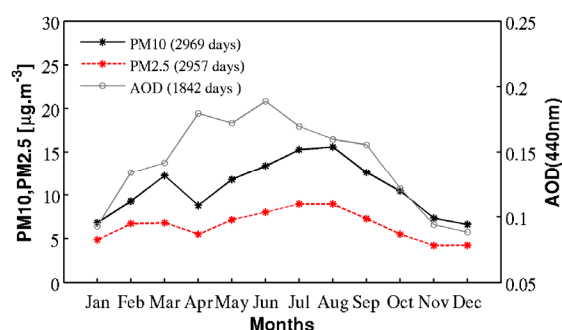


Fig. 1. Mean annual cycle of the PM₁₀, PM_{2.5} and AOD(440 nm) representative of the north-central area of the Iberian Peninsula, based on the sites of Peñausende (EMEP) and Palencia (AERONET), during the period 2003-2011.

3 RESULTS

3.1 Annual cycle

In Figure 1, the 9-year climatological annual cycle of PM₁₀ is represented with that of the AERONET AOD at 440 nm. For the AOD, the results have been taken from a previous study on AERONET data [4], and it was found that the site of Palencia is characterized by a daily AOD (440 nm) of 0.15±0.10 and an Ångström exponent (440-870 nm) of 1.29±0.35 on average. At Peñausende, PM₁₀

is $11.0 \pm 9.5 \mu\text{g}\cdot\text{m}^{-3}$ on average over the full period and $6.6 \pm 4.9 \mu\text{g}\cdot\text{m}^{-3}$ for $\text{PM}_{2.5}$. As shown on Figure 1(a) the climatological cycle of PM_{10} is characterized by high values in spring and summer, and low values in winter and fall, with two maxima in March and August of $12.2 \mu\text{g}\cdot\text{m}^{-3}$ and $15.6 \mu\text{g}\cdot\text{m}^{-3}$ respectively. The climatological curve of $\text{PM}_{2.5}$ presents the same variations and shape, with two maxima 6.8 and $9.0 \mu\text{g}\cdot\text{m}^{-3}$ occurring in the same months. This leads to a relative minimum in April of $8.8 \mu\text{g}\cdot\text{m}^{-3}$ for PM_{10} and $5.5 \mu\text{g}\cdot\text{m}^{-3}$ for $\text{PM}_{2.5}$. The bimodality reflects clearly the seasonal frequency of occurrence of mineral dust outbreaks over The Iberian Peninsula, which are frequent in summer, and generally in late-winter/early-spring. Indeed, many previous studies have already highlighted the fact that most high PM_{10} events are associated to the arrival of high-Saharan dust air masses over the Iberian Peninsula. Particularly in summer, when the mixing layer is higher, vertical mixing between the lower levels of the troposphere with high atmospheric air masses originating from North Africa is favoured. Although the summer occurrence of desert intrusions has been extensively studied, those of winter/spring are also of relevance as shown here. Besides, this behaviour can be almost extended to the entire Iberian Peninsula with a decreasing gradient from south to north.

The most obvious difference between the mean annual cycle of AOD and PM_x is precisely the presence of these two modes, instead of one for the AOD. Indeed, in spring no maximum emerges in the case of the AOD, moreover it must be noted that the variation is not well defined for the first semester of the year with a very irregular increase from to 0.09 in January to 0.16 in June. On the contrary, the decrease from summer to fall is more regular and gets steeper when the fall starts. As mentioned before, there has been a long gap of data during a period of about a year between 2009 and 2010, which could be a reason for observed shape difference. To discard this explanation, the climatological annual cycle was derived excluding year 2009 and 2010 from the datasets (not shown here), and no significant changes were observed in the results. Moreover, AERONET provides data only under cloud-free conditions, and therefore there are also some days with no available AOD data. Despite the difference in daily sampling, the climatological curves of coinciding days (1698) also lead to similar results (not shown here). However, given that available AOD data represent only 56% of the total period as compared to 90% for PM_x , it should not be completely excluded that for larger series the bimodality of the annual cycle could also be observed for the AOD. Indeed, this bimodality appears clearly when only desert dust contribution is considered as showed by [5].

Besides, the bimodality of the climatological annual cycle for the AOD has already been observed

at a site of the Iberian Peninsula, located in the south-western coast of Spain, in the area of the Gulf of Cadiz near the city of Huelva [6]. In this area of the Iberian Peninsula, mineral dust events are more frequent and stronger [7].

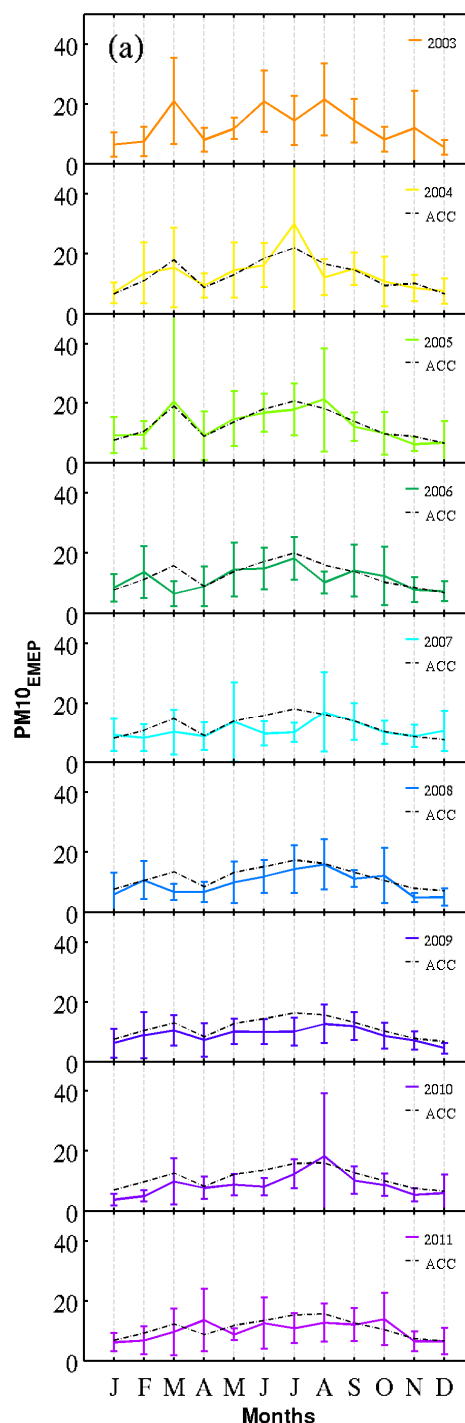


Fig. 2. Mean annual cycle of (a) PM_{10} data and (b) AOD (440 nm) [4], derived for each year (color solid line) and for cumulative multi-annual periods (black dotted line). The bars represent the standard deviation of the daily data for a given month-year. The black dotted line of the bottom graphs corresponds to the annual cycle based on the entire period 2003-2011 that is also shown on Figure 1.

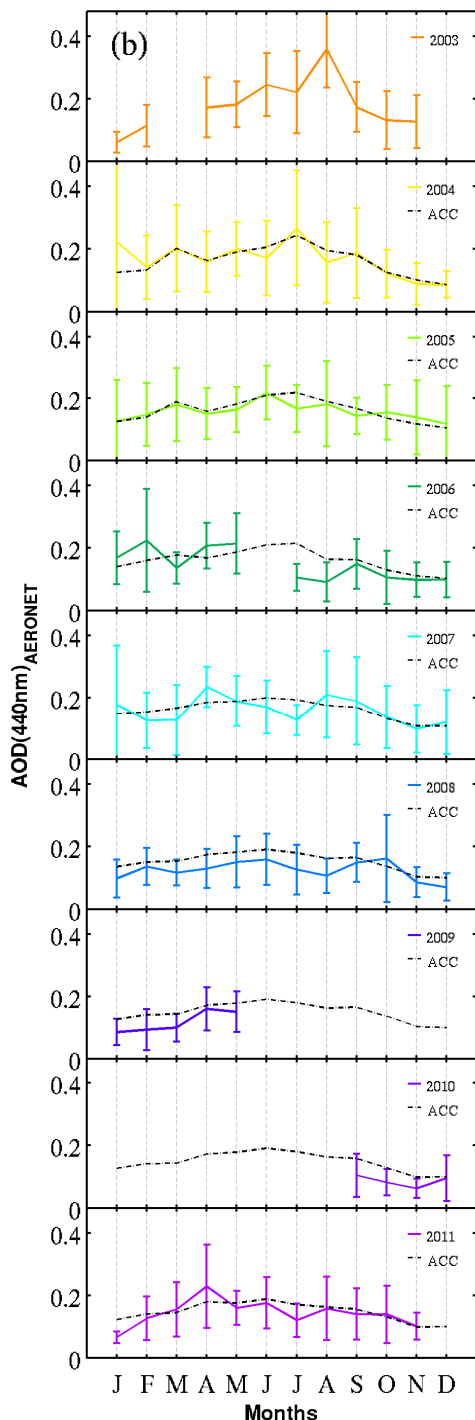


Fig. 2. Continued.

3.2 Interannual variability

In order to investigate year-to-year variations, Figure 2 presents the annual cycle of PM₁₀ and AOD for each year, together with the climatological curve as it gets built from the accumulation of the prior years. The PM₁₀ annual cycle (Figure 2(a)) for the individual years is in general similar to the mean climatological annual cycle, which indicates small

shape variations from one year to the other, making the accumulated or multi-annual values relatively stable. This can be seen from the "accumulated" curve which changes very little from the first (top) to the last (bottom). Despite this general tendency, a non neglected variability from one year to the other is observed.

The spring maximum occurs in March for most of the years (2003, 2004, 2005, 2009 and 2010), for some years in February (2006, 2008), but only rarely in April (2011) or even May (2007). It should be noted that the spring maximum is much higher in the first years (2003-2005) than later on. In 2009, PM₁₀ values are particularly low and no clear maximum appears. In summer, usually a single peak is observed although some years can present two peaks. The absolute maximum in summer is generally observed in August (2003, 2005, 2007, 2008 and 2010), but also in July (2004, 2009). For the whole period, the highest peak in summer is observed in July 2004, which corresponds to the strongest desert dust intrusion ever recorded over the Iberian Peninsula [8]. As regards the secondary peaks, in general they occur in early fall (e.g. 2008, 2011).

On the contrary, the annual cycle of the AOD (Figure 2(b)) can be very different from one year to the other. The "accumulated" curve show two maxima in the first years, but then gets smoothed as the maxima occurrence moves. Nevertheless, most maximums of PM₁₀ coincide with those of the AOD. Some exceptions are observed though for the years 2007 and 2009, when the spring maximum occurs a month later for the AOD as compared to PM₁₀. The correlation of these monthly means is analysed in details in the next section.

3.2 Relation PM_x-AOD

The relationship between PM₁₀ and AOD is presented in Figure 4. As expected, these two parameters are found to be moderately correlated (Figure 3 (a)) with a correlation coefficient of 0.56 for the daily data, lying between the 95% confidence interval (0.53-0.59). It should be noted that although the linear regression was not constrained to pass through the origin, the value at the origin falls within the error limits of PM_x measurements. The correlation is improved when considering the monthly means (Figure 3 (b)) rising up to 0.70. Here, it must be noted that the monthly means were computed using all available daily data from the individual datasets. When these monthly means are calculated using only coinciding days, the obtained results are sensibly the same ($R=0.69$, $Y=5.22+2.90$), and therefore are not affected by the sampling difference in the daily data.

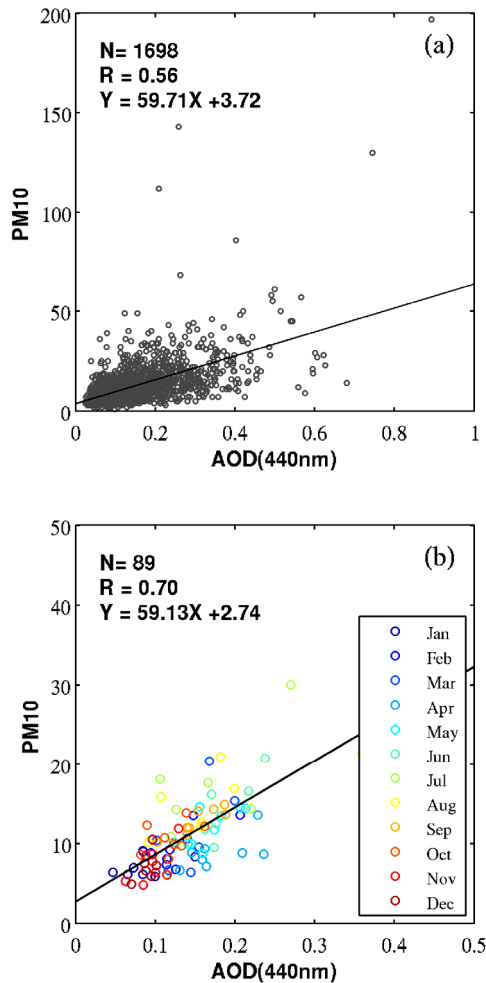


Fig. 3. Scatterplot and correlation of PM_{10} vs AOD (440 nm) for (a) daily values and (b) monthly means.

In Figure 4(a), both PM_{10} and $PM_{2.5}$ are represented as a function of the binned AOD at 440 nm using the 1698 coinciding data. Each point of the curve corresponds to the mean of PM_X in a given bin of AOD, and the associated standard deviation is represented by vertical bars. As it can be seen, PM_X increases slowly and regularly as the AOD reaches about 0.2, but above this value small maximums start to appear, one around 0.25 and another at 0.4, the highest peak being found for the AOD bin centered at 0.5 with nearly $50 \mu\text{g}\cdot\text{m}^{-3}$ and $25 \mu\text{g}\cdot\text{m}^{-3}$ for PM_{10} and $PM_{2.5}$ respectively. These high AOD values correspond to the occurrence of desert dust intrusions in the area. The existence of a few data with AODs above 0.7, as shown by the frequency histogram, are considered as exceptionally strong events, here related to that of July 2004.

These last results are corroborated by Figure 4(b) which is analogous to the previous Figure, this time with the fine-PM ratio instead of PM_X . Here the fine-PM ratio refers to the ratio of $PM_{2.5}$ with respect to PM_{10} . Indeed, the fine-PM ratio presents minima in the same AOD bin where the maxima are observed for the PM_X . For low AODs the fine-PM ratio remains of about 0.6 and drops as low as 0.45

for the AOD bin centered at 0.5. The fine-PM ratio can reach 0.3 for very high AODs, but as mentioned before, this only reflects the case of extreme desert dust outbreaks.

Besides, it should be noted that the apparent increase of the fine-PM ratio in the first AOD bins is an artefact of the AERONET data, as AOD values near zero become comparable to the uncertainty of the measurement (~ 0.02).

Figure 3 and 4 allow to underline that for AOD values above 0.5, as PM data decrease significantly where it would be expected to increase with the AOD. This explains the fact that there is no systematic correlation in the presence of strong events, thus frequently the values at the surface and those of the column appear uncoupled.

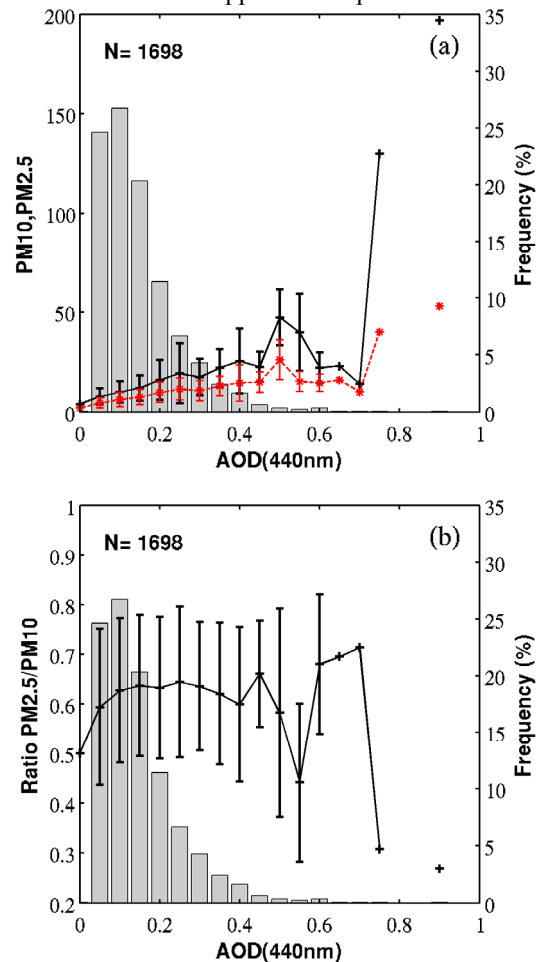


Fig. 4. (a) PM_{10} , $PM_{2.5}$ and (b) fine-PM ratio ($PM_{2.5}/PM_{10}$) as a function of binned AOD(440 nm).

4 CONCLUSIONS

In this study, long-term data of two rural background sites of the north-central region of Spain have been used to related PM_X and AOD.

It was found that the climatological annual cycle of PM_X is clearly modulated by the frequency of desert dust intrusions over the Iberian Peninsula, taking place mainly in late winter/early spring and in

the summer. However this bimodality is not present in the annual cycle of the AOD. When the interannual variability is examined, it appears that most maxima and minima of AOD and PM_X coincide. It is also observed that there is a significant variation from one year to the other, although the shape of the annual cycle is much more stable in the case of PM_X as compared to the AOD. The correlation between daily data is rather moderate, and clearly improved when considering monthly means. This may be explained by the fact that the poor sampling of sunphotometer data as compared to PM_X (56 % against 90 %). The availability of longer data series in the next years should help to verify whether the bimodality pattern of is also present in the AOD. Indeed, this bimodality is clearly manifested in the AOD when only the contribution of desert dust is estimated [7].

When strong desert dust events are studied, there is a high variability in the relation between PM_X and AOD, some for which column and surface data are highly correlated and other for which deposition breaks down this correlation.

ACKNOWLEDGMENTS

The authors are grateful to EMEP for providing observations from their network. Special thanks also go to NASA GSFC, PHOTONS and RIMA people for their long-standing collaboration and for operating and maintaining the AERONET network. The research leading to these results has received funding from the European Union Seventh Framework Programme (FP7/2007e2013) under grant agreement Nr. 262254 [ACTRIS]. Financial supports from the Spanish MINECO (projects of ref. CGL2011-23413, CGL2012-33576 and Acción Complementaria tipo E, CGL2010-09480-E, CGL2011-13085-E) are also gratefully acknowledged. We also thank the Environmental Council of the CyL Regional Government (Consejería de Medio Ambiente, Junta de Castilla y León) for supporting this research.

REFERENCES

- [1] Holben, B. N., Eck, T. F., Slutsker, I., Tanre, D., Buis, J. P., Setzer, A., Vermote, E., Reagan, J. A., Kaufman, Y. J., Nakajima, T., et al., AERONET - a federated instrument network and data archive for aerosol characterization. *Remote Sensing of Environment* 66 (1), 1e16 *Remote Sensing of Environment*, vol. 66(1), pp. 1-16, 1998.
- [2] Rodríguez S., Querol, X., Alastuey, A., Kallos, G. and Kakaliagou, O., "Saharan dust contributions to PM10 and TSP levels in Southern and Eastern Spain", *Atmospheric Environment*, 35(14), pp. 2433–2447, 2001.
- [3] Escudero M., Querol, X., Ávila, A. and Cuevas, E., "Origin of the exceedances of the European daily PM limit value in regional background areas of Spain", *Atmospheric Environment*, vol. 41(4), pp. 730–744, 2007.
- [4] Bennouna, Y., Cachorro, V., Torres, B., Toledano, C., Berjón, A., de Frutos, A. and Alonso Fernandez Coppel, I., "Atmospheric turbidity the annual cycle of aerosol optical depth over north-center Spain with ground (AERONET) and satellite (MODIS) remotely sensed data", *Atmospheric Environment*, vol. 67, pp. 352-364, 2013.
- [5] Cachorro, V.E., Burgos, M.A., Bennouna, Y., Toledano, C., and de Frutos, A., "Inventory of desert dust aerosols in the region of Castilla y León (2003-2012)", 1st Iberian Meeting on Aerosol Science and Technology (RICTA 2013), Évora, Portugal, 1-3 July 2013.
- [6] Bennouna, Y.S., Cachorro, V.E., Toledano, C., Berjón, A., Prats, N., Fuertes, D., Gonzalez, R., Rodrigo, R., Torres, B. and de Frutos, A., "Comparison of atmospheric aerosol climatologies over southwestern Spain derived from AERONET and MODIS", *Remote Sensing of Environment*, vol. 115, 1272-1284.
- [7] Toledano, C., Cachorro, V.E., de Frutos, A.M., Sorribas, M., Prats, N. and de la Morena, B.A., "Inventory of African desert dust events over the southwestern Iberian Peninsula in 2000–2005 with an AERONET Cimel Sun photometer", *Journal of Geophysical Research*, vol 112 (D21), 2007.
- [8] Cachorro, V.E., Toledano, C., Prats, N., Sorribas, M., Mogo, S., Berjón, A., Torres, B., Rodrigo, R., de la Rosa, J. and de Frutos, A.M. "The strongest desert dust intrusion mixed with smoke over the Iberian Peninsula registered with sun photometry", *Journal of Geophysical Research*, vol. 113 (D14), D14S04, 2008.

Spanish activities in the framework of the ChArMEx project since 2009: a summary

Michaël Sicard¹, Jorge Pey^{3,4}, Jose Carlos Cerro⁵, Diego Lange^{1,2}, Sandra Caballero⁶, Antonio Tovar-Sanchez⁷, Rafael Morales-Baquero⁸, Adolfo Comerón¹, Carles Bujosa⁹, Xavier Querol⁴, Begoña Artíñano¹⁰, Lucas Alados-Arboledas¹¹, Sara Basart¹², Andres Alastuey⁴, Jose Maria Baldasano¹², Francesc Rocadenbosch^{1,2}, Alvaro Muñoz¹, Constantino Muñoz¹, David García-Vízcaíno¹, Alejandro Rodríguez¹, Jordi Bach¹, Xavier Bush¹

Abstract — The ChArMEx (Chemistry-Aerosol Mediterranean Experiment) project is a French initiative aiming at developing and coordinating regional research actions for a scientific assessment of the present and future state of the atmospheric environment in the Mediterranean Basin, and of its impacts on the regional climate, air quality, and marine biogeochemistry. The target of ChArMEx is short-lived particulate and gaseous tropospheric trace species. In 2009 the project gained internationalization with the organization of the first international workshop held in Toulouse, France. Spain was the most represented country (after France) with 7 groups and 10 researchers. Up to date, the Spanish groups involved in ChArMEx have conducted research in several fields. Among them it is worth noting: a 3-year (2010 – 2012) in-situ study over a regional background environment in Mallorca plus 3 intensive measurement campaigns in that period; the installation in Mallorca and in the Sierra Nevada of two autonomous total deposition samplers performing weekly dust deposition on a network basis; and intensive in-situ and remote sensing measurements in Barcelona in the summer 2012 ChArMEx pre-campaign to give support to airborne observations. The paper gives a summary of all the activities led by Spanish researchers in the framework of ChArMEx. Preliminary results of the 3-year in-situ study in Mallorca and of the summer 2012 pre-campaign, as well as a brief description of the summer 2013 main campaign are presented.

Keywords — Aerosols, chemistry, atmosphere, climate, Mediterranean region, observations, remote sensing, modelling

1 INTRODUCTION

The international project ChArMEx (Chemistry-Aerosol Mediterranean Experiment) is a French

initiative whose goal is a scientific assessment of the present and future state of the atmospheric environment in the Mediterranean Basin, and of its impacts on the regional climate, air quality, and marine biogeochemistry. The target of ChArMEx is short-lived particulate and gaseous tropospheric trace species. The major stake is an understanding of the future of the Mediterranean region in a context of strong regional anthropogenic and climatic pressures [1].

Through seven work packages, ChArMEx addresses: emissions and source apportionment; chemical ageing of air masses with a focus on the formation of secondary organic aerosols; transport processes and their effect on air quality; direct radiative forcing by aerosols and its consequences on the water budget and regional climate; atmospheric deposition of nutrients and contaminants; recent trends and variability in atmospheric composition; and the future evolution of atmospheric chemistry at the horizon of 2030 and 2050.

Since 2009 several Spanish centers are involved in the project, in particular in the workpackages emissions and source apportionment, direct radiative forcing and deposition. This paper concentrates on the Spanish activities led in those 3 workpackages. A brief description of the summer 2013 main field campaign is also presented.

1. Remote Sensing Laboratory, Universidad Politècnica de Catalunya, Barcelona, Spain; E-mail: msicard@tsc.upc.edu; lange@tsc.upc.edu; comeron@tsc.upc.edu; roca@tsc.upc.edu; alvaro.munoz@etu.unistra.fr; constan@tsc.upc.edu; dgarcia@tsc.upc.edu; jordi.bach@gmail.com; xavier.bush@gmail.com
2. Centre de Recerca de l'Aeronàutica i de l'Espai - Institut d'Estudis Espacials de Catalunya, Universidad Politècnica de Catalunya, Barcelona, Spain
3. Aix-Marseille Université, Marseille, France; E-mail: jorge.pey@univ-amu.fr
4. Institute of Environmental Assessment and Water Research, IDAEA-CSIC, Barcelona, Spain; E-mail: xavier.querol@idaea.csic.es; andres.alastuey@idaea.csic.es
5. Illes Balears University, Spain; E-mail: jccerro@dgqal.caib.es
6. Atmospheric Pollution Laboratory, Miguel Hernández University, Spain; E-mail: san.cab@umh.es
7. Department of Global Change Research, IMEDEA (CSIC-UIB), Instituto Mediterráneo de Estudios Avanzados, Esporles, Spain; E-mail: atovar@imedea.uib-csic.es
8. Departamento de Ecología, Universidad de Granada, Granada, Spain; E-mail: rmorales@ugr.es
9. ENDESA, Spain; E-mail: carlesbu@gmail.com
10. CIEMAT, Madrid, Spain; E-mail: b.artinano@ciemat.es
11. Andalusian Centre for Environmental Research, Junta de Andalucía / Applied Physics Department, University of Granada, Granada, Spain; alados@ugr.es
12. Barcelona Supercomputing Center, Barcelona, Spain; sara.basart@bsc.es; jose.baldasano@bsc.es

2 SPANISH ACTIVITIES WITHIN THE WORKPACKAGE 1: EMISSIONS AND SOURCE APPORTIONMENT

The most relevant contribution in WP1 is the implementation in an existing regional background monitoring site situated in Can Llompart in Mallorca Island (Fig. 1) of additional instrumentation to fulfil some of the following objectives: a complete chemical characterization of the atmospheric aerosols and the identification of their main sources; the assessment of the levels of gaseous pollutants and atmospheric aerosols in different particles sizes; and the quantification and chemical characterization of the deposition fluxes. The additional instrumentation was installed during a period of 3 years between 2010 and 2012. Three intensive measurement campaigns took place in spring and in summer 2011 and in summer 2012.



Fig. 1. Map of the Spanish sites involved in ChArMEx.

2.1 Preliminary results at Can Llompart

The instrumentation already existing at Can Llompart allowed measuring hourly levels of NO, NO₂, SO₂, O₃, PM₁₀, air temperature, wind direction and velocity, atmospheric pressure and precipitation. The additional instrumentation consisted of:

- an optical particle counter (OPC) to determine real time concentrations of PM₁₀, PM_{2.5} and PM₁,
- two sequential high-volume (HV) sampler for PM₁₀ and PM₁ collection on quartz micro-fibre filters,
- an automatic collector of dry and wet (D/W) deposition of atmospheric particles,
- an ultra-fine particle (5-1000 nm) counter for number concentration,
- a multi-angle absorption photometer (MAAP) for continuous monitoring of black carbon concentrations, and
- measurements of NH₃ concentration.

Further details about their period and mode operation are given in Table 1. In total over the period 2010-2012 more than 450 valid samples of PM₁₀ and PM₁ have been collected. So far more than 400 of them have been analyzed for 60

inorganic compounds as well as organic and elemental carbon [2]. The PM₁₀ daily concentration over the period 2010-2012 is shown in Fig. 2. The mean annual PM₁₀ concentration over the whole period varies between 16 and 18 µg·m⁻³. All the daily PM₁₀ peaks exceeding the limit value of 50 µg·m⁻³ are related to Saharan dust outbreaks. The average chemical composition over the whole period is formed dominantly by 23 % of organics, 17 % of mineral dust, 14 % of SO₄²⁻ (coal-fired power plant), 10 % of sea spray, and to a lesser extent nitrate and ammonium (5% each component). However, significant seasonal variations are observed for most of these components, especially for sulphate and mineral dust, clearly enhanced in summer, and nitrate, significantly higher in wintertime owing to the occurrence of NH₄NO₃ which is not stable under warm atmospheric conditions.

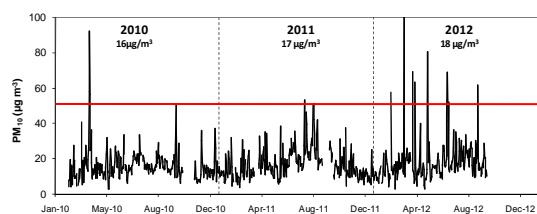


Fig. 2. PM₁₀ concentration over the period 2010-2012 in Can Llompart.

2.2 Results of the 2011 field campaigns

The 2011 spring campaign (15 March – 28 April) was planned to capture the impact at ground level of long-range transported plumes in the western Mediterranean [3]. Several African dust episodes occurred in March and coincided with large amounts of anthropogenic, European pollution exported from the continent. During the campaign a severe PM pollution episode from Europe was captured, as well as typical summer-type African dust episodes [3]. Photochemical nucleation was frequently observed during the spring campaign, with strong peaks at midday coinciding with very low black carbon concentrations (Fig. 3). During such episodes, the number of ultra-fine particles (5-1000 nm) increased up to 120.000 cm⁻³ as hourly mean value 2 to 3 hours after the slight traffic peaks.

The 2011 summer campaign (21 June – 15 September) was intended to characterize in detail the alternate of regional recirculation episodes and African dust episodes affecting the western Mediterranean. Both types of episodes give rise to a clear increase of atmospheric pollution in the western Mediterranean, and favour the ageing processes of the atmospheric PM. Fig. 4 shows the PM₁₋₁₀ fraction as well as the black carbon concentration. The accumulation of pollutants (regional recirculation) is indicated by upward red arrows in the BC plot, while the dust episodes, always coinciding with the end of the accumulation

of pollutants, are indicated by black arrows in the PM_{1-10} plot.

The chemical analyses of PM_{10} and PM_1 samples obtained during both intensive campaigns, as well as the 2012 summer campaign, are currently ongoing.

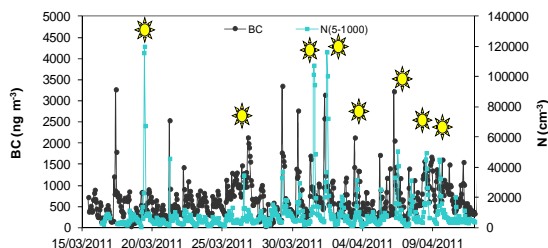


Fig. 3. Black carbon (BC) concentration and ultra-fine particle number (N) during the 2011 spring campaign in Can Llompart.

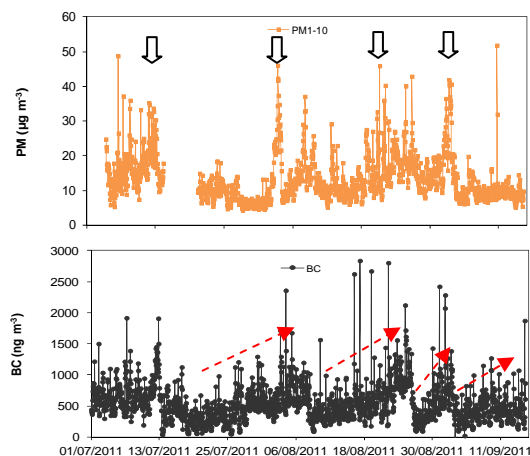


Fig. 4. Black carbon and PM_{1-10} during the 2011 summer campaign in Can Llompart.

3 SPANISH ACTIVITIES WITHIN THE WORKPACKAGE 4: RADIATIVE FORCING AND CLIMATE IMPACT

In the context of the 2012 ChArMEx pre-campaign, two field campaigns took place: TRAQA (Long distance transport and air quality in the Mediterranean Basin) and VESSAER (Vertical Structure and Sources of AERosols in the Mediterranean Region). The Spanish participation was mostly involved in the TRAQA campaign (25 June – 12 July). The main objectives of the campaign were [4]:

- Characterization of dynamic processes of exportation of contaminated air masses from source regions around the Mediterranean coast,
- Quantification of the exchanges between the boundary layer and the free troposphere above the Mediterranean Basin,
- Lagrangian track of the ageing and mixing of the contaminated plumes (aerosols and gases) in the low troposphere, and

- Analysis of the representativeness of the case study and the long-term series to evaluate the impact of the contaminated plumes on the air quality.

The meteorological conditions allowed for a total of 7 Intensive Observation Periods (IOP) with ~60 hours of flight of the instrumented ATR-42 research aircraft.

Intensive lidar measurements were performed in Barcelona to give support to the Saharan dust outbreak IOP (29 June), the pollution recirculation IOP (3-4 July) and the contamination structure along the Mediterranean coast IOP (10-11 July). Can Llompart measurements were intensified during the period 6 June – 15 August 2012.

In order to give a flavour of the ongoing analyses, Fig. 5 gives an illustration of the pollution recirculation IOP that took place in the area of Barcelona on 3 and 4 July. The MACC (Monitoring Atmospheric Composition and Climate) model first predicted an accumulation of pollutants in the area of Barcelona on 3 July that would travel northward on 4 July. The flights were set up accordingly to the prediction in order to 1) characterize locally the city plume on 3 July, and 2) sample the travelling plume in a Lagrangian manner on 4 July. The aircraft quicklook is a longitudinal cross section of approximately 200 km long. Barcelona is overpassed around 1405UT. The vertical structure observed by the airborne lidar is very similar to that observed from the ground. It is worth noting how the multi-layer structure observed above the city vanishes as the airplane moves away from the coast.

A comprehensive model-observation intercomparison exercise based on the 2012 dust IOP is ongoing and involves the NMMB/BSC-Dust model developed at the Barcelona Supercomputing Center (BSC) [5].

Related to the 2012 campaign subject, a potential operability exercise was performed by 10 EARLINET/ACTRIS and 2 non-EARLINET lidar stations around the northern Mediterranean basin for 72 hours (9 July 0600UT – 12 July 0600UT). EARLINET (European Aerosol Research Lidar Network) is the aerosol vertical profiling infrastructure of the European project ACTRIS (Aerosols, Clouds, and Trace Gases Research Infrastructure). The exercise itself is not linked to ChArMEx activities, but the data are being used by researchers actively involved in ChArMEx for a tentative to assimilate lidar profiles in an air quality model. The same data might also be used in the CALIOPE air quality modelling system [6] developed at BSC to assimilate lidar products, such as the planetary boundary layer height.

4 SPANISH ACTIVITIES WITHIN THE WORKPACKAGE 5: DEPOSITION

Deposition is a crucial parameter of the mass budget

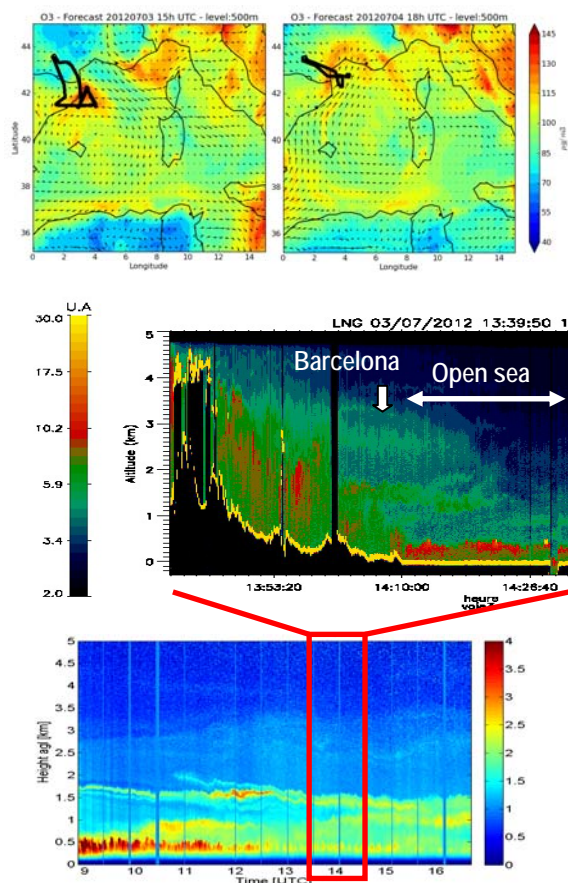


Fig. 5. Pollution recirculation IOP in the area of Barcelona: (top) MACC forecast of O₃ and aircraft track (black lines) for 3 and 4 July; (middle) airborne lidar quicklook on 3 July; (bottom) Barcelona lidar quicklook on 3 July.

of atmospheric particular matter far from their source. In aerosol regional transport models that parameter is not constrained because of the lack of adapted measurements [7][8]. In the marine biogeochemical cycle, the effects of deposition on processes such as phytoplankton bloom and concentration increase of dissolved metals, among others, are not well characterized [9].

To fill those gaps, a deposition network to assess the total insoluble deposition flux of atmospheric particular matter, and especially of Saharan dust, in the Mediterranean region has been set up with a new type of collector. This new collector is an autonomous deposition sampler called CARAGA (Collecteur Automatique de Retombés Atmosphériques à Grande Autonomie). Among the seven instruments currently installed in the western Mediterranean, two of them are in Spain: one in Ses Salines (at sea level and functioning since January 2012), in the Southeast of Mallorca, and one in Cañar (at 1729 m asl and functioning since August 2012), in the Southwest of Sierra Nevada (see Fig. 1). All systems are performing weekly dust deposition on a network basis. The chemical analyses of the first filters collected are ongoing.

In parallel to this network activity, weekly deposition of wet and dry particulate matter has been collected in Can Llompart since 2010. Fig. 6 shows the inorganic component speciation performed from the deposition measurements.

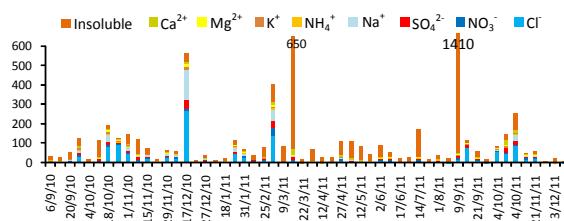


Fig. 6. Inorganic components (in $\mu\text{g}\cdot\text{m}^{-2}$) of the weekly deposition fluxes collected at Can Llompart.

5 SUMMER 2013 MAIN FIELD CAMPAIGN

The 2013 field campaign will take place between 10 June and 10 August 2013. Activities will be mainly in the western Mediterranean. As in the 2012 pre-campaign, the teams will be deployed on a dozen sites including ground measurement stations, balloon launch pad and aircraft bases. Ground operations will be continuous from June 10 to August 10 while airborne operations are organized into two periods of special observations (SOP): SOP-1a from June 12 to July 5 and SOP-1b from July 23 to August 9.

Like in 2012, the campaign is divided into two campaigns defined with different objectives: SOP-1a (ADRIMED, Aerosol Direct Radiative Impact on the regional climate in the MEDiterranean region) will focus on aerosol direct radiative forcing (column closure and regional scale) and SOP-1b (SAFMED, Secondary Aerosol Formation in the Mediterranean) will focus on organic chemistry and secondary aerosol formation.

Both research aircraft involved, the ATR-42 and the Falcon 20, will be based in Corsica, France. In-situ measurements will be performed at several surface stations, including supersites in Corsica, Lampedusa (Italy) and Mallorca. Drifting balloons equipped with an O₃ sonde or an optical particle counter will be launched from Menorca.

As far as Spain is concerned, lidar measurements will be performed in Barcelona and in Cap d'en Font, Menorca, and drifting balloons will be launched from the Sant Lluís aerodrome, Menorca, during SOP-1a; in-situ measurements will be performed in Cap Es Pinar in the north of Mallorca during SOP-1b (see Fig. 1). At the latter site, real time measurements of chemical composition of the gas and particle phases will be performed, as well as offline collection of PM onto filters for subsequent analysis of the organic and inorganic fraction as performed in Can Llompart.

6 CONCLUSIONS

The participation of the Spanish aerosol community either in field campaigns or in meetings and working groups related to the ChArMEx project is remarkable. Spanish researchers are actively involved in the workpackages 1 (emission and source apportionment), 4 (radiative forcing and climate impact) and 5 (deposition) of ChArMEx. Their participation also contributes, less directly, to workpackages 2 (ageing) and 3 (air quality and transport). In particular, the location of the Balearic Islands in the middle of the western Mediterranean Basin where the background conditions are usually clean is a strategic spot for investigating long-range transported aerosol issues such as chemistry, ageing and transport. Overall it makes no doubt that all activities led by Spanish researchers and their international collaborators will yield a better understanding of the Mediterranean aerosols, and an improvement of aerosol chemistry and climate models in the Mediterranean region.

ACKNOWLEDGMENT

This work is supported by the 7th Framework Programme project Aerosols, Clouds, and Trace Gases Research Infrastructure Network (ACTRIS) (grant agreement no. 262254); by the Spanish Ministry of Science and Innovation and FEDER funds under the projects TEC2012-34575, TEC2009-09106/TEC, CTM2011-14036-E and CGL2011-13580-E/CLI; and the grant SEV-2011-00067 from the Severo Ochoa Program. Deposition measurements in Sierra Nevada are funded by the project CEI-BioTic-UGR 20F12/24. ENDESA, through AMBILINE, is taking care of the routine instruments at Can Llompart. The authors would like to thank GESA-ENDESA and the Direcció General de Canvi Climàtic i Educació Ambiental, Illes Balears, for using their facilities and

their technical support.

REFERENCES

- [1] F. Dulac et al., “An update on ChArMEx (the Chemistry-Aerosol Mediterranean Experiment) activities and plans for aerosol studies in the Mediterranean region”, European Aerosol Conference, Granada, Spain, L. Alados Arboledas and F. J. Olmo Reyes (Eds.), 2 – 7 September 2012
- [2] J. C. Cerro, J. Pey, C. Bujosa, S. Caballero, A. Alastuey, M. Sicard, B. Artíñano, X. Querol, “Regional background aerosols over the Balearic Islands over the last 3 years: ground-based concentrations, atmospheric deposition and sources”, European Geosciences Union General Assembly, Vienna, Austria, 7 - 12 April 2013
- [3] J. Pey, C. Bujosa, S. Caballero, X. Querol, A. Alastuey, M. Sicard, B. Artíñano, “Two years of measurements at a regional background site in the Balearics: first results” , European Aerosol Conference, Granada, Spain, L. Alados Arboledas and F. J. Olmo Reyes (Eds.) , 2 – 7 September 2012
- [4] F. Dulac et al., “The summer 2012 Saharan dust season in the western Mediterranean with focus on the intense event of late June during the Pre-ChArMEx campaign” , European Geosciences Union General Assembly, Vienna, Austria, 7 - 12 April 2013
- [5] C. Pérez, K. Hausteiner, Z. Janjic, O. Jorba, N. Huneus, J.M. Baldasano, T. Black, S. Basart, S. Nickovic, R.L. Miller, J. Perlwitz, M. Schulz, M. Thomson, “Atmospheric dust modeling from meso to global scales with the online NMMB/BSC-Dust model – Part 1: Model description, annual simulations and evaluation”, Atmos. Chem. Phys., 11, 13001-13027, doi:10.5194/acpd-11-13001-2011, 2011
- [6] J. M. Baldasano, M.T. Pay, O. Jorba, S. Gassó, P. Jiménez-Guerrero, “An annual assessment of air quality with the CALIOPE modeling system over Spain”, Science of the Total Environment, 409, 2163–2178, doi: 10.1016/j.scitotenv.2011.01.041, 2011
- [7] C. Textor, et al., “Analysis and quantification of the diversities of aerosol life cycles within AeroCom”, Atmos. Chem. Phys., 6, 1777-1813, 2006
- [8] C. Textor et al., “The effect of harmonized emissions on aerosol properties in global models - an AeroCom experiment”, Atmos. Chem. Phys., 7, 4489-4501, 2007
- [9] A. Jordi, G. Basterretxea, A. Tovar-Sánchez, A. Alastuey, X. Querol, “Copper aerosols inhibit phytoplankton growth in the Mediterranean Sea”, Proc. National Academy Sciences, doi:10.1073/pnas.1207567110, 2012

Table 1. Additional instrumentation installed in Can Llompart during 2010-2012.

	OPC	HV sampler PM10	HV sampler PM1	D/W deposition	Number	MAAP	NH3
Routine	Non stop (1 hour)	Non stop (1 sample/4 day)		Non stop (weekly)			
Spring and summer 2011	Non stop (1 hour)	15/03-15/09 (143 samples)	16/03-21/07 (83 samples)	Non stop (weekly)	15/03-28/04 (44 days)	15/03-15/09 (185 days)	
Summer 2012	Non stop (1 hour)	06/06-15/08 (45 days)	06/06-15/08 (45 days)	Non stop (weekly)	06/06-06/08 (40 days)		06/06-15/08 (50 days)

Formaldehyde levels at a common pre-school playroom

M. Oliveira^{1,2}, K. Slezakova^{1,2}, C. Delerue-Matos¹, M.C. Pereira², S. Morais^{1*}

Abstract — As people spend most of their time indoors, the levels of indoor air pollution are important for the protection of public health. Due to their developing status, children represent the most susceptible group in regard to indoor air pollution exposure. Apart from homes, children spend most of the time at schools. The analysis of child exposure to air pollution in schools requires identification of the main pollution sources and measurement of the respective levels. In this context, formaldehyde is one of the priority pollutants. Thus the objective of this work was to assess the concentrations of formaldehyde in indoor air of one Portuguese pre-school (children 3–5 years old) and to compare the obtained levels with: (i) World Health Organization guidelines; (ii) current Portuguese legislation for indoor air; and (iii) other Portuguese studies. The indoor levels of formaldehyde were monitored during five weeks of 2012 in three different sampling points (A–C) of one naturally-ventilated playroom. The mean indoor concentration of formaldehyde was $14 \mu\text{g}/\text{m}^3$. All measured concentrations were below WHO guidelines and fulfilled Portuguese legislative limit. Finally, the indoor formaldehyde levels obtained within this study were comparable to those reported for other Portuguese schools.

Keywords — indoor air quality (IAQ), formaldehyde, schools, legislation

1 INTRODUCTION

Over the last decades the levels of exposure to harmful indoor air pollutants have been increasingly considered for the protection of human health. To assess those exposures, evaluation of the concentrations of indoor pollutants potentially toxic and/or carcinogenic is a matter of importance. Volatile organic compounds (VOCs) are among those pollutants that can considerably decrease indoor air quality. Various studies have shown that indoor exposure to VOCs can significantly contribute to adverse health effects [1]. The vast majority of human activities take place in indoor areas (homes, offices, schools, restaurants, shops and cars). Detailed investigations of the VOC pollution levels in such micro-environments are thus essential not only for the understanding of population exposure to these harmful substances, but also for epidemiological studies and eventually for the improvement of the indoor air quality.

Formaldehyde is one of the most known and studied VOC [2]. It is a colourless flammable gas that has at elevated concentrations a strong, pungent odour. Formaldehyde is ubiquitously found in the environment as it is formed by various natural processes (decomposition, biomass combustion of forest and bush fires, and through volcanoes) [3].

Traffic and industrial emissions are some of the major outdoor anthropogenic sources of formaldehyde; though it is also formed from secondary chemical reactions in the air. Whereas outdoor emissions are one of the relevant contributors of formaldehyde indoors, this pollutant is also released from a variety of indoor sources such as indoor combustion processes (wood burning, gas appliance use and cigarette smoking), insulating materials, particle board and plywood furniture containing formaldehyde-based resins, water based paints, household cleaning agents, pesticide formulations and other building materials containing urea formaldehyde resins [4]. Therefore, the use of low-emitting building materials and products, as well as preventing exposure to environmental tobacco smoke and other combustion emissions will minimize the risks associated with formaldehyde exposure [2].

Formaldehyde is classified by the International Agency for Research on Cancer as known carcinogen to humans (Group 1) [5]. Its exposure causes both short and long-term health effects. Irritation (skin, eye or upper respiratory tract), pulmonary edema, inflammation or even pneumonia are some of the acute health consequences [4], [6], [7] whereas chronic exposure to formaldehyde can cause worsening of allergies and adverse effects of the respiratory system, and even cancer [7], [8]. The major routes of exposure to formaldehyde are via ingestion and inhalation. As indoor inhalation exposure is specifically the dominant contributor (up to 98%) to personal exposure [3], formaldehyde is considered among the priority indoor air pollutants by World Health Organisation [3].

It is estimated that 3.6% of deaths of children under the age of 4 are caused by poor indoor air quality [3]. Children are more susceptible to indoor

1. Authors are with the REQUIMTE – Instituto Superior de Engenharia do Porto, Instituto Politécnico do Porto, Rua Dr. António Bernardino de Almeida 431, 4200-072 Porto, Portugal. E-mail: martamadalen@gmail.com, cmm@isep.ipp.pt, sbm@isep.ipp.pt.

2. Authors are with LEPAE - Departamento de Engenharia Química, Faculdade de Engenharia, Universidade do Porto, Portugal, Rua Dr. Roberto Frias, 4200-465 Porto. E-mail: slezakok@fe.up.pt; mcsp@fe.up.pt.

air pollution than adults, because their lung structure and immune system are not fully developed. In addition, increased physical activity and higher breathing rates may lead to higher levels of exposure for children and hence to more severe health outcomes [6], [9]. As children spend up to 10 hours in schools, the quality of indoor air in these specific environments is significant for child healthy development.

The objective of this study was to assess the concentrations of formaldehyde in indoor air of one Portuguese pre-school and to compare the obtained levels with: (i) World Health Organization guidelines; (ii) current Portuguese legislation for indoor air; and (iii) levels reported by other Portuguese studies.

2 MATERIAL AND METHODS

The study was conducted in one Portuguese pre-school in Oporto, Portugal. The school was situated in the direct vicinity of a highway exit point; traffic emissions are the major pollution source for the respective area [10], [11].

The levels of formaldehyde were monitored during five weeks (March to April) of 2012. During all weekdays, samples were collected before and after the classes (i.e. 8:30 and 16:30 h) using PPM Formaldemeter (HTV-M kit). The concentrations of formaldehyde were measured in indoor air of one playroom with 25 to 90 children present (3–5 years old). This room was naturally ventilated (with open windows), equipped with furniture (wood, PVC materials) and with PVC flooring. As the room area was approximately 150 m², the levels of formaldehyde were measured in three different sampling points (A–C) with various distance from windows, exits, and furniture. At each sampling point concentrations were assessed by three replicates.

During the whole period indoor temperature and relative humidity were continuously measured using the Mini data logger (Testo, model 174H) (Table 1).

For the data treatment, the Student's t-test was applied to determine the statistical significance ($P < 0.05$, two tailed) of the differences between the determined means.

3 RESULTS

The overall indoor mean concentration of formaldehyde was 14 µg/m³, with levels ranging up to 50 µg/m³. The statistical parameters (average, minimal and maximal values) obtained for each of the three sampling points (A–C) are shown in Fig. 1. The highest levels of formaldehyde were observed at sampling point A (mean concentration of 16 µg/m³). This point was the closest to the room walls (approximately 2 m). At both sampling points, B and

C mean concentrations of formaldehyde were 13 µg/m³. No significant differences ($P < 0.05$) were observed between the mean concentrations of formaldehyde at three different sampling positions of the playroom. In general, these findings thus indicate homogeneity of the air inside the playroom.

Table 1. Indoor temperature (°C) and relative humidity (%) during five weeks of sampling period

	Mean	SD	Range
T (°C)	18	5	17.1–22.1
RH (%)	59	9	32.6–82.3

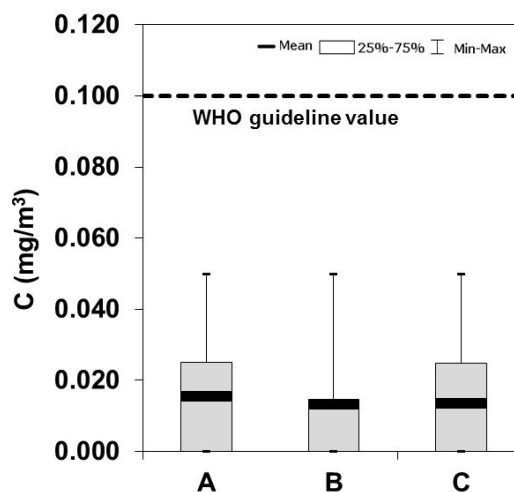


Fig. 1. Concentrations of formaldehyde at three different sampling points (A–C): means, minimal and maximal values, 25th and 75th percentiles. The horizontal dashed line represents WHO indoor guideline value (i.e. 0.1 mg/m³).

4 DISCUSSION

Considering formaldehyde as one of the priority pollutants, World Health Organisation (WHO) has established its guidelines in indoor air. WHO recommended threshold is 0.1 mg/m³ for short-term (i.e. 30 minute duration) exposure to formaldehyde in order to prevent sensory irritation. However, in order to also prevent effects on lung function as well as long-term effects (such as nasopharyngeal cancer and myeloid leukaemia), this threshold should not be exceeded at any 30-minute interval during a day [3]. The results in Fig. 1 clearly show that all indoor concentrations of formaldehyde measured in playroom (including maximal levels) were well below WHO guideline. Specifically, the maximal observed concentrations (0.05 mg/m³ at all sampling points) were twice lower than the WHO guideline value.

Because of the toxic nature of formaldehyde, Portuguese government has also established its limit in order to regulate the indoor exposure to

formaldehyde on national level. The National System for Energy and Indoor Air Quality Certification of Buildings (Regulamento dos Sistemas Energéticos de Climatização de Edifícios) sets an acceptable maximum value of 0.1 mg/m^3 of formaldehyde in indoor air of buildings. In agreement with previous results, all measured concentrations fulfilled the Portuguese legislative limits.

The results of the present work were also compared to other studies conducted in Portugal. The information of indoor air quality in Portuguese schools is rather limited concerning the levels of formaldehyde. The available information comes from three related studies [13], [14], [15], all of which evaluated indoor air quality of 14 primary and elementary schools in Lisbon during three seasons of 2009-2010. The reported concentrations of formaldehyde indoors were: $6.3\text{--}23.8 \text{ }\mu\text{g/m}^3$ (winter), $3.1\text{--}26.2 \text{ }\mu\text{g/m}^3$ (autumn), and $3.4\text{--}42.3 \text{ }\mu\text{g/m}^3$ (spring). Overall, the concentrations of formaldehyde obtained in pre-school in Porto were very similar and comparable to those reported for the spring season in Lisbon.

The indoor air quality in school environments is an emerging research area in many countries. The implementation of the legislative framework based on systematic studies and in agreement with interdisciplinary scientific authorities is crucial. The participation and role of professionals specializing in air quality, engineering, architecture and urban planning, public health, epidemiology, toxicology, catalysis and photochemistry of atmosphere is essential for the construction of healthy buildings and schools [16]. Proper ventilation, use low-emitting building materials, implementation of eco-labelling illustrative logos and clear indications that might help select products with reduced emission levels may significantly contribute to mitigate exposure to toxic pollutants, such as is formaldehyde [3], [16].

5 CONCLUSION

The mean indoor concentration of formaldehyde in the studied pre-school was $14 \text{ }\mu\text{g/m}^3$. Although the obtained levels ranged widely (up to $50 \text{ }\mu\text{g/m}^3$), all measured concentrations were below WHO guidelines and fulfilled Portuguese legislative limit. In addition, concentrations of formaldehyde obtained within this study were comparable to those reported for other Portuguese schools.

ACKNOWLEDGEMENTS

This work was supported by IJUP project PP_IJUP2011 121. M. Oliveira and K. Slezakova are grateful to *Fundação para a Ciência e a Tecnologia* for their fellowships SFRH/BD/80113/2011 and

SFRH/BPD/65722/2009, respectively.

REFERENCES

- [1] O. Geiss, G. Giannopoulos, S. Tirendi, J. Barrero-Moreno, B.R. Larsen, D. Kotzias, "The AIRMEX Study - VOC Measurements in Public Buildings and Schools/Kindergartens in Eleven European Cities: Statistical Analysis of the Data", *Atmos Environ*, vol. 45, pp. 3676–3684, 2011.
- [2] C.J. Weschler, "Changes in Indoor Pollutants since the 1950s", *Atmos Environ*, vol. 4, pp. 153–169, 2009.
- [3] World Health Organization, *Guidelines for Indoor Air Quality: Selected Pollutants*. Denmark Copenhagen: WHO Regional Office for Europe, 2010.
- [4] D.A. Sarigiannis, S.P. Karakitsios, A. Gotti, I.L. Liakos, A. Katsoyiannis, "Exposure to Major Volatile Organic Compounds and Carbonyls in European Indoor Environments and Associated Health Risk", *Environ Int*, vol. 37, pp. 743–765, 2011.
- [5] International Agency for Research on Cancer, "Formaldehyde, 2-butoxyethanol and 1-tert-butoxypropan-2-ol", *IARC Monographs on the Evaluation of the Carcinogenic Risk of Chemicals to Humans*, vol. 88, pp. 39–325, 2006.
- [6] P. Le Cann, N. Bonvallet, P. Gloennec, S. Deguen, C. Goeury, B. Le Bot, "Indoor Environment and Children's Health: Recent Developments in Chemical, Biological, Physical and Social Aspects", *Int J Hyg Environ Health*, vol. 215, pp. 1–18, 2011.
- [7] G. McGwin Jr., J. Lienert, J.I. Kennedy Jr., "Formaldehyde Exposure and Asthma in Children: a Systematic Review", *Environ Health Persp*, vol. 118, pp. 313–317, 2010.
- [8] J. Heinrich, "Influence of Indoor Factors in Dwellings on the Development of Childhood Asthma", *Int J Hyg Environ Health*, vol. 214, pp. 1–25, 2011.
- [9] S. Salvi, "Health Effects of Ambient Air Pollution in Children", *Paediatr Respir Rev*, vol. 8, pp. 275–280, 2007.
- [10] K. Slezakova, J.C.M. Pires, D. Castro, M.C.M. Alvim-Ferraz, C. Delerue-Matos, S. Morais, M.C. Pereira, "PAH Air Pollution at a Portuguese Urban Area: Carcinogenic, Risks and Sources Identification", *Environ Sci Pollut Res*, vol. 20, pp. 3932–3945, 2013.
- [11] K. Slezakova, D. Castro, C. Delerue-Matos, M.C.M. Alvim-Ferraz, S. Morais, M.C. Pereira, "Impact of Vehicular Traffic Emissions on Particulate-bound PAHs: Levels and Associated Health Risks", *Atmos Res*, vol. 127, pp. 141–144, 2013.
- [12] Decreto Lei 79/2006, "O Regulamento dos Sistemas Energéticos de Climatização em Edifícios", *Diário da República*, 1 série-A 67, pp. 2414–2497, 2006.
- [13] P. Nascimento Pegas, M.G. Evtugina, C.A. Alves, T. Nunes, M. Cerqueira, M. Franchi, C. Pio, S.M. Almeida, M.C. Freitas, "Outdoor/Indoor Air Quality in Primary Schools in Lisbon: A Preliminary Study", *Quim Nova*, vol. 33, pp. 1145–1149, 2010.
- [14] P.N. Pegas, C.A. Alves, M.G. Evtugina, T. Nunes, M. Cerqueira, M. Franchi, C.A. Pio, S.M. Almeida, M.C. Freitas, "Indoor Air quality in Elementary Schools of Lisbon in Spring", *Environ Geochem Health*, vol. 33, pp. 455–468, 2011.
- [15] P.N. Pegas, C. A. Alves, M.G. Evtugina, T. Nunes, M. Cerqueira, M. Franchi, C.A. Pio, S.M. Almeida, S. Cabo Verde, M.C. Freitas, "Seasonal Evaluation of Outdoor/Indoor Air Quality in Primary Schools in Lisbon", *J Environ Monit*, vol. 13, pp. 657–667, 2011.
- [16] C.A. Alves, "Formaldeído em Escolas: Uma Revisão", *Quim Nova*, vol. 35, pp. 2025–2039, 2012.

Pointing error and field of view of AERONET Cimel-318 Sun photometers

B. Torres^{1,2}, C. Toledano¹, A.J. Berjón³, D. Fuertes¹, V. Molina¹, R. González¹, M. Canini⁴,
V.E. Cachorro¹, P. Goloub², T. Podvin², L. Blarel², O. Dubovik², Y. Bennouna¹, A.M. de
Frutos¹

Abstract — Two new measurements, namely cross and matrix, have been added to the Cimel 318 radiometer, which is the standard instrument of the Aerosol Robotic Network (AERONET). These are both designed for the evaluation of the pointing error, although the matrix scenario also allows measuring the solid view angle of the instrument. First we have developed a method to derive the pointing error based on the cross and matrix data, including a correction for the Sun movement during the measurement, which must be taken into account for a correct evaluation of the pointing error. Both measurements reach similar results, with differences under 0.01° in the estimated pointing errors. Second, the pointing error of AERONET field instruments has been monitored by means of the cross measurement, that has been added to the standard measurement sequence of 10 photometers belonging to AERONET-Europe. The pointing errors are generally smaller than 0.1° although in some instruments values up to 0.3° have been observed. Moreover, the pointing error evaluation has shown that this measure can be used to detect mechanical problems in the robots or dirtiness in the quadrant detector due to the stable behavior of the values, for example with respect to time and solar zenith angle. Third, the matrix scenario can be used to derive the solid view angle of the radiometers. In order to provide a validation to the field of view measurement, a comparison with the field of view obtained with the vicarious calibration method was developed. The differences between both methods, which are completely independent, are under 3%.

Keywords — Aeronet, Pointing error, Field of view

1 INTRODUCTION

The Aerosol Robotic Network (AERONET [1]) program was started by the National Aeronautics and Space Administration (NASA) in the 90's, in collaboration with PHOTONS (Laboratoire d'Optique Atmosphérique-LOA, University of Lille), as a federation of networks with regional or national extent deployed on ground in the form of stations for monitoring atmospheric aerosols. AERONET aims at providing reliable monitoring of global aerosol optical and microphysical properties, to facilitate the characterization of the aerosol properties, the validation of satellite products related to the aerosol as well the synergy with other instrumentation (lidar, surface radiation, etc.).

The standard AERONET instrument is the CE-318 manufactured by Cimel Electronique. This is an automatic sun and sky radiometer, equipped with 8 or 9 spectral channels covering the spectral range 340–1640 nm. It performs both direct Sun measurements and sky radiance observations in the almucantar and principal plane configurations [1].

The AERONET inversion algorithm, described in

[2] (also in [3], [4] and [5]), provides the aerosol information from two kinds of measurements: spectral data of direct Sun radiation extinction (i.e. aerosol optical depth) and angular distribution of sky radiance. In the work [3], an accuracy analysis of the AERONET inversion code considering different error sources is developed. One of the most important results of the study is that an accurate pointing is critical for the characterization of desert dust aerosol.

However, an evaluation of the pointing error in the Cimel CE-318 sun-photometers has not been done yet. The present work analyzes the first results of two new measurements, denominated “cross” and “matrix” and integrated in the CE-318, which have been developed for a characterization of the pointing error.

Finally, the matrix scenario allows to calculate the field of view (FOV) of the sun photometer. This characteristic is of great importance in any sun photometer but the need of an accurate determination arises from the fact that the field of view can be used to calibrate the radiance channels using the vicarious method.

2 THEORETICAL BASIS

2.1 Pointing Error

Pointing error is defined as the angle between the Sun position (correct pointing) and the erroneous pointing direction. As sun-photometers are moved

1. Group of Atmospheric Optics, Valladolid University, Valladolid, Spain.

2. Laboratoire d'Optique Atmosphérique, Université des Sciences et Technologies de Lille, Villeneuve d'Ascq, France.

3. Izaña Atmospheric Research Center, Spanish Meteorological Agency (AEMET), Tenerife, Spain.

4. CIMEL Electronique, Paris, France.

by two motors, azimuth and zenith axes, the value of the pointing error, Θ_ξ , is normally given in spherical coordinates:

$$\Theta_\xi = \Theta_\xi(\xi_\varphi, \xi_\theta) \quad \text{Eq.1}$$

However, the scenarios conceived to estimate the pointing error calculate ξ_φ and ξ_θ but not the “total” pointing error Θ_ξ . Note, here, that if the pointing error is sufficiently small, it can be considered as an infinitesimal displacement (with $dr = 0$) and therefore the relation in Eq. (1) could be defined as an infinitesimal displacement in spherical coordinates:

$$\Theta_\xi = \sqrt{\xi_\theta^2 + \sin^2\theta_s \xi_\varphi^2} \quad \text{Eq.2}$$

One of the first results that we obtained with the tests made to characterize the sun-photometer pointing was precisely that the zenith component of the error, ξ_θ , was constant and the azimuth one, ξ_φ , was also constant if it was multiplied by $\sin(\theta_s)$; this result indicated that the pointing error should be understood as the scattering angle between the Sun beam and the direction where the detector is pointing. In order to make the description easier, from now on, the factorization of the total pointing error in spherical coordinates, $\Theta_{\xi\theta} = \xi_\theta$ and $\Theta_{\xi\varphi} = \xi_\varphi \sin(\theta_s)$, will be named as total vertical and horizontal error, respectively, keeping the names of zenith and azimuth error for ξ_θ and ξ_φ which are related to the two motor movements: zenith and azimuth.

2.2 Field of view

The field of view is an important characteristic of the sun photometers: in radiance measurements, a large field of view can yield to undesired averaging of radiances at sky regions near the sun in which the change of radiance with the scattering angle is steep. On the other hand, the direct solar irradiance measurements get biased by the amount of aureole radiation that is assumed to be direct solar radiation. An investigation on this particular topic in the frame of AERONET has been recently published [6]. According to the Cimel company, manufacturer of the sun-photometer Cimel-318, the value of the field of view in the current sun-photometers is 1.2° while in the old versions it was 2.4° .

Another important aspect which motivates the characterization of the sun photometers field of view is the so-called Vicarious calibration method [7], which provides a radiance calibration when the irradiance calibration and the solid view angle are known. In the cited work [7], the authors derive the solid view angle from a set of irradiance and radiance calibrations, the latter made using an integrating sphere with known radiance output. In this work, we will apply the vicarious method to

derive the field of view. This estimation is based on the AERONET direct sun and radiance calibrations, therefore it is independent of the geometrical measurements of the field of view that are described in the next section. A comparison of results from 3 instruments will be presented to make a first consistency check between methods.

3 NEW SCENARIOS: MATRIX AND CROSS

Before describing the new scenarios, it is necessary to briefly explain how the Cimel sun photometer points at the Sun during its automated operation. The photometer robot has origin positions in both the zenith and azimuth motors. These are found with the so-called PARK procedure or “scenario”. Once the parking position is achieved, the instrument tries to find the sun following an astronomical calculation (GOSUN scenario) based on site coordinates and time. Due to incorrect levelling or robot orientation this position is usually not perfect. Finally a 4-quadrant detector is used (TRACK scenario) to find the exact solar position. The 4-quadrant must be previously adjusted (initially by the manufacturer) so that the instrument finds the position of maximum signal on the detector while pointing at the sun or a solar simulator, which is assumed to be the optical axis of the system. The adjustment can be lost due to several reasons: incorrect manipulation for example during transport, dirtiness on the 4-quadrant window, deficient alignment during maintenance, etc.

3.1 Matrix measurement

The matrix measurement starts with go-sun and track scenarios (pointing to the Sun) and afterwards the Cimel moves towards right $\Delta\varphi=1^\circ$ and down $\Delta\theta=-1^\circ$. From this point it starts scanning the area around the Sun, going from down to up and right to left by steps of 0.01 until $\Delta\varphi=-1^\circ$ and down $\Delta\theta=1^\circ$ resulting in a total of 441 measurements. The total time used for the whole matrix measurement is 3.5 min. An example of a matrix measurement is given in the Fig. 1 (on the right) taken in Lille site on 22 September 2010 at 12:47:07 LT.

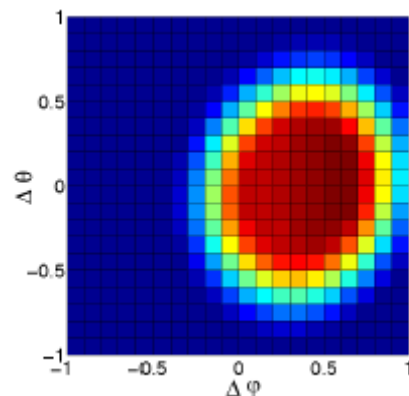


Fig. 1. Example of a matrix scenario taken in Lille site on 22 September 2010 at 12:47:07LT.

The image produced by the matrix (Fig. 1) seems to be wrong at first glance. The responsible of this strange result is the Sun movement during the matrix measurement.

Using the Sun movement algorithm presented in [8] a Sun movement correction is applied to all the matrix data, and re-sizing the matrix, the same matrix as in Fig. 1 is plotted in Fig. 2.

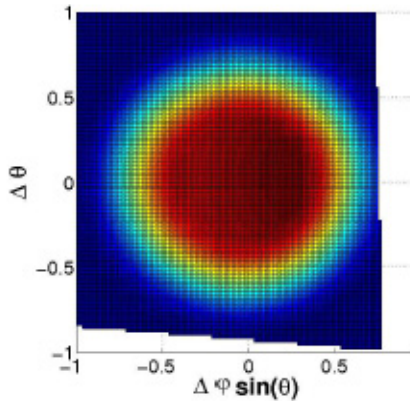


Fig. 2. Same matrix scenario as in fig.1 but corrected for the Sun displacement and with the azimuth displacement multiplied by $\sin(\theta_s)$.

3.2 Cross measurements

The Sun cross measurement starts tracking the Sun and then it moves downwards, $\Delta\theta = -4^\circ$. From this point, it moves up recording data for every step of 0.2° (scenario 0). Once it gets $\Delta\theta = 4^\circ$ it repeats the movements but backwards (scenario 1). Afterwards, it points to the Sun again and moves right, $\Delta\phi = 4^\circ$. From there, it moves left recording data every 0.2° , as well, until $\Delta\phi = -4^\circ$ (scenario 2), and then it repeats the movement towards right until $\Delta\phi = 4^\circ$ again (scenario 3).

Cross measurements need a correction of solar displacement too. Checking the timing recorded in the data files, from the beginning of the two tracking (considering tracking moment the time recorded in the scenario 0 and 2) until the end of scenario 1 and 3 the Sun photometer uses approximately 40 s. The correction is especially critical for azimuth angles during the summer season when a bias of 0.4° would appear otherwise.

4 POINTING ERROR ESTIMATIONS

4.1 Methodology

After describing the scenarios and the Sun movement correction, we will describe the methodology used to obtain the pointing bias with the matrix and the cross measurements. The analysis of the matrix measurements consists of obtaining the contour maps for levels between 20 and 80% of the

maximum value (with steps of 5%) for the different matrix. Every line level describes an ellipse, as shown in the example in Fig. 3.

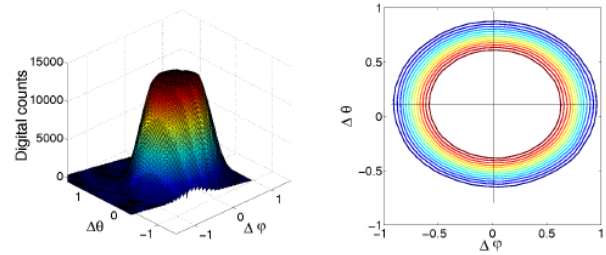


Fig. 3. Figure on the left, matrix measurement done in Valladolid site on 5 August 2010 at 13:41 LT with a SZA of 54.77° , on the right its contour map for levels from 20 to 80% of its maximum value (every 5%).

The value of the pointing error is estimated calculating all the centres and averaging them. A similar procedure is followed for the cross measurements. Using the data from scenarios 0 and 1 and scenarios 2 and 3 the data is interpolated at different heights of its maximum value, in this case from 20 to 80% with steps of 10%.

4.2 Preliminary results

The first tests with the matrix and cross measurements were done in Valladolid during summer 2010 with photometer #353, and in Lille during the early autumn 2010 with photometers #042 and #047. We also did some tests with photometers #420 and #143 in Valladolid during the autumn. Table 1 includes the dates and the description of all the data collected. Therefore, for these first tests, data were collected using 5 different sun-photometers. The measurements from #047 are split because two different robots were used during the measurement; when it was installed on the first robot, it showed some disagreements which are discussed separately. Once the photometer was set on the second robot, the disagreements disappeared.

Tables 2 and 3 contain the average and the standard deviation of the pointing error for all the data, except for the photometer #047(1) due to its fore-mentioned problems. Table 2 shows the results obtained for the horizontal pointing error (azimuth pointing error multiplied by $\sin(\theta_s)$) and Table 3 for vertical pointing error (or zenith pointing error). The same scheme is used for both tables, the column on the left, presents the results obtained by the matrix, the second column the result obtained by the cross while third and four columns present the results for every cross branch individually. The two scenarios provide practically the same pointing errors with absolute differences under 0.01° between them. This is a very important result as the scenarios are independent and the methodology followed to calculate the pointing error was done separately. Another important result is that the sun-photometers

point the Sun with an error under 0.01° except the photometer #143 whose tracking system seems to be biased 0.2° in both axes.

4.2 Pointing error monitoring in the field

The previous analysis suggested that matrix and cross measurements are both valid methods to estimate the pointing errors as well as good indicators of different issues, such as robot problems or dirtiness in the quadrant detector. After this, the cross measurement was proposed to be integrated as a part of the AERONET standard measurement protocol.

In order to integrate the cross measurement in the measurement protocol, the Cimel company designed a new E-eprom (5.20h), that adds 2 cross scenarios per day to the usual measurement protocol. These are all CE-318NE (“extended” model with 1640nm channel). Note that the pointing measurements in previous sections with the matrix and cross measurements, were based on the 1020nm Sun channel exclusively. Cimel sunphotometers have 2 optical channels (with 2 collimator tubes). Depending on the Cimel models, the sky measurements are taken with the second optical channel (standard model) or with the same optical channel (extended model), given that extended models use the second channel for short-wave infrared measurements at 1640 nm wavelength.

The 4-quadrant detector is unique though, therefore the parallelism between tubes may play a role. The choice of extended Cimel model for these measurements allows evaluating the pointing in both physical channels and provides an estimation of the parallelism between the two optical axes. This gives an estimation of the pointing error of the sky measurements in standard Cimels.

Seven sun-photometers belonging to AERONET-Europe, have been operated with these routine cross measurements twice a day for more than a year. As explained above, these are all CE-318NE (“extended” model). As an example, Fig. 4 shows the pointing error derived from crosses during 2012 for sun photometer #627 in both physical channels, corresponding to the UV-Visible and Infrared channels respectively. The two channels have different pointing axis and both of them stay within the prescribed specifications.

The pointing error observations derived from cross measurements have shown to be very stable over time, therefore they would allow: (a) correction of the pointing in the sky radiances, that could improve the inversion-derived products; (b) detection of mechanical problems. In Fig. 5, the time series of pointing error in the azimuth and zenith directions is shown for instrument #383. In the analyzed period the instrument was deployed at several sites (Autilla, Valladolid and Izaña). A mechanical problem of the first robot used at Autilla is clearly highlighted by the azimuth pointing error.

The problem is solved after the change of mounting robot. The installation in Valladolid shows very low and stable pointing errors. The last period in Izaña seems to present some deficiency in the zenith direction, very likely due to some robot problem again.

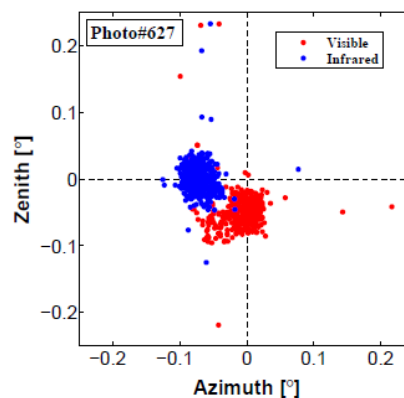


Fig. 4. Zenith and azimuth pointing error derived from cross measurements for sunphotometer #627 during 2012.

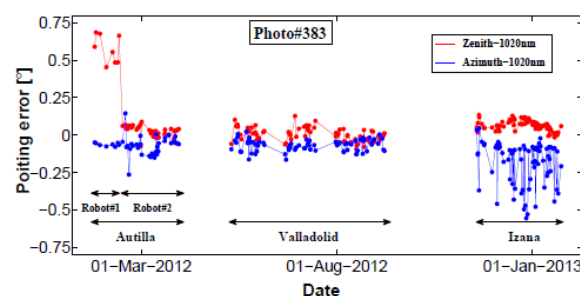


Fig. 5. Time series of zenith and azimuth pointing error derived from cross measurements for sun-photometer #383 during 2012.

Finally, Table 4 shows basic statistics on pointing errors for the photometers in the field for the 7 sun-photometer under analysis. The results are indicative of good pointing adjustment overall, with average pointing error below 0.01 in both directions for all the photometers except #421. For this photometer the average of the zenith pointing error is 0.24 and 0.14 , for visible and infrared channel respectively, though values up to 0.3 have been registered in specific measurements. Note, that most of the instruments were master instruments operating in calibration platforms (Izaña, Valladolid and Autilla) therefore it could be expected that different results are obtained from normal field instruments.

5 FIELD OF VIEW CALCULATIONS

In the work [9] a method is proposed to estimate the field of view of the solar radiometer PREDE (standard instrument of the Skynet network) from similar measurements to the matrix scenario.

Apart from the use of the Sun as a source, we also propose using a laser beam in the laboratory. The

utilization of a punctual source results not only in the value of the field of view but also with the opportunity to estimate the shape of the response of the field of view in the sun-photometer. Figure 6 shows an example of a matrix measurement in photometer #143 using the laser beam in the laboratory.

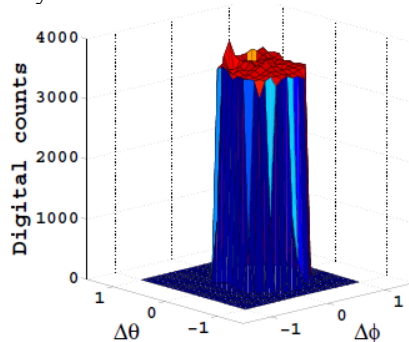


Fig. 6. Example of a matrix measurement using a laser beam with photometer #143.

The result of the tests are in accordance with those obtained in the field (using the sun as a source) with differences under 5% as shown in Table 5. The FOV calculations from the vicarious method are also represented in Table 5 and the results agree better than 3% with respect to the other technique for both light sources.

6 CONCLUSIONS

The pointing error of Cimel-318 sun-photometer has been determined through the utilization of two new measurement scenarios: cross and matrix. However, the raw data produced by these new scenarios have been shown insufficient for a correct evaluation of the pointing error and a correction to account for Sun movement during the measurement has been also implemented. In a preliminary study on several sun-photometers applying the methodology proposed in this work, the results obtained have revealed that both scenarios, cross and matrix, are equivalent with differences in the evaluation of the pointing error below 0.01. For this reason, and due to the large amount of memory that is needed to record the data of matrix scenario, only the cross scenario has been integrated as a part of the AERONET standard protocol for field measurements. The analysis of the first results has indicated that, in general, the value of the pointing error in AERONET sun-photometers is smaller than 0.01 though in some instruments values up to 0.03 have been registered. Moreover, the pointing error has shown a stable behaviour during the time and independent of the solar zenith angle, which can be used to detect other problems during the measurement process such as mechanical problems in the robots or dirtiness in the quadrant detector.

Using the matrix scenario, the field of view of three sun-photometers has been characterized using the sun and a laser beam as a punctual source. Both results have been compared with those obtained by the vicarious method showing differences under 3% between them.

ACKNOWLEDGMENT

The authors are grateful to NASA-GSFC, PHOTONS and RIMA teams for their long-standing collaboration and for operating and maintaining the AERONET network. The research leading to these results has received funding from the European Union Seventh Framework Programme (FP7/2007e2013) under grant agreement Nr. 262254 [ACTRIS]. Financial supports from the Spanish MINECO (projects of ref. CGL2009-09740, CGL2011-23413, CGL2012-33576 and Acción Complementaria CGL2011-13085-E) are also gratefully acknowledged. We also thank the Environmental Council of the CyL Regional Government (Consejería de Medio Ambiente, Junta de Castilla y León) for supporting this research.

REFERENCES

- [1] Holben, B., Eck, T., Slutsker, I., Tanre, D., Buis, J., Setzer, A., Vermote, E., Reagan, J., Kaufman, Y., Nakajima, T., Lavenu, F., Jankowiak, I., and Smirnov, A.: AERONET - A federated instrument network and data archive for aerosol characterization, *Remote Sens. Environ.*, 66, 1–16, 1998.
- [2] Dubovik, O. and King, M.: A flexible inversion algorithm for retrieval of aerosol optical properties from Sun and sky radiance measurements, *J. Geophys. Res.-Atmos.*, 105, 20 673–20 696, 2000.
- [3] Dubovik, O., Smirnov, A., Holben, B., King, M., Kaufman, Y., Eck, T., and Slutsker, I.: Accuracy assessments of aerosol optical properties retrieved from Aerosol Robotic Network (AERONET) Sun and sky radiance measurements, *J. Geophys. Res.-Atmos.*, 105, 9791–9806, 2000.
- [4] Dubovik, O., Holben, B., Eck, T., Smirnov, A., Kaufman, Y., King, M., Tanre, D., and Slutsker, I.: Variability of absorption and optical properties of key aerosol types observed in worldwide locations, *J. Atmos. Sci.*, 59, 590–608, 2002.
- [5] Dubovik, O., Sinyuk, A., Lapyonok, T., Holben, B. N., Mishchenko, M., Yang, P., Eck, T., Volten, H., Munoz, O., Veihelmann, B., Van Der Zande, W. J., Leon, J., Sorokin, M., and Slutsker, I.: Application of spheroid models to account for aerosol particle nonsphericity in remote sensing of desert dust, *J. Geophys. Res.-Atmos.*, 111, 2006.
- [6] Sinyuk, A., Holben, B. N., Smirnov, A., Eck, T. F., Slutsker, I., Schafer, J. S., Giles, D. M., and Sorokin, M.: Assessment of error in aerosol optical depth measured by AERONET due to aerosol forward scattering, *Geophys. Res. Lett.*, 39, 90–108, 2012. 302
- [7] Li, Z., Blarel, L., Podvin, T., Goloub, P., Buis, J.-P., and Morel, J.-P.: Transferring the calibration of direct solar irradiance to diffuse-sky radiance measurements for CIMEL Sun-sky radiometers, *Appl. Optics*, 47, 1368–1377, 2008.
- [8] Reda, I. and Andreas, A.: Solar position algorithm for solar radiation applications (vol. 76, p. 577, 2004), *Sol. Energy*, 76, 577–589, 2007.
- [9] Nakajima, T., Tonna, G., Rao, R., Boi, P., Kaufman, Y., and Holben, B.: Use of sky brightness measurements from ground for remote sensing of particulate polydispersions, *Appl. Optics*, 35, 2672–2686, 1996.

Table 1. Summary of the cross and matrix measurements done in the preliminary result tests.

Station	Photometer	Starting date	Ending date	Valid measur.
Valladolid	#353	04/08/2010	06/08/2010	19
Lille	#042	22/09/2010	24/09/2010	38
Valladolid	#143	08/10/2010	17/10/2010	110
Lille	#047(1)	09/10/2010	12/10/2010	107
Valladolid	#420(1)	18/10/2010	18/10/2010	34
Lille	#047(2)	21/10/2010	28/10/2010	65
Valladolid	#420(2)	09/11/2010	11/11/2010	27

Table 2. Summary of the horizontal pointing error ($\Theta_{\xi\phi} = \xi_{\phi} \sin(\theta_s)$) for several sun photometers in the preliminary result tests.

Photo.	MATRIX		CROSS		Cross - Scen(2)		Cross - Scen(3)	
	mean	std	mean	std	mean	std	mean	std
#353	0.041	0.021	0.050	0.024	0.044	0.023	0.057	0.023
#042	-0.058	0.018	-0.062	0.016	-0.065	0.016	-0.059	0.016
#143	0.163	0.019	0.156	0.020	0.148	0.029	0.163	0.021
#420(1)	0.115	0.017	0.118	0.019	0.115	0.019	0.120	0.020
#047(2)	-0.110	0.027	-0.108	0.024	-0.109	0.023	-0.107	0.025
#420(2)	-0.082	0.015	-0.069	0.017	-0.093	0.130	-0.067	0.019

Table 3. Summary of the vertical pointing error ($\Theta_{\xi\theta} = \xi_{\theta}$) of several sun photometers in the preliminary result tests.

Photo.	MATRIX		CROSS		Cross - Scen(0)		Cross - Scen(1)	
	mean	std	mean	std	mean	std	mean	std
#353	0.079	0.020	0.079	0.015	0.084	0.014	0.073	0.016
#042	0.021	0.018	0.020	0.018	0.022	0.018	0.019	0.019
#143	-0.199	0.021	-0.208	0.022	-0.210	0.024	-0.207	0.029
#420(1)	0.025	0.019	0.019	0.015	0.023	0.015	0.016	0.015
#047(2)	-0.046	0.020	-0.049	0.025	-0.034	0.023	-0.064	0.026
#420(2)	0.052	0.019	0.053	0.023	0.065	0.050	0.049	0.023

Table 4. Pointing error statistics for the 7 analyzed photometers in the azimuth (Az) and zenith (Zn) directions for the visible (vis) and infrared (ir) channels.

	Az_{vis}	Zn_{vis}	Az_{ir}	Zn_{ir}	Valid measur.
383	-0.06	0.03	-0.06	0.04	92
390	-0.06	-0.06	-0.08	-0.06	43
419	-0.05	-0.08	-0.08	-0.09	150
421	-0.02	0.24	-0.04	0.14	411
513	-0.04	0.01	-0.02	0.05	51
544	-0.07	0.10	-0.10	0.02	161
627	-0.01	-0.05	-0.07	0.00	287
Total	-0.04	0.07	-0.06	0.04	1196

Table 5. Comparison of the field of view results obtained using the Sun and a laser beam as a source.

Photo.	Sun	Laser	Vicarious
#353	1.30	1.30	1.30
#143	1.14	1.19	1.17
#420	1.32	1.29	1.31

A comparison between almucantar and principal plane retrieval products within AERONET network

B. Torres^{1,2}, C. Toledano¹, O. Dubovik², V. Cachorro¹, A.J. Berjón¹, T. Lapyonak², P. Goloub²

Abstract — Aerosol Robotic Network (AERONET) data are widely used for characterizing the aerosol optical and microphysical properties, which are retrieved from direct Sun and almucantar radiance measurements by inversion procedure. The network also measures radiances in the principal plane geometry which are susceptible to be inverted. In this study, the aerosol products from both retrievals are compared. In particular, the differences in the AERONET retrievals from near simultaneous principal plane and almucantar measurements have been analyzed at three different key sites: Mongu (biomass burning), Beijing (urban) and Solar Village (desert dust). The analyzed parameters have been the size distribution, the single scattering albedo and the refractive index. Differences in the size distribution are generally under 10% for radii between 0.1 μ m and 5 μ m. Outside this size range, the differences can be as large as 50%. With respect to the optical parameters, the observed differences are within AERONET estimated uncertainties. The largest differences have been found for the retrievals of desert dust.

Keywords — Aeronet, Aerosol retrieval, Inversion

1 INTRODUCTION

The AEROSOL ROBOTIC NETWORK (AERONET [1]) program was started by the National Aeronautics and Space Administration (NASA) in the 90's, in collaboration with PHOTONS (Laboratoire d'Optique Atmosphérique, LOA, University of Lille), as a federation of networks with regional or national extent deployed on ground in the form of stations for monitoring atmospheric aerosols. AERONET aims at providing reliable monitoring of global aerosol optical and microphysical properties, to facilitate the characterization of the aerosol properties, the validation of satellite products related to the aerosol as well the synergy with other instrumentation (lidar, surface radiation, in situ aerosol, etc.).

The standard AERONET instrument is the Cimel Electronique 318. This is an automatic sun and sky radiometer, equipped with 8 or 9 spectral channels covering the spectral range 340-1640 nm. It performs both direct Sun measurements and sky radiance observations in the almucantar and principal plane configurations.

All AERONET are processed by a common algorithm at NASA and uploaded to the website in near real time. Level 1.0 data are unscreened and level 1.5 are cloud screened, although these may not have the final calibration applied and therefore they are not quality assured. After the calibration post-deployment, the data are reprocessed (assuming

linear change rate in the calibration coefficients) and manually inspected, following set of criteria (http://aeronet.gsfc.nasa.gov/newweb/PDF/AERONETcriteria_final1.pdf). If the data fulfil the criteria, they are raised to the level 2.0 (quality assured data [2]). The data are distributed through the AERONET website. The unique source of data ensures that the latest version of the data processing is used. Note that the network database is being constantly upgraded, improving the quality and the amount of the products provided as new requirements and algorithms are implemented. Since 2006 the Version 2 Direct Sun and Inversion Algorithm is operational [2]. It has introduced notable improvements respect to Version 1; for instance, the treatment of particle nonsphericity (see [3]) or the use of a database for the surface reflectance. More details and their references can be gained in the AERONET website (http://aeronet.gsfc.nasa.gov/new_web/data.html).

The AERONET inversion algorithm, described in [4] allows the network to provide columnar optically effective aerosol properties (for instance, volume size distribution, refractive index and single scattering albedo) from both radiance measurements and the AOD retrieved through direct sun measurements.

The inversion strategy together with the accuracy of the AERONET data achieved by strict protocols, have produced valuable information about aerosol properties at key sites after several years of continuous measurements. Although the inversion strategy presented by [4] is not related to the geometry of the radiance measurement, most of the works found in the literature, using AERONET data, have been obtained exclusively using almucantar measurements. The main reason for this is that, even

1. *Group of Atmospheric Optics, Valladolid University, Valladolid, Spain.*
2. *Laboratoire d'Optique Atmosphérique, Université des Sciences et Technologies de Lille, Villeneuve d'Ascq, France.*
3. *Izana Atmospheric Research Center, Spanish Meteorological Agency (AEMET), Tenerife, Spain.*

though radiance measurement are carried out within AERONET following principal plane and almucantar geometries, only retrievals obtained from the latter are shown in AERONET webpage. The symmetry existing in almucantar confers a greater confidence to this geometry since averaging left and right branches of the measurements is possible. Also, the symmetry allows cloud screening which cannot be easily implemented for the principal plane.

Nevertheless, principal plane measurements are also processed and internally available. The main advantages of principal plane retrievals is that they provide more stable inversion results around noon due to the observation of larger scattering angle range. There are known limitations in the inversion of almucantar data at low solar zenith angles (SZA) as reported by [5].

The present study tries to shed some light on the comparison between the retrieved aerosol properties from both geometries. For this purpose, we have analyzed the differences in the retrievals from almost simultaneous principal plane and almucantar measurements at three different key sites: Mongu (biomass burning), Beijing (urban) and Solar Village (desert dust). The retrieved parameters analyzed have been the size distribution, the single scattering albedo and the refractive index.

2 METHODOLOGY AND DATA

Data from three AERONET sites characteristic of three different types of aerosol were chosen in order to compare the results obtained from the inversion of principal plane and almucantar. Mongu (Zambia, 15.25° S-23.15° E, 1107.0 msl) was chosen for the analysis of biomass burning aerosol, Beijing (China, 39.98° N-116.38° E, 92.0 msl) for urban aerosol and Solar Village (Saudi Arabia, 24.90° N-46.40° E, 790 msl) for desert dust aerosol. We have only selected data which accomplished the next four requirements: 1.- Data belonging to AERONET Level 2.0 (quality assured); 2.- Data from those days where the division of the standard deviation by the average of the aerosol optical depth values was smaller than 0.1 (evaluated for the four wavelengths used by the inversion 440, 670, 870 and 1020 nm). This requirement was established in order to assure that the analysis was done for stable aerosol conditions. 3.- The pairs almucantar and principal plane were selected only if both measurements took place within a maximum delay of 30 minutes. 4.- Finally, only those days presenting at least 4 pairs matching the previous three conditions were chosen for the comparison. Following these previous requirements, a total of 174 pairs were taken for the comparison, of which 65 pairs belong to biomass burning, 59 pairs to urban aerosol and 50 pairs to desert dust.

3 RESULTS

As commented in the introduction, the comparison between the aerosol properties retrieved from almucantar and principal plane measurements has been done for the aerosol size distribution, the single scattering albedo and the refractive index. Relative differences have been used to represent the results for the size distribution, while for the optical parameters absolute differences have been chosen. The sign has been kept to distinguish in every case which results are larger from both retrievals. In the criteria selected positive differences correspond to higher values in principal plane retrievals while negative differences mean that the almucantar retrievals reach higher values.

3.1 Size Distribution

Figure 1 represents the mean and standard deviation (error bars) of the relative differences obtained for the comparison of the size distribution in the three analyzed cases: biomass burning (upper part of the figure), urban (central part of the figure) and desert dust (lower part of the figure).

Observing the figure, we can see how the comparisons for the three aerosol types present some common characteristics. If we first evaluate the part for radii between 0.1 μ m and 5 μ m, we can note that the average of the relative differences as well as the standard deviation present the lowest values in this region. These results indicate that the differences are not strongly biased even though the almucantar values are slightly higher: the values of the average of the relative differences are mostly negative and under 10%, except for the radii around 2 μ m where the average is a bit higher reaching maximum values up to 20%. On the other hand, the results show that this zone present the highest similarity in the retrievals (principal plane vs almucantar) with values of the standard deviation bounded by 15%.

Urban type shows the lowest differences for radii between 0.1 < r < 5 μ m (middle figure). The comparison is even better between 0.2 μ m and 1 μ m where the values of the relative differences are smaller than 4%. On the contrary, biomass burning presents the highest values for this zone, in fact, the maximum value (19.5%) is obtained for this aerosol type. The desert dust type exhibits intermediate values in this size range with maximum values around 15%. Finally, it is worth mentioning that even though the almucantar values are mostly higher in this size range than the principal plane ones (negative values of relative differences), there is a small region where the principal plane results are higher for the three aerosol types. The maximum positive value in this size range is 11.3% and is obtained for the desert dust at r = 0.76 μ m. Moving to the extremes, for radii shorter than 0.1 μ m or larger than 5 μ m, the comparison is much worse than in the previous analyzed region. In this manner, the means

of the relative differences are much larger and positive (up to 60%), indicating that the values in the size distribution obtained from the almucantar are systematically lower than those obtained using the principal plane. At the same time, the standard deviations of the differences are much larger too, reaching values up to 40%.

Among the three aerosol types, the biomass burning shows the smallest discrepancies in the extremes; for this aerosol type, the differences are under 22% except for the last bin (at 15 μm) where the relative difference is 44%. Desert dust case presents the worst behaviour, especially in the coarse mode, where for several bins the relative differences exceed 40% reaching the maximum of 60% at 11.4 μm .

These larger discrepancies in the extremes were expected since as it was pointed out in [5] the contribution of these particles to the measured optical characteristics is significantly smaller than for particles of intermediate sizes, and therefore, the errors associated to these radii are much larger. Nevertheless, the values of the volume concentration in these zones are normally quite lower compared to those obtained for 0.1 μm < r < 5 μm and consequently the absolute errors are also small.

3.2 Optical Parameters

The analysis of the optical parameters has been restricted to the single scattering albedo and the refractive index. Table 1 contains the mean values and the standard deviations obtained for both parameters in the analyzed days using only almucantar geometry. The values obtained for the biomass burning aerosol in Mongu and for the desert dust in Solar Village are similar to those presented in [6]. For instance, $\omega(440) = 0.85$ corresponding to the analysis of the biomass burning is comparable to the one obtained $\omega(440) = 0.88$. The values retrieved for the desert dust in Solar Village are in a better agreement being even within the typical ranges found in [6]. Finally, it should be noted that Beijing site was not included in the analysis done in [6]; however the mean values found for the urban aerosol of this analysis agree with the typical values of the several urban aerosol examples presented there.

Returning to the comparison between the principal plane and almucantar retrievals, the results for the single scattering albedo are shown in figure 2. The mean of the differences between both inversions are plotted against the wavelength for the three aerosol cases analyzed: biomass burning (gray), urban (blue) and desert dust (orange). Once again, the standard deviation of the differences is represented using the error bar.

As it can be seen in the plot, the average of the differences is under 0.01 for the three analyzed cases and for the four wavelengths, reaching the highest value (0.007) at 440 nm for the desert dust. The

standard deviation is under 0.01 for the biomass burning and the urban aerosol, being a bit higher for the desert dust aerosol where values around 0.02 are obtained.

Figure 3 shows the results for the real part of the refractive index. While the standard deviation does not depend on the aerosol type, with a value about 0.03 for the three cases, we observe that the average of the difference is higher for the desert dust than for the other two cases. The averaged values of the difference for biomass burning and urban aerosol are lower than 0.005 indicating that there is no tendency between principal plane and almucantar differences; on the contrary, the average for the desert dust is about 0.03, or in other words, the values of the real part of the refractive index retrieved using principal plane are on average significantly higher than the ones obtained using almucantar for the desert dust.

The last part of the analysis regarding optical parameters contains the comparison for the imaginary part of the refractive index. Figure 4 depicts the averages and the standard deviations of the absolute differences for the three aerosol examples and the four wavelengths. Contrary to the previous cases, the highest standard deviations of the absolute differences are reached for the biomass burning aerosol presenting values around 0.003. On the other hand, the values for desert dust and urban aerosol are enclosed between 0.0014 and 0.002. It should be remembered (table 1), that the absolute values of the imaginary part of the relative index for the biomass burning are one order of magnitude higher than those for the desert dust and around twice as large as the ones for the urban aerosol. Therefore, in relative terms, the best comparison is obtained again for biomass burning and urban aerosol.

The strong correlation between the imaginary part of the refractive index and the single scattering albedo makes, that the mean values of the two magnitudes present their sign exchanged for the three cases and the four wavelengths. Using table 1, we observe that the average of the differences, principal plane vs almucantar, of the imaginary part of the refractive index are at maximum 8% for the desert dust aerosol, 6% for the urban aerosol and 4% for biomass burning. Adding this result to the ones obtained for the single scattering albedo and the real part of the refractive index, we can conclude that there is an excellent agreement between the optical parameters retrieved by principal plane and almucantar geometries.

4 CONCLUSIONS

The comparison presented in the previous section involving 174 pairs of data reveals that, in general, the agreement between the retrieved aerosol parameters obtained from principal plane and almucantar measurements is within the estimated

uncertainties given by AERONET for almucantar retrievals. Indeed, if we limit the study to biomass burning and urban aerosol, the differences in the optical parameters are almost negligible (e.g. absolute differences in the single scattering albedo under 0.01). Analyzing the results of the size distribution for the same aerosol types, we observe that the relative differences are generally under 10% for radii between 0.1 μm and 5 μm , though growing rapidly when moving to the extremes. This result was expected due to, basically, the loss of sensitivity of the retrievals to particles of those sizes for the wavelengths used in AERONET [5].

ACKNOWLEDGMENT

The authors are grateful to NASA-GSFC, PHOTONS and RIMA teams for their long-standing collaboration and for operating and maintaining the AERONET network. The research leading to these results has received funding from the European Union Seventh Framework Programme (FP7/2007e2013) under grant agreement Nr. 262254 [ACTRIS]. Financial supports from the Spanish MINECO (projects of ref. CGL2009-09740, CGL2011-23413, CGL2012-33576 and Acci3n Complementaria CGL2011-13085-E) are also gratefully acknowledged. We also thank the Environmental Council of the CyL Regional Government (Consejer3a de Medio Ambiente, Junta de Castilla y Le3n) for supporting this research.

REFERENCES

- [1] Holben, B., Eck, T., Slutsker, I., Tanre, D., Buis, J., Setzer, A., Vermote, E., Reagan, J., Kaufman, Y., Nakajima, T.,

- Lavenu, F., Jankowiak, I., and Smirnov, A.: AERONET - A federated instrument network and data archive for aerosol characterization, *Remote Sens. Environ.*, 66, 1–16, 1998.
 Holben, B. N., Eck, T. F., Slutsker, I., Smirnov, A., Sinyuk, A., Schafer, J., Giles, D., and Dubovik, O.: AERONET's Version 2.0 quality assurance criteria, in: *Remote Sensing of the Atmosphere and Clouds*, edited by Tsay, S., Nakajima, T., Singh, R., and Sridharan, R., vol. 6408 of Proc. SPIE, p. Q4080, doi:10.1117/12.706524, conference on Remote Sensing of the Atmosphere and Clouds, Goa, INDIA, NOV 13-16, 2006, 2006.
 [2] Dubovik, O., Sinyuk, A., Lapyonok, T., Holben, B. N., Mishchenko, M., Yang, P., Eck, T., Volten, H., Munoz, O., Veihelmann, B., Van Der Zande, W. J., Leon, J., Sorokin, M., and Slutsker, I.: Application of spheroid models to account for aerosol particle nonsphericity in remote sensing of desert dust, *J. Geophys. Res.-Atmos.*, 111, 2006.
 [3] Dubovik, O. and King, M.: A flexible inversion algorithm for retrieval of aerosol optical properties from Sun and sky radiance measurements *J. Geophys. Res.-Atmos.*, 105, 20 673–20 696, 2000.
 [4] Dubovik, O., Smirnov, A., Holben, B., King, M., Kaufman, Y., Eck, T., and Slutsker, I.: Accuracy assessments of aerosol optical properties retrieved from Aerosol Robotic Network (AERONET) Sun and sky radiance measurements, *J. Geophys. Res.-Atmos.*, 105, 9791–9806, 2000.
 [5] Dubovik, O., Holben, B., Eck, T., Smirnov, A., Kaufman, Y., King, M., Tanre, D., and Slutsker, I.: Variability of absorption and optical properties of key aerosol types observed in worldwide locations, *J. Atmos. Sci.*, 59, 590–608, 2002.

Table 1. Mean values and standard deviations obtained for the single scattering albedo and the refractive index in the analyzed days using only almucantar geometry.

Wavelength [nm]		$\omega(\lambda)$				$n(\lambda)$				$k(\lambda)$			
		440	670	870	1020	440	670	870	1020	440	670	870	1020
Bio. Burn. (Mongu)	mean	0.85	0.81	0.78	0.76	1.53	1.53	1.54	1.54	0.032	0.032	0.030	0.027
	std	0.03	0.05	0.05	0.05	0.04	0.03	0.03	0.03	0.012	0.013	0.012	0.011
Urban (Beijing)	mean	0.92	0.92	0.90	0.89	1.48	1.49	1.49	1.49	0.016	0.011	0.012	0.012
	std	0.05	0.03	0.04	0.04	0.03	0.03	0.04	0.03	0.009	0.005	0.005	0.005
Desert dust (Solar Vil.)	mean	0.90	0.92	0.94	0.94	1.51	1.54	1.54	1.54	0.006	0.004	0.004	0.004
	std	0.02	0.03	0.03	0.03	0.05	0.03	0.03	0.03	0.003	0.003	0.002	0.002

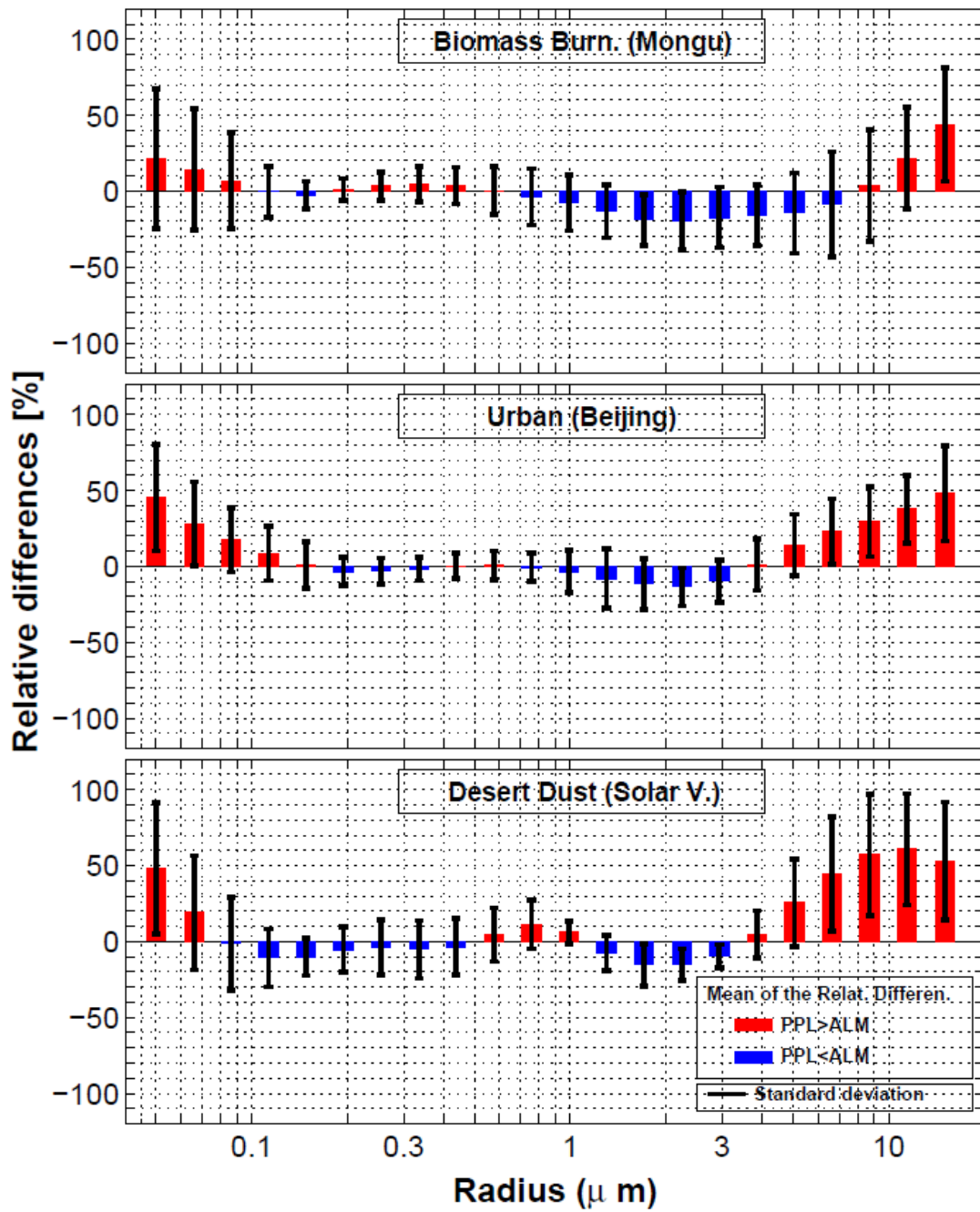


Fig. 1. Relative differences found in the size distribution between the inversion obtained by almucantar and principal planes for the three analyzed cases: biomass burning (upper part of the figure) urban (central part of the figure) and desert dust (lower part of the figure).

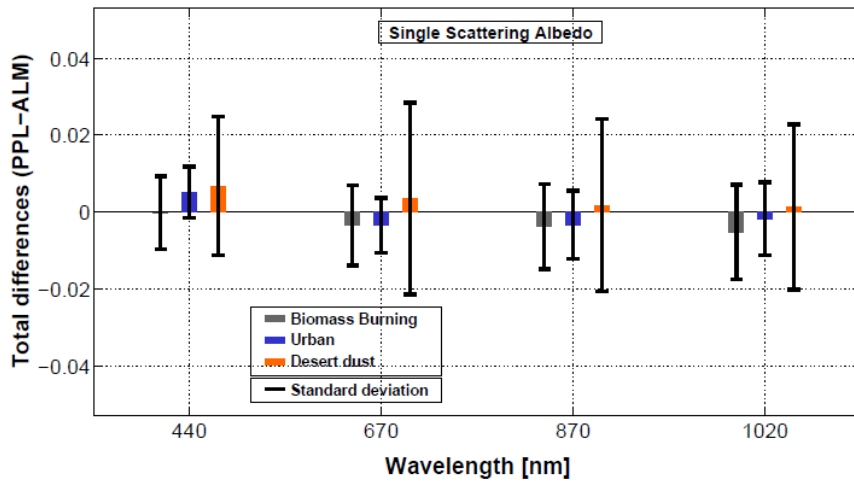


Fig. 2. Absolute differences found in the single scattering albedo between the inversion obtained by almucantar and principal planes for the three analyzed cases: biomass burning (gray) urban (blue) and desert dust (orange). Bars indicate the standard deviation of the differences

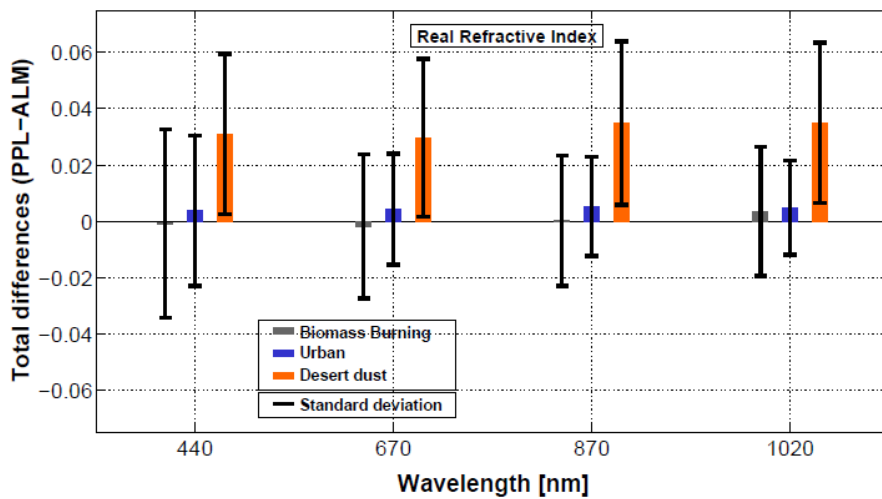


Fig. 3. Absolute differences found in the real part of refractive index between the inversion obtained by almucantar and principal planes for the three analyzed cases: biomass burning (gray bar) urban (blue bar) and desert dust (orange bar).

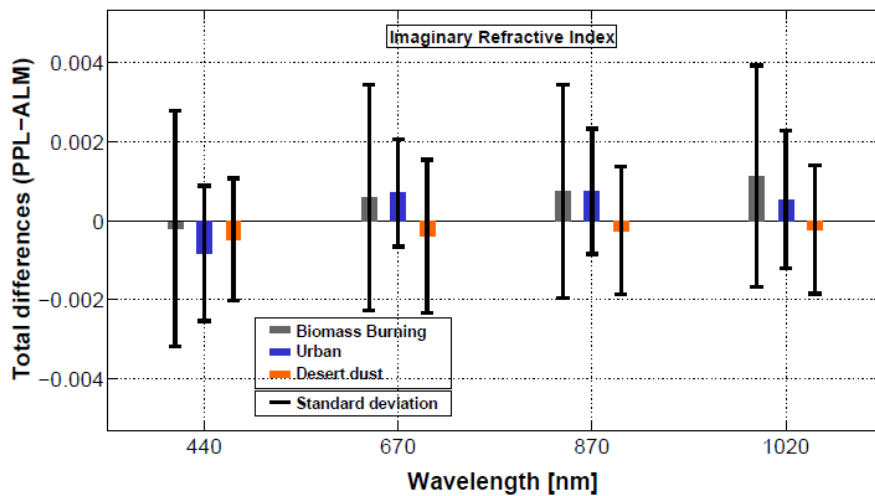


Fig. 4. Absolute differences found in the imaginary part of refractive index between the inversion obtained by almucantar and principal planes for the three analyzed cases: biomass burning (gray bar) urban (blue bar) and desert dust (orange bar).

Study of aerosol hygroscopic growth inside a well-mixed boundary layer by means of multi-wavelength Raman lidar

F. Molero, A.J. Fernández, F. J. Gómez-Moreno, E. Alonso, M. Becerril, M. Pujadas & B. Artíñano

Abstract — The radiative budget of the earth is influenced by atmospheric aerosols and water content, both with highly variable spatial and temporal distributions. Lidar techniques represent a powerful tool to study them because of their capability to provide aerosol optical properties and water vapor profiles with high resolution both in time and vertical dimension. The primary objective of this work is to investigate the hygroscopic growth of aerosol inside a well-mixed boundary layer, with the aim to study the influence of aerosols on cloud formation processes. Profiles from a multi-wavelength Raman lidar, supported by ground-level measurements, were measured on a relevant synoptic situation. The aerosol optical properties can yield information about the growth of aerosols as a function of relative humidity. The vertically-resolved experimental results obtained for those parameters were compared with numerical calculations based on Mie theory, using size distributions measured at ground-level, in order to establish theoretically the effect of humidity on these parameters. Several relevant features observed on the case analyzed are commented.

Keywords — Aerosols, hygroscopic growth, lidar, Raman

1 INTRODUCTION

The complex relationship between atmospheric aerosols and cloud properties represents one of the largest uncertainties in aerosol radiative forcing of climate [1]. The clearest observational evidence for this indirect aerosol effect [2] is provided by ship tracks [3], which are trails caused by effluent from ships that change the cloud microstructure by redistributing their water into a larger number of smaller droplets than ambient low-level clouds. The drizzle that normally occurs in marine stratocumulus clouds in clean air would be inhibited from the clouds with reduced droplet size, thereby increasing the cloud water content and longevity [4]. Recently, ship track-like features in clouds over land, created by major urban and industrial pollution sources, were observed from weather satellites [5].

An accurate understanding of the interdependent microphysical, chemical, and dynamic processes that characterize the aerosol-cloud system in the atmosphere, is required to quantify the effect of aerosols on the albedos and lifetimes of clouds, the so-called first [6] and second [4] indirect effects. The rates at which cloud particles form, grow and fall out of clouds depend on the concentrations, sizes and chemical compositions of the aerosol particles, but also on the humidity, temperature and vertical velocity of the airmass [7]. Anthropogenic modification of the concentrations and chemical compositions of aerosol particles might therefore

influence cloud properties, weather and climate. Anthropogenic particles are most highly concentrated in the lower atmosphere, so the indirect effect is expected to be most important in low-level clouds, especially on convective clouds on top of the planetary boundary layer (PBL hereafter), that ingests air mainly through its base, rich in PBL aerosols. Over a continental site, two main types of aerosols may be distinguished, continental aerosol confined to the PBL and background aerosol in the free troposphere. This background aerosol can be regarded as an aged continental aerosol.

Atmospheric aerosol particles change their size with relative humidity due to uptake or release of water [8]. This hygroscopic growth of aerosols affects their optical properties, such as the scattering of light by aerosols that will be enhanced because of the water absorbed and condensed on aerosols and the size growth of aerosols. This influence on the optical properties and the fact that the aerosol-cloud interaction occurs at altitudes where the atmospheric parameters reach cloud formation conditions, make remote sensing techniques suitable candidates to study this effect. Lidar techniques represent a powerful tool because of their capability to provide aerosol and water vapour profiles simultaneously with high resolution both in time and vertical dimension.

In this work we present the results obtained by the CIEMAT-Madrid multi-wavelength Raman Lidar system in relevant meteorological situation, especially cases with well-mixed PBL under a cloud deck, when the relative humidity profile increases smoothly from its surface value up to 100% at cloud base. Lidar-derived optical parameters yield

1. All authors are with the Department of Environment, CIEMAT, Madrid, 28040, Spain. E-mail: f.molero@ciemat.es

information about the growth of aerosols as a function of relative humidity. Numerical calculations based on Mie theory, using size distributions measured at ground-level help to establish theoretically the effect of humidity on these parameters.

2 EXPERIMENTAL

2.1 site description

Experimental data were taken at Madrid (40.45°N, 3.73°W, 663 m asl). The experimental site was the CIEMAT (Centro de Investigaciones Energéticas, Medioambientales y Tecnológicas) premises, located in the Madrid northwest city outskirts, which can be considered as an urban background site. The Madrid metropolitan area is located in the center of the Iberian Peninsula, bordered to the north–northwest by a high mountain range (Sierra de Guadarrama) 40 km from the city, and to the northeast and east by lower mountainous terrain. The population of the metropolitan area of Madrid is nearly 6 million inhabitants, with a car fleet of almost 3 million vehicles. Since its industrial activity consists mainly of light factories, the Madrid atmosphere is typically urban, fed by traffic emission and also by domestic heating in winter.

2.2 Instrumentation

The multiwavelength Raman Lidar system is based on a monostatic biaxial configuration pointing vertically to the zenith and emits the fundamental, second and third harmonic of a Nd:YAG 30 Hz laser. Lidar signal was registered in 1-min integrated time, with vertical resolution of 3.75 m. The receiving line consists of a 30-cm-diameter Newtonian telescope with a multiwavelength detection module based on dichroic mirrors and interferential filters. The collected radiation is split into seven channels allowing the detection of elastic signals at 1064, 532 and 355 nm and three Raman channels at 387 and 607 nm (nitrogen Raman-shifted signal from 355 and 532 nm, respectively) and 408 nm (water vapor Raman-shifted signal from 355 nm). This experimental configuration allows simultaneous retrieving of vertically-resolved water vapor and aerosols properties. The water profiles are determined by the ratio between the water vapor 355 nm-Raman-shifted signal and the nitrogen 355 nm-Raman-shifted signal [9] and are provided in mixing ratio units. Multi-wavelength lidars provide additional information on aerosol microphysical properties due to the wavelength dependence of the backscattering and extinction coefficients [10].

At ground level, the temporal evolution of particle number and dry ambient sub-micrometer size distributions in the size range of 0.015–0.661 μm were monitored at the site by using a Scanning

Mobility Particle Sizer (TSI SMPS 3936), combining a long Differential Mobility Analyzer (DMA) and a Condensation Particle Counter (CPC model 3775) working in the scanning mode. For particles in the size range of 0.3–20.0 μm , an Optical Particle Counter (GRIMM 1108) was used, obtaining a single plot for number distributions between 0.015 to 20 μm by joining the data from both instruments.

3 RESULTS

Regular lidar measurements are performed at the CIEMAT site since May 2012. For instance, Fig 1 shows a 150 min color-coded plot of the 7 May 2013 measurement between 01:18 and 03:47 UTC. This night, a cloud deck (red) about 1 km width was observed over the PBL, placed between 2 and 3 km height agl. The sub-cloud layer (yellow) is expected to be well-mixed due to the influence of shear-induced mixing but also due to top-down mixing related to the destabilization of the boundary layer associated to the cloud top radiative cooling. Thus, the relative humidity profile is expected to increase smoothly from its surface value up to 100% at cloud base. Also, aerosol concentration is more likely to be uniform with height in a neutrally stratified (well-mixed) boundary layer. In order to assess them, the lidar signals were averaged 30 min, between 01:35 and 02:05 UTC. The backscattering coefficients and relative humidity profiles are shown in fig 3 and 4 respectively. Measurements were taken at nighttime due to the strong effect of the solar light on the Raman channels, which prevent an accurate measurement of the humidity at daytime. The meteorological situation and cloud microphysical properties for that day were studied using MODIS images.

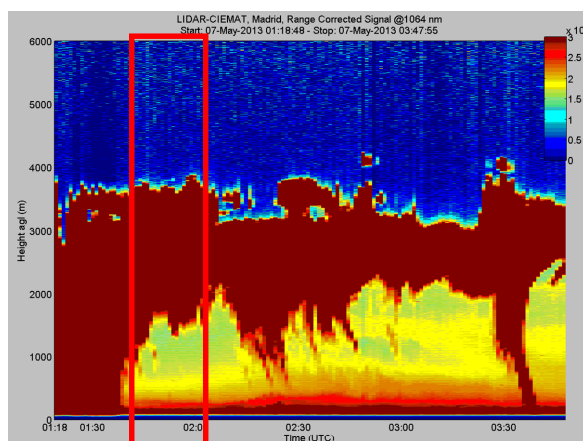


Fig. 1 Color-coded plots of the range-corrected 1064 nm lidar signals vs time and height from surface up to 6 km agl for the measurement session of 7 May 2013, between 01:18 and 03:47 UTC. Red box indicate the time period averaged for optical properties study

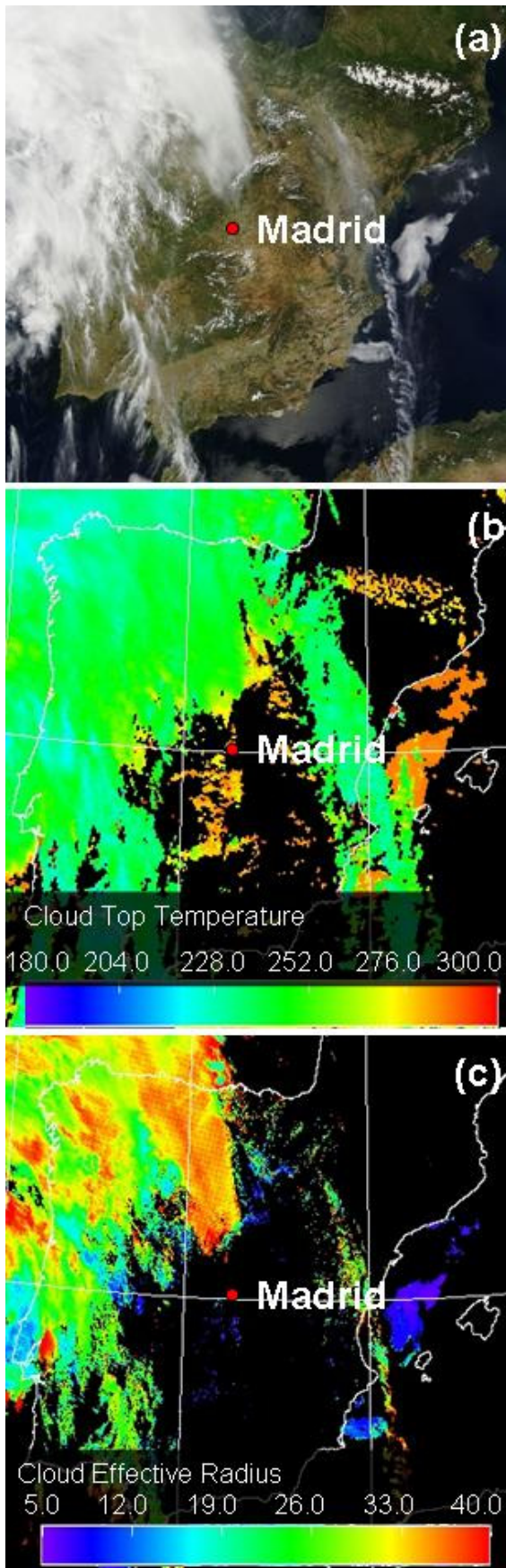


Fig. 2 MODIS images for 6 May 2013 11:10 UTC. (a) RGB image. (b) Cloud top temperature and (c) cloud effective radius

Fig 2 shows the true color image obtained on the 11:10 UTC Terra satellite overpass (top panel), the Cloud top temperature, converted from cloud pressure calculated using radiances measured in spectral bands located within the broad $15 \mu\text{m}$ CO_2 absorption region [11], through the use of gridded meteorological products, and the cloud effective radius obtained combining the 0.645, 2.13 and $3.75 \mu\text{m}$ bands [12]. As it can be observed, a thick cloud mass arrived from the Northwest, but it did not reach the Madrid site, indicated by a red dot in the middle of the Iberian Peninsula. Warm low-level clouds developed over the site, with cloud top temperatures above $276 \text{ }^\circ\text{K}$ and effective radius around $5 \mu\text{m}$. These clouds are influenced by aerosols confined in the PBL, as the lidar profiles will show later. In contrast, two bands of clouds, one to the east and another to the west presented different characteristics, with lower temperatures, around $252 \text{ }^\circ\text{K}$ and larger effective radii, above $26 \mu\text{m}$, well above the threshold value for precipitation indicated by Rosenfeld and Gutman [5]. The convective clouds developed over the PBL were studied by the lidar system. Fig 3 shows the backscattering coefficient (betas, hereafter) profiles for the three elastic wavelengths obtained by averaging measurements between 01:35 and 02:03 UTC. The betas suffer a strong increase from 1 km agl up to 2.8 km agl, where the peak of the cloud was observed and the betas reached values over $100 \text{ Mm}^{-1} \text{ sr}^{-1}$. Above 4 km the attenuation of the laser signals prevented inversion of the betas. Fig. 4 shows the relative humidity measured simultaneously, and the temperature and relative humidity profiles provided by the Barajas airport, 13.5 Km away from the site to the east, radiosounding launched at 23:15 UTC, about 2h and 30 min before the start of the lidar measurement.

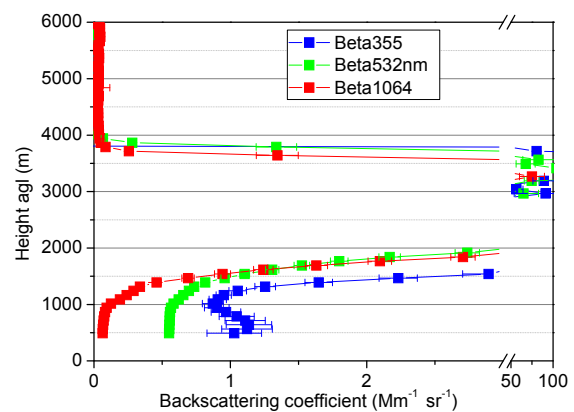


Fig. 3 Vertically-resolved aerosol backscattering coefficient profiles obtained by averaging signals between 01:35 and 02:05 UTC

Good agreement can be observed for altitudes above 500 m agl, with the expected increase of RH with height up to the cloud base at 2.8 km with values

between 60% and 70% near the surface increasing to values above 100% in the upper portion of the sub-cloud layer. The closer-to-ground layer disagree due to the temporal and spatial difference.

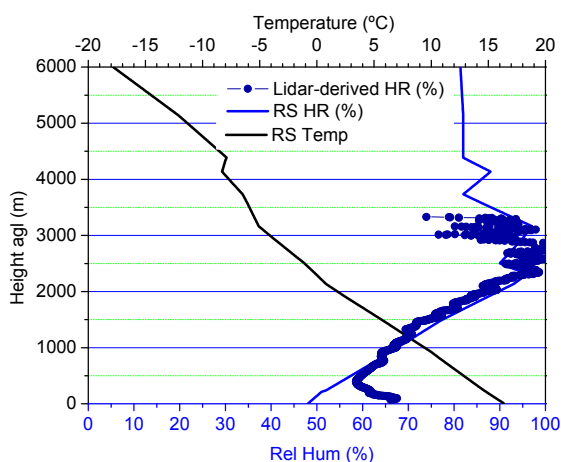


Fig. 4 Relative humidity (blue) and Temperature (black) profiles provided by the Barajas airport radiosounding (RS) and derived from the lidar measurements (blue dots) between 01:35 and 02:05 UTC

By measuring the aerosol betas as a function of height up until cloud base, the influence of the hygroscopic factor on aerosol optical properties can be studied. The observed increase in backscattering coefficient is most certainly related to the swelling of the aerosols as they are picking up water with increasing RH. A scatterplot of backscattering coefficient for the three elastic wavelengths versus relative humidity is plotted in Fig. 5 by selection altitudes with RH growing from 60 to 100 in 5% steps. It can be observed that changes in RH below 70% do not influence the backscattering coefficient, but further grow produce a net increase in this parameter.

Effect of humidity on aerosol lognormal distribution can be estimated using Köhler theory [13, 14] in order to calculate the backscattering coefficients, backscattering-to-extinction ratios and angstrom exponents theoretically and compared with those retrieved by the lidar at cloud-formation altitudes. Several assumptions are required in order to modify the size distribution measured at ground-level to take into account the effect of the relative humidity as the aerosols ascent along the PBL.

4 CONCLUSIONS

Data from the CIEMAT-Madrid site has been used to characterize the aerosol backscattering as a function of relative humidity. The analysis has shown that the relative humidity profile in particular synoptic situations, when convective clouds develop over the planetary boundary layer forming a cloud deck, help to study the hygroscopic growth that

aerosols experience as they ascent along the atmosphere. More detailed analysis of lidar data is required, in conjunction with modelling of aerosol

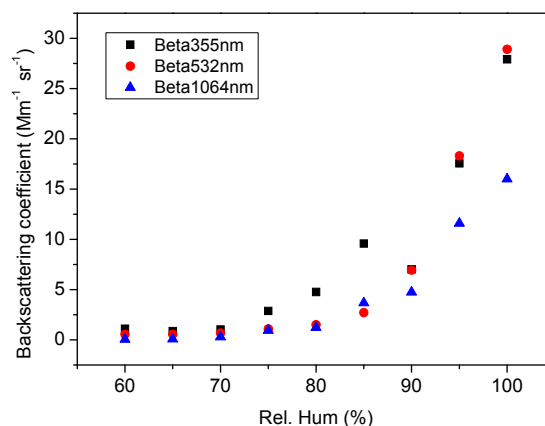


Fig. 5 Relationship between backscattering coefficient vs relative humidity derived from the lidar measurements between 01:35 and 02:05 UTC

behaviour to better characterize the hygroscopic growth of aerosols present in the boundary layer on the particular day studied.

ACKNOWLEDGMENT

The work was supported by the MINECO (Spanish Ministry of economy) through project CGL2010-17777 (PHAESIAN). We acknowledge the use of Rapid Response imagery from the Land Atmosphere Near-real time Capability for EOS (LANCE) system operated by the NASA/GSFC/Earth Science Data and Information System (ESDIS) with funding provided by NASA/HQ.

REFERENCES

- [1] IPCC: Climate Change 2007: The Physical Science Basis. Contribution of Working Group I to the Fourth Assessment Report of the Intergovernmental Panel on Climate Change, edited by: Solomon, S., Qin, D., Manning, M., Chen, Z., Marquis, M., Averyt, K., Tignor, M., and Miller, H. L., Cambridge University Press, Cambridge and New York, 996 pp., 2007.
- [2] Penner, J. E., Dong, X., and Chen, Y.: Observational evidence of a change in radiative forcing due to the indirect aerosol effect, *Nature*, 427, 231–234, 2004.
- [3] J. A. Coakley Jr., R. L. Bernstein, P. A. Durkee, “Effect of Ship-Stack Effluents on Cloud Reflectivity “ *Science* 237, 1020-1022. 1987
- [4] B. A. Albrecht, “Aerosols, cloud microphysics and fractional cloudiness” *Science* 245, 1227-1230. 1989
- [5] D. Rosenfeld, and G. Gutman, “Retrieving microphysical properties near the tops of potential rain clouds by multispectral analysis of AVHRR data”. *J. Atmos. Res.*, 34, 259–283. 1994
- [6] S. Twomey, “The influence of pollution on the shortwave albedo of clouds” *J. Atm Sciences*, 34, pp. 1149-1152. 1977
- [7] Pruppacher, H. R. and Klett, J. D.: *Microphysics of clouds and precipitation*, Kluwer Academic Publishers, 1997.
- [8] Hänel G. “The properties of atmospheric aerosol particles as function of the relative humidity at thermodynamic

- equilibrium with the surrounding moist air". *Adv. Geophys.* 19, 73-188. 1976
- [9] Whiteman, D N; Melfi, S H; Ferrare, R A, "Raman lidar system for the measurement of water vapor and aerosols in the Earth's atmosphere" *Applied Optics* 31.3068-3082. 1992
- [10] Müller, D., U. Wandinger, D. Althausen, and M. Fiebig "Comprehensive particle characterization from 3-wavelength Raman-lidar observations: Case study", *Appl. Opt.*, 40(27), 4863–4869. 2001
- [11] Menzel, W. P., R. A. Frey, H. Zhang, D. P. Wylie., C. C. Moeller, R. A. Holz, B. Maddux, B. A. Baum, K. I. Strabala, and L. E. Gumley: "MODIS global cloud-top pressure and amount estimation: algorithm description and results". *Jour of App Meteor and Clim.*, 47, 1175-1198 2008.
- [12] King, Y. J. Kaufman, W. P. Menzel and D. Tanré, "Remote sensing of cloud, aerosol and water vapor properties from the Moderate Resolution Imaging Spectrometer (MODIS)" *IEEE Trans. Geosci. Remote Sens.*, 30, 2–27. 1992
- [13] Kohler H. "The nucleus in and the growth of hygroscopic droplets". *Trans. Faraday Soc.* 32, 1152-1161. 1936
- [14] M. D. Petters and S. M. Kreidenweis "A single parameter representation of hygroscopic growth and cloud condensation nucleus activity" *Atmos. Chem. Phys.*, 7, 1961–1971, 2007

Relation between solar UVB and UV erythemal radiation at the surface

Vanda Salgueiro¹, Maria João Costa², Ana Maria Silva³, Daniele Bortoli⁴

Abstract —The relation between solar UVB and UV erythemal irradiances, measured at the surface in Évora between August 2011 and December 2012, presents a small dispersion with RMSE and R^2 values of 0.0022 W/m^2 and 0.9989 , respectively. This small dispersion was investigated through an analysis to aerosols, which revealed that this parameter has a very small contribution to the observed spread in the data. Thus, the equation expressing the relation between UVery and UVB was applied to a set of measured data, being obtained a BIAS of -0.0009 W/m^2 and a RMSE of 0.0027 W/m^2 from the comparison between UVery calculated, with the equation proposed, and the measured UVery.

Keywords — Aerosols, solar ultraviolet radiation

1 INTRODUCTION

Solar ultraviolet irradiance, UV (100 to 400nm), constitutes about 9% of the solar spectrum at the top of the atmosphere. However, only a fraction of this UV irradiance is transmitted to the Earth's surface depending on the absorption and scattering processes. The UV radiation can be subdivided in three spectral bands: UVC (100-280nm), which is completely absorbed by ozone and oxygen before reaching the Earth's surface, UVB (280-315nm), which is partly absorbed by ozone and UVA (315-400nm) that is weakly absorbed by ozone and therefore partly reaching the surface. Although the fraction of UVB at the surface level is less than 10% of the total UV irradiance [1], the UVB is more effective causing biological damage since the erythemal function (relation between solar UV irradiance and the erythemal UV) is essentially dependent of UVB being equal to unit at wavelengths lower than 298nm [2] (Fig.1). A means to inform people about the erythemal UV (UVery) strength, defined as the integral of the product between the spectral UV irradiance and the erythemal function [2], is the UV index, which is a standard measure being calculated as the product between the UVery and a constant of $40 \text{ m}^2\text{W}^{-1}$.

Since several years, the Évora Geophysics Centre (CGE) monitors the ultraviolet radiation in the A, B and AB spectral regions (UVA, UVB and UVAB). Only recently the UVery radiation started to be measured at the CGE Atmospheric Physics

Observatory in Évora and therefore the temporal series of UVery and UV Index (UVI) are limited to the last couple of years. This work aims at obtaining a parameterization of the surface UVery radiation and thus of the UV index, using ground-based UVB irradiance measurements. This parameterization is useful to the estimation of the UVery and UVI temporal series for the historical UVB data series available in the study region. On the other hand, this parameterization may be useful to obtain the UVery irradiance as well the UVI in places where we only have radiometers that measure in the UVB spectral band, as is the case of Cabo da Roca (Lisbon area).

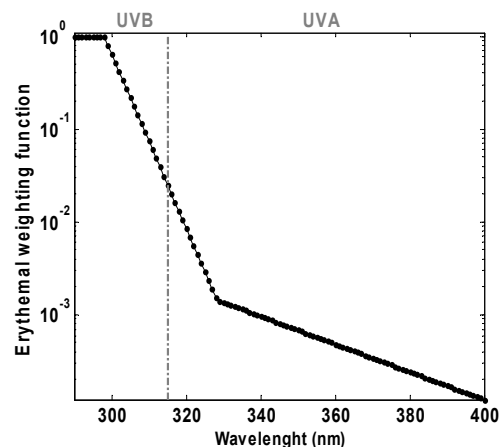


Fig. 1. Erythemal action spectrum CIE [3] as a function of the wavelength. The grey line represents the limit, at 315nm, between UVB and UVA.

The variability of UVB radiation that reaches the surface depends mainly on the solar zenith angle (SZA; angle between the local vertical and the center of the solar disk, being a function of latitude, day of the year and time of the day) and of cloud cover [4]. Other factors that affect the quantity of UV at the surface are ozone, aerosols, albedo, altitude and seasonal variations of the Sun-Earth distance. Since, the aim of this work is to obtain a

1. Evora Geophysics Centre, R. Romao Ramalho, 59, 7000 Evora. Portugal. E-mail: vsalgueiro@uevora.pt
2. Evora Geophysics Centre and Physics Department of University of Evora, R. Romao Ramalho, 59, 7000 Evora. Portugal. E-mail: mjcosta@uevora.pt
3. Evora Geophysics Centre, R. Romao Ramalho, 59, 7000 Evora. Portugal. E-mail: asilva@uevora.pt
4. Evora Geophysics Centre and University of Evora, R. Romao Ramalho, 59, 7000 Evora. Portugal. E-mail: db@uevora.pt

parameterization of the UV_{ery}, the methodology followed implies the analysis of the relationship between the measured UV_{ery} and UVB to all atmospheric conditions, from clear sky to overcast, during a year and a half. On the other hand, an analysis of the aerosol effects on UV irradiance is performed based in simulated UV irradiances in order to verify the influence of aerosols on the surface UV irradiance variability at surface.

The next section presents the methodology followed and the data considered in this work. In section 3, the results are presented and discussed and finally the conclusions are presented in section 4.

2 METHODOLOGY AND DATA

2.1 Solar UV Radiation - Measured Data

The solar UV irradiance data, used in this work, were measured at the Atmospheric Physics Observatory of the CGE (38°34' N, 7°54' W, and 300m above mean sea level) with Kipp&Zonen radiometers (Fig.2). These radiometers measure the global UV irradiance in three different spectral ranges: UV-A (315 – 400nm), UV-B (280 – 315nm) and erythemic active UV with response function of the human skin [3]. The radiometers voltage output is proportional to the irradiances in Wm⁻². The conversion of the radiometers signal to irradiance units is made using the calibration methodology proposed by [5], which depends on the solar zenith angle and on the ozone column value. The ozone column value used is obtained from the OMI (Ozone Monitoring Instrument) instrument onboard AURA satellite (<ftp://toms.gsfc.nasa.gov/pub/omi/data/overpass/>). In this work, the 10 minutes UVB and UV_{ery} irradiance measurements were used, from August 2011 until the end of December 2012, for all sky conditions from clear sky to overcast.



Fig. 2. Set of Kipp&Zonen radiometers that are installed in CGE atmospheric observatory.

2.2 Solar UV Radiation - Calculated Data

The UV_{ery} and the UVB irradiances were simulated using the LibRadtran-1.4 [6] (library for radiative transfer) code. The simulations were made for clear sky conditions, considering minimum and maximum AOD values in the UV region, being considered 0.01 as minimum and 0.3 as maximum. These values are deemed representative of Évora conditions based on AERONET measurements. The solar zenith angle ranges between 15° and 90° with a step of 1° and the ozone column value was varied between 250 and 400 DU. The UV irradiance was calculated once a month, starting in the day 15 of the year with a step of 30 days, being the atmospheric profile (mid latitude summer or mid latitude winter) chosen according with the day of the year. Aerosol data were obtained from the Aerosol RObotic NETwork (AERONET) CIMEL sun-photometer [7] also installed in CGE observatory (Évora site). The aerosol optical depth (AOD) at 340nm was considered and a precipitable water value of 14.05mm considering the AERONET data from 2003 to 2010. The surface was characterized by an albedo of 0.035 (http://snowdog.larc.nasa.gov/surf/pages/lat_lon.html).

3 RESULTS AND DISCUSSION

3.1 Experimental relationship between UV_{ery} and UVB radiation

In this section the relationship between the UV_{ery} and the UVB measured irradiances is presented. The data are presented in Fig.3 and correspond to a total of 36279 individual measurements taken for all sky situations, from clear to overcast skies. Yet the data points correspond to a range of solar zenith angles from 15.1°, the minimum angle measured in the study site, to 90°. The relationship obtained between UV_{ery} and UVB and presented as Eq. (1) is rather good, being translated by the small spread of the data with a root mean square error (RMSE) of 0.0022 Wm⁻² and by a high determination coefficient (R²) of 0.9989. McKenzie et al. (2004) had already obtained a relation between UVB and UV_{ery}, for a set of measured data for ozone ranging between 260 to 320DU, and the small spread observed was justified as being due to cloud effects. In the next section an analysis of the contribution of the aerosols to the small spread observed in the data of Fig. 3 is done. In addition, in this section the results of the application of Eq. (1) to a set of UVB measured data are presented.

$$y = 0.0084x^2 + 0.1183x + 0.0023 \quad (1)$$

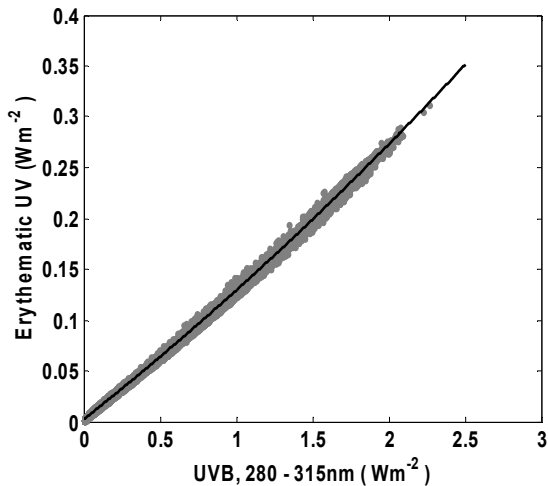


Fig. 3. Regression between erythemal UV and UVB measured irradiances corresponding to 36279 individual measurements from August 2011 until the end of December 2012.

3.2 Erythemal UV obtained from the relationship between measured erythemal UV and UVB

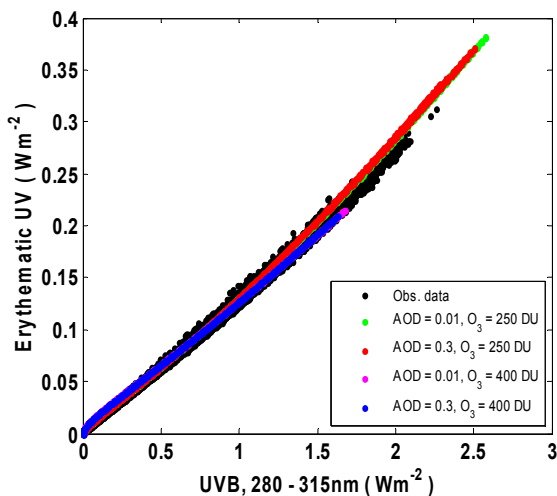


Fig. 4. Erythemal UV irradiance as a function of UVB measured irradiances (black dots) and calculated irradiances (colored dots). The colored dots are in accordance with the AOD and ozone values as indicated in the legend of the figure.

The U_{Very} and UVB calculated for the conditions described in section 2.2 are presented in Fig. 4. The measured UV is also presented (black dots) for comparison purposes. It can be observed that the contribution of aerosols to the spread of the measured UV radiation is very small. This becomes evident when considering the minimum and

maximum values of AOD (0.01 and 0.3). In fact the green and red symbols, as well as the magenta and blue symbols, both pairs corresponding to constant ozone and maximum AOD variation (0.01 to 0.3), are practically superimposed. The RMSE values obtained from the set of data relative to the minimum and the maximum values of AOD and constant values of ozone were between 0.0011 Wm⁻² and 0.0016 Wm⁻² being these values lower than the RMSE of the experimental data (0.0022 Wm⁻²). The change in AOD introduces only little variation in the calculated UV irradiances; however the ozone contribution is rather important, explaining great part of the observed dispersion.

Eq. (1) was applied to a set of UVB measured data corresponding to July 2012, in order to determine the U_{Very} and accordingly also the UVI may be obtained. The equation was applied to all atmospheric conditions, from clear sky to overcast and to aerosols and ozone values variations, and considering only solar zenith angles lower than 70° resulting in 2002 data points. Two examples are presented in Fig. 5 and in Fig. 6, where the calculated U_{Very} (blue line) and the measured U_{Very} (black line) can be observed for clear sky conditions (Fig. 5) and for cloudy conditions (Fig. 6). A comparison between the U_{Very} obtained from the equation and the measured U_{Very} values was done, in order to verify the reliability of the equation to infer U_{Very} from UVB. From this comparison a BIAS of -0.0009 Wm⁻² was obtained (normalized BIAS of -0.31%), meaning that the calculated U_{Very} presents a very low tendency to underestimate the measured U_{Very}. The U_{Very} data also presents a small dispersion translated by absolute and normalized RMSE values of 0.0027 Wm⁻² and 0.98%, respectively.

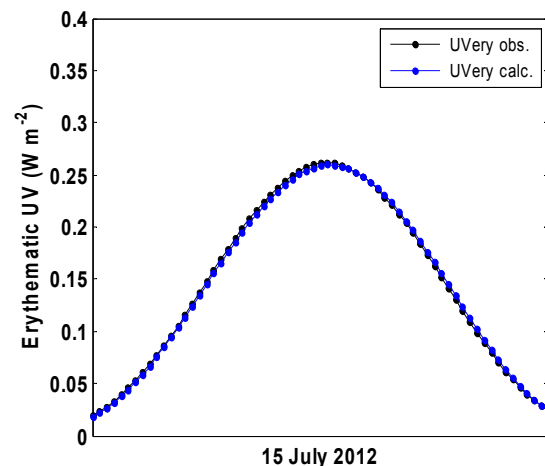


Fig. 5. Erythemal UV irradiance calculated (blue points) and measured (black points) in Évora on 15 July 2012 for clear sky conditions.

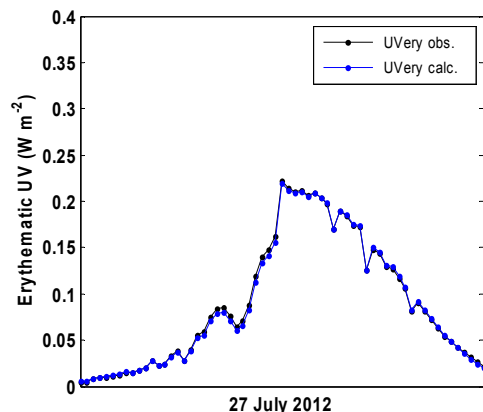


Fig. 6. Erythemic UV irradiance calculated (blue points) and measured (black points) in Évora on 27 July 2012 to cloudy conditions

8 CONCLUSIONS

The relationship between the solar UVB and UVery irradiances measured at the surface in Évora was investigated. It was verified that the correlation between both irradiances is quite good with high R^2 (0.9989) and low RMSE (0.0022 Wm^{-2}) values. This small dispersion cannot be explained by the aerosols, since the calculations showed that for the maximum AOD variation considered (0.01 to 0.3) the irradiance curves are practically superimposed. Other dependences are already being investigated.

The equation translating the experimental relation between UVery and UVB was applied to UVB data of July 2012. The comparison between modelled and measured UVery, yields small BIAS and RMSE values. Even considering all atmospheric conditions, from clear sky to overcast, including AOD and ozone column variations, as was the case here, only a small dispersion of the UVery data was obtained. The results of this work are important because the equation obtained may constitute a valuable tool to determine the UVery and consequently the UV index in places where only UVB measurements are available, as is the case of Cabo da Roca in the area of Lisbon.

ACKNOWLEDGMENT

This work was financed through FEDER (Programa Operacional Factores de Competitividade – COMPETE) and National funding through FCT – Fundação para a Ciência e a Tecnologia in the framework of project FCOMP-01-0124-FEDER-009303 (PTDC/CTE-ATM/102142/2008). The authors also acknowledge the funding provided by the Évora Geophysics Centre, Portugal, under the contract with FCT (the Portuguese Science and Technology Foundation), PEst-

OE/CTE/UI0078/2011. The authors thank Samuel Bárias for maintaining instrumentation used in this work.

REFERENCES

- [1] A. Serrano, M. Antón, M.L. Cancillo and V.L.Mateos, Daily and annual variations of erythemal ultraviolet radiation in Southwestern Spain. *Ann. Geophys.*, 24, pp. 427-441, 2006.
- [2] Richard McKenzie, Dan Smale and Michael Kotkamp, Relationship between UVB and erythemally weighted radiation. *Photochem. Photobiol. Sci.*, 3, 252-256, 2004.
- [3] McKinlay, A.F. and Diffey, B.L.: A reference spectrum for ultraviolet induced erythema in human skin, *CIE Journal*, 6, pp. 21-27, 1987.
- [4] Richard L. McKenzie, Lars Olof Björn, Alkiviadis Bais and Mohammad Ilyasd, Changes in biologically active ultraviolet radiation reaching the Earth's surface, *Photochem. Photobiol. Sci.*, 2, pp. 5-15, 2003.
- [5] J.M. Vilaplana, A. Serrano, M. Antón, M.L. Cancillo, M. Parias, J. Gröbner, G. Hülsen, G. Zablocky, A. Díaz, and B.A. de la Morena, Report of the "El Arenosillo"/INTA-COST Calibration and Intercomparison Campaign of UVER Broadband Radiometers, http://www-medphysik.vuwien.ac.at/uv/cost726/COST726_Dateien/Results/Report_El_Arenosillo.pdf. 2007.
- [6] B. Mayer and A., Kylling, Technical note: The LibRadtran software package for radiative transfer calculations – description and examples of use. *Atmos. Chem. Phys.*, 5, pp. 1855–1877, 2005.
- [7] Holben B.N., T.F.Eck, I.Slutsker, D.Tanre, J.P.Buis, A.Setzer, E.Vermote, J.A.Reagan, Y.Kaufman,T.Nakajima, F.Lavenu, I.Jankowiak, and A.Smirnov, AERONET - A federated instrument network and data archive for aerosol characterization, *Rem. Sens. Environ.*, 66, pp. 1-16, 1998.

NanoScan SMPS - Key Characteristics of an Innovative, Portable Instrument for Sizing and Counting of Nanoparticles

Torsten Tritscher¹, Sherrie Elzey², Michael Beeston³, Eric Filimundi⁴, Axel F. Zerrath², Thomas J. Krinke¹, Oliver F. Bischof¹

Abstract — Nanoparticles are ubiquitous in both outdoor and indoor environments due to a large variety of natural and anthropogenic sources. Key parameters for characterizing nanoparticles include their size distribution and number concentration. A novel, portable and compact nanoparticle sizing instrument, the NanoScan SMPS, has been designed for applications such as monitoring of industrial process emissions and workplaces, mobile studies, in-vehicle and air quality measurements. The instrument's measurement technique is based on the electrical mobility sizing that is used in Scanning Mobility Particle Sizer (SMPS) spectrometers. The innovation of the NanoScan lies in the use of a Radial Differential Mobility Analyzer and an integrated, isopropanol-based Condensation Particle Counter (CPC), which make it both compact and portable. Number size distributions in the range from 10 to 420 nm can be obtained, and the size range can be easily extended to a wide range of 10 nm to 10 μm by complementing its measurement with an additional portable instrument, the Optical Particle Sizer (OPS). Measurement data from NanoScan SMPS and OPS can be combined with user-friendly software. We present an evaluation of key performance characteristics as well as measurements from different sources and locations. These include test aerosols generated in the laboratory, emissions during material testing and processing as well as a mobile study. NanoScan SMPS compares well with established methods such as the research-grade SMPS from TSI. Results demonstrate the capability of this measurement tool to characterize particle emissions, identify sources of nanoparticles and increase workplace safety by reliable mobile measurement of number-based size-distributions over a wide size range.

Keywords — Atmospheric measurements, Nanoparticle, Scanning Mobility Particle Sizer, Workplace exposure

1 INTRODUCTION

There are numerous sources of nanoparticles, including anthropogenic sources such as engineered nanoparticles and particles from combustion and industrial processes. However, nanoparticles are also ubiquitous in ambient air, both indoors and outdoors. The size distribution, number concentration, and surface area of nanoparticles represent key parameters in the determination of their risk. Measuring exposure to nanoparticles has typically been conducted within academic research using research-grade instrumentation and sophisticated software. For many applications, e.g. in the field of indoor air quality and occupational health and safety, this type of instrumentation may not always be necessary and even complicate the acquisition of

data in real-life applications.

In this paper we are evaluating a novel instrument by direct comparison to the established Scanning Mobility Particle Sizer (SMPS) spectrometer. The data we present offer insight into the application of the NanoScan SMPS to the measurement of nanometer-sized aerosols within environments that would be more challenging for a research-grade SMPS, which is most frequently used in laboratory research.

The NanoScan SMPS model 3910 (TSI Inc., St. Paul, MN, USA) was designed to provide size resolution and accuracy for field measurements with a performance that is similar to the one of a research-grade component SMPS. It has been designed to obtain number size distributions of nanometer-sized airborne particles in the range from 10 to 420 nm. This measurement range can be extended to coarse particles with an additional portable instrument, the Optical Particle Sizer (OPS) model 3330 (TSI Inc., St. Paul, MN, USA). Combined these two instruments can cover the full range from 10 nm to 10 μm . Both instruments include a built-in computer, can be battery-powered and do not contain hazardous substances that might restrict its use to designated areas.

1. Authors are with TSI GmbH, Particle Instruments, Neukoellner Str. 4, 52068 Aachen, Germany. Email: Torsten.Tritscher@tsi.com
2. Authors are with TSI Incorporated, 500 Cardigan Road, Shoreview, MN 55126, USA.
3. Author is with TSI Ltd, Stirling Road, Cressex Business Park, High Wycombe, Bucks, HP12 3ST, UK
4. Author is presenting Author at the conference and is with TSI France Inc. Hotel technologique BP 100, Technopôle de Château-Gombert, 13382 Marseille cedex 13, France. Email: Eric.Filimundi@tsi.com

2 INSTRUMENTATION

2.1 NanoScan SMPS

The NanoScan SMPS consists of four main components: an inlet cyclone, a unipolar charger, the Radial Differential Mobility Analyzer (RDMA), and the isopropanol-based CPC. There are two key features of the instrument that enable its portable use: a patented opposed flow unipolar diffusion charger [1], which works without a radioactive source and thus avoids licensing, and transportation issues, and the incorporation of the RDMA. RDMA technology was introduced by Pourpax and Daval (1990) [2], and further characterized and developed through work done by Mesbath, 1994 [3], Zhang et al., 1995 [4] and Fissan et al., 1998 [5]. The internal operation of the NanoScan SMPS is outlined in Fig. 2. The exterior of the compact NanoScan SMPS and the color touch-screen display is shown in Fig. 1.

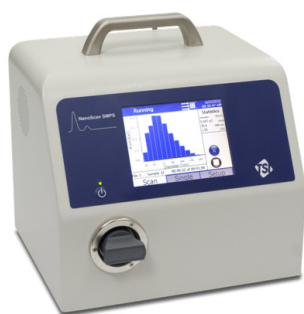


Fig. 1. View of the NanoScan SMPS model 3910 (TSI Inc.).

On entering the instrument, the aerosol flow of 0.75 L/min is pre-conditioned by an inlet cyclone with a cut point (D50) of 550 nm (see Fig. 2). The cyclone is crucial for long-term use of the instrument as it prevents issues related to plugging

that could occur when using an inlet impactor. Subsequently, the sample aerosol enters unipolar charger. This patented charger works by introducing an opposed flow that is filtered with both an active carbon filter and a HEPA filter. After passing over the charger needle, a jet of positive ions flows into the field-free mixing chamber, allowing the interaction of ions with the sample flow by an opposed flow technique, which improves mixing and charge repeatability.

After an internal flow splitting, 0.25 L/min of the sample flow enters the RDMA as polydisperse flow for the size analysis. The remaining flow enters as particle-free sheath air from the bottom outside edge of the RDMA into a circular channel. The polydisperse sample flow is introduced tangentially through an inlet channel at the top. The top plate of the RDMA is at ground, and the bottom plate is at a high negative voltage, thus creating an electric field. The size classified aerosol exits at the bottom center port of the RDMA through the monodisperse outlet and continues to the isopropanol-based CPC for the number concentration measurement. The integrated CPC is based on the design of the well-characterized (Hämeri et al., 2002 [6]) handheld CPC model 3007 (TSI Inc.). The excess flow exits through the top center port of the RDMA. During the course of a measurement the DMA's voltage is ramped up to scan the entire size range.

In the size distribution measurement mode of the NanoScan SMPS, a 45 second up-scan in which the measurement occurs and a 15 second down-scan (retrace) are completed, which combine to a total 60 seconds sampling time. In a second mode of operation, the so-called Single mode, the NanoScan SMPS can monitor the nanoparticle number concentration of a single electrical mobility diameter with a time resolution of 1 second. The mobility

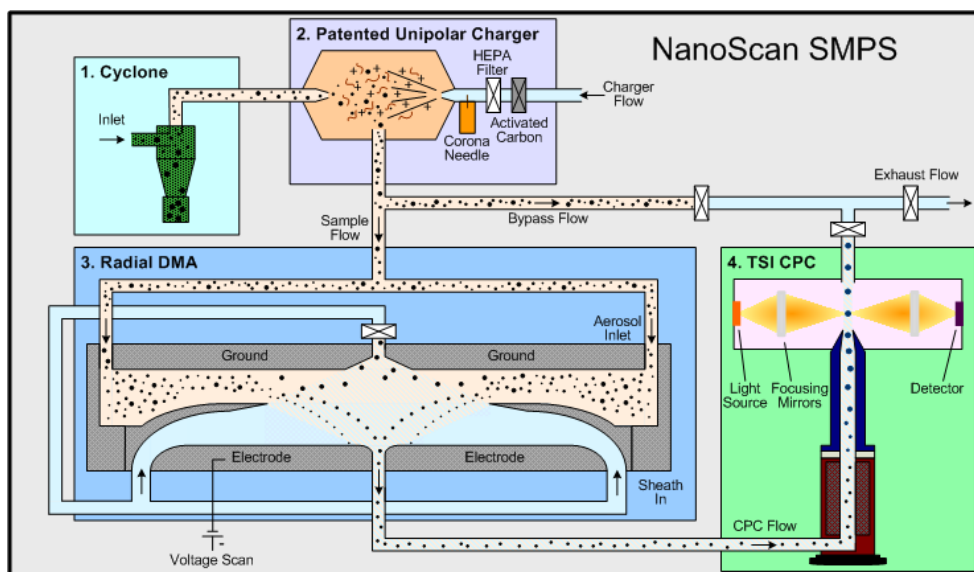


Fig. 2. Flow schematic of the NanoScan SMPS.

diameter can be set to any size between 10 and 420 nm by the operator. This single mode enables measurements such as the detection and tracing of a specific engineered nanomaterial of known size.

The NanoScan SMPS can run on battery power for several hours and provides on-board data storage sufficient for 8 to 10 days of continuous operation. Its USB storage drive option is useful to export the data. Data acquisition can be done conveniently via a computer with dedicated measurement software. This is especially useful when the instruments runs in its extended mode on A/C power and with an external working fluid reservoir connected.

2.2 Extended Size Range: Optical Particle Sizer

The size range of the NanoScan SMPS can be extended to coarse particles with an additional compact, portable instrument, the Optical Particle Sizer (OPS) model 3330 (TSI Inc.), which measures particles in the size range from 0.3 to 10 μm in up to 16 adjustable size channels. The OPS uses a laser and a photodetector to size and count particles passing through a sensing volume illuminated by the laser. The light scattered by the particles is collected by an elliptical mirror and focused onto the photodetector. The processed measurement result is a number size distribution based on optical-equivalent diameter.

Combined these two compact instruments can measure the number size distribution of particles over the full range from 10 nm to 10 μm . An external view of the OPS instrument is shown in Fig. 3.



Fig. 3. The Optical Particle Sizer (OPS) model 3330 (TSI Inc.).

2.3 Data Merge: Multi-Instrument Manager

Data from the NanoScan SMPS and the OPS can be merged with an easy-to-use software tool called Multi-Instrument Manager (MIM). It allows reviewing, averaging, curve fitting and merging data from component SMPS, NanoScan SMPS and OPS instruments. Merging size distributions based on electrical mobility and optical-equivalent diameter typically requires a fitting of the data. MIM software allows to curve fit distributions using up to three modes of lognormal distribution. Data from two

particle sizing instruments can be merged and fitted to display measurements over a wide size range.

The MIM software offers three merge and curve fit options: No Correction, Minimum Gap, and Calibration Data. The No Correction option merges two distributions with no correction. The Minimum Gap option minimizes the gap between the NanoScan SMPS and OPS data by adjusting the refractive index. The Calibration Data option includes custom OPS calibration data based on reference particle sizes. The software can take the optical properties into account by automatically determining the effective refractive index of the aerosol. The data can be viewed as number-, surface area-, or mass-weighted size distributions.

Fig. 4 shows particle size distributions acquired using the NanoScan SMPS and OPS sampling ambient air in an urban environment. MIM software was used to merge and curve fit the data as number-weighted (panel A) and mass-weighted (panel B) size distributions.

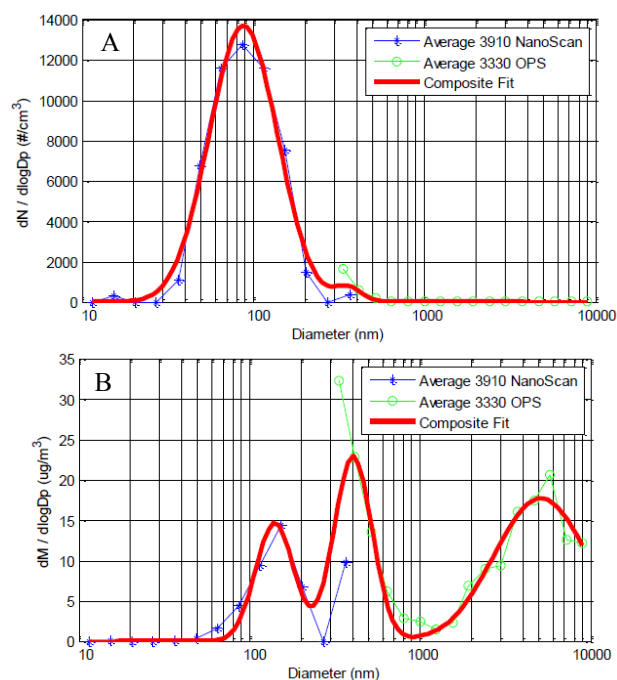


Fig. 4. Multi-Instrument Manager Software merge and curve fit of urban aerosol measurements from the NanoScan SMPS (blue diamonds) and OPS (green circles). Data are shown as number-weighted (panel A) and mass-weighted (panel B) size distributions.

3 RESULTS AND DISCUSSION

3.1 NanoScan SMPS Validation

A direct comparison was made between the NanoScan SMPS and a research-grade component SMPS system commonly used in the laboratory (TSI 3936L76). The proven technology of the SMPS was used as the reference in several applications. The

tests involved challenging the NanoScan SMPS with both monodisperse and polydisperse aerosols. The monodisperse aerosol was polystyrene latex spheres (PSL) having NIST-traceable certified particle diameters ranging from 20 nm to 300 nm. The PSL aerosol was generated using an electrospray aerosol generator (TSI 3480). The polydisperse aerosol was NaCl generated using an atomizer (TSI 3076). Polydisperse NaCl was used to compare the concentration linearity of the NanoScan SMPS to the component SMPS and a reference CPC (TSI 3776).

Fig. 5 shows results for 200 nm PSL, comparing particle size distributions measured using the NanoScan SMPS and component SMPS and the corresponding total concentration measured by each SMPS system. The 200 nm PSL data are representative of the similarities and differences in size distribution measurements between the NanoScan SMPS and component SMPS for monodisperse samples. The total particle number concentrations agree well (within 5%), as do the median particle diameters (within 5%). The NanoScan SMPS tends to show broader distributions of lower intensity, due to the lower resolution, i.e., wider size channels.

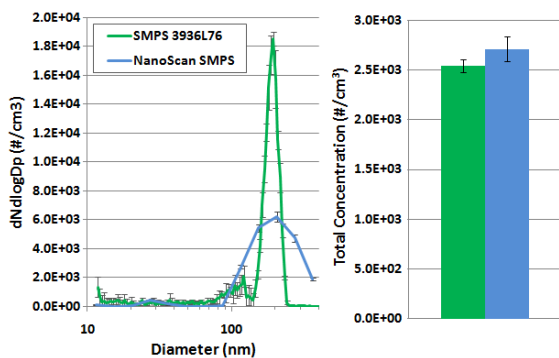


Fig. 5. Size distributions (left) and total concentration in bar chart (right) for 200 nm PSL measured by the NanoScan SMPS (blue) and component SMPS (green).

Fig. 6 shows polydisperse NaCl size distributions measured using the NanoScan SMPS and component SMPS. Five consecutive scans are shown, demonstrating the reproducibility of the measurements

Fig. 7 shows the concentrations of NaCl measured over four orders of magnitude. The data demonstrate the close agreement between the NanoScan SMPS and component SMPS, as well as the linearity of the NanoScan SMPS concentration ($R^2 > 0.99$).

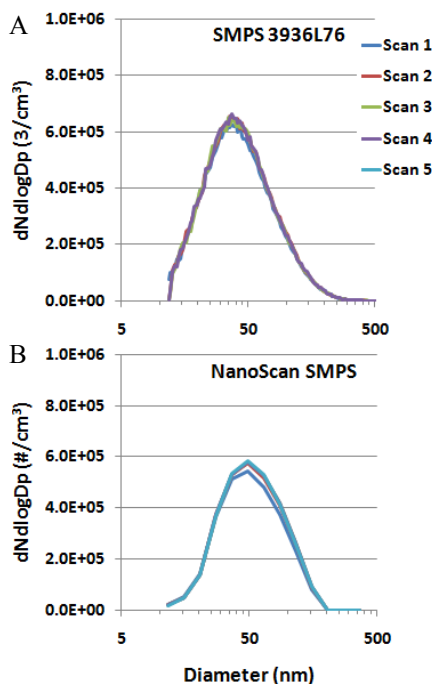


Fig. 6. Size distributions of polydisperse NaCl measured using the component SMPS (panel A) and the NanoScan SMPS (panel B).

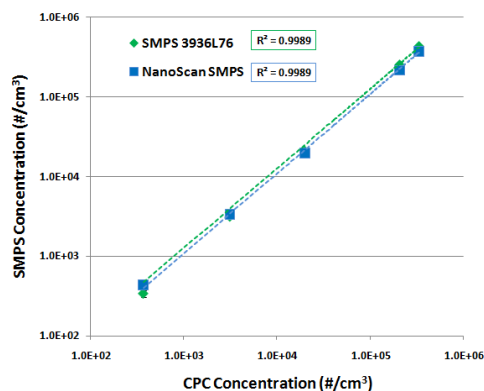


Fig. 7. Concentration linearity of NanoScan SMPS

3.1 Mobile Study

A mobile study of in-vehicle measurements was conducted as an example for a possible application for the NanoScan SMPS showing the easy handling of the instrument. Cabin air or in-vehicle air was continuously measured during a 380 km journey from Cologne to Bremen in Germany. The NanoScan SMPS was placed on the front seat of the car with its sampling port open to sample the cabin air of the vehicle. The measurements were completed coupled with a GPS tracker to enable the accurate correlation of data reported by the instrument with the sampling environment.

Fig. 8 shows the total number concentration plotted on a Google Earth map for the full journey. A wide range of particle concentrations was found as the result of continuous size distributions measurements.

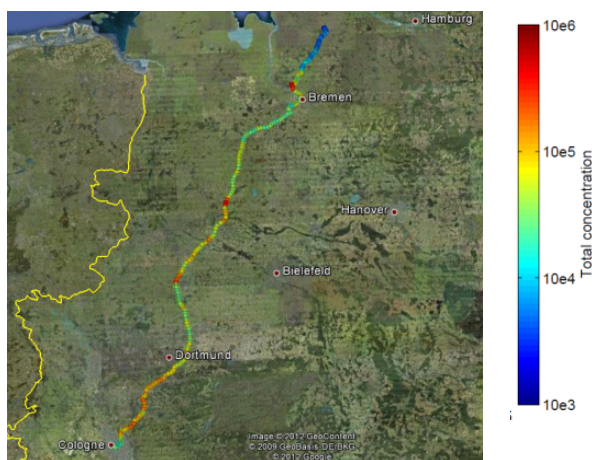


Fig. 8. The summed size distributions of NanoScan SMPS shown as total particle number concentration during the mobile study in Germany plotted in Google maps. Blue colors indicate a low concentration and warmer colors indicate higher particle concentrations.

The total number concentration and the geometric mean diameter of the measurements calculated from individual recorded number size distributions are varying throughout the journey

In total more than 250 scans were recorded and Fig. 9 shows just five examples. The variation in the total number concentration measured along the route highlights a number of distinct high particle number hot spots such as in Munster where a concentration of 227444 particle/cm³ was recorded. It is clear from the size distribution measured that the majority of the particles within this situation are very small, with diameters smaller than 20 nm. The largest particles were found at a construction site along the highway at the Lohne-Dinklage location. Here the mode of the distribution is at 86.6 nm. The results taken at Bremervörde are the example for low concentration and show again a different nature of particle size distributions along the route. Here the mode of the distribution is at 36.5 nm.

The combined information from total particles number, mean diameter and individual size distributions allows to some extent a source apportionment and characterization of the present aerosol. This study demonstrates the value of such data but also shows that nanoparticle concentrations at common “work” places such as inside a vehicle can be very high.

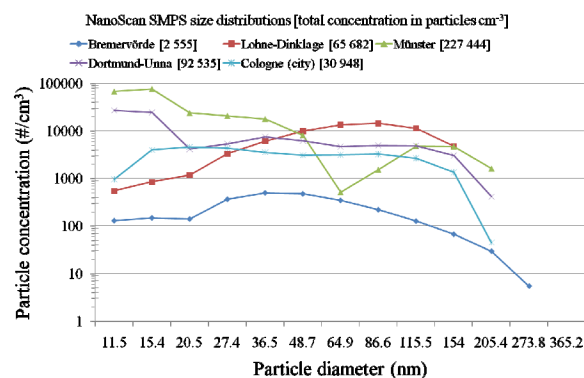


Fig. 9. Size distributions from NanoScan SMPS from selected locations from northern Germany (Bremervörde) to the southern part of the journey in Cologne on logarithmic scale. The total concentration is given in brackets for each location.

3.2 Workplace Exposure

An important area of environmental monitoring includes nanoparticles at indoor workplaces. Different working steps and processes can result in the generation of nanoparticles which pose a known risk within a work place. Hence, the NanoScan SMPS was tested in a production facility environment.

Nanoparticles from metal inert gas soldering were studied in an exposure laboratory with a Fast Mobility Particles Sizer (FMPS, TSI 3091) and the NanoScan SMPS in parallel. The mode diameter changed from 107 and 115 nm to 143 and 154 nm after few minutes for FMPS and NanoScan SMPS, respectively. Also the total number concentrations of 2.16×10^6 and 1.29×10^5 cm⁻³ (FMPS) agreed well with the NanoScan SMPS values 2.28×10^6 and 1.37×10^5 cm⁻³.

The NanoScan SMPS was used in another case study for the assessment of worker exposure during several work scenarios. These ranged from material tests like abrasion and extrudability to measurements done during milling of the same material. The background particle concentrations in indoor air and exposure levels during the material processing were determined at each site and at several sampling points within the rooms. Exposure to nanoparticles was measured in the breathing zone. The background data recorded from the ventilation diffusers supplying fresh air to the rooms were measured, along with the breathing zone during all processes.

The total number concentration in the fresh air supplied through diffusers from the ventilation system was on average around 6100 particles/cm³ in the nanoparticle size range (<500 nm). In contrast the total number concentration of particles in the breathing zone during the various processes was on

the order of 12000 particles/cm³. The dominant peaks in the size distribution within the breathing zone were at approximately 15 and 37 nm. In the background signal a third peak was determined at about 116 nm, which is a particle size not uncommon for indoor aerosols.

The efficiency of enclosures employed as a safety measure is highlighted from the analysis of the measurements during a composite mixing process, which took place in a ventilated enclosure. The particle counts in the room air measured at the ventilation diffuser were equal to the background measurements in the enclosure. The total number concentration was determined to be about 4700 particles/cm³. The number concentration within the enclosure increased by a factor of four to about 20000 particles/cm³ as the material is processed within the enclosure. Therefore it is evident that the enclosure was able to capture the majority of the particles emitted. Studies like this allow the evaluation of measures taken (here the use of an enclosure) to protect workers from enhanced Nanoparticles exposure.

4 CONCLUSIONS

This paper presents the novel, compact NanoScan SMPS model 3910 (TSI Inc.) and highlights its capabilities for reliable nanoparticle measurements within the size range from 10 to 420 nm in real-time. This size range can be extended to 10 µm with an additional portable instrument, the OPS. MIM software can be used as a user-friendly tool to merge data from both instruments using several fitting options.

The NanoScan SMPS provides the means to employ SMPS technology in a compact and portable format that can be easily utilized in the field. The incorporation of a unipolar charger, RDMA and isopropanol-based CPC removes transport and application limitations currently in place for component SMPS technology.

The NanoScan SMPS demonstrated concentration linearity and provided good comparability to the laboratory-based reference component SMPS system when challenged with monodisperse and polydisperse particles.

Case studies with the NanoScan SMPS showed the wide range of possible applications. Coupling continuous in-vehicle measurements with GPS technology enabled an easy characterization of the particle size distributions while driving on a highway in Germany. This allowed, for instance, highlighting distinct hotspots and sources of interest. It also enabled an assessment of the exposure to nanoparticles in the vehicle.

Exposure assessment of an industrial workplace demonstrated another application of the NanoScan SMPS. Measurements within a production test

facility showed the variation between the nature of the nanoparticles in ventilation diffusers compared to those detected in the breathing zone. It also demonstrated how to evaluate the effectiveness of protection or exposure reduction measures.

ACKNOWLEDGMENT

The authors would like to acknowledge the input and support by a number of colleagues at TSI. We also thank Ines Engel for helping create the map-based plots of the mobile study.

REFERENCES

- [1] Medved, A., Dorman, F., Kaufman, S.L. and A. Pöcher, A New Corona-based Charger for Aerosol Particles. *Journal of Aerosol Science*, 31:S616-S61, 2000
- [2] Pourpax, M. and J. Daval, Electrostatic precipitation of aerosol on wafers, a new mobility spectrometer. In 'Aerosols: Science, Industry, Health and Environment', Pro. of the Third Int. Aerosol Conference, 24–27 Sept., 1990, Kyoto, Japan, Vol. II, edited by S. Masuda and K. Takahashi, Pergamon Press, 1990
- [3] Mesbath, B., Le spectrometre de mobilite electrique circulaire; Performance et applications, Thesis de Doctorat a l'Universite Paris XII, 4 Juil., Creteil, France, 1994
- [4] Zhang S.H., Akutsu Y., Russell L.M., Flagan R.C. and J.H. Seinfeld, Radial Differential Mobility Analyser. *Aerosol Science & Technology*, 23: 357-375, 1995
- [5] Fissan, H.; Pöcher, A.; Neumann, S.; Boulaud, D. and M. Pourpax, Analytical and empirical transfer functions of a simplified spectromètre de mobilité électrique circulaire (SMEC) for nano particles. *Journal of Aerosol Science* 29, 3: 289-293, 1998
- [6] Hämeri, K, Koponen, I.K., Aalto, P.P., and M. Kulmala, The particle detection efficiency of the TSI-3007 condensation particle counter. *Journal of Aerosol Science* 33, 1463-1469, 2002

Germination Rate of Three Anemophilous Pollen Types After In Vitro Exposure to Gaseous Atmospheric Pollutants

L. Duque¹, H. Ribeiro¹, C. R. Gomes^{2,3}, J. C. G. Esteves da Silva^{2,4}, I. Abreu^{1,5}

Abstract — While airborne, pollen fertility may be affected by several environmental factors such as air pollution. In this work we investigated how the germination rate of three anemophilous pollen types (*Acer negundo*, *Platanus x acerifolia* and *Quercus robur*) varies after exposure to gaseous atmospheric pollutants in a simulated atmospheric environment. Pollen was in vitro exposed to CO, NO₂, O₃ and SO₂ for 6 hours in an environmental chamber. Two concentration levels were tested for each gas: around and above the limit values for human health protection fixed by the European Union in the Directive 2008/50/EC of 21 May on “Ambient Air Quality and Cleaner Air for Europe”. Subsequent to the exposure, pollen was germinated in optimized media, according to pollen type. Non-exposed pollen served as control. Most of the exposed pollen samples presented a significant decrease in pollen germination rate when compared to non-exposed samples. However, some samples, namely those of *P. x acerifolia* exposed to NO₂, did not present a decreased germination rate. Moreover, in some cases, significant differences in pollen germination rates were observed between pollen exposed to the two different concentration levels of the same pollutant.

Keywords — Atmospheric pollution, Environmental chamber, Gaseous pollutants, Pollen fertility

1 INTRODUCTION

Plants' male fitness is a major feature of sexual plant reproduction and, ultimately, an important aspect in a plant's selective force in evolution. Male reproductive success is determined by a wide number of features that may include, among others, anther and pollen production, pollen dispersal and germination and pollen tube growth. These aspects can be affected by environmental factors [1], [2]. Amongst these factors we can distinguish abiotic (e.g. resources availability: water and soil fertility, soil and air temperature, carbon dioxide concentration) and biotic factors (e.g. herbivory and plant-pollinator interactions).

The ability of pollen to germinate is an essential aspect in the evaluation of male fitness in higher plants. In the case of anemophilous pollen, it is likely that it will be further influenced by atmospheric factors that entomophilous pollen, since the air is there vehicle of transportation. When

pollen becomes airborne, its characteristics may be affected by the other components of the aerosol.

Particulate matter, lead, benzene and gaseous pollutants such as carbon monoxide (CO), nitrogen oxides (NO_x), ozone (O₃) and sulphur dioxide (SO₂) are some of the components of the aerosol that are currently being monitored in Europe because they are considered to have harmful effects on people's health [3].

Besides their negative effects on humans, NO_x, O₃ and SO₂ also cause damage to vegetation. Most studies performed so far show a negative impact of O₃ in the reproductive development of plants [4], [5]. Fewer studies have been conducted on the effect of the other gaseous pollutants and the results are not conclusive.

In this work we investigated how the germination rate of three anemophilous pollen types (*Acer negundo*, *Platanus x acerifolia* and *Quercus robur*) varies after exposure to four gaseous atmospheric pollutants (CO, NO₂, O₃ and SO₂) in a simulated atmospheric environment.

2 MATERIAL AND METHODS

2.1 Pollen Gathering and Storage

Inflorescences of *Acer negundo*, *Platanus x acerifolia* and *Quercus robur* were collected from the trees in public gardens and sidewalks in the city of Porto, Portugal. Then they were dried at 27 °C and passed through a column of sieves of different mesh sizes to get pure pollen. Pollen thus obtain was kept at -20°C.

1. Author is with Grupo do Ambiente, Centro de Geologia, Universidade do Porto, Portugal

2. Author is with Departamento de Química e Bioquímica, Faculdade de Ciências, Universidade do Porto, Portugal

3. Author is with CIIMAR- Centro Interdisciplinar de Investigação Marinha e Ambiental, Universidade do Porto, Portugal

4. Author is with Centro de Investigação em Química (CIQ-UP), Departamento de Química e Bioquímica, Faculdade de Ciências, Universidade do Porto, Portugal

5. Author is with Departamento de Biologia, Faculdade de Ciências, Universidade do Porto, Portugal, ianoronh@fc.up.pt

Table 1. Average gas concentrations (ppm) during exposure experiments

Gas	Limit values for human health protection [#]	<i>Acer negundo</i>		<i>Platanus x acerifolia</i>		<i>Quercus robur</i>	
		+	++	+	++	+	++
CO	8.73	9.14	18.35	8.68	18.51	8.77	18.57
NO ₂	0.11	0.13	0.22*	0.11	0.22*	0.13	0.22*
O ₃	0.061	0.068	0.251	0.060	0.227	0.058	0.233
SO ₂	0.13	0.16	0.26	0.17	0.28	0.14	0.28

* Estimated concentration. [#] The limit values for human health protection were fixed by the European Union in the Directive 2008/50/EC of 21 May and refer to: NO₂ and SO₂- one hour mean; CO and O₃- daily maximum 8-hour mean. + - about the limit values for human health protection; ++ - about twice (CO, NO₂ and SO₂) and four times (O₃) the limit value for human health protection.

2.2 In Vitro Exposure of Pollen to Gaseous Pollutants

Each pollen type was in vitro exposed, during 6 hours, to each of four gaseous pollutants: CO, NO₂, O₃ and SO₂, at two different concentration levels (Table 1). The lowest levels (+) are about the limit values for human health protection for each gas fixed by the European Union in the Directive 2008/50/EC of 21 May on “Ambient Air Quality and Cleaner Air for Europe”. The highest levels (++) are about twice those values, except for O₃ which was exposed to four times the limit value for human health protection.

The exposure was performed in an environmental chamber previously described by Sousa et al. [6]. This chamber is equipped with a solar simulator (Newport Oriol 96000 150 W), a fan to homogenize the air and gas sensors (Aeroqual).

Pollen was put in a tube, with both edges closed with a 23 µm pore length mesh (SEFAR PET 1000), and the tube was placed over a 12 V DC fan that impelled the air within the chamber to pass through the tube. Because of its smaller size, two layers of mesh were used when exposing *P. x acerifolia* pollen.

To obtain the desired concentrations of pollutants, small volumes of gas were introduced in the chamber through a septum placed in the front chamber wall. The interval between injections was dependent of the gas reactivity: around 2 h for NO₂ and SO₂, around 12 min for O₃, and, for CO, a sole injection was performed in the beginning of the experiment.

After exposure, pollen was kept at -20°C until in vitro germination assays were performed. For each pollen type, a non-exposed pollen sample was used as control.

2.3 Pollen Germination

Pollen was in vitro germinated in optimized media at 27°C. Table 2 summarizes the composition of the media used.

A. negundo and *Q. robur* pollen was incubated in the germination media for 48 h, whilst *P. x acerifolia* was incubated for 6 h. After incubation, random groups of 100 pollen grains were observed using a light microscope (Leica DMLS) and germinated pollen was distinguished from non-germinated pollen. A pollen grain was classified as germinated when its tube was longer than the pollen’s diameter.

For each sample, only the five replicates which scored the highest germination rates were considered for statistical analysis.

Table 2. Composition of media used for germination of the three pollen types

	<i>A. negundo</i>	<i>P. x acerifolia</i>	<i>Q. robur</i>
H ₃ BO ₃ (ppm)	100	100	186
CaCl ₂ (ppm)	100	300	-
Ca(NO ₃) ₂ .4H ₂ O (ppm)	-	-	400
Sucrose (%)	15	12	14
Agar (%)	0.5	0	0.7
pH	5.0	-	-

2.4 Statistical analysis

SPSS v.18 was used for statistical analysis. The normality of the acquired data was assessed by the Shapiro-Wilk test. An ANOVA test was performed to test the differences between the germination rate of the exposed and the non-exposed samples. When this test would point to statistical differences, a Tukey’s test was performed to test the differences between pairs of samples.

3 RESULTS

Germination rate of control pollen differed between pollen types. Control *Quercus robur* pollen presented the highest percentage of germination

(82.0%), followed by *Acer negundo* (65.4%) and *Platanus x acerifolia* (37.6%).

All samples exposed to O₃ and SO₂ presented a decrease in germination rate in relation to the non-exposed samples (Fig. 1). For NO₂ and CO most of the exposed pollen samples also presented significant decrease in germination rate. Exceptions were observed for *P. x acerifolia* exposed to NO₂, *A. negundo* pollen sample exposed to the lowest level of NO₂ and *P. x acerifolia* pollen sample exposed to the lowest level of CO, which did not present a significant decrease in germination rate.

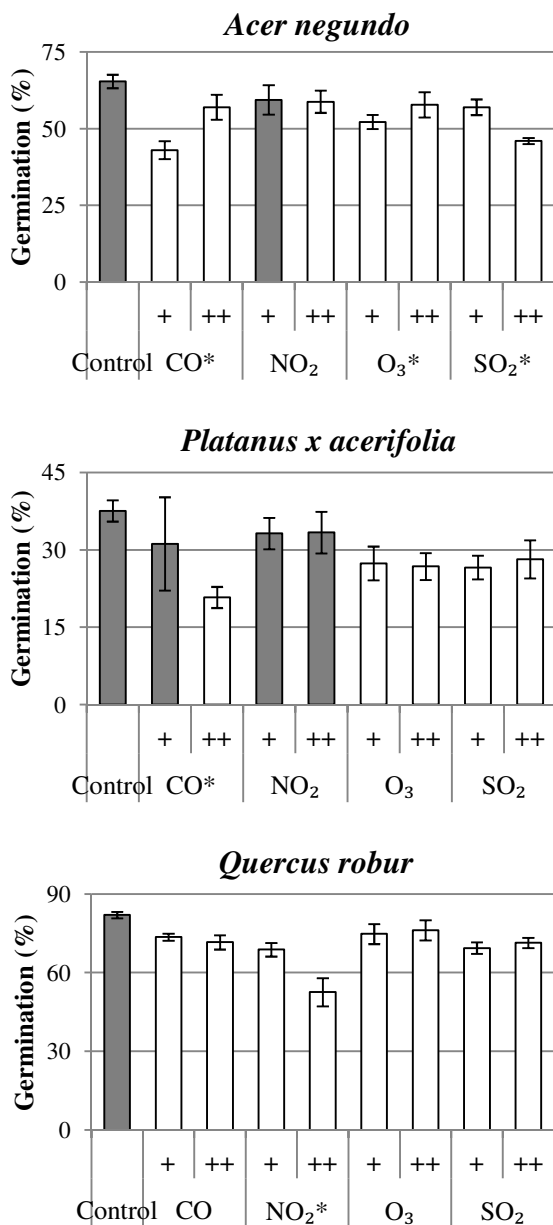


Fig. 1. Germination rate of *Acer negundo*, *Platanus x acerifolia* and *Quercus robur* pollen before and after exposure to gaseous pollutants at different concentration levels. + and ++ indicate lowest and highest concentration levels. White bars indicate samples which had a germination rate statistically different from the control sample ($p < 0.05$). * indicate statistical differences ($p < 0.05$) in germination rate between the two concentration levels.

In some cases, significant differences in germination rates of pollen exposed to the two different concentration levels of the same pollutant were observed: *A. negundo* pollen exposed to CO, O₃ and SO₂; *P. x acerifolia* exposed to CO and *Q. robur* pollen exposed to NO₂. Nevertheless, in the cases of *A. negundo* pollen exposed to CO and O₃, the highest decrease in pollen germination rate was observed in the samples exposed to the lowest rather than the highest concentration of gas.

Quercus robur pollen was the only pollen type which showed a decrease in germination rate of all gas-exposed samples.

4 DISCUSSION

Our results show that the germination rate of pollen exposed to gaseous pollutants is generally lower than that of non-exposed pollen. Analogous results were obtained by Gottardini et al. [7] when comparing pollen collected in stations with different levels of air pollution. Their results showed that the highest pollen germination rate and tube length growth occurred in the no road traffic situation. Nevertheless, the lowest pollen germination rate was registered in the light road traffic site and not in the heavy road traffic site, similarly to our results of *A. negundo* pollen exposed to CO and O₃, which showed the lowest germination rate in the samples exposed to the low gas concentration level. This may indicate that others factors, that we don't control, like temperature and relative humidity in our case, and soil fertility in Gottardini's situation can be influencing the results. However, Gottardini et al. [7] consider that the pollen germination rate is not a reliable pollution indicator, because of the difficulties in identifying the most suitable medium for germination and the difficulty to reproduce the method by different operators. They recommend the implementation of viability tests like TTC-test (2,3,5 tryphenil-tetrazolium-chloride test) or FCR-test (fluorochromatic reaction test using fluorescein diacetate solution) to monitor air quality. Their results showed a positive correlation between pollen viability and O₃ concentration and negative correlations between pollen viability and SO₂, NO_x and NO₂ concentrations. However, in our results, effects, when existing, were negative for all gases.

When testing pollen viability, others authors also found a negative effect of pollutants on pollen grains. When evaluating the effects of NO₂, Gottardini et al. [8] reported that the viability of pollen was significantly lower in the areas where the concentration of NO₂ was higher. However, according to Iannotti et al. [9] not all species can be used as bio-indicators of air quality through pollen viability since some species are very well adapted to urban environments, showing the highest pollen viability in polluted areas. But even if pollen viability is a good trait to test which plant species

can adapt to urban areas, we consider that viability tests are not enough, because many pollen grains that are considered viable fail to germinate and therefore fail to achieve their goal.

Duro et al. [10] tested the correlation between pollen germination rate and gas concentration in the sites where samples were collected and their results also suggest that pollen sensitivity to pollution is species-dependent. In our results, *Quercus robur* was the only pollen type which showed a decrease in germination rate in all exposed samples, possibly meaning that this pollen type is more susceptible to pollution than the other pollen types studied.

Chichiriccò and Picozzi [11] reported that fumigating pollen for 2 hours with high concentrations of CO (up to 250 ppm), NO₂ (up to 11 ppm) and O₃ (up to 1.5 ppm) did not affect its capacity to emit a tube which penetrated stigma papillae. When, after in vivo pollination, pollen and stigma were fumigated, these gases temporarily inhibited pollen germination. However, and in spite of the high gas concentrations, the inhibition was temporary and pollen grains could recover the ability to germinate after cessation of fumigation.

Hormaza et al. [12] exposed pollen from different fruit and nut species to O₃ after dusting it onto germination medium. Their results showed that most species were moderately tolerant to O₃, registering reduced pollen germination in samples exposed to ozone concentrations of 0.4 and 0.6 ppm but not to 0.2 ppm. In our study, however, the germination of all samples fumigated with O₃ was reduced, independently of the pollen type.

5 CONCLUSIONS

The reduction in pollen germination rate, which occurred in pollen grains when they were in the presence of gaseous pollutants, negatively affects male fertility. Because of pollen grains essential role in plants' reproduction, more studies should be conducted to find out which processes are involved in the lost of germination capability.

ACKNOWLEDGMENTS

This work was supported by FEDER funds through the Operational Program Competitiveness Factors - COMPETE and National Funds through FCT - Foundation for Science and Technology in the projects Ref^o PTDC/AAC-AMB/102796/2008 and PEst-OE/CTE/UI0039/2011- UI 39. Second author benefits from a scholarship (SFRH/BDP/43604/2008) financed by QREN-POPH and FCT.

REFERENCES

- [1] L.F. Delph, M.H. Johannsson and A.G. Stephenson 1997 "How environmental factors affect pollen performance: Ecological and evolutionary perspectives" *Ecology* **78** 1632-9
- [2] R.N. Schaeffer, J.S. Manson and R.E. Irwin 2013 "Effects of abiotic factors and species interactions on estimates of male plant function: a meta-analysis" *Ecology Letters* **16** 399-408
- [3] E.E. Agency 2012 "Air quality in Europe - 2012 report" (Luxembourg: Office for Official Publications of the European Union)
- [4] V.J. Black, C.R. Black, J.A. Roberts and C.A. Stewart 2000 "Impact of ozone on the reproductive development of plants" *New Phytologist* **147** 421-47
- [5] C.P. Leisner and E.A. Ainsworth 2012 "Quantifying the effects of ozone on plant reproductive growth and development" *Glob. Change Biol.* **18** 606-16
- [6] R. Sousa, L. Duque, A.J. Duarte, C.R. Gomes, H. Ribeiro, A. Cruz, J.C.G. Esteves da Silva and I. Abreu 2012 "In vitro exposure of *Acer negundo* pollen to atmospheric levels of SO₂ and NO₂: effects on allergenicity and germination" *Environmental Science & Technology* **46** 2406-12
- [7] E. Gottardini, F. Cristofolini, E. Paoletti, P. Lazzeri and G. Pepponi 2004 "Pollen viability for air pollution bio-monitoring" *Journal of Atmospheric Chemistry* **49** 149-59
- [8] E. Gottardini, A. Cristofori, F. Cristofolini, S. Maccherini and M. Ferretti 2008 "Ambient levels of nitrogen dioxide (NO₂) may reduce pollen viability in Austrian pine (*Pinus nigra* Arnold) trees - Correlative evidence from a field study" *Sci. Total Environ.* **402** 299-305
- [9] O. Iannotti, G. Mincigrucci, E. Bricchi and G. Frenguelli 2000 "Pollen viability as a bio-indicator of air quality" *Aerobiologia* **16** 361-5
- [10] A. Duro, V. Piccione and D. Zampino 2013 "Air quality biomonitoring through pollen viability of Fabaceae" *Environmental monitoring and assessment* **185** 3803-17
- [11] G. Chichiriccò and P. Picozzi 2007 "Reversible inhibition of the pollen germination and the stigma penetration in *Crocus vernus* ssp *vernus* (Iridaceae) following fumigations with NO₂, CO, and O₃ gases" *Plant Biology* **9** 730-5
- [12] J.I. Hormaza, K. Pinney and V.S. Polito 1996 "Correlation in the tolerance to ozone between sporophytes and male gametophytes of several fruit and nut tree species (Rosaceae)" *Sexual Plant Reproduction* **9** 44-8

Long range transport of European fine particulate nitrate in the Central Iberian Peninsula

M. A. Revuelta*, L. Núñez, F. J. Gómez-Moreno, M. Pujadas, B. Artíñano**

Abstract — The atmospheric long-range transport of particulate nitrate is difficult to assess due to its high chemical reactivity and thermal instability. However, nitrate can be transported over long distances. The literature shows that, under some meteorological situations, a flow of this pollutant from Central Europe into the Iberian Peninsula can be established. In this work, nine events of this type have been detected on an 8-years time series of fine nitrate measured at an urban background site in Madrid, in spite of the dominance of local sources. The events have been identified attending the hourly evolution of pollutants as well as backtrajectory information. One of them took place on March 2010 and was also detected simultaneously at EMEP rural stations in the Peninsula. During the course of this episode the spatial pattern of nitrate on EMEP stations was altered from the mean annual pattern registered on 2010.

Keywords — Fine particulate nitrate, European long-rang transport

1 INTRODUCTION

Chemically stable aerosol compounds can travel thousands of kilometers in the atmosphere. It is recognised that long-range transport of particulate sulphate can have a significant impact on the surface ambient concentrations of fine aerosol [1]. The fast chemical reactivity and thermal decomposition of some particulate nitrate (NO_3^-) compounds makes more difficult the identification of transport events, however, nitrate can also be transported over long distances under some circumstances.

References to regional pollutant transport in the Madrid air basin are frequent in literature [2], [3]. However, the studies of long-range transport of secondary inorganic compounds (SIC) of the aerosols into the Madrid air basin are rare, and probably limited to the study of Salvador et al (2008) [4]. Using back-trajectory clustering during the 1999–2005 period, the authors identified the highest SIC concentrations in TSP and PM10 for clusters representing:

1- low speed air circulation or regional transport. The cluster contained short trajectories of air mass recirculating within the Iberian Peninsula. This situation occurred predominantly in the summer and early autumn months.

2- transport of air masses from the European Continent towards the Iberian Peninsula, through the Mediterranean Sea. On average March, June and December were the months with a higher occurrence of this transport pattern.

The second kind corresponds to long-range

transport from Central Europe and the Western Mediterranean. Despite the predominance of the general Western circulation, polluted air masses from the European continent may reach the Peninsula through the Mediterranean basin or the Gulf of Biscay. The existence of other source areas which might contribute to sulphate and nitrate levels in the Madrid air basin must not be discarded either. North-African anthropogenic emissions are increasingly being considered in air pollution studies [5]. Recently, studying transport patterns and trends in precipitation chemistry of a rural site in North-Eastern Spain in the period 1984-2009, Izquierdo et al (2012) [6] discovered that industrialisation in Eastern Europe and North Africa seemed to be acquiring a greater role in the recent period. In the time period studied, NO_3^- sources areas from central Europe strikingly increased.

At Madrid, local episodes giving rise to high concentrations of urban fine nitrate have been described by [7]. These episodes take place under typical winter anticyclonic situations. The stagnation of air during winter thermal inversions favours concentration in a local scale during the coldest months of the year. PM accumulates under stable atmospheric conditions favoured by the presence of high pressures at surface level. Peaks attributed to regional transport were also identified.

In this work, individual episodes giving rise to high concentrations of fine nitrate attributed to transport from the European continent have been identified. These events have been detected at ground level in an urban background site in Madrid, in spite of the dominance of locally generated nitrate during most of the year. They have been distinguished from local episodes attending the hourly evolution of pollutants, since local accumulation leads to characteristic daily cycles that

Department of Environment, CIEMAT, Madrid, ES-28040, Spain. *mrevueltam@aemet.es, **b.artinano@ciemat.es

are inhibited under transport conditions [8: 187-208]. One of these episodes, which took place on March 2010 at the urban background site in Madrid and EMEP stations, is described in detail in this work.

2 METHODOLOGY

2.1 Sampling Sites and Techniques

The Madrid Metropolitan Area is located in the centre of the Iberian Peninsula. The population is nearly 6 million inhabitants, involving a car fleet of almost 3 million vehicles with very intense traffic on weekdays. Since industry consists essentially of light factories, the Madrid plume is typically urban. Hence, nitrate and NO_x precursor emissions come essentially from traffic. Pollutant and meteorological measurements data were recorded at the CIEMAT site (urban background) for the period 2004-2011. Particulate nitrate concentrations on PM_{2.5} were semi-continuously measured by a Rupprecht and Patashnick Series 8400N Ambient Particulate Nitrate Monitor. This instrument shows the highest efficiency of detection for ammonium nitrate (NH₄NO₃). Meteorological information was obtained from a permanent tower with the following parameters and heights: wind direction and speed at 52 m agl, precipitation and solar radiation at 31 m agl, temperature and humidity at 4m agl and pressure at ground level. Gaseous species (NO and NO₂) were measured by a DOAS spectrometer (OPSIS AR-500).

EMEP is a network for monitoring reactive gases, particulate matter and chemical precipitation under the European Monitoring and Evaluation Programme and is managed in Spain by the Spanish Meteorological Agency (AEMET). It is formed by 13 stations located throughout the Iberian Peninsula and the Balearic Islands. The EMEP network takes samples of PM₁₀ filters on a 24-h basis. Particulate nitrate concentrations are determined by Ion Chromatography.

2.2 Data Analysis Tools and Models

Nitrate concentration maps for the EMEP sites in Spain have been depicted using the Openair software (<http://www.openair-project.org>).

Backtrajectory information has been obtained using the FLEXTRA model outputs (<http://www.nilu.no/projects/ccc/trajectories>).

3 RESULTS

A time series of nitrate in PM_{2.5} has been studied at the CIEMAT site for the period 2004-2011. Transport events have been identified attending the short-scale time evolution of pollutants and

meteorological parameters. Nine of these events coincide with FLEXTRA backtrajectories originated in Central Europe. Fig. 1 (bottom) shows daily nitrate at CIEMAT during the measurement period. Transport events E1 to E9 have been marked with arrows. All of them took place in the cold season, between the months of December and April. It must be remembered that March, June and December were the months with the highest occurrence of transport of air masses from the European Continent towards the Iberian Peninsula. In this work fine nitrate transport episodes have not been detected in June probably due to the thermal decomposition of ammonium nitrate. These data have been compared with the nitrate in PM₁₀ registred at the EMEP site ES09 (Campisábalos), a rural site 100 km away from Madrid city (Fig. 1, top). The arrows show the moments when the events identified at CIEMAT occurred if ES09 data are available. The volatility of nitrate, together with the difference of techniques and aerosol size fractions measured at both sites result in a great difficulty in the identification of simultaneous events. The PM₁₀ fraction measured at EMEP is highly affected by the thermal-stable mineral fraction of coarse nitrate. In contrast, fine nitrate measured at CIEMAT is dominated by the thermally-unstable ammonium nitrate. Recently, Perrone et al (2013) [9] studied the input of fine aerosol received by a Central Mediterranean site in Italy. The authors found mineral nitrate and ammonium sulphate transport, but did not observe the ammonium nitrate transport. On the British Islands, Charron et al (2013) [10] identified long-range transport of both ammonium nitrate and sulphate originated at Central Europe. The authors used concentration field map methods and EMEP emissions information. In spite of the inherent difficulties of the study, in occasions nitrate long-range transport episodes at rural sites at the Central Iberian Peninsula and the urban background CIEMAT site can be seen. The most outstanding of the episodes recorded is event E8, which took place during the second week of March 2010 (green arrow). During E8 the nitrate concentrations reached at the urban background site at Madrid are lower than during the typical winter accumulation episodes. Nevertheless, the March monthly concentration (2.07 ± 0.06) is higher than on February (1.49 ± 0.05), in contradiction with the temperature-dependant nitrate seasonal pattern registered at the site [11]. This fact suggests an additional nitrate input in March 2010.

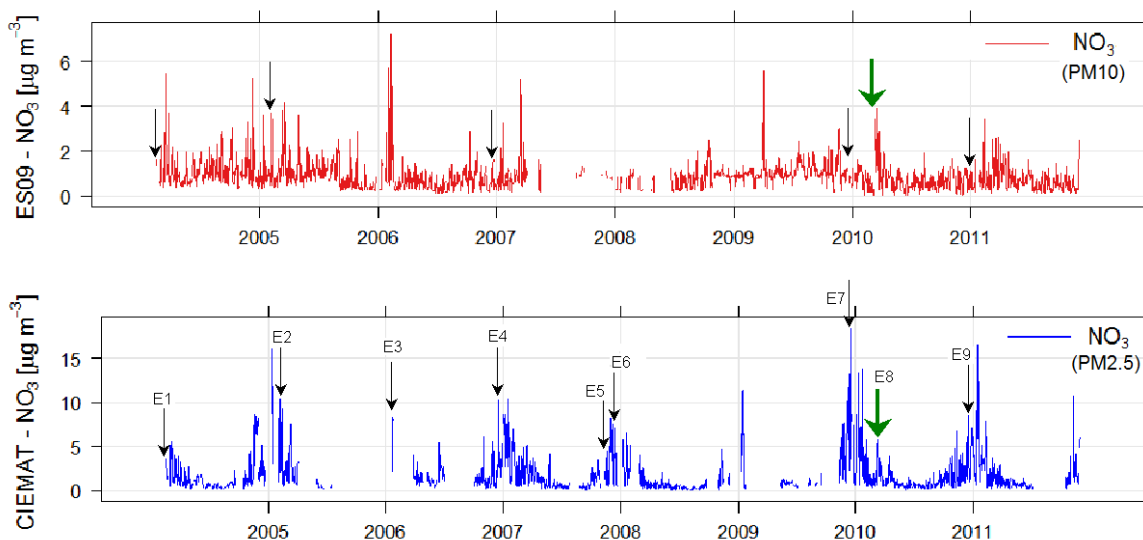


Fig. 1: Time series of daily particulate nitrate at ES09 and CIEMAT

Fig. 2 shows the short-time evolution (10 min) of meteorological parameters and pollutant concentrations at CIEMAT during E8. Between 10-14 March nitrate showed high concentrations not correlated to the NO or NO₂ precursors evolution. On March 12, wind speeds over 6 m·s⁻¹ coincide with a sharp nitrate increase. Maximum short-term concentrations are ~9 µg·m⁻³. This behavior contrasts with that

observed during local pollution events, when typical hourly evolutions of pollutants are seen. During winter accumulation episodes concentrations can be above 20 µg·m⁻³. These values reflect the dominance of local sources and thus the difficulty of detecting long-range transport events at an urban background station except with this type of short-term analysis.

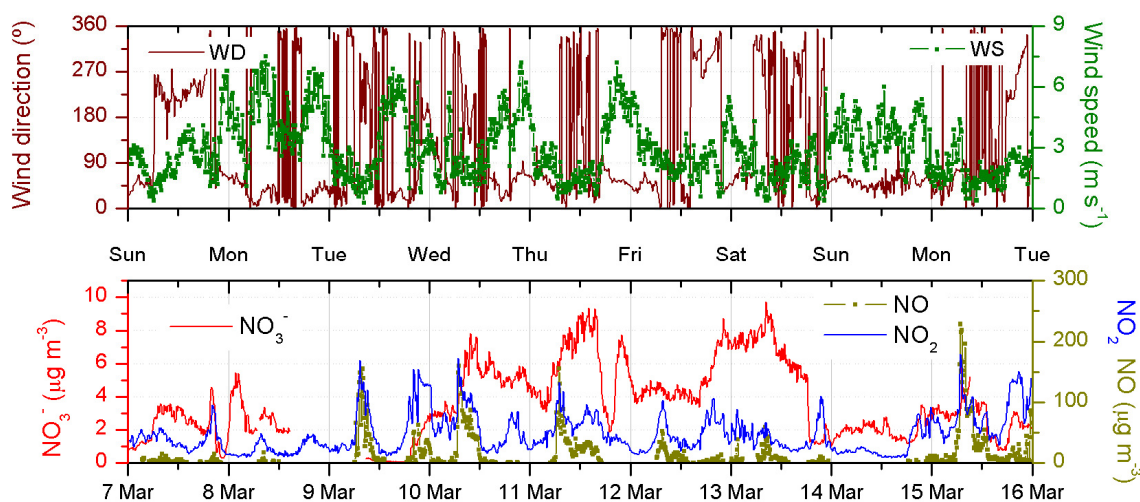


Fig. 2: Wind direction, wind speed (top) and PM2.5 nitrate, NO₂, NO (bottom) at CIEMAT during E8

Fig. 3 (left) shows European air mass origin at the three altitudes provided by FLEXTRA on March 12 2010 at 12 UTC. Fig. 3 (right) shows the daily evolution of particulate nitrate concentration at CIEMAT and three EMEP

stations at the Central Iberian Peninsula during March 2010. This evolution is similar at all the stations, which registered maximum levels during the main event between days 10 to 13, and also on three subsequent occasions.

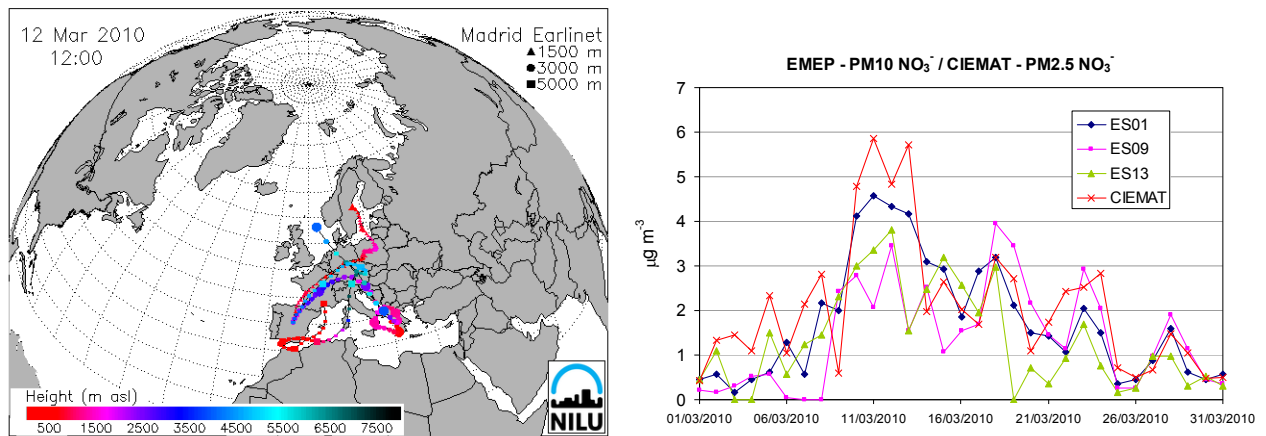


Fig. 3: FLEXTRA back-trajectories during E8 (left). Daily nitrate evolution at the Central Iberian Peninsula during March 2010 (right).

Fig. 4 shows mean nitrate concentrations maps at the 13 EMEP rural stations for four different periods. The top left map depicts 2010 annual averages. A spatial pattern is seen with the highest concentrations (over 1.5 $\mu\text{g}\cdot\text{m}^{-3}$) at the East Iberian coast, Balearic Islands and Huelva (ES17). Lower annual mean concentrations

(below 1.3 $\mu\text{g}\cdot\text{m}^{-3}$) were registered at the Central and Western Peninsula. This gradient was previously observed by [12] for the period 1999-2005. The authors attributed this result to the higher ammonia levels along the Mediterranean coast caused by emissions from intensive cultivation and farming.

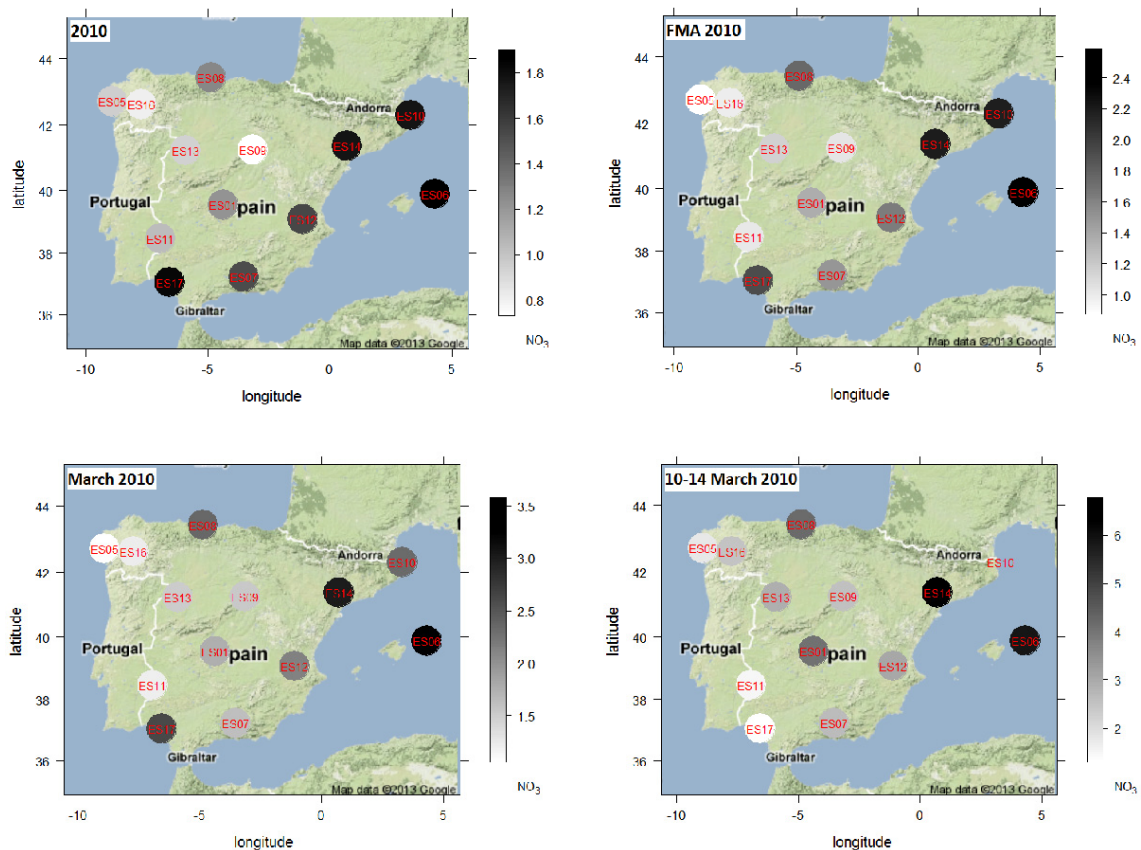


Fig. 4: Mean PM10 nitrate concentration [$\mu\text{g}\cdot\text{m}^{-3}$] maps at EMEP sites

This spatial pattern remains similar when we restrict the analysis to the period February-March-April (FMA) 2010 (top right), although concentrations are higher due to the effect of the low temperatures. During this three-month period, the highest concentrations were recorded on March (bottom left). In this month the pattern is significantly altered from the annual means. On 10-14 March (bottom right) a spatial pattern clearly different from the annual gradient is found, showing the highest concentrations at the North-Eastern stations. Nitrate concentrations decrease towards the South-Western direction reaching minimum values at ES11 and ES17 (Badajoz and Huelva).

The behaviour observed at the Madrid urban background site as well as the EMEP stations is consistent with the atmospheric transport of high concentrations of particulate nitrate from Central Europe towards the Iberian Peninsula. These results allow identifying E8 as an example of the impact of the European nitrate input in the Peninsula.

4 CONCLUSIONS

A major fraction of fine nitrate in the atmosphere is on the form of the thermally unstable ammonium nitrate. This fact implies a great difficulty in assessing the long-range transport of this pollutant.

In this work, the impact of fine nitrate inputs transported from Central Europe at an urban background site in Madrid has been identified. Back-trajectory information together with short-time evolution of pollutants served to detect 9 events along an 8-year time period. Out of them, event E8 has been selected and analysed in detail, since it is the one most clearly observed simultaneously at the rural stations in the Central Iberian Peninsula. E8 took place in March 2010. A peak is observed on the monthly concentration of both fine nitrate at the urban background site and nitrate in PM10 at the rural stations. The short-term concentrations reached ($\sim 9 \mu\text{g}\cdot\text{m}^{-3}$) were half of the maximum concentrations registered during local accumulation events at the urban background site.

In 2010, an annual spatial pattern of nitrate concentration at the EMEP stations was observed, with the highest concentrations at the Eastern and Southern stations. This pattern was altered during E8, when the highest concentrations were reached at the North-Western stations decreasing towards the South-Eastern direction.

All these observations point to E8 as a long-range episode of transport of particulate nitrate.

These results provide information on the impact of the European nitrate input in the Iberian Peninsula.

ACKNOWLEDGMENTS

The Ministry of Science and Innovation is acknowledged for their economical support through the CGL2011-27020 project. The Openair software is a project of the Natural Environment Research Council (NERC) of the UK. The FLEXTRA model was developed by Andreas Stohl (NILU) in cooperation with Gerhard Wotawa and Petra Seibert (Institute of Meteorology and Geophysics, Vienna). Meteorological data was data provided by ECMWF.

REFERENCES

- [1] K. M. Wagstrom, S. N. Pandis. "Contribution of Long Range Transport to local Fine Particulate Matter Concerns". *Atmos. Environ.* 45, no. 16: 2730-35, 2011.
- [2] P. Salvador, Artiñano, B., Alonso, D. G., Querol, X., Alastuey, A. "Identification and characterisation of sources of PM10 in Madrid (Spain) by statistical methods". *Atmos. Environ.* 38(3): 435-447, 2004.
- [3] E. Coz, F. J. Gómez-Moreno, G. S. Casuccio, B. Artiñano. "Variations on morphology and elemental composition of mineral dust particles from local, regional, and long-range transport meteorological scenarios", *J. Geophys. Res.*, 115, D12204, 2010.
- [4] P. Salvador, Artiñano B., Querol X. Alastuey A. "A combined analysis of backward trajectories and aerosol chemistry to characterize long-range transport episodes of particulate matter: the Madrid air basin, a case study". *Sci. Tot. Environ.* 390/2-3 pp. 496-507, 2008.
- [5] S. Rodríguez, A. Alastuey, S. Alonso-Perez, X. Querol, E. Cuevas, J. Abreu-Afonso, M. Viana, N. Perez, M. Pandolfi, J. de la Rosa. "Transport of desert dust mixed with North African industrial pollutants, in the subtropical Saharan Air layer". *Atmos. Chem. Phys.* 11, 6663-6685, 2011.
- [6] R. Izquierdo, A. Avila, M. Alarcón. "Trajectory statistical analysis of atmospheric transport patterns and trends in precipitation chemistry of a rural site in NE Spain in 1984-2009". *Atmos. Environ.* 61, 400-408, 2012.
- [7] F. J. Gomez-Moreno, Nunez, L., Plaza, J., Alonso, D., Pujadas, M., Artiñano, B. "Annual evolution and generation mechanisms of particulate nitrate in Madrid". *Atmos. Environ.* 41(2): 394-406, 2007.
- [8] M. A. Revuelta. Study of secondary inorganic aerosol compounds in the urban atmosphere: temporal evolution and characterisation of episodes. PhD Thesis, Universidad Complutense de Madrid, 2013. (Pending publication).
- [9] M. R. Perrone, S. Becagli, J.A. Garcia Orza, R. Vecchi, A. Dini, R. Udisti, M. Cabello. The impact of long-range-transport on PM1 and PM2.5 at a Central Mediterranean site. *Atmos. Environ.* 71, 176-186, 2013.
- [10] A. Charron, C. Degrendele, B. Laongsri, and R. M. Harrison. Receptor modelling of secondary and carbonaceous particulate matter at a southern UK site. *Atmos. Chem. Phys.*, 13, 1879-1894, 2013.
- [11] M. A. Revuelta, R. M. Harrison, L. Nunez, F. J. Gomez-Moreno, M. Pujadas, B. Artinano. "Comparison of temporal features of sulphate and nitrate at urban and

Revuelta et al: Long range transport of European fine particulate nitrate in the Central Iberian Peninsula

- rural sites in Spain and the UK". *Atmos. Environ.*, 60, 383–391, 2012.
- [12] X. Querol, A. Alastuey, T. Moreno, M. M. Viana, S. Castillo, J. Pey, S. Rodríguez, B. Artiñano, P. Salvador, M. Sanchez, S. Garcia Dos Santos, M. D. Herce Garraleta, R. Fernandez-Patier, S. Moreno-Grau, L. Negral, M. C. Minguillon, E. Monfort, M. J. Sanz, R. Palomo-Marín, E. Pinilla-Gil, E. Cuevas, J. de la Rosa, A. Sanchez de la Campa. (Spatial and temporal variations in airborne particulate matter (PM₁₀ and PM_{2.5}) across Spain 1999-2005. *Atmos. Environ.* 42, 3964-3979, 2008.

The REDMAAS 2012 SMPS+UFP intercomparison campaign

F. J. Gómez-Moreno¹, E. Alonso¹, B. Artíñano¹, V. Juncal Bello², M. Piñeiro Iglesias²,
P. López Mahía^{2,3}, N. Pérez⁴, J. Pey⁴, A. Alastuey⁴, B. A. de la Morena⁵, M. I. García⁶,
S. Rodríguez⁶, M. Sorribas^{7,8}, G. Titos^{7,8}, H. Lyamani^{7,8} and L. Alados-Arboledas^{7,8}

Abstract — The Spanish network on environmental DMAs (Red Española de DMAs Ambientales, REDMAAS) is currently formed by six groups involved in the monitoring of atmospheric particle size distributions by means of Differential Mobility Analyzers (DMAs). The REDMAAS network is operative since 2010. One of the main activities developed in the network is an annual SMPS and UFP intercomparison. In this work we show the results obtained in the last intercomparison campaign: the DMA calibration checks with latex, the CPC intercomparison, the SMPS+UFP intercomparison results and additionally a study on particle losses in dryers. This last study tried to take into account the particle deposition in the dryer section because of the few results found in the literature. The DMA calibration checks showed very good agreement between the different instruments for 80 nm latex particles, with a deviation lower than 3% among them. The CPC intercomparison showed two groups of instruments measuring the same concentrations but with a 10% of deviation between the two groups. Six dryers were tested in the deposition study. The results showed differences in their individual behaviors, a possible age effect could be seen although other causes cannot be excluded, i.e. the inner tube could be twisted. A comparison with theoretical deposition was performed.

Keywords — Atmospheric aerosols, Particle size distribution, Aerosol dryers, SMPS

1 INTRODUCTION

One of the most important properties of atmospheric particles is their size, since it affects their behavior and provides information about its origin and history. Size distributions play an important role in understanding those processes where the aerosol is involved. For example, the radiation-matter interaction processes known as scattering and absorption depend on the particle size. Atmospheric particles play a key role in the Earth's radiative balance and thus influence climate change [1]. Some climate models indicate that aerosols are delaying the expected warming due to the greenhouse gases. Sulfate and organic particles have a particular influence on this delay; both kinds of particles are mainly in the ultrafine range.

The health effect studies need to know the particle size distribution to obtain the fraction of particles that are deposited in the lungs and other parts of the respiratory system, especially those able of penetrating into the bloodstream. Some studies have shown that the particle toxicity per mass unit increases as the particle size decreases [2, 3].

So, it is important to measure and know the

atmospheric size distributions of fine and ultrafine particles in order to fully understand their properties, both the particle dynamics and its influence in the environment. Thus, in addition to those works focused on particle formation by nucleation [4], the origin and distribution of ultrafine particles has been studied by SMPS instruments in several European and American cities, e.g. Birmingham [5], Helsinki [6], Pittsburgh [7], Barcelona [8], ... There have also been some studies on different types of non-urban stations: rural [9], regional background [10, 11], arctic and coastal background [12] or tropospheric background in Antarctica [13].

In the case of Spain, there are six research groups measuring the size distributions of atmospheric particles in different type of environments in the provinces of La Coruña (UDC), Barcelona (IDAEA-CSIC), Madrid (CIEMAT), Huelva (El Arenosillo-INTA), Granada (UGR) and the island of Tenerife (CIAI-AEMET). These groups have to solve similar problems, so the cooperation between them has allowed the optimization of the facilities and the results obtained.

The SMPSs are instruments widely used to measure particle size distributions in the atmosphere [14]. It is formed by a DMA [15] and a CPC [16] working in a scanning mode [17]. The DMA classifies the particles according to their electrical mobility and later the CPC counts them obtaining so the size distribution. The Ultrafine Particle Monitor [18], UFP, is also composed by a DMA, but the particles are counted by electrometers.

In 2010 the REDMAAS (Spanish Network of Environmental DMAs) is established in Spain. Its objective is to promote the exchange and transfer of

1. Department of Environment, CIEMAT, Madrid, E-28040, Spain, First Author E-mail: F.J.Gomez@ciemat.es
2. Institute of Environment, University of A Coruña (IUMA-UDC), A Coruña, E-15179, Spain
3. Dept. Analytical Chemistry, University of A Coruña, A Coruña, E-15071, Spain
4. Institute of Environmental Assessment and Water Research (IDAEA-CSIC), Barcelona, E-08034, Spain
5. Atmospheric Sounding Station 'El Arenosillo', INTA, Mazagón-Huelva, E-21130, Spain
6. Izaña Atmospheric Research Centre, (IARC/CIAI), AEMet, Santa Cruz de Tenerife, E-38001, Spain
7. Andalusian Environmental Centre (CEAMA), University of Granada, E-18071 Granada, Spain
8. Applied Physics Department, University of Granada, E-18071 Granada, Spain

knowledge between the groups and to optimize the use of such instrumentation, the SPMS. This is reached through a series of activities to ensure the quality of the measurements and the cooperation between the groups. One of the activities of the REDMAAS is an annual campaign where DMA calibration checks, CPC and SMPS intercomparisons are performed. In this paper we introduce the results obtained during the 2012 campaign where 7 CPCs, 5 SMPSs and 1 UFP were deployed, all of them manufactured by TSI.

2 CAMPAIGN LOCATION

The intercomparison campaign was held in the Atmospheric Sounding Station El Arenosillo (37.10°N, 6.73°W, 40 m asl) belonging to Instituto Nacional de Técnica Aeroespacial (INTA) (www.inta.es/atmosfera). The observatory is located on the Atlantic coast of Andalusia, in the province of Huelva and within the Natural Area of the Doñana National Park. Around the observatory, from W to SE and clockwise over several tens of kilometers, it is possible to find a tree forest with predominance of pine. The Atlantic Ocean is in the SE-W clockwise area and less than 1 km from the observatory.

Due to good weather conditions with predominance of clear days and the provision of general services, this observatory has exceptional conditions for the development of intercomparison campaigns. This has allowed to perform several campaigns since 1999 for different kinds of instruments.

This campaign was performed from November 11th to 20th, 2012. The instrument deployment used during the campaign can be found in Fig. 1.



Fig. 1. In this picture it is possible to see three SMPSs on the left side and two SMPSs and an UFP on the right side during the instrument intercomparison. The flow splitter is in the top side

3 RESULTS

3.1 DMA Calibration Checks

First of all, a general routine maintenance was performed to the different instruments to ensure proper operation. After the verification of the flow rates using primary standards (Gilibrator bubble flowmeters), the DMA calibrations were checked using latex particles. Two particle sizes were chosen: 80 and 190 nm. The latex particles were suspended in water and were aerosolized using a Collision atomizer [19].

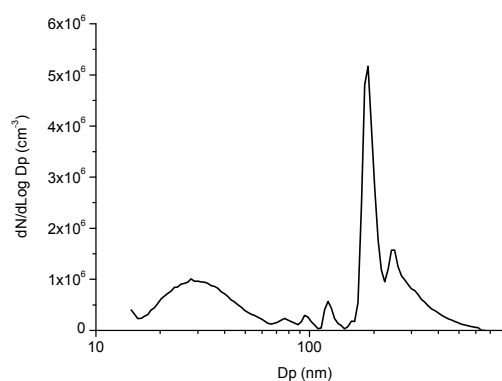


Fig. 2. Calibration check of DMA-5 using 190-nm latex particles. The peak around 30 nm is due to water residue and the tail after 190 nm is caused by particle agglomeration.

An example of the results can be found in Fig.2. In this case, the DMA-5 was calibrated using 190-nm particles. All instruments had deviations less than 3% for the 80-nm particles and only two of them had above this value for 190-nm particles.

3.2 CPC Intercomparison

The second activity was the CPC intercomparison. In this case, 6 TSI CPCs were deployed in the lab, being the following models: 3772, 3775, 3025, 3785, 3776 (2). All of them use butanol as condensation liquid but the 3785, using water. Ambient air was sampled from a common flow splitter, which was connected to an external probe. Another CPC 3010 was later used in the campaign, but it could not participate in the CPC intercomparison.

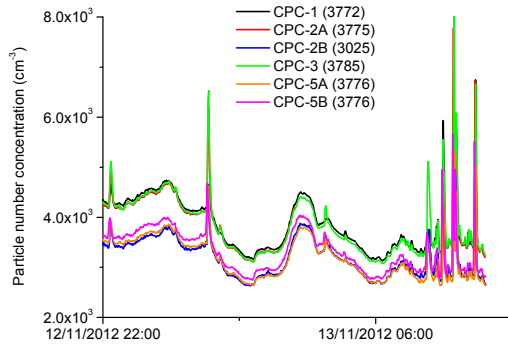


Fig. 3. CPC intercomparison results. There were 7 CPCs during the 2012 campaign, but only 6 of them could be compared.

These results show that there are two different groups of measurements. The first group (3785, 3772 and 3775) has a deviation around 9% above the average value, while a second group has two counters with a deviation of 9.5% and another with 5% below that value. This second group corresponds to those counters (models 3025 and 3776) that can measure smaller particle sizes, down to 3 nm. Both models work in a similar way, taking a sample flow and using only a small fraction of it in the sensor section.

The TSI UFP (model 3031) was compared with a CPC3776. Both had a similar behavior, with an average difference between them of -0.4%.

3.3 SMPS Intercomparison

In the Fig. 4 it is possible to find an SMPS intercomparison for a selected period. In this figure, the particle sizes have been grouped in 6 intervals. In all of them, the concentrations measured by the instruments are very similar. The biggest differences were observed for the smaller particles, below 30 nm, where the diffusion losses can affect the instruments. In order to avoid this, the pipe lengths and the flow rates were the same for all the measurements.

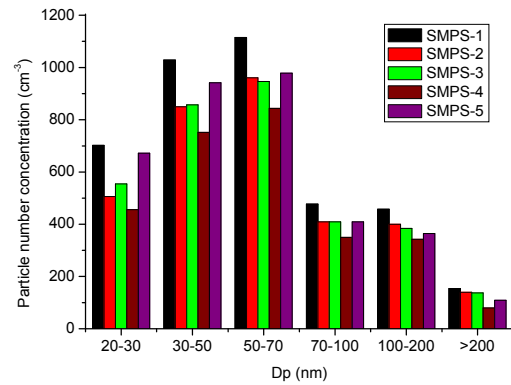


Fig. 4. SMPS intercomparison during the campaign. These data were taken the November 15th, 17:20-18:20.

3.3 Particle losses in dryers

During the 2012 intercomparison campaign, especial attention was paid to the particle deposition in sampling lines and an experimental study was performed to analyze the deposition in the dryers. Since there are only few studies on this issue [14], the quantification of such losses is actually needed. To this end, the sampled air was first dried and then a flow splitter divided the flow into two. Two SMPSs measured the particle size distribution in parallel, the first of them didn't have any dryer and the second had the testing one. These two SMPSs previously had shown to measure the same distributions. The pipes lengths from the splitter to the SMPS were the same for both of them, so the differences in the measurements were caused by the particle deposition in the dryer. Six dryers (5 Permapure Nafion dryers SS12" and 1 dryer SS24") were tested. An example of the results can be found in Fig. 5 for the long dryer (Nafion SS24").

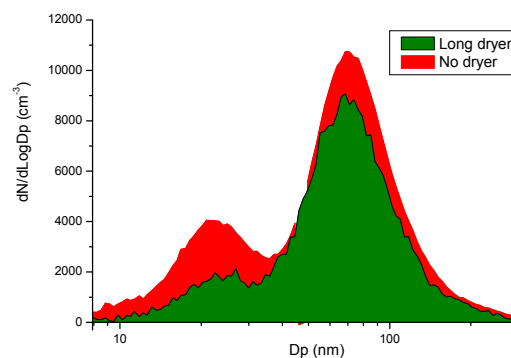


Fig. 5. A dry aerosol measured with and without dryer (Nafion SS24"). The difference between the two measurements is the particle deposition in the dryer.

The results have shown a different behavior for every individual dryer. These differences could be

caused by an aging effect, although other possibilities are open, e.g. the nafion tube could be twisted and this could produce a higher deposition by turbulent impaction. A comparison with theoretical deposition has been done [20], showing a higher deposition in the experiments. This is because not all the deposition mechanisms are included in the theoretical estimation, e.g. the turbulent impaction.

4 CONCLUSIONS

It has been observed that the instruments belonging to the Spanish network on environmental DMAs (REDMAAS) have similar sensitivities in terms of particle size classification and aerosol concentration. The calibrations with latex particles have given a low deviation from its nominal value. The CPC intercomparison has shown two different groups of instruments, probably because of two different technologies for particle detection. The SMPSs have given similar measurements. The study of particle deposition in dryers has shown a different behavior for every dryer, with experimental values higher than those theoretical ones

ACKNOWLEDGMENT

This network is financed by the Ministry of Science and Innovation (CGL2011-15008-E & CGL2011-27020).

REFERENCES

- [1] Climate change 2007: synthesis report. In: *Contribution of Working Groups I, II and III to the Fourth Assessment Report of the Intergovernmental Panel on Climate Change*, R.K Pachauri, A. Reisinger, eds. IPCC, Geneva, Switzerland, 2007.
- [2] J.J.N Lingard, A.S. Tomlin, A.G. Clarke, K. Healey, A. Hay and C.P. Wild, "A study of trace metal concentration of urban airborne particulate matter and its role in free radical activity as measured by plasmidstrand break assay," *Atmos. Environ.*, 39, pp. 2377-2384, 2005.
- [3] G. Oberdorster, "Toxicology of ultrafine particles: in vivo studies," *Phil. Trans. R. Soc. A*, 358, 2719-2740, 2000.
- [4] M. Kulmala, H. Vehkamäki, T. Petäjä, M. Dal Maso, A. Lauri, V.-M. Kerminen, W. Birmili and P.H. McMurry, "Formation and growth rates of ultrafine atmospheric particles: a review of observations," *J. Aerosol Sci.*, 35, pp. 143-176, 2004.
- [5] R.M. Harrison, M. Jones and G. Collins, "Measurements of the physical properties of particles in the urban atmosphere," *Atmos. Environ.*, 33, pp. 309-321, 1999.
- [6] T. Hussein, A. Puustinen, P.P. Aalto, J.M. Mäkelä, K. Hämeri and M. Kulmala, "Urban aerosol number size distributions," *Atmos. Chem. Phys.*, 4, pp. 391-411, 2004.
- [7] C.O. Stanier, A.Y. Khlystov and S.N. Pandis, "Ambient aerosol size distributions and number concentrations measured during the Pittsburgh Air Quality Study (PAQS)," *Atmos. Environ.*, 38, pp. 3275-3284, 2004.
- [8] J. Pey, S. Rodríguez, X. Querol, A. Alastuey, T. Moreno, J. P. Putaud and R. Van Dingenen, "Variations of urban aerosols in the western Mediterranean," *Atmos. Environ.*, 42, pp. 9052-9062, 2008.
- [9] J.M. Mäkelä, P. Aalto, V. Jokinen, T. Pohja, A. Nissinen, S. Palmroth, T. Markkanen, K. Seitsonen, H. Lihavainen and M. Kulmala, "Observations of ultrafine aerosol particle formation and growth in boreal forest," *Geophys. Res. Lett.*, 24, pp. 1219-1222, 1997.
- [10] M. Cusack, N. Pérez, J. Pey, A. Alastuey and X. Querol. "Source apportionment of fine PM and sub-micron particle number concentrations at a regional background site in the western Mediterranean: a 2.5 yr study," *Atmos. Chem. Phys. Discuss.* 13, pp. 3915-3955, 2013, submitted for publication in ACP.
- [11] M. Cusack, N. Pérez, J. Pey, A. Wiedensohler, A. Alastuey and X. Querol, "Variability of sub-micrometer particle number size distributions and concentrations in the Western Mediterranean regional background," *Tellus B*, 65, pp. 19243, 2013.
- [12] M. Sorribas, V.E. Cachorro, J.A. Adame, B. Wehner, W. Birmili, A. Wiedensohler, A.M. De Frutos and B.A. de la Morena, "Sub-micrometric aerosol size distributions in Southwestern Spain: Relation with meteorological parameter". ICNAA. Galway (Irlanda), 2007.
- [13] J. L. Gras, "Condensation nucleus size distribution at Mawson, Antarctica: micro-physics and chemistry," *Atmos. Environ.*, 27, Part A, pp. 1417-1425, 1993.
- [14] A. Wiedensohler, W. Birmili, A. Nowak, A. Sonntag, K. Weinhold, M. Merkel, B. Wehner, T. Tuch, S. Pfeifer, M. Fiebig, A. M. Fjåraa, E. Asmi, K. Sellegri, R. Depuy, H. Venzac, P. Villani, P. Laj, P. Aalto, J. A. Ogren, E. Swietlicki, P. Williams, P. Roldin, P. Quincey, C. Hüglin, R. Fierz-Schmidhauser, M. Gysel, E. Weingartner, F. Riccobono, S. Santos, C. Gröning, K. Faloon, D. Beddows, R. Harrison, C. Monahan, S. G. Jennings, C. D. O'Dowd, A. Marinoni, H.-G. Horn, L. Keck, J. Jiang, J. Scheckman, P. H. McMurry, Z. Deng, C. S. Zhao, M. Moerman, B. Henzing, G. de Leeuw, G. Löschau and S. Bastian, "Mobility particle size spectrometers: harmonization of technical standards and data structure to facilitate high quality long-term observations of atmospheric particle number size distributions," *Atmos. Meas. Tech.*, 5, pp. 657-685, 2012.
- [15] E.O. Knutson, and K.T. Whitby, "Aerosol classification by electric mobility: apparatus, theory and applications," *J. Aerosol Sci.*, 6, 443-451, 1975.
- [16] J.K. Agarwal and G.J. Sem, "Continuous Flow Single-Particle-Counting Condensation Nuclei Counter," *J. Aerosol Sci.*, 11, pp. 343-357, 1980.
- [17] S.C. Wang, R.C. Flagan, "Scanning electrical mobility spectrometer," *Aerosol Sci. and Tech.* 13, pp. 230-240, 1990.
- [18] L. Hillemann, A. Zschoppe and R. Caldow, "Aerosol mobility spectrometry based on diffusion charging," European Aerosol Conference 2007, Salzburg, Abstract T05A008, 2007.
- [19] K.R. May, "The Collision Nebulizer. Description, Performance & Application," *J. Aerosol Sci.*, 4, pp. 235-243 1973.
- [20] J.E. Brockmann. "Sampling and transport of aerosol". Chapter 6 in *Aerosol Measurement*, K. Willeke and P.A. Baron, eds., New York, Van Nostrand Reinhold, pp. 77-111, 1993.

Inventario del Aerosol Desértico en la Región de Castilla y León (2003 - 2012)

V.E. Cachorro¹, M.A. Burgos¹, Y. Bennouna¹, C. Toledano¹, B. Torres^{1,2}, A. Herguedas³,
J. González Orcajo³, A.M. de Frutos¹

Abstract — As part of the columnar aerosol characterization and establishment of a climatology representative of the north-centre region of Spain (Castilla and León), a study on the discrimination and classification of aerosol types has been carried out. This work focuses on the estimation of the desert type aerosol which is transported to this region, using a detailed inventory of the events, associated days and frequency, and other characteristics of this type of intrusion over a period of 10 years, between 2003 and 2012. The method employed here is similar to that documented in [1] which is based on a few threshold criteria on the values of aerosol parameters AOD-Alfa, adapted to the particularity of this region of study, characterized as clean continental. The detection of an episode or intrusion of desert type is not complicated, but it can be difficult to determine the exact number of days, mainly at the end of episodes, which correspond to mixed aerosols, with high values of the Alfa parameter, above 1 (low values being observed only in the case of strong events). For this reason it was chosen to distinguish between the days with Alfa values below 1 for pure desert dust, in comparison with those of mixed aerosol called DC (Desert-Continental), with Alfa between 1 and 1.5. With the aim to improve the classification of the days, additional information on PM10 data from the background station of Peñausende (Zamora) belonging to the EMEP network, have been used. Moreover, air mass backtrajectories from the HYSPLIT model and satellite images from the MODIS sensor, synoptic maps as well as forecast maps from the NAAPS model were examined, with the aim to perform a better discrimination, characterization and estimation. The combination of the entire information has facilitated the manual inventory, which will constitute a basis for the validation of an automatic method for future precise detection and estimation of this type of aerosol in the studied region.

Palabras Clave — Aerosol desértico, Espesor óptico de aerosoles, Exponente de Ångström, Inventario.

1 INTRODUCCIÓN

La presencia de aerosol desértico modifica sustancialmente la estimación de la radiación tanto a nivel de atmósfera como a nivel de superficie. Debido a ello, los efectos radiativos globales de los aerosoles minerales en el clima están sujetos a un intenso estudio desde la década de los 70. El desierto del Sahara es la principal fuente de aerosol mineral en el hemisferio Norte, afectando directamente nuestra zona de estudio. Tomando como base el inventario realizado en el sur-oeste de la Península Ibérica [1], y siguiendo una misma línea de procedimientos y análisis, se pretende extender dicho trabajo al norte de la Meseta Castellana, a la vez que ampliar el periodo de estudio.

Utilizando las técnicas de detección remota basadas en las medidas de radiómetros solares a nivel de suelo, podemos detectar y evaluar estas intrusiones desérticas y también caracterizar las propiedades ópticas de éstos aerosoles.

En este trabajo hemos desarrollado un inventario de los episodios desérticos ocurridos en un periodo de diez años, comprendido entre enero de 2003 y diciembre de 2012, a partir de los datos obtenidos con un fotómetro solar en el marco de la red

AERONET en la estación de Palencia. El fotómetro solar permite obtener información real (“ground truth”) sobre los aerosoles desérticos bajo condiciones de cielo despejado, útil para evaluar su influencia en los niveles de AOD.

El propósito de este trabajo es el de proveer de un inventario fiable de eventos desérticos en esta zona de estudio, pero no el de dar una caracterización detallada de sus propiedades ópticas. Por tanto, el inventario que hemos realizado determina el número, la duración y la intensidad de los eventos correspondientes a las intrusiones de aerosol desértico. A su vez pretende servir de estudio complementario al realizado por [2] sobre la climatología de éstos y en [3] sobre la comparativa de los valores de PM10 y AOD para evaluar la influencia de los aerosoles desérticos sobre los valores totales. Sin embargo, debemos mencionar que el estudio en [2] se realiza con datos de PM10 y AOD conjuntamente, mientras que el presente trabajo se realiza tomando como datos básicos los de aerosol en columna obtenidos con el fotómetro Cimel.

Cabe señalar que las medidas de los fotómetros están únicamente disponibles en condiciones de cielo despejado, por lo que los episodios que ocurran bajo condiciones de lluvia o cielo nublado serán parcialmente o no detectados. Estos episodios requerirán de otros mecanismos de detección y evaluación, y es por ello que hemos utilizado información complementaria como se explica en la

1. Grupo de Óptica Atmosférica (GOA-UVA), Universidad de Valladolid, 47071, Valladolid, España, Autor Correspondiente: e-mail: chiqui@goa.uva.es
2. Laboratoire d'Optique Atmosphérique, UMR8518, Université des Sciences et Technologies de Lille, Villeneuve d'Ascq, France.
3. Departamento de Control de Calidad y Cambio Climático. Consejería de Fomento y Medio Ambiente de la Junta de Castilla y León. Valladolid, España.

metodología. Con todo, es previsible pensar que este inventario pueda producir una estimación a la baja de la ocurrencia de eventos desérticos, pero esta es mínima y entra dentro del error de la estimación, tanto en lo concerniente al número de eventos desérticos como al número de días asociados a los mismos.

Este trabajo se estructura de la siguiente manera: en primer lugar describiremos la estación de medida así como la instrumentación utilizada y los datos aportados. Seguiremos explicando la metodología empleada para terminar mostrando los principales resultados obtenidos.

2 ESTACIÓN DE MEDIDA E INSTRUMENTACIÓN

La localización geográfica de la principal estación utilizada, Palencia, es 41.9N, 4.5W (750 metros de altura sobre el nivel del mar). Dicha ciudad pertenece a la comunidad autónoma española de Castilla y León y se encuentra en la zona centro-norte de la Península Ibérica, concretamente en la llamada Meseta Norte, que tiene una altitud promedio de 700 metros.

La comunidad autónoma de Castilla y León es la tercera comunidad menos poblada de España debido a su gran superficie (94.193 km²) y su poca población (2.543.413 habitantes censados en 2012), teniendo una densidad de población de poco más de 27 habitantes por km². La estación de Palencia se encuentra en ésta pequeña ciudad (~100.000 habitantes) que está situada en un área rural, bien aislada de grandes núcleos urbanos e industriales y desde donde se pueden observar con claridad las intrusiones de polvo desértico.

Los datos proporcionados por esta estación de Palencia son los correspondientes al fotómetro Cimel que ha estado realizando medidas de las propiedades ópticas de los aerosoles dentro de la red AERONET durante este periodo de estudio de 2003 a 2012 (y continúa operativo). Sin embargo, destacamos que no ha estado operativo durante todos los años quedando así los meses de junio a diciembre de 2009 y de enero a septiembre de 2010 sin datos en esta estación. Los datos de estos periodos han sido reemplazados por los medidos en la estación de Autilla del Pino, a 7 Km. de la ciudad. Los detalles sobre este periodo de estudio pueden verse en [4]. Más detalles sobre la instrumentación se pueden encontrar en la propia página Web de AERONET.

3 METODOLOGÍA

Los datos de AERONET en la estación de Palencia nos permiten calcular el espesor óptico de los aerosoles (AOD) y derivar a partir de éste el exponente de Ångström, "Alfa", en el rango espectral de 440-870 nm. Los valores de AOD y

Alfa constituyen la herramienta fundamental para nuestro análisis.

El proceso que seguiremos para detectar las intrusiones desérticas es una inspección manual que se basa en establecer unos valores umbrales para estos dos parámetros AOD-Alfa, que dependen de la zona de estudio y están basados en la climatología de la zona y nuestra experiencia en este tipo de datos. A su vez esta información base va acompañada de un análisis detallado de información complementaria como indicamos más adelante.

Según vemos en [3], la climatología de la estación de Palencia nos indica un valor promedio de AOD (440 nm) de 0.15 ± 0.10 y un valor promedio de Alfa de 1.29 ± 0.35 en el periodo de 2003 a 2011.

Por tanto, en primer lugar se detectan los episodios utilizando los siguientes valores umbrales: $AOD > 0.18$ y $Alfa < 1$, referido a los valores puntuales o instantáneos de Cimel (medidas quinceminutales). Estos valores son escogidos basándonos en nuestra experiencia sobre los datos de AOD en la estación de estudio y en otras estaciones, así como en la literatura y en la climatología del aerosol. Este primer paso permite detectar el episodio en sí, pues los días centrales del mismo o los más intensos son determinados fácilmente.

El segundo paso y más complicado (el relativo al número de días del evento) es acotar la duración de cada episodio, señalando su primer y último día, así como descartar datos poco fiables, por ejemplo los debidos a la contaminación por la nubosidad que no hayan sido correctamente descartados por AERONET con anterioridad, o bien la falta de datos en sí.

En esta inspección manual clasificamos si un evento es D (Desértico Puro) o DC (Desértico mezclado con Continental). La principal diferencia entre ambos, que nos muestran valores AOD superiores a 0.18, radica en el parámetro Alfa. En el caso de los días con clara intrusión desértica (D), éste se encuentra por debajo de 1, mientras que si tenemos una situación en que conviven el aerosol desértico con el aerosol continental propio de la zona o con recirculaciones de masas de aire, tendremos un aerosol mezcla (DC), obteniendo valores de Alfa que oscilarán entre 1 y 1.5.

En este tipo de aerosol mezcla, que denominamos DC (aerosol desértico no puro), lo que queremos indicar es que no hay una prevalencia marcada de aerosol desértico. Sin embargo, asignar porcentajes de mezcla de uno u otro no es una tarea fácil, y por ahora, únicamente haremos la distinción D y DC sin cuantificar la mezcla que tenemos.

Cuando un evento irrumpe en nuestra área de estudio, los datos muestran un ascenso por encima del valor umbral de AOD así como un descenso por debajo del valor umbral de Alfa y cuando el evento termina, se recobran los valores de fondo de la estación. Este patrón es generalmente sencillo de reconocer. Los eventos más intensos son los que

muestran un mayor incremento de AOD a la vez que un mayor descenso del parámetro Alfa, en ocasiones incluso, llegando a valores próximos a cero.

Para acotar de forma precisa los días de comienzo y finalización de los eventos, nos servimos de otra información como son los valores de PM10 en la estación de Peñausende (Zamora), así como las retro trayectorias proporcionadas por el modelo HYSPLIT, evaluadas a 500, 1500 y 300 metros. Estas fuentes nos permiten contrastar los datos obtenidos con los fotómetros y nos ayudan a solucionar posibles dudas sobre si incluir o no ciertos días de comienzo o de fin de los episodios. También contrastamos con imágenes de satélite MODIS, mapas sinópticos y predicciones del modelo NAAPS, para descartar posibles datos contaminados por nubes que podrían presentar valores de AOD y Alfa similares a los de una intrusión desértica.

4 RESULTADOS Y DISCUSIÓN

Mostraremos en este apartado los resultados de nuestro estudio centrándonos fundamentalmente en el inventario, de donde obtendremos la distribución por años y la climatología de las intrusiones, así como la contribución del aerosol desértico a la carga total de aerosol de la zona de estudio.

Tabla 1. Principales resultados del inventario relativos a: a) Todos los días de eventos desérticos; b) días D o desértico puro; c) días DC o mezcla de desértico y continental. (Sigma = desviación estándar)

a)	2003	2004	2005	2006	2007	2008	2009	2010	2011	2012	Total	Por año
N.Episodios	19	16	20	20	19	17	15	13	16	16	171	17.10
N.Días (D+DC)	49	47	46	61	52	35	33	20	32	33	408	40.80
Porcentaje días, %	13.4	12.8	12.6	16.7	14.3	9.6	9.0	5.5	8.8	9.0	11.2	11.2
Duración media, días	2.58	2.94	2.30	3.05	2.74	2.06	2.20	1.54	2.00	2.06	2.39	--
AOD (440nm) Medio	0.32	0.34	0.24	0.26	0.31	0.27	0.23	0.32	0.27	0.30	0.29	--
Sigma AOD (440nm)	0.11	0.15	0.05	0.10	0.14	0.10	0.15	0.13	0.09	0.10	0.04	--
Alfa Medio	0.96	0.93	0.93	0.80	1.05	0.99	0.86	0.81	0.91	0.77	0.90	--
Sigma Alfa	0.37	0.37	0.41	0.32	0.36	0.46	0.35	0.50	0.37	0.47	0.09	--

b)	2003	2004	2005	2006	2007	2008	2009	2010	2011	2012	Total	Por año
N.Días D	28	26	28	38	26	19	24	11	17	23	240	24
Porcentaje días D, %	57.1	55.3	60.9	62.3	50.0	54.3	72.7	55.0	53.1	69.7	--	58.80
Porcentaje días D%*	7.67	7.10	7.67	10.41	9.86	5.19	6.58	3.01	4.66	6.28	--	6.58

4.1 Inventario de Eventos desérticos en el Periodo 2003-2012

Siguiendo los criterios mencionados en el apartado anterior, se lleva a cabo el inventario de las intrusiones desérticas en el centro norte de España. Mostramos en la Tabla 1 los principales resultados extraídos del inventario. Así, por ejemplo, vemos que durante este periodo se recogen un total de 171 eventos formados por 408 días de aerosol desértico. En promedio, anualmente tendremos 17.1 episodios y 40.8 días, que representan el 11.2 % de días respecto del año, aunque es destacable la alta variabilidad interanual.

En el inventario se detallan la duración exacta de cada evento (día inicial hasta día final), los valores promedio para cada día tanto de AOD (440 nm) y Alfa (440-870 nm) como de PM10, así como información acerca de las retro trayectorias de las masas de aire a 500, 1500 y 3000 m.

En la Tabla 1 recogemos una estadística de este inventario de la siguiente manera: Tabla 1.a) considerando los días clasificados tanto D como DC; Tabla 1.b) sólo se tienen en cuenta aquellos días clasificados como desérticos puros (D) y Tabla 1.c) considerando únicamente los días de tipo DC.

Cabe señalar que el porcentaje que se indica de días de tipo D+DC es respecto a los días totales de cada año mientras que el porcentaje de días D o DC se hace de dos maneras, las cuales nos ofrecen información complementaria. En primer lugar, es el porcentaje respecto a los días totales del año y en segundo lugar (*) se calcula respecto al número total de días D+DC (es decir, dentro de los días considerados con intrusión desértica, indicando qué porcentaje es únicamente D o únicamente DC).

AOD(440nm) Medio	0.30	0.36	0.25	0.27	0.37	0.29	0.24	0.36	0.31	0.33	0.31	--
Sigma AOD (440nm)	0.12	0.17	0.06	0.11	0.19	0.13	0.17	0.12	0.11	0.11	0.05	--
Alfa Medio	0.68	0.68	0.60	0.65	0.70	0.62	0.72	0.47	0.61	0.52	0.63	--
Sigma Alfa	0.27	0.28	0.22	0.25	0.24	0.30	0.28	0.22	0.24	0.34	0.08	--

c)	2003	2004	2005	2006	2007	2008	2009	2010	2011	2012	Total	Por año
N.Días DC	21	21	18	23	26	16	9	9	15	10	168	16.80
Porcentaje días DC, %	42.9	44.7	39.1	37.7	50.0	45.7	27.3	45.0	46.9	30.3	--	41.20
Porcentaje días DC, % *	5.75	5.74	4.93	6.30	7.12	4.37	2.47	2.47	4.11	2.73	--	4.60
AOD(440nm) Medio	0.33	0.32	0.23	0.23	0.27	0.26	0.20	0.28	0.23	0.23	0.26	--
Sigma AOD (440nm)	0.10	0.12	0.04	0.07	0.07	0.05	0.06	0.13	0.04	0.05	0.04	--
Alfa Medio	1.26	1.27	1.32	1.14	1.30	1.38	1.27	1.18	1.23	1.33	1.27	--
Sigma Alfa	0.18	0.16	0.16	0.17	0.16	0.22	0.20	0.44	0.15	0.15	0.07	--

Podemos observar como el número de días y de episodios presenta una importante variabilidad interanual, oscilando entre 13 episodios en 2010 con apenas 20 días de aerosol desértico a 20 episodios en 2006 con 61 días de aerosol desértico. Ambos, años excepcionalmente bajo y alto, respecto a la media. La presencia de aerosoles en la zona de estudio varía entre un 5.5% y un 16.7%, dependiendo del año.

En la evaluación global o cómputo total de número de eventos y número de días asociados a estos eventos, debemos asociar una incertidumbre o error, sin embargo, estos errores no son fáciles de establecer. Por ejemplo, es difícil de asegurar en verano, cuándo hay episodios consecutivos o no, debido a las frecuentes recirculaciones de las masas de aire. No obstante, si el valor de AOD desciende a valores inferiores al valor umbral por más de dos días consecutivos, se considerarán dos eventos distintos.

En la Fig.1.a) podemos ver el número de eventos por año. Se observa como los cinco primeros años muestran más días con presencia de aerosol mientras que los cinco siguientes descienden en número. Esta tendencia también se pone de manifiesto, siendo más acusada aún, si consideramos el número de días con evento desértico (Fig.1.b), tanto D, DC como la suma de ambos.

En la Fig.2.a) representamos la distribución mensual de los eventos con presencia de aerosol y en la Fig. 2.b) la misma distribución para el número de días con evento tanto D, DC y la suma de ambos.

Es en estas gráficas donde encontramos la principal característica de los eventos desérticos en Castilla y León, pues se ve un patrón que muestra dos máximos, uno en Marzo y otro en Mayo/Junio así como dos mínimos, uno en abril y otro durante los meses de invierno.

El patrón de la climatología anual de los aerosoles desérticos en esta zona, centro-norte de la Península Ibérica, relativo al número de eventos y

número de días, reaparece como era de esperar al evaluar el peso o la influencia del aerosol desértico sobre el valor total del AOD, como se muestra en el apartado 4.3.

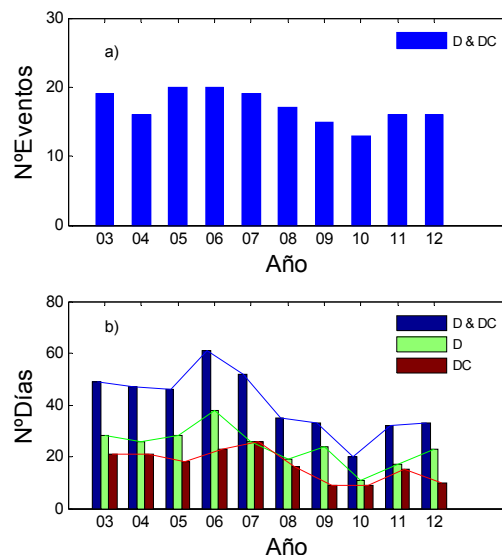
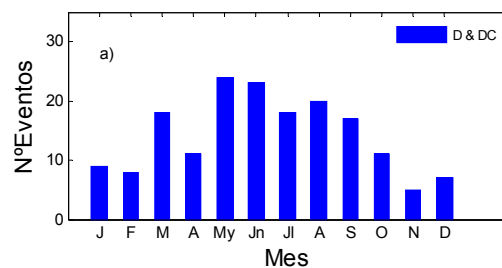


Fig.2. Distribución interanual de a) número de eventos desérticos; b) número de días correspondientes a los eventos totales de aerosol desértico (D&DC), con aerosol desértico puro (D), y con aerosol mezcla (DC).



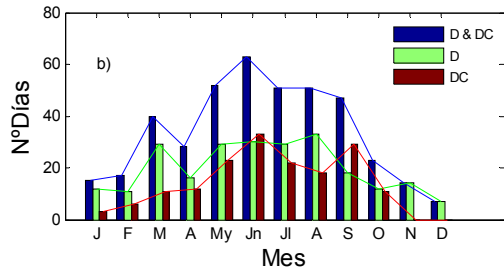


Fig.2. Distribución mensual de a) número de eventos desérticos totales; b) número de días correspondientes a los eventos totales de aerosol desértico (D&DC), con aerosol desértico puro (D), y con aerosol mezcla (DC).

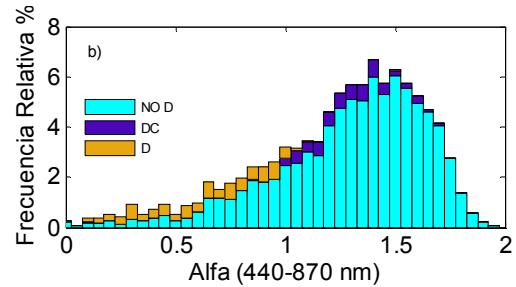


Fig.3. Histogramas de frecuencias de a) AOD (440 nm) y b) Alfa, para eventos de tipo D, DC y todos los demás días de 2003 a 2012.

4.2 AOD y Alfa durante Episodios Desérticos

Una vez que el inventario de episodios desérticos está establecido, vamos a buscar las principales características de los parámetros AOD y Alfa durante estos días.

Para ello, representamos el histograma de frecuencias de AOD y Alfa que se muestra en las Fig.3. a) y Fig.3.b) respectivamente. En ellos se ven en diferente color los días que han sido clasificados como D, DC y todos los demás. Vemos que el histograma tiene un máximo de frecuencia de AOD en valores en torno a 0.04, apareciendo los eventos desérticos por encima de valores 0.18. No son, sin embargo, únicamente eventos desérticos aquellos que pueden tener un AOD superior al valor umbral de 0.18.

En el histograma de frecuencia de Alfa, vemos como los valores se reparten entre 0 y 2, teniendo un máximo de frecuencia en torno a 1.40 y apareciendo los eventos D en valores por debajo de 1, los DC en valores entre 1 y 1.5 y los demás días con otro tipo de intrusión o sin evento, indistintamente en todo el rango.

4.3 Influencia de los Eventos Desérticos en los Niveles de AOD/ Climatología

Los promedios mensuales para el AOD en Palencia, se representan en la Fig. 4. Las barras corresponden a los promedios mensuales para todos los días de medida en la estación (barras azules), promedios mensuales para todos los días exceptuando aquellos clasificados como desérticos (barras verdes), diferencia absoluta entre ellos (barras marrones) y diferencia relativa (línea azul).

Si comparamos la diferencia absoluta o relativa con las Fig.2.a) y Fig.2.b), encontramos un comportamiento o forma estacional muy parecido. Es decir, volvemos a encontrar dos picos a lo largo del año, el primero en Marzo y el segundo a final de primavera o principio de verano, así como también podemos observar los mínimos que se producen en Abril y en los meses de invierno. Es cierto que los máximos de mayo y junio son más acusados, pero es posible que con un número mayor de años, la forma pueda llegar a ser idéntica.

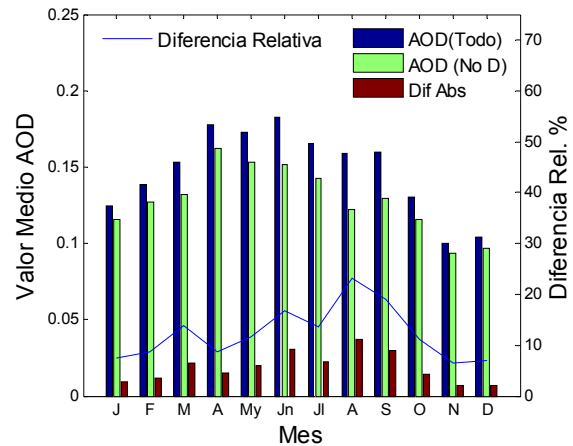
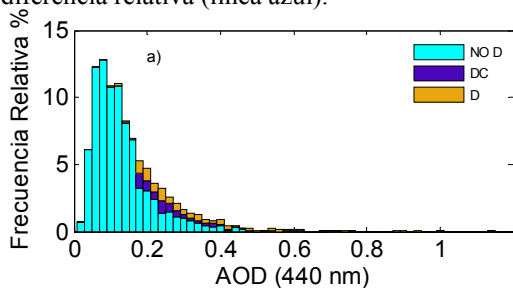


Fig.4. Valores promedio de AOD (440 nm) para todos los días, para todos los días exceptuando aquellos con aerosol desértico y diferencia absoluta entre ellos.



Por otro lado esta modulación que crea el aerosol desértico y que vemos al representar la diferencia absoluta o relativa, no se observa al representar la climatología anual del aerosol total, a diferencia de lo que ocurría en [1] para la estación de El Arenosillo. Allí, la modulación introducida por el aerosol desértico es tan fuerte que se manifiesta claramente en la representación mensual del aerosol total. Sin embargo la forma anual del aerosol desértico es la misma en las dos estaciones (observe como ahora la contribución del aerosol desértico en mayo y junio es más baja que en agosto), aunque la carga sea menor, habiendo un gradiente sur-norte de disminución, como era de esperar.

5 CONCLUSIONES

Los valores de AOD-Alfa de los aerosoles en Palencia se han monitoreado desde el año 2003 hasta el año 2012 con un fotómetro Cimel de la red AERONET. Se ha realizado con estos datos un inventario de las intrusiones desérticas detectadas en el centro norte de la península ibérica, partiendo como base de las medidas espectrales del parámetro AOD (440 nm).

Los episodios desérticos muestran un claro patrón con una ocurrencia máxima en Marzo y en Mayo/Junio y dos mínimos, en Abril e invierno.

Este inventario servirá como base para un análisis completo de las propiedades microfísicas y ópticas del aerosol desértico en la zona de estudio y sus efectos en el clima. También se llevarán a cabo estudios detallados que relacionen las masas de aire con los eventos desérticos encontrados así como diversos inventarios a través de inspecciones automáticas tomando como datos principales únicamente el AOD, o únicamente el PM10, con el fin de comparar ambos sistemas y encontrar las similitudes y diferencias en los resultantes inventarios tras utilizar AOD o PM10 como dato principal.

Las intrusiones desérticas son las responsables de una gran parte de los eventos de alta turbiedad en la estación, modulando el patrón climatológico del AOD en menor medida que en otras estaciones como puede ser El Arenosillo, debido a su diferente ubicación geográfica.

Respecto a la distribución interanual del número de episodios durante este periodo, no se ha podido observar ningún patrón.

El análisis manual completo de estos eventos constituirá la base para la validación de un método automático de identificación y evaluación de episodios desérticos en las series de datos de los fotómetros. Los resultados obtenidos en este trabajo nos muestran que el AOD espectral es suficiente para llevar a cabo inventarios de eventos desérticos, que son necesarios para evaluar el impacto sobre el clima del aerosol en una escala global.

AGRADECIMIENTOS

Los autores agradecen en primer lugar al MINECO del Gobierno de España por la beca FPI con referencia BES-2012-051868.

Agradecemos también a la gente de NASA GSFC, PHOTONS y RIMA por su larga colaboración y por operar y mantener la red AERONET a la vez que a EMEP por proveernos de datos gracias a las observaciones de su red.

El estudio que lleva a estos resultados ha recibido fondos de the European Union Seventh Framework Programme (FP7/2007e2013) bajo la beca Nr. 262254 [ACTRIS]. Agradecemos nuevamente el soporte financiero recibido desde el MINECO del Gobierno de España (proyectos con referencia CGL2009-09740, CGL2011-23413, CGL2012-33576 y la Acción Complementaria, CGL2011-13085-E) y damos las gracias al Gobierno de la Comunidad Autónoma de Castilla y León (Consejería de Medio Ambiente de la Junta de Castilla y León) por apoyar esta investigación.

REFERENCIAS

- [1] C.Toledano, V.E. Cachorro, A.M de Frutos, M. Sorribas, N. Prats, B.A. de la Morena, "Inventory of African desert dust events over the southwestern Iberian Peninsula in 2000-2005 with an AERONET Cimel Sun photometer," *Journal of Geophysical Research*, vol. 112, Nov. 2007.
- [2] Y.S.Bennouna, V.E.Cachorro, B.Torres, C.Toledano, A. Berjón, A.M.de Frutos, I.Alonso Fernández Coppel, "Atmospheric turbidity determined by the annual cycle of the aerosol optical depth over north-center Spain from ground (AERONET) and satellite (MODIS)," *Atmospheric Environment*, vol.46, pp.352-364, Jan.2012.
- [3] Y.Bennouna, V.Cachorro, M.A.Burgos, C.Toledano,A.M.de Frutos. "The relations between AOD and PMx from long term data for north-central Spain," *RICTA 2013*.
- [4] X.Querol,J.Pey,M.Pandolfi,A.Alastuey,M.Cusack,N.Pérez,T .Moreno,M.Viana,N.Mihalopoulos,G.Kallos,S.Kleanthous. "African dust contributions to mean ambient PM10 mass-levels across the Mediterranean Basin,"*Atmospheric Environment*,43(2009).

Variability of the levels of Particulate Matter in the Madrid Metropolitan Area, during the 1999-2012 period

P. Salvador¹, B. Artiñano¹, F. Molero¹, M. Viana², A. Alastuey², X. Querol²

Abstract — During the periods 1999-2000, 2007-2008 and 2011-2012, PM₁₀ and PM_{2.5} samples were collected at an urban-traffic site in the Madrid metropolitan area. From 1999 to 2012 PM₁₀ and PM_{2.5} average concentration decreased by 36% and 47% respectively. From 1999-2000 to 2007-2008 a noticeable reduction was found in the mean concentration of PM_{2.5} (39%) but not in PM₁₀ (13%). It was attributed to a reduction in the carbonaceous (OM+EC) and SO₄²⁻ content in PM as a consequence of the reduction of the emissions from residential coal burning and the higher proportion of diesel vehicles in the Madrid car fleet. On the contrary, from the 2007-2008 to the 2011-2012 period, a higher reduction in the coarse (26% in PM₁₀) than the fine (13% in PM_{2.5}) PM levels were detected. No significant downward trend in the carbonaceous content was detected in this period. However the secondary inorganic compounds (SO₄²⁻, NO₃⁻ and NH₄⁺) mean contribution decreased by 45% and 38% in PM₁₀ and PM_{2.5} respectively. This could be partly attributed to the reductions in permitted sulphur in fuels, the low levels of ammonia and humidity in the Madrid atmosphere, which favor the volatilization of nitrate and the economical crisis effects. However, the reduction in the contribution of mineral dust in the coarse fraction was less pronounced across both periods. Thus, future strategies aimed at reducing levels of PM₁₀ in the Madrid metropolitan area, should focus on mineral content due to anthropogenic activities and natural phenomena, aside from road traffic and fossil fuel consumption.

Keywords — PM₁₀, PM_{2.5}, fossil fuels, trend analysis

1 INTRODUCTION

This work analyses the evolution of particulate matter (PM) air pollution in the Madrid metropolitan area over the 1999-2012 period. This is one of the main factors which presently affect air quality in most cities all over the world. In fact, there are many health evidences suggesting that short-term as well as long-term exposures to coarse and smaller fractions of PM, are associated with adverse respiratory and cardiovascular health effects, including premature mortality [1]. Epidemiological and toxicological studies have shown PM mass comprises fractions (PM_{2.5} and PM₁₀: particle matter with aerodynamic diameter lower than 10 and 2.5 μm, respectively) with varying types and degrees of health effects suggesting a role for both the chemical composition and physical properties. For this reason, a number of European Directives (1999/30/EC and 2008/50/EC) made PM₁₀ and PM_{2.5} be the control parameters for PM pollution. Public administrations have been testing management strategies addressed to reduce

emissions of primary PM and precursors of secondary organic and inorganic aerosol. In the Madrid metropolitan area, different data sets were obtained during experimental studies performed in the 1999-2012 period. They were carried out to characterize mean PM₁₀ and PM_{2.5} concentration levels and their chemical composition at a representative urban-traffic site. The time series of concentration of PM and gases, recorded at the stations of the Air Quality Network (AQN) operating in this area during this period, were also collected. These data sets have been analyzed with the aim of analyzing the temporal variations produced in the PM levels and composition during the last years and to evaluate the impact of the abatement policies on pollutant emissions.

2 METHODOLOGY

2.1 The Study Area

The Madrid metropolitan area is one of the most densely populated regions in Spain with more than 5 million inhabitants, including Madrid City and the surrounding towns. It is located at the centre of the Iberian Peninsula, within an air shed (the Madrid Air Basin) bordered to the north-northwest by the Guadarrama Range 40 km from the metropolitan area and to the south by the Toledo Mountains (Fig. 1). Industrial activity in this area consists essentially of light factories. Hence, the Madrid plume is typically urban, fed by traffic emissions and by

1. P. Salvador, B. Artiñano and F. Molero are with the Environmental Department of the Research Center for Energy, Environment and Technology (CIEMAT). Avenida Complutense 22, 28040 Madrid. Spain. E-mails: pedro.salvador@ciemat.es; b.artinano@ciemat.es; f.molero@ciemat.es

2. M. Viana, A. Alastuey and X. Querol are with the Institute of Environmental Assessment and Water Research (IDÆA-CSIC). Provisional address: c) Lluís Solé i Sabarís S/N, 08028 Barcelona. Spain. E-mails: mar.viana@idaea.csic.es; andres.alastuey@idaea.csic.es; xavier.querol@idaea.csic.es

domestic heating. Fuel used by the heating facilities includes natural gas, gasoil, coal and, to a lesser extent, propane and butane.

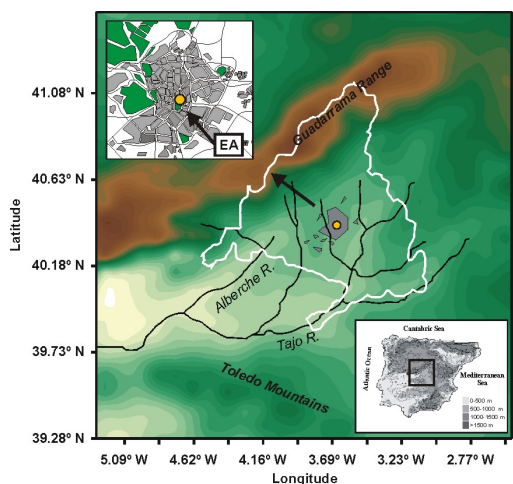


Fig. 1. Bi-dimensional topography of the Madrid Air Basin. The metropolitan area, represented by the city of Madrid (up-left) and satellite towns has been shaded. The location of the Escuelas Aguirre-EA monitoring site is shown. White line represents the boundary of the Madrid province territory.

2.2 PM measurements and Sampling

Sampling campaigns were conducted at an urban-traffic site (Escuelas Aguirre; 3.68° W, 40.42° N, 672 m a.s.l.) adjacent to one automatic monitoring station of the Madrid city Air Quality Network. These studies were carried out from June 1999 to June 2000, from January 2007 to April 2008 and from January 2011 to January 2012. PM10 and PM2.5 samples were obtained using manual gravimetric high-volume samplers, cut-off inlets and quartz micro-fibre filters. Following sampling and standard gravimetric determination of the PM mass concentration levels, major and trace elements and compounds were analysed in PM filters, with a maximum of 57 determinations per sample in the better cases. Procedures are described in [2]. Manual sampling was carried out at a rate of 2 moving days per week with the exception of the first period, when only one PM2.5 sample was collected per week. A number of PM10 and PM2.5 filters were collected (67 and 38 in 1999-2000, 95 and 104 in 2007-2008 and 83 and 74 in 2011-2012). During this study the chemical components were grouped into several categories: (a) crustal component (sum of elements typically found in rock-forming minerals, including Al_2O_3 , SiO_2 , CO_3^{2-} , Ca, Fe, K, Mg, Mn, Ti and P); (b) marine component (sum of Cl^- , Na^+ and marine SO_4^{2-}); (c) OM+EC or organic matter plus elemental carbon (value obtained after applying a 1.2 factor to the OC concentrations as in [3]); (d) secondary inorganic compounds (SIC, as the sum of the non-

marine SO_4^{2-} , NO_3^- and NH_4^+ concentrations) and (e) metals.

3 RESULTS AND DISCUSSION

Tables 1 and 2 summarize mean concentration values of major and trace elements of PM during the experimental studies. Mean PM10 concentrations reached $48 \mu\text{g}/\text{m}^3$ in 1999/2000, $41 \mu\text{g}/\text{m}^3$ in 2007/2008 and $31 \mu\text{g}/\text{m}^3$ in 2011/2012. PM2.5 concentrations decreased from $34 \mu\text{g}/\text{m}^3$ in 1999/2000 to $21 \mu\text{g}/\text{m}^3$ in 2007/2008 and $18 \mu\text{g}/\text{m}^3$ in 2011/2012. In brief PM average concentration decreased by 36% and 47% in PM10 and PM2.5 respectively, from the 1999-2000 to the 2011-2012 period.

Table 1. Mean concentrations (in $\mu\text{g}/\text{m}^3$) and relative contributions to the total mass (%) of major and trace elements of PM10 registered at EA

PM10	1999-2000	2007-2008	2011-2012
PM	47.7	41.4	30.5
Crustal	14.6 (31%)	12.8 (31%)	11.6 (38%)
OM+EC	22.2 (47%)	12.7 (31%)	12.0 (39%)
SIC	7.6 (16%)	7.0 (17%)	3.8 (13%)
SO_4^{2-}	4.5 (9%)	3.2 (8%)	1.7 (6%)
NO_3^-	2.1 (4%)	2.4 (6%)	1.3 (4%)
NH_4^+	1.2 (2%)	1.5 (4%)	0.81 (3%)
Marine	0.72 (1.5%)	1.20 (2.9%)	0.52 (1.7%)
Metals	0.34 (0.7%)	0.40 (1.0%)	0.26 (0.9%)
Unknown	2.2 (5%)	7.2 (17%)	2.3 (7%)

Table 2. Mean concentrations (in $\mu\text{g}/\text{m}^3$) and relative contributions to the total mass (%) of major and trace elements of PM2.5 registered at EA

PM2.5	1999-2000	2007-2008	2011-2012
PM	34.1	20.7	18.0
Crustal	5.3 (16%)	2.5 (12%)	1.4 (8%)
OM+EC	21.2 (62%)	9.8 (47%)	11.1 (62%)
SIC	6.5 (19%)	5.3 (26%)	3.3 (18%)
SO_4^{2-}	3.8 (11%)	2.4 (11%)	1.5 (8%)
NO_3^-	1.3 (4%)	1.5 (7%)	0.92 (5%)
NH_4^+	1.4 (4%)	1.5 (7%)	0.86 (5%)
Marine	0.47 (1.4%)	0.60 (2.9%)	0.13 (0.7%)
Metals	0.21 (0.6%)	0.19 (0.9%)	0.08 (0.4%)
Unknown	0.4 (1%)	2.3 (11%)	2.0 (11%)

A noticeable reduction in the mean concentration of PM2.5 (39%) was found from 1999-2000 to 2007-2008. It was a consequence of a strong abatement in the carbonaceous and SO_4^{2-} content in

PM2.5 (54% and 38%, respectively). The drop in the concentrations of PM10 between these periods was less dramatic (13%). On the contrary, from the 2007-2008 to the 2011-2012 period, a higher reduction in the coarse (26% in PM10) than the fine (13% in PM2.5) PM levels was detected. Throughout this period carbonaceous content did not change in a noticeable amount in comparison with the former one (12.7 and 12.4 $\mu\text{g}/\text{m}^3$ in 2007-2008 and 2011-2012, respectively). However the SIC mean contribution, decreased by 45% and 38% in PM10 and PM2.5 respectively. In fact, SO_4^{2-} , NO_3^- and NH_4^+ mean contribution reduced by 45-46% in PM10 and by 37-42% in PM2.5.

The reduction in the crustal contribution in the coarse fraction, was less pronounced across both periods (12% from 1999-2000 to 2007-2008 and 9% from 2007-2008 to 2011-2012). In fact, mineral dust in PM10, reached similar levels in the 2007-2008 and 2011-2012 periods (12.8 and 11.6 $\mu\text{g}/\text{m}^3$ respectively). In the fine fraction the evolution of the mineral dust mean contribution is different. It decreased from 5.3 $\mu\text{g}/\text{m}^3$ in 1999/2000 to 2.5 $\mu\text{g}/\text{m}^3$ in 2007/2008 and 1.4 $\mu\text{g}/\text{m}^3$ in 2011/2012. Moreno et al. [4] associated hourly profile concentrations of crustal components recorded at EA, with traffic rush hour patterns and daytime construction-demolition activities.

With the aim to interpret these changes in PM levels and composition, trend estimates of PM10 and gaseous pollutants concentrations at the EA automatic monitoring station were undertaken, using the OpenAir data analysis tools [5]. Results are shown in Table 3. The magnitude of the trend was expressed as a slope (pollutant concentration per unit time) using the Theil-Sen method [6]. Bootstrap resampling techniques were used to quantify whether the trends in concentrations of pollutants were statistically significant “[5], [6]”.

Table 3. Results of the Theil-Sen trend analysis for the 1999-2012 period at EA. Statistically significant values of the trend line slope estimators of pollutants concentrations, at the 99% confidence level.

	Slope estimator
PM10	-1.18 ($\mu\text{g}/\text{m}^3$)/year
CO	-0.06 (mg/m^3)/year
SO ₂	-0.81 ($\mu\text{g}/\text{m}^3$)/year
NO	-2.82 ($\mu\text{g}/\text{m}^3$)/year
NO ₂	-2.23 ($\mu\text{g}/\text{m}^3$)/year
O ₃	0.83 ($\mu\text{g}/\text{m}^3$)/year

Statistically significant ($p < 0.01$) downward trends were detected in PM10, SO₂, CO, NO₂ and NO_x concentrations during the 1999-2012 period. On the contrary, O₃ concentrations showed an upward trend ($p < 0.01$). PM2.5 concentrations were recorded at the EA station since the year 2009.

Consequently, no trend estimation could be obtained.

The smoothed trend, in the monthly mean concentrations of SO₂ at EA, represented in Fig. 2, depicts the monotonic downward trend for SO₂ concentrations during the study period. Salvador et al. [7] demonstrated that this behaviour could be partly attributed to a reduction in the number of coal fed domestic heating devices in Madrid during the 1999-2008 period.

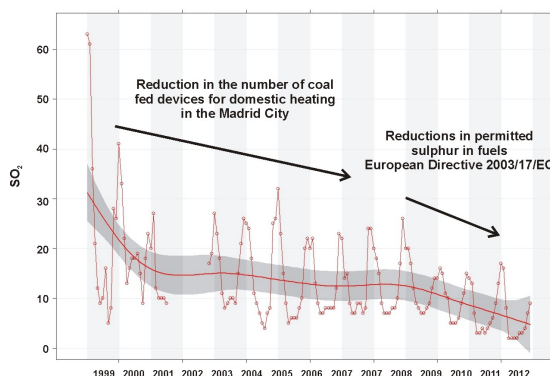


Fig. 2. Monthly mean evolution and smooth trend in concentrations of SO₂ registered at EA from 1999 to 2012.

Moreover the consumption of gasoil for this purpose, decreased by 54% from 1999 to 2011 in the Madrid metropolitan area (Fig. 3). It is a consequence of the exchange of coal and gasoil fed heating devices by natural gas fed ones, promoted by the Madrid Municipality Air Quality administration. This is part of its management strategies to reduce pollutant emissions.

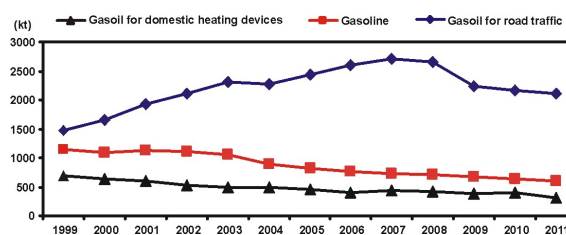


Fig. 3. Annual total consumption of gasoil (for domestic heating and traffic) and gasoline in the Madrid Metropolitan Area in the 1999-2011 period.

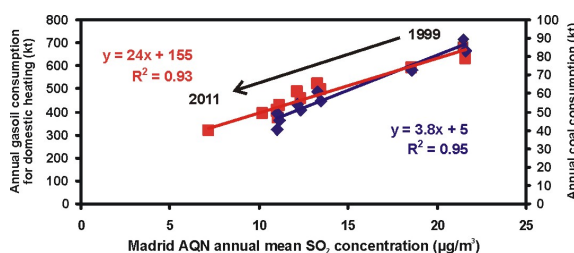


Fig. 4. Cross-correlation plots of the annual gasoil for domestic heating and coal consumption in Madrid with the annual mean SO₂ concentrations registered in the Madrid AQN.

Fig. 4 shows the strong association between the mean annual levels of SO₂ recorded at the Madrid City Air Quality Network and the total consumption of gasoil ($r^2=0.93$). It should be also taken into account the reduction in permitted sulphur in fuels required by the European Directive 2003/17/EC which came into force on 1 January 2009. Consequently, Fig. 2 clearly depicts a stronger decrease in the monthly mean concentrations of SO₂ from 2009 onwards.

The downward tendency in the SO₂ levels clearly influenced the levels of SO₄²⁻ recorded in PM10 and PM2.5 at EA. SO₄²⁻ mean contribution in PM10 decreased by 61% from 1999 to 2012, both in PM10 and PM2.5.

The mean annual levels of CO recorded at the Madrid City AQN exhibited a good correlation with the annual levels of gasoline consumption ($r^2=0.91$) in the Madrid metropolitan area (Fig. 5). The reduction in the number of vehicles fed by gasoline, comprising 72% of the Madrid car fleet in 1999 and 42% in 2011 and 2012, could partly explain the downward tendency in the CO levels exhibited during the study period. An outstanding reduction in the gasoline annual consumption was produced in this period (Fig. 3).

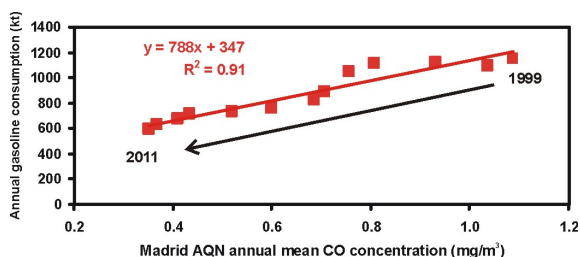


Fig. 5. Cross-correlation plots of the annual gasoline in Madrid with the annual mean CO concentrations registered in the Madrid AQN.

It should be mentioned that the Madrid car fleet increased by 35%, from 1999 to 2008. From 2008 onwards it remains unchanged, probably as a consequence of the worldwide economical crisis. Moreover, the proportion of diesel vehicles in the Madrid car fleet rose from 29% in 1999 to 55% in 2008. Since then it also remains unaltered.

In spite of the fact that the increased use of diesel vehicles in many European car fleets, which incorporate catalytic particle filters, resulted in lower emissions of carbonaceous PM but also in higher levels of NO_x than gasoline vehicles with a higher proportion of primary NO₂ [8], the economical crisis results in lower consumption of gasoil since the year 2008 (Fig. 3). As a consequence, mean levels of nitrogen oxides (NO and NO₂) showed a downward trend during the study period. The progressive decrease on ambient NO levels at EA, resulted in an increase on O₃ levels.

It could be concluded that the reduction during the last years, in the use of fossil fuels (coal, gasoil

for domestic heating and road transport and gasoline) in the Madrid metropolitan area, resulted in a decrease in the mean levels of OM+EC, SO₄²⁻ and NO₃⁻ in PM10 and PM2.5 at EA. The drastic reduction of the NO₃⁻ levels produced from the 2007-2008 to the 2011-2012 period, could be also attributed to the low levels of ammonia and humidity currently existing in the Madrid atmosphere, which favor its volatilization.

A reduction in the daily road traffic flows and the intensity of construction-demolition and roadworks activities in the Madrid Metropolitan Area could be also attributed during the last years to the economical crisis. This reduction would probably originate lower levels of resuspended road dust and crustal material emissions, presumably in the fine range.

4 CONCLUSIONS

A noticeable decrease in the mean contributions of coarse and fine PM in the Madrid metropolitan area, was detected during the 1999-2012 period. In a first stage, from 1999 to 2007, a noticeable reduction in the levels of PM2.5 was found. Afterwards, from 2008 to 2012 a higher reduction in the PM10 than PM2.5 was produced.

This fact could be mainly attributed to the reduction in the use of fossil fuels, due to the abatement policies on anthropogenic emissions promoted by public administrations, but also to the economical crisis. As a consequence, mean levels of carbonaceous material, SO₄²⁻ and NO₃⁻ in PM10 and PM2.5 strongly decreased at EA from 1999 to 2012.

However, the reduction in the contribution of mineral dust in the coarse fraction was less pronounced across this period. Thus, future strategies aimed at reducing levels of PM10 in the Madrid metropolitan area, should focus on mineral content due to anthropogenic activities and natural phenomena, aside from road traffic and fossil fuel consumption.

ACKNOWLEDGMENT

This work was funded by the Ministry of Agriculture, Food and Environment (UCA 2009020083) and the Spanish R&D Plan under MICROSOL (CGL2011-27020), and GRACCIE CONSOLIDER (CSD2007:00067) Projects.

REFERENCES

- [1] "Review of evidence on health aspects of air pollution - REVIHAAP Project" First results. World Health Organization 2013. Regional office for Europe (www.euro.who.int)
- [2] X. Querol, A. Alastuey, M.M. Viana, S. Rodriguez, B. Artiñano, P. Salvador, S. Garcia, R. Fernandez, C. Ruiz, J. de la Rosa, A. Sanchez, M. Menendez and J.Gil, "Speciation

- and origin of PM₁₀ and PM_{2.5} in Spain” *Journal of Aerosol Science* 35 pp. 1151-1172, 2004
- [3] X. Querol, A. Alastuey, T. Moreno, M.M. Viana, S. Castillo, J. Pey, S. Rodriguez, B. Artíñano, P. Salvador, M. Sánchez, S. Garcia, M.D. Herce, R. Fernandez, S. Moreno, L. Negral, M. Minguillón, E. Monfort, M. Sanz, R. Palomo, E. Pinilla, E. Cuevas, J. de la Rosa J. and A. Sanchez, “Spatial and temporal variations in airborne particulate matter (PM₁₀ and PM_{2.5}) across Spain 1999-2005” *Atmospheric Environment* 42 pp. 3964-3979, 2008
- [4] T. Moreno, A. Karanasiou, F. Amato, F. Lucarelli, S. Nava, G. Calzolari, M. Chiari, E. Coz, B. Artíñano, J. Lumbreras, R. Borge, E. Boldo, C. Linares, A. Alastuey, X. Querol and W. Gibbons, “Daily and hourly sourcing of metallic and mineral dust in urban air contaminated by traffic and coal-burning emissions” *Atmospheric Environment* 68, pp. 33-44, 2013
- [5] D.C. Carslaw and K. Ropkins, “openair - an R package for air quality data analysis” *Environmental Modelling & Software* 27-28 pp. 52-61
- [6] D.C. Carslaw, "The openair manual – open-source tools for analysing air pollution data" *Manual for version 0.5-16*, King’s College London
- [7] P. Salvador, B. Artíñano, M. Viana, A. Alastuey and X. Querol, “Evaluation of the changes in the Madrid metropolitan area influencing air quality: analysis of 1999-2008 temporal trend of Particulate Matter” *Atmospheric Environment* 57, pp. 175-185, 2012
- [8] D.C. Carslaw, S.D. Beevers, J.E. Tate, E.J. Westmoreland and M.L. Williams, "Recent evidence concerning higher NO_x emissions from passenger cars and light duty vehicles” *Atmospheric Environment* 45, pp. 7053-7063, 2011

Physical, Chemical and Optical Properties of Aerosol at Ny Ålesund, Svalbard: a Closure Study

Christian Lanconelli¹, Maurizio Busetto¹, Mauro Mazzola¹, Angelo Lupi¹, Silvia Becagli², Daniele Frosini², Aki Virkkula³, and Vito Vitale¹

Abstract — Continuous measurements of aerosol scattering and absorption coefficients, size distribution and chemical analysis were performed during the periods April-Aug 2010 and 2011 at Gruvebadet laboratory, Ny-Ålesund. A closure study, aimed to match measured aerosol optical properties, with those calculated with Mie theory from size distribution and chemical properties, is developed and results discussed. Particular attention was devoted to the modelling of the scattering coefficient. It was found to agree within 1% with measurements, assuming particle mass densities within 1.4 g/cm³ to 2.0 g/cm³ and real part of the refractive index to vary between 1.4 and 1.8, along the whole campaigns. Retrieved values of refractive index are finally compared with diurnal chemical composition in order to verify the results of the procedure.

Keywords — Size distribution, Scattering Coefficient, Absorption Coefficient, Mie Theory.

1 INTRODUCTION

Aerosols play an important role in the energy budget of the Earth-atmosphere system, both directly, by radiation scattering and absorption, and indirectly, modifying the clouds optical properties and life-time [1]. Relatively high aerosol concentration were found even in the Arctic region during spring and early summer, when the Arctic-haze phenomena takes place. In the framework of the Italian PRIN, the Climate Change Tower Integrated Project (CCT-IP) and the international Cooperative Investigation of Climate-Cryosphere Interaction (CICCI), the Gruvebadet laboratory in Ny-Ålesund was equipped with a series of instruments aimed to measure physical and optical properties of aerosols at ground level from spring (Arctic haze) to late summer. In addition a winter-over campaign occurred between 2011 and 2012 for spectral absorption coefficient.

2 RESEARCH DESIGN

The scattering coefficient (K_{sca}) at 530 nm was measured by a Radiance Research M903 nephelometer and stored as minute average. The absorption coefficient (K_{abs}) was measured at three wavelength (467, 530 and 660 nm) using a Radiance Research PSAP [2], [3], [4].

The combination of K_{sca} and K_{abs} at the common 530 nm wavelength was used to obtain the aerosol extinction coefficient K_{ext} and the single scattering albedo (SSA).

The size distribution was characterized with a TSI Scanning Mobility Particle Sizer (SMPS mod. 3034) for mobility diameters D_m varying from 10 to 487 nm, and a TSI Aerodynamic Particle Sizer (APS mod.3321) for aerodynamic diameters D_a from 0.5 μ m to 20 μ m. Both instruments classify particles in 54 size classes, each with a geometrical width $dlogD$ equal to 32. Aerodynamic diameters D_a were converted to geometrical diameter $D_p \sim D_m$, as needed by Mie theory, using the following formula given in [5],

$$D_p = D_a \sqrt{\frac{C_a \chi \rho_0}{C_p \rho_p}} \quad (1)$$

in which C_a and C_p are the “Cunnighan” slip factors that could be considered to approach unity for the condition of operation [6], χ is the particle dynamic shape factor that should not assume values greater than 1.1-1.2 for water soluble inorganic particle [7], ρ_p is the particle density in g/cm³ and $\rho_0=1.0$ g/cm³. Considering that in Eq. 1 the contribution due to the combined effects the slip and the dynamic shape factors are likely to be negligible with respect to the effect of particle density, we adopted a simplified formulae in this work,

$$D_p = D_a \sqrt{\frac{1}{\rho_p}} \quad (2)$$

We assumed three values of the particle density

1. C. Lanconelli is with Institute of Atmospheric Sciences and Climate, the National Research Council, via Gobetti, 101, I-40129, Bologna, Italy. E-mail: c.lanconelli@isac.cnr.it
2. S. Becagli is with the Department of Chemistry of the University of Florence, via della Lastruccia 3, I-50019 Sesto Fiorentino, Firenze Italy. E-mail: silvia.becagli@unifi.it
3. A. Virkkula is with the Finnish Meteorological Institute, P.O. Box 503, FI-00101 Helsinki Finland, E-mail: Aki.Virkkula@fmi.fi

ρ_p (1.4, 1.7 and 2.0 g/cm³) defining three corresponding SMPS-APS composite size distributions $dV/d\log D_p(\rho_p)$ in the SMPS-APS combined diameter range from 10nm to 10 μ m. The density values adopted here should be considered as indicative of the presence of different fraction of chemical compounds, being they representative of organic matter (1.4 g/cm³), water soluble (1.7 g/cm³), sea salt or crustal material (2.0 g/cm³) [8].

An example of the dependence of the size distribution from the particle mass density is given in Figure 1 for a SMPS-APS composite scanning (14 March 2010 00:00 UTC). It is clear that with increasing ρ_p the total volume decreases, and APS modes shift to lower values of D_p .

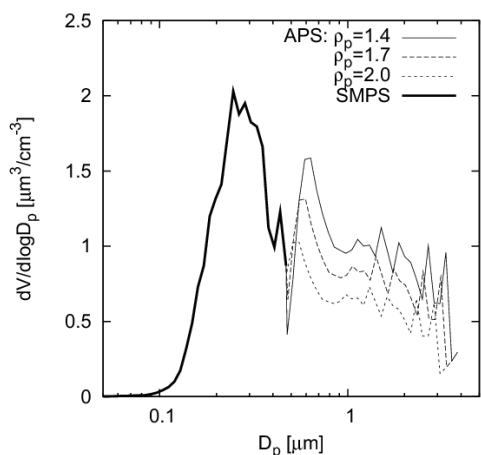


Figure 1: Composite volume size distribution from SMPS (solid black line) and APS (thin) as function of particle density.

Khlystov et al. [5], adopted a method based on the correspondence of $dV/d\log D$ values obtained by SMPS and corrected APS in the resulting overlapping channels. This method could not be applied here because of the lack of channels overlap, due to the limited upper range of the mod. 3034 SMPS (487 μ m) with respect to mod. 3936L10 used in other experiments. Nevertheless a qualitative idea could be obtained by virtually extent the SMPS distribution until it fits with APS corrected size distribution. Chemical analysis relative to the same period reported in Figure 1 evidence a predominant fraction of sulphate aerosols with respect to sea salt that yields to a probable intermediate density of 1.8-1.9 g/cm³, that likes to produce a mode with a diameter of 0.5-0.6 micron.

The scheme adopted in this work to study closures between physical, optical and chemical measurements is summarized in Figure 2. Assuming three combined SMPS-APS size distributions, each representing a different assumption on average particle density, Mie theory was used to compute scattering and absorption coefficient. The real part

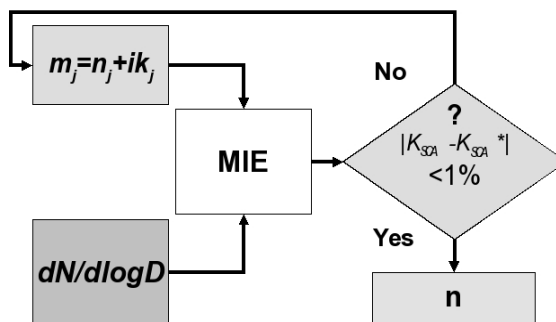


Figure 2: Schematic of the algorithm used to estimate the real part of the refractive index.

of the refractive index n has been varied until to reproduce measured K_{sca} within 1% error. The Mie algorithm for spherical dry particles of the 6S computer code was adopted (Vermote et al., 1997). The imaginary part k of the refractive index was set to zero considering that poorly absorbing aerosols were observed over the whole period ($SSA > 0.95$) and that the scattering coefficient is appreciably affected only for values of k greater than 10^{-2} [9].

3 PHYSICAL AND OPTICAL CLOSURE

A sensitivity analysis of the K_{sca} dependence with respect to ρ_p and n was performed for the monthly averaged size distributions of March (Arctic haze) and Aug 2010. Approximately linear monotonic variations of $-0.5 \cdot 10^{-5} \text{ m}^{-1}/\text{unit } \rho_p$ and $-0.1 \cdot 10^{-5} \text{ m}^{-1}/\rho_p$, was observed for March and August respectively, assuming a fixed value of the real refractive index $n=1.5$. Conversely, the real part of the refractive index causes a variation of K_{sca} with a rate of $+2 \cdot 10^{-5} \text{ m}^{-1}/n$ (Mar) and $+0.3 \cdot 10^{-5} \text{ m}^{-1}/n$ (Aug), for a fixed density of 1.7 g/cm³. Such results were also given in Figure 3.

Moreover, because of the evidence of a correlation between the time series of K_{sca} and total number given by the APS, a simple parametrization of K_{sca} with respect to N_{APS} was investigated. Daily averages of K_{sca} and N_{APS} are well correlated with purely parametric relations of the form,

$$K_{sca} [m^{-1}] = 2.29 \cdot 10^{-6} N_{APS} [cm^{-3}] \quad (3)$$

with an $r^2=0.82$, and

$$K_{sca} = 3.16 \cdot 10^{-6} N_{APS}^{0.73} \quad (4)$$

with an $r^2=0.90$, the latter giving evidence of two main regimes of optical particle properties, being the slope higher for the lower particle concentration occurring during summer. Scattering coefficient time series are poorly correlated with the total particle counts from SMPS accordingly to Mie theory for 530 nm, for which the maximum

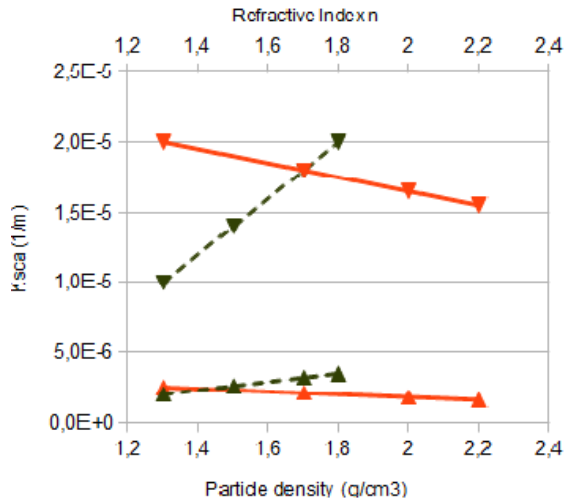


Figure 3: Dependence of calculated K_{sca} from particle density with $n=1.5$ (orange) and real part of the refractive index for a fixed density of 1.7 g/cm^3 . Triangles are for August while reverse triangle are for March.

efficiency is expected to be for a size parameter $x = \pi D/\lambda$, nearly to 4, hence $D \sim 700 \text{ nm}$.

Roughly speaking assuming a δ -Dirac particle size-distribution centred on diameter D , provides that equation

$$K_{sca} = \int \pi r^2 Q_{sca} (dN / d \log D) d \log D \quad (5)$$

reduces to the simpler

$$K_{sca} = \sigma_{sca} N \quad (6)$$

An annual indicative scattering cross section could be considered given by the slope of the first parametrization as $2.26 \cdot 10^{-4} \text{ cm}^2$. The slope of the second equation could be used to seasonally characterize this parameter considering that lower values of K_{sca} pertains to summer and higher values to Arctic haze period (March-April). The volume scattering coefficient average values of April and Aug 2010 was estimated to be respectively $5.02 \cdot 10^{-6} \text{ m}^{-1}$ and $2.36 \cdot 10^{-6} \text{ m}^{-1}$, and correspondingly scattering cross sections was observed to be $1.93 \cdot 10^{-4} \text{ cm}^2$ and $2.52 \cdot 10^{-4} \text{ cm}^2$.

4 COMPARISON WITH CHEMICAL MEASUREMENTS

Analogously, a good correlation was observed between daily averages of K_{sca} and PM_{10} , presenting an annual linear relationship

$$K_{sca} [\text{m}^{-1}] = 1.31 \cdot 10^{-6} PM_{10} [\text{g}/\text{m}^3] \quad (7)$$

with an $r^2=0.65$. Here the slope has the physical

meaning of a specific scattering cross section equal to $1.31 \text{ m}^2/\text{g}$. This value is similar to that adopted by OPAC for a maritime clean model ($1.29 \text{ m}^2/\text{g}$, [10]).

Inversions for n was made for each SMPS-APS size-distributions performed every 10 minutes, and for the three values of particle density as described in Figure 2. Some examples are shown in Figure 4, where the retrieved values of the refractive index n for two values of the particle density are given for two periods 14-29 Mar (part a) and May 22-Jun 5 (part b) 2010.

In part a) of Figure 4, the retrieved n is shown to vary between 1.4 and 1.5, for particle density of 1.5 g/cm^3 . It increases by less than 0.1 when an higher density is assumed (1.7 g/cm^3). In both cases, n lays between typical values for sea salt (1.38 g/cm^3) and NH_4HSO_4 (1.48 g/cm^3).

In part b) of Figure 4, the methodology retrieves values of n that are greater than those related to the main species expected to be present and measured in chemical composition (from 1.40 to 1.53 for H_2SO_4 and $(\text{NH}_4)_2\text{SO}_4$ respectively, 1.38 for sea salt). A certain amount of crustal component with n varying from 2 to 4 should likely be present, even if undetermined by the chemical analysis.

Agreement with the chemical measures was appreciable. In particular, when sea salt component

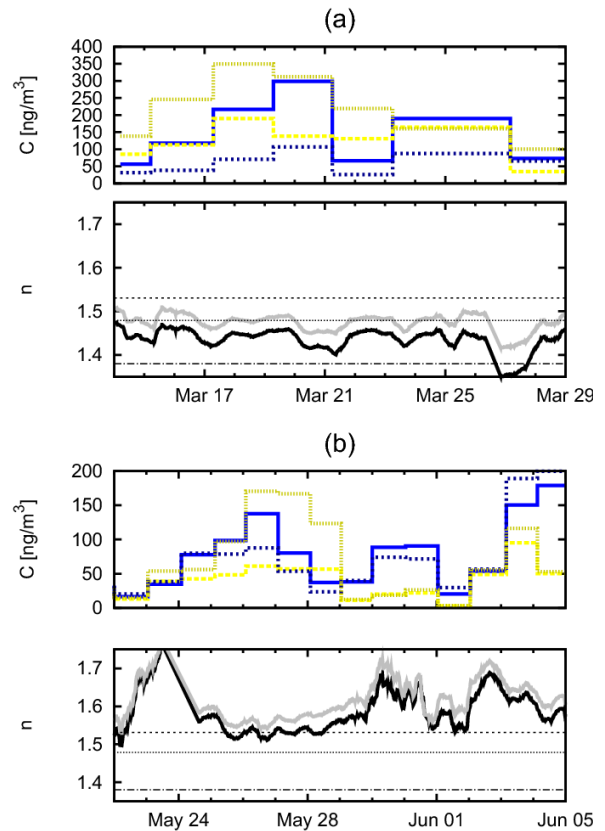


Figure 4: Time patterns of the daily chemical analysis (Na^+ solid blue, NH_4^+ solid yellow, Cl^- dotted blue, SO_4^{2-} dotted dark-yellow), and of the retrieved refractive index for $\rho=1.4 \text{ g/cm}^3$ (black) and $\rho=1.7 \text{ g/cm}^3$ (gray). Constants refer to $(\text{NH}_4)_2\text{SO}_4$ (dashed), NH_4HSO_4 (dotted) and NaCl (dash-dotted).

increases, the refractive index is found to decrease, accordingly to lower relative values of sea salt with respect to sulphate real refractive index. A particular period between May 30 to Jun 1st do not follows this rule and requires additional investigation.

5 CONCLUSIONS

An experiment of closure between physical, chemical and optical properties of aerosols, was approached in order to verify the possibility of the retrieval of the refractive index using Mie theory and size distributions and scattering coefficient measurements. A linear as well as a power law relationship between volume scattering coefficient K_{sca} and total APS number density, and K_{sca} and PM10 were parametrized, with correlation coefficient greater than 0.8. and 0.60 respectively. An iterative procedure to retrieve the best real part of refractive index that provides modelled volume scattering coefficient within 1% difference with measurements was set up for three different particle density from 1.4 to 2. The quality of inversions was discussed qualitatively in terms of comparisons with chemical analysis. The results obtained encourage deeper investigations involving the absorption coefficient and imaginary part of the refractive index, particle density closures with chemical analysis, and the role of the non sphericity of particle. Chemical undetermined fraction of PM10, by varying between 20% to 80% remains a key question that requires to wait for laboratory additional analysis. Considering that a TSI 3-wavelength nephelometer replaced M903 single wavelength instrument in 2012, and that measurements are going on increasing statistics, the closure results are likely to be expanded in next future to obtain better closures. Optical and physical properties daily based graphs can be accessed at

<http://www.isac.cnr.it/~radiclim/cctower/>.

REFERENCES

- [1] IPCC, 2007: Climate Change 2007: considered to be a more representative quantity for the geometric diameter of the particle. The Physical Science Basis. Contribution of Working Group I to the Fourth Assessment Report of the Intergovernmental Panel on Climate Change [Solomon, S., D. Qin, M. Manning, Z. Chen, M. Marquis, K.B. Averyt, M. Tignor and H.L. Miller (eds.)]. Cambridge University Press, Cambridge, United Kingdom and New York, NY, USA, 996 pp.
- [2] Bond T.C., T.L. Anderson, and D. Campbell, Calibration and Intercomparison of Filter-Based Measurements of Visible Light Absorption by Aerosols, *Aerosol Science and Technology*, 30, 582–600, 1999.
- [3] Weiss, R.E., and P.V., Hobbs, Optical Extinction Properties of Smoke from the Kuwait Oil Fires, *J. Geophys. Res.*, 97, 14, 14.537-14.540, 1992.
- [4] Virkkula A., Backman J., Aalto P.P., Hulkkonen M., Riuttanen L., Nieminen T., Dal Maso M., Sogacheva L., De Leeuw G., and Kulmala M., Seasonal cycle, size dependencies, and source analyses of aerosol optical properties at the SMEAR II measurement station in Hyytiälä, Finland, *Atmos. Chem. Phys.*, 11, 4445–4468, 2011
- [5] Khlystov, A., C. Stanier, and S. N. Pandis, An Algorithm for Combining Electrical Mobility and Aerodynamic Size Distributions Data when Measuring Ambient Aerosol, *Aer. Sci. Tech.*, 38, 229-238, 2004.
- [6] Gussman, On the Aerosol Particle Slip Correction Factor, *J. Appl. Meteor.*, 8, 999-1001, 1969.
- [7] Zelenyuk A., Y. Cai and D. Imre, From Agglomerates of Spheres to Irregularly Shaped Particles: Determination of Dynamic Shape Factors from Measurements of Mobility and Vacuum Aerodynamic Diameters, *Aer. Sci. Tech.*, 40, 197–217, 2006.
- [8] Hand, J. L., and S. M. Kreidenweis, A New Method for Retrieving Particle Refractive Index and Effective Density from Aerosol Size Distribution Data, *Aer. Sci. Tech.*, 36, 1012–1026 (2002)
- [9] Raut J.-C. and P. Chazette, Retrieval of aerosol complex refractive index from a synergy between lidar, sunphotometer and in situ measurements during LISAIR experiment, *Atmos. Chem. Phys.*, 7, 2797-2815, 2007
- [10] Hess, M., P. Koepke, and I. Schult, 1998: Optical Properties of Aerosols and Clouds: The software package OPAC. *Bull. Amer. Meteor. Soc.*, 79, 831–844., 1998

Raman lidar observations of Iberian forest fires smoke layers over Portugal

Sérgio Pereira^{1,2}, Jana Preißler¹, Juan Luis Guerrero-Rascado^{1,2,3},
Frank Wagner¹, Ana Maria Silva¹

Abstract — Optical properties of aerosols from forest fires, in the Iberian Peninsula, measured with a multi-wavelength Raman lidar, are presented. The observations of the smoke layers, in the free troposphere, were carried out in Évora, Portugal, during 18 and 19 October 2011. In several occasions, particle backscatter coefficients greater than $5 \text{ Mm}^{-1}\text{sr}^{-1}$ and particle extinction coefficients close to 300 Mm^{-1} , at 355 nm, could be observed in the center of the layers aloft. The particle intensive optical properties acquired during the different periods were comparable and average properties of the smoke particles are reported; in conjunction with back-trajectories analysis they suggest the presence of relatively fresh biomass burning. The wavelength dependence of the mean lidar ratios at 355 and 532 nm (56 sr) was small. Moreover, the mean values of extinction and backscatter related Ångström exponents (about 1.4 for the 355/532 nm wavelength pair) were also quite similar. The particle linear depolarization ratio at 532 nm was consistently low, around 5%. These results add further experimental support to previous observations of fresh biomass burning particles in the free troposphere.

Keywords — Aerosol remote sensing, forest fires smoke, lidar

1 INTRODUCTION

Smoke aerosols from biomass burning are one of the key aerosol types in climate research [1], [2], but their optical properties in free tropospheric layers are still insufficiently studied. The presence of smoke at these elevated layers permits its transport throughout long distances, either transcontinental or even around the globe [3] - [7].

The influence of smoke in terms of direct and indirect radiative forcing, atmospheric chemistry and visibility reduction is significant (see e.g. [8]-[10]). Also, the impact of smoke aerosols on health [11] and biological processes [12] were documented. Concerning Portugal, in the period of 2001-2011 an average area close to 150.000 ha per year was burnt, particularly during the summer periods [13].

During October 2011 multiple forest fires were occurring on the Iberian Peninsula, with more intensity in the north-western areas, but also in other regions. Smoke layers in the free troposphere were detected at Évora, Portugal, with a Raman lidar in October 2011, and the respective optical properties acquired on 18-19 October 2011 are here presented.

2 INSTRUMENTATION AND METHODOLOGY

2.1 Measurement site

Évora (38.5° N, 7.9° W, ~300 m above sea level (a.s.l)) is located inland in the south-western region of the Iberian Peninsula. The city (< 60000 inhabitants) is the capital of Alentejo, a rural region in Southern Portugal, which covers about one third of the area of Portugal but has a low population density. The distance to the capital, Lisbon, is about 130 km. No polluting industries exist in the vicinity of Évora. Local anthropogenic pollution is caused by traffic and, in winter, domestic fuel burning. Occasionally, anthropogenic aerosol from Europe, forest fire smoke from the north and centre of Portugal and from Spain or desert dust from the Sahara are transported to the site (see e.g. [14]-[17]).

2.2 The Raman lidar installed at Évora

The Portable Aerosol and Cloud Lidar (PAOLI) of the Évora Geophysics Center (CGE) is a multi-wavelength Raman lidar of the type Polly^{XT} [18] and is regularly operated at CGE since September 2009. It is part of both the European Aerosol Research Lidar Network (EARLINET) [19] and the Spanish and Portuguese Aerosol Lidar Network (SPALINET) [20]. A Nd:YAG based laser is emitted at 1064 nm, which is further doubled and tripled in the wavelengths 532 and 355 nm. Elastically backscattered photons are detected at the wavelengths 355, 532 and 1064 nm and inelastically backscattered photons are detected at 387 and 607

1. Evora Geophysics Centre and University of Evora, R. Romão Ramalho, 59, 7000 Evora. Portugal.
2. Andalusian Center for Environmental Research (CEAMA), University of Granada – Autonomous Government of Andalusia, Av. del Mediterráneo s/n, 18006, Granada, Spain
3. Dpt. Applied Physics, University of Granada, Fuentenueva s/n, 18071, Granada, Spain.

nm (corresponding to the Raman-shift on nitrogen molecules of radiation at 355 and 532 nm, respectively); additionally, the cross-polarized component is detected at 532 nm.

The profiles of particle extinction coefficients, $\alpha(z)$, at 355 and 532 nm, particle backscatter coefficients, $\beta(z)$, at 355, 532 and 1064 nm as well as the particle linear depolarization ratio, $\delta_p(z)$, at 532 nm, can be obtained from PAOLI measurements [16], [18], [21].

2.3 Data analysis

During nighttime periods the particle backscatter and extinction coefficients profiles, at 355 and 532 nm, were obtained with the Raman method [22]. It is based on the independent measurements at the laser wavelength as well as at the wavelength of the inelastic backscattered light. For applying this method, no assumption of the lidar ratio is necessary for the calculation of particle extinction and backscatter coefficients. From the obtained Raman profiles of the extinction and backscatter coefficients, the lidar ratios at 355 and 532 nm, S_{355} and S_{532} respectively, were derived.

During daytime periods, the particle backscatter profiles were obtained with the Klett method [23] assuming height-constant extinction-to-backscatter ratios.

The wavelength dependence of the backscatter and extinction coefficients can be determined, for the wavelength pair 355/532 nm, via the Ångström exponents, $\hat{\alpha}_\beta$ and $\hat{\alpha}_\alpha$, respectively. These parameters indicate the proportion of the coarse particles relative to smaller particles.

Backward trajectories at different heights in the free troposphere were computed with the Hybrid Single Particle Lagrangian Integrated Trajectory Model (HYSPPLIT) [24], which allowed estimating the source regions from where the particles were transported to the measurement site. Products of the space-borne instrument MODIS (Moderate Resolution Imaging Spectro radiometer) were also used in order to obtain information on the forest fires occurring on the Iberia Peninsula (see e.g. [25])

3 RESULTS

The smoke plumes over Portugal and Spain and the atmospheric turbidity caused by those fires are particularly evident in figure 1 for 18 October 2011. The 72-hour backward trajectories shown in figure 2 were computed for the height range between 2 and 4 km and for times close to the available lidar measurements. They are representative of other adjacent periods during 18 and 19 October 2011, when lidar measurements were available. They indicated that the smoke particles observed over Évora were transported from the forest fires occurring in the northwest of the Iberian Peninsula. All backward trajectories suggested a relatively

short transport time, between about 1-2 days.

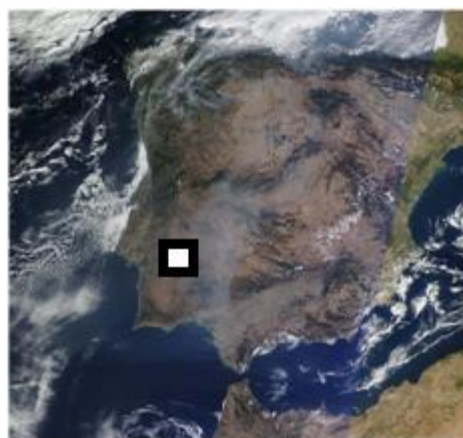


Fig. 1. MODIS-Terra image (1km x 1km) for 18 October 2011. The square on the image shows the region where Évora is located.

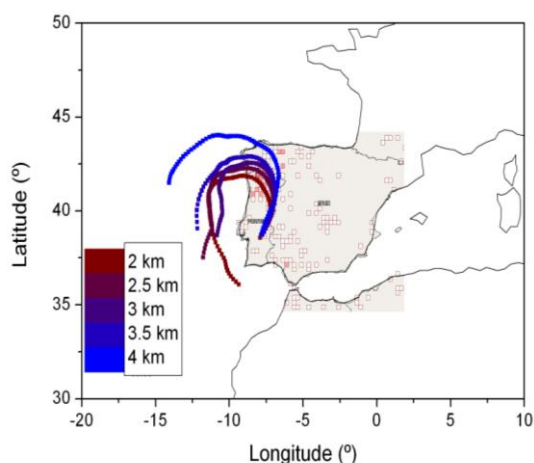


Fig. 2. 72-h back-trajectories ending at Évora on 18 October 2011, at 2000 UTC for heights between 2000 and 4000 m agl. The airflow pattern was quite constant during the whole period analysed. Also shown are the fire hot spots detected by MODIS on board the Terra and Aqua satellites.

Figure 3 shows two examples of the particle backscatter and extinction coefficients, at 355 nm, for two different measurement periods on 18 October 2011, namely 20:00 - 21:00 UTC and 21:45-22:00 UTC. Two layers in the free troposphere with enhanced backscatter and extinction coefficients are apparent, in particular regarding the second period shown in figure 3. Particle backscatter coefficients higher than $5 \text{ Mm}^{-1} \text{sr}^{-1}$ and extinction coefficients close to 300 Mm^{-1} could be observed.

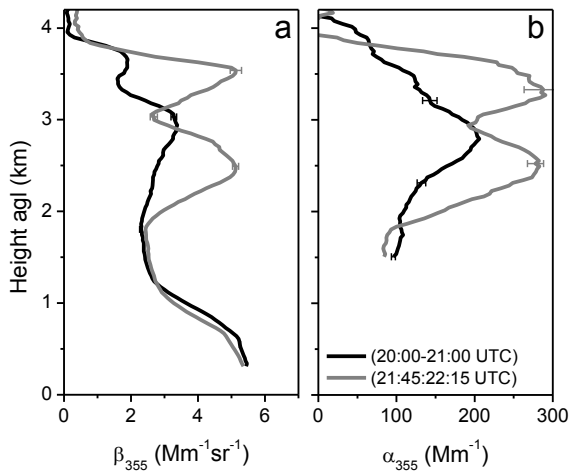


Fig. 3. Profiles of the particle (a) backscatter and (b) extinction coefficients at 355 nm, obtained with the Raman method for 18 October 2011 in the periods between 20:00 - 21:00 UTC and 21:45-22:15 UTC.

Despite the variability in both the intensity and the heights of the layers, revealed by the backscatter and extinction coefficients, the mean $\hat{\alpha}_\beta$ and $\hat{\alpha}_\alpha$ (wavelength pair 355/532 nm) were consistent throughout the studied period and were similar over the considered height range. As figure 4a illustrates, the average $\hat{\alpha}_\beta$ and $\hat{\alpha}_\alpha$ present a similar behavior and a mean value of about 1.4 was found for both parameters.

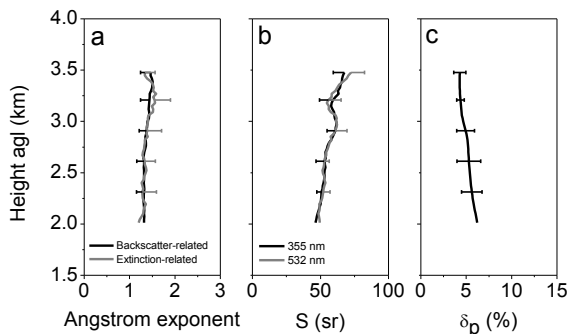


Fig. 4. Mean profiles and standard deviation (error bars) of (a) backscatter and extinction related Ångström exponents (355/532 nm), (b) lidar ratios at 355 and 532 nm and (c) particle linear depolarization ratio at 532 nm.

These types of magnitudes of the Ångström exponents indicate a predominance of fine mode particles and are comparable to the findings of [26]. They studied a “fresh biomass burning aerosol” plume over Granada (Spain) and obtained a similar range of 1.0-1.5 for the backscatter and extinction related Ångström exponents. As aforementioned, analysis of the backward trajectories suggested travel times in the order of less than 48 hours for the smoke plumes observed at Évora. However, the uncertainties of the travel times were high because of the large number of fires and the different source

regions contributing to the aerosol load. In any case, those estimated travel times, in conjunction with the range of observed $\hat{\alpha}$, are consistent with the conclusions of [2] on the increase in size of smoke particles with ageing. It was previously noticed that aged smoke, after long range transport (about 1-2.5 weeks), is characterized by lower Ångström exponents, ranging from about 1 down to near zero [27]-[29]. Thus, our results of the Ångström exponents suggest that the smoke plumes here described were relatively fresh.

Figure 4b shows the average lidar ratio profiles at 355 and 532 nm, S_{355} and S_{532} (retrieved with the Raman method), which present small wavelength dependence. They were mainly in the range of 50-60 sr and an average value of 56 ± 6 sr was found for both S_{355} and S_{532} . Lidar ratios between 40-70 sr represent 90% of the observations. These values show consistency with the values reported by [26], who found lidar ratios between 60 and 65 sr. Catrall et al [30] compiled a set of mean lidar ratios for biomass burning aerosols (table 3 and references therein), directly measured by Raman lidars, which were in the range of 50 and 69 sr (at wavelengths between 490 and 550 nm). Moreover, lidar ratios from 40 to 100 sr at 355 nm were observed over East Europe [27], with increasing values being correlated with the increasing age of the smoke particles. Müller et al [30] reported mean values of 46 and 53 sr, respectively at 355 and 532 nm, for aged smoke advected from North America and Siberia to Germany. In the case of smoke from Siberia, observed in Japan after approximately four days of transport, lidar ratios of 40 and 65 at 355 and 532 nm, respectively, were reported by [31]. The wavelength dependence of the lidar ratios was previously suggested as an indicator of the smoke aging. For long-range transported smoke the ratio of the lidar ratios (S_{355}/S_{532}) is less than one ([31], [4], [29]), whereas [26] obtained a value “around unity” for fresh biomass burning aerosol. This is also the average value obtained in the present study (1.00 ± 0.03), which corroborates the previous results and gives additional support to the assumption that relatively fresh smoke was observed in the free troposphere over Évora during this period.

The average value of the particle linear depolarization ratio was $5.0 \pm 0.6\%$ (figure 4c). In all investigated periods, consistently small particle depolarization ratios were found, mainly in the range of 4-6%. Our results are in agreement with what should be expected for small size particles which were likely close to sphericity and which have small capability for depolarizing the light emitted by the lidar. Comparable values were also reported by other authors ([29], [31]).

4 CONCLUSIONS

Free tropospheric smoke plumes were detected over Évora, Portugal, with Raman lidar in October 2011. The analysis of the optical properties and transportation paths suggested the presence of relatively fresh smoke, with a transportation time of about 1-2 days. The mean values of extinction and backscatter related Ångström exponents were similar and of high magnitude, about 1.4 for the 355/532 nm wavelength pair, which represent a significant wavelength dependence of α and β . This high wavelength dependence indicates the presence of small particles over the site. Particle backscatter coefficients greater than $5 \text{ Mm}^{-1}\text{sr}^{-1}$ and particle extinction coefficients close to 300 Mm^{-1} , at 355 nm, were observed in the center of the layers aloft. The mean lidar ratios at 355 and 532 nm of 56 sr presented small wavelength dependence. Moreover, the particle linear depolarization ratio at 532 nm was consistently low with about 5%.

Acknowledgments

This work was supported by FCT (Fundação para a Ciência e a Tecnologia) through the National Re-equipment Program under REDE/1527/RNG/2007, through the project PTDC/CTEATM/65307/2006, and through the project PTDC/AAC-CLI/104925/2008. The authors also acknowledge the funding provided by the Évora Geophysics Centre, Portugal, under the contract with FCT (the Portuguese Science and Technology Foundation), PESt-OE/CTE/UI0078/2011.

We also acknowledge for the FCT grants SFRH/BPD/81132/2011 and SFRH/BD/47521/2008. CGE benefits from the membership in SPALINET, EARLINET and ACTRIS. ACTRIS Research Infrastructure Project is supported by the European Union Seventh Framework Programme (FP7/2007-2013) under grant agreement number 262254). This work was also supported by the Andalusia Regional Government through the project P10-RNM-6299. We also thank the lidar team of the Leibniz-Institute for Tropospheric Research in Leipzig, Germany for their support with PAOLI. The authors gratefully acknowledge the NOAA Air Resources Laboratory (ARL) for the provision of the HYSPLIT transport and dispersion model and/or READY website (<http://ready.arl.noaa.gov>) used in this publication.

REFERENCES

[1] Dubovik, O., Holben, B., Eck, T. F., Smirnov, A., Kaufman, Y. J., King, M. D., Tanré, D and Slutsker, I., 2002: Variability of Absorption and Optical Properties of Key Aerosol Types Observed in Worldwide Locations. *J. Atmos. Sci.*, 59, 590–608.
 [2] Müller, D., I. Mattis, A. Ansmann, U. Wandinger, C. Ritter, and D. Kaiser (2007), Multiwavelength Raman lidar

observations of particle growth during long-range transport of forest-fire smoke in the free troposphere, *Geophys. Res. Lett.*, 34, L05803, doi:10.1029/2006GL027936.
 [3] Damoah, R., N. Spichtinger, C. Forster, P. James, I. Mattis, U. Wandinger, S. Beirle, T. Wagner, and A. Stohl (2004), Around the world in 17 days - Hemispheric-scale transport of forest fire smoke from Russia in May 2003, *Atmos. Chem. Phys.*, 4, 1311–1321.
 [4] Müller, D., I. Mattis, U. Wandinger, A. Ansmann, D. Althausen, and A. Stohl (2005), Raman lidar observations of aged Siberian and Canadian forest fire smoke in the free troposphere over Germany in 2003: Microphysical particle characterization, *J. Geophys. Res.*, 110, D17201, doi:10.1029/2004JD005756.
 [5] Fabian, P., R. Rollenbeck, N. Spichtinger, L. Brothers, G. Dominguez, and M. Thiemens (2009): Sahara dust, ocean spray, volcanoes, biomass burning: pathways of nutrients into Andean rainforests, *Adv. Geosci.*, 22, 85–94.
 [6] Guerrero-Rascado, J. L., F. J. Olmo, F. Molero, F. Navas-Guzmán, M. J. Costa, A. M. Silva, M. Pujadas, M. Sicard, L. Alados-Arboledas, 2010. Characterization of atmospheric aerosol for a long-range transport of biomass-burning from North America over the Iberian Peninsula. Proceedings of the 25th International Laser Radar Conference, 5–9 July 2010, St.-Petersburg, Russia. ISBN 978-5-94458-109-9.
 [7] Val Martin, M., J. A. Logan, R. A. Kahn, F. Y. Leung, D. L. Nelson, and D. J. Diner, Smoke injection heights from fires in North America: analysis of 5 years of satellite observations, *Atmos. Chem. Phys.*, 10, 1491-1510, 2010.
 [8] Kaufman, Y. J., et al., Smoke, Clouds, and Radiation—Brazil (SCAR-B) experiment, *J. Geophys. Res.*, 103, 31,783–31,808, 1998
 [9] Lyamani, H., Olmo, F.J., Alcántara, A., Alados-Arboledas, L. (2006), Atmospheric aerosols during the 2003 heat wave in southeastern Spain II: microphysical columnar properties and radiative forcing. *Atmos. Environ.*, 40, 6465–6476.
 [10] Alves, C., Gonçalves, C., Fernandes, A. P., Tarelho, L., Pio, C. (2011), Fireplace and woodstove fine particle emissions from combustion of western Mediterranean wood types. *Atmospheric Research*, 101, 692–700.
 [11] Stedman, J.R. (2004), The predicted number of air pollution related deaths in the UK during the August 2003 heatwave. *Atmos. Environ.*, 38, 1087–1090.
 [12] Allen, A.G., Cardoso, A.A., Rocha, G.O. (2004), Influence of sugar cane burning on aerosol soluble ion composition in Southeastern Brazil. *Atmos. Environ.*, 38, 5025–5038.
 [13] Direção de Unidade de Defesa da Floresta (2012). Relatório anual de áreas aridas e ocorrências em 2011 (http://www.icnf.pt/portal/florestas/dfici/Resource/ficheiros/relatorios/relatorioanualincendios2011_afndedef).
 [14] Elias, T., A. M. Silva, N. Belo, S. Pereira, P. Formenti, G. Helas, and F. Wagner (2006), Aerosol extinction in a remote continental region of the Iberian Peninsula during summer, *J. Geophys. Res.*, 111, D14204, doi:10.1029/2005JD006610.
 [15] Pereira, S., F. Wagner, and A. M. Silva (2008), Scattering properties and mass concentration of local and long-range transported aerosols over the South Western Iberia Peninsula, *Atmos. Environ.*, 42, 7623–7631.
 [16] Preißler, J., F. Wagner, S. N. Pereira, and J. L. Guerrero-Rascado (2011), Multi-instrumental observation of an exceptionally strong Saharan dust outbreak over Portugal, *J. Geophys. Res.*, 116, D24204, doi:10.1029/2011JD016527.
 [17] Pereira, S. N., Wagner, F., and Silva, A. M. (2012), Long term black carbon measurements in the southwestern Iberia Peninsula. *Atmos. Environ.*, 57, 63-71.
 [18] Althausen, D., R. Engelmann, H. Baars, B. Heese, A. Ansmann, D. Müller, and M. Komppula (2009), Portable Raman lidar PollyXT for automated profiling of aerosol backscatter, extinction, and depolarization, *J. Atmos. Oceanic Technol.*, 26, 2366–2378.
 [19] Bösenberg, J., et al. (2003), Executive summary, in EARLINET: A European Aerosol Research Lidar Network to Establish an Aerosol Climatology, Rep. 348, pp. 6–31, Max Planck Inst. for Meteorol., Hamburg, Germany.

- [20] Sicard, M., et al. (2011), SPALINET: The Spanish and Portuguese aerosol lidar network, *Opt. Pura Apl.*, 44, 1–5.
- [21] Preißler, J. (2012), Vertically resolved monitoring of atmospheric aerosols over Portugal with a multi-wavelength Raman lidar. Ph.D Thesis (European Doctorate), 129 pp, University of Évora, Portugal.
- [22] Ansmann, A., U. Wandinger, M. Riebesell, C. Weitkamp, and W. Michaelis (1992), Independent measurement of extinction and backscatter profiles in cirrus clouds by using a combined Raman elastic-backscatter lidar, *Appl. Opt.*, 31, 7113–7131.
- [23] Klett, J. D. (1981), Stable analytical inversion solution for processing lidar returns, *Appl. Opt.*, 20, 211–220.
- [24] Draxler, R.R. and Rolph, G.D., 2012. HYSPLIT (HYbrid Single-Particle Lagrangian Integrated Trajectory) Model access via NOAA ARL READY Website (<http://ready.arl.noaa.gov/HYSPLIT.php>). NOAA Air Resources Laboratory, Silver Spring, MD.
- [25] Giglio, L., J. Descloitres, C. O. Justice, and Y. J. Kaufman. 2003. An enhanced contextual fire detection algorithm for MODIS. *Remote Sens. Environ.*, 87, 273-282
- [26] Alados-Arboledas, L., D. Müller, J. L. Guerrero-Rascado, F. Navas-Guzmán, D. Pérez-Ramírez, and F. J. Olmo (2011), Optical and microphysical properties of fresh biomass burning aerosol retrieved by Raman lidar, and starand sun-photometry, *Geophys. Res. Lett.*, 38, L01807, doi:10.1029/2010GL045999.
- [27] Amiridis, V., Balis, D.S., Giannakaki, E., Stohl, A., Kazadzis, S., Koukouli, M.E., Zanis, P., 2009. Optical characteristics of biomass burning aerosols over southeastern Europe determined from UV–Raman lidar measurements. *Atmospheric Chemistry and Physics* 9, 2431–2440.
- [28] Wandinger U., Müller, D., Böckmann, C., et al.: Optical and microphysical characterization of biomass burning and industrial pollution aerosols from multiwavelength lidar and aircraft measurements, *J. Geophys. Res.*, 107, doi:10.1029/2000 JD000202, 2002.
- [29] Müller, D., A. Ansmann, I. Mattis, M. Tesche, U. Wandinger, D. Althausen, and G. Pisani (2007), Aerosol-type-dependent lidar ratios observed with Raman lidar, *J. Geophys. Res.*, 112, D16202, doi:10.1029/2006JD008292.
- [30] Catrall, C., J. Reagan, K. Thome, and O. Dubovik (2005), Variability of aerosol and spectral lidar and backscatter and extinction ratios of key aerosol types derived from selected Aerosol Robotic Network locations, *J. Geophys. Res.*, 110, D10S11, doi: 10.1029/2004JD005124.
- [31] Murayama, T., D. Müller, K. Wada, A. Shimizu, M. Sekiguchi, and T. Tsukamoto (2004), Characterization of Asian dust and Siberian smoke with multi-wavelength Raman lidar over Tokyo, Japan in spring 2003, *Geophys. Res. Lett.*, 31, L23103, doi:10.1029/2004GL021105.

Influence of atmospheric aerosol characterization on satellite remote sensing of water quality parameters

M. Potes¹, M. J. Costa², R. Salgado³

Abstract — Changes in the atmospheric aerosol composition affect the amount of radiation that reaches the surface and consequently the energy budget between atmosphere and Earth. The study of surface water properties from satellite remote sensing techniques requires the correction of the atmospheric effects. In this work the influence of aerosol optical thickness and aerosol type are tested varying the aerosol characteristics in the radiative transfer calculations to determine atmospherically corrected satellite spectral reflectance. The impact of these variations is then assessed through comparisons of the water quality parameters derived using empirical algorithms under different atmospheric aerosol conditions.

Keywords — aerosol optical thickness, atmospheric correction, lake water quality, remote sensing

1 INTRODUÇÃO

A região do Alentejo, localizada a sul de Portugal, representa aproximadamente um terço do país e tem aproximadamente 5% da população nacional. O Alentejo é uma região que há muito tempo é conhecida pela irregularidade na disponibilidade hídrica como consequência da irregularidade da precipitação média anual. Assim, com o objectivo de constituir um reservatório de água essencial na região, foi construída a barragem de Alqueva, dando origem à respectiva albufeira que permite a preservação e uso de água, até durante os períodos de seca extensos. O Alqueva, localizado na secção portuguesa do Rio Guadiana e incluído na bacia hidrográfica do Guadiana, é um dos maiores lagos artificiais da Europa quanto à área superficial (250 km²) e representa um bom exemplo da importância do controle de qualidade de água em lagos artificiais, devido à sua importância na região onde está localizado. Este controle é realizado através de um programa de monitorização que tem por objectivo representar uma estimativa segura da qualidade da água do reservatório. Normalmente esta avaliação é realizada através da medição de vários parâmetros significativos com uma determinada frequência temporal e espacial [1].

O estudo das propriedades de superfície a partir de técnicas de detecção remota de satélite necessita que seja feita a correcção dos efeitos da atmosfera. A

transferência radiativa serve de mecanismo para a transferência de energia entre a atmosfera e a superfície subjacente e entre as diferentes camadas da atmosfera. Para a modelação dos efeitos atmosféricos é necessário o tratamento completo da absorção pelos gases atmosféricos (geralmente a absorção pelos aerossóis é pequena) e da dispersão pelos aerossóis presentes na coluna atmosférica. Neste trabalho é avaliado o peso quantitativo e qualitativo dos aerossóis na obtenção de parâmetros de qualidade da água através de detecção remota por satélite.

2 MÉTODOS

Para a correcção atmosférica dos dados de satélite foi utilizado o código de transferência radiativa (CTR) 6S (Second Simulation of the Satellite Signal in the Solar Spectrum). Segundo este CTR, podem modelar-se os efeitos atmosféricos nas regiões espectrais do visível e infravermelho [2].

A absorção por gases atmosféricos no espectro solar é principalmente devida ao oxigénio (O₂), ozono (O₃), vapor de água (H₂O), dióxido de carbono (CO₂), metano (CH₄) e óxido nitroso (N₂O). As concentrações de O₂, CO₂, CH₄ e N₂O são consideradas constantes, uniformemente misturados na atmosfera, enquanto as concentrações de H₂O e O₃ variam no tempo e no espaço. Estes dois últimos são os gases mais importantes para o código uma vez que apresentam importantes bandas de absorção na região espectral abrangida pelo CTR embora existam janelas atmosféricas adequadas, no espectro solar, para a detecção remota feita por satélites.

Uma vez que este estudo foi realizado para um dia de céu limpo a correcção atmosférica depende essencialmente do tipo e quantidade de aerossóis presentes na atmosfera. Medições de espessura

1. Author is with the Evora Geophysics Centre and University of Evora, R. Romão Ramalho, 59, 7000 Evora. Portugal. E-mail: mpotes@uevora.pt

2. Author is with the Department of Physics, University of Evora, R. Romão Ramalho, 59, 7000 Evora. Portugal. E-mail: mjcosta@uevora.pt

3. Author is with the Department of Physics, University of Evora, R. Romão Ramalho, 59, 7000 Evora. Portugal. E-mail: rsal@uevora.pt

óptica (AOT) e de índice de refração complexo são continuamente obtidas no observatório do Centro de Geofísica de Évora (CGE) a partir da inversão de medidas de radiação espectral obtidas por um fotómetro solar que faz parte da AEROSOL ROBOTIC NETWORK (AERONET). Devido à proximidade da albufeira de Alqueva (50 km aproximadamente) não são de esperar variações significativas no tipo de aerossol.

Para se obter a concentração dos pigmentos são necessárias regressões empíricas baseadas na razão entre bandas espectrais de reflectância de superfície [3]. Os algoritmos utilizados permitem estimar a concentração de clorofila, densidade de cianobactérias e turbidez sobre toda a superfície do Alqueva numa visão global da distribuição destes parâmetros que condicionam a qualidade da água da Albufeira [4],[5].

Para a avaliação do peso quantitativo e qualitativo dos aerossóis na obtenção de parâmetros de qualidade da água foram realizados quatro casos de estudo (Tabela 1). Um caso de referência em que foi utilizado a caracterização dos aerossóis medida pelo CIMEL de Évora (Fig. 1). E três casos em que a AOT e o índice de refração imaginário (RI) foram alterados um de cada vez de modo a quantificar os efeitos nos parâmetros analisados neste trabalho, como mostra a Tabela 1.

Tabela 1 – Caracterização dos aerossóis para os vários casos de estudo. Espessura óptica (AOT) e índice de refração imaginário (RI) aos 550 nm.

	AOT	RI
Referência	0.038	0.0260
Caso 1	0.050	0.0260
Caso 2	0.500	0.0260
Caso 3	0.038	0.0026

3 RESULTADOS

A Fig. 1 mostra concentração de clorofila a ($\mu\text{g L}^{-1}$), densidade de cianobactérias (10^3 células mL^{-1}) e turbidez (NTU – Nephelometric Turbidity Units) à superfície da albufeira de Alqueva para o dia 11 de Fevereiro de 2009, 10:52 UTC. Estes mapas de referência foram realizados com a caracterização dos aerossóis obtidos pelo CIMEL de Évora. O valor de AOT aos 550 nm foi obtido às 10:53 UTC e o valor de RI aos 550 nm foi obtido às 10:48 UTC.

O mapa de concentração de clorofila a (Fig. 1a) mostra que a zona mais a sul e os trechos mais estreitos apresentam valores elevados e superiores a $100 \mu\text{g L}^{-1}$ enquanto as zonas interiores apresentam valores mais baixos. Este comportamento também é visível no mapa de densidade de cianobactérias (Fig. 1b). De salientar que o pigmento clorofila a é o único que está presente em todas as plantas incluindo as cianobactérias. O mapa de turbidez (Fig. 1c) apresenta grande variabilidade espacial em toda a albufeira, sem um padrão definido.

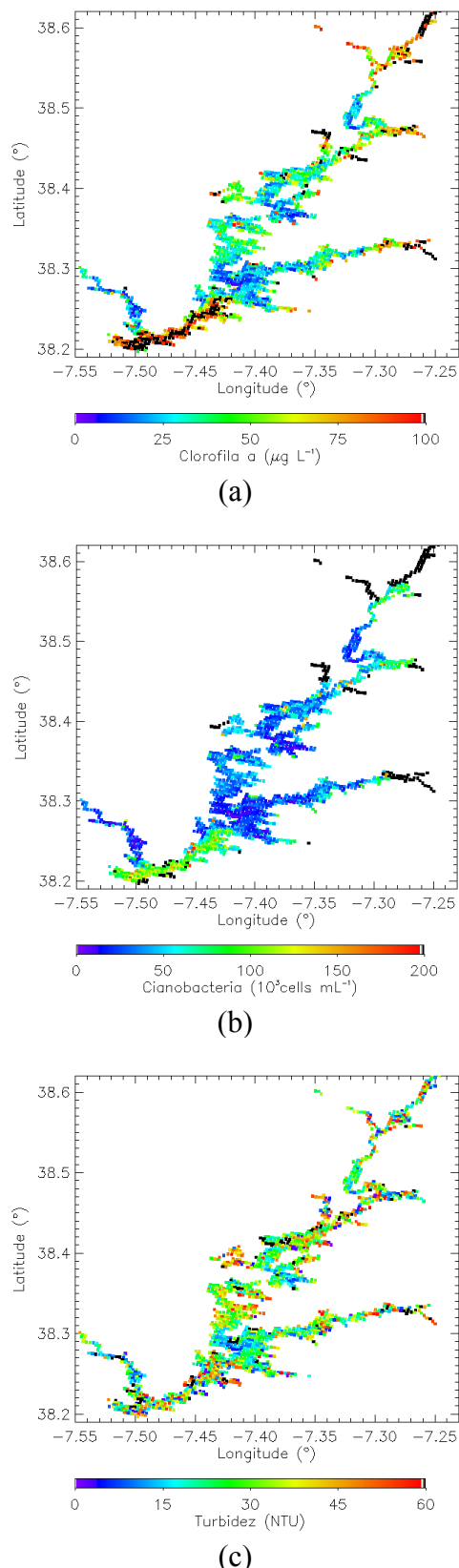
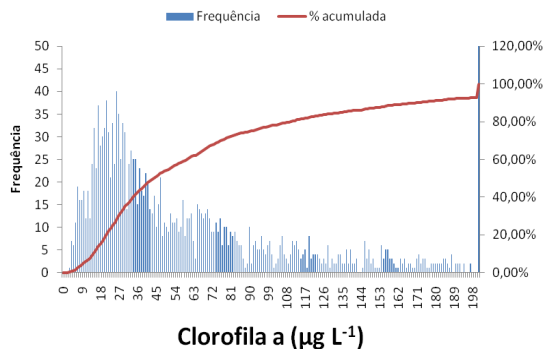
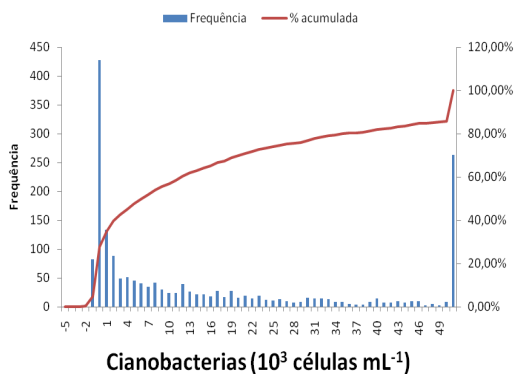


Figura 1 – Mapas da albufeira de Alqueva no dia 11 de Fevereiro de 2009 com: (a) concentração de clorofila a ; (b) densidade de cianobactérias; (c) turbidez da água. Caso de referência.

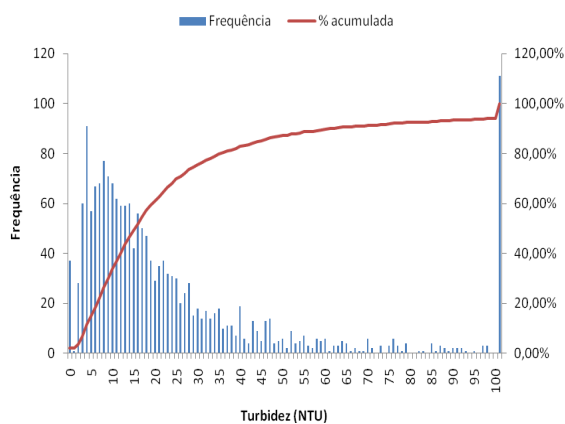
Para o caso 1 foi utilizado um valor de AOT ligeiramente superior ao valor de referência (Tabela 1), mantendo o mesmo RI, o que permite avaliar o efeito de um aumento da espessura óptica dos aerossóis atmosféricos na obtenção dos mesmos parâmetros de qualidade da água. Foi calculada a anomalia em relação ao caso de referência e na Fig. 2 estão representados os gráficos da frequência absoluta e relativa dessa anomalia para os três parâmetros em estudo.



(a)



(b)

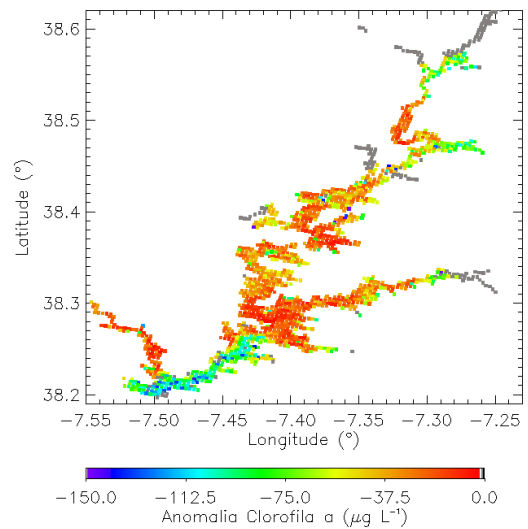


(c)

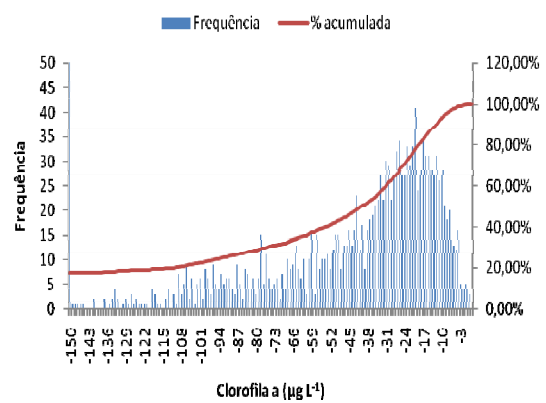
Figura 2 – Gráficos de frequência absoluta e relativa da anomalia da concentração de clorofila *a*, densidade de cianobactérias e turbidez da água entre o caso 1 (AOT=0.05) e o caso de referência, para a albufeira de Alqueva no dia 11 de Fevereiro de 2009.

Verifica-se que este ligeiro aumento de AOT vai provocar um aumento nas estimativas da concentração de clorofila *a* e da turbidez (anomalia positiva – Figs. 2a e 2c). Na estimativa da densidade de cianobactérias (Fig. 2b) há um ligeiro decréscimo (anomalia negativa) em cerca de 30% da albufeira e um aumento (anomalia positiva) na área restante da albufeira.

Para o caso 2 foi utilizado um valor de AOT bastante superior ao valor de referência (Tabela 1), mantendo uma vez mais o RI. Nas Figs. 3 e 4 estão representados os mapas de anomalia entre o caso 2 e o caso de referência e respectivos gráficos de frequência absoluta e relativa para a concentração de clorofila *a* e turbidez, respectivamente. Para a densidade de cianobactérias os valores deixaram de ter significado físico, não sendo por isso aqui apresentados.

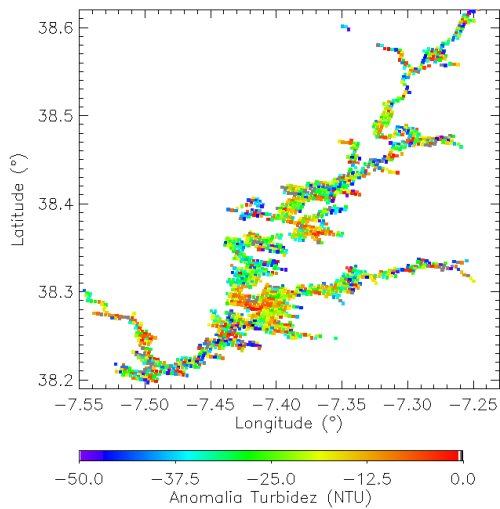


(a)

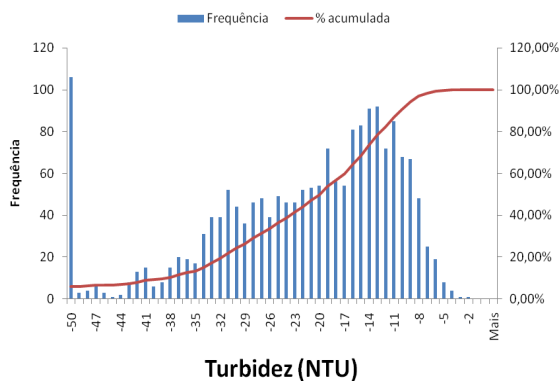


(b)

Figura 3 – Mapa da anomalia de concentração de clorofila *a* entre o caso 2 e o caso de referência e respectivo gráfico de frequência absoluta e relativa, para a albufeira de Alqueva no dia 11 de Fevereiro de 2009.



(a)

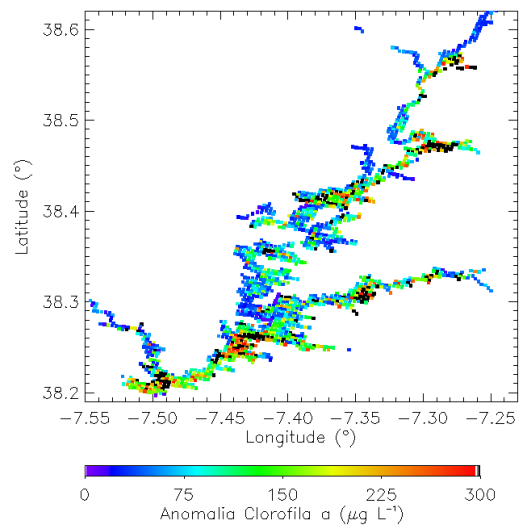


(b)

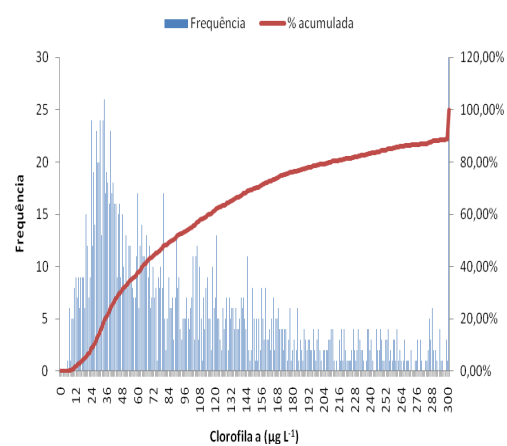
Figura 4 – Mapa da anomalia da turbidez entre o caso 2 (AOT=0.5) e o caso de referência e respectivo gráfico de frequência absoluta e relativa, para a albufeira de Alqueva no dia 11 de Fevereiro de 2009.

Verifica-se que um valor de AOT muito superior vai levar a uma diminuição nas estimativas da concentração de clorofila *a* e da turbidez (anomalia negativa). A anomalia da concentração de clorofila *a* é mais acentuada onde a concentração é superior no caso de referência (Fig. 1). A anomalia da turbidez apresenta a mesma variabilidade espacial que o caso de referência.

Para o caso 3 foi utilizado o valor de AOT de referência e um valor de RI com uma ordem de grandeza inferior (Tabela 1), simulando um tipo de aerossóis que absorvem menos radiação solar. Nas Figs. 5, 6 e 7 estão representados os mapas de anomalia entre o caso 3 e o caso de referência e respectivos gráficos de frequência absoluta e relativa para a concentração de clorofila *a*, densidade de cianobactérias e turbidez, respectivamente.



(a)



(b)

Figura 5 – Mapa da anomalia de concentração de clorofila *a* entre o caso 3 e o caso de referência e respectivo gráfico de frequência absoluta e relativa, para a albufeira de Alqueva no dia 11 de Fevereiro de 2009.

Verifica-se que esta diminuição de RI vai provocar um aumento nas estimativas da concentração de clorofila *a* e da turbidez (anomalia positiva – Figs. 5 e 7). Na estimativa da densidade de cianobactérias há um ligeiro decréscimo (anomalia negativa) em cerca de 40% da albufeira e também um aumento (anomalia positiva) no restante da albufeira (Fig. 6). De salientar o comportamento similar com o caso 1 onde a AOT foi ligeiramente aumentada. Embora neste caso a anomalia da concentração de clorofila *a* e da turbidez seja superior (ver Figs. 5 e 7).

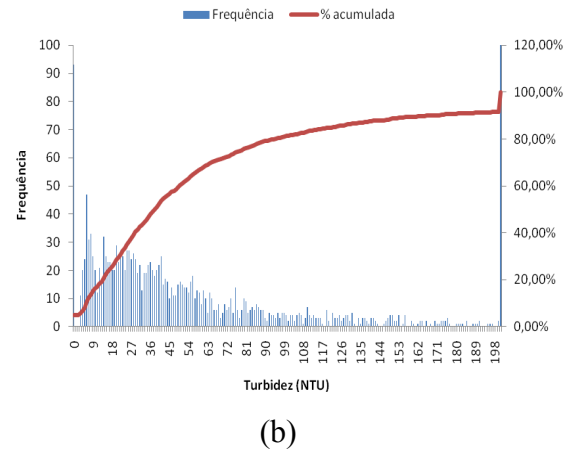
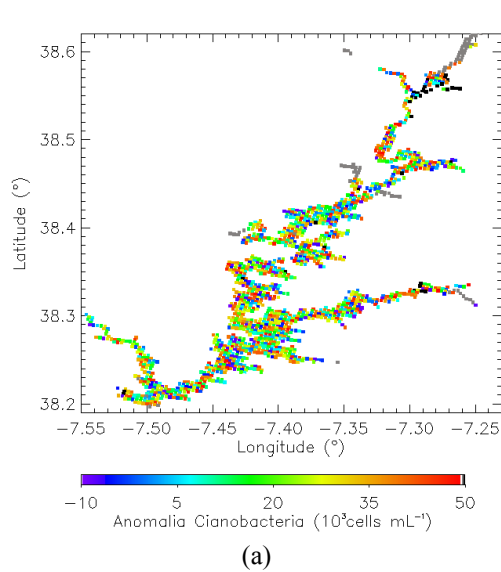


Figura 7 – Mapa da anomalia da turbidez entre o caso 3 e o caso de referência e respectivo gráfico de frequência absoluta e relativa, para a albufeira de Alqueva no dia 11 de Fevereiro de 2009.

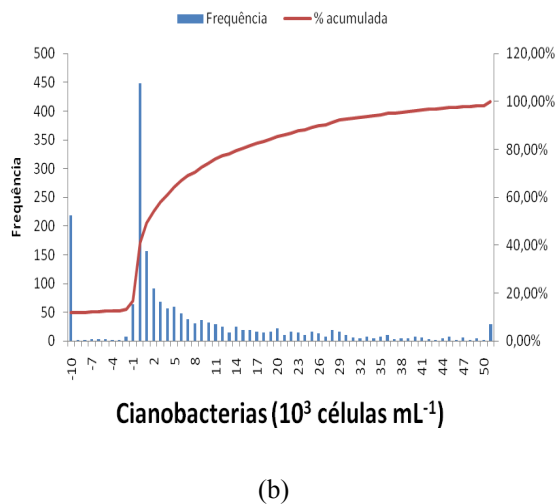
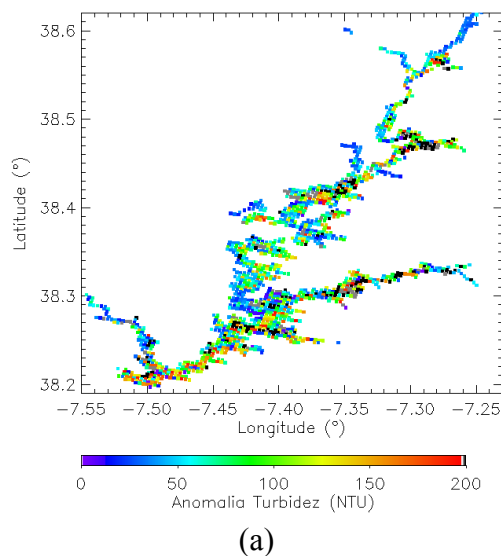


Figura 6 – Mapa da anomalia da densidade de cianobactérias entre o caso 3 e o caso de referência e respectivo gráfico de frequência absoluta e relativa, para a albufeira de Alqueva no dia 11 de Fevereiro de 2009.



4 CONCLUSÕES

Foi utilizada a metodologia desenvolvida em [4], [5] para obter concentração de parâmetros biológicos e turbidez, que condicionam a qualidade da água, através da combinação de medições da reflectância espectral de superfície. Uma questão crítica na obtenção de parâmetros de qualidade de água a partir de medidas de satélite é a existência de medições de alguns parâmetros atmosféricos que permitam uma adequada correcção atmosférica das imagens de satélite. Demonstra-se aqui que a caracterização precisa dos aerossóis, nomeadamente a espessura óptica e índice refracção imaginário, é de extrema importância na obtenção da concentração de clorofila a , densidade de cianobactérias e turbidez.

AGRADECIMENTOS

Este trabalho foi financiado pelo FEDER (Programa Operacional Factores de Competitividade – COMPETE), pela FCT (Fundação para a Ciência e a Tecnologia) no âmbito da bolsa de doutoramento SFRH/BD/45577/2008 e pelo projecto FCOMP-01-0124-FEDER-009303 (PTDC / CTE-ATM / 102142 / 2008). Os autores querem agradecer o financiamento disponibilizado pelo Centro de Geofísica de Évora, Portugal, através do contracto com a FCT - PEst-OE/CTE/UI0078/2011. Os autores querem também agradecer o financiamento do projecto da Comunidade Europeia - Research Infrastructure Action under the FP7 "Capacities" specific programme for Integrating Activities, ACTRIS Grant Agreement no. 262254.

REFERÊNCIAS

- [1] Serafim, A., Morais, M., Guilherme, P., Sarmiento, P., Ruivo, M. and Magriço, A. 2006. Spatial and temporal heterogeneity in the Alqueva reservoir, Guadiana river, Portugal. *Limnetica* 25, 771-786.
- [2] Vermote, E.F., Tanré, D., Deuzé, J-L., Herman, M. and Morcrette, J-J. 1997. Second simulation of the satellite signal in the solar spectrum: An overview. *IEEE Trans. Geosci. Rem. Sens.* 35, 675-686.
- [3] Bukata, R.P., Jerome, J.H., Kondratyev, K.Ya. and Pozdnyakov, D.V. 1995. *Optical Properties and Remote Sensing of Inland and Coastal Waters*, CRS Press, 362pp.
- [4] Potes, M., Costa, M.J., Silva, J.C.B., Silva, A.M. and Morais, M. 2011. Remote sensing of water quality parameters over Alqueva reservoir in the south of Portugal. *Int. J. Remote Sens.* 32:12, 3373-3388.
- [5] Potes, M., Costa, M. J., Salgado, R. 2012. Satellite remote sensing of water turbidity in Alqueva reservoir and implications on lake modeling. *Hydrol. Earth Syst. Sci.* 16, 1623-1633.

Sensitivity study of longwave radiative forcing to dust particle properties

Santi Bertolín¹, Michaël Sicard^{1,2}, Marc Mallet³, Philippe Dubuisson⁴, Adolfo Comerón¹

Abstract — The aerosol radiative effect in the longwave spectral range is often neglected in atmospheric aerosol forcing studies, hence very few research is conducted in this field at local scale, and even less at regional scale. However, strong absorbing aerosols, like mineral dust, can have a small, but non-negligible heating effect in the longwave which can slightly counteract the aerosol cooling effect in the shortwave. The objective of this research is to perform a sensitivity study of an aerosol radiative transfer model as a function of dust particle properties. The model used is GAME [Dubuisson et al., 1996] which can compute the radiative forcing of aerosol layers in both the shortwave and the longwave regions under different input conditions. Preliminary radiative forcing simulations in the longwave have shown an important sensitivity to the following parameters: aerosol size and refractive index, aerosol vertical distribution, humidity, surface temperature and albedo.

Keywords — radiative transfer model, longwave, sensitivity study, mineral dust

1 INTRODUCTION

Atmospheric aerosols have a remarkable effect on the Earth-atmosphere radiative budget [1]. Nowadays many radiative transfer models (RTM) have been developed to estimate locally the aerosol direct radiative forcing (RF). A large number of recent studies focused only in the estimation of the shortwave (SW) RF arguing that the contribution of the longwave (LW) range was negligible [2][3][4]. Few studies, such as [5][6], have considered the LW range despite the difficulties to parameterize accurately the model and the lack of knowledge of the aerosol properties in the LW range.

It is true that the RF of most aerosol types in the LW range is small compared to their forcing in the shortwave. However large, highly absorbing particles such as mineral dust (MD) have revealed to have a significant forcing in the LW [5][6]. Mineral dust is an atmospheric aerosol present all around the world, even though it is originated only in a few delimited sources. In Europe the nearest source is the Sahara desert, which is the largest one, emitting half of the world atmospheric MD [10]. During its transport, MD properties are modified in such a manner that only a medium-size distribution remains (very small and very large particles are deposited through wet scavenging and sedimentation mechanisms, respectively) [11]. In order to focus on MD, the establishment of a climatology is proposed

to characterize the properties of the “typical” transported MD observed in our region.

In this study we propose to evaluate the sensitivity of a state-of-the-art radiative transfer model to aerosol properties (particle size, fine/coarse mode proportions, etc.) and aerosol layer properties (layer height, aerosol optical thickness, etc.) in order to identify situations inducing high RF in the LW range. The paper first presents a rather complete review of the existing knowledge of the aerosol microphysical properties in the LW spectral range. Then we perform a climatology study with almost nine years of AERONET (Aerosol Robotic Network) data to retrieve the mean characteristics of MD in the region of interest: Barcelona, Spain. Finally we present a sensitivity study of a transfer radiative model.

2 MINERAL DUST MODEL IN BARCELONA

Among the broad literature available on atmospheric aerosol microphysics, many works deal with the microphysical characterization of MD particles. MD particles are well characterized by remote sensing observations [12] and laboratory experiments [13][14], or a combination of both [15][16][17]. In the LW spectral range, the available literature reduces significantly. In order to find a model of MD particles representative of long-range transported particles over Barcelona several references have been used, as well as a climatology of their optical properties in Barcelona.

Yang et al. [18] showed that “the nonsphericity effect of dust particles is significant at short wavelengths, however, not at the thermal infrared wavelengths.” For this reason particles are assumed to be spherical and the classical Mie theory is employed to compute their optical properties used in the RTM.

1. Remote Sensing Laboratory, Universidad Politècnica de Catalunya, Barcelona, Spain; E-mail: santiberto@gmail.com; msicard@tsc.upc.edu; comeron@tsc.upc.edu

2. Centre de Recerca de l'Aeronàutica i de l'Espai - Institut d'Estudis Espacials de Catalunya, Universidad Politècnica de Catalunya, Barcelona, Spain

3. Laboratoire d'Aérodynamique, Université de Toulouse / CNRS, Toulouse, France; Marc.Mallet@aero.obs-mip.fr

4. Laboratoire d'Optique Atmosphérique, Université de Lille 1, Lille, France; philippe.Dubuisson@univ-lille1.fr

2.1 Refractive index

Contrary to the shortwave range, small spectral variations in the refractive index in the LW can result in significant changes in the optical coefficients. Hence a good spectral resolution is needed.

The behavior of the real and the imaginary part of the refractive index of MD particles as a function of wavelength in the LW has been reported for the first time in a limited number of studies in the eighties [13][14][19]. Later, reference books about atmospheric aerosols such as [15][16] gave also the refractive index versus wavelength but corrected with respect to different other sources.

The measurements considered here were taken in Meppen in western Germany [14][16]. MD particles, including soot, one of the main drivers of the absorption, were obtained after removal of water solubles and of particles with radii greater than $1.5 \mu\text{m}$ [14]. Fig. 1 shows the variation of the refractive index as a function of wavelength from 0.2 to $40 \mu\text{m}$. For comparison indexes from [13], [15] and [17] are also reported. There is only one significant difference between the model selected and [13] and [17]: the imaginary part in the 3 to $8 \mu\text{m}$ range is clearly above the others, by a value of ~ 0.05 . The refractive index from [15] is in general below the values from the other references. The most probable reason for that subestimation is the MD origin: [15] uses measurements of soil dust obtained by evaporation of rain and snow water [20], without referring directly to MD.

2.2 Size distribution and concentration

The aerosol size distribution and their concentration have been retrieved by long-term AERONET sun-photometer measurements in Barcelona during the period 23/12/2004 – 15/09/2012. Only level 2 data have been considered. In the above mentioned period a total of 4529 size distribution inversions are available.

MD particles have been discriminated by applying the method described in [21] and [22] that classifies the aerosols as MD when the Ångström exponent, $AE(440,870)$, is less than 0.75 , and the difference $\delta AE = AE(440,675) - AE(675,870)$ is less than 0.3 . To guarantee errors less than 30% [21] recommends to apply an additional criterion on the aerosol optical thickness (AOT): $AOT(1020) > 0.15$. The distribution of all points in a δAE versus AE plot is shown in Fig. 2. The total number of measurements representative of MD particles according to the discrimination described above is 134, distributed over 54 days. For those measurements the mean values of the fine and coarse volume median radii, r_{Vgf} and r_{Vgc} , the fine and coarse standard deviations, σ_f and σ_c , and the fine and coarse volume concentrations, C_{Vf} and C_{Vc} , are reported in Table. 1.

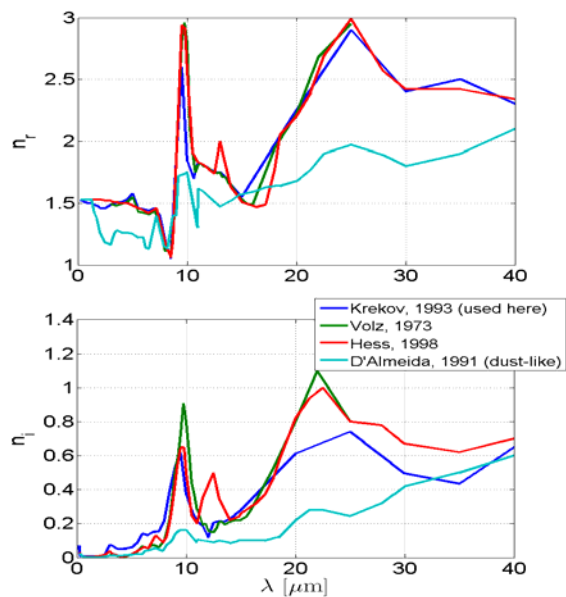


Fig. 1. Spectral dependency of the (top) real part, n_r , and (bottom) imaginary part, n_i , of the refractive index from different sources.

The input of our Mie code is the lognormal median radii, r_g , its standard deviation, σ_g , and the number concentration, N . The conversion of AERONET volumetric products to those parameters are given in the appendix.

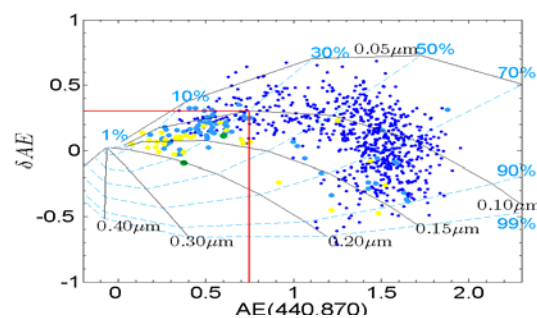


Fig. 2. δAE versus AE plot diagram for $n_r = 1.4$ and $n_i = 0.001$. Small, dark blue dots correspond to $0.15 < AOT < 0.30$, large, light blue dots to $0.3 < AOT < 0.4$, yellow dots to $0.4 < AOT < 0.7$ and green dots to $0.7 < AOT < 1$.

Table. 1. Characteristics of the MD model.

	Fine mode	Coarse mode
Refractive index	Krekov, 1993 (blue line in Fig. 1)	
r_{Vg} (r_g) [μm], σ	0.146 (0.057), 0.56	2.001 (0.632), 0.61
C_V [$\mu\text{m}^3/\mu\text{m}^2$]	0.036	0.176

2.3 MD particle optical properties

The extinction coefficient, α , the scattering albedo, ω_0 , and the asymmetry factor, g , are retrieved with a Mie code at a number of 115 wavelengths ranging from 4 to $50 \mu\text{m}$ (wavenumber from 2500 to 200 cm^{-1}). The MD particle density

has been taken as $2.6 \text{ g}\cdot\text{cm}^{-3}$ [17]. The spectral behaviour of all three parameters is shown in Fig. 3.

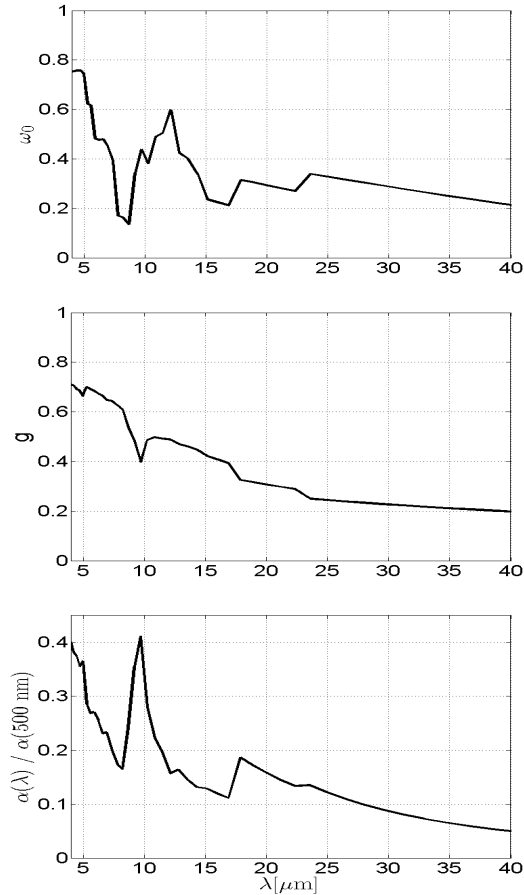


Fig. 3. Optical properties of the bimodal distribution of MD defined in Table 1. (top) Single scattering albedo, (middle) asymmetry factor, (bottom) extinction coefficient normalized at 500 nm.

3 RADIATIVE TRANSFER MODEL

Irradiances have been calculated using a fast yet accurate RTM, referred to as the GAME code. GAME allows to retrieve up and down fluxes, F , at the bottom (BOA) and top (TOA) of the atmosphere in the infrared spectral range, i.e. between 4 and 50 μm , in 40 vertical levels between ground and 100 km. Aerosol forcing has been calculated as:

$$\Delta F_{BOA} = F_{BOA}^w - F_{BOA}^o \quad \text{and} \quad (1)$$

$$\Delta F_{TOA} = -\left(F_{TOA}^w - F_{TOA}^o\right), \quad (2)$$

where F^w and F^o are the net fluxes with and without aerosols. With this convention, a negative sign of the daily ΔF implies an aerosol cooling effect.

3.1 Model description

GAME accounts for thermal emission, absorption and scattering, as well as their interactions, using the Discrete Ordinates Method (DISORT) [23]. This

accurate method allows calculating fluxes at any atmospheric level with the assumption of a vertically inhomogeneous media, stratified into plane and homogeneous layers. Gaseous absorption is treated from the correlated k-distribution [24]. The impact of the absorption continua is modelled using the CKD (Clough, Kneizys and Davis) formulation [25].

GAME also includes aerosol absorption and scattering.

The spectral optical properties of aerosols are defined for each atmospheric layer, including the phase function, the single scattering albedo and the extinction optical thickness.

3.2 Model parameterization

Besides aerosol optical properties, the RTM is sensitive to atmospheric parameters such as the relative humidity and air temperature profile, surface albedo and temperature or the aerosol vertical distribution.

The mid-latitude summer profile is taken from the U.S. Standard Atmosphere, 1976 model. The profiles of PTU, O_3 and CO_2 concentrations are represented in the same 40 vertical levels used in GAME. In a first approximation, the surface temperature is set to the temperature of the first level of the atmospheric profile used.

Contrary to the shortwave region, where reflectivity ρ can be highly directional, in the LW it is possible to approximate surface as lambertian. If Earth is considered in thermodynamic equilibrium, the emissivity, ε , is related to the reflectivity, ρ , by $\varepsilon = 1 - \rho$. The surface emissivity has been calculated as the mean value in the range 8 to 13 μm of the soil sample from [26]. The corresponding surface albedo is 0.041.

The aerosol vertical distribution was set to the MD layer characteristics based on observations over a period of 3 years [27]. The MD layer base mean is $1434 \pm 441 \text{ m}$ and the top mean is $3608 \pm 1605 \text{ m}$. Since our mid-latitude summer profile has a vertical resolution of 1000 m, the MD vertical distribution in Barcelona has been set to 1500 – 3500 m. All the generic parameters are listed in Table. 2.

Table. 2. Generic parameters for the sensitivity study.

Atmospheric profile	mls40
Surface albedo	0.041
Surface temperature	294.2 °K
Zenith sun angle	0 °
AOT	1
Aerosol vertical distribution	1.5-3.5 km

Other features are involved in the process but are not commented here, either because they have a negligible effect on the LW RF, like the sun position, or because they are different for every particular event, like the AOT or the aerosol stratification (layer thickness and height).

4 SENSITIVITY STUDY IN THE LONGWAVE

Fig. 4 shows the RF at BOA and TOA as a function of AOT at 500 nm. MD has a heating effect at both BOA and TOA, with a quasi-linear relationship with the AOT. Fig. 5 shows the behaviour of the RF as a function of the MD layer height, assuming a MD layer thickness of 1 km. Aerosols scatter in all directions, a little more in the forward direction ($g \approx 0.5$ in the 8 to 13 μm range), and absorb radiation and re-emit it also in all directions, therefore, a percentage of radiation turns back. Earth surface is the principal source of LW radiation so that the closest the aerosol layer from the surface, the more radiation will be reflected. This is well reproduced in Fig. 5 where the LW RF is high near the surface and decrease with increasing height while at TOA it behaves oppositely.

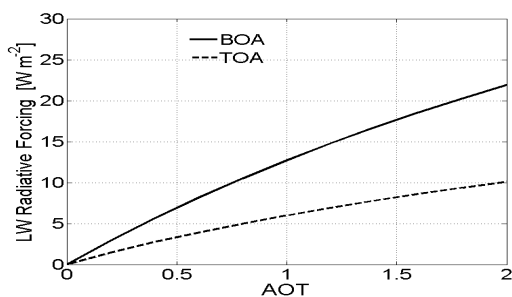


Fig. 4. LW RF at BOA and TOA as a function of AOT at 500 nm.

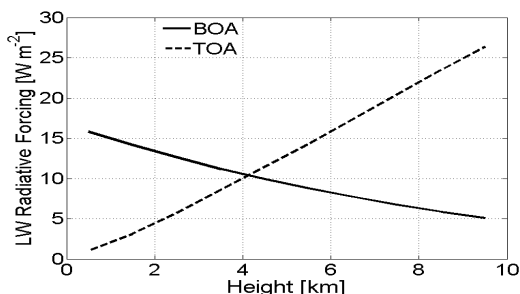


Fig. 5. LW RF at BOA and TOA as a function of MD layer height. For this figure, 1 km height layers have been used, between 0-1 km, 1-2 km, etc.

Fig. 6 shows the LW RF as a function of wavelength. Most of the radiation occurs in the atmospheric window of 8 to 13 μm . At TOA large particles have also a non-negligible effect on the RF in the 15 to 22 μm range. The effect of small particles represents approximately 10 % of the total RF.

Fig. 7 shows the particle size dependency of the LW RF for a constant AOT of 1 at 500 nm. The size distribution is monomodal here. The peak around $r_g = 0.005 \mu\text{m}$ is related to high values of extinction (figure not shown) and single scattering albedos close to 0 which indicates that the particles are nearly only absorbing. Above $0.005 \mu\text{m}$ the absorption decreases until $0.5 \mu\text{m}$. From $0.5 \mu\text{m}$, the

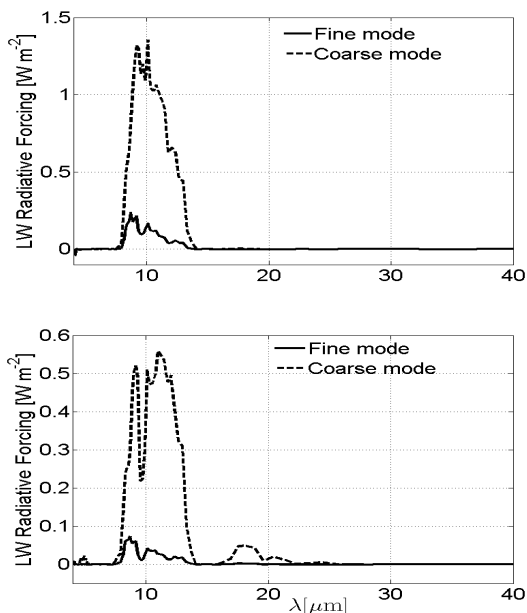


Fig. 6. LW RF as a function of wavelength at (top) BOA and (bottom) TOA.

absorption as well as the scattering increase, hence the increase in the RF seen in Fig. 7. Fig. 8 shows the LW RF as a function of the particle size (again a monomodal distribution is considered) maintaining the total volume constant and equal to that of Table 1. To maintain the total volume constant for small particles, it is necessary to increase the particle number to excessively and unrealistic values, so that the figure has to be taken with caution. For particles with a radius lower than $0.1 \mu\text{m}$ nearly all the extinction is due to absorption ($\omega_0 = 0$), while for greater radius the optical properties are similar to those of Fig. 3. For very large particles ($r_g > 10 \mu\text{m}$), $\omega_0 \approx 0.5$ and N is very low. This produces the LW RF to be nearly 0.

Finally Fig. 9 shows the RF dependency on the the ratio of mode concentration, N_c/N_f . One sees that the effect of small particles is less than 14 % at BOA and less than 10 % at TOA compared to large particles. The range of the mode concentration ratio in which the LW RF varies is comprised between 0.0001 and 0.1.

5 APPLICATION TO A REAL CASE

The LW RF is estimated on a real case of MD outbreak in Barcelona which took place on 22-23 July, 2009. The SW RF of that event has already been studied by [4]. The LW estimation is made for the MD plume observed by lidar on 22 July at 1212 UT [4] with the following parameters:

- refractive index as in Table 1;
- size distribution and concentration from the sun-photometer on 23 July at 0606 UT;
- atmospheric profile from local radiosounding taken at 22 July at 1200 UT;

- surface emissivity (0.983) and temperature (302.8 °K) from CERES (Clouds and the Earth's Radiant Energy System) products;
- MD stratification: AOT distributed between 0 and 6 km accordingly to the lidar profile [4].

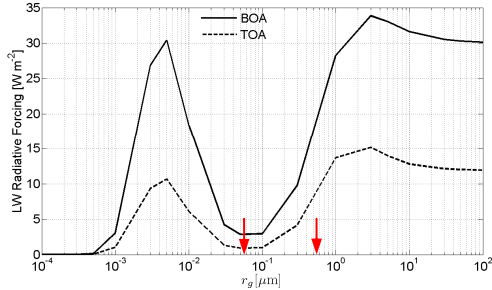


Fig. 7. LW RF at BOA and TOA vs. particle median radius and maintaining AOT(500 nm) = 1. The red arrows indicate the fine and coarse modes of the MD model.

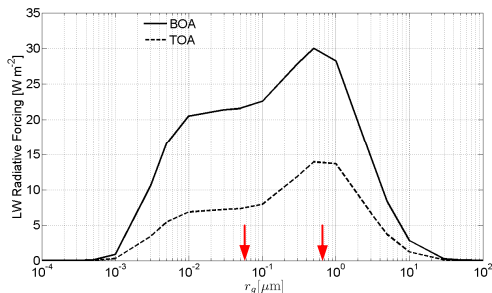


Fig. 8. LW RF at BOA and TOA vs. particle median radius and maintaining the volume concentration to that of Table 1. The red arrows indicate the fine and coarse modes of the MD model.

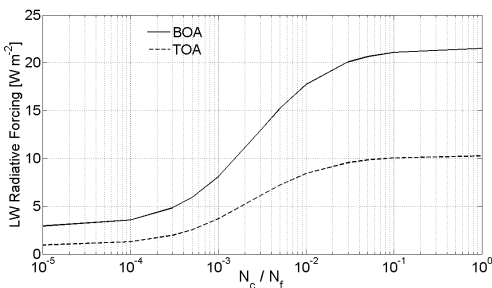


Fig. 9. RF at BOA and TOA vs. ratio of mode concentration, N_c/N_f . Beyond the displayed range, the RF values remain constant.

In order to validate the fluxes simulated by GAME, the TOA upward flux has been compared to CERES/TERRA measurements in its “window” spectral range defined between 8 and 12 μm . We found that GAME TOA upward flux is $97.8 \text{ W}\cdot\text{m}^{-2}$ and CERES flux (measured on 22 July at 1104 UT) over Barcelona is $101.3 \text{ W}\cdot\text{m}^{-2}$, resulting in a difference lower than 3.5 %. Further analyses focused on both GAME input uncertainties and CERES measurement errors are necessary to conclude on those differences.

The LW RF of the MD observed on 22 July is given in Table 3. SW RF from [4] are also reported for comparison. The surface LW forcing slightly counteracts the SW one, producing a heating effect that reduces the total cooling by $\sim 10\%$. The LW contribution at TOA is, in relative terms, much more important as the LW effect sums up $\sim 68\%$ of the SW RF.

Table 3. RF on 22 July, 2009, at 1212 UT.

	SW Forcing	LW Forcing
BOA [$\text{W}\cdot\text{m}^{-2}$]	-93	8.87
TOA [$\text{W}\cdot\text{m}^{-2}$]	8	5.47

6 APPENDIX

AERONET size distributions are bimodal volumetric lognormal distributions:

$$\frac{\partial V(r)}{\partial \ln r} = V(r) \frac{\partial N(r)}{\partial \ln r} = \frac{4}{3} \pi r^3 \frac{\partial N(r)}{\partial \ln r} \quad (3)$$

The median lognormal parameters are calculated as:

$$r_g = r_{vg} e^{-3\sigma^2} \quad \text{and} \quad (4)$$

$$\sigma_g = \sigma_{vg}. \quad (5)$$

The volume concentration value refers to the integration of the lognormal volumetric distribution between minimum and maximum radius.

$$C_v = \int_{r_{min}}^{r_{max}} \frac{\partial V(r)}{\partial \ln r} \partial \ln r \quad (6)$$

From this definition and Eq. (3) it is possible to derive the number concentration as:

$$N = \frac{3\sigma C_v}{\sqrt{2\pi} r_{vg}^3 e^{\frac{9}{2}\sigma^2}} \frac{1}{\left[\text{Erf} \left(\frac{\ln r_{max} - \ln r_{vg}}{\sqrt{2}\sigma} \right) - \text{Erf} \left(\frac{\ln r_{min} - \ln r_{vg}}{\sqrt{2}\sigma} \right) \right]} \quad (7)$$

7 CONCLUSIONS

This work demonstrates and quantifies the dependency of the aerosol RF in the LW spectral range on several particle characteristics: the AOT, the plume height, the size distribution and the mode concentration ratio. The real case presented and the comparison of the RF in both the SW and the LW proves that under given circumstances the LW contribution cannot be neglected, especially at TOA where the LW RF has been estimated to be half of the SW RF.

The aerosol properties, such as size distribution and concentration, are highly variable with transport. In spite of our capabilities to properly characterize aerosol properties at a local scale, MD particles remain difficult to accurately parameterize in regional climate models.

ACKNOWLEDGMENTS

This work is supported by the 7th Framework Programme project Aerosols, Clouds, and Trace Gases Research Infrastructure Network (ACTRIS) (grant agreement no. 262254); by the Spanish Ministry of Science and Innovation and FEDER funds under the projects TEC2012-34575, TEC2009-09106/TEC and CGL2011-13580-E/CLI.

REFERENCES

- [1] Forster, P., Ramaswamy, V., Artaxo, P., Bernsten, T., Betts, R., Fahey, D. W., Haywood, J., Lean, J., Lowe, D. C., Myhre, G., Nganga, J., Prinn, R., Raga, G., Schulz, M., and Van Dorland, R.: Changes in atmospheric constituents and in radiative forcing, in *Climate Change 2007*, in: The Physical Science Basis. Contribution of Working Group I to the Fourth Assessment Report of the Intergovernmental Panel on Climate Change, edited by: Solomon, S., Qin, D., Manning, M., Chen, Z., Marquis, M., Averyt, K. B., Tignor, M., and Miller H. L., Cambridge Univ. Press, Cambridge, United Kingdom, 129–234, 2007.
- [2] J. Roger, M. Mallet, P. Dubuisson, H. Cachier, E. Vermote, O. Dubovik and S. Despiou, “A synergetic approach for estimating the local direct aerosol forcing: Application to an urban zone during the Expérience sur Site pour Contraindre les Modeles de Pollution et de Transport d’Emission (ESCOMPTE) experiment”, *Journal of Geophysical Research*, vol. 111, d13208, doi: 10.1029/2005jd006361, 2006.
- [3] M. Mallet, V. Pont, C. Lioussé, L. Gomes, J. Pelon, S. Osborne, J. Haywood, J. Roger, P. Dubuisson, A. Mariscal, V. Thouret and P. Goloub, “Aerosol direct radiative forcing over Djougou (northern Benin) during the African Monsoon Multidisciplinary Analysis dry season experiment (Special Observation Period-0)”, *Journal of Geophysical Research*, vol. 113, d00c01, doi: 10.1029/2007jd009419, 2008.
- [4] M. Sicard, M. Mallet, D. García-Vizcaíno, A. Comerón, F. Rocadenbosch, P. Dubuisson and C. Muñoz-Porcar, “Intense dust and extremely fresh biomass burning in Barcelona, Spain: characterization of their optical properties and estimation of their radiative forcing”, *Environment Research Letters*, vol. 7, 034016, doi:10.1088/1748-9326/7/3/034016, 2012.
- [5] H. Liao and J. Seinfeld, “Radiative Forcing by mineral dust aerosols: sensitivity to key variables”, *Journal of Geophysical Research*, vol. 103, d24, pp. 31,637-31,645, 1998.
- [6] J. Dufresne, C. Gautier and P. Ricchiazzi, “Longwave scattering effects of mineral aerosols”, *American Meteorological Society*, vol. 59, pp. 1959-1966, 2002.
- [7] P. Dubuisson, D. Dessailly, M. Vesperini and R. Frouin, “Water Vapor Retrieval Over Ocean Using Near-Infrared Radiometry”, *Journal of geophysical research*, vol 109, d19106, doi:10.1029/2004/JD004516, 2004.
- [8] P. Dubuisson, J. Roger, M. Mallet and O. Dubovik, “A Code to Compute the Direct Solar Radiative Forcing: Application to Anthropogenic Aerosols during the Escompte Experiment. International Radiation Symposium (IRS 2004) on Current Problems in Atmospheric Radiation,” edited by H. Fischer, B.-J. Sohn and A. Deepak, Hampton, pp. 127-130, 2006.
- [9] P. Dubuisson, V. Giraud, O. Chomette, H. Chepfer and J. Pelon, “Fast radiative transfer modeling for infrared imaging radiometry”, *Journal of Quantitative Spectroscopy & Radiative Transfer*, vol. 95(2), pp. 201-220, 2005.
- [10] D. Santos, M. J. Costa, A. M. Silva and R. Salgado “Modeling Saharan Desert Dust Radiative Effects on Clouds,” Proceedings of the global conference on Global Warming 2011, Lisbon, Portugal, 2011.
- [11] B. Marticorena and G. Bergametti, “Modeling the atmospheric dust cycle: 1. Design of a soil derived dust emission scheme”, *Journal of Geophysical Research*, vol. 100, d8, pp. 16,415-16,430, 1995.
- [12] O. Dubovik, B. Holben, T. Eck, A. Smirnov, Y. Kaufman, M. King, D. Tanré and I. Slutsker, “Variability of Absorption and Optical Properties of Key Aerosol Types Observed in Worldwide Locations”, *Journal of the Atmospheric Sciences*, vol. 59, pp. 590, 2002.
- [13] F. Volz, “Infrared optical constant of ammonium sulfate, Sahara dust, volcanic pumice, and flash”, *Applied Optics*, vol. 12, 3, 1973.
- [14] F. Volz, “Infrared optical constants of aerosols at some locations”, *Applied Optics*, vol. 22, 23, 1983.
- [15] G. d’Almeida, P. Koepke and E. Shettle, *Atmospheric aerosols: global climatology and radiative characteristics*, A Deepak Pub, 1991.
- [16] G. M. Krekov, “Models of atmospheric aerosols”. In *Aerosol Effects on Climate*, S.G. Jennings, ed., U. of Arizona Press, Tucson, Ariz., 1993
- [17] M. Hess, P. Koepke and I. Schult, “Optical Properties of Aerosols and Clouds: The Software Package OPAC”, *American Meteorological Society*, vol. 79, 5, 1998.
- [18] P. Yang, Q. Feng, G. Hong, G. W. Kattawar, W. J. Wiscombe, M. I. Mishchenko, O. Dubovik, I. Laszlo, I. N. Sokolik, “Modeling of the scattering and radiative properties of nonspheroidal dust-like aerosols”. *Aerosol Science*, vol. 38, pp. 995–1014, 2007.
- [19] Y. Fouquart, B. Bonnel, G. Brogniez, J. Buriez, L. Smith, J. Morcrette, and A. Cerf, “Observations of Saharan aerosols: Results of ECLATS field experiment. Part II: Broadband radiative characteristics of the aerosols and vertical radiative flux divergence”, *Journal of Climate Meteorology*, vol. 26, pp. 38–52, 1987.
- [20] F. Volz, “Infrared Refractive Index of Atmospheric Aerosol Substances”, *Applied Optics*, vol. 11, 4, 1972.
- [21] G. P. Gobbi, Y. J. Kaufman, I. Koren and T. F. Eck, “Classification of aerosol properties derived from AERONET direct sun data”, *Atmospheric Chemistry and Physics*, vol. 7, pp. 453–458, 2007.
- [22] S. Basart, C. Pérez, E. Cuevas, J. M. Baldasano and G. P. Gobbi, “Aerosol characterization in Northern Africa, Northeastern Atlantic, Mediterranean Basin and Middle East from direct sun AERONET observations”, *Atmospheric Chemistry and Physics*, vol. 9, pp. 8265–8282, 2009.
- [23] K. Stamnes, S. Tsay, W. Wiscombe and K. Jayaweera, “Numerically stable algorithm for discrete-ordinate-method radiative transfer in multiple scattering and emitting layered media”, *Applied Optics*, vol. 27, pp. 2502-2509, 1988.
- [24] A. Lacis and V. Oinas, “A description of the correlated k-distribution method”, *Journal of Geophysical Research*, vol. 96, pp. 9027-9064, 1991.
- [25] S. Clough, F. Kneizys and R. Davies, “Line shape and the water vapor continuum”, *Atmospheric Research*, vol. 23, pp. 229–241, 1989.
- [26] K. Wang, Z. Wan, P. Wang, M. Sparrow, J. Liu, X. Zhou, S. Haginoya, “Estimation of surface longwave radiation and broadband emissivity using Moderate Resolution Imaging Spectroradiometer (MODIS) land surface temperature/emissivity products”, *Journal of Geophysical Research*, vol. 110, d11109, doi: 10.1029/2004jd005566, 2005.
- [27] A. Papayannis, V. Amiridis, L. Mona, G. Tsaknakis, D. Balis, J. Bösenberg, A. Chaikovski, F. De Tomasi, I. Grigorov, I. Mattis, V. Mitev, D. Müller, S. Nickovic, C. Pérez, A. Pietruczuk, G. Pisani, F. Ravetta, V. Rizi, M. Sicard, T. Trickl, M. Wiegner, M. Gerding, R. E. Mamouri, G. D’Amico and G. Pappalardo, “Systematic lidar observations of Saharan dust over Europe in the frame of EARLINET (2000–2002)”, *Journal of geophysical research*, vol. 113, d10204, doi: 10.1029/2007jd009028, 2008.

